

AD-A120 426

EFFECT OF STATE OF STRESS ON VELOCITY OF LOW-AMPLITUDE  
SHEAR WAVES PROPAG. (U) TEXAS UNIV AT AUSTIN  
GEOTECHNICAL ENGINEERING CENTER D P KNOX ET AL MAR 82

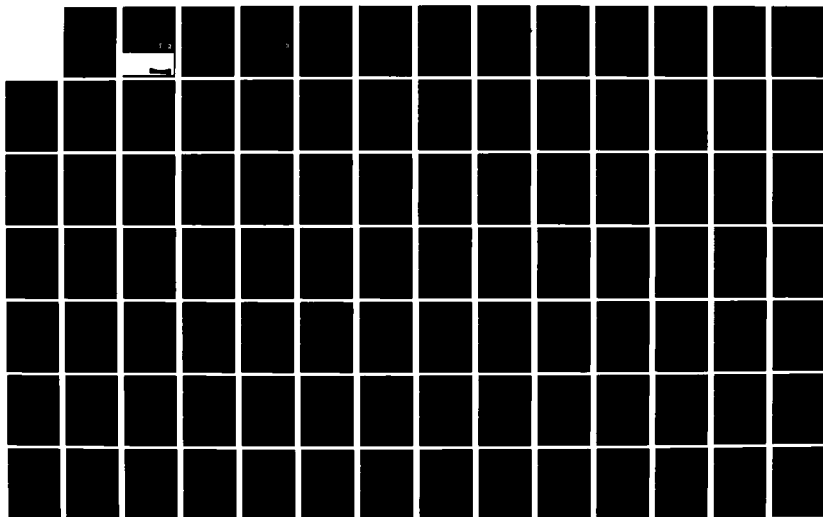
1/6

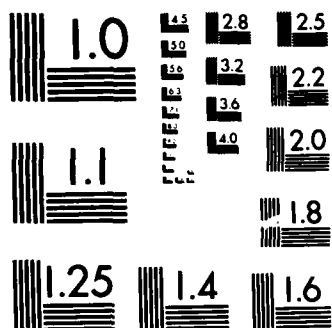
UNCLASSIFIED

GR82-23 AFOSR-TR-82-0908 AFOSR-80-0031

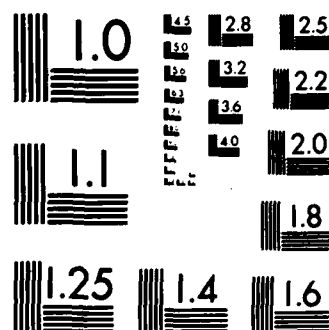
F/G 20/11

NL

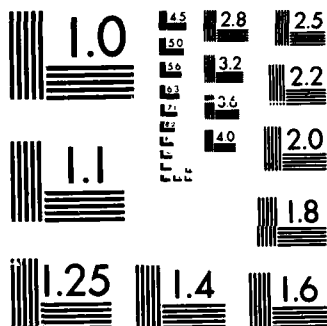




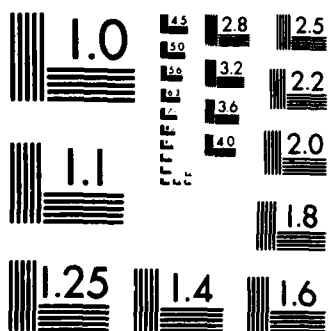
MICROCOPY RESOLUTION TEST CHART  
NATIONAL BUREAU OF STANDARDS-1963-A



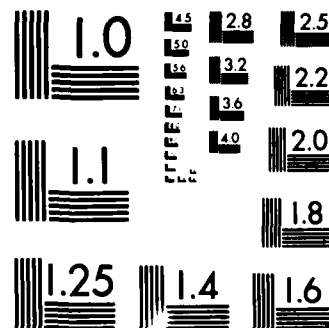
MICROCOPY RESOLUTION TEST CHART  
NATIONAL BUREAU OF STANDARDS-1963-A



MICROCOPY RESOLUTION TEST CHART  
NATIONAL BUREAU OF STANDARDS-1963-A



MICROCOPY RESOLUTION TEST CHART  
NATIONAL BUREAU OF STANDARDS-1963-A



MICROCOPY RESOLUTION TEST CHART  
NATIONAL BUREAU OF STANDARDS-1963-A

(10)

**EFFECT OF STATE OF STRESS ON VELOCITY OF  
LOW-AMPLITUDE SHEAR WAVES PROPAGATING ALONG  
PRINCIPAL STRESS DIRECTIONS IN DRY SAND**

AD A120426

D. P. Knox, K. H. Stokoe II  
and S. E. Kopperman

a report on research  
sponsored by  
United States Air Force  
Office of Scientific Research  
Bolling Air Force Base

DTIC  
SELECTED  
OCT 17 1982  
S H D

82 10 18 224

Qualified requestors may obtain additional copies from  
the Defense Technical Information Service.

### **Conditions of Reproduction**

Reproduction, translation, publication, use and disposal  
in whole or in part by or for the United States  
Government is permitted.



UNCLASSIFIED

SECURITY CLASSIFICATION OF THIS PAGE (When Data Entered)

REPORT DOCUMENTATION PAGE		READ INSTRUCTIONS BEFORE COMPLETING FORM
1. REPORT NUMBER <b>AFOSR-TR- 82-0908</b>	2. GOVT ACCESSION NO. <b>AD-A720 426</b>	3. RECIPIENT'S CATALOG NUMBER
4. TITLE (and Subtitle) EFFECT OF STATE OF STRESS ON VELOCITY OF LOW-AMPLITUDE SHEAR WAVES PROPAGATING ALONG PRINCIPAL STRESS DIRECTIONS IN DRY SAND		5. TYPE OF REPORT & PERIOD COVERED ANNUAL 1 Oct 79 - 31 Dec 81
		6. PERFORMING ORG. REPORT NUMBER
7. AUTHOR(s) DAVID P. KNOX, KENNETH H. STOKOE, II, AND STEWART E. KOPPERMAN		8. CONTRACT OR GRANT NUMBER(s) AFOSR-80-0031
9. PERFORMING ORGANIZATION NAME AND ADDRESS UNIVERSITY OF TEXAS AT AUSTIN DEPARTMENT OF CIVIL ENGINEERING AUSTIN, TX 78712		10. PROGRAM ELEMENT, PROJECT, TASK AREA & WORK UNIT NUMBERS 61102F 2307/C1
11. CONTROLLING OFFICE NAME AND ADDRESS AIR FORCE OFFICE OF SCIENTIFIC RESEARCH/NA BOLLING AFB, DC 20332		12. REPORT DATE March 1982
		13. NUMBER OF PAGES 421
14. MONITORING AGENCY NAME & ADDRESS (if different from Controlling Office)		15. SECURITY CLASS. (of this report) Unclassified
		15a. DECLASSIFICATION/DOWNGRADING SCHEDULE
16. DISTRIBUTION STATEMENT (of this Report)  Approved for Public Release; Distribution Unlimited.		
17. DISTRIBUTION STATEMENT (of the abstract entered in Block 20, if different from Report)  DTIC ELECTE OCT 19 1982		
18. SUPPLEMENTARY NOTES  H		
19. KEY WORDS (Continue on reverse side if necessary and identify by block number)  SHEAR WAVES                      TRIAXIAL TESTING                      STRUCTURAL ANISOTROPY SEISMIC VELOCITY                BIAXIAL TESTING SHEAR MODULUS                  LOW AMPLITUDE BODY WAVES DAMPING                           STRESS HISTORY		
20. ABSTRACT (Continue on reverse side if necessary and identify by block number)  The effect of state of stress on shear wave velocity was examined for shear waves propagated as body waves through a sand mass. Testing was performed in a triaxial testing device, which was designed to hold a cubic soil sample measuring 7 ft (2.1 m) on a side and which was used to apply an isotropic, biaxial or triaxial state of stress to the sample. The triaxial device is essentially a steel box, constructed of reinforced steel, which uses rubber membranes to apply a confining pressure along each of the principal axes		

EFFECT OF STATE OF STRESS ON VELOCITY OF LOW-AMPLITUDE  
COMPRESSION WAVES PROPAGATING ALONG PRINCIPAL  
STRESS DIRECTIONS IN DRY SAND

D. P. Knox, K. H. Stokoe, II,  
and S. E. Kopperman

AIR FORCE OFFICE OF SCIENTIFIC RESEARCH (AFSC)  
NOTICE OF TRANSMITTAL TO DTIC  
This technical report has been reviewed and is  
approved for public release IAW AFR 190-12.  
Distribution is unlimited.  
MATTHEW J. KERPER  
Chief, Technical Information Division

a report on research  
sponsored by  
United States Air Force  
Office of Scientific Research  
Bolling Air Force Base

March, 1982

Geotechnical Engineering Report GR82-23  
Geotechnical Engineering Center  
Civil Engineering Department  
The University of Texas at Austin  
Austin, Texas

## ACKNOWLEDGEMENTS

The authors wish to acknowledge the following people for their valuable assistance in this project:

- Dr. Jose M. Roeset, for his assistance during this project,
- geotechnical engineering graduate students at The University of Texas at Austin, especially Joseph E. Baka, J. Scott Heisey, and Juan B. Bernal, for their invaluable assistance with this project,
- Ms. Sarah C. Clark, for her unending energy in the typing of this report,
- Mr. W. Howell, for his help with the design of the triaxial cube,
- Mr. T. Rose, for his efforts in constructing the triaxial cube,
- the personnel of the Balcones Research Center of The University of Texas at Austin, especially Mr. G. Moden, Mrs. L. Golding, and Mr. G. Hinckley, for their assistance with this research, and
- the United States Air Force Office of Scientific Research (AFOSR), Bolling Air Force Base, Washington, D.C., for supporting this research under grant AFOSR 80-0031A, with Lt. Col. John J. Allen as the project manager.



Accession Per	<input checked="" type="checkbox"/> <input type="checkbox"/> <input type="checkbox"/>		
DTIC ORLAI			
DTIC T-3			
Unprocessed			
Justification			
By			
Distribution/			
Availability Codes			
Avail and/or			
Dist Special			

## ABSTRACT

The effect of state of stress on shear wave velocity was examined for shear waves propagated as body waves through a sand mass. Testing was performed in a triaxial device, which was designed to hold a cubic soil sample measuring 7 ft (2.1 m) on a side and which was used to apply an isotropic, biaxial or triaxial state of stress to the sample. The triaxial device is essentially a steel box, constructed of reinforced steel, which uses rubber membranes to apply a confining pressure along each of the principal axes of the cube. Dry sand was placed in the cube for this initial testing program.

Shear waves were propagated along the principal axes of the cube over the pressure range from 10 to 40 psi (68.9 to 276 kPa). Shear wave particle motion was monitored by three-dimensional accelerometers embedded in the sand. Stress cells and strain sensors were also embedded in the sand mass to examine stress-strain properties of the sand for the applied loading. All wave testing was performed at low-amplitude strains and at wave frequencies less than 2400 Hz. Therefore, it was assumed that the shear modulus was rate independent in this study.

Based on the results of this study, shear wave velocity was found to depend about equally on the principal stresses in the

direction of wave propagation and particle motion and was determined to be relatively independent of the principal stress in the out-of-plane direction (the direction in which no shear wave particle motion occurs). As a result, the typical procedure of relating shear wave velocity to the mean effective principal stress is not correct, since the mean effective stress involves all three of the principal stresses. Stress history was found to have no significant effect on shear wave velocity for this sand. Structural anisotropy was found to cause up to an 18 percent variation in shear wave velocity, with velocities apparently grouped according to planes of motion, the plane determined by the direction of wave propagation and particle motion.

## TABLE OF CONTENTS

	Page
ACKNOWLEDGEMENTS . . . . .	i
ABSTRACT . . . . .	ii
TABLE OF CONTENTS . . . . .	iv
LIST OF TABLES . . . . .	x
LIST OF FIGURES . . . . .	xiii
LIST OF SYMBOLS . . . . .	xxv
 CHAPTER 1. INTRODUCTION . . . . .	 1
CHAPTER 2. REVIEW OF LITERATURE . . . . .	5
2.1 INTRODUCTION . . . . .	5
2.2 TESTING DEVICES . . . . .	5
.1 Resonant Column Device . . . . .	7
.2 Piezoelectric Crystals . . . . .	8
.3 Test Chamber . . . . .	9
.4 Soil Cube . . . . .	11
.5 Cyclic Triaxial Test . . . . .	15
.6 Cyclic Simple Shear Test . . . . .	16
.7 Cyclic Torsional Shear Test . . . . .	17
.8 Cyclic Multiaxial Test Devices . . . . .	18
2.3 EFFECT OF ISOTROPIC CONFINEMENT . . . . .	19
2.4 EFFECT OF ANISOTROPIC CONFINEMENT . . . . .	27
.1 Lawrence (1965) . . . . .	28
.2 Hardin and Black (1966) . . . . .	30
.3 Schmertmann (1978) . . . . .	33
.4 Hardin (1978) . . . . .	36
.5 Roelser (1979) . . . . .	37
2.5 SUMMARY . . . . .	41

	Page
CHAPTER 3. SUMMARY OF TRIAXIAL TESTING DEVICE . . . . .	43
3.1 INTRODUCTION . . . . .	43
3.2 STRUCTURE OF THE CUBE . . . . .	43
3.3 LOADING SYSTEM . . . . .	45
3.4 EXCITATION SYSTEM . . . . .	47
3.5 MONITORING AND RECORDING SYSTEM . . . . .	48
3.6 STRESS MEASUREMENT . . . . .	49
3.7 STRAIN MEASUREMENT . . . . .	49
3.8 TEST SAMPLE . . . . .	50
3.9 SUMMARY . . . . .	52
CHAPTER 4. ENGINEERING PROPERTIES OF SAND . . . . .	53
4.1 INTRODUCTION . . . . .	53
4.2 SAND CLASSIFICATION . . . . .	53
4.3 DRAINED SHEARING STRENGTH . . . . .	56
4.4 ISOTROPIC DYNAMIC TESTING . . . . .	59
.1 Low-Amplitude Dynamic Properties . . . . .	60
.2 Intermediate-Amplitude Dynamic Properties . . . . .	66
4.5 SUMMARY . . . . .	67
CHAPTER 5. SUMMARY OF TESTING PROGRAMD AND PROCEDURES . . . . .	72
5.1 INTRODUCTION . . . . .	72
5.2 TESTING PROGRAM . . . . .	72
5.3 TESTING PROCEDURES . . . . .	73
5.4 SUMMARY . . . . .	78

	Page
CHAPTER 6. ISOTROPIC CONFINEMENT . . . . .	79
6.1 INTRODUCTION . . . . .	79
6.2 SIMPLIFIED CONDITION OF ISOTROPIC CONFINEMENT . . . . .	79
6.3 DESCRIPTION OF SHEAR WAVES . . . . .	82
.1 Nomenclature . . . . .	83
.2 Shear Wave Records . . . . .	85
.3 Shear Wave Data Reduction . . . . .	90
6.4 ANALYSIS OF SHEAR WAVE VELOCITIES . . . . .	91
.1 Comparison of Direct and Interval Velocities . . . . .	91
.2 Short and Long Intervals . . . . .	95
6.5 EFFECT OF STRESS HISTORY . . . . .	102
6.6 EFFECT OF ISOTROPIC CONFINING PRESSURE . . . . .	103
6.7 STRUCTURAL ANISOTROPY . . . . .	116
6.8 SHEAR WAVE CHARACTERISTICS . . . . .	123
.1 Predominant Frequency . . . . .	123
.2 Wavelength . . . . .	124
.3 Shearing Strain Amplitude . . . . .	125
6.9 SUMMARY AND CONCLUSIONS . . . . .	127
CHAPTER 7. BIAXIAL CONFINEMENT . . . . .	130
7.1 INTRODUCTION . . . . .	130
7.2 BIAXIAL STATES OF STRESS . . . . .	130
.1 Notation of Stress Components . . . . .	131
.2 Patterns of Stress Variation . . . . .	135
.3 Review of Simplifications and Data Analysis . . . . .	137



	Page
7.3 TESTING WITH A VARIABLE MEAN EFFECTIVE PRINCIPAL STRESS . . . . .	138
.1 Effect of Each Stress Component on $V_s$ .	140
.2 Effect of Principal Stress in Direction of Wave Propagation . . . . .	141
.3 Effect of Principal Stress in Direction of Particle Motion . . . . .	144
.4 Effect of Principal Stress in the Out-of-Plane Direction . . . . .	150
.5 Summary of Effect of Principal Stresses on $V_s$ . . . . .	154
.6 Comparison Between Measured and Predicted Shear Wave Velocities .	160
.7 Effect of Principal Stresses on Shear Modulus . . . . .	161
7.4 STRUCTURAL ANISOTROPY . . . . .	170
7.5 TESTING WITH A CONSTANT MEAN EFFECTIVE PRINCIPAL STRESS . . . . .	172
.1 Effect of Shearing Stress with Constant $\bar{\sigma}_o$ . . . . .	175
.2 Comparison <sup>o</sup> Between Measured and Predicted Shear Wave Velocities . . . .	188
7.6 SUMMARY AND CONCLUSIONS . . . . .	189
CHAPTER 8. TRIAXIAL CONFINEMENT . . . . .	199
8.1 INTRODUCTION . . . . .	199
8.2 TRIAXIAL STATES OF STRESS . . . . .	200
.1 Notation of Stress Components . . . . .	200
.2 Patterns of Stress Variation . . . . .	201
.3 Review of Simplifications and Data Analysis . . . . .	201
.4 Principal Stress Ratio . . . . .	203
8.3 TESTING WITH A VARIABLE MEAN EFFECTIVE PRINCIPAL STRESS . . . . .	204
.1 Effect of Each Stress Component on $V_s$ .	205
.2 Effect of Principal Stress in Direction of Wave Propagation . . . . .	207

	Page
.3 Effect of Principal Stress in Direction of Particle Motion . . . . .	211
.4 Effect of Principal Stress in the Out-of-Plane Direction . . . . .	218
.5 Summary of Effect of Principal Stresses on $V_s$ . . . . .	222
.6 Comparison of $\sigma_s$ Stress Component Relationships for Isotropic, Biaxial, and Triaxial Confinement . . . . .	225
.7 Effect of Principal Stresses on Shear Modulus . . . . .	227
8.4 STRUCTURAL ANISOTROPY . . . . .	231
8.5 TESTING WITH A CONSTANT MEAN EFFECTIVE PRINCIPAL STRESS . . . . .	232
.1 Effect of Shearing Stress with Constant $\sigma_o$ . . . . .	233
.2 Comparison Between Measured and Predicted Shear Wave Velocities . . . . .	249
8.6 SUMMARY AND CONCLUSIONS . . . . .	250
CHAPTER 9. RE-EXAMINATION OF RESULTS FROM PREVIOUS EXPERIMENTS . . . . .	257
9.1 INTRODUCTION . . . . .	257
9.2 REVIEW OF PREVIOUS EXPERIMENTS . . . . .	258
9.3 SUMMARY OF EFFECT OF STRESS COMPONENTS ON $V_s$ . . . . .	260
9.4 VARIATION OF $V_s$ WITH DOMINANT STRESS COMPONENTS . . . . .	262
9.5 SUMMARY AND CONCLUSIONS . . . . .	267
CHAPTER 10. SUMMARY, CONCLUSIONS AND RECOMMENDATIONS FOR FUTURE WORK . . . . .	268
10.1 SUMMARY AND CONCLUSIONS . . . . .	268
.1 Triaxial Testing Device . . . . .	268
.2 Stress-Strain Measurements . . . . .	270
.3 Effect of State of Stress on $V_s$ . . . . .	271
.4 Importance to Laboratory and Field Testing . . . . .	275

	Page
10.2 RECOMMENDATIONS FOR FUTURE WORK . . . . .	275
APPENDIX A. TRIAXIAL TESTING DEVICE . . . . .	279
APPENDIX B. TESTING PROGRAM AND PROCEDURES . . . . .	332
APPENDIX C. SET OF RECORDED WAVEFORMS, DATA INPUT, AND COMPUTER OUTPUT FOR A REPRESENTATIVE ISOTROPIC TEST . . . . .	381
APPENDIX D. SET OF RECORDED WAVEFORMS, DATA INPUT, AND COMPUTER OUTPUT FOR A REPRESENTATIVE BIAXIAL TEST . . . . .	393
APPENDIX E. SET OF RECORDED WAVEFORMS, DATA INPUT, AND COMPUTER OUTPUT FOR A REPRESENTATIVE TRIAXIAL TEST . . . . .	405
REFERENCES . . . . .	417

## LIST OF TABLES

Table		Page
2.1	Parameters Affecting Shear Modulus of Sands for Complete Stress Reversal (after Hardin and Drnevich, 1970) . . . . .	22
2.2	Summary of Values Presented in the Literature for the Slope of the $\log V_s - \log \bar{\sigma}_o$ or $\log V_p - \log \bar{\sigma}_o$ Relationship . . . . .	24
2.3	Effect of Stress Ratio on Shear Wave Velocity at a Mean Effective Principal Stress of 10 psi (69 kPa) (from Schmertmann, 1978) . . . . .	35
2.4	Effect of Stress Ratio on Compression Wave Velocity at a Mean Effective Principal Stress of 10 psi (69 kPa) (from Schmertmann, 1978) . . . .	35
6.1	Nomenclature Used to Identify the Six Different Shear Waves . . . . .	84
6.2	Comparison of $\log V_s - \log \bar{\sigma}_o$ Relationship Determined from Short and Long Intervals for Isotropic Confinement . . . . .	98
6.3	Values of Constants $C_1$ and $m$ from Eq. 6.1 for the Six Different Shear Waves . . . . .	109
6.4	Values for the Six Different Shear Waves of Constant, $C$ , and Slope, $n$ , from Eq. 6.4 . . . . .	115
6.5	Values for the Three Shear Wave Groups of Constants and Slopes of Eqs. 6.1 and 6.4 . . . . .	122
7.1	Stress Components for the Six Different Shear Waves for One State of Biaxial Confinement . . . . .	134
7.2	Variation of Stress Components for Biaxial Test Series . . . . .	136
7.3	Effect on $V_s$ of Principal Stress in Direction of Wave Propagation for Biaxial Confinement . . . .	146

Table		Page
7.4	Effect on $V_s$ of Principal Stress in Direction of Particle <sup>s</sup> Motion for Biaxial Confinement . . . .	151
7.5	Effect on $V_s$ of Principal Stress in Out-of-Plane Direction for Biaxial Confinement . . . . .	155
7.6	Summary of Effects on $V_s$ of Orientation of Principal Stresses Relative to Planes of Motion for Biaxial Confinement . . . . .	157
7.7	Comparison of the Effect of Principal Stresses on Shear Wave Velocity for Isotropic and Biaxial Confinement States . . . . .	159
7.8	Effect on $G_{max}$ of Orientation of Principal Stresses Relative to Planes of Motion Associated with the Shear Wave . . . . .	169
7.9	Variation of Shear Wave Velocity with Shearing Stress for Tests Performed with a Constant $\bar{\sigma}_o$ for Biaxial Confinement . . . . .	180
7.10	Effect on $V_s$ of Principal Stresses in Directions of Wave Propagation and Particle Motion . . . . .	187
8.1	Variation of Stress Components for Triaxial Test Series . . . . .	202
8.2	Effect on $V_s$ of Principal Stress in Direction of Wave Propagation for Triaxial Confinement . . .	212
8.3	Effect on $V_s$ of Principal Stress in Direction of Particle <sup>s</sup> Motion for Triaxial Confinement . . .	217
8.4	Effect on $V_s$ of Principal Stress in Out-of-Plane Direction for Triaxial Confinement . . . . .	221
8.5	Summary of Effects on $V_s$ of Orientation of Principal Stresses Relative to Planes of Motion for Triaxial Confinement . . . . .	223
8.6	Comparison of Average Effect of Principal Stress Orientation on Shear Wave Velocity for Isotropic, Biaxial, and Triaxial Confinements . . . . .	226

Table		Page
8.7	Comparison of Influence on $V_s$ of Orientation of Principal Stresses Relative to Planes of Shear Wave Motions for Biaxial and Triaxial Confinements . . . . .	228
8.8	Influence on $G_{max}$ of Orientation of Principal Stresses Relative to Planes of Shear Wave Motions . . . . .	230
8.9	Variation of Shear Wave Velocity with Shearing Stress for Tests Performed with a Constant $\bar{\sigma}_o$ for Triaxial Confinement . . . . .	241
8.10	Variation of $V_s$ with Principal Stresses in Directions of Wave Propagation and Particle Motion for Triaxial Confinement . . . . .	248
9.1	Influence on Shear Wave Velocity of Orientation of Principal Stresses from Data Presented by Lawrence (1965), Hardin and Black (1966) and Roesler (1979) . . . . .	261
9.2	Variation of Shear Wave Velocity with Directions of Wave Propagation and Particle Motion for Data Presented by Lawrence (1965), Hardin and Black (1966) and Roesler (1979) . . . . .	266
10.1	Summary of Values of Constants Determined for Eqs. 10.1 and 10.2 for Each Plane of Motion for Isotropic, Biaxial, and Triaxial States of Stress.	274
B.1	Pressure Loading Sequences . . . . .	334
B.2	Densities and Void Ratios of Sand at Various Elevations in the Cube . . . . .	354
B.3	Source-Accelerometer Distances Determined After Placement . . . . .	359

## LIST OF FIGURES

Figure		Page
2.1	Triaxial Cell Converted for Shear Wave Velocity Measurements by Lawrence (1965) . . . . .	10
2.2	Schematic of Test Chamber Used by Schmertmann (1978) . . . . .	12
2.3	Accelerometer Pattern in Plane Through Axis of Test Chamber Used by Schmertmann (1978) . . . . .	12
2.4	Cubical Sand Sample with Shear Wave Exciter and Transducers Used by Roesler (1979) . . . . .	14
2.5	Principles of Shear Wave Exciter Used by Roesler (1979) . . . . .	14
2.6	Exploded View of Multiaxial Test Cell Patterned After Cell Used by Ko et al (from Berends, 1974) .	20
2.7	Influence of Shear Stress on Shear Wave Velocity in Ottawa Sand (from Lawrence, 1965) . . . . .	29
2.8	Results of Shear Wave Velocity Tests Replotted from Fig. 2.7 (from Lawrence, 1965) . . . . .	31
2.9	Variation of Shear Wave Velocity with Principal Stress in (a) Direction of Wave Propagation, (b) Direction of Particle Motion, and (c) Out-of-Plane Direction (from Roesler, 1979) . . . . .	39
4.1	Grain Size Analysis of Washed Mortar Sand . . . . .	54
4.2	Failure Envelopes for Loose and Dense Sand Samples from Consolidated, Drained Triaxial Tests.	58
4.3	Variation in Low-Amplitude Shear Modulus with Effective Confining Pressure . . . . .	62
4.4	Variation in Low-Amplitude Shear Wave Velocity with Effective Confining Pressure . . . . .	64

Figure		Page
4.5	Variation in Low-Amplitude Material Damping Ratio with Effective Confining Pressure . . . . .	65
4.6	Variation in Shear Modulus with Shearing Strain .	68
4.7	Variation in Material Damping with Shearing Strain . . . . .	69
6.1	Typical Shear Wave Record Using Reversed Impulses to Aid in Identification of Initial Shear Wave Arrival . . . . .	86
6.2	Typical Set of Shear Wave Data from Recording All Three Accelerometers Along One Axis of the Cube . . . . .	87
6.3	Illustration of the Two Extremes in Quality of Shear Wave Records . . . . .	89
6.4	Comparison of $\log V_s - \log \bar{\sigma}_0$ Relationship Based on Direct and $s$ Interval Velocities for Isotropic Tests . . . . .	93
6.5	Comparison of $\log V_s - \log \bar{\sigma}_0$ Relationship Based on Short- and $s$ Long-Interval Velocities . . .	96
6.6	Stress History Effect on Shear Wave Velocity for Isotropic Confinement . . . . .	104
6.7	Variation of Shear Wave Velocity with Mean Effective Principal Stress for Propagation in Top-Bottom Direction . . . . .	105
6.8	Variation of Shear Wave Velocity with Mean Effective Principal Stress for Propagation in North-South Direction . . . . .	106
6.9	Variation of Shear Wave Velocity with Mean Effective Principal Stress for Propagation in East-West Direction . . . . .	107
6.10	Variation of Average Shear Wave Velocity for Each Shear Wave with Isotropic Confinement . . .	112
6.11	General Least-Square Fit of All Shear Wave Velocities Determined Under Isotropic Confinement.	113



Figure		Page
6.12	Planes of Motion for Shear Wave Exhibiting Similar $\log V_s - \log \bar{\sigma}_0$ Relationships . . . . .	118
6.13	Variation of Shear Wave Velocity with Mean Effective Principal Stress for Waves in the TB-EW Plane . . . . .	119
6.14	Variation of Shear Wave Velocity with Mean Effective Principal Stress for Waves in the TB-NS Plane . . . . .	120
6.15	Variation of Shear Wave Velocity with Mean Effective Principal Stress for Waves in the EW-NS Plane . . . . .	121
6.16	Recorded Waveforms Showing Reflected Shear Wave (R) Returning to Third Accelerometer After Initially Generated Shear Wave is Fully Recorded .	126
7.1	Illustration of Notation Used to Describe Directions of Effective Principal Stresses Relative to Shear Wave Motions . . . . .	133
7.2	Variation of Shear Wave Velocity with Principal Stress in Direction of Wave Propagation for TB-NS Plane of Motion for Biaxial Confinement . .	142
7.3	Variation of Shear Wave Velocity with Principal Stress in Direction of Wave Propagation for TB-EW Plane of Motion for Biaxial Confinement . .	143
7.4	Variation of Shear Wave Velocity with Principal Stress in Direction of Wave Propagation for NS-EW and NS-TB Planes of Motion for Biaxial Confinement . . . . .	145
7.5	Variation of Shear Wave Velocity with Principal Stress in Direction of Particle Motion for TB-NS Plane of Motion for Biaxial Confinement . . . . .	147
7.6	Variation of Shear Wave Velocity with Principal Stress in Direction of Particle Motion for TB-EW Plane of Motion for Biaxial Confinement . . . . .	148
7.7	Variation of Shear Wave Velocity with Principal Stress in Direction of Particle Motion for TB-NS and EW-NS Planes of Motion for Biaxial Confinement	149

Figure		Page
7.8	Variation of Shear Wave Velocity with Principal Stress in Out-of-Plane Direction for NS-EW Plane of Motion for Biaxial Confinement . . . . .	152
7.9	Variation of Shear Wave Velocity with Principal Stress in Out-of-Plane Direction for TB-EW Plane of Motion for Biaxial Confinement . . . . .	153
7.10	Comparison of Measured and Predicted Shear Wave Velocities for $\frac{S_{TB}}{\sigma_o}$ -Wave for Biaxial Confinement with a Varying $\sigma_o$ . . . . .	162
7.11	Comparison of Measured and Predicted Shear Wave Velocities for $\frac{S_{TB}}{\sigma_o}$ -Wave for Biaxial Confinement with a Varying $\sigma_o$ . . . . .	163
7.12	Comparison of Measured and Predicted Shear Wave Velocities for $\frac{S_{NS}}{\sigma_o}$ -Wave for Biaxial Confinement with a Varying $\sigma_o$ . . . . .	164
7.13	Comparison of Measured and Predicted Shear Wave Velocities for $\frac{S_{NS}}{\sigma_o}$ -Wave for Biaxial Confinement with a Varying $\sigma_o$ . . . . .	165
7.14	Comparison of Measured and Predicted Shear Wave Velocities for $\frac{S_{EW}}{\sigma_o}$ -Wave for Biaxial Confinement with a Varying $\sigma_o$ . . . . .	166
7.15	Comparison of Measured and Predicted Shear Wave Velocities for $\frac{S_{EW}}{\sigma_o}$ -Wave for Biaxial Confinement with a Varying $\sigma_o$ . . . . .	167
7.16	Variation of Shearing Stress and Principal Stress Ratio for the Biaxial Test Series with a Constant Mean Effective Principal Stress . . . . .	174
7.17	Variation of Shear Wave Velocity with Principal Stress Ratio for TB-NS Plane of Motion for Biaxial Confinement . . . . .	176
7.18	Variation of Shear Wave Velocity with Principal Stress Ratio for TB-EW Plane of Motion for Biaxial Confinement . . . . .	177

Figure		Page
7.19	Variation of Shear Wave Velocity with Principal Stress Ratio for NS-EW Plane of Motion for Biaxial Confinement . . . . .	178
7.20	Variation of Shear Wave Velocity with Directions of Wave Propagation and Particle Motion for TB-NS Plane of Motion for Biaxial Confinement with a Constant $\bar{\sigma}_0$ . . . . .	184
7.21	Variation of Shear Wave Velocity with Directions of Wave Propagation and Particle Motion for TB-EW Plane of Motion for Biaxial Confinement with a Constant $\bar{\sigma}_0$ . . . . .	185
7.22	Variation of Shear Wave Velocity with Directions of Wave Propagation and Particle Motion for NS-EW Plane of Motion for Biaxial Confinement with a Constant $\bar{\sigma}_0$ . . . . .	186
7.23	Comparison of Measured and Predicted Shear Wave Velocities for $S_{TB/NS}$ -Wave for Biaxial Confinement with a Constant $\bar{\sigma}_0$ . . . . .	190
7.24	Comparison of Measured and Predicted Shear Wave Velocities for $S_{TB/EW}$ -Wave for Biaxial Confinement with a Constant $\bar{\sigma}_0$ . . . . .	191
7.25	Comparison of Measured and Predicted Shear Wave Velocities for $S_{NS/TB}$ -Wave for Biaxial Confinement with a Constant $\bar{\sigma}_0$ . . . . .	192
7.26	Comparison of Measured and Predicted Shear Wave Velocities for $S_{NS/EW}$ -Wave for Biaxial Confinement with a Constant $\bar{\sigma}_0$ . . . . .	193
7.27	Comparison of Measured and Predicted Shear Wave Velocities for $S_{EW/TB}$ -Wave for Biaxial Confinement with a Constant $\bar{\sigma}_0$ . . . . .	194
7.28	Comparison of Measured and Predicted Shear Wave Velocities for $S_{EW/NS}$ -Wave for Biaxial Confinement with a Constant $\bar{\sigma}_0$ . . . . .	195
8.1	Variation of Shear Wave Velocity with Principal Stress in Direction of Wave Propagation for NS-TB Plane of Motion for Triaxial Confinement . . . . .	208

Figure		Page
8.2	Variation of Shear Wave Velocity with Principal Stress in Direction of Wave Propagation for NS-EW Plane of Motion for Triaxial Confinement . . . . .	209
8.3	Variation of Shear Wave Velocity with Principal Stress in Direction of Wave Propagation for TB-NS and TB-EW Planes of Motion for Triaxial Confinement . . . . .	210
8.4	Variation of Shear Wave Velocity with Principal Stress in Direction of Particle Motion for TB-NS Plane of Motion for Triaxial Confinement . . . . .	213
8.5	Variation of Shear Wave Velocity with Principal Stress in Direction of Particle Motion for EW-NS Plane of Motion for Triaxial Confinement . . . . .	214
8.6	Variation of Shear Wave Velocity with Principal Stress in Direction of Particle Motion for TB-NS and TB-EW Planes of Motion for Triaxial Confinement . . . . .	216
8.7	Variation of Shear Wave Velocity with Principal Stress in Out-of-Plane Direction for TB-EW Plane of Motion for Triaxial Confinement . . . . .	219
8.8	Variation of Shear Wave Velocity with Principal Stress in Out-of-Plane Direction for NS-EW Plane of Motion for Triaxial Confinement . . . . .	220
8.9	Variation of Shear Wave Velocity with Principal Stress Ratios $K_{13}$ and $K_{23}$ for $S_{TB/NS}$ -Wave for Triaxial Confinement with a Constant $\bar{\sigma}_0$ . . . . .	234
8.10	Variation of Shear Wave Velocity with Principal Stress Ratios $K_{13}$ and $K_{23}$ for $S_{TB/EW}$ -Wave for Triaxial Confinement with a Constant $\bar{\sigma}_0$ . . . . .	235
8.11	Variation of Shear Wave Velocity with Principal Stress Ratios $K_{13}$ and $K_{23}$ for $S_{NS/TB}$ -Wave for Triaxial Confinement with a Constant $\bar{\sigma}_0$ . . . . .	236
8.12	Variation of Shear Wave Velocity with Principal Stress Ratios $K_{13}$ and $K_{23}$ for $S_{NS/EW}$ -Wave for Triaxial Confinement with a Constant $\bar{\sigma}_0$ . . . . .	237

Figure		Page
8.13	Variation of Shear Wave Velocity with Principal Stress Ratios $K_{13}$ and $K_{23}$ for $S_{EW/TB}$ -Wave for Triaxial Confinement with a Constant $\bar{\sigma}_0$ . . . . .	238
8.14	Variation of Shear Wave Velocity with Principal Stress Ratios $K_{13}$ and $K_{23}$ for $S_{EW/NS}$ -Wave for Triaxial Confinement with a Constant $\bar{\sigma}_0$ . . . . .	239
8.15	Variation of Shear Wave Velocity with Directions of Wave Propagation and Particle Motion for TB-NS Plane of Motion for Triaxial Confinement with a Constant $\bar{\sigma}_0$ . . . . .	244
8.16	Variation of Shear Wave Velocity with Directions of Wave Propagation and Particle Motion for TB-EW Plane of Motion for Triaxial Confinement with a Constant $\bar{\sigma}_0$ . . . . .	245
8.17	Variation of Shear Wave Velocity with Directions of Wave Propagation and Particle Motion for NS-EW Plane of Motion for Triaxial Confinement with a Constant $\bar{\sigma}_0$ . . . . .	246
8.18	Comparison of Measured and predicted Shear Wave Velocities for TB-NS Plane of Motion for Triaxial Confinement with a Constant $\bar{\sigma}_0$ . . . . .	251
8.19	Comparison of Measured and Predicted Shear Wave Velocities for TB-EW Plane of Motion for Triaxial Confinement with a Constant $\bar{\sigma}_0$ . . . . .	252
8.20	Comparison of Measured and Predicted Shear Wave Velocities for NS-EW Plane of Motion for Triaxial Confinement with a Constant $\bar{\sigma}_0$ . . . . .	253
9.1	Variation of Shear Wave Velocity with Directions of Wave Propagation and Particle Motion Based on Data Presented by Lawrence (1965) . . . . .	263
9.2	Variation of Shear Wave Velocity with Directions of Wave Propagation and Particle Motion Based on Data Presented by Hardin and Black (1966) . . . . .	264
9.3	Variation of Shear Wave Velocity with Directions of Wave Propagation and Particle Motion Based on Data Presented by Roesler (1979) . . . . .	265

Figure		Page
A.1	Schematic Diagram of Model Cube and Associated Systems . . . . .	281
A.2	Cut-Away, Isometric View of Triaxial Cube Showing Top Reinforcement Details . . . . .	284
A.3	Cross-Sectional View Along Central Vertical Plane in Triaxial Cube . . . . .	285
A.4	Cross-Sectional View Along Central Horizontal Plane in Triaxial Cube . . . . .	288
A.5	Isometric View of Triaxial Cube Showing Side Reinforcement Details . . . . .	289
A.6	Sand Filling Operation in Progress with Wood Scaffolding in Place . . . . .	292
A.7	Completed Cube Structure . . . . .	293
A.8	Exploded View of Triaxial Cube . . . . .	295
A.9	Construction of First-Design Membranes . . . . .	299
A.10	Membrane Used to Apply Load to Sand Sample in Cube	304
A.11	Schematic of Air/Water System Used to Pressurize the Membranes . . . . .	306
A.12	Panel Board Used to Pressurize Membranes in Cube .	307
A.13	Excitation Hammer in Each Port of Triaxial Cube .	309
A.14	Close-up View of Excitation Port Without Impulse Hammer . . . . .	310
A.15	Typical Travel Time Records for Surface Source and Embedded Receivers . . . . .	313
A.16	Schematic of Monitoring and Recording Systems . .	315
A.17	Isometric View of 3-D accelerometer Package. . . .	316
A.18	Three-Dimensional Accelerometer Block with Accelerometers Installed . . . . .	317

Figure		Page
A.19	Accelerometer Being Placed into a 3-D Accelerometer Block . . . . .	319
A.20	Accelerometer Orientation in 3-D Packages Relative to Impulse of Source . . . . .	321
A.21	Soil Stress Cell and Control Unit (from Terra Technology literature) . . . . .	323
A.22	Typical 2-in. Diameter Soil Strain Gage . . . . .	325
A.23	Original Sand Placement System . . . . .	329
B.1	Variation in Confining Pressure Along Each Axis of the Cube with Time . . . . .	338
B.2	Mohr-Coulomb Envelope for Biaxial Confinement with Constant Mean Effective Principal Stress . . . . .	340
B.3	Mohr-Coulomb Envelope for a Typical Test under Triaxial Confinement . . . . .	342
B.4	Rubber Membranes Being Attached to the North and West Faces of the Cube . . . . .	346
B.5	Layer of Oil Being Applied to Plastic Sheet on West Face of Cube . . . . .	347
B.6	Sand Being Air-Dried in Outdoor Storage Bin . . . . .	350
B.7	Location of Density Measurements Taken During Filling of Cube . . . . .	352
B.8	Location of Stress and Strain Measuring Devices in Cube When Looking West Through the Cube . . . . .	356
B.9	Horizontal Location of Stresses and Strain Measuring Devices at Mid-Height of Cube . . . . .	357
B.10	Personnel Cage Used in Placement of Electronics into Sand During Filling Operation . . . . .	360
B.11	Placement of Total Stress Cells When the Cube Was Half Filled . . . . .	361

Figure		Page
B.12	Total Stress Cell for Vertical Stress Measurement Placed on Sand Surface During Building of Sample .	362
B.13	Total Stress Cell for Horizontal Stress Measurement Placed on Sand Surface During Building of Sample . . . . .	363
B.14	Wires from Stress Cells Fed Through East Wall of Cube . . . . .	364
B.15	Placement of Strain Sensors When the Cube was Partially Filled . . . . .	367
B.16	Horizontal Strain Sensors Placed in the Sand During the Building of the Sample . . . . .	368
B.17	Sand Surface upon Completion of Building of the Sample . . . . .	371
B.18	Stress-Strain Curves for Each Axis of the Cube Based on Strain Gages . . . . .	374
B.19	Stress-Strain Curves for Each Axis of the Cube Based on Water Flowing Into and Out of Membranes .	376
B.20	Stress Cell Reading versus Pressure Determined by Panel Board Gage for Each Axis of the Cube . . . .	378
C.1	Accelerometer Records of $S_{TB/NS}$ -Wave for Sample Isotropic Data . . . . .	382
C.2	Accelerometer Records of $S_{TB/EW}$ -Wave for Sample Isotropic Data . . . . .	383
C.3	Accelerometer Records of $S_{NS/TB}$ -Wave for Sample Isotropic Data . . . . .	384
C.4	Accelerometer Records of $S_{NS/EW}$ -Wave for Sample Isotropic Data . . . . .	385
C.5	Accelerometer Records of $S_{EW/TB}$ -Wave for Sample Isotropic Data . . . . .	386
C.6	Accelerometer Records of $S_{EW/NS}$ -Wave for Sample Isotropic Data . . . . .	387



Figure		Page
C.7	Data Input of All Shear Wave Types for Sample Isotropic Data . . . . .	388
C.8	Computer Output of All Shear Wave Types for Sample Isotropic Data . . . . .	390
D.1	Accelerometer Records of $S_{TB/NS}$ -Wave for Sample Biaxial Data . . . . .	394
D.2	Accelerometer Records of $S_{TB/EW}$ -Wave for Sample Biaxial Data . . . . .	395
D.3	Accelerometer Records of $S_{NS/TB}$ -Wave for Sample Biaxial Data . . . . .	396
D.4	Accelerometer Records of $S_{NS/EW}$ -Wave for Sample Biaxial Data . . . . .	397
D.5	Accelerometer Records of $S_{EW/TB}$ -Wave for Sample Biaxial Data . . . . .	398
D.6	Accelerometer Records of $S_{EW/NS}$ -Wave for Sample Biaxial Data . . . . .	399
D.7	Data Input of All Shear Wave Types for Sample Biaxial Data . . . . .	400
D.8	Computer Output of All Shear Waves for Sample Biaxial Data . . . . .	402
E.1	Accelerometer Records of $S_{TB/NS}$ -Wave for Sample Triaxial Data . . . . .	406
E.2	Accelerometer Records of $S_{TB/EW}$ -Wave for Sample Triaxial Data . . . . .	407
E.3	Accelerometer Records of $S_{NS/TB}$ -Wave for Sample Triaxial Data . . . . .	408
E.4	Accelerometer Records of $S_{NS/EW}$ -Wave for Sample Triaxial Data . . . . .	409
E.5	Accelerometer Records of $S_{EW/TB}$ -Wave for Sample Triaxial Data . . . . .	410
E.6	Accelerometer Records of $S_{EW/NS}$ -Wave for Sample Triaxial Data . . . . .	411

Figure		Page
E.7	Data Input of All Shear Wave Types for Sample Triaxial Data . . . . .	412
E.8	Computer Output of All Shear Wave Types for Sample Triaxial Data . . . . .	414

## LIST OF SYMBOLS

A	= peak particle (or strain) amplitude
A	= constant
A <sub>1</sub>	= amplitude of accelerometer record
A <sub>2</sub>	= double amplitude of accelerometer record
B	= dynamic bulk modulus
$\bar{C}$	= apparent effective cohesion
C	= dimensionless constant
C	= grain characteristics, grain shape, grain size, grading, minerology
C <sub>1</sub>	= constant
Cu	= coefficient of uniformity
d	= distance
dia	= diameter
D	= material damping ratio
D <sub>10</sub>	= effective grain size
e	= void ratio
E	= Young's Modulus
F(e)	= $0.3 + 0.7e^2$
f	= wave frequency
f <sub>n</sub>	= natural frequency
g	= acceleration of gravity

- $G$  = shear modulus  
 $G_{ij}$  = elastic shear modulus in  $ij$  plane  
 $G_{\max}$  = low-amplitude shear modulus  
 $G_s$  = specific gravity of solid particles  
 $h$  = height from water elevation in panel board accumulator  
to top of cube  
 $H$  = ambient stress history  
 $ID$  = inside diameter  
 $k$  = factor based on plasticity index  
 $K_o$  = lateral pressure coefficient for at-rest conditions  
 $K_{13}$  = principal stress ratio, defined as  $\bar{\sigma}_1/\bar{\sigma}_3$   
 $K_{23}$  = principal stress ratio, defined as  $\bar{\sigma}_2/\bar{\sigma}_3$   
 $m$  = slope of  $\log V_s - \log \bar{\sigma}_o$  relationship  
 $ma$  = slope of  $\log V_s - \log \bar{\sigma}_a$  relationship  
 $\max$  = maximum value  
 $mb$  = slope of  $\log V_s - \log \bar{\sigma}_b$  relationship  
 $mc$  = slope of  $\log V_s - \log \bar{\sigma}_c$  relationship  
 $\min$  = minimum value  
 $n$  = slope of  $\log G_{\max} - \log \bar{\sigma}_o$  relationship  
 $na$  = slope of  $\log G_{\max} - \log \bar{\sigma}_a$  relationship  
 $nb$  = slope of  $\log G_{\max} - \log \bar{\sigma}_b$  relationship  
 $nc$  = slope of  $\log G_{\max} - \log \bar{\sigma}_c$  relationship  
 $NS-EW$  = plane of motion defined by north-south and east-west  
directions of the cube  
 $OCR$  = overconsolidation ratio

$P_a$	= atmospheric pressure
$P_c$	= actual pressure at center of cube
$P_G$	= pressure read on gage in panel board
PI	= Plasticity Index of a soil
R	= over-registration ratio
SD	= standard deviation
$S_{ij}$	= dimensionless elastic shear stiffness parameter
$S_r$	= degree of saturation
$S_s$	= soil structure
$S_{EW/NS}$	= shear wave with wave propagation in the east-west direction and particle motion in the north-south direction
$S_{EW/TB}$	= shear wave with wave propagation in the east-west direction and particle motion in the top-bottom direction
$S_{NS/EW}$	= shear wave with wave propagation in the north-south direction and particle motion in the east-west direction
$S_{NS/TB}$	= shear wave with wave propagation in the north-south direction and particle motion in the top-bottom direction
$S_{TB/EW}$	= shear wave with wave propagation in the top-bottom direction and particle motion in the east-west direction
$S_{TB/NS}$	= shear wave with wave propagation in the top-bottom direction and particle motion in the north-south direction
t	= the sum of ( $m_a + m_b + m_c$ )
t	= secondary effects that are functions of time
t	= travel time
$t_1$	= time of initial arrival

- $t_2$  = time of arrival of first trough  
 $t_3$  = time of arrival of first peak  
 $T$  = period  
 $T$  = temperature effects  
 TB-EW = plane of motion defined by top-bottom and east-west  
           directions of the cube  
 TB-NS = plane of motion defined by top-bottom and north-south  
           directions of the cube  
 $\dot{u}$  = particle velocity  
 $V$  = wave velocity  
 $V_p$  = compression wave velocity for a body wave  
 $V_s$  = shear wave velocity for a body wave  
 $\Delta V_s$  = change in shear wave velocity  
 $\ddot{z}$  = particle acceleration  
 $\gamma$  = single-amplitude shearing strain  
 $\gamma$  = unit weight  
 $\gamma_d$  = dry unit weight of sand  
 $\gamma_w$  = unit weight of water  
 $\delta$  = logarithmic decrement  
 $\lambda$  = wavelength  
 $\nu$  = Poisson's ratio  
 $\pi$  = 3.14159 ...  
 $\rho$  = mass density =  $\gamma/g$   
 $\bar{\sigma}_a$  = effective principal stress in direction of wave  
           propagation

$\bar{\sigma}_b$	= effective principal stress in direction of particle motion
$\bar{\sigma}_c$	= effective principal stress in out-of-plane direction (direction perpendicular to $\bar{\sigma}_a$ and $\bar{\sigma}_b$ )
$\bar{\sigma}_{EW}$	= effective principal stress along the east-west axis
$\bar{\sigma}_{NS}$	= effective principal stress along the north-south axis
$\bar{\sigma}_v$	= effective principal stress along the vertical (top-bottom) direction
$\bar{\sigma}_o$	= mean effective principal stress
$\bar{\sigma}_1$	= major principal stress
$\bar{\sigma}_2$	= intermediate principal stress
$\bar{\sigma}_3$	= minor principal stress
$\Delta\sigma$	= change in stress
$\tau_{ij}$	= shearing stress in $ij$ plane
$\tau_o$	= octahedral shearing stress
$\bar{\phi}$	= effective angle of internal friction

## CHAPTER ONE

## INTRODUCTION

Shear and compression wave velocities of soils are often obtained from field testing or laboratory measurements. Once velocities are determined, shear and Young's moduli of the soil are calculated. These soil moduli are used in dynamic soil-structure interaction analyses for small-strain problems such as machine foundations, or as reference levels for larger-strain problems such as earthquake shaking or blast loading. A thorough understanding of the inter-relationship between wave velocity and state of stress is, therefore, required for the prediction of ground response under dynamic loading. The relationship of wave velocity in soil with isotropic confinement has been examined in depth. However there has been little research, until very recently, investigating the effect of biaxial and triaxial states of stress on the propagation velocity of shear and compression waves in soil.

This study was undertaken to determine the effects on shear and compression wave velocities of the general state of stress in soil. This knowledge is required for the proper analysis of measurements from laboratory and field seismic testing. In addition, understanding in situ wave behavior is necessary in the modeling of dynamic soil behavior, and it may be of value in the estimation



of initial states of stress in soil. The portion of the study presented herein focuses on the effect on shear wave velocity of state of stress. That portion of the study dealing with compression wave velocity may be found in Kopperman et al (1982).

The study of the relationship between propagation velocity of body waves and state of stress in soil was conducted in a large-scale triaxial testing device. The triaxial device was designed and constructed by Mr. Kopperman and the writer for this study and was the subject of much effort in the task of preparing the device for operation. The triaxial device is essentially a cube structure constructed of reinforced steel which was designed to hold a cubic soil sample measuring 7 ft (2.1 m) on a side. Rubber loading membranes were oriented along the three principal planes of the cube, between the soil and three mutually perpendicular walls of the cube. The membranes were hydraulically pressurized to attain an isotropic, biaxial, or triaxial state of stress. Compression and shear waves were generated along each principal axis of the cube, with wave motion monitored by accelerometers embedded in the sand mass. Stress and strain measurement equipment were also embedded in the sand sample to determine stress-strain properties under the applied confinement. The design and construction of the triaxial device (referred to as the cube) is briefly summarized in Chapter 3 and is discussed in detail in Appendix A.

An initial series of wave propagation tests was performed as part of this research on one sample of dry washed mortar sand. A discussion of the engineering properties of the sand is presented in Chapter 4. The testing program of the states of stress at which wave propagation tests were conducted and the details of the construction of the sand sample in the cube are summarized in Chapter 5 and detailed in Appendix B.

Results of the effect on shear wave velocity of isotropic, biaxial, and triaxial states of stress are presented in Chapters 6, 7, and 8, respectively. Also discussed in these chapters are the effects on shear wave velocity of stress history and structural anisotropy for the sand. Results of the re-examination of previous research, in light of the results of this study, are presented in Chapter 9. A discussion of previous related research is contained in Chapter 2.

A summary of the major conclusions of this study are presented in Chapter 10. These results show, that for any state of stress, shear wave velocity for body waves is controlled primarily by the principal stresses in the direction of wave propagation and particle motion and is relatively independent of the principal stress in the out-of-plane direction, the direction in which no particle motion occurs for the shear wave. Shear wave velocity seems to be about equally dependent on the directions of wave propagation and particle motion, although this proportion may vary for other soils. For instance, for a different sand, Roesler (1979)

found that shear wave velocity was slightly more dependent on the direction of wave propagation than particle motion, with the out-of-plane direction having no effect on shear wave velocity. It follows then, that the typical procedure of relating shear velocity to the mean principal effective stress,  $\bar{\sigma}_0$ , which involves all three of the principal stress directions, including the out-of-plane direction, is not correct.

As expected, stress history was found to have no significant effect on shear wave velocity for this sand and, therefore, was neglected. On the other hand, structural anisotropy was found to have a significant effect on shear wave velocity. Shear wave velocities appeared to be grouped according to planes of motion, that is the plane determined by the directions of wave propagation and particle motion, with up to an 18 percent variation in shear wave velocity measurements with the planes of motion. This difference in shear wave velocity between planes of motion did not, however, affect the relationship between shear wave velocity and the principal stresses in the direction of wave propagation and particle motion.

## CHAPTER TWO

### REVIEW OF LITERATURE

#### 2.1 INTRODUCTION

The general purpose of this research is to evaluate the effect of the three-dimensional state of stress on compression and shear wave velocities of dry sand. The work reported herein deals with the shear-wave portion of this research. The effect of isotropic confinement on shear wave velocity has been extensively investigated, principally within the last two decades. Much less research has been directed at investigating the effect of the biaxial state of stress on shear wave velocity. For the case of triaxial confinement, there is a virtual absence of research on the effect of this state of stress on  $V_s$ . The following sections contain a review of the literature pertinent to the scope of this study.

#### 2.2 TESTING DEVICES

One of the focal points of past research has been on testing methods used to measure dynamic shear modulus and constrained modulus (which are directly related to shear and compression wave velocities of body waves, respectively) of various soils. It was felt that it would be helpful to the reader to include a brief description of the various devices used to measure dynamic soil properties.

As such, a short summary of the devices used by those researchers referenced in the later sections is included. For a more complete description, the reader is referred to the referenced articles and Woods (1973), who reviewed the current state-of-the-art with regard to laboratory and field testing for dynamic property measurement.

Generally speaking, testing devices fall into three categories which are conveniently divided according to experimental technique. The three categories are: 1. resonance methods, 2. pulse methods, and 3. cyclic methods. Resonance methods are based upon the relationship between the natural frequency of a soil column and its stiffness (hence, wave velocity). Pulse methods are based upon causing a disturbance at one point in the soil sample and defining its arrival at another point from which the time to travel between these points is determined. If the distance of travel is known, wave velocity can then be computed. Cyclic methods are based upon subjecting a laboratory sample to simulated field conditions of stress in order to evaluate soil properties. The soil properties are determined from the stress-strain behavior of the soil as a load is cycled. Different cyclic tests can determine the modulus of elasticity,  $E$ , or shear modulus,  $G$ , of soils as a function of various parameters.

One major difference between resonance and pulse methods is that resonance methods require somewhat larger deformations of the soil sample relative to the pulse methods. Because

of this, frequencies that the soil samples are subjected to may be higher for pulse methods. Nevertheless, results from both testing methods seem to yield similar wave velocities. Of the following devices discussed, the resonant column device pertains to the resonance method, while pulse method devices include piezoelectric crystals, test chambers (Schmertmann, 1978), and soil cubes (Roesler, 1979).

Although cyclic tests were conceived to represent actual field loading conditions, each of the test devices has limitations. One of the major difficulties with trying to simulate real loading conditions is the mechanical performance of the test device. Another problem with cyclic tests is the distribution and redistribution of stress and strain within the sample during testing. Test devices which pertain to the cyclic method include the cyclic triaxial, cyclic simple shear, and cyclic torsional shear devices, and the multiaxial (true triaxial) devices (Atkinson and Ko, 1973).

#### 2.2.1 Resonant Column Device

The resonant column device is a laboratory device employed to evaluate the dynamic moduli and material damping of soils. The resonant column is based on the theory of wave propagation in elastic rods, relating the dynamic modulus of the column of soil to its natural frequency. Shearing strain amplitudes can range from about 0.0001 to nearly 1.0 percent.

There are a number of designs of resonant column devices, each design a function of the boundary conditions imposed on the soil column. These boundary conditions determine the driving conditions for the soil and the method of analysis used to determine the shear modulus (and shear wave velocity). Either shear or compression waves may be propagated through the soil column depending on the particular orientation of the device. A cylindrical soil sample is subjected to torsional or longitudinal vibration to determine the first-mode natural frequency of the column. Soil samples can be solid or hollow when torsional vibration is used.

Although commonly designed for isotropic confinement only, Hardin and Black (1966) and Hardin and Drnevich (1970) designed resonant column devices which permitted independent control of the axial load and cell pressure during testing. This independent control permits biaxial confinement of the soil sample.

#### 2.2.2 Piezoelectric Crystals

Piezoelectric crystals are often used in the pulse method of determining dynamic soil properties. Waves of ultrasonic frequency (500 kilocycles/sec) are generated and received using these crystals. The wave amplitude is generally very low, typically less than 0.0001 percent. Either compression or shear waves can be generated in the soil depending on the orientation and type of piezoelectric crystal used. This approach uses the wave travel

times and travel distance to compute a velocity from which the modulus (G or E) is calculated.

Piezoelectric crystals were used by Lawrence (1963) to generate one-dimensional dilatational waves through sand and glass beads. The device consisted of the test sample in a Shelby tube, which was confined longitudinally by two load pistons and then placed in a load frame. The load frame applied an axial pressure on the soil. Lawrence (1965) conducted shear wave velocity measurements in sand and clay, using a modified triaxial cell with piezoelectric crystals mounted in the cells top cap and base pedestal as shown in Fig. 2.1. The crystals were connected in parallel and oriented so that, if pulsed, a torsional distortion would occur at the sample's end. Crystals were also used to measure any torsional displacement at the other end of the sample.

### 2.2.3 Test Chamber

Schmertmann (1978) designed a test chamber to measure shear and compression wave velocities in dry sand, in accordance with the pulse method. The chamber was constructed of steel and was used to confine a soil sample 4 ft (1.22 m) in height and with a diameter of 4 ft (1.22 m). A sample of this size helped reduce any boundary effects on the wave velocities. With the chamber, independent control of side pressure and axial load was possible so that an isotropic or biaxial state of stress could be induced in the soil sample. The side pressures were created by water



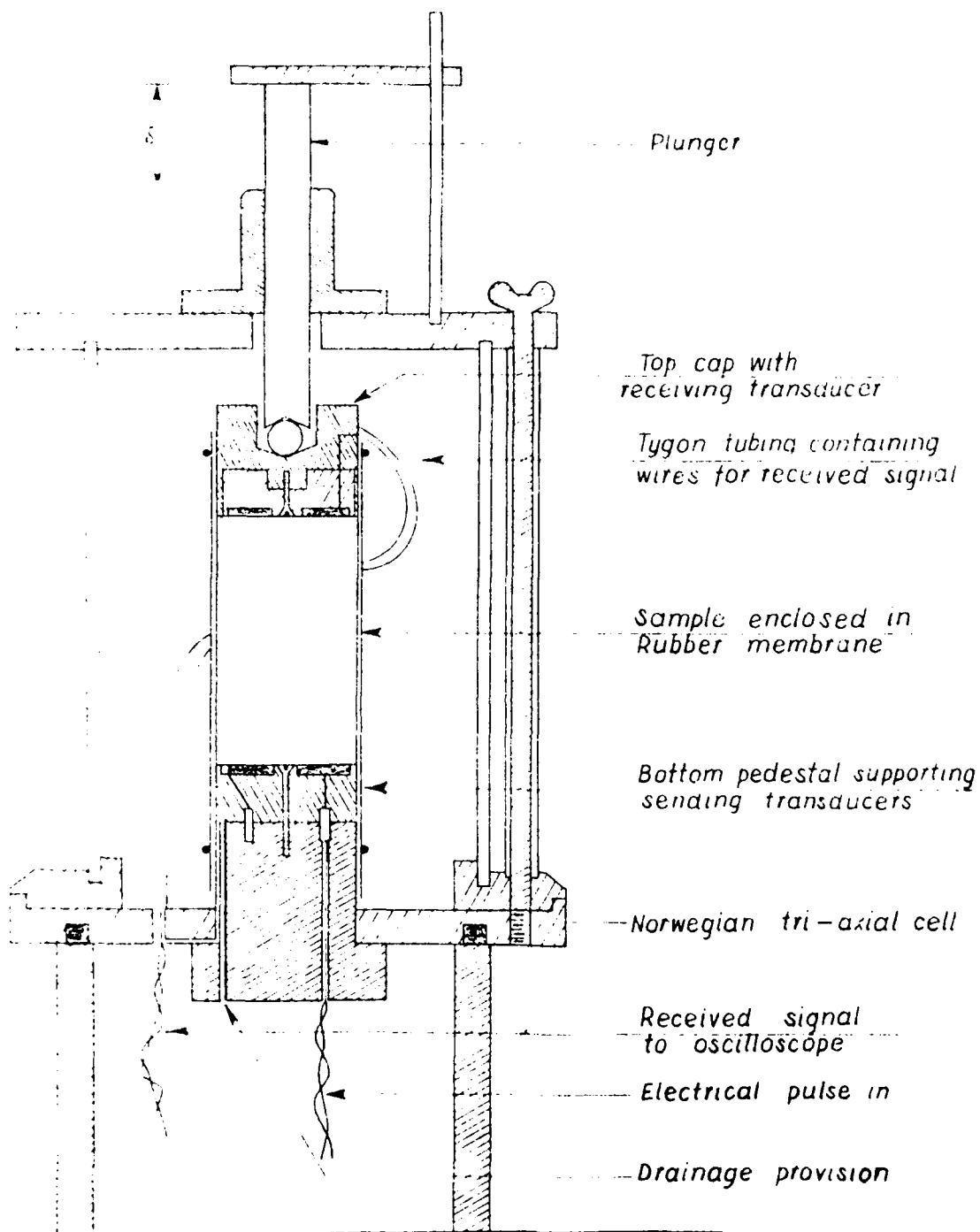


Fig. 2.1 - Triaxial Cell Converted for Shear Wave Velocity Measurements by Lawrence (1965)

pressure around the circumferential boundary of the chamber and the axial pressure was created by a reaction weight on top of the chamber, as shown in Fig. 2.2.

Schmertmann placed several accelerometers within the sand mass, oriented in such a manner as to measure wave velocities horizontally, vertically, and diagonally across the sample. Waves were generated at the outer edge of the sample and the wave arrivals were recorded by accelerometers along several wave paths as shown in Fig. 2.3. Differences in direct arrival times were used to compute wave velocities. Tests were performed over a pressure range of from 5 to 20 psi (34.5 to 137.8 kPa).

By varying the method used to generate the initial impulse, either shear or compressive waves were measured. Two circular plates were buried 1.2 in. (3 cm) beneath the top surface of the sand, one plate in the center of the surface and the other plate near the outer edge of the chamber. The vertical rod had a horizontal brace connected to it. When the rod was hit in the vertical direction, mostly compression waves were generated. When the horizontal brace was hit, the plates rotated within the sample, generating shear waves. Sandpaper was glued to the bottom of the plates in order to improve the plate-soil coupling.

#### 2.2.4 Soil Cube

Roesler (1979) used the pulse method and an approach similar to Schmertmann's but with a rather unique device. Roesler

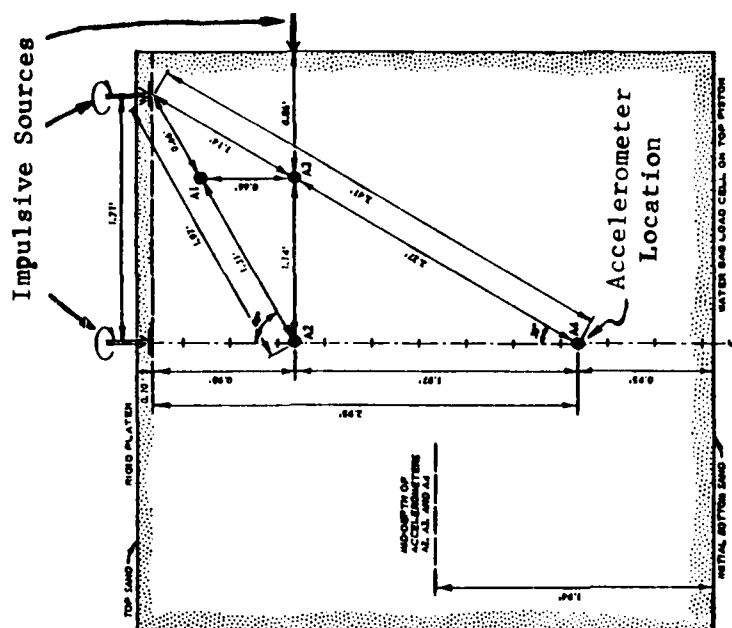


**Fig. 2.3 - Accelerometer Pattern in Plane Through Axis of Test Chamber Used by Schmertmann (1978)**

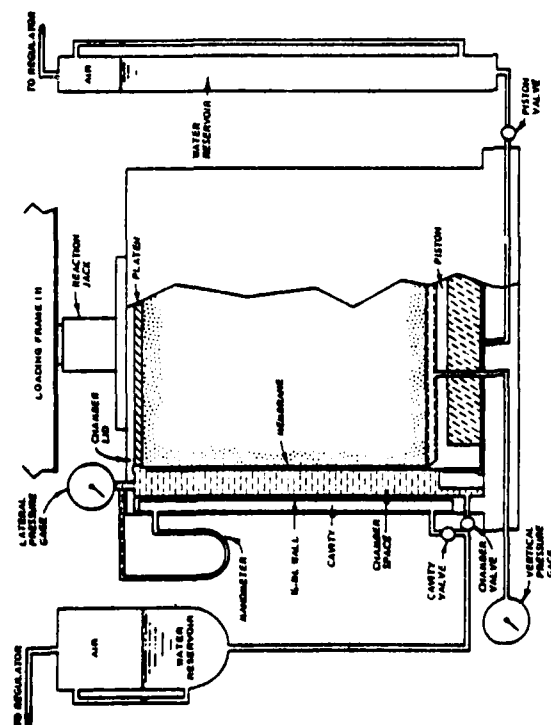


Fig. 2.2 - Schematic of Test Chamber  
Used by Schmertmann (1978)

conducted shear wave velocity measurements with a cubical sand sample measuring 30 cm (11.4 in.) on a side. The sample was constructed in an airtight, PVC-lined, plexiglas box. Once the sand sample was evacuated, the plexiglas sides were removed, leaving a PVC covered cube of soil. As shown in Fig. 2.4, a shear wave exciter was placed in the sand sample in line with two transducers which were used to measure arrival times of the shear waves. The shear wave exciter was designed to minimize volumetric strain and thus minimize the generation of compression waves. The exciter, shown in Fig. 2.5, consisted of a direct-current motor which rotated and reacted against a casing embedded in the sand. The reaction of the casing against rotation produced the shear waves.

The sand sample could be subjected to an isotropic evacuation pressure and an axial load so that either isotropic or biaxial confinement could be induced in the sand. Test pressures ranged from 5.8 to 23.2 psi (40 to 160 kPa).

A unique feature of this device was that the sand cube was stable (being evacuated) and could be rotated. Therefore the axial load could be placed along any principal axis of the cube at any one time. This arrangement permitted varying any one of the axial pressures while holding the other two constant, thereby examining the change in  $V_s$  as a function of just one of the axial stresses. Further, the shear wave exciter and transducer arrangement could be oriented parallel or perpendicular to the sand

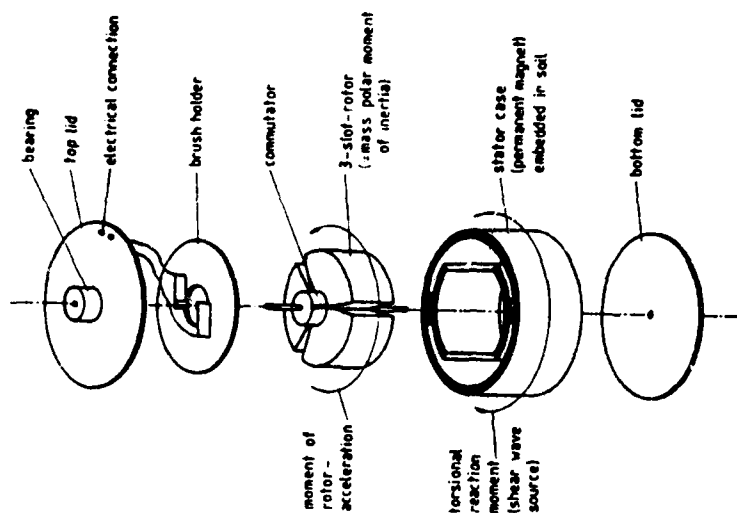


Fig. 2.5 - Principles of Shear Wave Exciter Used by Roesler (1979)

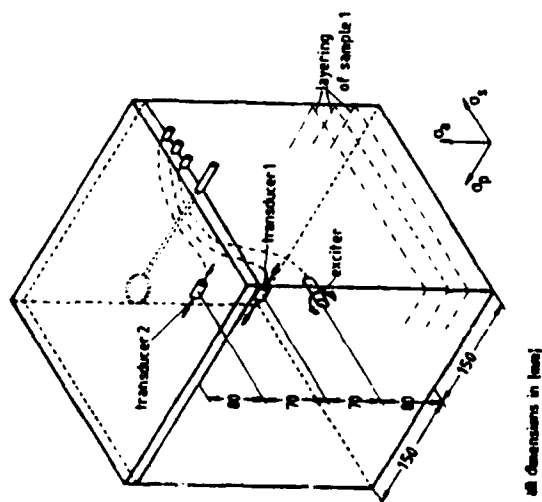


Fig. 2.4 - Cubical Sand Sample with Shear Wave Exciter and Transducers Used by Roesler (1979)

layering, caused by sample construction, to investigate the effect of sample anisotropy.

#### 2.2.5 Cyclic Triaxial Test

Cyclic triaxial devices are universally used testing devices to measure dynamic soil properties. With these devices, cylindrical samples are placed within a cell chamber and usually consolidated under an isotropic confining pressure. For the theoretical simulation of actual field loading, the axial stress is increased to create the level of shear stress to which it is desired to subject the sample. At the same time, the cell pressure is reduced by an amount equal to the increase in axial stress. The original axial stress and cell pressure are then reversed by the same level so that the shear stress is cycled on the sample. This procedure allows a constant normal stress on a 45-degree plane through the sample while a shear stress is developed and reversed on that 45-degree plane.

Although this loading may simulate field conditions (on horizontal planes during earthquake loading) the test is frequently performed with a constant cell pressure and with the axial stress having twice the shear stress level cycled along that axis. This, in effect, results in the correct level of shear stress acting upon the sample. Both patterns of cycling result in similar levels of shear stress on the soil testing conditions.

Triaxial tests can be performed as stress controlled or strain controlled tests. Stress controlled tests are most common and use a cyclic axial load on the sample. Strain controlled tests also cycle the axial load but the deformation is controlled. By doing this,  $E$  is calculated from the stress-strain relationships from which  $G$  is calculated by assuming a value for Poisson's ratio.

The cyclic triaxial test does have limitations, including:

1. stress concentrations at the cap and base of the specimen,
2. rotation of the major principal stress by 90 degrees during cycling,
3. necking of the sample at large cyclic strains, and
4. difficulty in obtaining accurate shear strain measurements below 0.01 percent.

#### 2.2.6 Cyclic Simple Shear Test

The cyclic simple shear test simulates most closely idealized field loading during earthquakes. There are two main designs for this apparatus. The NGI/SGI apparatus uses a sample with a circular cross section with non-rigid vertical boundaries (either stacked rings or wire-wound membrane). The Cambridge design of the simple shear device employs a sample with a square cross-section and rigid vertical boundaries.

In the simple shear test, the sample is first axially loaded to initially consolidate the soil under  $K_0$  conditions. With the axial load still applied, the base of the sample

is subjected to the desired shear stress, resulting in the base of the sample moving laterally while the top remains fixed. The lateral movement creates strains over the entire sample height. The shear stress is then reversed, with the stress-strain behavior of the sample recorded. As with the cyclic triaxial test, the cyclic simple shear test may be performed as either a stress controlled or strain controlled test. For the stress controlled test, the desired level of shear stress is cycled, with no control on the lateral strains. The strain controlled test, on the other hand, control the lateral strain of the base with no regard to the stress in the sample.

Problems also exist in the simple shear test which include: 1. sample preparation, 2. development of non-uniform strains in the sample, 3. stress concentrations within the sample, and 4. the lack of application of shear stresses on vertical boundaries of the sample.

#### 2.2.7 Cyclic Torsional Shear Test

The cyclic torsional shear device was first devised to reduce some of the problems inherent with the cyclic simple shear device. Two soil sample configurations were developed for the torsional shear test. The configurations are: 1. solid or hollow cylindrical samples with height to width ratios of 2 to 1, and 2. hollow samples with the height varying proportionally to the radius of the sample. The linear variation of height with



radius for the second configuration results in a greater sample height near the outside boundary and sloping to a shorter height on the inside boundary. The variation in height is often created on the bottom face of the hollow sample.

Hollow samples were developed to reduce the variation of shearing strains along the radius of the sample. The sloping base of the second configuration should, theoretically, produce more uniform strains along the sample radius.

#### 2.2.8 Cyclic Multiaxial Test Devices

One of the most complex test apparatus is the multiaxial test device, with involved mechanical design problems. The multiaxial devices fall into two general categories which involve:

1. the use of a hollow cylindrical sample subjected to an external pressure, internal pressure, and axial or torsional load, and
2. the use of cubical soil samples subjected to principal stresses along the three axes of the cube. Only the second approach will be reviewed in this section.

Several cubical multiaxial devices have been constructed. These devices allow independent control of the principal stresses along each of the principal axes of the cube. The tests are performed as either stress controlled or strain controlled tests, depending on how the principal stresses are applied along the sample boundaries. These boundary conditions may be categorized as: 1. flexible boundaries, 2. rigid boundaries, or 3. a

combination of flexible and rigid boundaries. Flexible boundaries (Ko and Scott, 1967) are synonymous with stress controlled devices and rigid boundaries (Pearce, 1971) are used for strained controlled devices. The combination flexible-rigid boundary device (Sutherland and Mesdary, 1969) uses flexible boundaries for two directions and a rigid boundary for the third direction. Each of these boundary conditions has its own advantages and disadvantages.

Only one cubical test device will be discussed in this section. This device, described by Ko and Sture (1967) and Atkinson and Ko (1978), uses flexible boundaries. The apparatus was initially designed to test 4-in. (10.2 cm) cubical samples. The device, shown in Fig. 2.6, can apply triaxial stresses up to 20 ksi ( $1.38 \times 10^5$  kPa) with flexible pads subjected to hydraulic pressure. Strains are monitored by proximeters situated along the walls of the device (sides of the sample). These proximeters have a sensitivity of  $1 \times 10^{-5}$  in. ( $2.54 \times 10^{-5}$  cm), and each wall has three mounted in a triangular pattern on it.

### 2.3 EFFECT OF ISOTROPIC CONFINEMENT

The effect of isotropic confinement on compression and shear wave velocities is well defined. Several investigators (Hardin and Richart, 1963; Hardin and Drnevich, 1970; and Hardin and Drnevich, 1972) have performed extensive studies of the parameters affecting wave velocity using resonant column and torsional shear devices, and their results are summarized in this section.

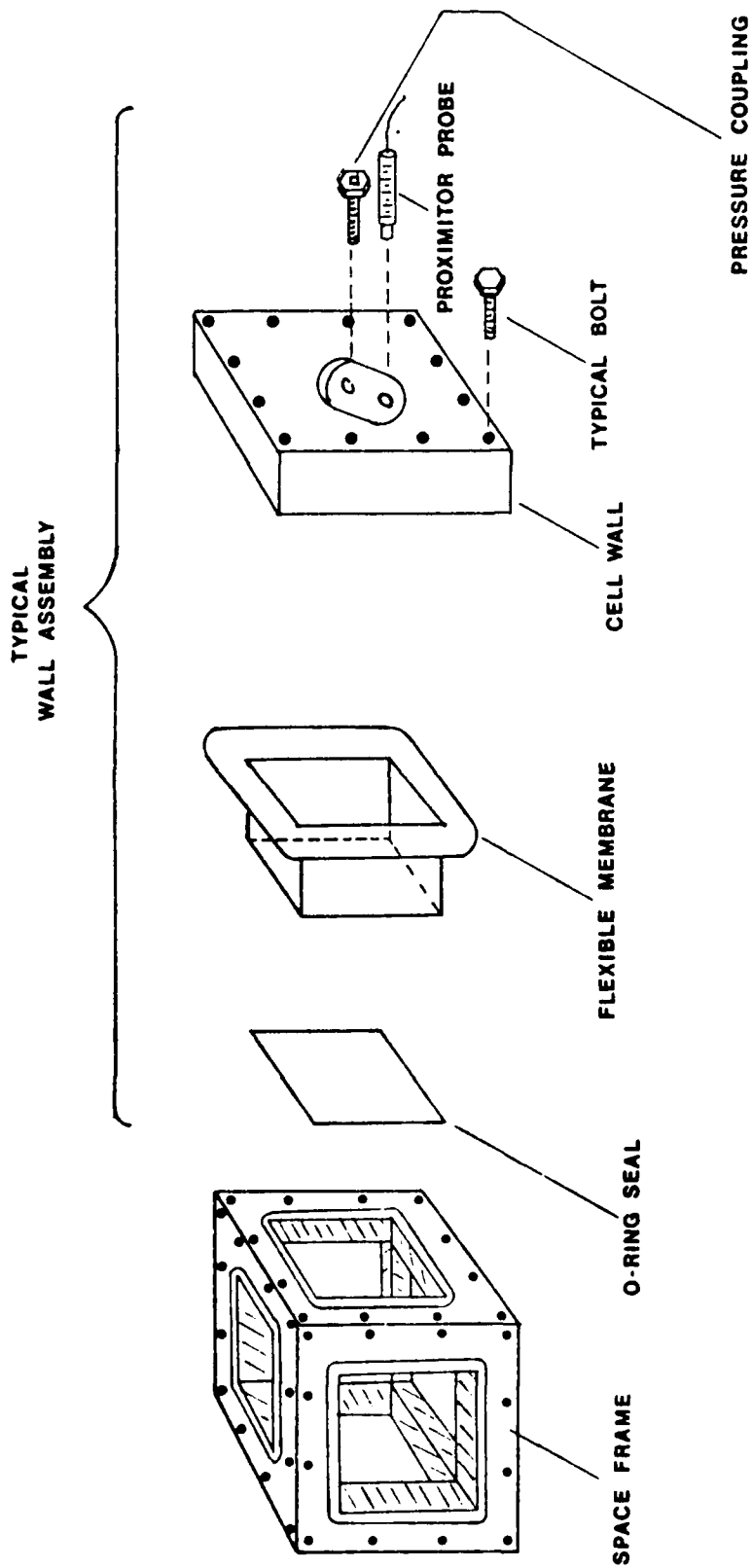


Fig. 2.6 - Exploded View of Multiaxial Test Cell Patterned After Cell Used by Ko, et al (from Berends, 1974)

The shear modulus is a function of many parameters, each parameter varying in importance. Equation 2.1 (after Richart, Hall, and Woods, 1970) summarizes those parameters recognized as affecting  $G$ , for all soils:

$$G = f(\bar{\sigma}_o, e, H, S_r, \tau_o, C, A, f, t, S_s, T) \quad (2.1)$$

where:  $\bar{\sigma}_o$  = mean effective principal stress,

$e$  = void ratio,

$H$  = ambient stress history,

$S_r$  = degree of saturation,

$\tau_o$  = octahedral shear stress,

$C$  = grain characteristics, grain shape, grain size, grading, minerology,

$A$  = strain amplitude,

$f$  = frequency of vibration,

$t$  = secondary effects that are functions of time, and magnitude of load increment,

$S_s$  = soil structure, and

$T$  = temperature, including freezing.

The importance to  $G$  of many of these parameters is summarized in Table 2.1.

Based on Table 2.1, mean effective principal stress is a very important parameter affecting  $G$  and  $V_s$ . Results show that shear wave (and compression wave) velocity increases as  $\bar{\sigma}_o$  increases, with the rate of increase typically varying from the 1/5 to 1/4

TABLE 2.1

Parameters Affecting Shear Modulus of Sands  
for Complete Stress Reversal  
(after Hardin and Drnevich, 1970)

Soil Parameter	Importance to Shear Modulus
(1)	(2)
Strain Amplitude	Very
Mean Effective Principal Stress	Very
Void Ratio	Very*
Degree of Saturation	Very**
Octahedral Shear Stress	Less
Overconsolidation Ratio	Less
Frequency of Loading	Less
Secondary Effects	Less**
Grain Characteristics, Size, Shape, Gradation, Minerology	Little**
Soil Structure	Little**
Temperature	Little**

\* Only one void ratio used in this study so not discussed in this section.

\*\* Beyond the scope of this study.

power of confining pressure. The  $\log V_s - \log \bar{\sigma}_0$  relationship then plots as a straight line, with the slope of the line equal to the power of confining pressure. Results from a number of authors, as shown in Table 2.2, indicate that the slope of this line may vary substantially for sands. For confining pressures less than 14 psi (96.5 kPa), the slope of this relationship may be slightly higher, varying with the  $1/3$  to  $1/4$  power of the confining pressure.

The effect of strain amplitude on shear wave velocity can also be quite important. The shear modulus decreases rapidly strain amplitude increases. In fact, at strains of 0.1 percent, the shear modulus can easily differ by a factor of three from the modulus measured at 0.001 percent. Although there is no apparent level of strain below which  $G$  is constant, it has been shown for sands that for strain amplitudes below 0.001 percent, the measured shear modulus is essentially equal to  $G_{\max}$ . Therefore, for strain amplitudes less than 0.001 percent,  $G_{\max}$  (and so  $V_s$ ) is assumed constant.

Other factors that effect  $V_s$  and can be considered important parameters include void ratio, degree of saturation, and the number of cycles of loading. Since only one void ratio was involved in this study, it will only be said the shear modulus decreases as the void ratio increases. Because the degree of saturation was essentially zero for this study (the sand was tested in a nearly dry state) a discussion of its effects on  $V_s$  will

TABLE 2.2

Summary of Values Presented in the Literature  
for the Slope of the  $\log V_s - \log \bar{\sigma}_o$  or  
 $\log V_p - \log \bar{\sigma}_o$  Relationship

Reference	Slope for Shear Wave Velocity	Slope for Compression Wave Velocity
(1)	(2)	(3)
Hardin and Richart (1963)		
< 14 psi	0.25 to 0.33	0.25 to 0.33
> 14 psi	0.20 to 0.25	0.20 to 0.25
Schmertmann (1978)	0.20	0.20
Roesler	0.26	
Hardin and Drnevich (1970)	0.25	
Wilson and Miller (1962)	0.15 to 0.20	0.20 to 0.25
Hardin and Black (1966)	0.25	0.25
Lawrence (1963)		0.20 to 0.25
Lawrence (1965)	0.25	

be omitted. Similarly, the number of cycles of loading is inappropriate for this study and will not be discussed in this section.

The effect on shear modulus of the remaining parameters can be considered less important. Several of these parameters were examined in detail in this study. These parameters include stress history, octahedral shear stress, and frequency of vibration. Stress history (preloading) has a small effect on  $V_s$  for sands, with the velocity varying from one to four percent from that of the virgin specimen. The importance of stress history is dependent on the Plasticity Index of the soil (the PI of sand is zero). It was assumed, therefore, that the effect on  $G$  (and so  $V_s$ ) of stress history could be ignored for this study. A discussion of the experimental effects on  $V_s$  of stress history is presented in Section 6.5.

The effect of frequency of vibration (really strain rate) on  $V_s$  varies with soil type and frequency range. Generally, for low-amplitude loading of sands and for frequencies in the range from 200 to 2500 cps (Hertz), it can be assumed that the frequency of vibration has no effect on wave velocities. For this study it was assumed that the frequencies would be between 200 and 2500 cps, and therefore, the effect on  $V_s$  of frequency was ignored (see Section 6.8.1).

The effect of octahedral shear stress on  $G$  was also investigated in this study. Results of two previous investigations



(Hardin and Black, 1966; Lawrence, 1965) indicate that the level of shear stress has little effect on  $G$ . The cube results show these results are an oversimplification. Shear wave velocity was determined to depend primarily on the principal stresses in the directions of wave propagation and particle motion. Therefore, as discussed in Section 7.5.1, if these two stresses are known, shear wave velocity can be predicted.

The remainder of the parameters which could affect  $G$  will not be reviewed in this section because they do not pertain to this study. These parameters include grain characteristics (only one type of sand was tested), secondary time effects, soil structure, and temperature effects (the last three parameters are beyond the scope of this study).

Hardin (1978) studied the importance of each of these parameters and presented a general equation for shear modulus at small strain amplitudes as:

$$G_{\max} = \frac{A \text{OCR}^k}{0.3 + 0.7e^2} P_a^{1-n} \frac{\sigma_o}{\sigma_o^n} \quad (2.2)$$

where:  $G_{\max}$  = shear modulus in desired units,

$A$  = constant (dimensionless),

$\text{OCR}$  = overconsolidation ratio,

$k$  = function of soil plasticity ( $k = 0$  for sands),

$e$  = void ratio,

$P_a$  = atmospheric pressure in units of  $G_{\max}$ ,

$n$  = slope of  $\log G_{\max} - \log \bar{\sigma}_o$  relationship, and  
 $\bar{\sigma}_o$  = mean effective principal stress in units of  $G_{\max}$ .

This expression was determined to predict the shear modulus within  $\pm 10$  percent of values measured by Hardin for shearing strain amplitudes less than 0.001 percent. Those parameters which Hardin considered most important in their effect on  $G$  are incorporated into the equation.

#### 2.4 EFFECT OF ANISOTROPIC CONFINEMENT

For the case of anisotropic (biaxial) confinement, five studies have been conducted: Hardin and Black (1966), Lawrence (1965), Schmertmann (1978), Hardin (1978), and Roesler (1979). The results from each study are presented separately so that the results of each author may be presented in an orderly manner.

The change from an isotropic to anisotropic state of stress necessitates varying the principal stresses independently. Biaxial testing can be performed by: 1. varying the ratio of the major and minor principal stresses while holding the mean effective principal stress constant, (Hardin and Black, 1966; Schmertmann, 1978), 2. varying the mean effective confining pressure by changing  $\bar{\sigma}_1$  and  $\bar{\sigma}_3$  simultaneously while noting the level of shear stress (Lawrence, 1965), and 3. varying one of the principal stresses ( $\bar{\sigma}_1$  or  $\bar{\sigma}_3$ ) while holding the remaining principal stress constant and noting the level of shear stress (Roesler, 1979). The first two variations of stress requires that two principal

stresses be equal and vary in unison while the third principal stress varies accordingly. Consequently, all three axial stresses are varying for each test sequence. The effect on wave velocity of each principal stress, therefore, is difficult to isolate. The third variation of stress allows for individual examination of the effect of each axial stress on  $V_s$ , since only one stress is changing during the test sequence.

#### 2.4.1 Lawrence (1965)

Lawrence (1965) performed tests on dry sand with piezo-electric crystals as shear wave generators. The crystals were radially situated in a modified triaxial cell in which the axial load and cell pressure were controlled independently. The mean effective principal stress varied from 10 to 110 psi (68.9 to 757.9 kPa) and stress ratios (defined as  $\bar{\sigma}_1 / \bar{\sigma}_3$ ) varied from 1 to 1.4. Shear waves were generated vertically through a cylindrical soil sample.

The results obtained by Lawrence are shown in Fig. 2.7, in which shear wave velocities were determined at different shear stresses and mean effective principal stresses. The circles plotted on the figure represent individual shear wave velocity measurements, with the values of  $V_s$  shown next to the circles. Lawrence drew lines of constant  $V_s$  which are shown as vertical lines in the figure. Therefore, Lawrence concluded that  $V_s$  was effected only by  $\bar{\sigma}_0$  and was independent of the level of shear stress.

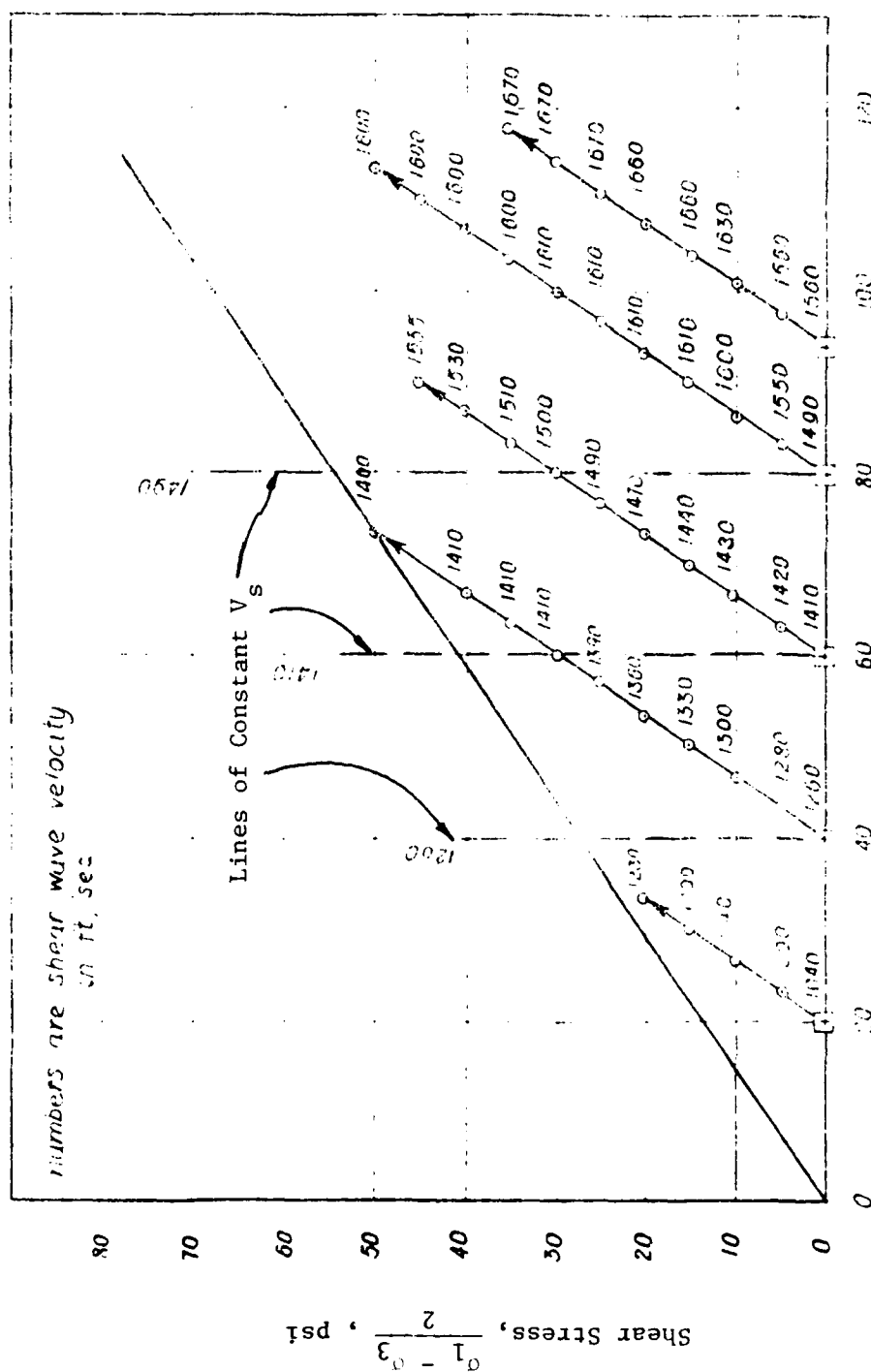


Fig. 2.7 - Influence of Shear Stress on Shear Wave Velocity in Ottawa Sand  
(from Lawrence, 1965)

Lawrence did note that the change of shear wave velocity with  $\bar{\sigma}_0$  was not a linear variation. Figure 2.8 shows the five loading paths of Fig. 2.7 redrawn as a plot of  $V_s$  and  $\bar{\sigma}_0$ . The shear stress increases with the increase in  $\bar{\sigma}_0$ . As shown by this figure, the shear wave velocity increased slightly as the shear stress (and  $\bar{\sigma}_0$ ) increased. Lawrence attributed this change in  $V_s$  to a reduction in void ratio as the shear stress increased.

#### 2.4.2 Hardin and Black (1966)

Hardin and Black (1966) performed resonant column tests on sand samples. They vibrated the samples only with small amplitude torsional excitation. The dynamic shear modulus was determined while the samples were subjected to an isotropic confining pressure and an additional, independently controlled, axial load. Loading stress paths followed the trend of increased isotropic confining pressure with unloading paths reversing the trend. For some sets of tests, the shear stress was varied while  $\bar{\sigma}_0$  remained constant. Principal stress ratios varied from approximately 1 to 2, and almost all tests were conducted in the normally consolidated state. The test apparatus was designed so that small angles of twist, on the order of  $10^{-5}$  radians per in. of specimen length, were applied to the sample.

Test results indicate that the measured  $G_{\max}$  was essentially independent of the deviatoric component of stress and depended only on the mean effective principal stress. For a principal

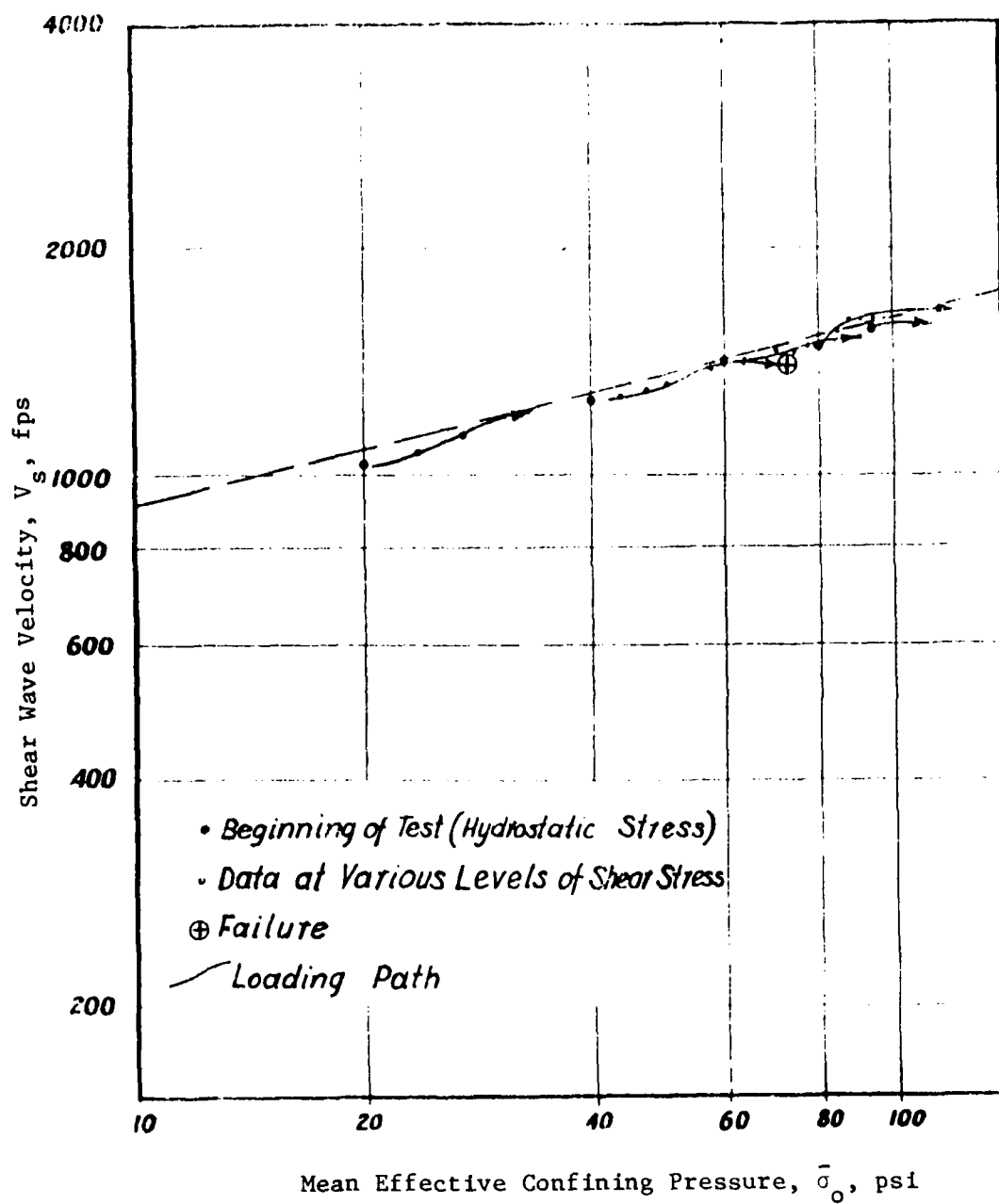


Fig. 2.8 - Results of Shear Wave Velocity Tests  
 Replotted from Fig. 2.7 (from Lawrence, 1965)

stress ratio ranging from 1 to 2 and a constant  $\bar{\sigma}_o$ , measured values of  $G_{\max}$  had less than a 2 percent scatter. Based on the conclusion that the level of shear stress did not effect  $G_{\max}$ , the equations for  $G$  at small strain amplitudes for sand presented by Hardin (1965) were:

for sands with round grains:

$$\bar{\sigma}_o < 2000 \text{ psf} \quad G_{\max} = \frac{(32.17-14.80e)^2}{(1+e)} \bar{\sigma}_o^{1/2} \quad (2.3)$$

(96.5 kPa)

$$\bar{\sigma}_o > 2000 \text{ psf} \quad G_{\max} = \frac{(22.52-10.6e)^2}{(1+e)} \bar{\sigma}_o^{3/5} \quad (2.4)$$

(96.5 kPa)

and for sands with angular grains:

$$G_{\max} = \frac{(30.09-19.12e)^2}{(1+e)} \bar{\sigma}_o^{1/2} \quad (2.5)$$

where:  $G_{\max}$  = low-amplitude shear modulus in psi,  
 $e$  = void ratio,  
 $\bar{\sigma}_o$  = mean effective principal stress in psf.

When these equations were used to compare predicted values of  $G$  with measured values obtained by Hardin and Black, a maximum scatter of 8.9 percent was found.

Several tests were conducted for unloading to examine the stress history effect on  $G_{\max}$ . The results indicated that stress history (preloading) had only a small effect of decreasing  $G_{\max}$ , with a maximum decrease in  $G_{\max}$  measured as 10.8 percent. The

decrease in  $G_{\max}$  was found to diminish as the overconsolidation ratio decreased. Generally, it was felt that the change in shear modulus due to preloading could be neglected for sands.

#### 2.4.3 Schmertmann (1978)

Schmertmann (1978) performed laboratory tests on dry sand with a triaxial chamber in which a soil sample 4 ft (1.2 m) in diameter and 4 ft (1.2 m) high was constructed. The radial and vertical stresses were varied independently in the chamber from 5 to 20 psi (34.5 to 137.8 kPa) with the stress ratio varying from 1 to 3 (with the stress ratio defined here as the vertical stress over the radial stress).

Schmertmann studied the variation in bulk modulus,  $B$ , with anisotropic confinement, by studying the variation in  $V_s$  and  $V_p$  with the direction of wave propagation. The bulk modulus is a function of both  $V_p$  and  $V_s$  and is defined as:

$$B = \rho(V_p^2 - 4/3 V_s^2) \quad (2.6)$$

where:  $B$  = dynamic bulk modulus in psf,  
 $\rho$  = mass density =  $\gamma/g$  in lb-sec<sup>2</sup>/ft<sup>4</sup>,  
 $V_p$  = compression wave velocity in fps, and  
 $V_s$  = shear wave velocity in fps.

Because Schmertmann was investigating the magnitude and directional effects of  $V_p$  and  $V_s$  on  $B$ , he performed an extensive analysis of both waves. Waves were generated in several directions through the



sand sample (vertically, horizontally, and diagonally). Wave arrivals were detected by accelerometers placed in the sand, with the velocities determined from interval velocities of initial arrivals.

Velocity measurements indicated that, for isotropic confinement, both  $V_p$  and  $V_s$  were slightly faster in the horizontal direction than in the vertical direction. This suggested that the sand had some degree of inherent anisotropy present due to the method of sand placement. This inherent anisotropy will be referred to as structural anisotropy herein. (In fact, researchers have found it impossible to construct a truly isotropic sand sample.)

Schmertmann found that by varying the stress ratio while holding  $\bar{\sigma}_0$  constant,  $V_s$  was not significantly affected (less than  $\pm 10$  percent) for any direction of propagation. The results, summarized in Table 2.3, indicate that  $V_s$  depended primarily on  $\bar{\sigma}_0$  and was much more insensitive to the level of shear stress. It can be noted from Table 2.3 that varying the stress ratio from 1 to 3 (increasing the vertical  $\bar{\sigma}_1$  relative to the radial  $\bar{\sigma}_3$ ) at constant  $\bar{\sigma}_0$  had the effect of slightly increasing  $V_s$  for the vertically propagating shear wave, while slightly decreasing  $V_s$  for the horizontally propagating shear wave. The change in  $V_s$  with stress ratio was  $\pm 2$  percent. Although this could be due to experimental scatter, it could also be indicative of a relationship

TABLE 2.3

Effect of Stress Ratio on Shear Wave Velocity  
at a Mean Effective Principal Stress of 10 psi (69 kPa)  
(from Schmertmann, 1978)

Direction of Wave Propagation	Stress Ratio ( $\bar{\sigma}_1/\bar{\sigma}_3$ )	Shear Wave Velocity* fps
(1)	(2)	(3)
Vertical	1	916
	3	933
Horizontal	1	1026
	3	1059

\* Based on an average of tests at two sand densities.

TABLE 2.4

Effect of Stress Ratio on Compression Wave Velocity  
at a Mean Effective Principal Stress of 10 psi (69 kPa)  
(from Schmertmann, 1978)

Direction of Wave Propagation	Stress Ratio ( $\bar{\sigma}_1/\bar{\sigma}_3$ )	Compression Wave Velocity* fps
(1)	(2)	(3)
Vertical	1	1376
	3	1701
Horizontal	1	1506
	3	1460

\* Based on an average of tests at two sand densities.

between  $V_s$  and the direction of propagation and axial stress as found in this study (see Section 7.5).

On the other hand, Schmertmann found that  $V_p$  was significantly affected by the stress ratio, as shown in Table 2.4. There was essentially no change in  $V_p$  for horizontal propagation as the vertical stress was varied. However,  $V_p$  was significantly affected by changes in the vertical stress when the wave was propagated in the vertical direction. It was concluded that measured  $V_p$  values were dependent on the effective principal stress in the direction of propagation.

#### 2.4.4 Hardin (1978)

Hardin (1978) in his state-of-the-art paper attempts to form a three-dimensional stress-strain relation for soils. Included in the relation is consideration of the stress path followed during loading of the soil and its affect on the stresses. A general form for shear modulus is:

$$G_{ij}^e = \frac{S_{ij} \text{OCR}^k}{(1+\nu) F(e)} p_a^{1-n} \left( \frac{1}{(\bar{\sigma}_o + \tau_{ij})^{-n} + (\bar{\sigma}_o - \tau_{ij})^{-n}} \right) \quad (2.7)$$

where:  $G_{ij}^e$  = elastic shear modulus in  $ij$  plane,  
 $S_{ij}$  = dimensionless elastic shear stiffness parameters  
in proposed stress-strain relation,  
OCR = overconsolidation ratio,  
 $k$  = elastic parameter dependent on soil Plasticity Index,

$\nu$  = elastic Poisson's ratio,

$F(e)$  = function of void ratio ( $F(e) = 0.3 + 0.7e^2$ ),

$n$  = slope of  $\log G - \log \bar{\sigma}_0$  relationship,

$\bar{\sigma}_0$  = effective mean principal stress in same units as

$G_{ij}$ , and

$\tau_{ij}$  = shear stress on  $ij$  plane.

This general equation can be simplified for the isotropic state of stress where  $\tau_{ij} = 0$  and is modified for certain stress paths. This approach is the beginning of a general framework in using soil dynamics to predict soil behavior.

#### 2.4.5 Roesler (1979)

Roesler (1979) performed shear wave measurements using a 30 cm (11.8 in.) cubical sand sample. The sand was subjected to a vacuum as the confining pressure and a vertically acting axial load. A torsional shear wave exciter was used to generate torsional shear waves in the sample, and wave arrivals were detected by two transducers, aligned along one axis of the cube, upon which the generator was also located. Wave velocities were determined from the interval velocities of initial arrivals to the two transducers. The sample could be rotated so that the axial load could be applied along any of the three principal axes of the sand cube.

For the shear wave testing, the internal vacuum was held constant and the axial load was increased so that the axial

stress in only one direction was changed. By doing this, neither the stress ratio or  $\bar{\sigma}_0$  remained constant for the test series. However, the effect of varying only one axial stress could be studied. Since the cube could be rotated and the axial load transferred to each of the principal axes of the cube, the effect of each of the principal stress directions on  $V_s$  for the same shear wave (constant directions of wave propagation and particle motion relative to the cube axes) could be evaluated. Test pressures ranged from 5.8 to 23 psi (40 to 158 kPa) with a maximum stress ratio of 1.8 used for the tests.

Test results showed an increase in  $V_s$  with increasing isotropic stress, with the results comparing favorably with existing equations. As the stresses became anisotropic,  $V_s$  was found to vary only with the principal stresses in the directions of wave propagation and particle motion, and not with the principal stress in the third, orthogonal direction, as shown in Fig. 2.9.

This effect on  $V_s$  by only these two stress directions was explained by the fact that shear waves create shear strains only in the directions of propagation and particle motion, and so it was logical that only these stress directions should affect  $V_s$ . The plots shown in Fig. 2.9 were analyzed to express  $V_s$  as a mathematical function of the summation of all three stress directions, resulting in the following relationship (after Roesler, 1979):

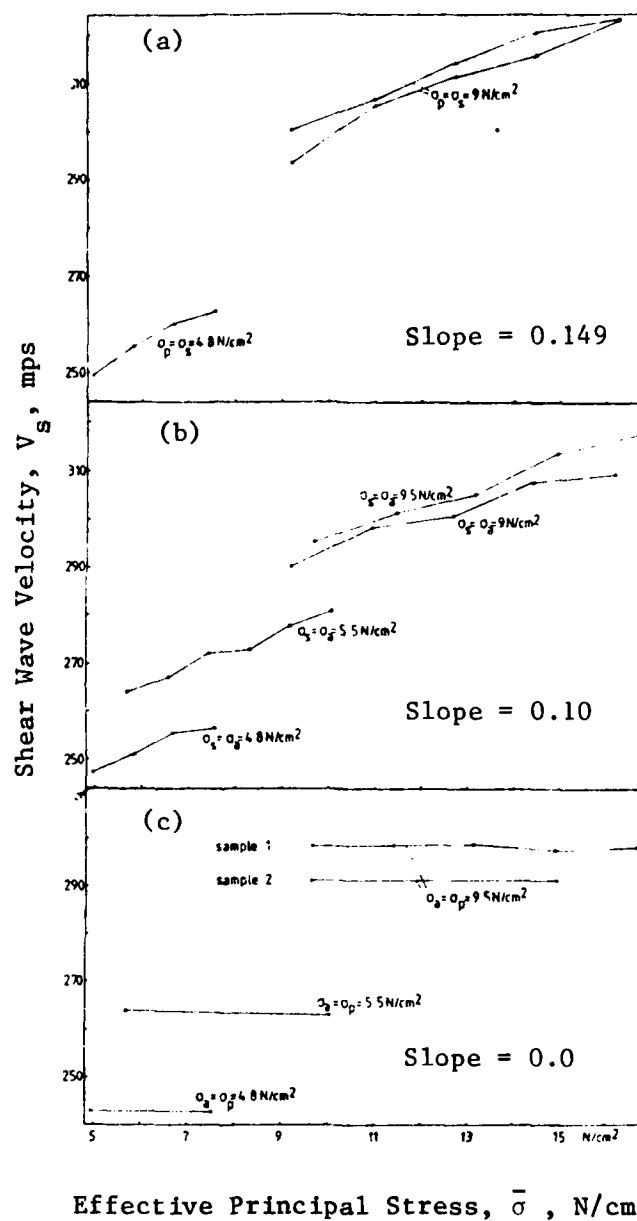


Fig. 2.9 - Variation of Shear Wave Velocity with Principal Stress in (a) Direction of Wave Propagation, (b) Direction of Particle Motion, and (c) Out-of-Plane Direction (from Roesler, 1979)

$$V_s \approx \bar{\sigma}_a^{0.149} \bar{\sigma}_b^{0.107} \bar{\sigma}_c^0 \quad (2.8)$$

where:  $V_s$  = shear wave velocity  
 $\bar{\sigma}_a$  = stress in direction of wave travel,  
 $\bar{\sigma}_b$  = stress in direction of particle motion, and  
 $\bar{\sigma}_c$  = stress in direction perpendicular to the  $\bar{\sigma}_a$  and  $\bar{\sigma}_b$   
direction.

These exponents were based on the average values of the measured  $V_s$  as each of the stress components was varied in turn. The difference between the mean values and the minimum and maximum values was approximately 23 percent. Roesler attributed most of this experimental scatter to stress history effects for the sand, though previous experiments have suggested that stress history has little effect on  $V_s$ .

It is interesting to note that the sum of the three stress exponents equals 0.256. This value is in agreement with the values obtained by a number of authors for isotropic confinement.

Roesler also experienced structural anisotropy in the sand sample due to the method of sand placement. The degree of anisotropy could be estimated in the sample by the reorientation of the transducer-generator arrangement. The electronics configuration was first placed parallel to the sand layering created during placement and  $V_s$  was measured. The electronics were then rotated so that they were aligned perpendicular to sand layering (in a

newly constructed sample), and the measurements were repeated. Structural anisotropy was, in this manner, studied along both directions.

## 2.5 SUMMARY

The general purpose of this study is to evaluate the effect of the three-dimensional state of stress on  $V_s$ . Although the effect of isotropic confinement has been thoroughly investigated, the effects of biaxial and especially triaxial confinement have had much less study devoted to them.

There are many types of testing devices to determine dynamic soil properties. These devices are generally categorized according to the method of analysis used to determine the properties. These methods are the resonance method (resonant column device), the pulse method (piezoelectric crystals, test chambers, and soil cubes), and cyclic methods (cyclic triaxial, cyclic simple shear, cyclic torsional shear, and multiaxial test devices). Each of these devices has its own advantages and disadvantages in determining dynamic soil properties. One of the most important considerations for any of these devices is the shearing strain amplitude to be used for testing.

Shear modulus (and so  $V_s$ ) can be greatly affected by a number of parameters. Those explicitly considered within the scope of this study include mean effective principal stress, strain amplitude, frequency of vibration, stress history, and shearing



stress. Generally, both  $V_p$  and  $V_s$  vary with the  $1/5$  to  $1/4$  power of  $\bar{\sigma}_0$ . For shearing strain amplitudes less than 0.001 percent,  $G_{\max}$  can be assumed to remain constant for sands. Similarly, frequencies of vibration between 200 and 2500 Hz can be assumed to have no effect on  $G$ . For sands, stress history can also be neglected, with  $V_s$  typically varying by less than a few percent for loading and unloading in the range of stresses from zero to 100 psi (0 to 689 kPa). The results of this study showed that  $V_s$  was dependent mainly on the principal stress in the directions of wave propagation and particle motion. Therefore the level of shear stress is unimportant as long as these two principal stresses are known.

The state of biaxial confinement becomes more involved for  $V_p$  and  $V_s$ . Compression wave velocity appears to be dependent only on the principal stress in the direction of wave propagation. Shear wave velocity, on the other hand, depends on  $\bar{\sigma}_0$ .

Based on Roesler's experimental results, shear wave velocity is a function of the stresses in the directions of wave propagation and particle motion, with  $V_s$  independent of the stress in the third, orthogonal direction.

For all the investigators cited in this chapter, it was impossible to construct a truly isotropic sample. Typically, wave velocity is different in the vertical and horizontal directions due to structural anisotropy.

## CHAPTER THREE

### SUMMARY OF TRIAXIAL TESTING DEVICE

#### 3.1 INTRODUCTION

Since the major element of this study was fabrication of a triaxial testing device and associated equipment, much of the effort in the study was directed toward the design, construction, and readiness of this system for testing. The triaxial cube is essentially a steel box with interior dimensions of 7 ft (2.1 m) on a side. The associated equipment for the testing device is used to:

1. place the sand in a uniform state within the cube,
2. pressurize the soil sample to a desired state of stress,
3. excite compression and shear waves in the sand,
4. monitor and digitally record these waveforms, and
5. monitor the stress and strain throughout the soil mass during testing.

This chapter briefly summarizes the design and development of the triaxial device and associated equipment. A full description of this system is presented in Appendix A which is taken directly from Kopperman, et al (1982) and is added to this report for completeness.

#### 3.2 STRUCTURE OF THE CUBE

The cube was planned to permit wave propagation testing through a soil sample 7 ft (2.1 m) on a side under various states of stress. A large soil sample was desired so that the central

portion of the soil cube would be relatively free from boundary effects. In addition, it was desired to exert a confining pressure on the sand of 50 psi (345 kPa) over any side. Finally the cube had to have a reasonable cost of fabrication.

A final design was decided upon which combined steel plate for the six faces of the cube with steel reinforcement of angles, I-beams, and plate sections. The sides of the cube were constructed of 0.357-in. (0.95 cm) thick, steel plate, approximately 7 ft (2.1 m) square. Each plate had steel angles of various sizes welded to it to resist bending of the thin steel plates used for the faces of the cube. To resist bending further, I-beams were welded longitudinally to each of the four side plates, forming four rings encircling the sides of the cube.

The cube was designed to be built in three separate sections (the bottom with four base legs, the four sides, and the top) which are then bolted together to form the completed structure. Typically only the top section would be removed as soil samples are constructed or removed from the cube. The base legs were added to the bottom section to permit access to the excitation port (see Section 3.3) on the bottom face. The cube was designed to be a free-standing structure which can be moved with the lifting lugs provided on the top section. Excitation ports were provided at the center of each face of the cube so that wave testing can be performed at a variety of locations.

### 3.3 LOADING SYSTEM

The loading system was designed to apply confining stresses on the soil mass which attempt to simulate those three-dimensional stresses which may exist in the field. To better simulate field conditions, non-rigid, stress controlled boundaries were used to confine the soil mass. As a result, the loading system utilized three membranes to apply confining stresses along the principal axes of the cube with one membrane along the top and one membrane along each of two adjacent sides of the cube. Each membrane is confined around its perimeter to prevent the tendency of the membrane to expand and burst. The confinement also isolates each membrane so that it only exerts stresses along its respective axis of the cube.

Several design options were considered as solutions for the loading membranes, which included: 1. using a currently manufactured product (either directly or modified as required), 2. having the membranes professionally constructed as per specifications, and 3. building the membranes ourselves as per specifications. Each of these options was examined based on the following design criteria: 1. maximum working pressure of 50 psi, 2. operational safety, 3. durability, 4. ease of handling, 5. simplicity of operation, and 6. cost of membranes. An additional consideration was that water rather than air would be used to pressurize the membranes. Water was selected because the incompressibility of water would make it safe to use. Further,

water had a better vertical pressure gradient than air when added to the sand forces. Finally, any possible leaks in the membranes could be discovered more easily if the membranes were filled with water.

Based on the design criteria, the decision was made to construct the membranes ourselves. Approximately 7 ft (2.1 m) square sheets of 0.063-in. (0.16 cm) thick, Butyl rubber was used to form the membranes. The Butyl sheets were cemented together and waterproofed with a lap sealant. Two inflow/outflow ports were installed in the membranes through which water would enter the membranes. A sheet of filter fabric was included so that the water pressure would be evenly distributed over the entire face of the soil cube lined by the membranes.

During initial testing of these membranes, leaks were discovered. It was eventually concluded that correction of the leakage would be too costly, either directly in dollars or indirectly in time. Therefore, the design options were reviewed and it was decided to use a currently manufactured product which would be modified as required for the cube. The best choice of the products manufactured appeared to be water pressure bags from Goodyear Aerospace Corporation. The water pressure bags were constructed of Nylon reinforced sheets of 0.063-in. (0.16 cm) thick rubber which were vulcanized together to form a single unit and were available in a variety of sizes which could sustain a working pressure of at least 40 psi (276 kPa). Two inflow/outflow ports

were included as required, although filter fabric could not be included because of the danger of melting during vulcanization. However, it was felt that a sheet of paper inside the membrane which was used in the vulcanization process, would serve a similar purpose as the filter fabric.

Hydraulic loading was used to pressurize the membranes for the working pressure range from 10 to 40 psi (6.9 to 276 kPa). Air pressure was transformed into water pressure at an air-water accumulator for each membrane. The pressure was controlled by a panel board which contained the accumulators and that independently regulated the pressure in each membrane.

### 3.4 EXCITATION SYSTEM

To generate shear and compression waves in the soil mass, a mechanism was needed to generate these waves at the soil boundary. Access to the soil was facilitated by fabrication of excitation ports (holes in the cube walls) at the center of three mutually perpendicular sides of the cube (the bottom and two adjacent sides). A source hammer was attached to the cube at each excitation port and was composed of an excitation anvil which contacts the soil, an external frame, an external adjustment screw to maintain contact between the soil and anvil, an internal frame, and a hand-held hammer to strike the anvil.

The type of wave generated (shear or compression) was determined by the direction of the hammer blow. Shear and

compression waves were generated by applying hammer blows parallel to the face of the cube or perpendicular to the face, respectively. The source hammer was in direct contact with the soil so that distinct waveforms were generated. The base of the anvil was knurled to improve the hammer-soil contact. The base of the anvil was chosen to be 3 in. (7.6 cm) square after an examination of the quality of waveform generated for various soil-hammer contact areas.

### 3.5 MONITORING AND RECORDING SYSTEM

The waveforms of the shear and compression waves propagating through the soil mass were monitored by a spacial array of three dimensional (3-D) accelerometer packages buried in the soil. Each 3-D accelerometer package was composed of three Endevco Isoshear accelerometers (sensitivity of 0.001 g) rigidly attached to a wooden block with a similar stiffness to the sand. One accelerometer was oriented along each of the principal axes of the cube. Three, 3-D accelerometers were aligned along each principal axis of the cube with the middle 3-D accelerometer being the same for each axis. The accelerometers were spaced 1.5 ft (0.46 m) apart and were placed far enough from the cube walls so that reflections did not interfere with the recorded wave. A pair of digital oscilloscopes were used to record the output of the three accelerometers which were oriented along the correct principal axis of the cube and which had the correct direction of

sensitivity to monitor the generated particle motion. Since each oscilloscope had only two channels with which to record, two oscilloscopes were required to record the output from three accelerometers, with the center accelerometer output repeated on both oscilloscopes as a reference. The oscilloscopes were electronically triggered when the hand-held hammer struck the anvil, initiating a voltage drop in a resistance-capacitance circuit which started the recording cycle of the oscilloscopes. Each waveform was recorded on a floppy diskette for storage and later recall.

### 3.6 STRESS MEASUREMENT

Stresses in the sand within the cube were monitored by three total pressure cells (stress cells) embedded in the sand and by a pressure gage measuring the water pressure in the membranes. The stress cells were included to insure that the pressure measured in the sand by the cells was the same as the pressure applied by the loading membranes. One stress cell, manufactured by Terra Technology, was used to monitor sand pressure along each principal axis of the cube. A control unit automatically converted the signal from the embedded stress cell into digital output of the desired units of the measurement.

### 3.7 STRAIN MEASUREMENT

Six pairs of soil strain gages were embedded in the sand during sample construction to monitor strains in the sample for



each state of stress. Soil strain gages from Bison Instruments were used, with each pair of gages consisting of two, free-floating, disc-shaped sensors embedded in the sand and separated by a known distance. Both 2-in. (5.1 cm) and 4-in. (10.2 cm) diameter sensors were used with separation distances of about two diameters between sensors. One sensor acted as a driving coil and the other as a receiving coil with the electro-magnetic coupling between the sensors related to the separation distance. Strains were calculated from the difference between initial and final spacing of the sensors for any pressure application. Two pairs of sensors were positioned to measure the strains along each principal axis of the cube.

### 3.8 TEST SAMPLE

For a uniform stress to exist throughout the soil sample, no shearing stresses in the form of friction can exist along the soil-cube boundaries. To model frictionless boundaries, two plastic sheets were placed between all six faces of the cube and the sand sample. A thin coat of WC-40 oil (a lubricant) was applied between the sheets of plastic.

The sand placement system was designed to fill the cube with sand of a uniform density over the full height of the sample. When compared with other methods, the raining of sand through the air was chosen because of the uniformity of placement obtainable with this method. For sands rained from heights greater than

2.5 ft (0.76 m), samples could be consistently obtained of a uniformly medium-dense nature (Marcusson and Bieganousky, 1977). Raining of the sand was also found by Marcusson and Beiganousky to yield variations in density of only  $\pm 0.5$  pcf for a constant height of fall.

An initial design for the raining system was centered around a sand hopper suspended over and moved across the top of the cube. The hopper was supported by a wood collar which was bolted around the top of the cube. Sand was poured into the hopper from a concrete bucket suspended from an overhead crane. A gate system was then opened in the bottom of the hopper to permit the sand to rain into the cube at a controlled rate. Screens were included in the base of the hopper to disperse the sand as it left the hopper. This version of sand raining was modified (see Appendix B) during the first filling of the cube because of difficulties with the gates of the hopper.

As the sand was rained into the cube, density measurements were taken at four elevations and at various horizontal locations in the sample. Plexiglas density containers were constructed with a volume of 0.05 cu ft (142 cu cm). These containers were placed on the sand surface during the filling operation, and sand was rained into them. When they were full, the containers were removed, and the sand contents weighed to determine densities. The average density of the sand was 96.6 pcf ( $1547 \text{ kg/m}^3$ ), and the

standard deviation was only about two percent of this value, or 1.9 pcf ( $30 \text{ kg/m}^3$ ).

### 3.9 SUMMARY

The triaxial testing device was designed and constructed to hold a soil sample measuring 7 ft (2.1 m) on a side. Loading membranes were purchased to apply a confining pressure of up to 40 psi (276 kPa) on the soil. A system to generate shear and compression waves was fabricated, and the electronics to monitor and record these waveforms was assembled, as was the equipment to measure the stresses and strains occurring in the soil in the cube. The triaxial testing device and associated equipment was completed with the addition of a method to rain the sand into the cube with a uniform density.

## CHAPTER FOUR

### ENGINEERING PROPERTIES OF SAND

#### 4.1 INTRODUCTION

The sand used in the initial wave propagation testing was selected in June, 1980 and was delivered to the Ferguson Structural Engineering Laboratory at the Balcones Research Center in August, 1980. The sand was selected because it is available locally in large quantities and because it fulfills several requirements as discussed in Section 4.2. Enough sand was initially ordered to form at least two separate cube samples. Since delivery to the Ferguson Laboratory, the sand has been located in an outdoor storage bin adjacent to the laboratory. The outdoor bin is not covered but has 3-ft (0.91 m) high concrete walls and a concrete floor.

#### 4.2 SAND CLASSIFICATION

The sand is a medium to fine, washed mortar sand with a specific gravity of 2.67. The sand classifies as SP in the Unified Soil Classification System. The results of grain size analyses performed on five different sand samples are shown in Fig. 4.1. Based on the average grain size curve, the sand has an effective grain size,  $D_{10}$ , of 0.28 mm and a uniformity coefficient,  $C_u$ , of 1.71. A soil with a uniformity coefficient smaller than 2.0 is considered uniform. Therefore, the average grain size curve shows

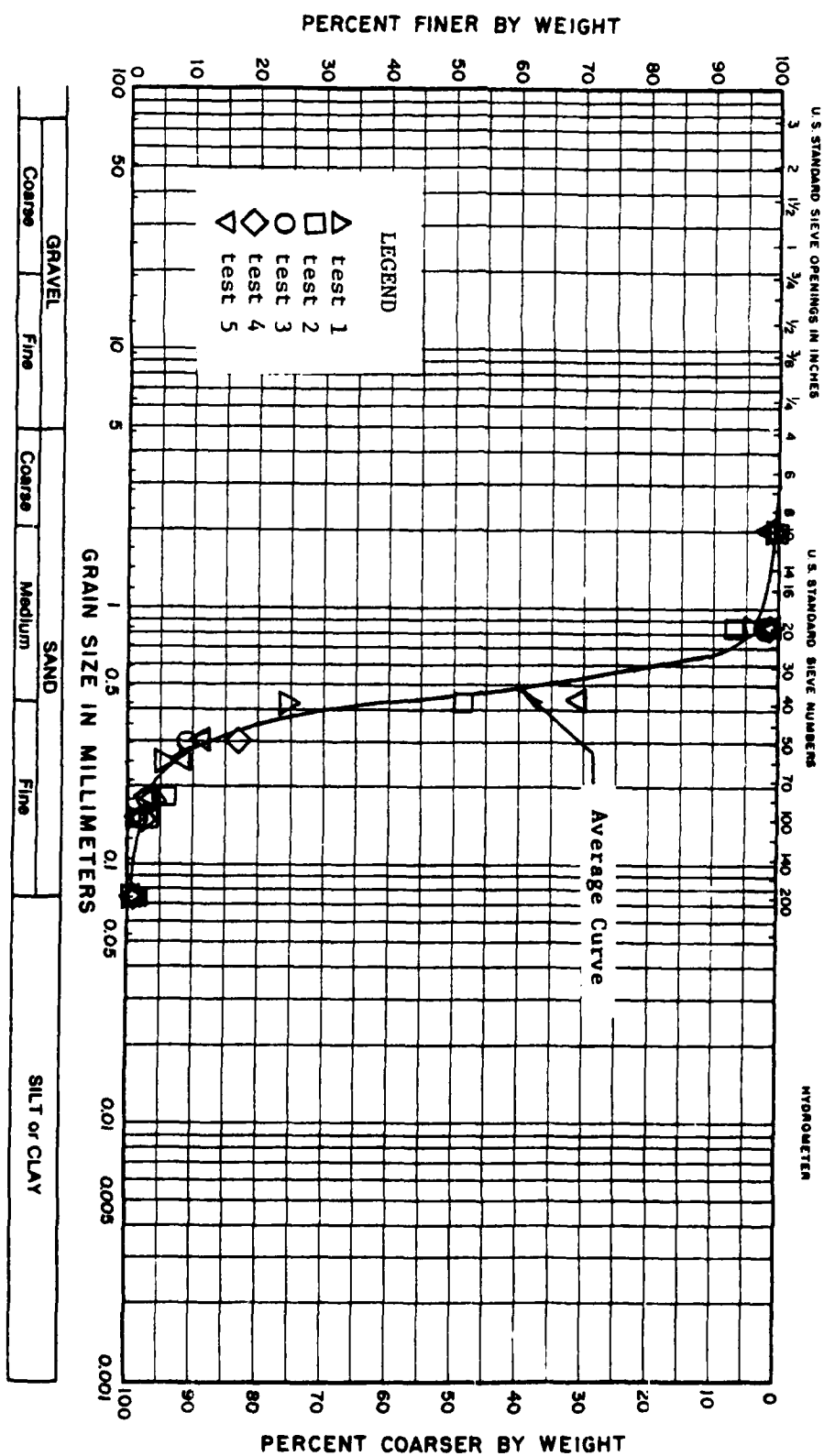


Fig. 4.1 - Grain Size Analysis of Washed Mortar Sand

the uniform grading of this mortar sand which makes the sand well-suited for the planned testing. Because of the relatively uniform size of the sand grains, the sand can be rained into the triaxial cube without significant segregation, an important consideration in this test series. The ability to rain the sand into the cube without significant segregation coupled with raining the sand from a minimum height of 3 ft (0.91 m) (Marcuson and Bieganousky, 1977) ensures not only uniform samples but also reproducible samples for each test.

Sand samples were taken from the storage bin from the time the sand was first delivered in August 1980 until the time the sand was used to fill the cube in June 1981. Since there is little scatter in the grain size curve, it can be concluded that there was no significant alteration of the original sand material with time. Therefore, the amount of fines can be expected to remain reasonably constant from one sample to the next. Sand fines are important to the quality of waves generated in the sand mass and to the density of the sand sample.

In the initial testing, the sand was tested in a dry state. The sand was dried in the sun to a water content of less than 0.5 percent. At this water content the sand did not tend to clump due to surface water on the sand grains. Small portions of sand were raked out in one-inch (2.54 cm) layers over a large area to dry in the heat of the sun. The sand was constantly raked and turned over to ensure complete drying. Dried sand was then placed

in piles and protected from moisture in the air by covering the piles with sheet plastic.

#### 4.3 DRAINED SHEARING STRENGTH

A series of consolidated drained (S-type) triaxial tests was performed with the sand to determine the effective strength parameters: friction angle,  $\bar{\phi}$ , and apparent cohesion,  $\bar{c}$ . The tests were performed with 1.5-in. (3.81-cm) diameter samples which had heights of 3 in. (7.62 cm). The sand was air dried prior to testing and had an average water content of 0.4 percent.

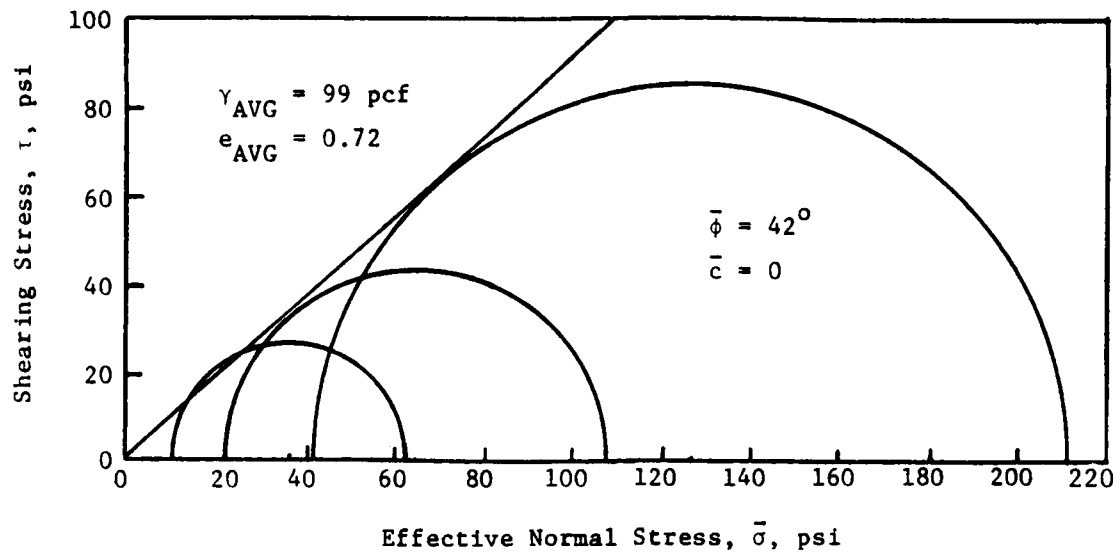
To determine the variation in  $\bar{\phi}$  and  $\bar{c}$  with density, the sand was tested at two different average dry densities, 83 and 99 pcf (1343 and 1602 kg/m<sup>3</sup>) which represents loose and dense states for the sand, respectively. To obtain a dense sample, sand was rained into the sample mold (on the base pedestal of the triaxial device) from a height of 3 ft (0.91 m). This was done by permitting the sand to fall freely through a 3-ft (0.91 m) long tube into the mold. Loose sand samples were constructed by pouring the sand through a funnel with the spout kept just above the top of the sample in the mold. The sand was poured slowly but continuously into the mold to minimize any tendency to segregate and layer. None of the samples were compacted after the sand was placed in the mold since the sand mass in the cube was not going to be compacted after it was placed. In fact, it was felt that the dense sand samples would most closely represent the sand after it was placed (by raining) in the cube.

Failure envelopes for the loose and dense sand samples are shown in Fig. 4.2. Based on the failure envelopes,  $\bar{\phi}$  increases as density increases, ranging from 37 degrees for the loose samples to 42 degrees for the dense samples. The value of  $\bar{c}$  can be considered essentially zero for both the loose and dense states.

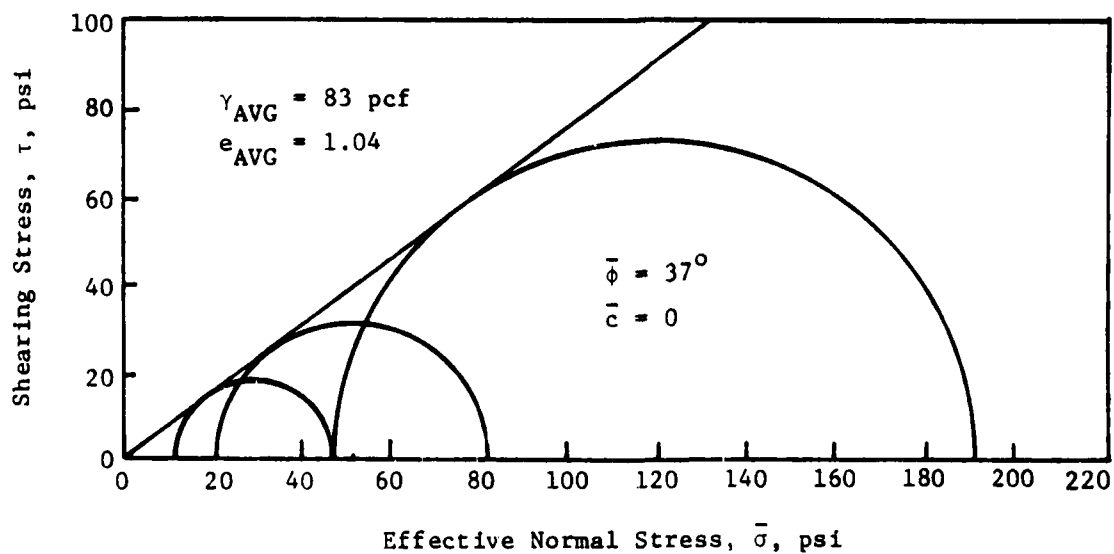
Once the failure envelopes were determined, the stress difference between the three principal stress axes was studied to determine if any combination of triaxial stresses would cause the sand to fail in the cube while being loaded. From this study (using a conservative value of 40 degrees for  $\bar{\phi}$ ) it was concluded that with a major and minor principal stress combination of 40 and 5 psi (275.6 and 34.5 kPa) respectively, the sand sample would fail. Therefore, this combination of principal stresses was excluded from testing.

The principal stress combination was limited further by the nonuniform vertical stresses in the sand. There is a variation of vertical stress with depth acting on the sand because of body forces within the cube. These body forces are due to the increase in total weight of sand with depth and the increase in total weight of water with depth in the loading membranes. The variation of vertical geostatic stress ranges from zero at the top of the sample to 4.52 psi (31.1 kPa) at the bottom with an average value of 2.3 psi (15.8 kPa) in the middle. It was desired to reduce the significance of body forces on wave propagation, and so it was decided to test only at confining pressures where the body forces





a. Dense Sand Sample



b. Loose Sand Sample

Fig. 4.2 - Failure Envelopes for Loose and Dense Sand Samples from Consolidated, Drained Triaxial Tests

at the middle of the sample were less than 25 percent of the applied pressure. With this approach, 10 psi (68.9 kPa) was selected as the minimum pressure at which any wave testing would be conducted. As a result, 10 psi and 40 psi (68.9 and 275.6 kPa) represent the minimum and maximum principal stresses in this study, with  $\bar{\sigma}_3$  being large enough to overshadow the body forces and with  $\bar{\sigma}_1 - \bar{\sigma}_3$  satisfying the stress difference requirements based on  $\bar{\phi}$ .

#### 4.4 ISOTROPIC DYNAMIC TESTING

Dynamic soil property tests were performed on the sand at the Soil Dynamic Laboratory at the University of Texas at Austin. Resonant column equipment was used to evaluate the shear modulus,  $G$ , shear wave velocity,  $V_s$ , and material damping ratio,  $D$ , of the sand, which are defined as,

$$G = \rho V_s^2 \quad (4.1)$$

$$D = \frac{\delta^2}{\sqrt{4\pi^2 + \delta^2}} \quad (4.2)$$

where:  $\rho$  = mass density of the sand, and

$\delta$  = log decrement determined from the free-vibration-decay-curve.

Isotropic confining pressures were maintained through resonant column testing with hydrostatic confining pressures ranging from 2.5 to 80 psi (17.2 to 551.2 kPa). Sand samples experienced

two-way cyclic loading, undergoing complete stress reversal. Both low-amplitude and intermediate-amplitude tests were used to evaluate  $V_s$ ,  $G$  and  $D$ . Low-amplitude tests are defined as those tests in which the single-amplitude shearing strain,  $\gamma$ , did not exceed 0.001 percent. Intermediate-amplitude tests are those tests in which shearing strains were in the range of 0.001 to about 0.01 percent.

The significance of low-amplitude testing is that dynamic soil properties are essentially constant in this strain range (Hardin and Drnevich, 1972a and b), and it is the strain range expected in the initial tests in the triaxial cube. At shearing strains above 0.001 percent, dynamic soil properties may be influenced by strain amplitude depending on several variables such as the soil type, strain amplitude, and confining pressure.

#### 4.4.1 Low-Amplitude Dynamic Properties

Three series of low-amplitude tests were performed to determine the effect of the effective mean principal stress,  $\bar{\sigma}_o$ , on  $V_s$ ,  $G$  and  $D$ . Different initial void ratios of 0.59, 0.70 and 0.76 were achieved in the different test series. In addition, the second and third test series included unloading pressure sequences to study the effect of overconsolidation and stress history on the dynamic properties. The second test series had one cycle of loading and unloading while the third test series included 2.5 load cycles (load-unload-reload-unload-reload).

The variation in the low-amplitude  $G$  with effective hydrostatic confining pressure is shown in Fig. 4.3. A linear relationship between  $\log G$  and  $\log \bar{\sigma}_o$  exists with the shear modulus increasing as confining pressure increases. In addition, the shear modulus decreases as void ratio increases at any confining pressure. However, the decrease in shear modulus with increasing void ratio does not significantly change the slope of the  $\log G - \log \bar{\sigma}_o$  relationship.

Based on low-amplitude resonant column tests, the shear modulus can be expressed in the form of (Hardin, 1978):

$$G_{\max} = \frac{A \text{ OCR}^k}{0.3 + 0.7e^2} P_a^{1-n} \bar{\sigma}_o^n \quad (4.3)$$

where:  $G_{\max}$  = shear modulus in psi,  
 $A$  = constant (dimensionless),  
 $\text{OCR}$  = overconsolidation ratio (dimensionless),  
 $k$  = factor based on Plasticity Index of soil (for sand,  $k = 0$ ),  
 $e$  = void ratio,  
 $P_a$  = atmospheric pressure in psi,  
 $\bar{\sigma}_o$  = mean effective confining pressure in psi, and  
 $n$  = slope of the  $\log G - \log \bar{\sigma}_o$  relationship.

Average values for  $A$  and  $n$  were determined for these tests and found to be 705 and 0.48, respectively. These values of  $A$  and  $n$  result in an average ratio of calculated shear modulus divided by

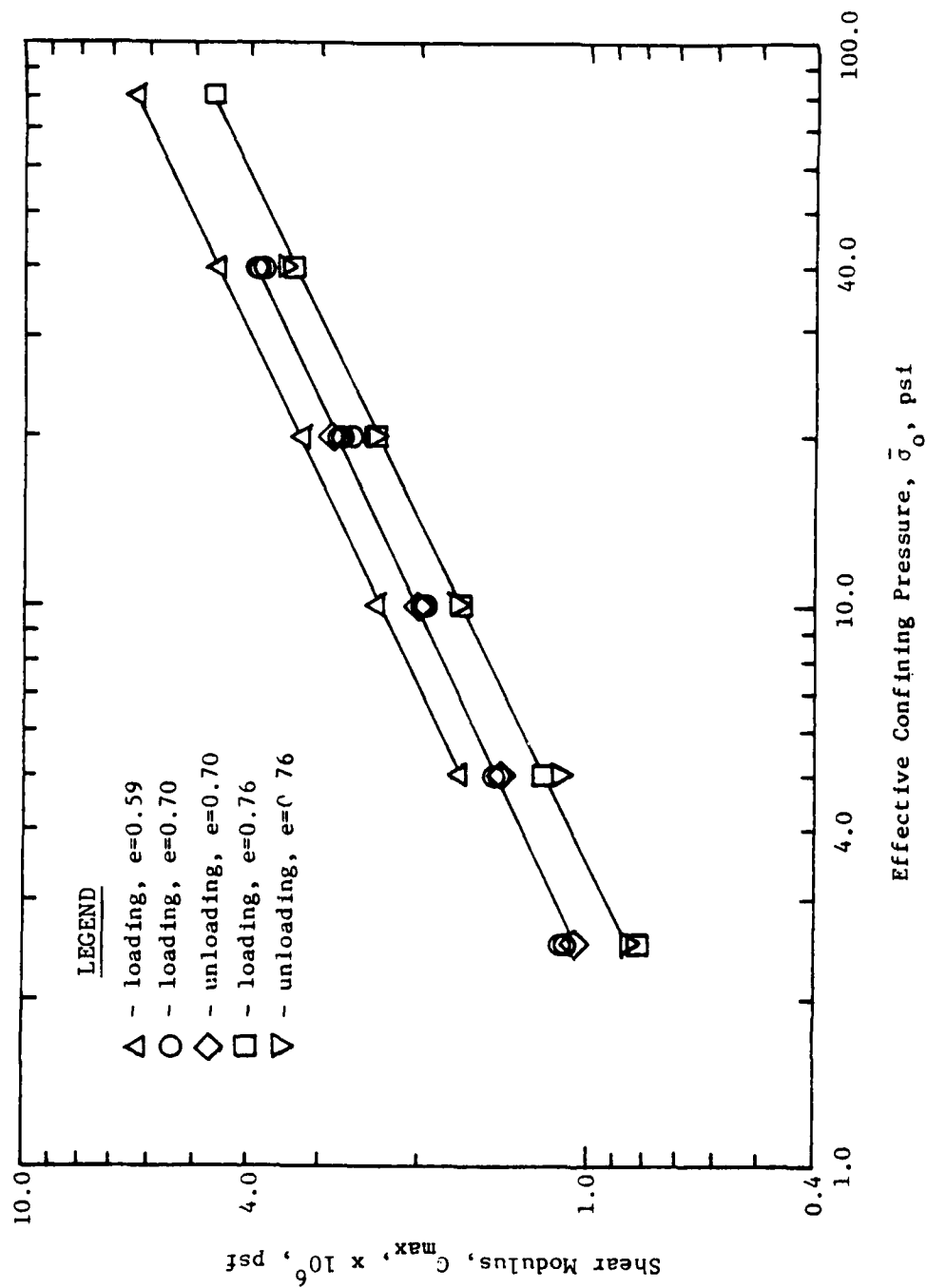


Fig. 4.3 - Variation in Low-Amplitude Shear Modulus with Effective Confining Pressure

measured shear modulus from the resonant column test for all the tests equal to 0.99 with a standard deviation of 0.05. A maximum deviation of  $\pm 11$  percent was found between the calculated and measured shear moduli. Therefore Eq. 4.3 can be used to predict the shear modulus (and hence shear wave velocity) of the sand in the triaxial cube when the loading is hydrostatic.

The unloading pressure sequence shown in Fig. 4.3 indicates that previous stress history (for stress-controlled boundaries) has little effect on the shear modulus and shear wave velocity of this sand and, for practical purposes, can be neglected. This behavior represents an important consideration in conducting the tests in the cube because it means that stress history can be ignored in performing the low-amplitude tests.

Shear wave velocity is related to shear modulus, as indicated by Eq. 4.1, by the one half power. The variation in  $V_s$  with effective hydrostatic confining pressure is shown in Fig. 4.4. A linear relationship also exists between  $\log V_s$  and  $\log \bar{\sigma}_o$  with the shear wave velocity increasing as confining pressure increases. Also, shear wave velocity decreases as void ratio increases at any confining pressure. As with the shear modulus, the decrease in shear wave velocity with increasing void ratio does not significantly change the slope of the  $\log V_s - \log \bar{\sigma}_o$  relationship.

The variation in low-amplitude material damping ratio with confining pressure is shown in Fig. 4.5 for the sand tested at all three void ratios. The results show that  $D$  tends to decrease

AD-A120 426

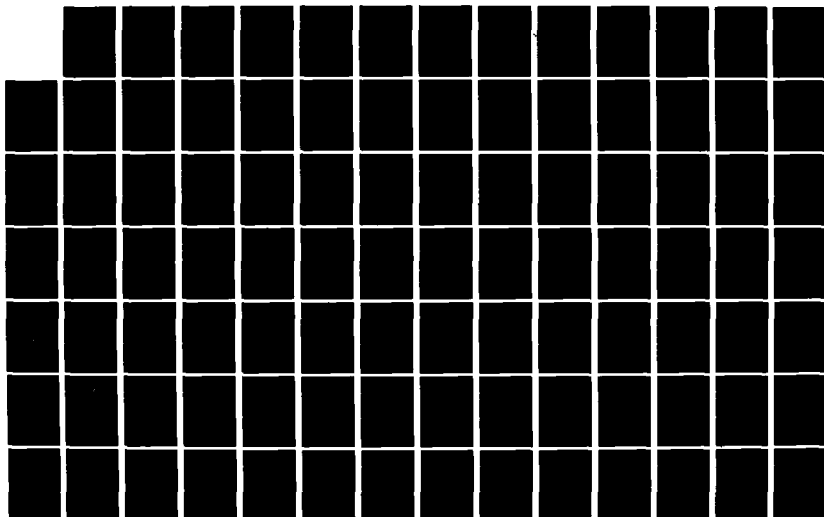
EFFECT OF STATE OF STRESS ON VELOCITY OF LOW-AMPLITUDE  
SHEAR WAVES PROPAG. (U) TEXAS UNIV AT AUSTIN  
GEOTECHNICAL ENGINEERING CENTER D P KNOX ET AL. MAR 82  
GR82-23 AFOSR-TR-82-0908 AFOSR-80-0031

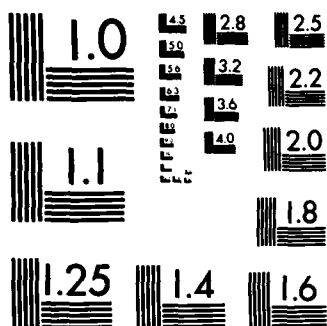
2/6

UNCLASSIFIED

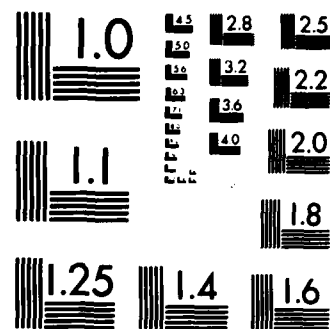
F/G 20/11

NL

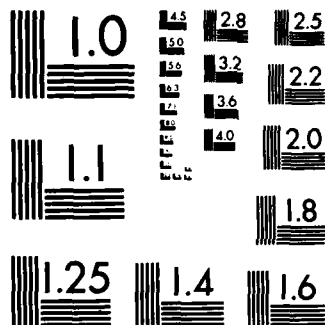




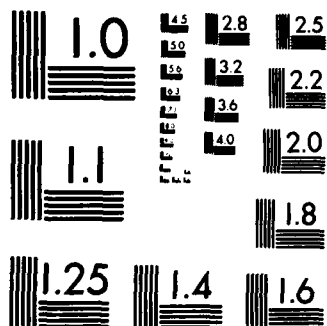
MICROCOPY RESOLUTION TEST CHART  
NATIONAL BUREAU OF STANDARDS-1963-A



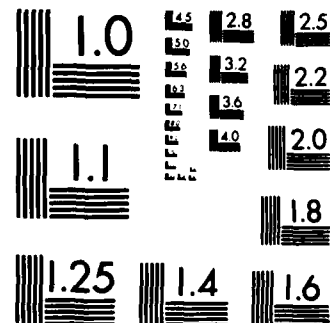
MICROCOPY RESOLUTION TEST CHART  
NATIONAL BUREAU OF STANDARDS-1963-A



MICROCOPY RESOLUTION TEST CHART  
NATIONAL BUREAU OF STANDARDS-1963-A



MICROCOPY RESOLUTION TEST CHART  
NATIONAL BUREAU OF STANDARDS-1963-A



MICROCOPY RESOLUTION TEST CHART  
NATIONAL BUREAU OF STANDARDS-1963-A



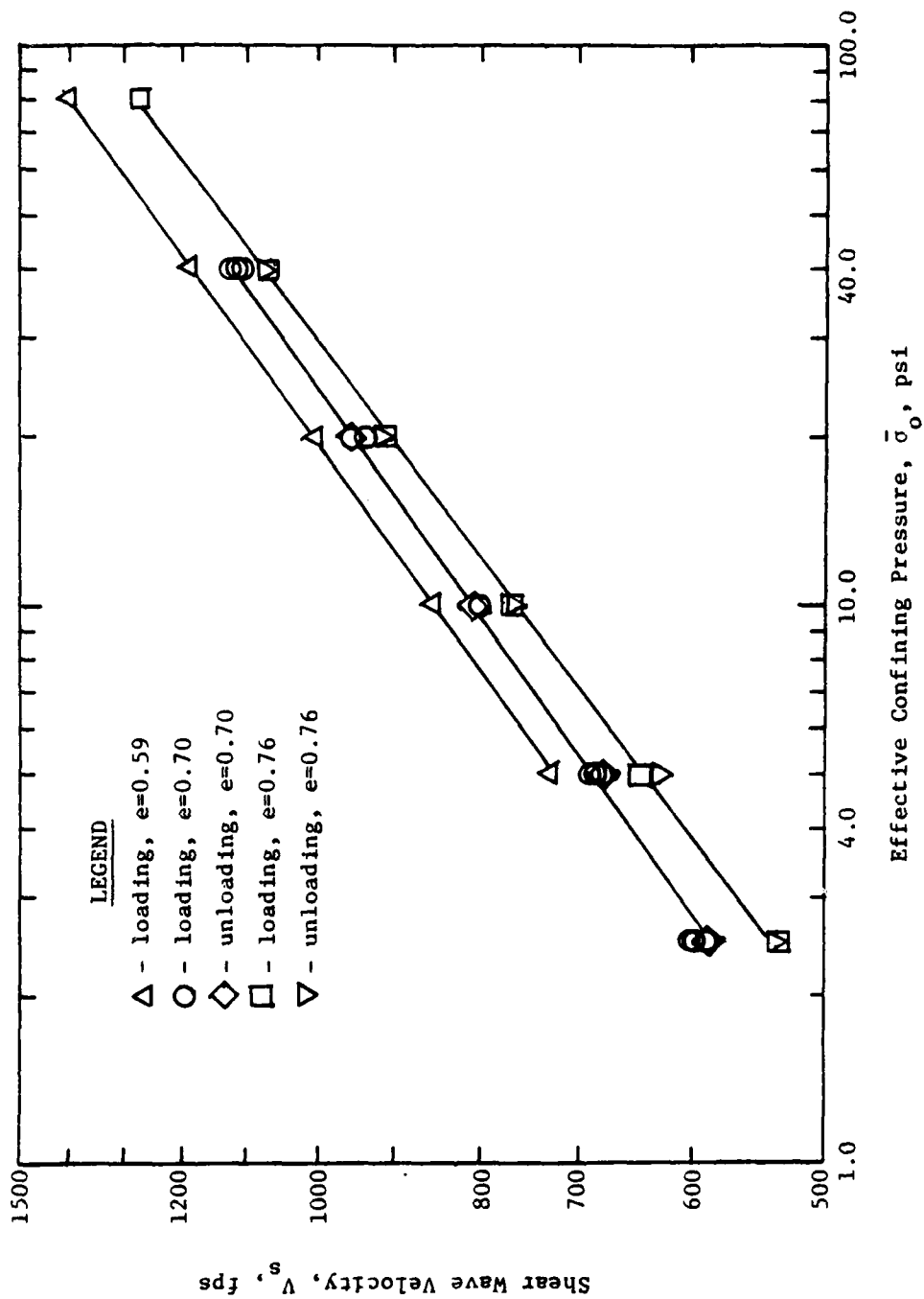


Fig. 4.4 - Variation in Low-Amplitude Shear Wave Velocity with Effective Confining Pressure

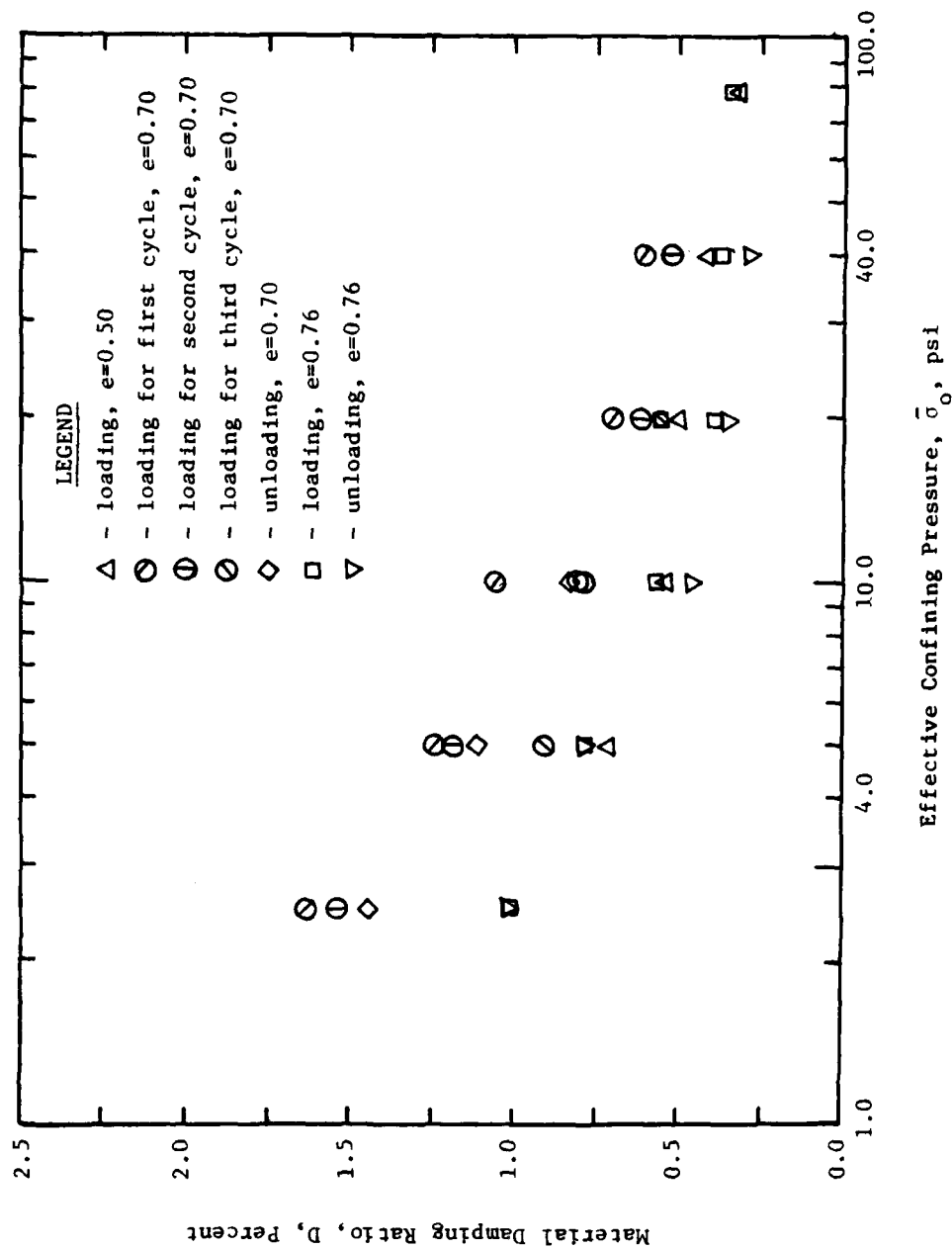


Fig. 4.5 - Variation in Low-Amplitude Material Damping Ratio with Effective Confining Pressure

as confining pressure increases, with the rate of decrease becoming less significant as confining pressure increases. Significant scatter in the damping data exists, and because of this scatter, the effect of void ratio upon damping of the sand at any confining pressure is not obvious. Hardin and Drnevich (1972a) indicate that damping ratio decreases as void ratio increases for undisturbed natural soils. However this trend is not shown by this sand. As a result, only a range for  $D$  can be given to compare with the results from the cube. Attention may also have to be paid to the effect of stress history on material damping of the sand.

Although the value of  $D$  at any void ratio is similar for both loading and unloading, as shown in Fig. 4.5, the large scatter in the data ( $\pm 30$  percent typical,  $\pm 40$  percent maximum) masks any lesser variation of  $D$  with stress history. Nevertheless, the resonant column data indicate that  $D$  varies, on the average, from 1.3 percent at low effective confining pressure to 0.3 percent at higher effective confining pressures.

#### 4.4.2 Intermediate-Amplitude Dynamic Properties

One intermediate-strain-amplitude test series was performed to determine the effect of shearing strain amplitude on the shear modulus and material damping of the sand in this strain range. This test series was performed at the same set of confining pressures as the low-amplitude tests for the sample with an initial void ratio of 0.76 and was performed on the loading sequence with this sample.

The variation in shear modulus with shearing strain amplitude at each confining pressure is shown in Fig. 4.6. As seen in the figure, shear modulus decreases slightly with increasing shearing strains for confining pressures less than about 40 psi (275.6 kPa). For confining pressures of 40 psi (275.6 kPa) or above, shear modulus is essentially constant over the magnitude of shearing strains tested. However, for testing purposes in the triaxial cube, shear modulus can be considered constant unless  $\gamma$  exceeds 0.003 percent. As a result, shear wave velocity can also be considered constant up to this strain amplitude.

The variation in material damping ratio with shearing strain amplitude is shown in Fig. 4.7 at each of the confining pressures tested. The figure shows that damping ratio increases with increasing strain amplitude and for shearing strains above about 0.001 percent. This variation is largest at the lowest confining pressure. These results show that for testing in the cube above a strain of 0.001 percent, care must be taken in analyzing the data to account properly for the effect of strain amplitude.

#### 4.5 SUMMARY

The sand used in this stage of wave propagation testing is a uniform, medium to fine, washed mortar sand which classifies as SP in the Unified Soil Classification System. Because of the uniformity of the sand, no segregation should occur as the sand is rained into the cube, and, as such, a more uniform and reproducible

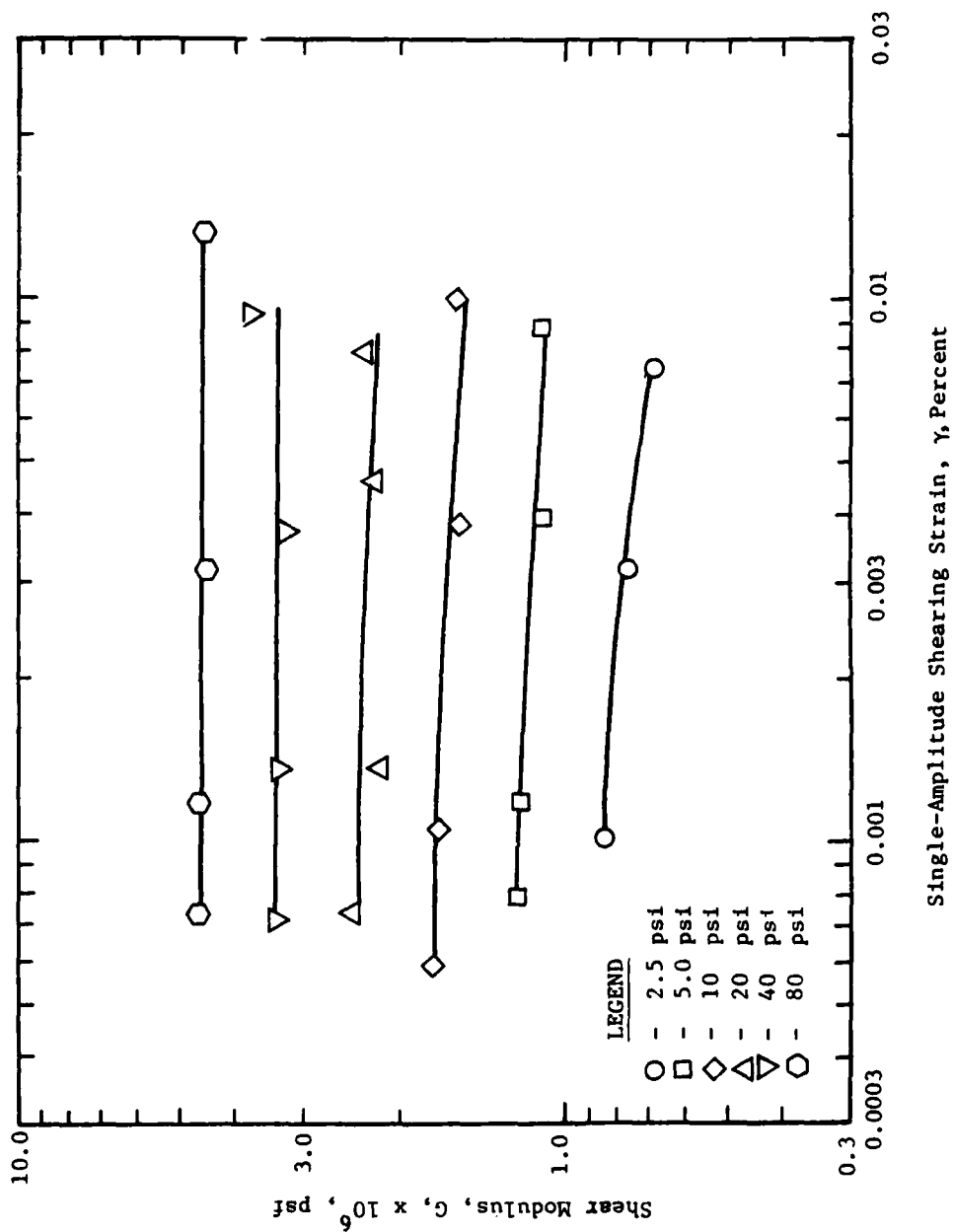


Fig. 4.6 - Variation in Shear Modulus with Shearing Strain

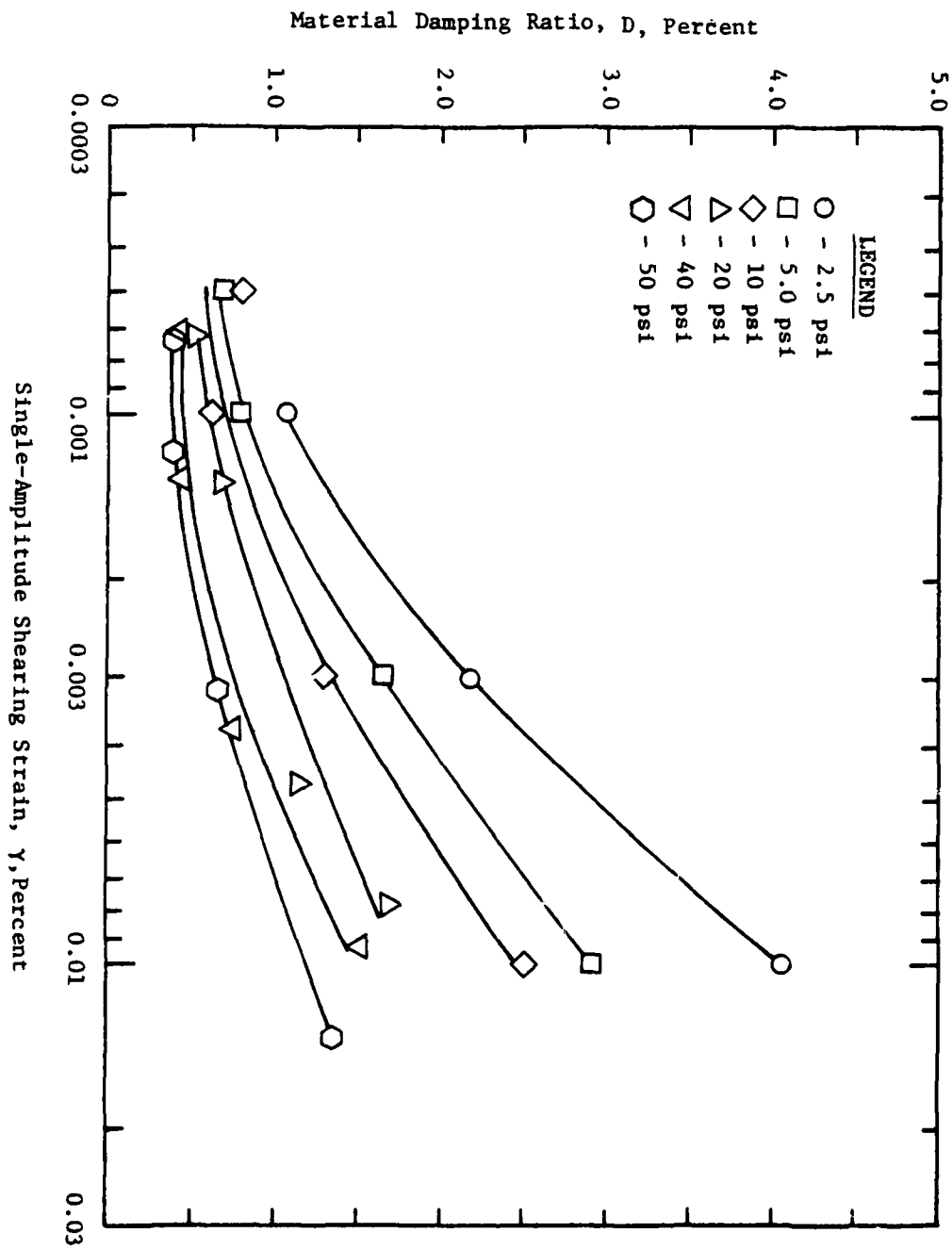


Fig. 4.7 - Variation in Material Damping Ratio with Shearing Strain

sand sample is possible from test to test. The sand was tested in an air-dried state with a water content of less than 0.5 percent.

Results from consolidated drained triaxial tests show that  $\bar{\phi}$  for the sand varies with the density, ranging from 35 degrees in a loose state (83 pcf, 1343 kg/m<sup>3</sup>) to 42 degrees in a dense state (99 pcf, 1602 kg/m<sup>3</sup>). The value of  $\bar{c}$  was essentially zero for any density. Because of the limitation of the maximum allowable stress difference (based on the failure envelope with a  $\bar{\phi}$  of 40 degrees) and to reduce the mathematical significance of body forces acting on the sample, the applied pressures within the cube were selected to range from 10 to 40 psi (68.9 to 275.6 kPa).

Both low-amplitude and intermediate-amplitude resonant column tests were performed on sand samples with an effective hydrostatic pressure varying from 2.5 to 80 psi (17.2 to 551.2 kPa). Low-amplitude tests with shearing strains less than 0.001 percent were performed at three different void ratios. Results from the low-amplitude tests show that a linear relationship exists for  $\log G$  (and therefore  $\log V_s$ ) and  $\log \bar{\sigma}_o$ , with the shear modulus (and shear wave velocity) increasing as the confining pressure increases. Shear modulus (and shear wave velocity) decreases as void ratio increases, although this decrease does not change the slope of the  $\log G - \log \bar{\sigma}_o$  (or  $\log V_s - \log \bar{\sigma}_o$ ) relationship. Previous stress history had no significant effect on the value of shear modulus (or shear wave velocity) for these tests. Material damping ratio decreases as effective confining pressure increases. The range of

average D varies from 1.3 percent at low confining pressures to 0.3 percent at high confining pressures, with  $\pm$  30 percent scatter typical.

An intermediate-amplitude resonant column test was performed on one sample for a pressure range of from 2.5 to 80 psi (17.2 to 551.2 kPa). Results show that the shear modulus decreases slightly with increasing shearing strains above 0.003 percent for confining pressures less than 40 psi (275.6 kPa). For testing purposes in the triaxial cube, the shear modulus (and shear wave velocity) can be considered constant at any pressure unless the shearing strain exceeds 0.003 percent. Material damping ratio decreases as shearing strain increases for strains above 0.001 percent, with the variation largest at the lower confining pressures. For shearing strains greater than 0.001 percent, care must be taken to account for strain amplitude effects on D.



## CHAPTER FIVE

## SUMMARY OF TESTING PROGRAM AND PROCEDURES

## 5.1 INTRODUCTION

Initial testing in this study consisted of the measurement of velocity and attenuation characteristics of compression and shear waves. The waves were propagated through a sample of dry sand of medium density. The following sections contain a summary of the testing program and procedures used to prepare the sand sample. A full description is presented in Appendix B, which is taken directly from Kopperman et al (1982) and is added for completeness.

## 5.2 TESTING PROGRAM

The testing program was composed of three sequences of pressure variation. Testing was first performed for a series of isotropic states of stress to determine the relationship between shear wave velocity and mean effective principal stress,  $\bar{\sigma}_0$ . These tests were followed by a second series of tests with a constant  $\bar{\sigma}_0$  in which both biaxial and triaxial states of stress were included. This series was designed to examine the relationship of shear wave velocity with shearing stress for a constant  $\bar{\sigma}_0$ . Hardin and Black (1966) concluded that shear wave velocity was proportional only to  $\bar{\sigma}_0$ , and independent of shearing stress.

A final series of biaxial and triaxial tests were performed in which the mean effective principal stress was varied. This series was performed to determine the relationship of wave velocity to the principal stresses along each axis of the cube. A complete list of the tests performed for these three sequences of pressure variation is given in Table B.1 and is shown graphically with time in Fig. B.1.

### 5.3 TESTING PROCEDURES

Preparation for testing began with construction of the sand sample. After two loading membranes were suspended on adjacent sides of the cube, oiled sheets of plastic were placed on the four sides and bottom of the cube. The purpose of these oiled sheets was to eliminate friction between the sand and walls of the cube so that no shearing stresses would develop.

With the interior of the cube lined, the raining of the sand began. After being dried in the sun to a suitable water content, the sand was screened and brought to the cube. Because of problems with the intended method of raining, it was decided to rain the sand from a concrete bucket with a limited rate of flow of sand. Based on sand density measurements, the average density of the sand sample was 96.6 pcf ( $1547 \text{ kg/m}^3$ ) with a standard deviation of 1.9 pcf ( $30 \text{ kg/m}^3$ ). Hence, the sand sample constructed with the modified raining system was quite uniform.

Construction of the sample was halted at five predetermined elevations so that electronics could be implanted in the sand sample. A spring-string system was used to indicate elevation of the sample within the cube. Electronics placed in the sample included 3-D accelerometer blocks, total pressure cells (stress cells), and strain sensors. Seven accelerometer blocks were situated in a spacial array in the sample so that three blocks were oriented along each principal stress direction of the cube. Careful measurements were taken of the distances between these blocks.

Three stress cells were placed on the horizontal plane at the mid-height of the cube. One cell was oriented along each principal axis to measure the stress from the corresponding loading membrane. Care was taken in the placement of these cells but significant scatter in the data was expected nonetheless because of the limited number of measurements (Hadala, 1967).

Six pairs of soil strain sensors were used to measure the strain in the sand along the principal axes of the cube. Two pairs of sensor discs were carefully oriented along each axis, one pair of sensors placed near the respective loading membrane and the other pair near the opposite face of the cube. The sensors have to be placed with certain surfaces of the discs facing each other. Because of equipment repair delays, these surfaces could not be determined when the sand was placed. Therefore, only four of the six pairs of sensors were later found to be operational.

While sand was being rained into the cube, the water in the two side membranes was being kept at an elevation approximately one in. (2.5 cm) above the level of the sand. The purpose of keeping the water elevation above the height of sand was to prevent the membranes from pinching together which might result in a nonuniform pressure over the face of the sand. If the pressures were not uniform, an unknown (and undetected) stress distribution would be present in the sand.

Raining of the sand was stopped with the sand height one in. (2.5 cm) below the top of the cube to allow room for placement of the top membrane. After oiled sheets were placed on the sand, the top membrane was laid on the sand. The cube was sealed with the bolting of the top face to the sides. Water was added to the top membrane to fill any air voids between the surface of the sand and top of the cube.

With the addition of the top, wave testing could then begin. Each membrane was connected to a separate pressure outlet in the panel board to permit independent control of the stresses along each axis of the cube. Testing proceeded through the various states of stress shown in Table B.1.

At each test pressure, nine sets of waveforms of shear and compression waves were recorded. For each principal axis of wave propagation, one compression and two mutually perpendicular shear waves were generated. Reversals were also recorded for each

shear wave to aid in identification of the shear wave arrival. Each set of waveforms consisted of the output from the three accelerometers oriented along the direction of wave propagation and with the correct direction of particle motion.

Each set of waveforms was generated by striking a source hammer in contact with the soil boundary. The direction of hit determined the direction of particle motion and the type of wave generated. All waveform sets were recorded by a pair of two-channel digital oscilloscopes which stored the data on magnetic storage diskettes. Output from the middle accelerometer was recorded on both oscilloscopes as a reference. Appendices C, D, and E show typical sets of shear wave traces for isotropic, biaxial, and triaxial states of stress, respectively. Data reduction is discussed in Chapter 6.

In addition, stress and strain data were collected, and an estimation was made as to the water volume change in the membranes as the pressure was varied from test to test.

Pressures were applied along the axes of the cube so that the planned state of stress occurred on the horizontal plane at the mid-height of the sample. This condition was attained with corrections made for overburden pressure of the sand, hydraulic gradient of the water, and differing piezometric elevations between the inlet ports on the membranes and the pressure controls of the panel board.

Unfortunately, problems occurred with the accumulation of stress and strain data. Delays in equipment repair allowed strain data to only be gathered during the second half of testing. Although reliable stress-strain properties cannot, therefore, be predicted, absolute strains measured by the strain sensors over the full pressure range were small (less than 0.3 percent).

A crude estimate of strain was made by estimating the water volume change in each membrane as the pressure was varied from test to test. Based on these estimations, there appeared to be an initial seating of the membranes as any air voids were filled between the sand and walls of the cube. After the initial seating, the stress-strain relationship was fairly linear with no evidence of stress history. Values of Young's Modulus, determined from the initial slopes of the stress-strain curves, ranged from 16,000 to 18,000 psi (110,000 to 124,000 kPa).

Stress cell measurements were subject to large scatter. The large scatter is inherent with these stress cells because of sand arching effects, compressibility of the sand, and non-linearity of the strain gages in the stress cells. Results from these cells showed that there was a linear variation in the stress-strain relationship after the initial seating. There was no direct correspondence between the stress applied by the loading membranes and the pressure read by the stress cell along each axis. Therefore, calibration curves should be made for future reference.

#### 5.4 SUMMARY

Testing was performed with the triaxial testing device for three sequences of pressure variation, including isotropic confinement, biaxial and triaxial confinement with a constant  $\bar{\sigma}_0$ , and biaxial and triaxial confinement with a variable  $\bar{\sigma}_0$ . Dry sand was used in this initial stage of testing and, therefore, the sand sample was constructed by a raining process. The raining process was interrupted to permit placement of accelerometers, stress cells, and strain sensors and to allow density measurements to be performed. The density tests indicated that the sample was quite uniform with an average density of 96.6 pcf (1547 kg/m<sup>3</sup>).

Problems with strain sensor equipment and data scatter with the stress cells prevented an in-depth investigation of the stress-strain properties of the sand. Based on the analyses made, stress and strain variation was almost linear, and there was no effect of stress history. An initial seating strain was observed as the membranes were initially loaded.

Dynamic testing was conducted at each test pressure. Shear and compression waves were generated along each principal axis. The method of analyzing the data is discussed in Chapter 6, and the results for isotropic, biaxial, and triaxial testing are presented in Chapters 6, 7, and 8, respectively.

## CHAPTER SIX

### ISOTROPIC CONFINEMENT

#### 6.1 INTRODUCTION

Wave propagation testing was first performed for the case of isotropic confinement ( $\sigma_1 = \sigma_2 = \sigma_3$ ) to understand the effect of an isotropic state of stress on shear wave velocity in the triaxial cube and to form a reference with which to compare results from anisotropic confinement. During the course of the testing program, ten tests were conducted with isotropic confinement. The shear wave velocity from these tests was examined: 1. to evaluate the effect of state of stress on  $V_s$ , 2. to compare these experimental results with other available data for isotropic confinement, and 3. to develop an understanding of the structural anisotropy of the sand sample. In this chapter, the characteristics of shear waves are briefly examined, and the variation of  $V_s$  with isotropic confinement and structural anisotropy are summarized.

#### 6.2 SIMPLIFIED CONDITION OF ISOTROPIC CONFINEMENT

Although the idealized condition of isotropic confinement was preferred, it was impossible to attain because of inherent pressure gradients in the triaxial cube. Horizontal and vertical pressure variations with depth resulted in a truly isotropic condition on only the horizontal plane at the mid-height of the



cube sample. Therefore, at only this level did the desired stresses exist. However, the pressure variations were relatively small and, therefore, were ignored in the data analysis.

Horizontal and vertical stresses within the sample increased with increasing depth in the sand. Vertical stress varied due to the increase in total weight of sand with increasing depth. Horizontal stress increased with depth because of the increase in total weight of water contained in the lateral membranes pressurizing the sand. Both of these pressure variations were a linear function of depth in the cube.

To account for the pressure variation in the cube and to have the horizontal plane in the middle of the cube subjected to a truly isotropic state of stress, the pressure set on the pressure gage was not the actual isotropic confining pressure. The vertical pressure in the top membrane was set on the pressure gage at 0.2 psi (1.4 kPa) less than the desired isotropic confining pressure at the center of the sample. This value of 0.2 psi resulted from a 2.4 psi (16.5 kPa) increase in pressure due to the weight of sand above the center and the water in the top membrane (3.5 ft (1.07 m) depth to center times 97 pcf ( $1554 \text{ kg/m}^3$ ) for sand times  $1/144 \text{ in.}^2/\text{ft}^2$  ( $0.00981 \text{ kPa/kg/m}^2$ ) + 0.083 ft (0.025 m)  $\text{H}_2\text{O}$  in membrane times 62.4 pcf ( $1000 \text{ kg/m}^3$ ) for  $\text{H}_2\text{O}$  times  $1/144 \text{ in.}^2/\text{ft}^2$  ( $0.00981 \text{ kPa/kg/m}^2$ ) = 2.4 psi (16.5 kPa)), and a 2.2 psi (15.2 kPa) decrease in pressure from the head loss because of the height difference between the level of air-water interface at the pressure board and inlet port

on top of the cube ( $0.036 \text{ lb/in.}^3$  ( $994 \text{ kg/m}^3$ ) unit weight of  $\text{H}_2\text{O}$  times 5 ft (1.53 m) head loss times 12 in./ft ( $0.00981 \text{ kPa/kg/m}^2$ ) = 2.2 psi (15.1 kPa)). The weight of the top membrane itself was negligible and was, therefore, ignored.

The horizontal pressure in both side membranes was set at the pressure gage at 0.9 psi (6.2 kPa) greater than the desired isotropic confining pressure at the center of the sample. This value of 0.9 psi resulted from a 1.3 psi (9.0 kPa) reduction in measured pressure to account for the weight of water in the side membranes (3.0 ft (0.92 m) of  $\text{H}_2\text{O}$  (the top six inches in the membrane contained air) times 62.4 pcf ( $1000 \text{ kg/m}^3$ ) for  $\text{H}_2\text{O}$  times  $1/144 \text{ in.}^2/\text{ft}$  ( $0.00981 \text{ kPa/kg/m}^2$ ) = 1.3 psi (9.0 kPa)), and a 2.2 psi (15.2 kPa) increase in pressure to account for head losses from the pressure gage to the inflow ports in the cube.

No attempt was made to correct  $V_s$  for these pressure gradients within the cube sample. Since all testing was performed at confining pressures from 10 psi to 40 psi (68.9 to 275.6 kPa) (measured at the center of the cube), the absolute variation in the vertical stress between the top and bottom accelerometers was 2.0 psi (13.8 kPa). This variation in pressure between accelerometers amounts to a  $\pm 10$  percent variation for a confining pressure of 10 psi (68.9 kPa) and a  $\pm 2.5$  percent variation for a confining pressure of 40 psi (275.6 kPa). The maximum horizontal pressure variation also occurred between the top and bottom vertical accelerometers and was equal to 1.3 psi (9.0 kPa). This horizontal

variation in pressure between the top and bottom accelerometers amounts to a  $\pm 7$  percent variation for a confining pressure of 10 psi (68.9 kPa) and a  $\pm 1.6$  percent variation for a 40 psi (275.6 kPa) confining pressure.

The variation in pressure between the top and bottom accelerometers was linear and was less than or equal to  $\pm 10$  percent of the confining pressure for all testing performed in this study. For the other five, 3-D accelerometers placed on the horizontal mid-height plane, a truly isotropic condition was assumed to exist. This assumption was based on the premise that the horizontal pressure was not a function of distance from the loading membranes but was continuous across the entire sample. The premise of a continuous pressure means that no shearing stresses existed on the sides of the cube without the loading membranes.

### 6.3 DESCRIPTION OF SHEAR WAVES

At each test pressure, six different shear waves were generated and recorded. The six different shear waves were based on directions of wave propagation and particle motion. Two directions of particle motion (polarization) were possible for each of the three directions of wave propagation. Each S-wave record was examined to identify travel times, wave amplitudes, and predominant frequencies.

### 6.3.1 Nomenclature

The triaxial cube was oriented so that the hammer in the bottom face generated a shear wave propagating in the top-bottom direction, and the two hammers in the sides generated waves propagating in the east-west and north-south directions. Wave identification was, therefore, arranged so that wave propagation and particle motion directions would correspond to these directions or axes of the cube. The six different shear waves were then designated using a nomenclature in which the first two symbols denote the direction of wave propagation and the second two symbols denote the direction of wave particle motion. For instance, for a shear wave propagating in the top-bottom (vertical) direction, particle motion could be in the east-west or north-south direction. These waves would be designated by the symbols  $S_{TB/EW}$  and  $S_{TB/NS}$ , respectively. Similarly, the other waves are represented by  $S_{NS/TB}$ ,  $S_{NS/EW}$ ,  $S_{EW/TB}$ , and  $S_{EW/NS}$ . A description of each wave is given in Table 6.1.

Wave reversals were also recorded for each shear wave. Reversed shear waves were generated with an impulse applied in a direction opposite to the impulse direction used to generate the "non-reversed" wave. These two waves, therefore, exhibit a reversal in the polarity of particle motion for the initial shear wave arrival. Because of the reversed polarity, recording a shear wave and its reversal aids in identification of the initial S-wave arrival (Schwartz and Musser, 1972). Initial-arrival identification becomes easier because the accelerometer output would be positive

TABLE 6.1

Nomenclature Used to Identify the Six  
Different Shear Waves

Wave Symbol*	Direction of Wave Propagation	Direction of Particle Motion
(1)	(2)	(3)
$S_{TB/NS}$	top-bottom	north-south
$S_{TB/EW}$	top-bottom	east-west
$S_{NS/TB}$	north-south	top-bottom
$S_{NS/EW}$	north-south	east-west
$S_{EW/TB}$	east-west	top-bottom
$S_{EW/NS}$	east-west	north-south

\* See Figure 6.12 showing the shear wave planes of motion.

for an initial upward particle motion and negative for an initial downward particle motion. This reversed polarity of the initial shear wave arrival (denoted by the "S" in the figure) for reversed impulses is illustrated in Fig. 6.1.

Reversed shear waves are different from non-reversed shear waves only in the fact that they have opposite polarity of particle motion. Relative wave features involving time and amplitude for the reversed shear wave correspond to the same features for the non-reversed shear wave. Therefore, all shear waves are designated by the symbols shown in Table 6.1 with no regard given to the polarity of particle motion.

#### 6.4.2 Shear Wave Records

Each wave record was examined to identify and quantify the following five features: 1. the time of the initial shear wave arrival; 2. the time of the first trough (which is one quarter of a cycle after the initial arrival); 3. the amplitude of this first trough; 4. the time of the first peak (which is three quarters of a cycle after the initial arrival); and 5. the amplitude of the first peak. Each shear wave was recorded by three accelerometers situated along the direction of propagation. Each test record, therefore, consisted of three waveforms, and three sets of the five wave features described above had to be identified. The sets of time and amplitude features for a typical test record are shown in Fig. 6.2. In this figure, the letter t or A

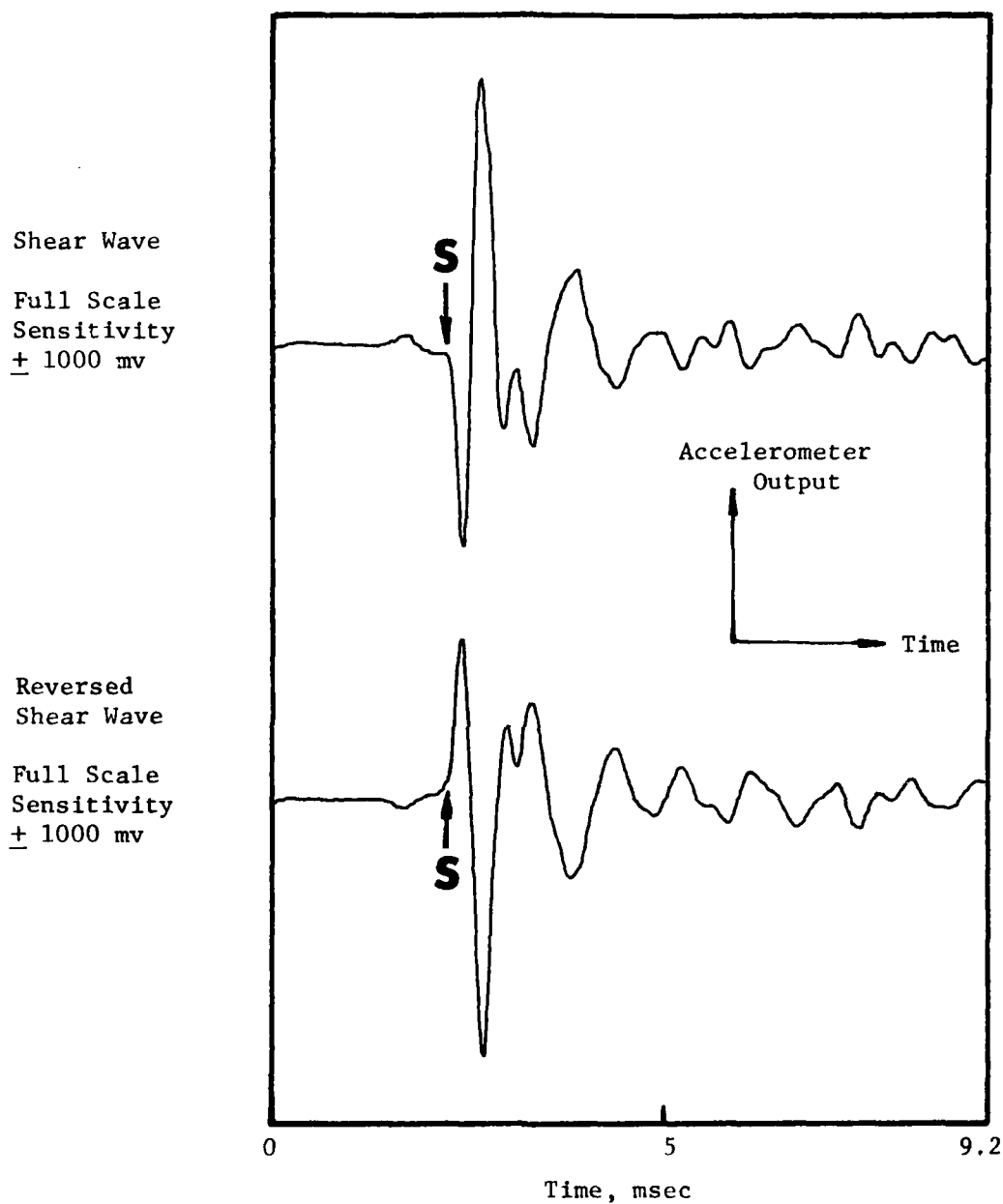


Fig. 6.1 - Typical Shear Wave Record Using Reversed Impulses to Aid in Identification of Initial Shear Wave Arrival

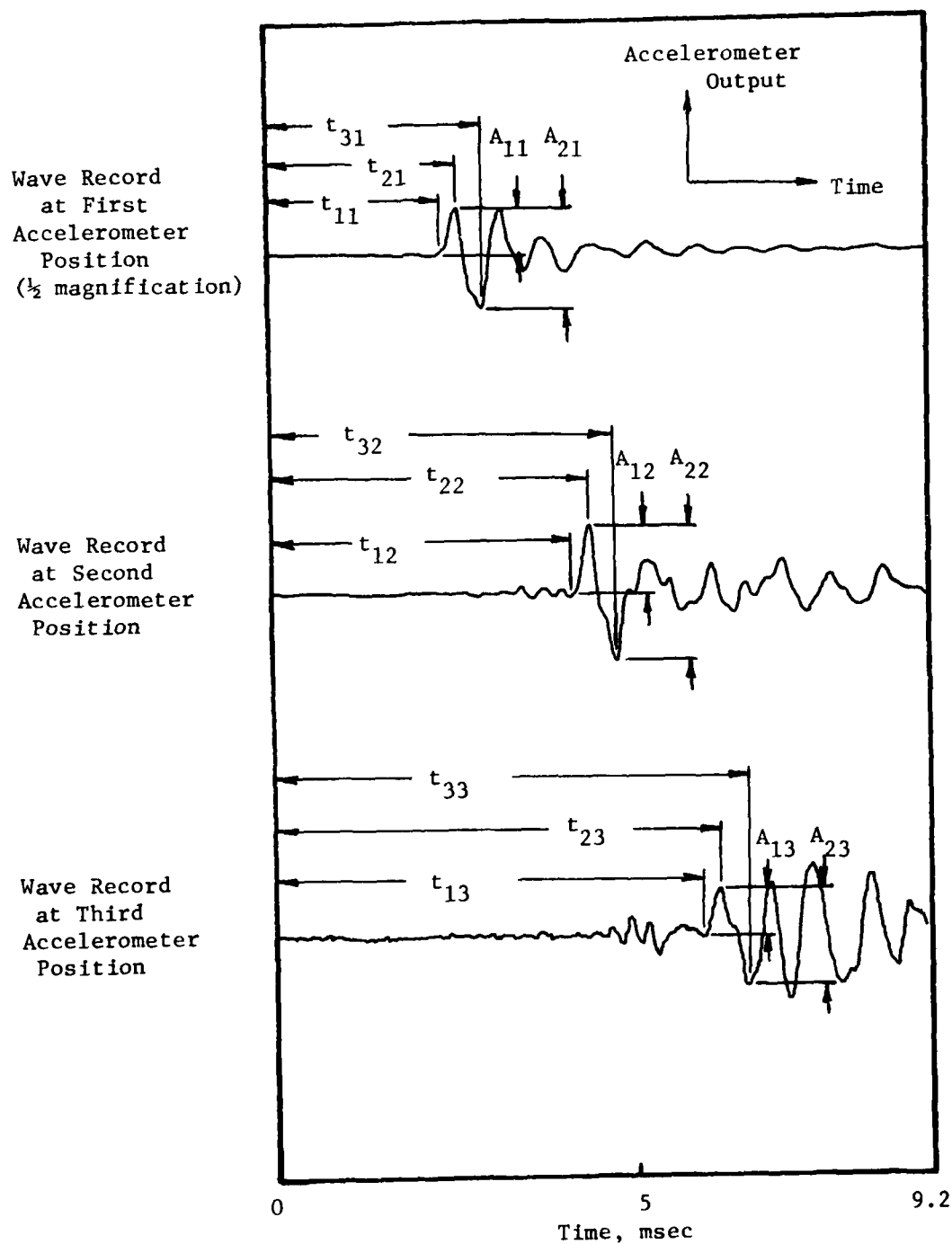


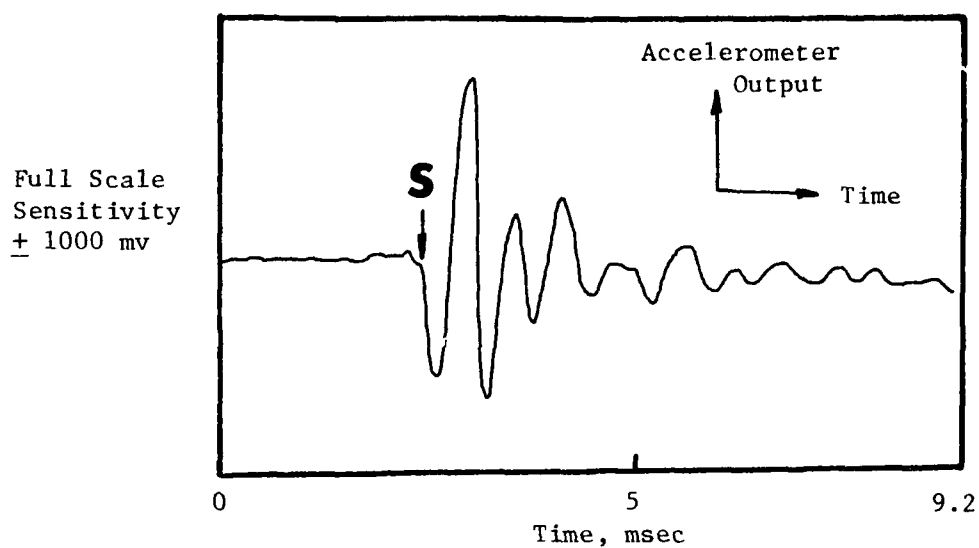
Fig. 6.2 - Typical Set of Shear Wave Data from Recording All Three Accelerometers Along One Axis of the Cube



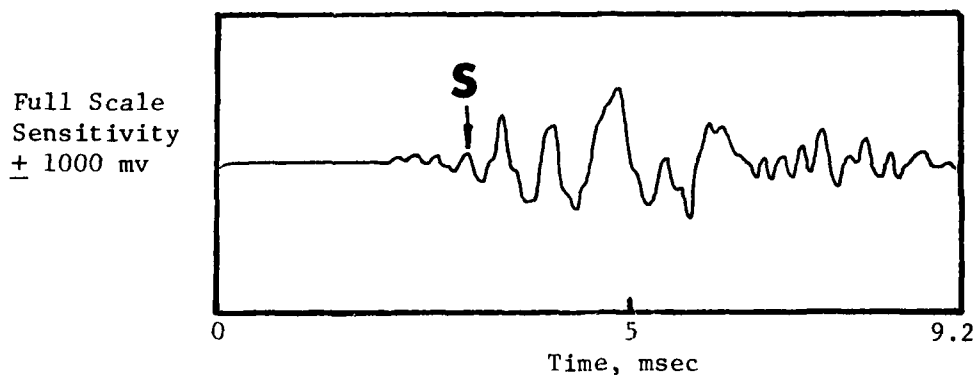
denotes a time or amplitude feature, respectively. The first subscripted numeral associated with the times represents: 1 for the direct arrival, 2 for the first trough, and 3 for the first peak. The first subscripted numeral associated with the amplitudes represents: 1 for the first trough, and 2 for the first trough to first peak. The second subscripted numeral denotes the accelerometer position along the axis: 1 for the accelerometer nearest to the source hammer, a distance of 2.0 ft (0.61 m), 2 for the center accelerometer, approximately 3.5 ft (1.07 m) from the source hammer, and 3 for the farthest accelerometer which was situated 5 ft (1.53 m) from the source hammer.

Generally, the shear wave records were quite easy to analyze, and the data displayed consistent trends. However, at times the shear wave records were erratic and difficult to analyze. Figure 6.3 shows two extremes in the shear wave records; the upper record being easy to analyze and the lower record requiring a great deal of judgement to analyze. When a record was difficult to analyze, the reasons seem to be traceable to problems with the source hammer; that is, the hammer-soil coupling, or the impulse applied to the hammer to generate the shear wave. Approximately 80 percent of the shear wave records were good records and easy to analyze.

The degree of hammer-soil coupling was reduced by small amounts of sand leakage from the sides of the two side hammers during testing (see Sect. 6.4). Although the hammer faces had been roughened to improve coupling, this leakage seemed to reduce the



a) Shear wave record which was easy to analyze



b) Shear wave record which was difficult to analyze

Fig. 6.3 - Illustration of the Two Extremes in Quality of Shear Wave Records

overall quality of hammer-soil coupling and thus distort the shear waves. This effect could sometimes be reduced by screwing the source hammer more tightly into the cube and so increasing the pressure of the hammer on the soil, although this was not always successful.

The hammer impulse was also quite important. Although an attempt was continuously made to keep the hammer blows constant, it was not possible. The differences in blows had the effect of exciting different frequencies in the shear waves. In particular, a "poor" hammer blow was one which excited high frequency interference in the shear wave record. When arrival times were chosen for the wave records with frequency interference, the process involved the smoothing of the shear wave to eliminate the undesirable frequencies. In general, those shear waves with lower predominant frequencies (in the range of 1000 Hz) were much easier to analyze.

As a final point, it must be noted that for a few of the tests, the accelerometers did not operate properly. The problems were intermittent, with the problems occurring in no discernible pattern. The reasons for the malfunctions were not determined but could have been associated with the fragile microdot cables and connectors, equipment overheating, or the switching boxes.

#### 6.3.3 Shear Wave Data Reduction

With the measured values from the waveforms cited above and the measured distances between accelerometers, a computer program was used to perform various calculations. The calculations

included: 1. velocity of the direct shear wave to each of the three accelerometers; 2. interval shear wave velocities (between accelerometers 1 and 2, 2 and 3, and 1 and 3) based on the initial arrivals, first troughs, and first peaks; and 3. shear wave frequencies based on the direct, first trough, and first peak arrival times. The computer program greatly eased the data reduction since the calculations were so repetitive and numerous. A printed version of the program may be found in the report by Kopperman, et al (1982).

A complete set of recorded waveforms, data input and resultant computer output for a representative test is included as Appendix C.

#### 6.4 ANALYSIS OF SHEAR WAVE VELOCITIES

##### 6.4.1 Comparison of Direct and Interval Velocities

The first step in evaluating the effect of the mean effective principal stress,  $\bar{\sigma}_0$ , on shear wave velocity was to compare the direct and interval velocities. The comparison was performed to determine both the data scatter and consistency of velocity changes with  $\bar{\sigma}_0$ .

Although similar in magnitude, direct velocities were lower than interval velocities. In almost all cases, direct velocities were on the order of five percent lower than interval velocities at a confining pressure of 10 psi (68.9 kPa) with the difference increasing to about 10 percent as  $\bar{\sigma}_0$  increased to 40 psi (275.6 kPa). In addition, the slope of the  $\log V_s \sim \log \bar{\sigma}_0$

relationship for direct velocities was on the order of one-half of that for the same relationship for interval velocities as shown in Fig. 6.4.

Differences between direct and interval velocities can be explained by two primary reasons: 1. delays in oscilloscope triggering (Hoar and Stokoe, 1978), and 2. nonuniform soil conditions. Since direct velocities depend upon absolute time, any delays between initiating and recording the wave will affect the wave velocity, as will any effects between the initiating point and the recording point. On the other hand, interval velocities depend only upon relative time or the time difference that a wave takes to travel between two points away from the source. Any time delays or soils changes between the source and first recording point do not affect an interval velocity measurement. Only variations in soil properties and soil-receiver coupling between the two measurement points affect interval velocity.

Triggering delays occur when the oscilloscope begins to record the waveform some finite time after the wave has actually been generated. This delay reduces the measured travel time and so, in effect, increases the apparent wave velocity. Triggering delays are typically nonuniform and intermittent.

Nonuniform soil density along the wave path will also cause direct velocities to differ from interval velocities. Wave velocity is a function of soil stiffness; that is, waves travel faster in dense or stiff soils and slower in loose or soft soils.

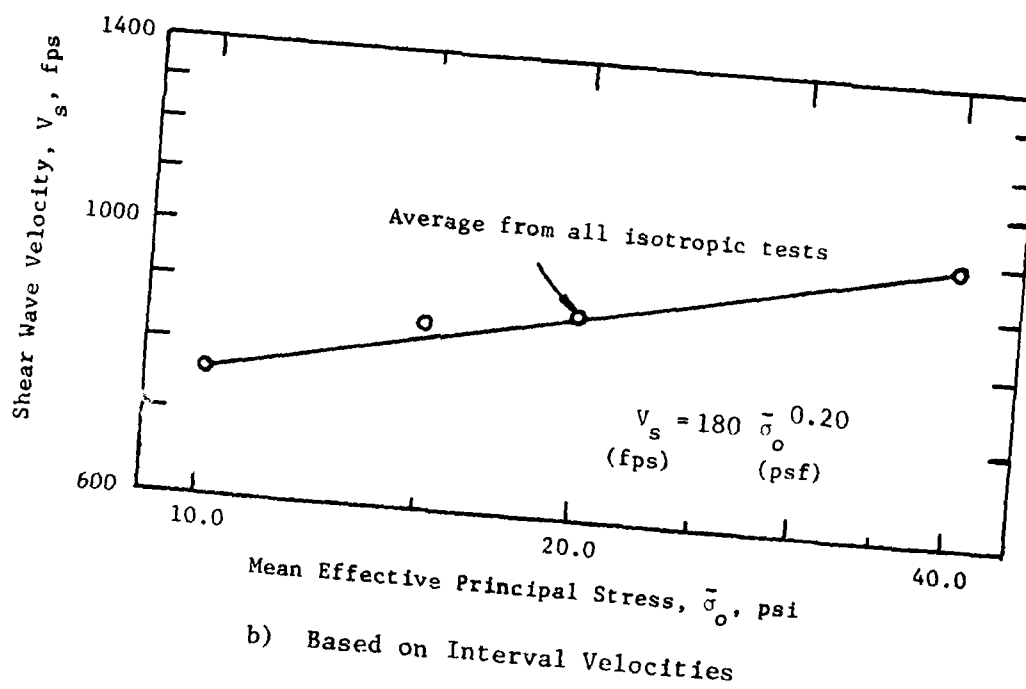
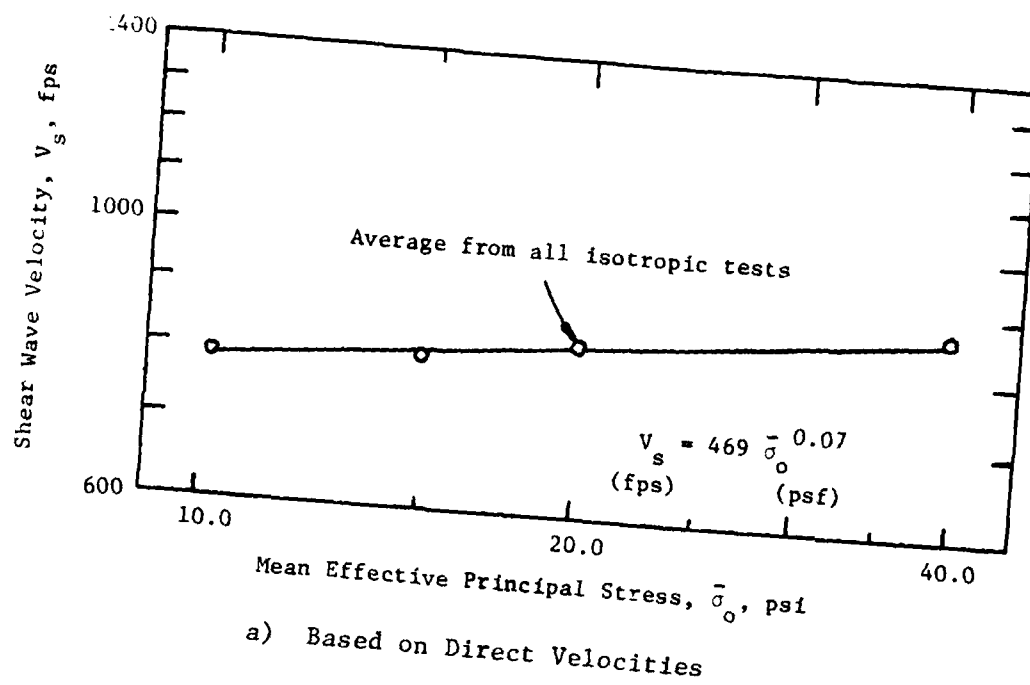


Fig. 6.4 - Comparison of Log  $V_s$  - Log  $\bar{\sigma}_o$  Relationship Based on Direct and Interval Velocities for Isotropic Tests

Therefore, should a loose or dense zone of soil occur along the wave path, the velocity will decrease or increase accordingly.

A loose zone of sand between the hammer and first accelerometer appears to be the most likely reason why direct velocities are lower than interval velocities. This loose zone would affect direct velocities only, leaving interval velocities unchanged. Uniform sample density along the boundary of the cube is very difficult to attain. Further, the intrusion of the source hammers into the sand sample make it difficult to form a uniform sample around the hammers. In addition, small amount of sand leaked from around both horizontal hammers during testing. Although only a small amount of sand escaped, it did leak continuously from about midway through the testing program. This leakage could easily create a soft zone around both of these hammers. It must be noted that the leakage of sand caused the east-west hammer to rotate slightly, which could cause formation of a soft zone in front of the hammer.

The likelihood of a soft zone around the hammers is reinforced by the rate of change of direct velocity with confining pressure. At the lower confining pressures, a soft zone would be less significant when considering the average pressure along the travel path. At higher confining pressures, the significance of the soft zone would become more important. This is shown in the direct velocity data with the lower slope for the  $\log V_s - \log \bar{\sigma}_o$  relationship. As the confining pressure increased, the soft zone

(which could result from lower stresses around the hammer) increasingly lowered the average direct velocity when compared to the interval velocity.

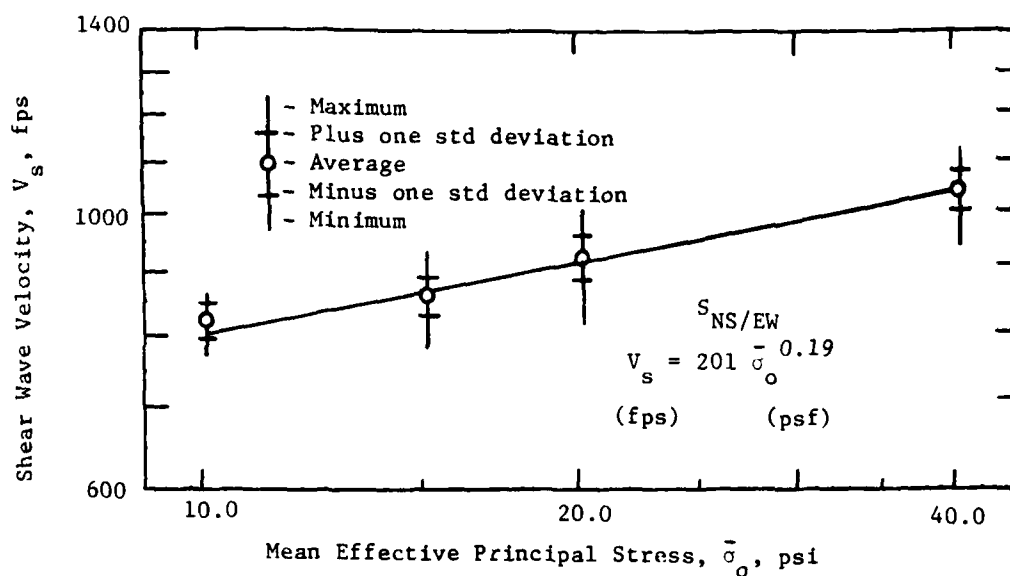
It was assumed, therefore, that direct velocities do not properly reflect the material properties. Hence, only interval velocities were used in this study to evaluate the effects of mean effective principal stress on shear wave velocity.

#### 6.4.2 Short and Long Intervals

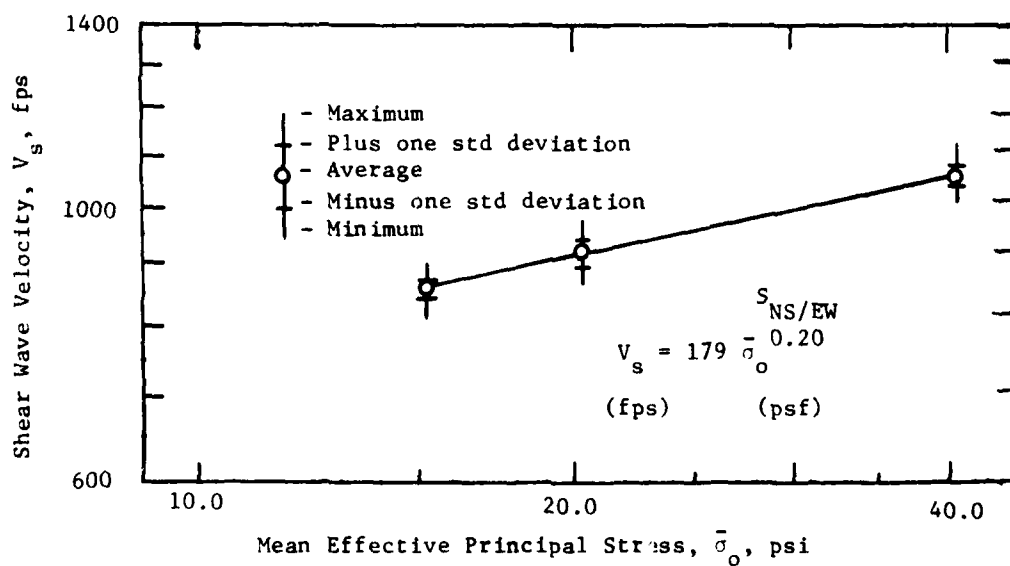
Three interval velocities were calculated for the shear waves: 1. between the first and second accelerometers (referred to herein as a short interval because it is 1.5 ft (0.46 m) in length); 2. between the second and third accelerometers (also referred to as a short interval because it is 1.5 ft (0.46 m) in length); and 3. between the first and third accelerometers (referred to as a long interval because it is 3.0 ft (0.92 m) in length). From analysis of the results, all three interval velocities agreed quite well.

Least-squares straight lines were fit to the data from the short and long intervals, and these lines had almost the same slopes for the  $\log V_s - \log \bar{\sigma}_0$  relationships. Figure 6.5 shows a comparison between the relationships based on the short and long intervals for the  $S_{NS/EW}$ -wave. This wave displayed the poorest correlation between the short- and long-interval velocities (based on Eq. 6.1, pg. 108). As can be seen in the figure, the slope of the  $\log V_s -$





a) Based on Short-Interval Velocities  
(between accelerometers 1 and 2, and  
2 and 3)



b) Based on Long-Interval Velocities  
(between accelerometers 1 and 3)

Fig. 6.5 - Comparison of Log  $V_s$  - Log  $\bar{\sigma}_o$  Relationship  
Based on Short- and Long-Interval Velocities

$\log \bar{\sigma}_0$  relationships varies from 0.19 for the short intervals to 0.20 for the long velocity. There was an 11 percent variation in the dimensionless constant for the least-squares straight lines fitted to the short and long intervals. There was no test data at 10 psi (68.9 kPa) in Fig. 6.5a because of equipment problems with the farthest accelerometer from the source hammer.

The slopes of the  $\log V_s - \log \bar{\sigma}_0$  relationships for the other five shear waves were identical, and the dimensionless constants of the relationships varied by less than four percent. A comparison between these values based on the short and long intervals is shown in Table 6.2. The small variation in slopes and constants indicates that it is unimportant whether short or long intervals are studied to examine the effect of  $\bar{\sigma}_0$  on shear wave velocity.

Upon examining Fig. 6.5, one can see that the scatter in velocities based on the short intervals is greater than the scatter in velocities based on the long interval. In fact, the standard deviation is practically halved for the long-interval velocity when compared to the short-interval velocity. The largest standard deviation at 15 psi (103.4 kPa) for the  $S_{NS/EW}$ -wave is reduced from about  $\pm 5$  percent of the average for the short-interval velocities to about  $\pm 2.2$  percent of the average for the long-interval velocities. Fig. 6.5 represents the data for the shear wave measurements which exhibited the poorest correlation, and for the other shear wave measurements the standard deviation for the long-interval velocities

TABLE 6.2

Comparison of  $\log V_s - \log \bar{\sigma}_0$  Relationships Determined from  
Short and Long Intervals for Isotropic Confinement

Shear Wave Type*	Isotropic Pressure (psi) (2)	Interval Type (3)	Average Velocity (fps) (4)	Standard Deviation (fps) (5)	Slope** (6)	Constant*** (7)
TB/NS	10	Short	753	23	0.19 0.19	191 191
		Long	753	17		
	15	Short	829	37		
		Long	829	10		
	20	Short	856	30		
		Long	856	12		
	40	Short	994	47		
TB/EW	10	Long	993	18		
		Short				
	15	Long				
		Short				
	20	Long				
		Short				
	Overall	Long				

TABLE 6.2 (Continued)

Shear Wave Type*	Isotropic Pressure (psi)	Interval Type	Average Velocity (fps)	Standard Deviation (fps)	Slope**	Constant***
(1)	(2)	(3)	(4)	(5)	(6)	(7)
TB/EW	40	Short Long	911 911	16 11		
	Overall	Short Long			0.22 0.22	136 135
NS/TB	10	Short Long	779 778	25 15		
	15	Short Long	840 840	28 9		
	20	Short Long	876 875	29 15		
	40	Short Long	1002 997	35 19		
	Overall	Short Long			0.18 0.18	208 210
NS/EW	10	Short Long	819 --- +	27 -- +		
	15	Short Long	853 853	29 17		

TABLE 6.2 (Continued)

Shear Wave Type*	Isotropic Pressure (psi)	Interval Type	Average Velocity (fps)	Standard Deviation (fps)	Slope**	Constant***
(1)	(2)	(3)	(4)	(5)	(6)	(7)
NS/EW	20	Short	916	37	0.19 0.20	202 184
		Long	912	23		
	40	Short	1038	34		
		Long	1042	19		
	Overall	Short Long				
EW/TB	10	Short	705	17	0.22 0.22	144 146
		Long	704	11		
	15	Short	790	13		
		Long	790	9		
	20	Short	830	25		
		Long	830	15		
	40	Short	974	43		
		Long	971	22		
	Overall	Short				
		Long				

TABLE 6.2 (Continued)

Shear Wave Type*	Isotropic Pressure (psi)	Interval Type	Average Velocity (fps)	Standard Deviation (fps)	Slope**	Constant***
(1)	(2)	(3)	(4)	(5)	(6)	(7)
EW/NS	10	Short	806	23		
		Long	806	16		
	15	Short	869	19		
		Long	869	15		
	20	Short	923	20		
		Long	923	14		
	40	Short	1032	48		
		Long	1039	24		
	Overall	Short			0.18	219
		Long			0.18	216

\*The first two letters denote the direction of wave propagation and the second two letters denote the direction of particle motion (TB = top-bottom, NS = north-south, EW = east-west).

\*\* Slope of  $\log V_s - \log \bar{\sigma}_0$  relationship as calculated by least-squares fit.

\*\*\* Constant in least-squares fit for the equation:  $V_s = C \bar{\sigma}_0^m$ , where  $\bar{\sigma}_0$  in units of psf.

+ Accelerometer 3 not operating so 1-3 interval not calculated.

is also reduced by a factor of about two from the standard deviation for the short-interval velocities. This condition stems from the fact that the shear waves have longer travel times over the long interval than the short intervals. When deciding upon arrival times, the exact time is subject to some interpretation and can vary, quite realistically, by as much as 0.05 milliseconds. The importance of this possible discrepancy becomes less important as the total travel time increases, and thus, the long-interval velocity will be more stable. Hence, the long interval provides more consistent shear wave velocity data while the short-interval velocities provide an idea of the maximum data variance.

For this study, lines were fit to the results of both interval velocities. Although more confidence was given to the long-interval velocities because of their stability, both long-interval and short-interval velocities were plotted. It was felt that this would be more representative of the experimental scatter in the shear wave data. Similar numerical results were obtained for both the short- and long-interval velocities.

#### 6.5 EFFECT OF STRESS HISTORY

Tests with isotropic confinement afforded an opportunity to study the effect of stress history on shear wave velocity and to compare these results with resonant column test results performed on the same sand. The resonant column tests showed that stress history has essentially no effect on the shear modulus (and shear wave velocity) for this sand.

During testing, several isotropic confining pressures were repeated to examine how the interval velocity changed. The repeated pressures included two at 40 psi (275.6 kPa), four at 20 psi (137.8 kPa), and three at 15 psi (103.4 kPa). Figure 6.6 shows the average of all interval velocities at each pressure for the  $S_{TB/EW}$ -wave on a  $\log V_s - \log \bar{\sigma}_o$  plot. This wave was chosen because it showed the most scatter in the results. As can be seen in the figure, average interval velocities differed by less than six percent at any  $\bar{\sigma}_o$ . This variation is considered quite acceptable for this type of testing. In addition, for the shear wave as a whole, average interval velocities differed by 3 percent for all test pressures.

This variance is well within acceptable experimental scatter for interval velocity and indicates that shear wave velocity is essentially unaffected by previous stress history. These results are in agreement with the resonant column tests. Since the shear wave velocity can be considered independent of stress history, the data for isotropic confinement was analyzed without regard to stress history.

#### 6.6 EFFECT OF ISOTROPIC CONFINING PRESSURE

The effect of isotropic confinement on wave velocity for each of the six shear waves is shown in Figs. 6.7, 6.8 and 6.9. For all cases, a linear variation in the  $\log V_s - \log \bar{\sigma}_o$  relationship was assumed, and a least-squares straight line was fit through the



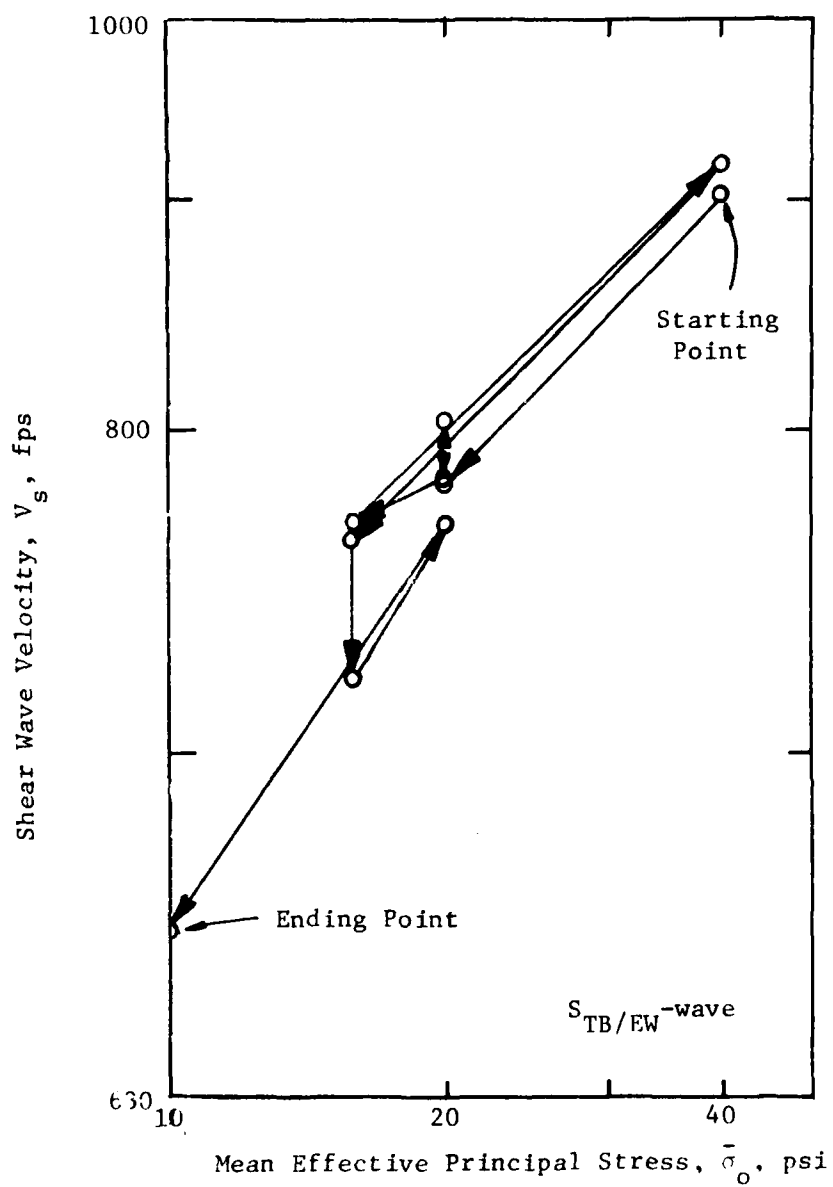
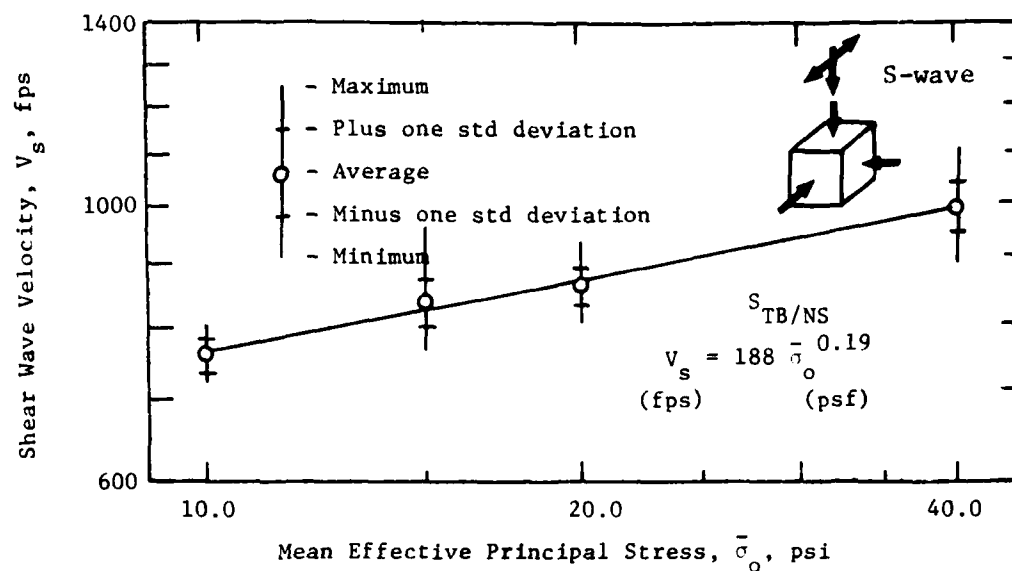
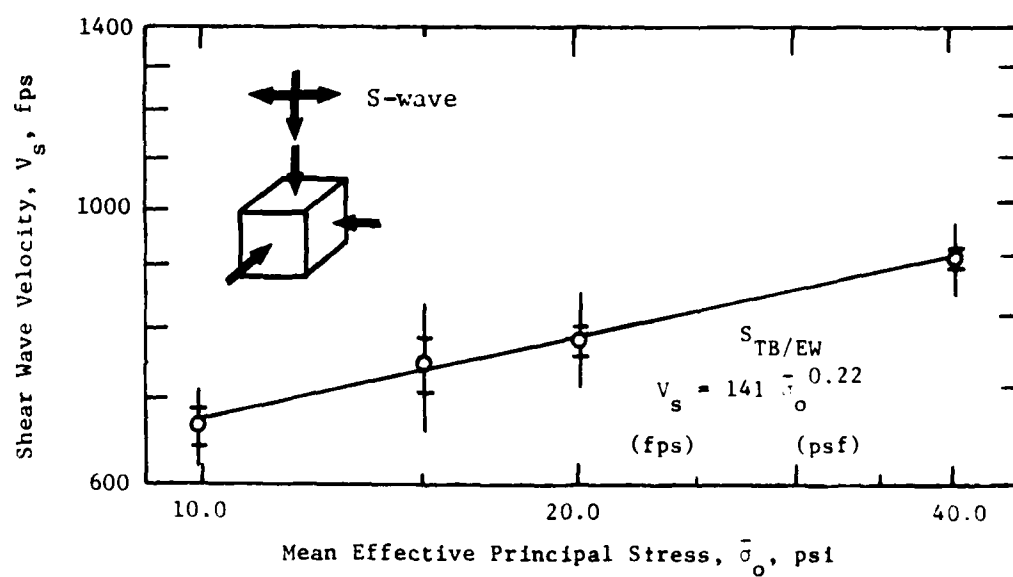


Fig. 6.6 - Stress History Effect on Shear Wave Velocity for Isotropic Confinement



a) For the  $S_{TB/NS}$ -Wave



b) For the  $S_{TB/EW}$ -Wave

Fig. 6.7 - Variation of Shear Wave Velocity with Mean Effective Principal Stress for Propagation in Top-Bottom Direction

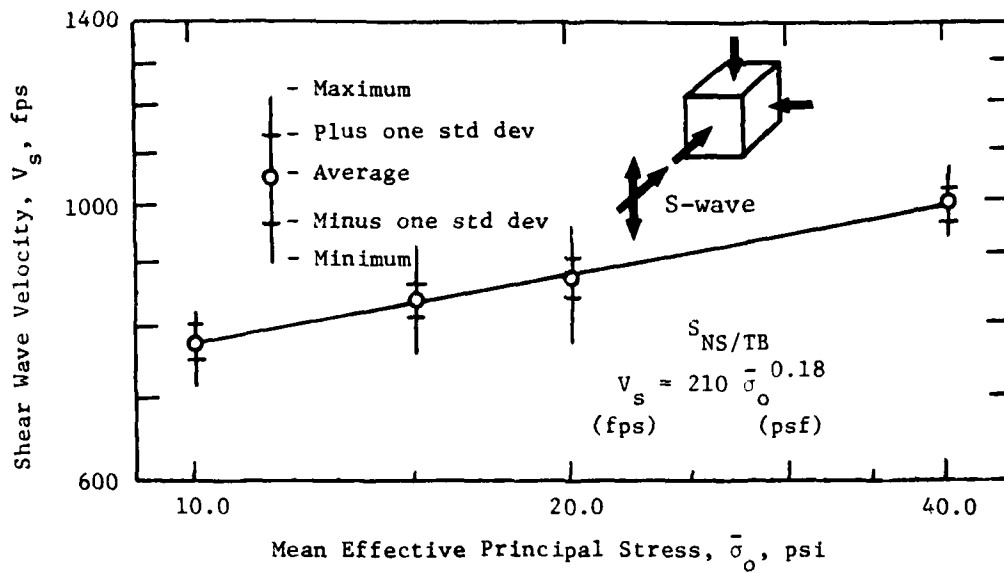
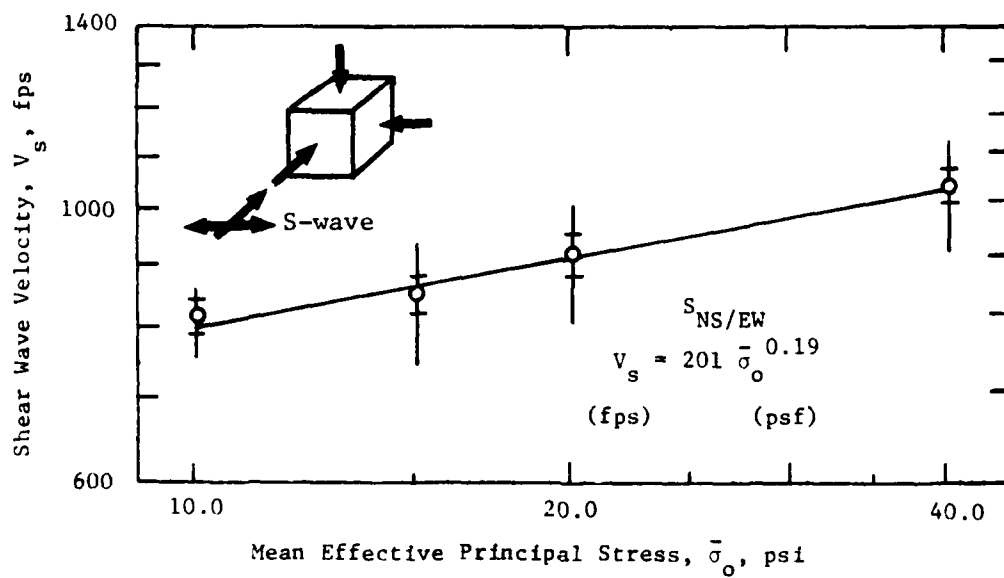
a) For the  $S_{NS/TB}$ -Waveb) For the  $S_{NS/EW}$ -Wave

Fig. 6.8 - Variation of Shear Wave Velocity with Mean Effective Principal Stress from Propagation in North-South Direction

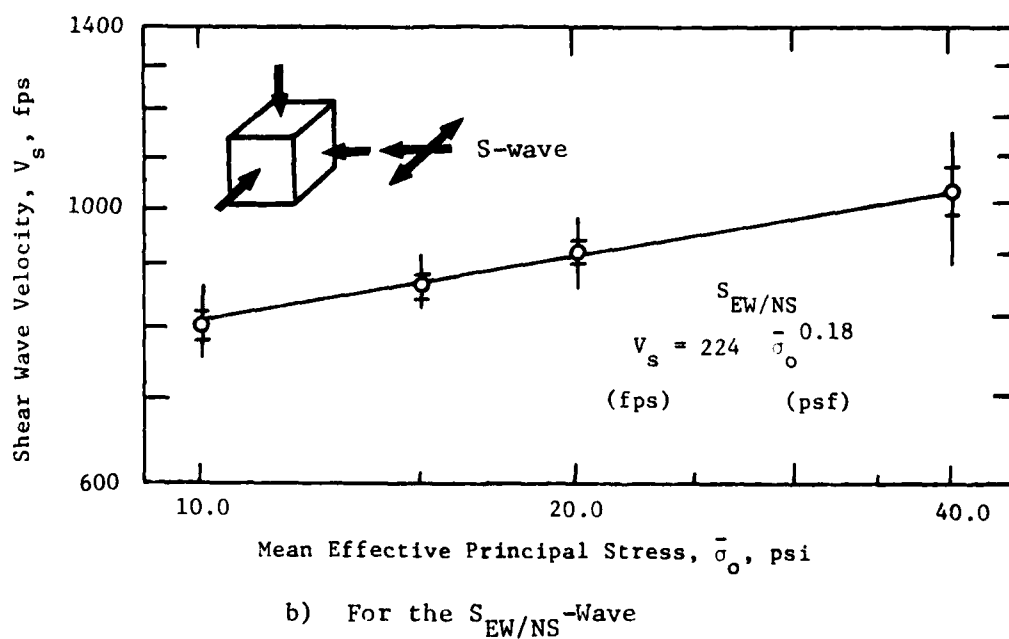
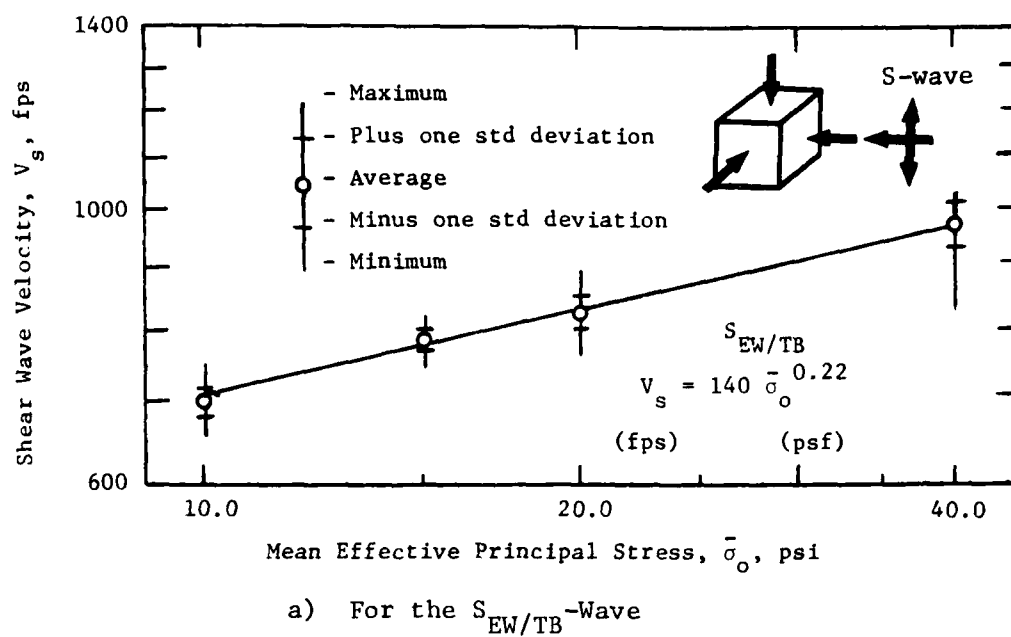


Fig. 6.9 - Variation of Shear Wave Velocity with Mean Effective Principal Stress for Propagation in East-West Direction

data. Each figure shows a sloping straight line depicting the least-squares line. Also shown at the various test pressures are a circle depicting the average of the test data for that pressure, a vertical line representing the scatter between the minimum and maximum values measured at that pressure, and two horizontal lines on the vertical line representing  $\pm$  one standard deviation from the average point.

Attempts were also made to fit the data with a polynomial function, a straight line on a linear scale, an exponential curve, and a power function. Quite surprisingly, all four approaches were reasonable in most cases. The power function, however, was consistently more accurate than the other three functions.

The linear variation of the  $\log V_s - \log \bar{\sigma}_o$  relationship turned out to be the most appropriate representation. Therefore, the expression for shear wave velocity as a function of isotropic pressure can be expressed in the form of (Hardin and Richart, 1963):

$$V_s = C_1 \bar{\sigma}_o^m \quad (6.1)$$

where:  $V_s$  = shear wave velocity in fps,

$C_1$  = constant,

$\bar{\sigma}_o$  = mean effective principal stress in psf, and

$m$  = slope of  $\log V_s - \log \bar{\sigma}_o$  relationship.

The values shown in Table 6.3 were computed for  $C_1$  and  $m$  for each shear wave. The coefficient of correlation of the fitted line for each relationship is also shown in the table. For each of the

TABLE 6.3

Values of Constants  $C_1$  and  $m$  from Eq. 6.1\* for  
the Six Different Shear Waves

Shear Wave Type**	$C_1$ *	$m$ *	Coefficient of Correlation
(1)	(2)	(3)	(4)
TB/NS	188	0.19	0.89
TB/EW	141	0.22	0.92
NS/TB	210	0.18	0.90
NS/EW	201	0.19	0.89
EW/TB	140	0.22	0.94
EW/NS	224	0.18	0.92

\* Eq. 6.1:  $V_s = C_1 \bar{\sigma}_o^m$ , (with  $V_s$  in fps and  $\bar{\sigma}_o$  in psf)

\*\* The first two letters denote the direction of wave propagation,  
and the second two letters denote the direction of particle  
motion (TB = top-bottom, NS = north-south, EW = east-west).

$\log V_s - \log \bar{\sigma}_o$  relationships, the scatter is less than nine percent from the average to  $\pm$  one standard deviation from the fitted line.

From Table 6.3, shear wave velocity varies with  $\bar{\sigma}_o$  raised to a power varying from 0.18 to 0.22. This range of  $m$  agrees well with published data, where typically the shear wave velocity varies with the confining pressure to the  $1/5$  to  $1/4$  power with an approximate experimental scatter in any particular case of about  $\pm 10$  percent (Lawrence, 1968; Hardin and Richart, 1963; Schmertmann, 1978; Roesler, 1978; Hardin and Black, 1966; Wilson and Miller, 1962). In addition, the computed value of  $m$  from the cube tests is similar to the 0.24 value determined from the resonant column tests performed on the same sand. The difference in  $m$  can probably be attributed to the different technique of sample construction and the different shear wave used in the resonant column. The value of  $m$  is a function of void ratio and intergranular contacts of the sand, and, hence, it will depend on how the sand samples are formed. Also, the different shear waves can affect the results because of structural anisotropy as discussed in Section 6.7.

The value of  $m$  does not appear to be constant but to be a function of the direction of wave travel. This is most likely due to the structural anisotropy of the sand sample. It is obvious that there does exist some degree of structural anisotropy within the sample since the values of  $C_1$  vary. If the confining pressure were equal to one psf (0.05 kPa), the shear wave velocity would be

equal to  $C_1$ . From Table 6.3 it can be seen that the value of  $C_1$  varies from an average value of 184 by  $\pm 23$  percent.

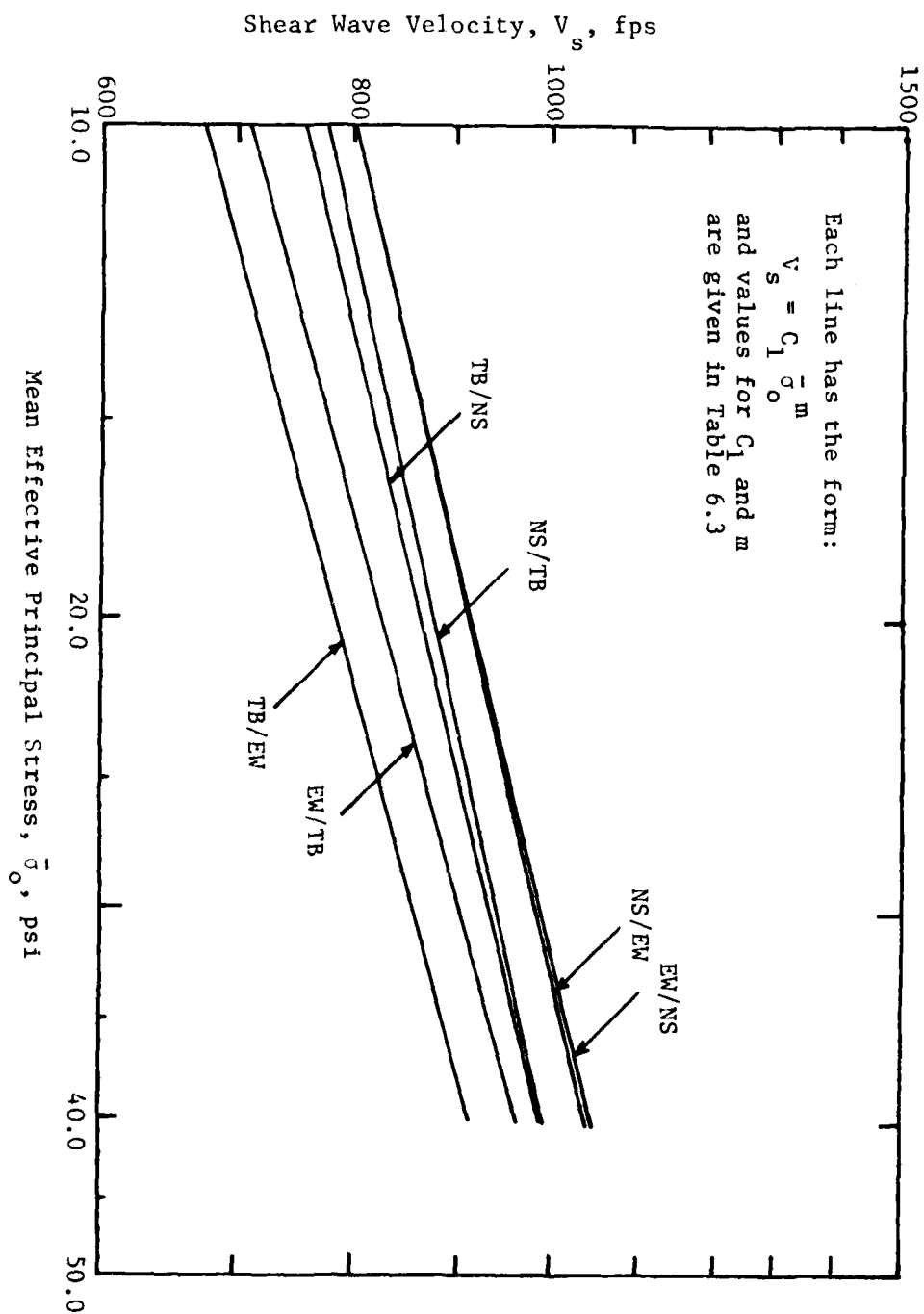
Even though some degree of anisotropy existed within the sample, it was desired to fit one general equation through all shear wave data. The individual shear wave equations from Table 6.2 are shown in Fig. 6.10 and clearly indicate the anisotropy (discussed in Sect. 6.7). The general equation fit to all this data is shown in Fig. 6.11 in which the average for all data at each  $\bar{\sigma}_0$  is shown by the circle with the full scatter and  $\pm$  one standard deviation also included. In the form of Eq. 6.1, the general equation can be expressed as:

$$V_s = 180 \bar{\sigma}_0^{0.20} \quad (6.2)$$

Fitting one equation to data which are offset due to structural anisotropy is reflected in the larger scatter for this equation than for the individual  $\log V_s - \log \bar{\sigma}_0$  equations. The variation from the fitted curve at each  $\bar{\sigma}_0$  to the  $\pm$  one standard deviation is increased to  $\pm 8$  percent at several test pressures with the maximum scatter in the data of  $\pm 18$  percent. The reduced accuracy of Eq. 6.2 in predicting values of  $V_s$  is also reflected in a lower coefficient of correlation of 0.77. It seems apparent that one equation for the relationship of velocity to confining pressure has the handicap of being affected by the structural anisotropy of the sand sample.



Fig. 6.10 - Variation of Average Shear Wave Velocity for Each Shear Wave with Isotropic Confinement



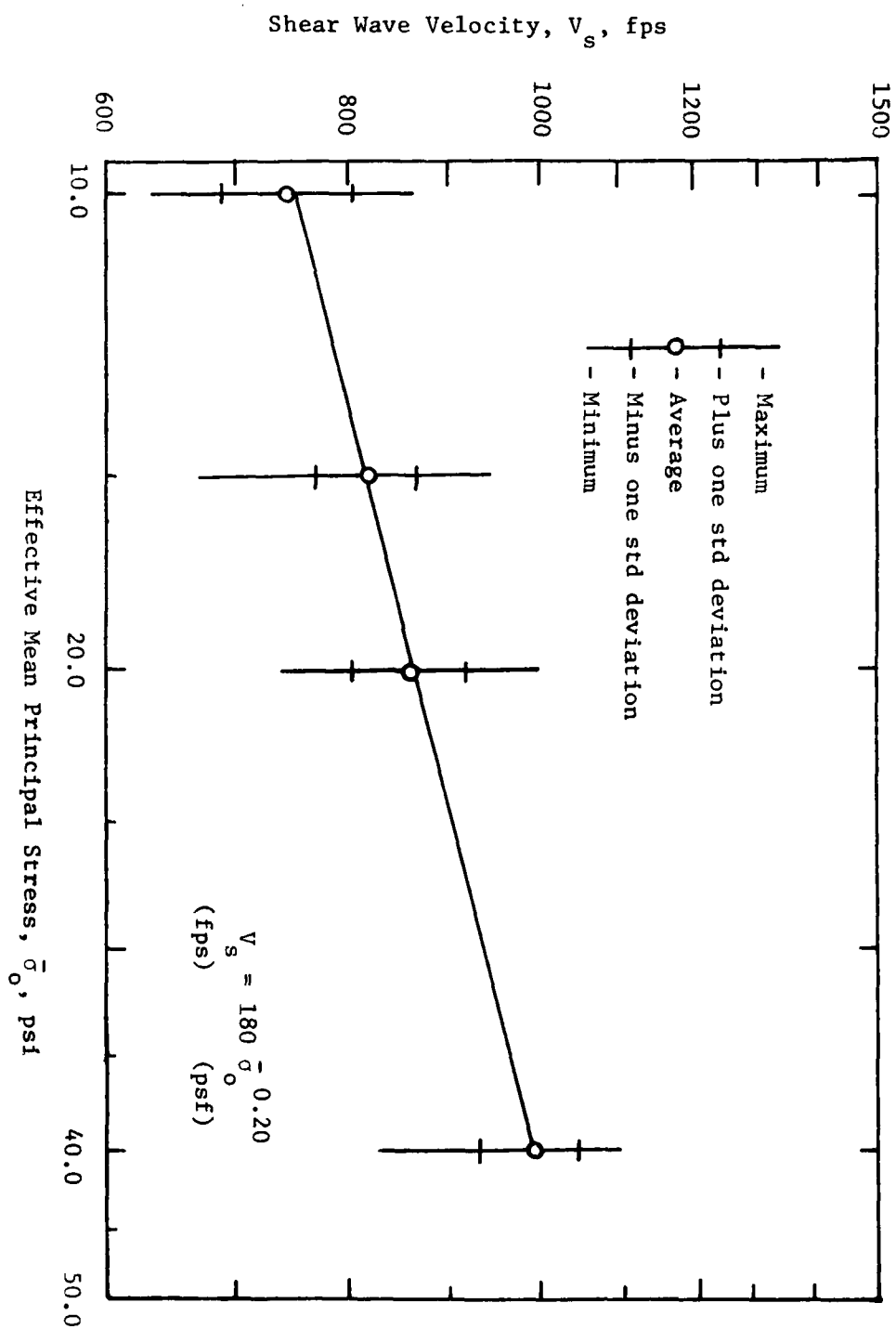


Fig. 6.11 - General Least-Square Fit of All Shear Wave Velocities Determined Under Isotropic Confinement

Based on the results shown in Table 6.3, the shear modulus can be expressed as (Hardin, 1978):

$$G_{\max} = \frac{C \text{ OCR}^k}{0.3 + 0.7e^2} P_a^{1-n} \bar{\sigma}_o^n \quad (6.3)$$

where:  $G_{\max}$  = shear modulus in desired units,

$C$  = constant (dimensionless),

OCR = overconsolidation ratio,

$k$  = factor related to soil plasticity (for sand,  $k = 0$ ),

$P_a$  = atmospheric pressure in same units as  $G_{\max}$ ,

$e$  = void ratio,

$\bar{\sigma}_o$  = mean effective principal stress in same units as

$G_{\max}$ , and

$n$  = slope of  $\log G - \log \bar{\sigma}_o$  relationship.

For the cube study, tests were conducted with only a void ratio of 0.73. Therefore, no conclusions can be drawn on the effects of void ratio within Eq. 6.3, and hence, the void ratio term is made a constant. The OCR term for sand becomes one because the coefficient  $k$  is zero since the sand is non-plastic. Equation 6.3 can then be simplified as:

$$G_{\max} = \frac{C}{0.673} P_a^{1-n} \bar{\sigma}_o^n \quad (6.4)$$

An equation of this form was computed for each different shear wave, and the calculated values of  $C$  and  $n$  are summarized in Table 6.4. Hardin (1978) determined values for  $C$  and  $n$  of 625 and 0.5, respectively, while resonant column tests performed on the

TABLE 6.4

Values for the Six Different Shear Waves of the  
Constant, C, and Slope, n, from Eq. 6.4\*

Shear Wave Type**	C*	n*
(1)	(2)	(3)
TB/NS	621	0.38
TB/EW	555	0.43
NS/TB	665	0.36
NS/EW	710	0.38
EW/TB	544	0.45
EW/NS	759	0.35

\* Eq. 6.4:  $G_{\max} = \frac{C}{0.673} Pa^{1-n} \bar{\sigma}_o^n$

\*\* The first two letters denote the direction of wave propagation, and the second two letters denote the direction of particle motion (TB = top-bottom, NS = north-south, EW = east-west).

sand used in the cube resulted in average values for  $C$  of 705 and for  $n$  of 0.48 (see Sect. 4.4.1). These values of  $C$  agree quite well with the calculated  $C$  for this study, which ranged from 544 to 759 with an average value of 642 for the six different shear waves. The calculated value of  $n$  for this study, however, was less than those values determined by either Hardin or the resonant column test.

#### 6.7 STRUCTURAL ANISOTROPY

As discussed in the preceeding section, the sand sample in the triaxial cube has some degree of structural anisotropy. Although it was hoped that raining the sand into the cube would produce a nearly isotropic sample, it is obvious that it did not. As other experimentors have found (Schmertmann, 1978; Roesler, 1979) it is not possible to construct a truly isotropic sand sample.

Structural anisotropy is the inherent anisotropy of the sand which is caused by the realignment of the sand grains as they are placed. Since shear wave velocity is a function, in part, of the inter-granular contacts between sand grains, particle alignment affects  $V_s$ . As the sand was rained into the cube, the sand bucket was swung only in the north-south direction (see Sect. 5.2.1). Therefore, sand grains should be aligned differently for the north-south and east-west directions, both of which will differ from the top-bottom direction.

To understand how confining pressure affected shear wave velocity, the degree of sample anisotropy had to be quantified. As discussed in Section 6.6, the degree of anisotropy is reflected in the values of  $C_1$  and  $m$  for each shear wave. Upon examination of Fig. 6.10, it can be seen that the  $\log V_s - \log \bar{\sigma}_0$  relationships fall into three distinct groups each composed of two different shear waves. It is interesting to note that the two shear waves in each wave group have a common plane of motion; that is, the directions of propagation and particle motion lie in the same plane. From Fig. 6.10, the plane of motion with the fastest apparent velocity due to structural anisotropy is the EW-NS plane, the plane determined by the east-west and north-south axes of the cube as shown in Fig. 6.12. Similarly the slowest velocities due to structural anisotropy involve the TB-EW plane of motion. Finally, the NS-TB plane of motion has an intermediate value of shear wave velocity.

These three wave groups were used to define the structural anisotropy of the sand sample. An equation was fit to each group of waves to determine three equations expressing the structural anisotropy for shear waves in the cube. These equations are shown in Figs. 6.13, 6.14 and 6.15 by the solid lines. The equations are also summarized in Table 6.5, following the same form as Eqs. 6.1 and 6.4.

Using these equations, a ratio of shear wave velocities for each plane of motion can be computed as follows:

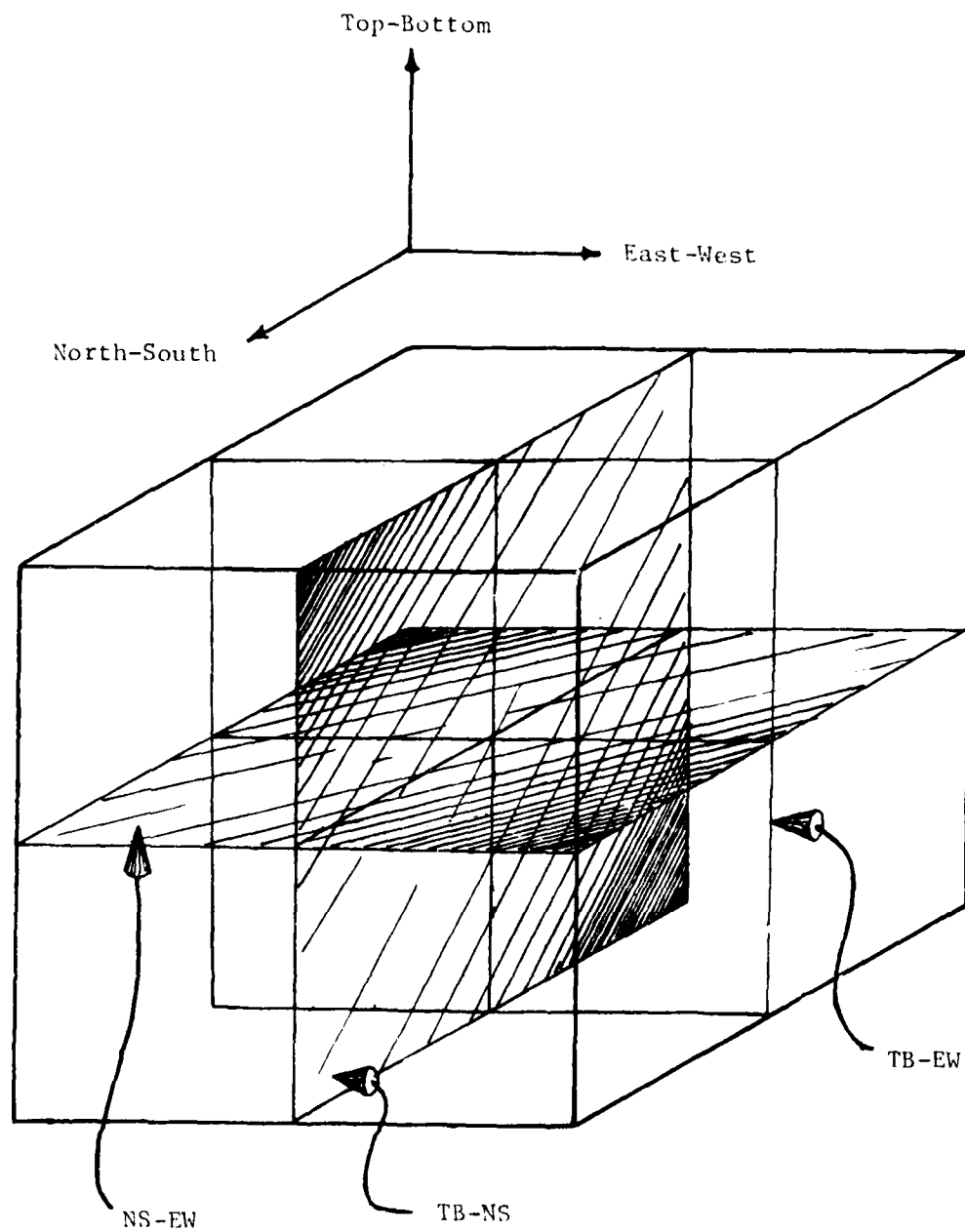


Fig. 6.12 - Planes of Motion for Shear Waves Exhibiting Similar  $\log V_s - \log \bar{\sigma}_0$  Relationships

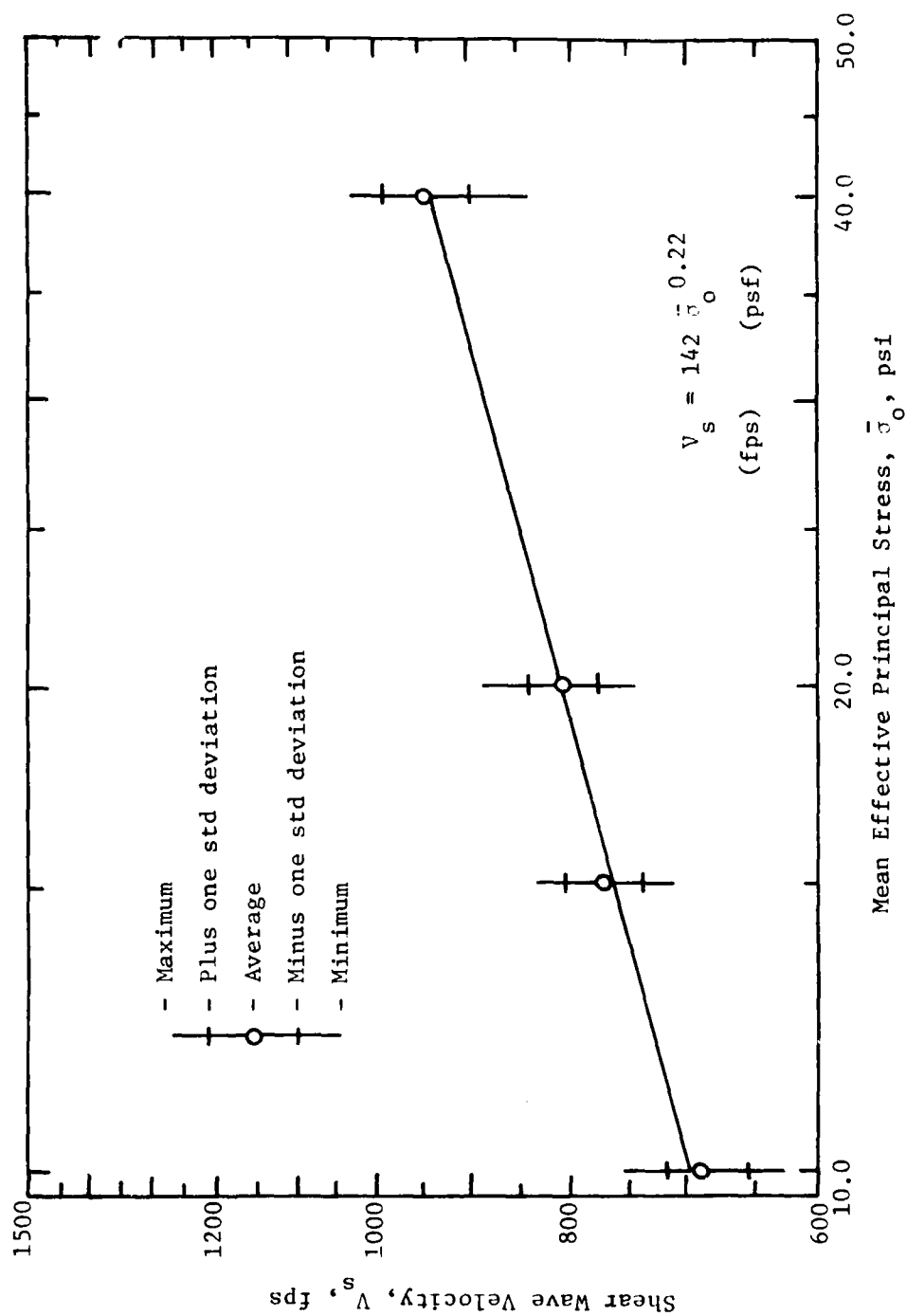


Fig. 6.13 - Variation of Shear Wave Velocity with Mean Effective Principal Stress for Waves in the TB-EW Plane



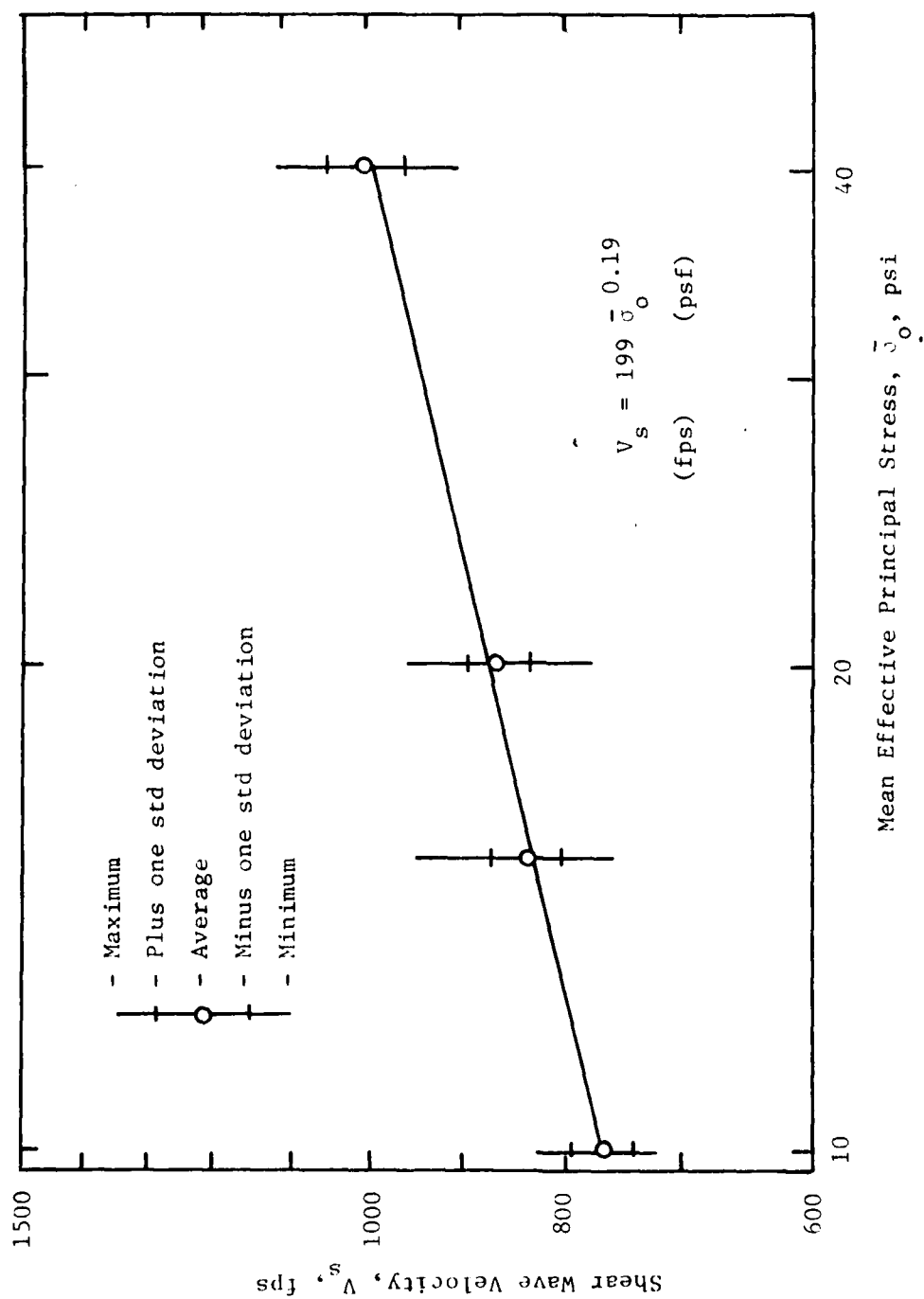


Fig. 6.14 - Variation of Shear Wave Velocity with Mean Effective Principal Stress for Waves in the TB-NS Plane

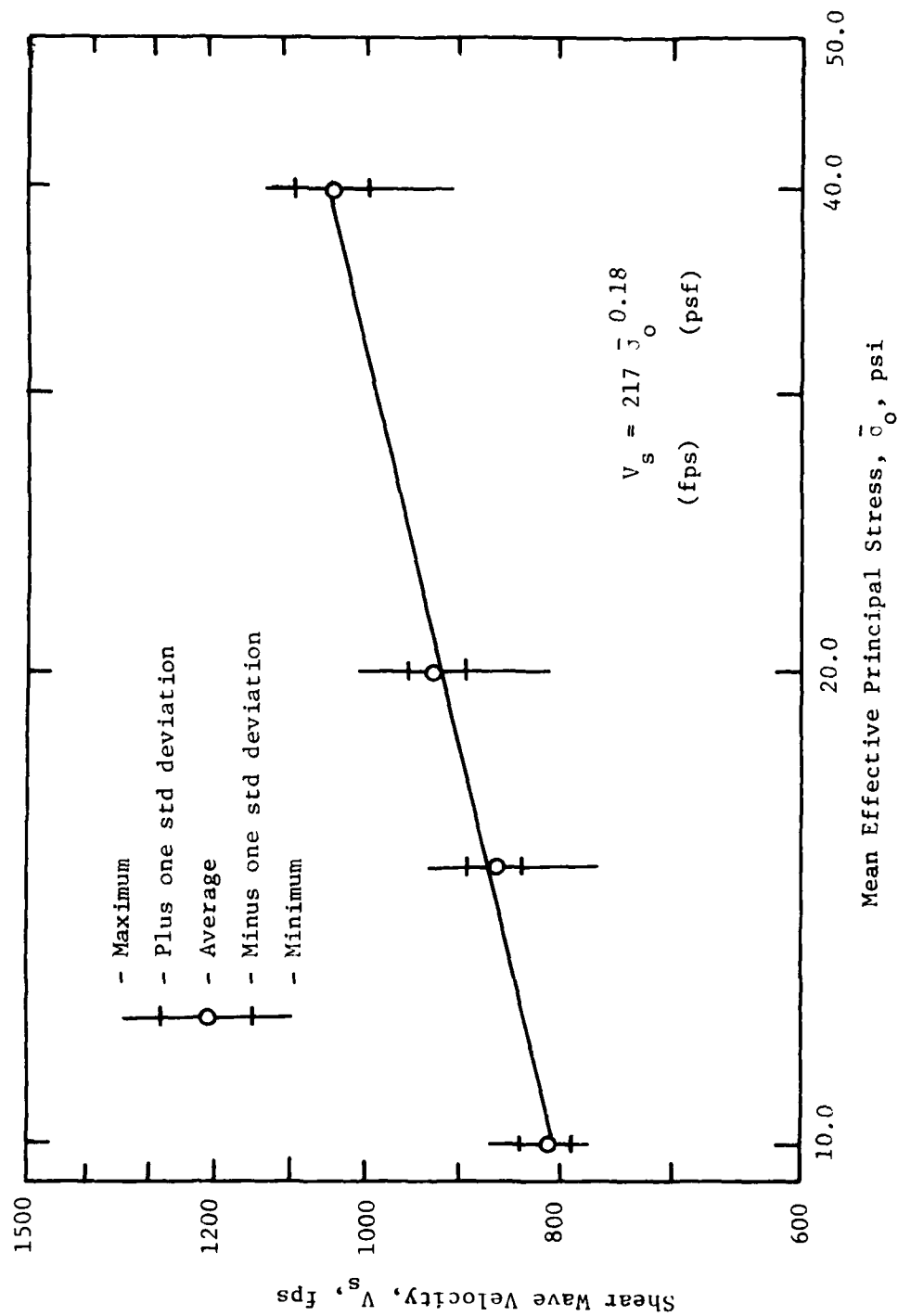


Fig. 6.15 - Variation of Shear Wave Velocity with Mean Effective Principal Stress for Waves in the EW-NS Plane

TABLE 6.5

Values for the Three Shear Wave Groups of Constants  
and Slopes of Eqs. 6.1\* and 6.4\*\*

Plane of Motion	$C_1^*$	$m^*$	Coefficient of Correlation	$C^{**}$	$n^{**}$
(1)	(2)	(3)	(4)	(5)	(6)
TB-EW	142	0.22	0.89	561	0.44
NS-EW	217	0.18	0.90	708	0.37
TB-NS	199	0.19	0.89	698	0.37

\* Eq. 6.1:  $V_s = C_1 \bar{\sigma}_o^m$ , (with  $V_s$  in fps and  $\bar{\sigma}_o$  in psf).

\*\* Eq. 6.4:  $G_{\max} = \frac{C}{0.673} \text{ Pa}^{1-n} \bar{\sigma}_o^n$

$$v_{TB-EW} = (0.65 \bar{\sigma}_o^{0.04}) v_{EW-NS} \quad (6.5)$$

$$v_{NS-TB} = (0.92 \bar{\sigma}_o^{0.01}) v_{EW-NS} \quad (6.6)$$

It is interesting to note that both of these equations involve a scalar factor and an exponential factor of  $\bar{\sigma}_o$ . The interdependence of the directional velocities can be assessed with these equations to predict how the velocities should vary from one principal plane to the next.

It is interesting to note that for these ratios, the velocity of the NS-TB plane (the plane along which the bucket was swung as the cube was filled) and the EW-NS plane (the plane perpendicular to the direction of fall for the sand) had approximately the same shear wave velocity, both velocities being larger than for the TB-EW plane. There is no obvious reason for the pattern, although it may be explained, in part, by the directions of sand placement as the cube was filled.

## 6.8 SHEAR WAVE CHARACTERISTICS

### 6.8.1 Predominant Frequency

Predominant frequencies were calculated for the first quarter cycle, first half cycle, and the first three-quarter cycle of particle motion. Frequency values typically ranged from 1000 to 1500 Hz, with frequencies as low as 700 Hz and as high as 2300 Hz recorded.

Values of frequency were higher for the first quarter cycle than the first half cycle. The three-quarter-cycle frequency was the average of these two values because of the method used to calculate this frequency. No apparent pattern of frequency change occurred with time, nor was the frequency dependent on the test pressure since there was no pattern in the calculated frequencies. The frequency did depend on how the source hammer was struck. This was particularly apparent for some waves where the reversals showed considerable difference in frequency from the non-reversed waves, although the interval velocities agreed quite well.

Since the frequencies were less than 2500 Hz for this sand, it can be assumed that the frequency of vibration had no effect on  $V_s$  (Hardin and Drnevich, 1972a).

#### 6.8.2 Wavelength

Wavelengths for the shear waves, based on the predominant frequency,  $f$ , and shear velocity,  $V_s$ , can be expressed as:

$$\lambda = \frac{V_s}{f} \quad (6.7)$$

where:  $\lambda$  = shear wavelength.

Calculated values ranged from 0.50 ft (0.15 m) to 1.5 ft (0.46 m).

Since frequencies were not observed to change through the course of the testing program (due to time or confining pressure variations), it can be concluded that the wavelength increased as the shear wave velocity increased.

The shear wavelength was less than the distance from the source to the first accelerometer. Therefore, it can be assumed at least one cycle of motion occurred before the shear wave encountered the first accelerometer. Further, since wavelengths were typically greater than seven times the accelerometer block width, it can be assumed that the accelerometer blocks themselves did not alter the measured shear waves by acting as a boundary. Finally, since the shear wavelength is less than the distance from the far cube face to the third accelerometer, there was no interference to the recorded wave due to wave reflections. This was shown in the wave records, whereas the reflected shear wave was observed at the last accelerometer some finite time after the generated shear wave had been completely recorded, as shown in Fig. 6.16. As can be seen in this figure, there is no interference on the initial wave arrival from the reflected shear wave.

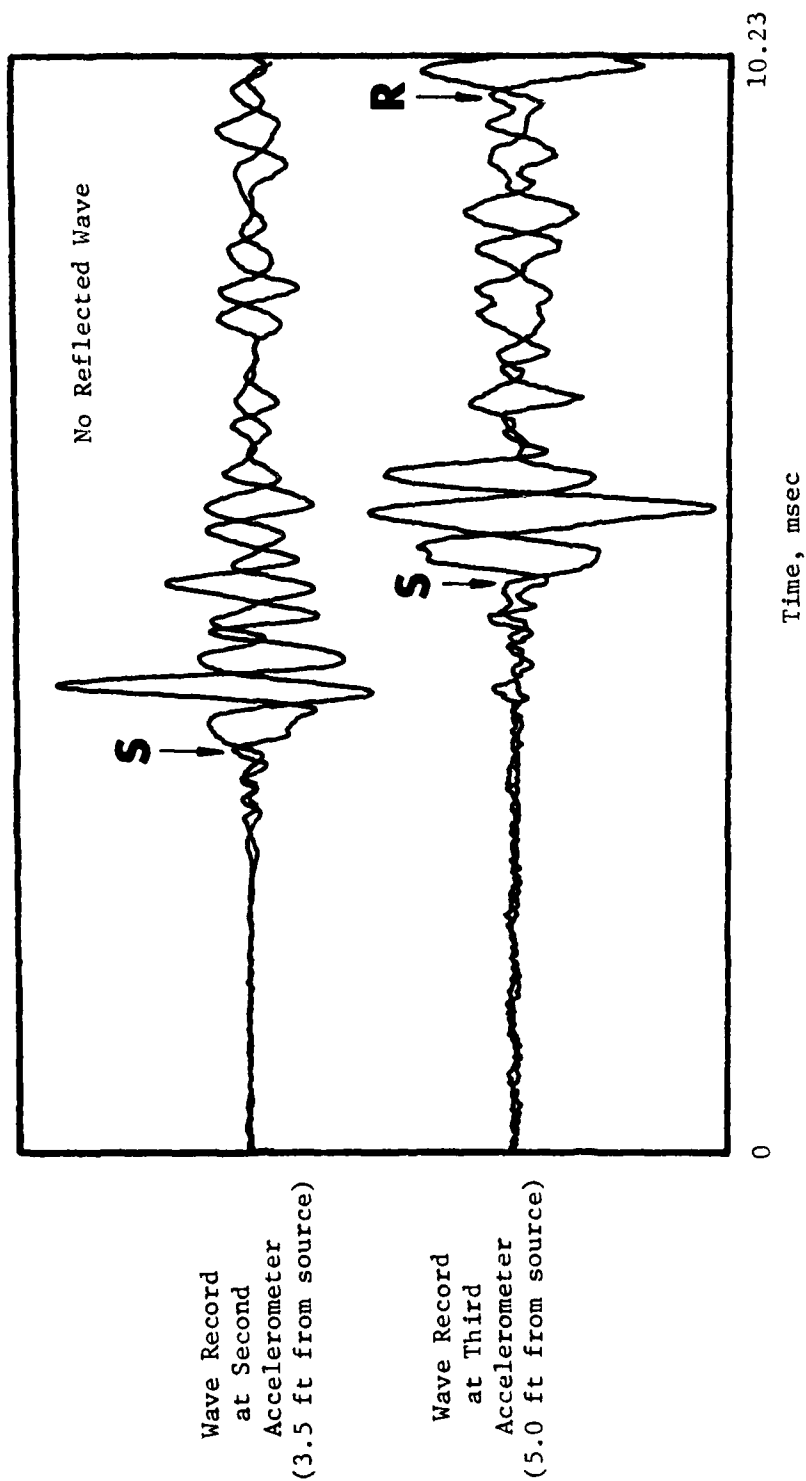
### 6.8.3 Shearing Strain Amplitude

Shearing strain amplitude was also computed in this study. Shearing strain amplitude,  $\gamma$ , can easily be determined from the frequency,  $f$ , particle acceleration,  $\ddot{z}$ , and shear wave velocity,  $V_s$ , if a plane wave assumption is made. By assuming harmonic motion, the strain amplitude is:

$$\gamma = \ddot{u}/V_s \quad (6.8)$$

and

$$\gamma = \frac{\ddot{z}}{(2 f V_s)}$$



Note: No Reflected Shear Wave at Second Accelerometer.

Fig. 6.16 - Recorded Waveforms Showing Reflected Shear Wave (R) Returning to Third Accelerometer After Initially Generated Shear Wave is Fully Recorded

where:  $\gamma$  = shearing strain amplitude,  
 $\dot{u}$  = particle velocity in ft/sec,  
 $\ddot{z}$  = particle acceleration in ft/sec<sup>2</sup>,  
 $f$  = frequency in Hertz, and  
 $V_s$  = shear wave velocity in ft/sec.

Calculations based on Eq. 6.8 showed that shearing strain amplitudes ranged from  $2 \times 10^{-5}$  percent to  $3 \times 10^{-4}$  percent. Based on these values, the assumption that only small strain testing would occur in determining the shear wave velocities is reasonable as shown by the laboratory resonant column tests (see Sect. 4.4). Therefore, shear wave velocity can be assumed to be independent of the amplitude of the impulse and distance of travel to the accelerometer for any given confining pressure. It should be remembered, however, that these calculations are only approximations because of the plane wave assumption, but they do show that testing was performed in the small-strain range where dynamic properties are essentially independent of strain amplitude and strain rate.

## 6.9 SUMMARY AND CONCLUSIONS

Although a truly isotropic state of stress was desired, the presence of inherent pressure gradients permitted this condition on only the horizontal plane at the mid-height of the cube sample. Examination of the pressure variations between accelerometers showed a  $\pm 10$  percent difference between the ideal isotropic confining pressure of 10 psi (68.9 kPa) and the actual stress conditions along



the shear wave travel path. This error was reduced to  $\pm 2.5$  percent for an ideal confining pressure of 40 psi (275.6 kPa). Because of these small differences, an isotropic state of confinement was assumed.

During the testing program, six different shear waves were generated. The six waves were based on the various combinations of directions of wave propagation and particle motion. Wave reversals were recorded for all shear waves to aid in identification of initial arrivals and both direct and interval velocities were determined.

In comparing direct and interval velocities, it was determined that direct velocities were incorrect due to triggering delays, nonuniform soil conditions, and a loose zone around the source hammer during testing. On the other hand, interval velocities were not affected by these variables. Interval velocities were measured over short (1.5 ft; 0.46 m) and long (3.0 ft; 0.92 m) intervals. It was found that short-interval velocities were representative of the maximum experimental scatter while long-interval velocities were more reliable and exhibited less scatter. However, there was no difference in the least-squares lines fit to the short- and long-interval velocities to evaluate the average effect of  $\bar{\sigma}_0$  on  $V_s$ .

In examining the effect of  $\bar{\sigma}_0$  on shear wave velocity, a linear relationship was found to exist between  $\log V_s$  and  $\log \bar{\sigma}_0$ .

The slope of the  $\log V_s - \log \bar{\sigma}_0$  relationship varied from 0.18 to 0.22 and agrees quite well with published data. However, this value of the slope is somewhat lower than the resonant column results (slope = 0.24) performed on this same sand. Equations were developed for each shear wave and a general equation was developed for all shear waves to express the effect of  $\bar{\sigma}_0$  on  $V_s$ . It was concluded that the equations for each shear wave are more accurate than the general equation because of structural anisotropy within the sand sample. Upon analyzing the structural anisotropy of the sample, the shear waves exhibited an anisotropic nature determined by the plane containing the shear wave. No effect of stress history were found for this sand.

Shear waves had predominant frequencies of from 1000 to 1500 Hz, wavelengths of from 0.50 to 1.5 ft (0.15 to 0.46 m), and shearing strain amplitudes of less than  $3 \times 10^{-4}$  percent. All these values are acceptable within the framework used to analyze the data.

## CHAPTER SEVEN

### BIAXIAL CONFINEMENT

#### 7.1 INTRODUCTION

Testing was performed for the case of biaxial confinement ( $\sigma_1 > \sigma_2 = \sigma_3$ ) to examine, in more detail, the effect of state of stress on shear wave velocity. During the course of this phase of testing, three different series of biaxial tests were performed. The test series were designed to study: 1. the variation of  $V_s$  under a constant mean effective principal stress with a varying deviatoric stress component, 2. the importance on  $V_s$  of each stress component with respect to direction of wave propagation, direction of particle motion, and the out-of-plane direction, and 3. the effect of the structural anisotropy on  $V_s$  under biaxial loading. Shear wave velocities were examined from all tests to study and to quantify each of these effects. In this chapter, the biaxial states of stress are briefly reviewed, and the variation of  $V_s$  with biaxial confinement and structural anisotropy are summarized.

#### 7.2 BIAXIAL STATES OF STRESS

To obtain the condition of biaxial confinement, the major effective principal stress,  $\bar{\sigma}_1$ , was applied along one axis of the cube, and the minor effective principal stress,  $\bar{\sigma}_3$ , was applied

along the remaining two axes. Typically, the major principal stress was oriented in the top-bottom (vertical) direction. However, for the biaxial test series which was designed to study structural anisotropy of the sand,  $\bar{\sigma}_1$  was rotated to the north-south axis of the cube.

#### 7.2.1 Notation of Stress Components

For isotropic confinement, the principal stresses were all equal. Therefore, the stress in the direction of wave propagation was the same as the stress in the direction of particle motion which was also the same as the stress in the out-of-plane direction (the third axis perpendicular to the plane containing the propagation and particle motion directions). As a result, attention could not be directed in isotropic confinement to investigating the effect on  $V_s$  of the stress components along the various axes.

For biaxial confinement, the principal stresses were no longer all the same, and the effect of the stress components on  $V_s$  could be investigated. It was necessary, therefore, to develop a notation to describe the directions of the principal stresses relative to the directions of the motions associated with the shear waves. This was accomplished by expressing the effective principal stresses as:

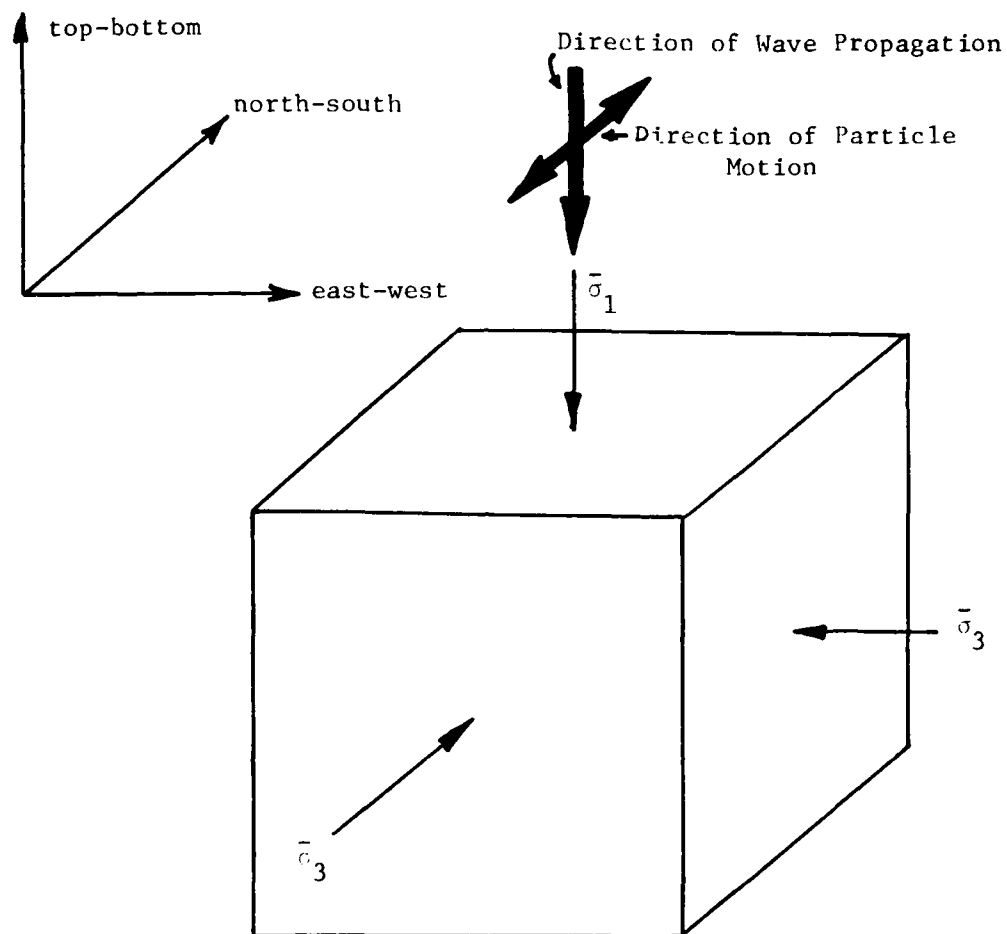
$$\bar{\sigma}_a = \text{effective principal stress in the direction of wave propagation,}$$

$\bar{\sigma}_b$  = effective principal stress in the direction of particle motion, and

$\bar{\sigma}_c$  = effective principal stress in the out-of-plane direction (the direction perpendicular to the  $\bar{\sigma}_a$  and  $\bar{\sigma}_b$  directions).

This stress notation is illustrated in Fig. 7.1 for a shear wave propagating in the top-bottom direction with particle motion polarized in the north-south direction, an  $S_{TB/NS}$ -wave.

Each of the six different shear waves has its own orientation with respect to the cube axes, as indicated by the notation used to describe the shear wave types:  $S_{TB/NS}$ ,  $S_{TB/EW}$ ,  $S_{NS/EW}$ ,  $S_{NS/TB}$ ,  $S_{EW/TB}$ ,  $S_{EW/NS}$ . The notation used to describe the type of shear wave is correlated with the stress components as shown in Table 7.1 for one state of biaxial confinement. The stress in the direction of the first two subscripted letters in the shear wave type (TB, NS or EW) is  $\bar{\sigma}_a$ . The stress in the direction of the second two subscripted letters used to describe the shear wave is  $\bar{\sigma}_b$ . The stress in the direction not appearing in the shear wave type is  $\bar{\sigma}_c$ . Since one of the purposes of this study is to examine how the stress component in any direction influences  $V_s$ , these designations of  $\bar{\sigma}_a$ ,  $\bar{\sigma}_b$ , and  $\bar{\sigma}_c$  will be used quite often for biaxial confinement and also for triaxial confinement discussed in Chapter 8.



In this case:

$$\bar{\sigma}_a = \bar{\sigma}_1$$

$$\bar{\sigma}_b = \bar{\sigma}_c = \bar{\sigma}_3$$

Fig. 7.1 - Illustration of Notation Used to Describe Directions of Effective Principal Stresses Relative to Shear Wave Motions

TABLE 7.1

Stress Components for the Six Different Shear Waves  
for One State of Biaxial Confinement\*

Shear Wave Type**	$\bar{\sigma}_a$ psi	$\bar{\sigma}_b$ psi	$\bar{\sigma}_c$ psi
(1)	(2)	(3)	(4)
TB/NS	40	15	15
TB/EW	40	15	15
NS/TB	15	40	15
NS/EW	15	15	40
EW/TB	15	40	15
EW/NS	15	15	40

\* Confinement State:  $\bar{\sigma}_1 = 40$  psi (top-bottom axis)  
 $\bar{\sigma}_3 = 15$  psi (north-south and east-west  
 axes)

\*\* The first two letters denote the direction of wave propagation and the second two letters denote the direction of particle motion (TB = top-bottom, NS = north-south, EW = east-west).

### 7.2.2 Patterns of Stress Variation

The variation in stresses for the three biaxial confinement series followed one of two general patterns. In the first pattern, one of the principal stresses ( $\bar{\sigma}_1$  or  $\bar{\sigma}_3$ ) was varied while the remaining principal stress was held constant. This method of stress variation is referred to as biaxial confinement with a variable mean effective principal stress. By varying the state of stress in this manner, the effect on  $V_s$  of the stress components relative to the wave motion directions was studied.

The variation of the stress components relative to wave motions for loading with a varying mean effective principal stress is shown in the first three rows in Table 7.2. Rows one and three describe those tests where only  $\bar{\sigma}_1$  was varied so that the effect of stress in only one direction was isolated and studied in detail. For row one in Table 7.2, where the varying  $\bar{\sigma}_1$  was oriented in the top-bottom (vertical) direction and a constant  $\bar{\sigma}_3$  was oriented along the two remaining axes of the cube, the  $S_{TB/NS}$ -wave reflected the effect on  $V_s$  of  $\bar{\sigma}_a$  alone, since only the stress in the direction of wave propagation was changing. Both  $\bar{\sigma}_b$  and  $\bar{\sigma}_c$  remained constant for this case.

For the series in which structural anisotropy was investigated (row three, Table 7.2) with  $\bar{\sigma}_1$  now varied along the north-south axis of the cube, the same  $S_{TB/NS}$ -wave reflected the effect on  $V_s$  of  $\bar{\sigma}_b$  alone, since the stress in the direction of particle motion was now changing.



TABLE 7.2  
Variation of Stress Components for Biaxial Test Series

Biaxial Test Series	Pattern of Stress Variation	Shear Wave Type*	Direction of Varying Stress Component
(1)	(2)	(3)	(4)
1a. Testing with a variable mean effective principal stress ( $\sigma_1$ varies)	Varying $\bar{\sigma}_1$ oriented along top-bottom direction with constant $\bar{\sigma}_3$ along north-south and east-west axes.	TB/NS TB/EW NS/TB NS/EW EW/TB EW/NS	Wave Propagation Wave Propagation Particle Motion Out-of-Plane Particle Motion Out-of-Plane
1b. Testing with a variable mean effective principal stress ( $\sigma_3$ varies)	Varying $\bar{\sigma}_3$ oriented along east-west and north-south axes with constant $\bar{\sigma}_1$ along top-bottom axis.	TB/NS TB/EW NS/TB NS/EW EW/TB EW/NS	Particle Motion and Out-of-Plane Particle Motion and Out-of-Plane Wave Propagation and Out-of-Plane Wave Propagation and Particle Motion Wave Propagation and Out-of-Plane Wave Propagation and Particle Motion
2. Testing with a variable mean effective principal stress to study structural anisotropy ( $\bar{\sigma}_1$ varies)	Varying $\bar{\sigma}_1$ oriented along north-south axis with constant $\bar{\sigma}_3$ along top-bottom and east-west axes.	TB/NS TB/EW NS/TB NS/EW EW/TB EW/NS	Particle Motion Out-of-Plane Wave Propagation Wave Propagation Out-of-Plane Particle Motion
3. Testing with a constant mean effective principal stress	Varying $\bar{\sigma}_1$ oriented along top-bottom axis with varying $\bar{\sigma}_3$ along the north-south and east-west axes.	TB/NS TB/EW NS/TB NS/EW EW/TB EW/NS	All components vary All components vary All components vary All components vary All components vary All components vary

\* The first two letters denote the direction of wave propagation and the second two letters denote the direction of particle motion (TB = top-bottom, NS = north-south, EW = east-west).

For those tests where only  $\bar{\sigma}_3$  was varied (row two in Table 7.2), the influence of the stress components on  $V_s$  could not be individually studied. Because  $\bar{\sigma}_3$  was applied along two cube axes, changing  $\bar{\sigma}_3$  varied two stress components at the same time. For  $\bar{\sigma}_3$  varying along the north-south and east-west axes of the cube, the  $S_{TB/NS}$ -wave reflected the effect of both  $\bar{\sigma}_b$  and  $\bar{\sigma}_c$ , because only  $\bar{\sigma}_a$  remained constant. Therefore a combined influence of  $\bar{\sigma}_b$  and  $\bar{\sigma}_c$  would be reflected in the variation of  $V_s$  for this shear wave.

The second pattern of stress variation involved changing both principal stresses simultaneously, while maintaining a constant mean effective principal stress, and is, therefore, referred to as biaxial loading with a constant mean effective principal stress. This stress pattern allowed  $V_s$  to be examined for constant  $\bar{\sigma}_0$  but with increasing levels of shear stress. The shear stress was a result of the stress difference between the major and minor principal stresses. Since both  $\bar{\sigma}_1$  and  $\bar{\sigma}_3$  varied, all stress components were changing, and hence, the stress components could not be studied individually. The combined influence of all the stress components is reflected in the variation of  $V_s$ .

### 7.2.3 Review of Simplifications and Data Analysis

As with isotropic confinement, the selected biaxial state of stress existed only on the horizontal plane at the mid-

height of the cube. This was due to inherent pressure gradients in the triaxial cube. These pressure gradients were ignored because of their small mathematical significance on  $V_s$  as discussed in Section 6.2.

Data analysis for biaxial confinement was the same as for isotropic confinement. Shear wave velocity is based upon the combination of short-interval and long-interval measurements because this approach yields the most representative experimental scatter. As with isotropic confinement, direct velocities were discarded as being unrepresentative of  $V_s$  (see Section 6.3).

A complete set of recorded waveforms, data input and resultant computer output for a representative test is included as Appendix D.

### 7.3 TESTING WITH A VARIABLE MEAN EFFECTIVE PRINCIPAL STRESS

Two series of tests were conducted with biaxial confinement in which the mean effective principal stress varied. The first series was designed to study the effect on  $V_s$  of the stress components in the directions of propagation, particle motion, and out-of-plane. The second series, presented in this section and in Section 7.4, was performed to examine the effect of structural anisotropy.

The first biaxial series began at an isotropic confining pressure of 15 psi (103.4 kPa). The vertical stress,  $\bar{\sigma}_1$ , was then increased in 5-psi (34.5 kPa) increments to 40 psi (275.6 kPa)

while  $\bar{\sigma}_3$  was held constant. The two horizontal stresses,  $\bar{\sigma}_3$ , were then increased in 5-psi (34.5 kPa) increments until an isotropic confinement of 40 psi (275.6 kPa) was reached. Shear wave velocity measurements were conducted after each incremental change in pressure. Table B.1 shows these tests as numbers 24 through 29 and 39 through 44, and the load history of the three principal axes can be seen in Fig. B.1 during the time of August 6 through August 11, 1981.

The complete biaxial series was then reversed to evaluate any effect of stress history on the sample. These tests are listed in Table B.1 as numbers 29 through 39, and the load history can be seen in Fig. B.1 during the time of August 6 through August 10, 1981. The principal stress ratio,  $K_{13}$ , defined as:

$$K_{13} = \frac{\bar{\sigma}_1}{\bar{\sigma}_3} \quad (7.1)$$

ranged for these tests from 1.0 to 2.67.

The second biaxial test series also began at an isotropic confining pressure of 15 psi (103.4 kPa). For this test series, however,  $\bar{\sigma}_1$  was re-oriented along the north-south axis. The major principal stress was increased from 15 to 40 psi (103.4 to 275.6 kPa) in 5-psi (34.5 kPa) increments while the top-bottom and east-west axis were maintained at a constant  $\bar{\sigma}_3$ . Tests were performed at 5-psi (34.5 kPa) increments in  $\bar{\sigma}_1$ , as shown in Table B.1 by test numbers 56 through 61. This load history can be

seen in Fig. B.1 during the time of August 17 and August 18, 1981. The principal stress ratio,  $K_{13}$ , for these tests also ranged from 1.0 to 2.67.

### 7.3.1 Effect of Each Stress Component on $V_s$

To examine how each stress component affects  $V_s$ , a variation of Eq. 6.1 was developed as (after Roesler (1979)):

$$V_s = C_1 \bar{\sigma}_a^{ma} \bar{\sigma}_b^{mb} \bar{\sigma}_c^{mc} \quad (7.2)$$

where:  $C_1$  = constant

$ma$  = slope of  $\log V_s - \log \bar{\sigma}_a$  relationship,

$mb$  = slope of  $\log V_s - \log \bar{\sigma}_b$  relationship, and

$mc$  = slope of  $\log V_s - \log \bar{\sigma}_c$  relationship.

In this equation, the mean effective principal stress is replaced by the stress components (expressed in psf) for shear wave motion. Ideally, the sum of the slopes for each stress component ( $ma + mb + mc$ ) should equal the slope  $m$  in Eq. 6.1 (slope of the  $\log V_s - \log \bar{\sigma}_o$  relationship for isotropic confinement) for each shear wave type. The constant,  $C_1$ , represents the physical characteristics of the sand used in testing, including the structural anisotropy of the sand sample.

For biaxial confinement, it was decided to solve Eq. 7.2 for each plane of motion (NS-EW, TB-NS, TB-EW) rather than for each of the six different shear waves. This was done because the structural anisotropy study for isotropic confinement showed that

the six shear waves could be paired into three wave groups with similar planes of motion (see Fig. 6.12). Therefore, a total of nine slopes (three values for each  $m_a$ ,  $m_b$ , and  $m_c$ ) are required for the three planes of motion.

### 7.3.2 Effect of Principal Stress in Direction of Wave Propagation

The first thing studied in the biaxial series was how  $\bar{\sigma}_a$  affected  $V_s$ . To evaluate the effect of  $\bar{\sigma}_a$ , only the stress component in the direction of wave propagation must vary. If more than one stress component is varied, then there is a cumulative effect on  $V_s$ , and the relationship of the individual stress component and  $V_s$  is not directly determined.

Those biaxial tests where the effect of  $\bar{\sigma}_a$  on  $V_s$  could be isolated involved varying only  $\bar{\sigma}_1$ . With  $\bar{\sigma}_1$  oriented along the top-bottom axis, tests were performed for both loading and unloading pressure variations for the TB-NS and TB-EW planes of motion. These results are shown in Figs. 7.2 and 7.3. Each figure shows a sloping straight line depicting the least-squares line. Also shown at the various pressures are a circle depicting the average of all test data for that pressure, a vertical line representing the scatter between the minimum and maximum values measured at that pressure, and two horizontal lines on the vertical line representing  $\pm$  one standard deviation from the average point.

For  $\bar{\sigma}_1$  oriented along the north-south axis of the cube (to examine structural anisotropy), tests were only performed for

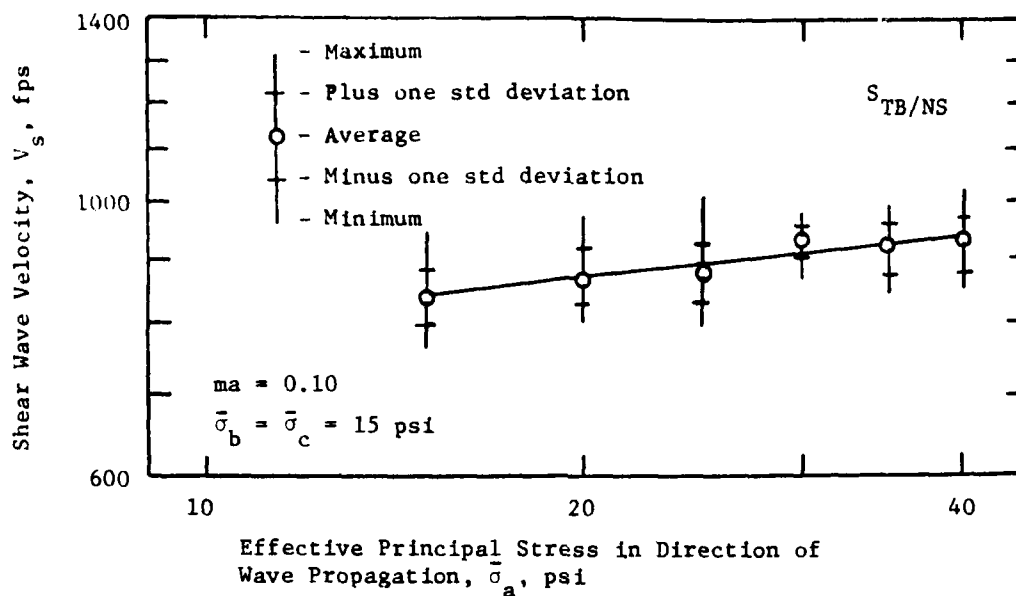
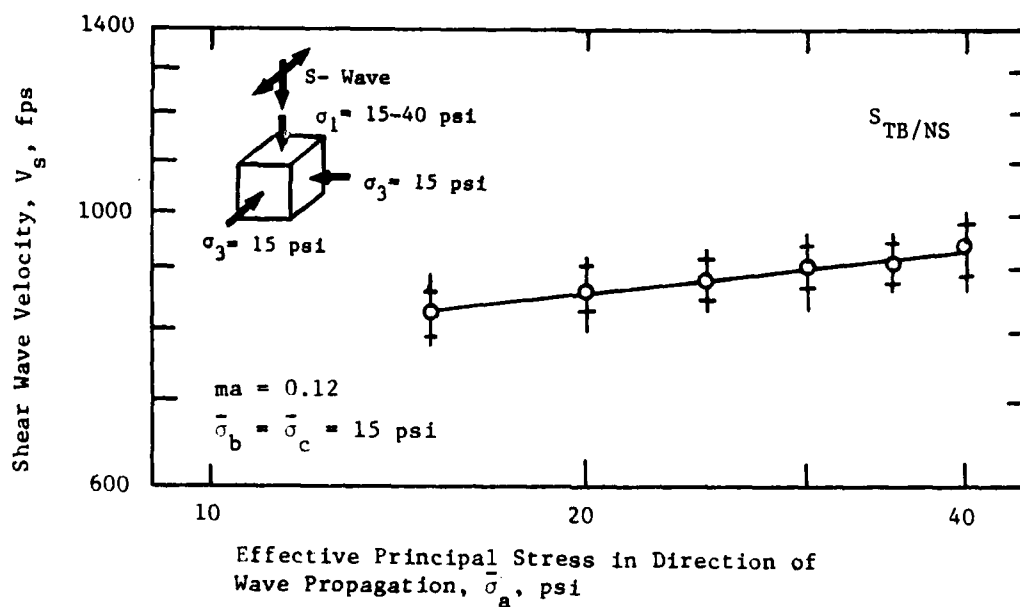
a) Loading Sequence with  $S_{TB/NS}$ -Waveb) Unloading Sequence with  $S_{TB/NS}$ -Wave

Fig. 7.2 - Variation of Shear Wave Velocity with Principal Stress in Direction of Wave Propagation for TB-NS Plane of Motion for Biaxial Confinement

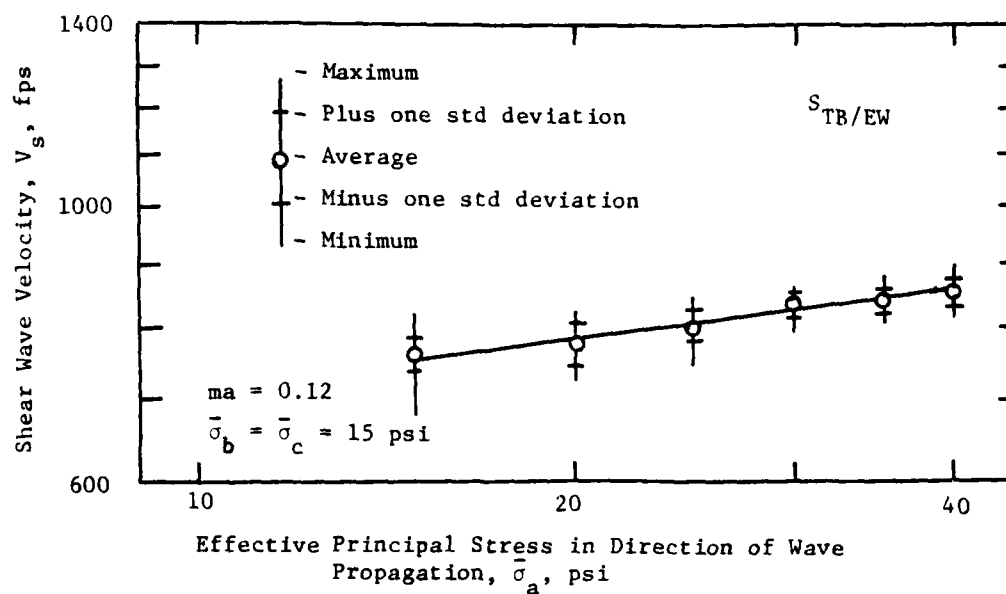
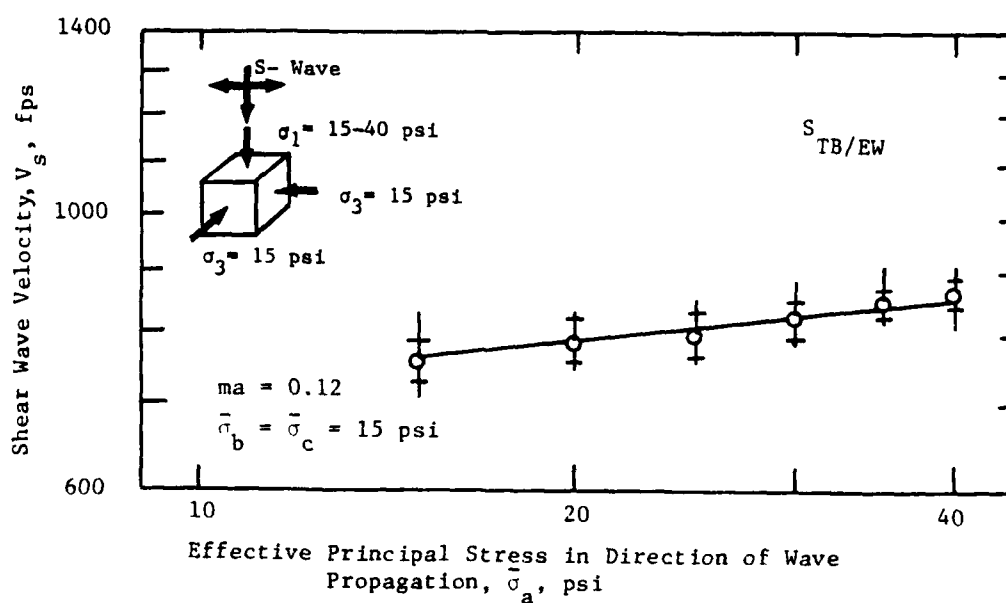
a) Loading Sequence with  $S_{TB/EW}$ -Waveb) Unloading Sequence with  $S_{TB/EW}$ -Wave

Fig. 7.3 - Variation of Shear Wave Velocity with Principal Stress in Direction of Wave Propagation for TB-EW Plane of Motion for Biaxial Confinement



a loading pressure sequence. The loading data are shown in Fig. 7.4 for this test, in which only  $\bar{\sigma}_1$  varied for the NS-TB and NS-EW planes of motion.

The results of the variation in  $V_s$  with  $\bar{\sigma}_a$  ( $\bar{\sigma}_b = \bar{\sigma}_c =$  constant) are summarized in Table 7.3, based on a least-squares fit to the data in Figs. 7.2, 7.3, and 7.4. From Table 7.3, the slope of the  $\log V_s - \log \bar{\sigma}_a$  relationship varies from 0.10 to 0.13 for all three wave groups. This variation in slope is well within the expected experimental scatter, and there are no apparent effects of structural anisotropy or stress history.

### 7.3.3 Effect of Principal Stress in Direction of Particle Motion

In a manner similar to that used to study the  $\log V_s - \log \bar{\sigma}_a$  relationship, those tests in which only  $\bar{\sigma}_1$  varied were used to examine the effect on  $V_s$  of  $\bar{\sigma}_b$ . For  $\bar{\sigma}_1$  oriented along the top-bottom axis of the cube, the  $\log V_s - \log \bar{\sigma}_b$  relationship for the TB-NS and TB-EW planes of motion are shown in Figs. 7.5 and 7.6, respectively, for both loading and unloading sequences. With  $\bar{\sigma}_1$  oriented along the north-south axis of the cube, Fig. 7.7 shows the effect on  $V_s$  of  $\bar{\sigma}_b$  for the TB-NS and EW-NS planes of motion for loading only. On all four of these figures are included the average of all interval velocity data for any test pressure, as well as the minimum and maximum values of the data and  $\pm$  one standard deviation from the average at each pressure.

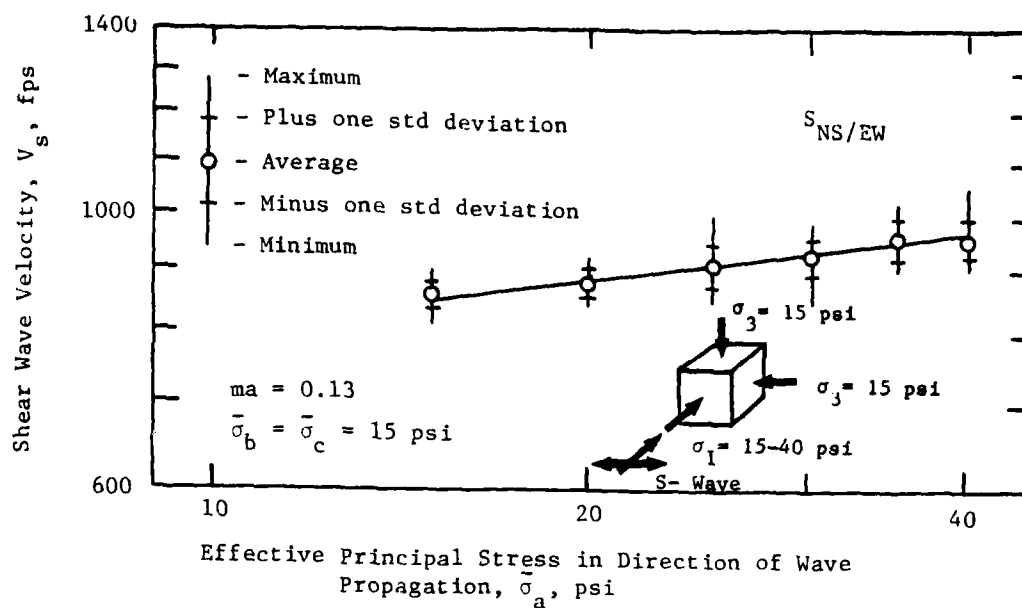
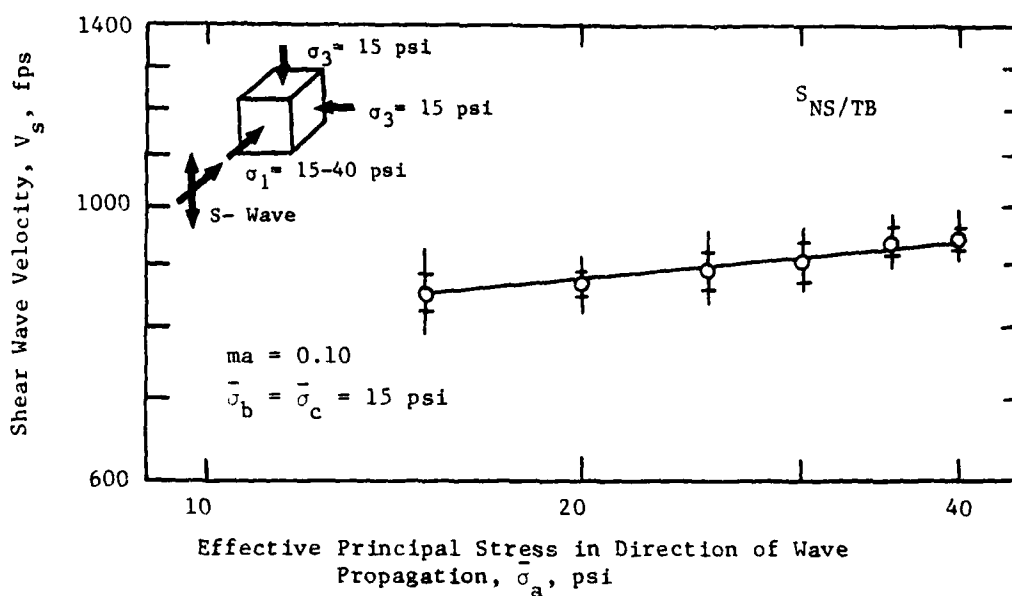
a) Loading Sequence with  $S_{NS/EW}$ -Waveb) Loading Sequence with  $S_{NS/TB}$ -Wave

Fig. 7.4 - Variation of Shear Wave Velocity with Principal Stress in Direction of Wave Propagation for NS-EW and NS-TB Planes of Motion for Biaxial Confinement

TABLE 7.3

Effect on  $V_s$  of Principal Stress in Direction  
of Wave Propagation for Biaxial Confinement

Plane of Motion	Slope of $\log V_s - \log \bar{\sigma}_a$ Relationship*		
	Loading ma	Unloading ma	Average ma
(1)	(2)	(3)	(4)
TB-NS	0.10	0.12	0.11
TB-EW	0.12	0.12	0.12
NS-EW	0.13	**	**

\* Eq. 7.2:  $V_s = C_1 \bar{\sigma}_a^{ma} \bar{\sigma}_b^{mb} \bar{\sigma}_c^{mc}$

\*\* Not determined because only performed loading pressure sequence.

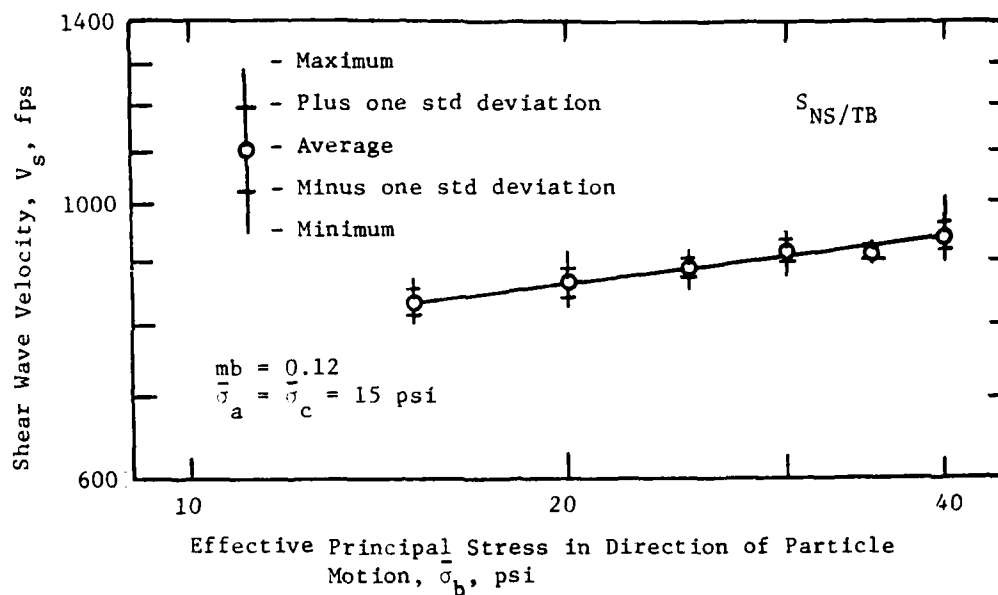
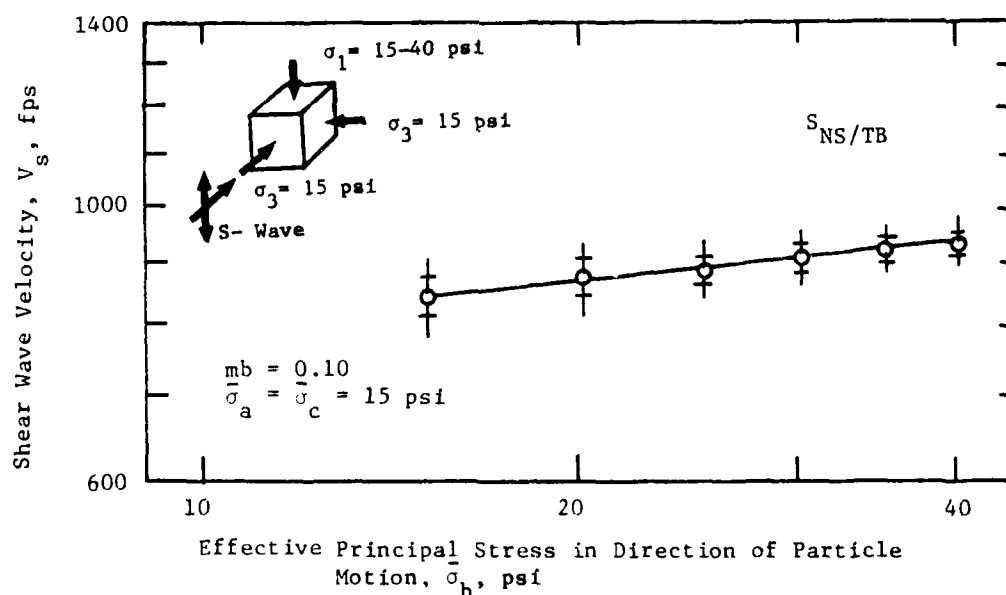
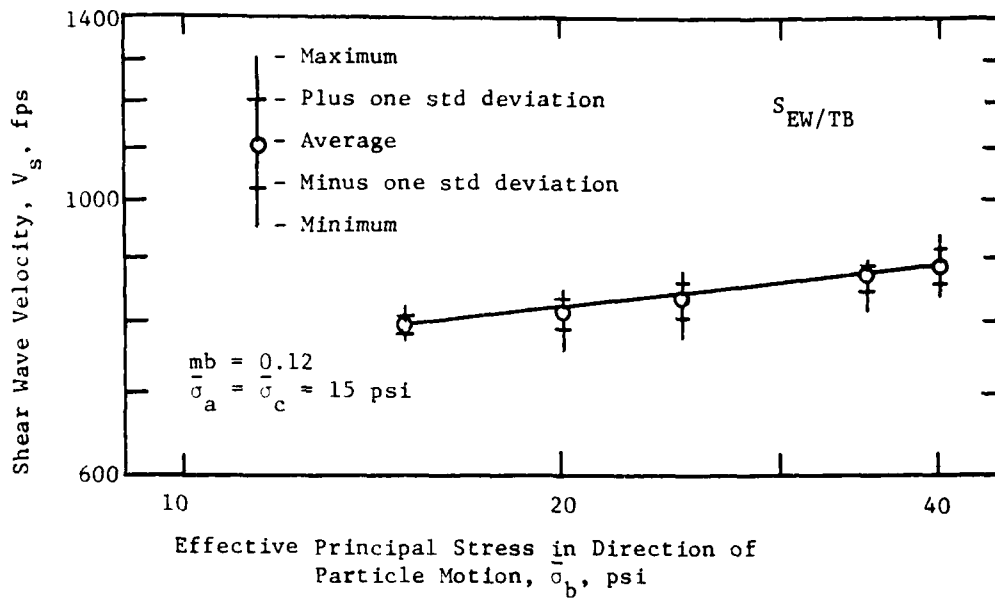
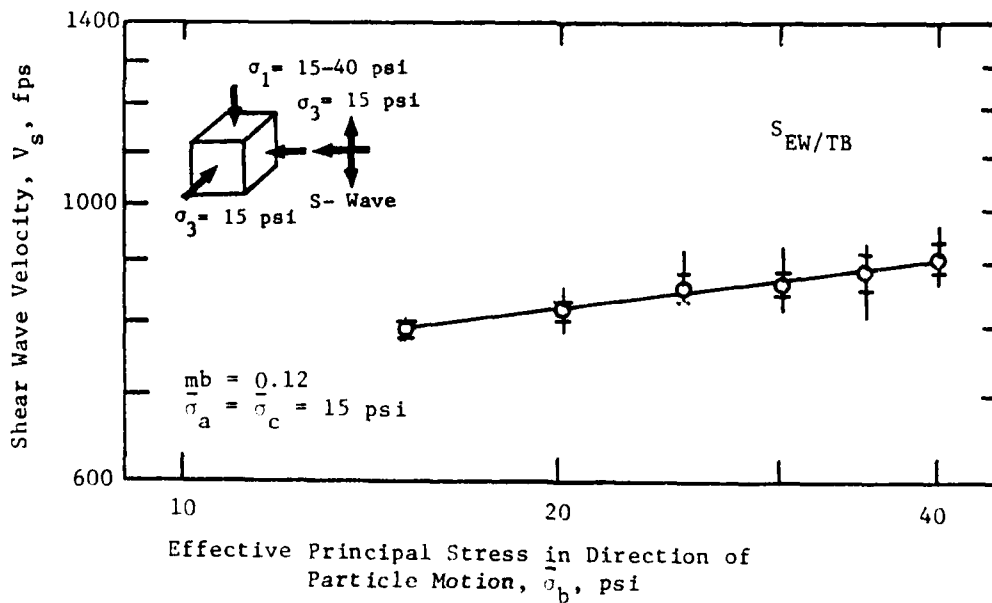
a) Loading Sequence with  $S_{NS/TB}$ -Waveb) Unloading Sequence with  $S_{NS/TB}$ -Wave

Fig. 7.5 - Variation of Shear Wave Velocity with Principal Stress in Direction of Particle Motion for TB-NS Plane of Motion for Biaxial Confinement

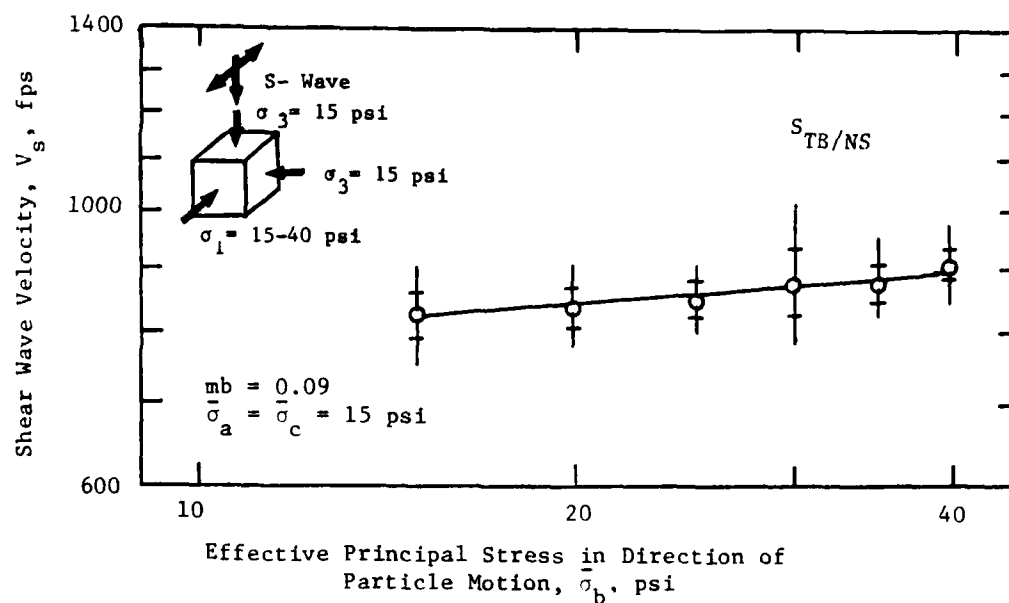


a) Loading Sequence with  $S_{EW/TB}$ -Wave

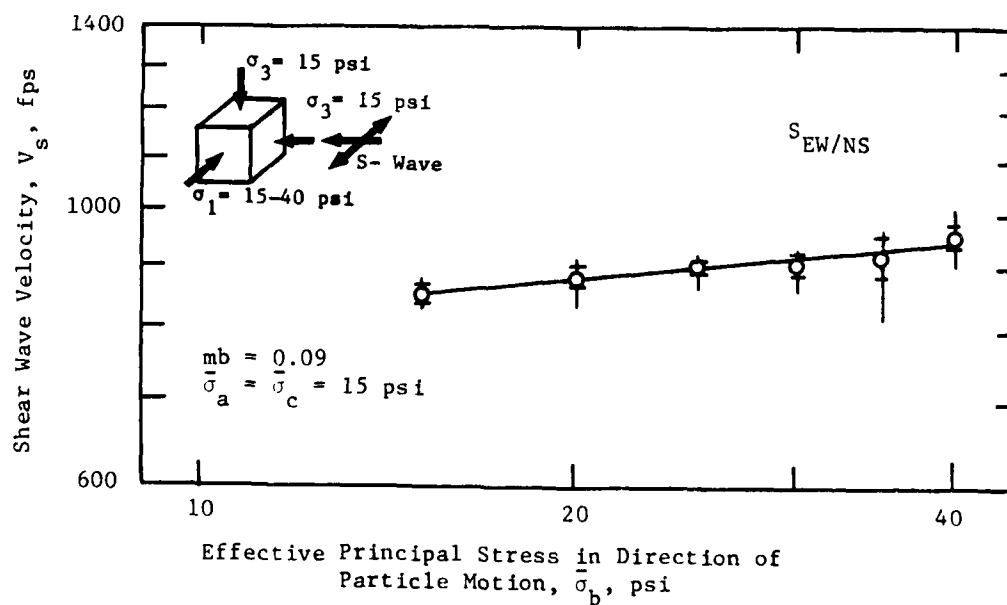


b) Unloading Sequence with  $S_{EW/TB}$ -Wave

Fig. 7.6 - Variation of Shear Wave Velocity with Principal Stress in Direction of Particle Motion for TB-EW Plane of Motion for Biaxial Confinement



a) Loading Sequence with  $S_{TB/NS}$ -Wave



b) Loading Sequence with  $S_{EW/NS}$ -Wave

Fig. 7.7 - Variation of Shear Wave Velocity with Principal Stress in Direction of Particle Motion for TB-NS and EW-NS Planes of Motion for Biaxial Confinement

A summary of the  $\log V_s - \log \bar{\sigma}_b$  relationships shown in Figs. 7.4, 7.5, and 7.6 are summarized in Table 7.4. Using a least-squares fit, the value of  $mb$  varies from 0.09 to 0.12 for the three wave groups. Stress history has no apparent effect on  $mb$  in that similar values were measured for both loading and unloading test sequences. Similarly, structural anisotropy had no apparent effect on the shear waves contained in any plane of motion. In general the values of  $mb$  are equal to or slightly less than the values of  $ma$  obtained in Section 7.3.2. This would tend to indicate that for this sand the shear wave velocity is equally dependent on the principal stresses in the directions of wave propagation and particle motion.

#### 7.3.4 Effect of Principal Stress in the Out-of-Plane Direction

The last stress component studied was  $\bar{\sigma}_c$ , the principal stress in the out-of-plane direction. As with  $\bar{\sigma}_a$  and  $\bar{\sigma}_b$ , the results presented are for those tests where only  $\bar{\sigma}_1$  varied, and therefore, only  $\bar{\sigma}_c$  varied. Figure 7.8 shows the  $\log V_s - \log \bar{\sigma}_c$  relationship for the NS-EW plane of motion for the loading and unloading pressure sequences. For this figure,  $\bar{\sigma}_1$ , was oriented along the top-bottom axis of the cube. Figure 7.9 shows the  $\log V_s - \log \bar{\sigma}_c$  relationship for the TB-EW plane of motion for those tests with  $\bar{\sigma}_1$  oriented along the north-south axis of the cube.

TABLE 7.4

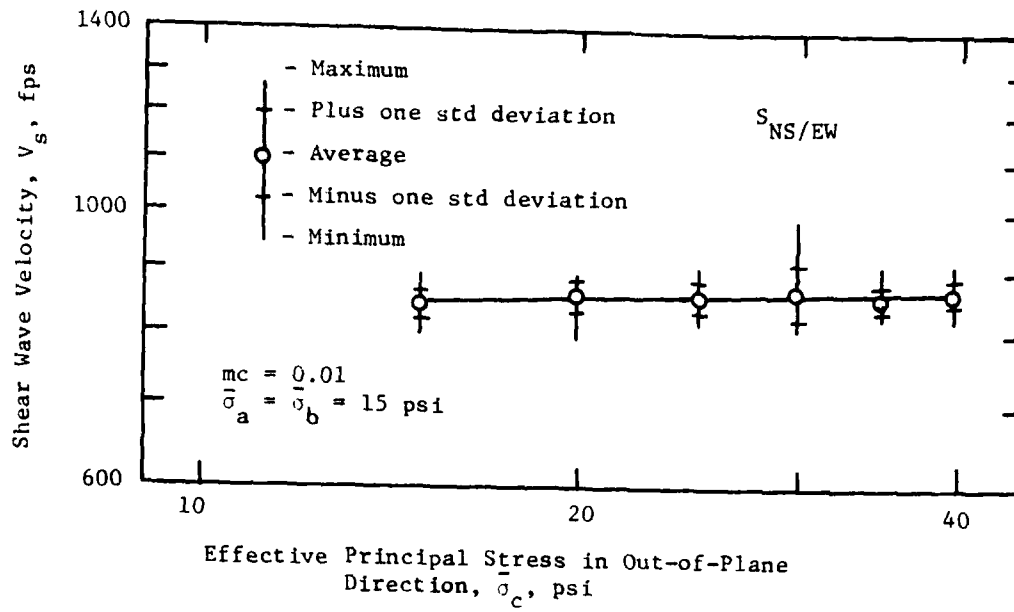
Effect on  $V_s$  of Principal Stress in Direction  
of Particle Motion for Biaxial Confinement

Plane of Motion	Slope of $\log V_s - \log \bar{\sigma}_b$ Relationship*		
	Loading mb	Unloading mb	Average mb
(1)	(2)	(3)	(4)
TB-NS	0.11	0.10	0.10
TB-EW	0.12	0.12	0.12
NS-EW	0.09	**	**

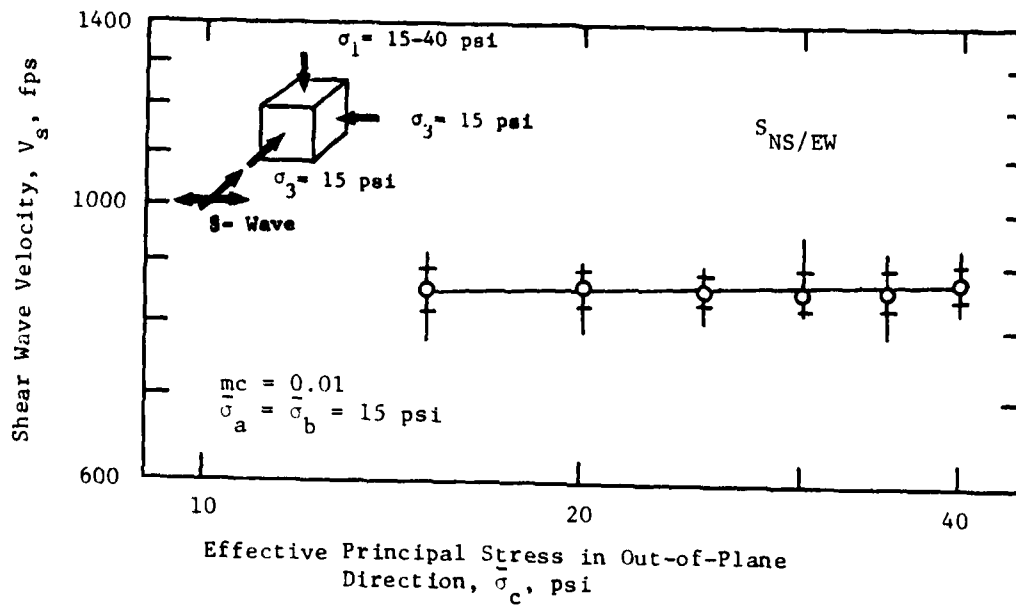
\* Eq. 7.2:  $V_s = C_1 \bar{\sigma}_a^{ma} \bar{\sigma}_b^{mb} \bar{\sigma}_c^{mc}$

\*\* Not determined because only performed loading pressure sequence.



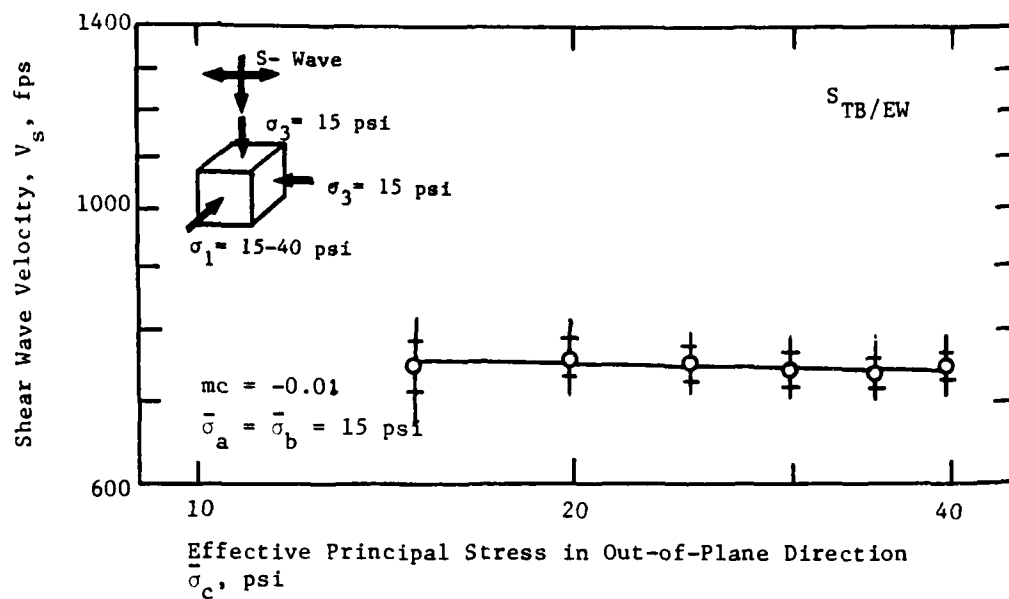


a) Loading Sequence with  $S_{NS/EW}$ -Wave

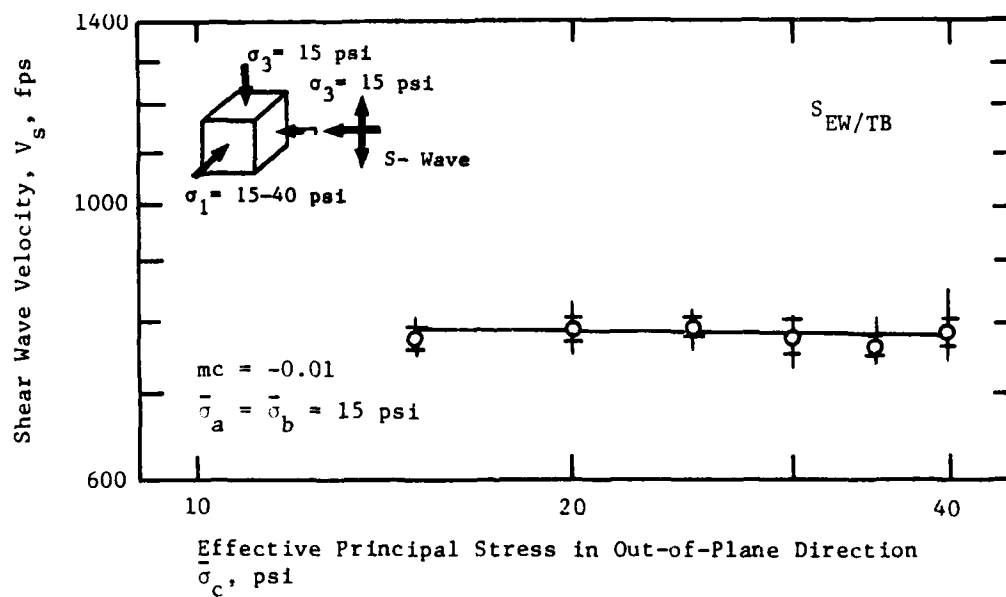


b) Unloading Sequence with  $S_{NS/EW}$ -Wave

Fig. 7.8 - Variation of Shear Wave Velocity with Principal Stress in Out-of-Plane Direction for NS-EW Plane of Motion for Biaxial Confinement



a) Loading Sequence with  $S_{TB/EW}$ -Wave



b) Loading Sequence with  $S_{EW/TB}$ -Wave

Fig. 7.9 - Variation of Shear Wave Velocity with Principal Stress in Out-of-Plane Direction for TB-EW Plane of Motion for Biaxial Confinement

The results of the least-square fit of the data for  $\bar{\sigma}_c$  are summarized in Table 7.5. As seen in this table, the value of  $m_c$  for the TB-EW plane of motion was slightly less than zero while the value of  $m_c$  for the NS-EW plane of motion was slightly greater than zero. These small values of  $m_c$  indicate that the shear wave velocity depends very little on the principal stress in the out-of-plane direction. As with  $\bar{\sigma}_a$  and  $\bar{\sigma}_b$ , stress history had no apparent effect on the value of  $m_c$ .

#### 7.3.5 Summary of Effect of Principal Stresses on $V_s$

The values of  $m_a$ ,  $m_b$ , and  $m_c$ , presented in Tables 7.3, 7.4, and 7.5, respectively, are incomplete. Values were not given for all planes of motion and for unloading portions of certain tests. This stems from the fact that in these initial tests not all the possible combinations of stress components and planes of motion had shear wave tests performed on them where only one principal stress varied.

To determine the complete set of values for  $m_a$ ,  $m_b$ , and  $m_c$ , the test series performed with an increasing  $\bar{\sigma}_3$  (while  $\bar{\sigma}_1$  remained constant) had to be used. For this test series with a variable  $\bar{\sigma}_3$ , two stress components were changing. The use of this test series, therefore, involved the implicit assumption that one of the two changing stress components is known so that the other component can be determined. For the calculations in this section, one of the stress components was assumed (based on the




TABLE 7.5

Effect on  $V_s$  of Principal Stress in Out-of-Plane  
Direction for Biaxial Confinement

Plane of Motion	Slope of $\log V_s - \log \bar{\sigma}_c$ Relationship*		
	Loading mc	Unloading mc	Overall mc
(1)	(2)	(3)	(4)
TB-NS	**	**	**
TB-EW	-0.01	**	**
NS-EW	0.01	0.01	0.01

\* Eq. 7.2:  $V_s = C_1 \bar{\sigma}_a^{ma} \bar{\sigma}_b^{mb} \bar{\sigma}_c^{mc}$

\*\* Not determined because only performed loading sequence  
or because stress component not varied for this plane  
of motion.

previous sections), and the other stress components were calculated based on a least-squares fit. The assumption was made that  $m_a$  was equal to  $m_b$ . That is, the shear wave velocity was equally affected by the stress in the direction of propagation and particle motion. The values determined for  $m_a$ ,  $m_b$ , and  $m_c$  are summarized in Table 7.6.

Once the various values of the slopes were evaluated, the constant  $C_1$  for Eq. 7.2 was determined for each plane of motion. This was accomplished by dividing the measured shear wave velocity for each test pressure by the three principal stress components for that test pressure raised to the appropriate power. The value of  $C_1$  for each plane of motion is also summarized in Table 7.6. The values of  $C_1$  reflect the physical characteristics of the sand used in the testing as well as the anisotropic nature of the sample (see Section 7.4.).

Based on the table, it is clear that each stress component does not contribute equally to the shear wave velocity for these body waves. The principal stresses in the directions of wave propagation and particle motion are dominant. It appears for this sand that the principal stresses in these directions can be assumed to contribute equally to the shear wave velocity. The principal stress in the out-of-plane direction affects the shear wave velocity very little and can be neglected.

TABLE 7.6

Summary of Effects on  $V_s$  of Orientation of Principal  
Stresses Relative to Planes of Motion for  
Biaxial Confinement

Variable in Equation 7.2*	Plane of Motion	Loading	Unloading	Average
(1)	(2)	(3)	(4)	(5)
ma	TB-NS	0.10	0.12	0.10
	TB-EW	0.13	0.11	0.12
	NS-EW	0.10	0.09	0.09
mb	TB-NS	0.11	0.10	0.10
	TB-EW	0.11	0.11	0.11
	NS-EW	0.09	0.09	0.09
mc	TB-NS	-0.01	-0.01	-0.01
	TB-EW	-0.01	-0.01	-0.01
	NS-EW	0.01	0.01	0.01
$C_1^{**}$	TB-NS	181	168	180
	TB-EW	113	145	132
	NS-EW	185	204	201

\* Eq. 7.2:  $V_s = C_1 \frac{\sigma_a}{\sigma_b} \frac{\sigma_a}{\sigma_c} \frac{\sigma_b}{\sigma_c}$

\*\*  $\frac{ft^{3-t}}{\text{sec lb}^t}$  where  $t = ma + mb + mc$

For all stress components, stress history has no marked effect on the values in Table 7.6. Therefore, stress history can be ignored for the case of biaxial confinement.

In comparing the  $V_s$  - stress-component relationships developed from this data with those obtained by Roesler (1979), there is a clear similarity. In both experiments, the stress component in the out-of-plane direction was found not to affect the shear wave velocity and, hence, could be ignored. Although absolute numbers are not important (due to the difference in sand samples), Roesler found that the stress component in the direction of wave propagation was more dominant than the component in the direction of particle motion ( $m_a$  equal to 0.15 versus  $m_b$  equal to 0.11). For this study, these two stress components were determined to affect the shear wave velocity almost equally, with the average slopes ranging for  $m_a$  from 0.09 to 0.12, and for  $m_b$  from 0.09 to 0.11.

A comparison can be made between the values of the sum of the slopes ( $m_a + m_b + m_c$ ) and  $C_1$  for biaxial confinement with the comparable values for isotropic confinement. Table 7.7 summarizes the values of these variables for each plane of motion for both isotropic and biaxial states of stress. As can be seen in the table, the results for both states of stress are in good agreement. For any plane of motion, the values of  $C_1$  are within 10 percent of the average for the isotropic and biaxial states of stress. The sum of the stress-component exponents for biaxial

TABLE 7.7

Comparison of the Effect of Principal Stresses on Shear Wave Velocity for Isotropic and Biaxial Confinement States

Plane of Motion	Type of Confinement	log $V_s$ - log $\bar{\sigma}$ Relationship*	
		(ma+mb+mc) or m	$C_1 \left( \frac{ft^{(3-t)}}{\text{sec lb}^t} \right)^{**}$
(1)	(2)	(3)	(4)
TB-NS	Biaxial	0.20	180
	Isotropic	0.18	217
TB-EW	Biaxial	0.23	132
	Isotropic	0.22	142
NS-EW	Biaxial	0.19	201
	Isotropic	0.19	199

\* Eq. 7.2 for biaxial confinement:  $V_s = C_1 \bar{\sigma}_a^{ma} \bar{\sigma}_b^{mb} \bar{\sigma}_c^{mc}$

Eq. 6.1 for isotropic confinement:  $V_s = C_1 \bar{\sigma}_o^m$

\*\* t = m for isotropic confinement or (ma + mb + mc) for biaxial confinement



AD-A120 426

EFFECT OF STATE OF STRESS ON VELOCITY OF LOW-AMPLITUDE  
SHEAR WAVES PROPAG. (U) TEXAS UNIV AT AUSTIN  
GEOTECHNICAL ENGINEERING CENTER D P KNOX ET AL. MAR 82

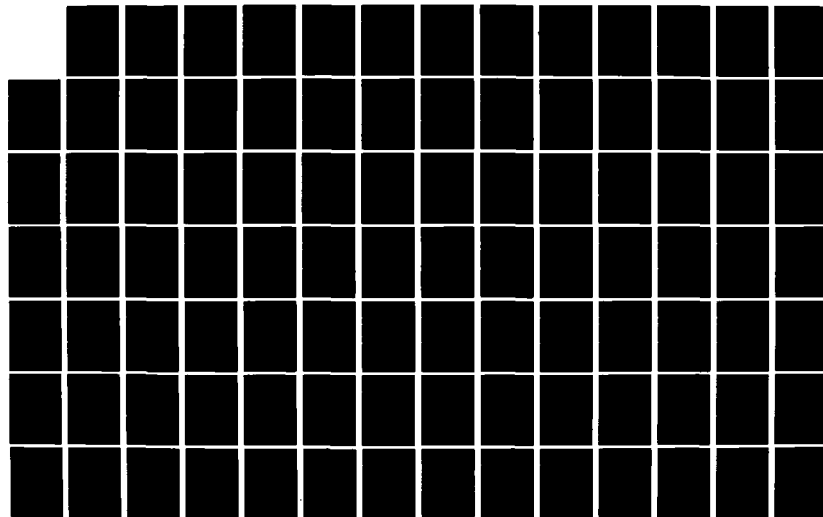
370

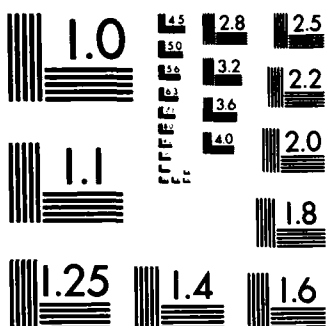
UNCLASSIFIED

GR82-23 AFOSR-TR-82-0908 AFOSR-80-0031

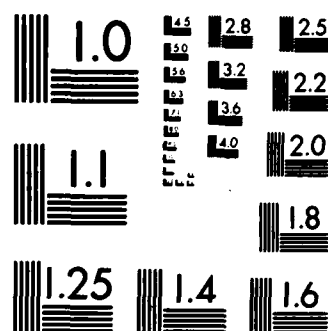
F/G 20/11

NL

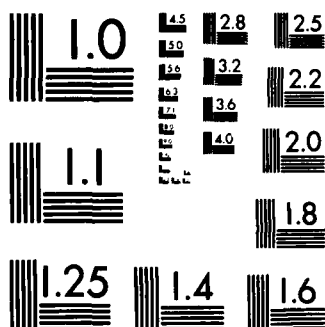




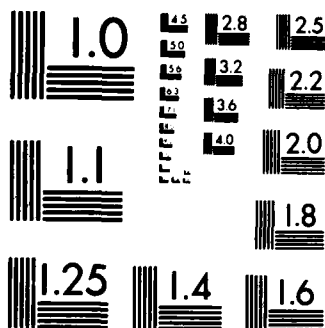
MICROCOPY RESOLUTION TEST CHART  
NATIONAL BUREAU OF STANDARDS-1963-A



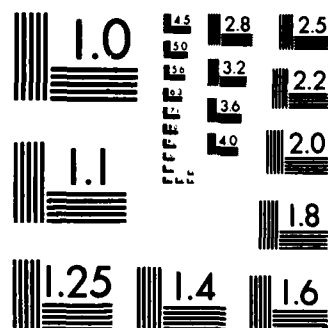
MICROCOPY RESOLUTION TEST CHART  
NATIONAL BUREAU OF STANDARDS-1963-A



MICROCOPY RESOLUTION TEST CHART  
NATIONAL BUREAU OF STANDARDS-1963-A



MICROCOPY RESOLUTION TEST CHART  
NATIONAL BUREAU OF STANDARDS-1963-A



MICROCOPY RESOLUTION TEST CHART  
NATIONAL BUREAU OF STANDARDS-1963-A

confinement are also within 10 percent of the value of the slope of the  $\log V_s - \log \bar{\sigma}_0$  relationship for isotropic confinement. The 10 percent difference in values can be attributed to experimental scatter in this study. Therefore, a good correlation was determined for the various factors affecting shear wave velocity for both isotropic and biaxial states of stress.

#### 7.3.6 Comparison Between Measured and Predicted Shear Wave Velocities

To estimate how accurately the equations developed in Table 7.6 predict shear wave velocity, measured values of  $V_s$  were compared with predicted values. This was done for the biaxial series where  $\bar{\sigma}_3$  varied for the east-west and north-south axes of the cube, while  $\bar{\sigma}_1$  remained constant for the top-bottom axis. The comparison was made for the three planes of motion and for the two shear wave types determined by each respective plane. Hence, for the TB-NS plane, both the  $S_{TB/NS}$ - and  $S_{NS/TB}$ -waves were compared.

The comparison between measured and predicted shear wave velocities was done in two ways. In the first method, measured data for each test pressure (average,  $\pm$  one standard deviation, and minimum and maximum values of the data) was shown on a plot of  $\log V_s$  versus  $\log \bar{\sigma}_3$ , where  $\bar{\sigma}_3$  equalled the varying principal stress components. The predicted shear wave velocity was included in the plot as a solid straight line based on the equations for each plane of motion shown in Table 7.6.

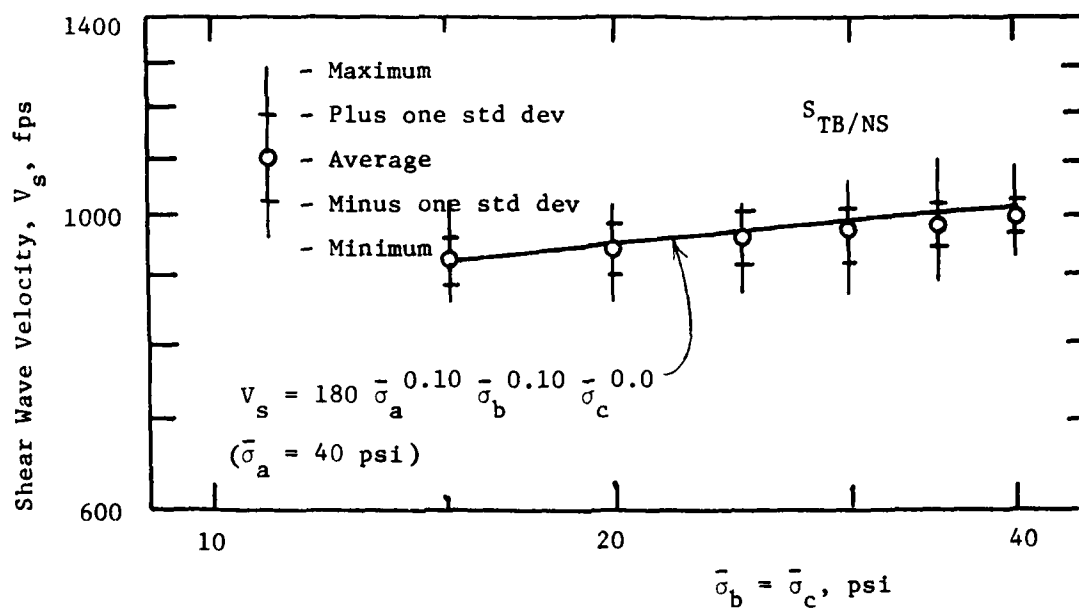
The second method of comparison involved the division of the measured  $V_s$  by the predicted  $V_s$  to obtain a ratio. A value for this ratio of one would indicate an exact correlation between these two values of  $V_s$ . The ratio was determined for the average,  $\pm$  one standard deviation from the average and the minimum and maximum data points for the measured data at each test pressure.

The results of these comparisons are shown in Figs. 7.10 through 7.15. Based on these figures, the ratio of measured to predicted  $V_s$  for  $\pm$  one standard deviation typically ranges from 0.95 to 1.05, although for the NS-EW plane of motion the values range from 0.90 to 1.14. These close comparisons indicate that the equations predict measured shear wave velocities within about  $\pm$  10 percent for each plane of motion. This difference between measured and predicted values of  $V_s$  is well within tolerable limits and is consistent with the  $\pm$  10 percent variance present throughout this study due to experimental scatter. The results of the comparison of values of  $V_s$  show good agreement and indicate that the equations developed in Table 7.6 can be used to predict  $V_s$  for this sand with sufficient accuracy.

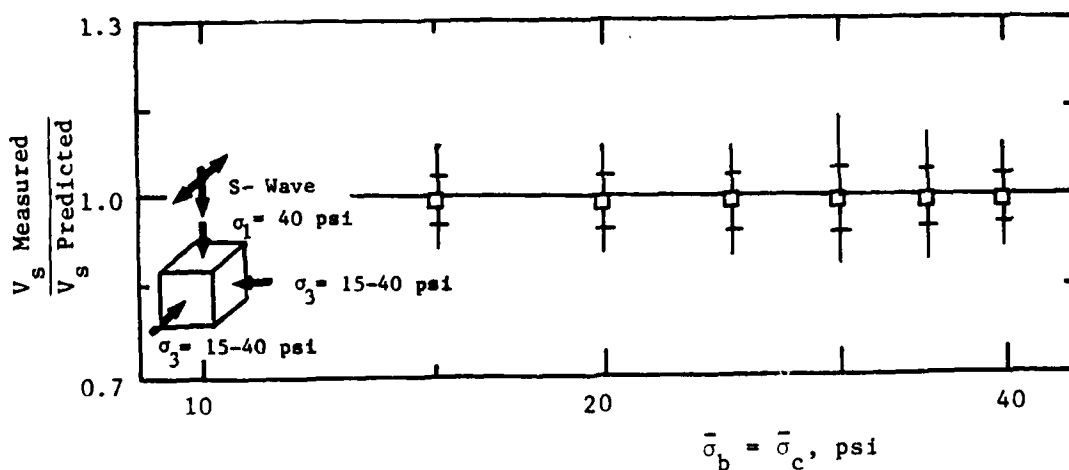
### 7.3.7 Effect of Principal Stresses on Shear Modulus

Based on the results presented in Table 7.6, the shear modulus can be expressed in a simplified form as (after Hardin (1978)):

$$G_{\max} = \frac{C}{0.673} P_a^{1-(n_a+n_b+n_c)} \frac{n_a}{\sigma_a} \frac{n_b}{\sigma_b} \frac{n_c}{\sigma_c} \quad (7.3)$$

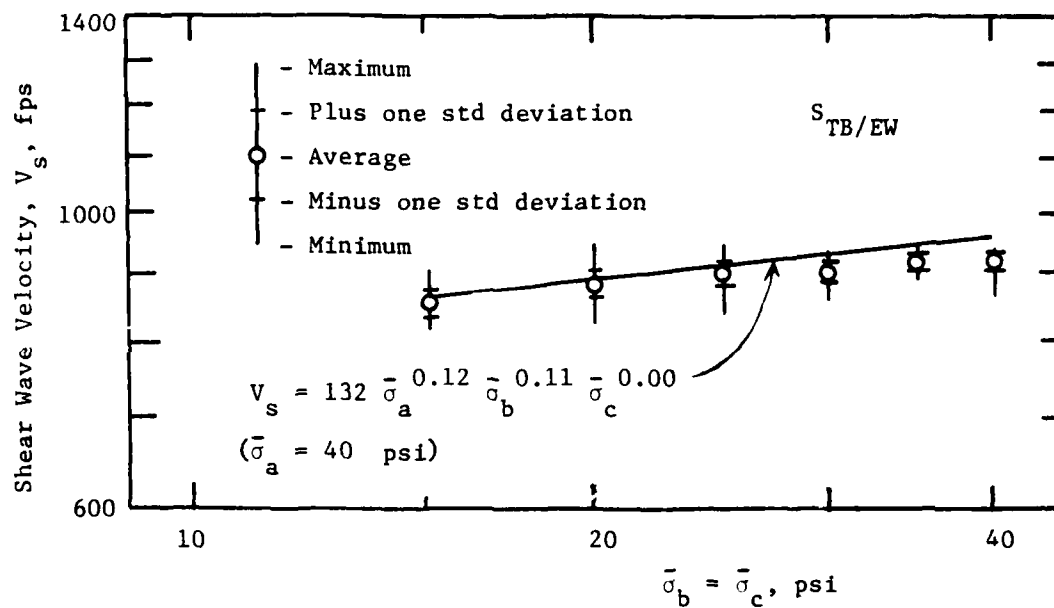


a) Absolute Values of Shear Wave Velocities

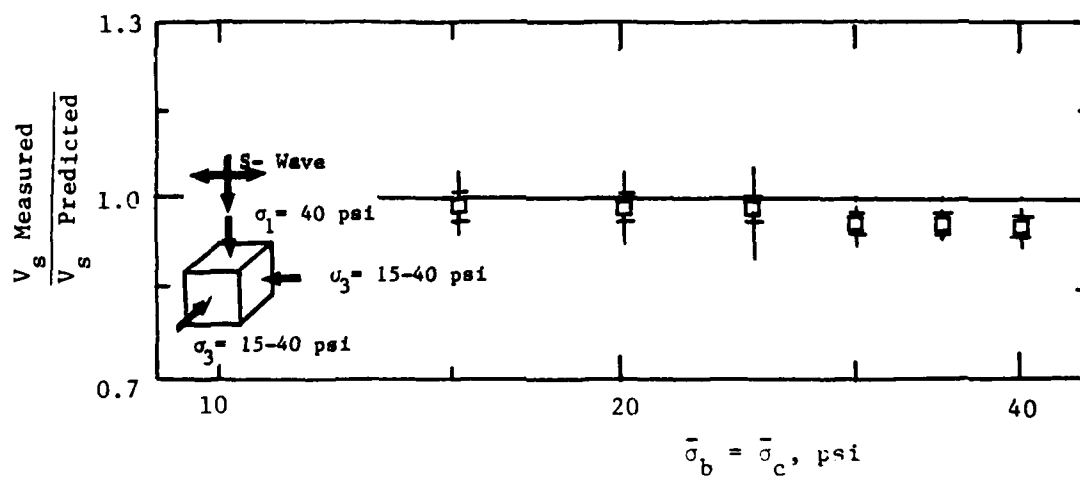


b) Ratio of Shear Wave Velocities

Fig. 7.10 - Comparison of Measured and Predicted Shear Wave Velocities for  $S_{TB/NS}$ -Wave for Biaxial Confinement with a Varying  $\bar{\sigma}_0$

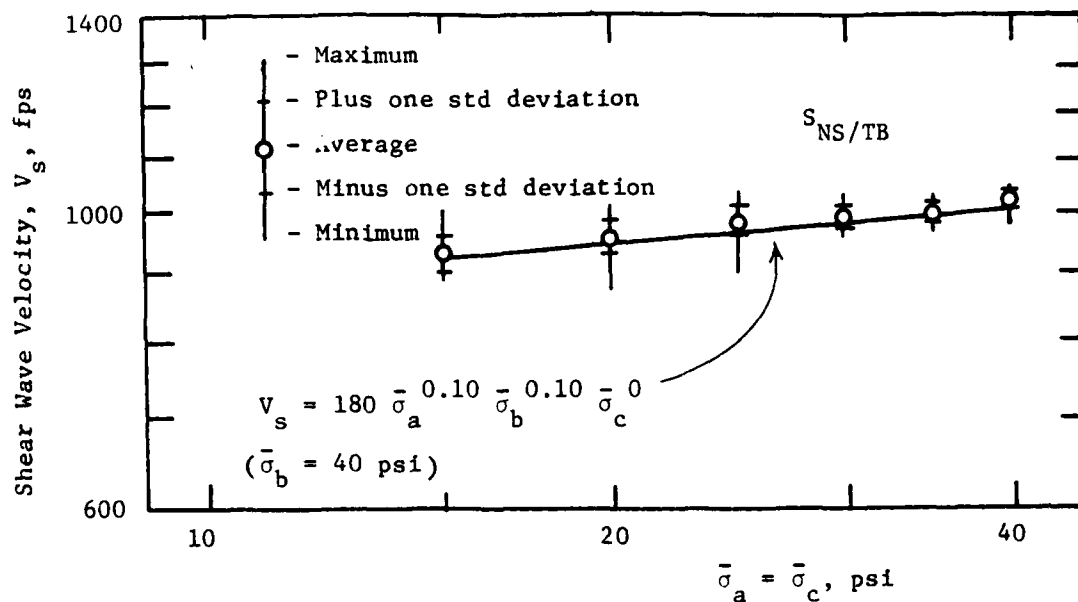


a) Absolute Values of Shear Wave Velocities

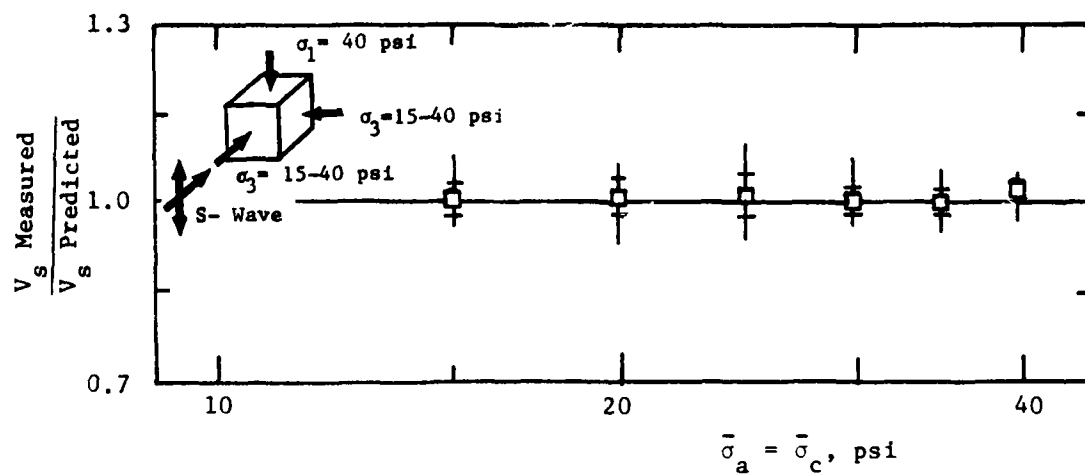


b) Ratio of Shear Wave Velocities

Fig. 7.11 - Comparison of Measured and Predicted Shear Wave Velocities for  $S_{TB/EW}$ -Wave for Biaxial Confinement with a Varying  $\bar{\sigma}_0$

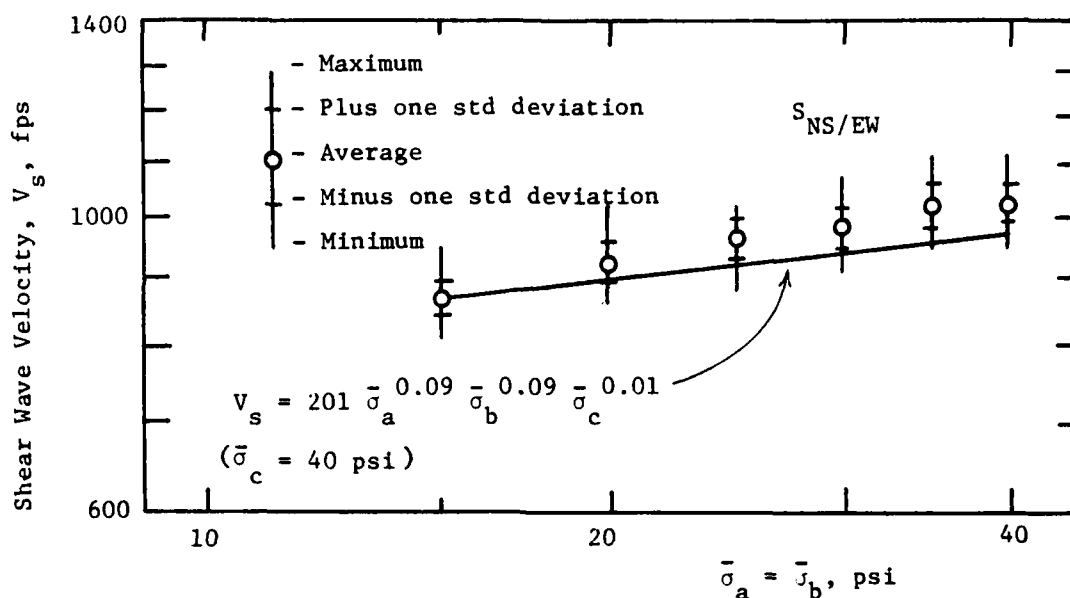


a) Absolute Values of Shear Wave Velocities

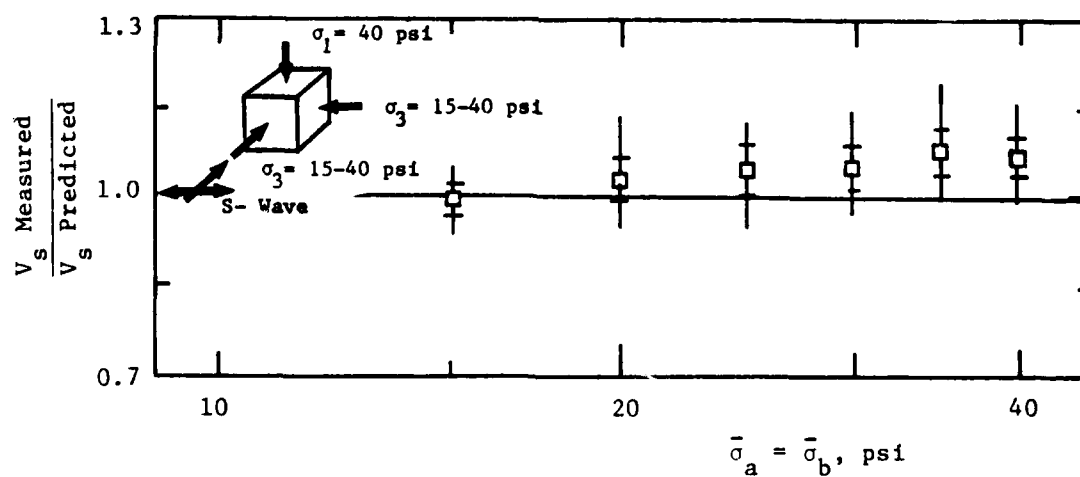


b) Ratio of Shear Wave Velocities

Fig. 7.12 - Comparison of Measured and Predicted Shear Wave Velocities for  $S_{NS/TB}$ -Wave for Biaxial Confinement with a Varying  $\bar{\sigma}_o$



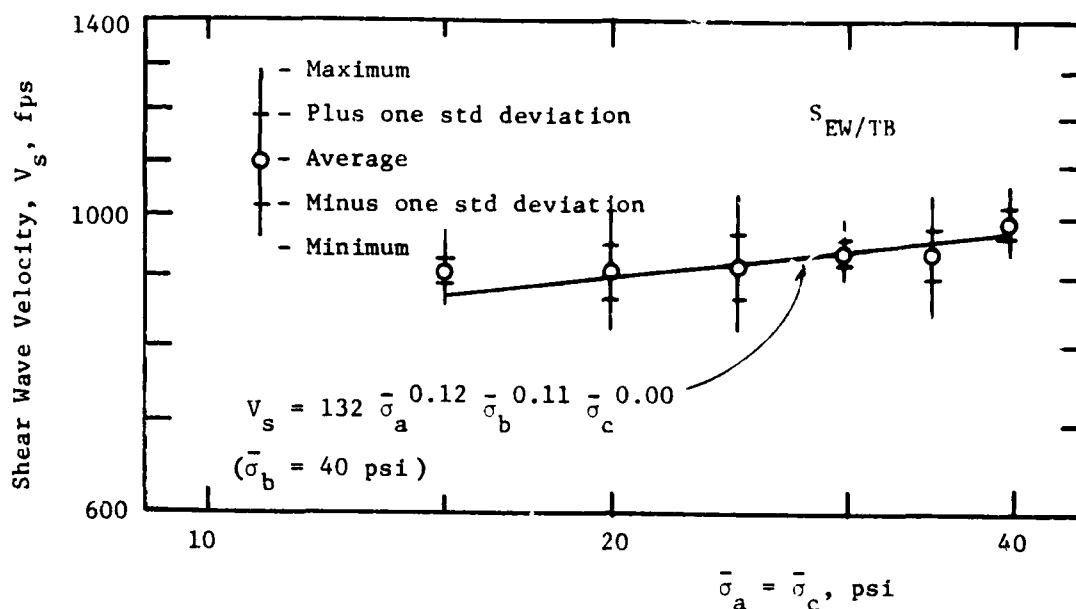
a) Absolute Values of Shear Wave Velocities



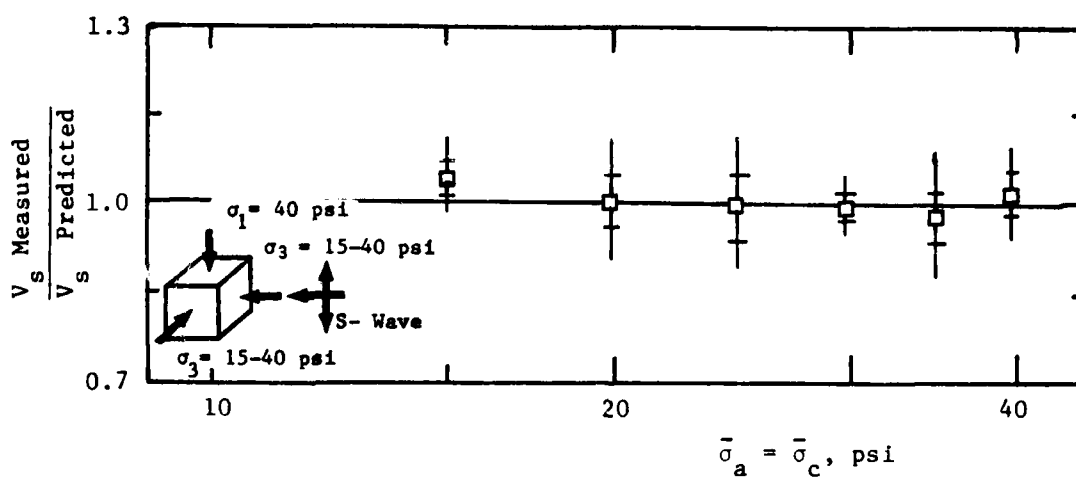
b) Ratio of Shear Wave Velocities

Fig. 7.13 - Comparison of Measured and Predicted Shear Wave Velocities for  $S_{NS/EW}$ -Wave for Biaxial Confinement with a Varying  $\sigma_o$



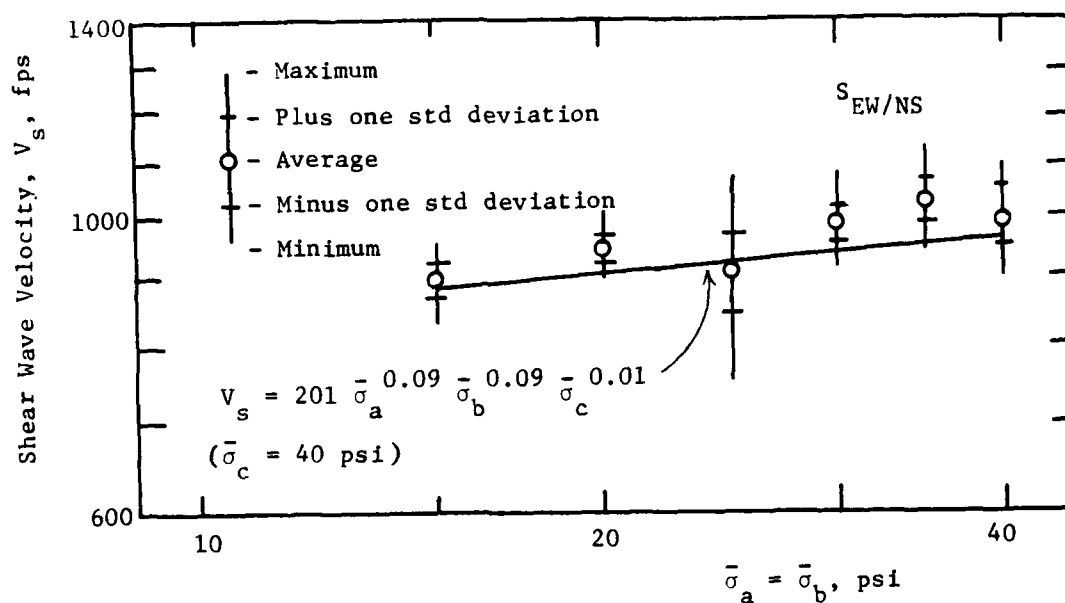


a) Absolute Values of Shear Wave Velocities

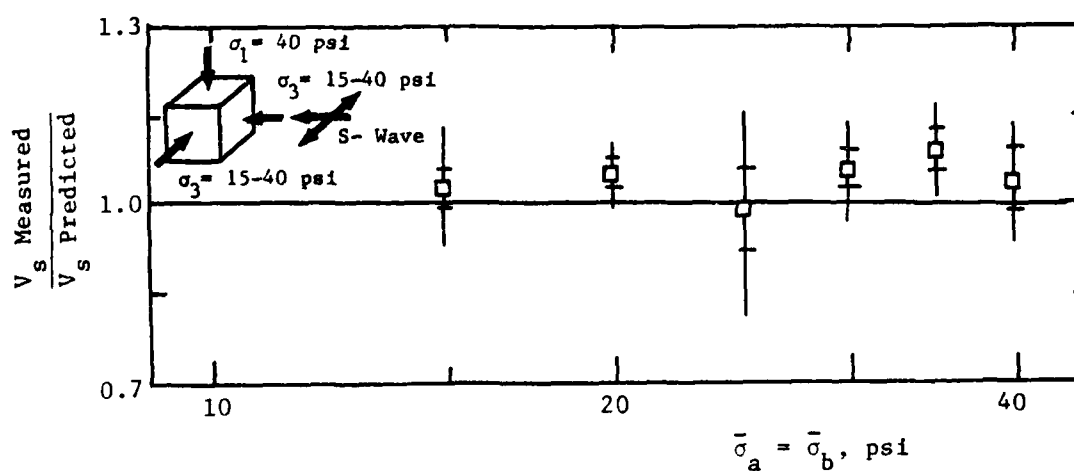


b) Ratio of Shear Wave Velocities

Fig. 7.14 - Comparison of Measured and Predicted Shear Wave Velocities for  $S_{EW/TB}$ -Wave for Biaxial Confinement with a Varying  $\bar{\sigma}_o$



a) Absolute Values of Shear Wave Velocities



b) Ratio of Shear Wave Velocities

Fig. 7.15 - Comparison of Measured and Predicted Shear Wave Velocities for  $S_{EW/NS}$ -Wave for Biaxial Confinement with a Varying  $\bar{\sigma}_o$

where:  $G_{\max}$  = shear modulus in desired units,  
 $C$  = dimensionless constant,  
 $na$  = slope of  $\log G_{\max} - \log \bar{\sigma}_a$  relationship,  
 $nb$  = slope of  $\log G_{\max} - \log \bar{\sigma}_b$  relationship,  
 $nc$  = slope of  $\log G_{\max} - \log \bar{\sigma}_c$  relationship,  
 $Pa$  = atmospheric pressure in same units as  $G_{\max}$ ,  
 $\bar{\sigma}_a$  = effective principal stress in direction of wave  
propagation in same units as  $G_{\max}$ ,  
 $\bar{\sigma}_b$  = effective principal stress in direction of particle  
motion in same units as  $G_{\max}$ , and  
 $\bar{\sigma}_c$  = effective principal stress in out-of-plane direction  
in same units as  $G_{\max}$ .

The shear modulus is related to the shear wave velocity as:

$$G = \frac{\gamma}{g} V_s^2 \quad (7.4)$$

where:  $\gamma$  = unit weight of material, and  
 $g$  = acceleration of gravity (32.17 ft/sec<sup>2</sup>; 9.81 m/sec<sup>2</sup>).

It follows then that the slope of the  $\log G - \log \bar{\sigma}$  relationship is directly related to the slope of the corresponding  $\log V_s - \log \bar{\sigma}$  relationship. The second-power relationship between  $G$  and  $V_s$  can be extended to the exponents by exponential multiplication so that the  $n$ -value exponents are equal to twice the value of the  $m$ -value exponents.

Equation 7.3 was evaluated for each plane of motion, and the results are presented in Table 7.8. The sum of the slopes

TABLE 7.8

Effect on  $G_{\max}$  of Orientation of Principal Stresses  
Relative to Planes of Motion Associated  
with the Shear Wave

Plane of Motion	na*	nb*	nc*	C*	na+nb+nc*
(1)	(2)	(3)	(4)	(5)	(6)
TB-NS	0.20	0.20	0.00	668	0.40
TB-EW	0.24	0.22	0.00	569	0.46
NS-EW	0.18	0.18	0.02	711	0.38

\* Eq. 7.3:  $G_{\max} = \frac{C}{0.673} P_a^{1-(na+nb+nc)} \frac{na}{\sigma_a} \frac{nb}{\sigma_b} \frac{nc}{\sigma_c}$

for the stress components ( $n_a+n_b+n_c$ ) was included to compare with the resonant column tests performed on the sand. In all cases, the sum of the slopes is less than the slope of 0.48 determined from the resonant column tests. However, the sum of slopes for biaxial confinement compare quite well with the slope  $n$  for the  $\log G - \log \bar{\sigma}_0$  relationship for isotropic confinement in the cube. The difference between the laboratory resonant column tests and the cube results could be explained by a difference in either testing procedures or the sand sample being tested. The reason or reasons, however, are unknown.

#### 7.4 STRUCTURAL ANISOTROPY

Since it was determined for isotropic confinement that the sand sample had some degree of structural anisotropy (see Section 6.7) it was decided to re-examine the structural anisotropy for biaxial confinement. Structural anisotropy is the inherent anisotropy of the sand caused by the realignment of the sand grains as they are placed. Due to the difference in placement of the sand for each axis of the cube, it was expected that some degree of anisotropy would be present in the sample.

The structural anisotropy was analyzed for each of the three planes of motion, using the equations summarized in Table 7.6. Based on these equations, a ratio of shear wave velocities for each plane of motion can be computed as follows:

$$V_{TB-EW} = (0.66 \bar{\sigma}_a^{0.03} \bar{\sigma}_b^{0.02} \bar{\sigma}_c^{-0.01}) V_{EW-NS} \quad (7.5)$$

$$V_{NS-TB} = (0.89 \bar{\sigma}_a^{0.01} \bar{\sigma}_b^{0.01} \bar{\sigma}_c^{-0.01}) V_{EW-NS} \quad (7.6)$$

As with isotropic confinement, these equations involve a scalar factor and an exponential factor for each stress component.

It is interesting to note that the sum of the exponents for biaxial confinement correspond exactly to the exponents for isotropic confinement from Eqs. 6.5 and 6.6. The exponents for biaxial confinement, however, incorporate a negative exponent. This negative exponent was not made zero since these equations are used to interrelate the planes of motion and not used to predict shear wave velocity. The scalar factors for biaxial confinement also correspond almost exactly to the scalar values for isotropic confinement.

The sum of the slopes for Eqs. 7.5 and 7.6 vary from 0.01 to 0.04 while the constant term varies from 0.66 to 0.89. This variance in the parameters amounts to a 20 percent scatter in the values of  $V_s$  among the three planes of motion. Although the values of the terms used to calculate  $V_s$  vary with each plane of motion, the relationships between these terms does not vary among the planes. That is, the domination of  $V_s$  by the directions of wave propagation and particle motion and the insignificance of the out-of-plane direction on  $V_s$  does not change due to the structural anisotropy.

Although the absolute values of  $C_1$ ,  $m_a$ ,  $m_b$  and  $m_c$  vary for each plane of motion, the general relationships between them is not changed by the structural anisotropy.

Therefore, the results show that the effect of structural anisotropy for this study has little effect on the  $\log V_s - \log \bar{\sigma}$  relationships for each principal stress component among the three planes of motion. Hence, calculations can be performed and similar trends expected for the effect on  $V_s$  of the stress components for each plane of motion, provided only shear waves within the respective plane of motion are used. The effect of structural anisotropy can be ignored within any one plane of motion, although the slight variance of  $V_s$  due to structural anisotropy must be accounted for when the comparison is made between planes of motion.

#### 7.5 TESTING WITH A CONSTANT MEAN EFFECTIVE PRINCIPAL STRESS

One biaxial series was conducted in which the mean effective principal stress remained constant. This test was designed to: 1. study the variation of  $V_s$  under a constant mean effective principal stress with a varying shearing stress component, and 2. provide additional shear wave velocity measurements to verify the validity of the expressions developed to predict shear wave velocity.

The series began at an isotropic confining pressure of 20 psi (137.8 kPa). The top-bottom principal stress,  $\bar{\sigma}_1$ , was then increased in two-psi (13.8 kPa) increments while at the same

time the side stresses,  $\bar{\sigma}_3$ , were decreased in one-psi (6.9 kPa) increments. Tests were performed after each incremental change in stress. The top-bottom stress,  $\bar{\sigma}_1$ , was increased to a maximum of 32 psi (220.5 kPa) with a corresponding minimum value of  $\bar{\sigma}_3$  of 14 psi (96.5 kPa).

At all times the sum of the principal stresses,  $\bar{\sigma}_o$ , remained constant at 20 psi (137.8 kPa). This value for  $\bar{\sigma}_o$  of 20 psi (137.8 kPa) was chosen because it was about one-half of the maximum possible confining pressure for the cube. As a result, a reasonable range for  $K_{13}$  was possible without: 1.  $\bar{\sigma}_1$  exceeding the design pressure of the cube, and 2. Mohr's circle formed by  $\bar{\sigma}_1$  and  $\bar{\sigma}_3$  touching the failure envelope for this sand with the resultant shearing stresses failing the sample. Figure 7.16 shows the variation of  $\bar{\sigma}_1$  and  $\bar{\sigma}_3$  for this test series along with the resultant shearing stress levels and the variations in  $K_{13}$ , which ranged from 1.0 to 3.0.

As the series continued, the stresses were decreased back to the isotropic confinement of 20 psi (137.8 kPa) with several tests conducted to examine the effect of stress history. Subsequently,  $\bar{\sigma}_1$  was increased once again, this time to a maximum value of 36 psi (248.0 kPa) with the necessary  $\bar{\sigma}_3$  of 12 psi (82.7 kPa). This was the final test conducted in this series, with intermittent triaxial confinement tests conducted during and after the biaxial tests. The complete biaxial series included tests 4A



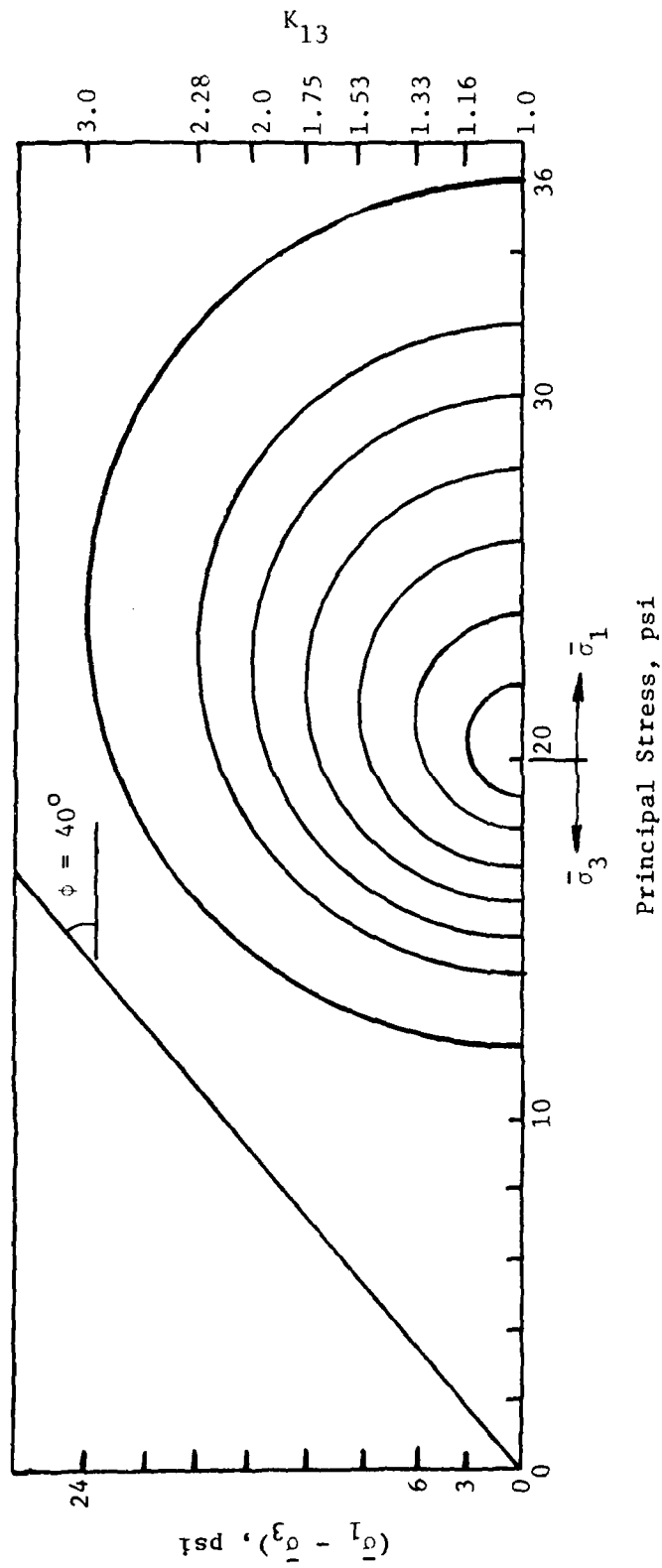


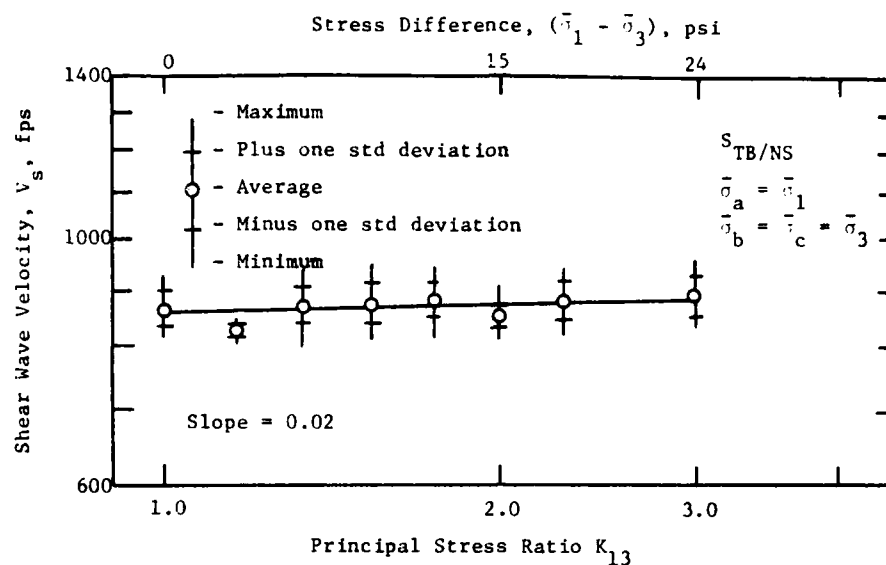
Fig. 7.16 - Variation of Shearing Stress and Principal Stress Ratio for the Biaxial Test Series with a Constant Mean Effective Principal Stress

through 13, 15, and 20 listed in Table B.1. The load history for these tests is shown in Fig. B.1 between the dates of July 7, 1981 and August 5, 1981.

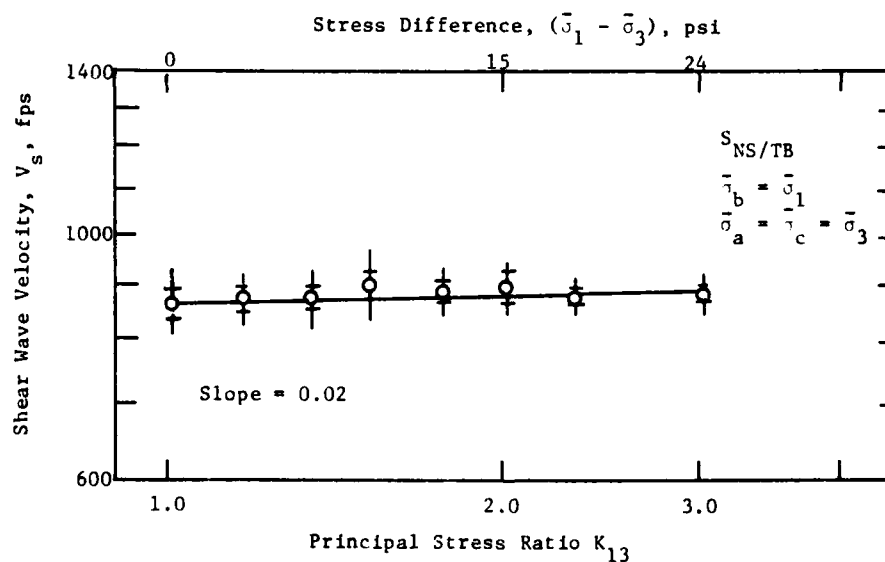
#### 7.5.1 Effect of Shearing Stress with Constant $\bar{\sigma}_o$

As stated, one of the primary purposes of this test series was to examine the effect on  $V_s$  of shearing stress when testing at a constant mean effective principal stress. Hardin and Black (1966) and Lawrence (1965) both determined, in separate experiments, that shear wave velocity was not a function of shearing stress in sand, except where the shearing stresses contributed to the mean effective principal stress for the test (or where the shearing stresses affected the void ratio of the sample tested).

The variation of  $V_s$  with  $K_{13}$  is presented in Figs. 7.17, 7.18, and 7.19 for the TB-NS, TB-EW, and NS-EW planes of motion, respectively. Each figure shows shear wave velocity data for each test pressure plotted against the logarithm of  $K_{13}$ . Hardin and Drnevich (1966) and Lawrence (1965) plotted logarithm of  $V_s$  against the logarithm of  $\bar{\sigma}_o$ . However, for this study, testing was performed for only one value of  $\bar{\sigma}_o$  (20 psi (137.8 kPa)) and so figures using axes of  $V_s$  and  $\bar{\sigma}_o$  would plot as a vertical line and, hence, be of little benefit. It was decided, therefore, to use  $K_{13}$  as the horizontal axis in place of  $\bar{\sigma}_o$  ( $\frac{1}{2}(\bar{\sigma}_a + \bar{\sigma}_b)$  is used later in this section) since  $K_{13}$  varied even though  $\bar{\sigma}_o$  remained constant. Similar values of  $K_{13}$  relate similar states of stress among the

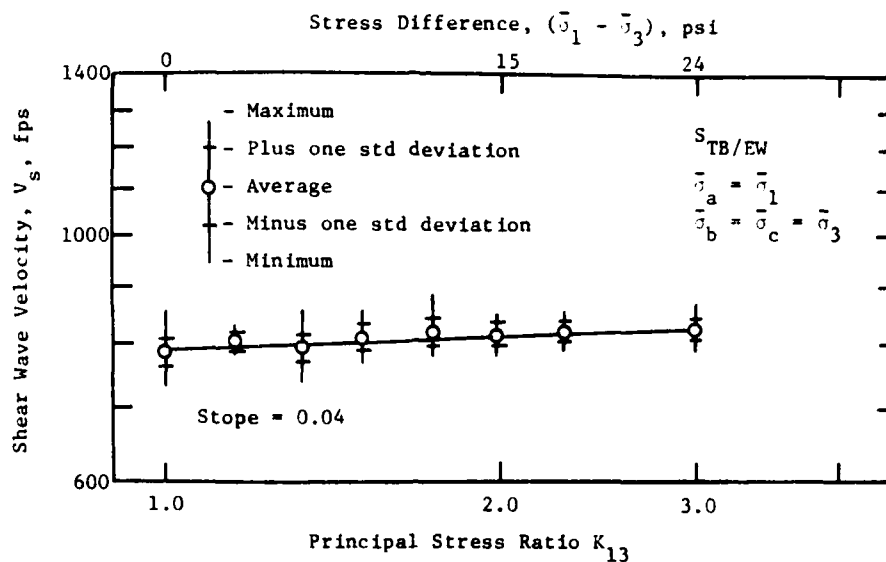


a) For the  $S_{TB/NS}$ -Wave

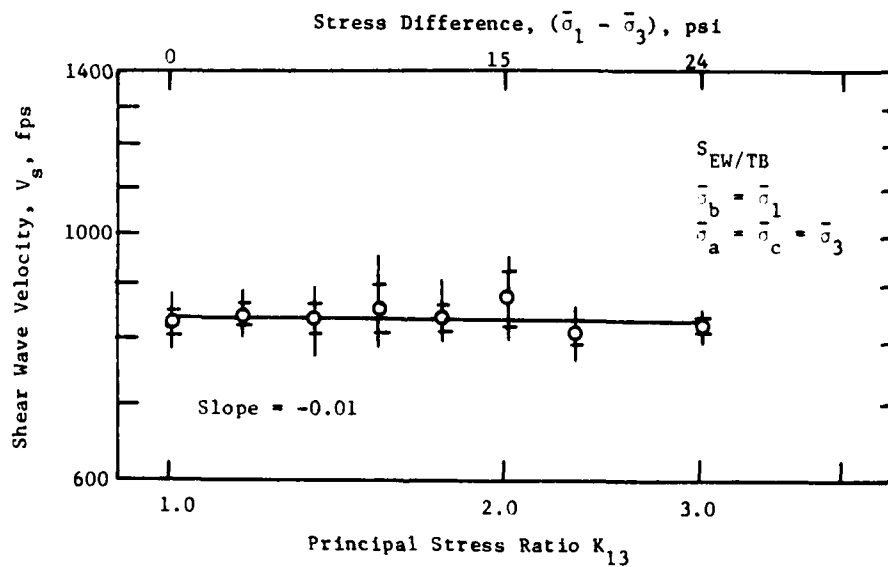


b) For the  $S_{NS/TB}$ -Wave

Fig. 7.17 - Variation of Shear Wave Velocity with Principal Stress Ratio for TB-NS Plane of Motion for Biaxial Confinement

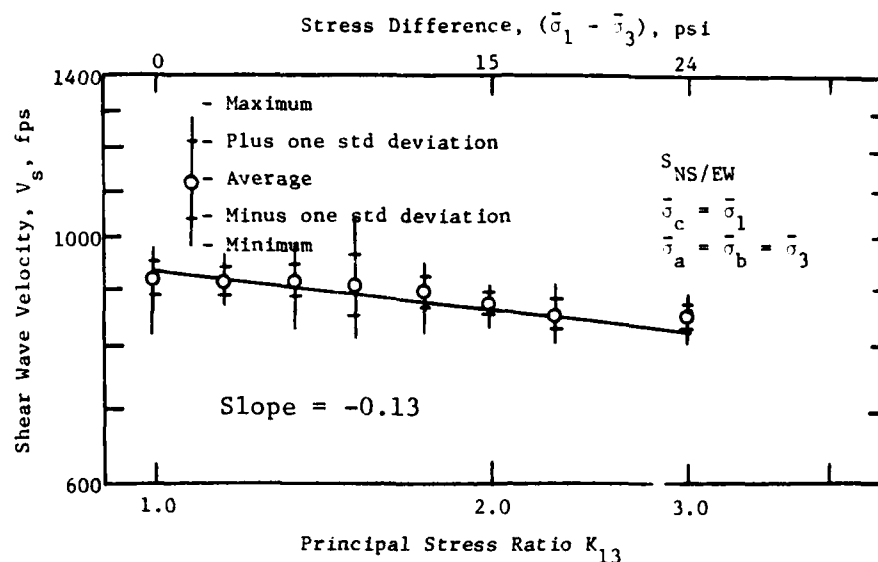


a) For the  $S_{TB/EW}$ -Wave

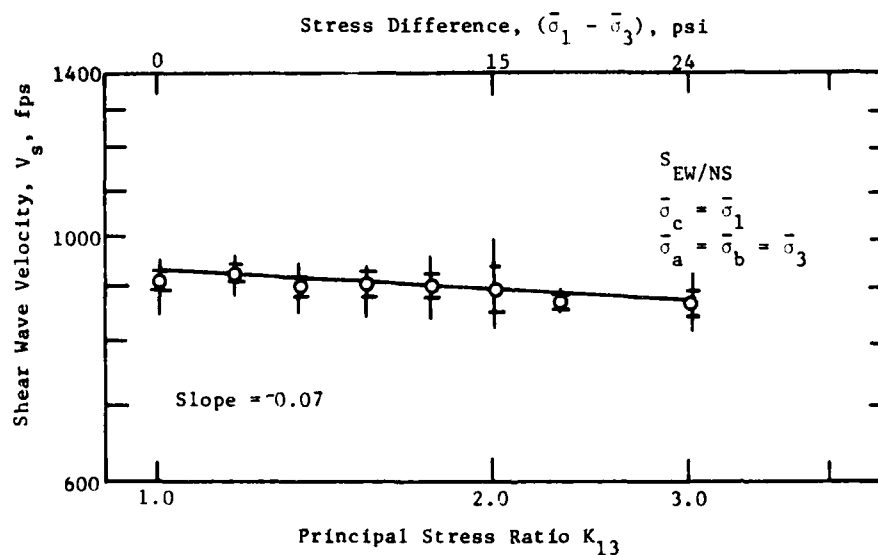


b) For the  $S_{EW/TB}$ -Wave

Fig. 7.18 - Variation of Shear Wave Velocity with Principal Stress Ratio for TB-EW Plane of Motion for Biaxial Confinement



a) For the  $S_{NS/EW}$ -Wave



b) For the  $S_{EW/NS}$ -Wave

Fig. 7.19 - Variation of Shear Wave Velocity with Principal Stress Ratio for NS-EW Plane of Motion for Biaxial Confinement

three planes of motion in terms of  $\bar{\sigma}_1$  and  $\bar{\sigma}_3$ . However, it must be noted that  $\bar{\sigma}_1$  and  $\bar{\sigma}_3$  in no way indicate the stress components relative to the directions of shear wave motion and that  $K_{13}$  may use any two of the stress components  $\bar{\sigma}_a$ ,  $\bar{\sigma}_b$ , or  $\bar{\sigma}_c$  for each of the planes of motion. Least-squares fit were performed to determine the slopes of the data presented in Figs. 7.17, 7.18, and 7.19, and the results are shown on these figures by solid lines. Each figure contains the results for the two shear waves possible for the particular plane of motion. A summary of these figures is given in Table 7.9.

Based upon Table 7.9,  $V_s$  does not appear to be sensitive to the level of shearing stress at a constant  $\bar{\sigma}_0$  for either the TB-NS or TB-EW planes of motion. The slopes of the  $\log V_s - \log K_{13}$  relationships ranged from -0.01 to 0.04, with an average value of 0.02. These slopes produced a maximum variation in  $V_s$  of only 4.3 percent for the range of  $K_{13}$  from 1.0 to 3.0. Hardin and Black (1966) obtained a one percent variation in  $V_s$  over the range in the principal stress ratio from 1.0 to 2.0. Although  $V_s$  did vary by a small amount for the cube data, the (erroneous) assumption could be made based on these figures that  $V_s$  is independent of the shearing stresses for a constant  $\bar{\sigma}_0$ , for the TB-NS and TB-EW planes of motion.

The remaining plane of motion, the NS-EW plane, did exhibit a distinct variation in  $V_s$  with shearing stress. The slopes of the  $\log V_s - \log K_{13}$  relationship ranged from -0.07 to -0.13,

TABLE 7.9

Variation of Shear Wave Velocity with Shearing Stress for Tests Performed with a Constant  $\bar{\sigma}_o$  for Biaxial Confinement

Plane of Motion	Shear Wave Type*	Principal Stress in Direction of Each Stress Component			Slope**	$V_s^{***}$	Percent Change in $V_s^{****}$
		$\bar{\sigma}_a$ (3)	$\bar{\sigma}_b$ (4)	$\bar{\sigma}_c$ (5)			
(1)	(2)				(6)	(7)	(8)
TB-NS	TB/NS	increasing $\bar{\sigma}_1$	decreasing $\bar{\sigma}_3$	decreasing $\bar{\sigma}_3$	0.02	18	2.1
	NS/TB	decreasing $\bar{\sigma}_3$	increasing $\bar{\sigma}_1$	decreasing $\bar{\sigma}_3$	0.02	19	2.2
TB-EW	TB/EW	increasing $\bar{\sigma}_1$	decreasing $\bar{\sigma}_3$	decreasing $\bar{\sigma}_3$	0.04	34	4.3
	EW/TB	decreasing $\bar{\sigma}_3$	increasing $\bar{\sigma}_1$	decreasing $\bar{\sigma}_3$	-0.01	-5	-0.6
NS-EW	NS/EW	decreasing $\bar{\sigma}_3$	decreasing $\bar{\sigma}_3$	increasing $\bar{\sigma}_1$	-0.13	-108	-11.7
	EW/NS	increasing $\bar{\sigma}_3$	decreasing $\bar{\sigma}_3$	increasing $\bar{\sigma}_1$	-0.07	-66	-6.5

\*The first two letters denote the direction of wave propagation, and the second two letters denote the direction of Particle motion (TB = top-bottom, NS = north-south, EW = east-west).

\*\* Slope of the  $\log V_s - \log K_{13}$  relationship.

\*\*\*  $V_s$  at  $K_{13} = 1.0$  minus  $V_s$  at  $K_{13} = 3.0$

\*\*\*\*  $(V_{K=1.0} - (V_{K=3.0}) / (V_{K=1.0}) \times 100\%$

with an average value of  $-0.10$ . This would amount to a 9 percent variation in  $V_s$  over the range in  $K_{13}$  used in this series. This percent variation is significant and as such cannot be accounted for by experimental scatter. The fact that  $V_s$  varies with this plane of motion means that the generalization cannot be made that  $V_s$  is independent of the level of shear stress for a constant mean effective principal stress.

To understand the effect of shearing stress on  $V_s$  for these planes of motion, one must note the similarity between the TB-NS and TB-EW planes of motions, and the difference between these two planes and the NS-EW plane of motion. This can be done by examining the stress components for each plane. As discussed in Section 7.3,  $\bar{\sigma}_a$  and  $\bar{\sigma}_b$  contribute about equally to  $V_s$  with respect to their exponents, while  $\bar{\sigma}_c$  was found to be unimportant to the magnitude of  $V_s$ .

For any of the shear waves in the TB-NS or TB-EW planes of motion,  $\bar{\sigma}_a$  and  $\bar{\sigma}_b$  for the shear waves involve both  $\bar{\sigma}_1$  and  $\bar{\sigma}_3$ . For any shear wave, whichever stress component ( $\bar{\sigma}_a$  or  $\bar{\sigma}_b$ ) was equal to  $\bar{\sigma}_1$ , the remaining component equalled  $\bar{\sigma}_3$ . For this biaxial test series,  $\bar{\sigma}_1$  was increased while  $\bar{\sigma}_3$  was decreased to keep  $\bar{\sigma}_0$  constant. Therefore, for any shear wave defined by the TB-NS or TB-EW planes of motion, if  $\bar{\sigma}_a$  was increasing,  $\bar{\sigma}_b$  was decreasing, and if  $\bar{\sigma}_a$  was decreasing,  $\bar{\sigma}_b$  was increasing.

This reversed trend for these two important stress components had a compensating effect on  $V_s$ . As the importance of



one of the stress components on  $V_s$  increased, the importance of the other component lessened. The net result of the compensation was a relatively constant  $V_s$  for varying levels of shearing stress (although the net effect was a slight increase in stress which is correctly reflected by the positive values of the average slopes shown in Figs. 7.17 and 7.18). The same results were shown in the experiments by Lawrence (1965) and Hardin and Black (1966). Although Lawrence used a modified triaxial cell while Hardin and Black performed their studies with the resonant column test device, both investigators used vertically propagating waves. For their tests,  $\bar{\sigma}_1$  and  $\bar{\sigma}_3$  were applied to the test specimens as cell pressure (an all-round confining pressure) and an axial load (vertically). This stress application dictated that, for vertically propagating shear waves,  $\bar{\sigma}_a$  and  $\bar{\sigma}_b$  involve both  $\bar{\sigma}_1$  and  $\bar{\sigma}_3$ . Therefore, it is not surprising that Lawrence and Hardin and Black observed essentially no variation in  $V_s$  for changes in level of shear stress, for they were, in effect, monitoring shear waves in the TB-NS and TB-EW planes of motion as defined by this study.

One of the important design considerations of the cube, though, is that velocity measurements can be made with the direction of wave propagation along any of the three cube axes and with the direction of particle motion along any one of the remaining two axes. Therefore, measurements of  $V_s$  were performed in this test series with shear waves for which  $\bar{\sigma}_a$  and  $\bar{\sigma}_b$  involved only  $\bar{\sigma}_3$  ( $\bar{\sigma}_c$  equaled to  $\bar{\sigma}_1$ ). These shear wave types involved the NS-EW plane of motion

in which both  $\bar{\sigma}_a$  and  $\bar{\sigma}_b$  increased (or decreased) simultaneously so that the compensation effect of reversed trends for  $\bar{\sigma}_a$  and  $\bar{\sigma}_b$  which occurred in the TB-NS and TB-EW planes of motion was eliminated. Without the compensating effect, there is a distinct trend of a varying  $V_s$  as the level of shear stress changes as shown in Fig. 7.19.

To illustrate the effect on  $V_s$  of only  $\bar{\sigma}_a$  and  $\bar{\sigma}_b$  at a constant  $\bar{\sigma}_c$ , it was decided to plot  $\log V_s$  versus  $\log \frac{1}{2}(\bar{\sigma}_a + \bar{\sigma}_b)$ . Such a plot is based on the assumptions that: 1.  $\bar{\sigma}_a$  and  $\bar{\sigma}_b$  equally affect  $V_s$ , and 2.  $\bar{\sigma}_c$  does not affect  $V_s$ . These results are shown in Figs. 7.20, 7.21, and 7.22 for the TB-NS, TB-EW, and NS-EW planes of motion, respectively. A least-squares fit to the data is shown by the solid lines in the figures.

Based upon these figures, it can be seen that shear wave velocity is not constant for varying shearing stresses at a constant  $\bar{\sigma}_c$ . Slopes of the  $\log V_s - \log \frac{1}{2}(\bar{\sigma}_a + \bar{\sigma}_b)$  relationship varied from -0.04 to 0.28. The values of the slopes should depend on the change in  $\bar{\sigma}_a$  and  $\bar{\sigma}_b$  for each of the planes of motion. As a means of comparison, the predicted values of shear wave velocity (based on Eq. 7.2 and the constants summarized in Table 7.6) are included as dashed lines in these figures. As can be seen, there is a good correlation between the predicted and measured values of shear wave velocity, with a typical variation of less than 10 percent. Table 7.10 summarizes the slopes of the  $\log V_s - \log \frac{1}{2}(\bar{\sigma}_a + \bar{\sigma}_b)$  relationship for the measured and predicted values of shear wave velocity in Figs. 7.20, 7.21, and 7.22.

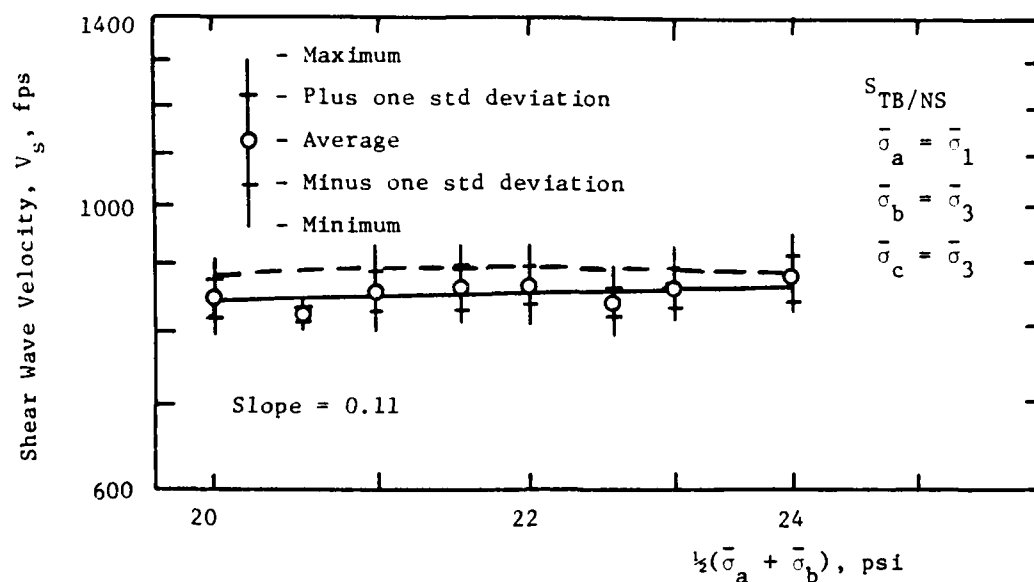
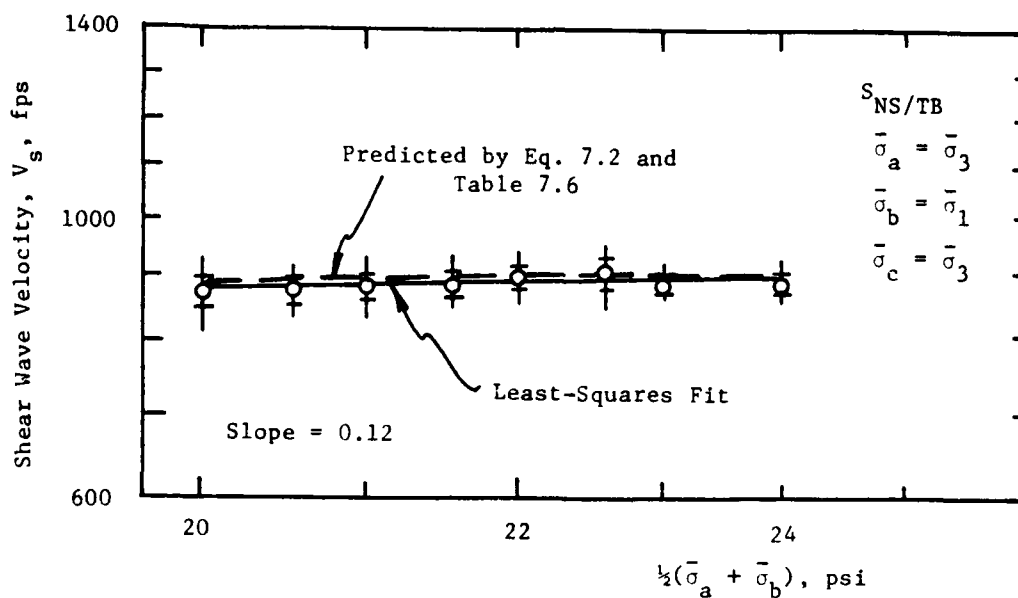
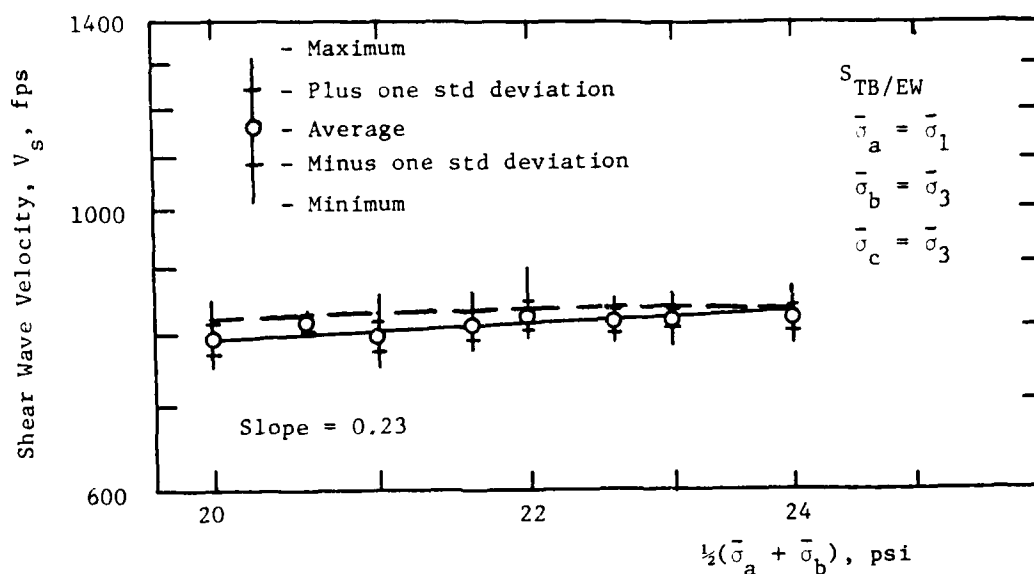
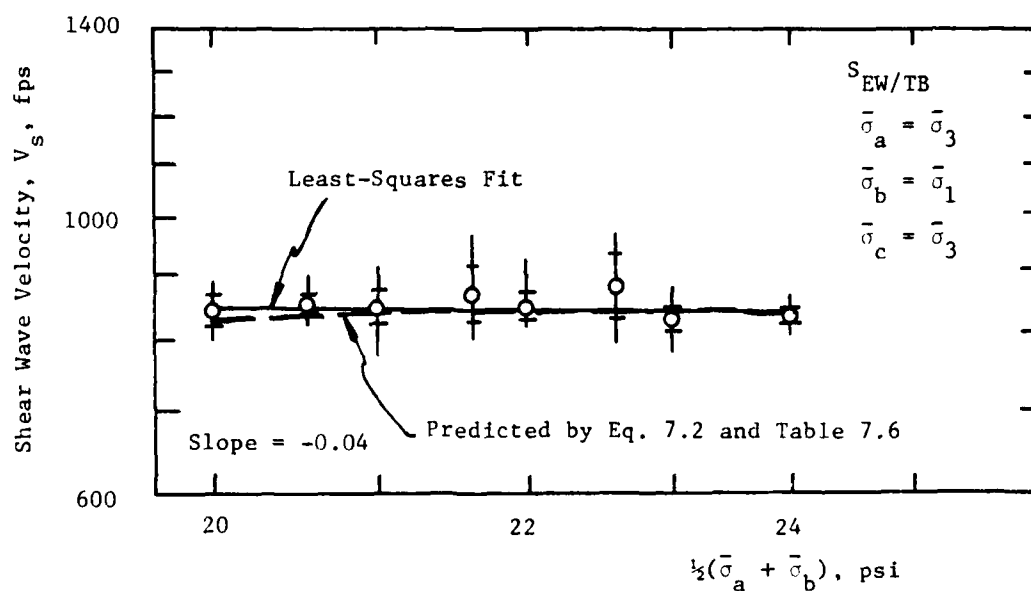
a) For the  $S_{TB/NS}$ -Waveb) For the  $S_{NS/TB}$ -Wave

Fig. 7.20 - Variation of Shear Wave Velocity with Directions of Wave Propagation and Particle Motion for TB-NS Plane of Motion for Biaxial Confinement with a Constant  $\bar{\sigma}_0$



a) For the  $S_{TB/EW}$ -Wave



b) For the  $S_{EW/TB}$ -Wave

Fig. 7.21 - Variation of Shear Wave Velocity with Directions of Wave Propagation and Particle Motion for TB-EW Plane of Motion for Biaxial Confinement with a Constant  $\bar{\sigma}_o$

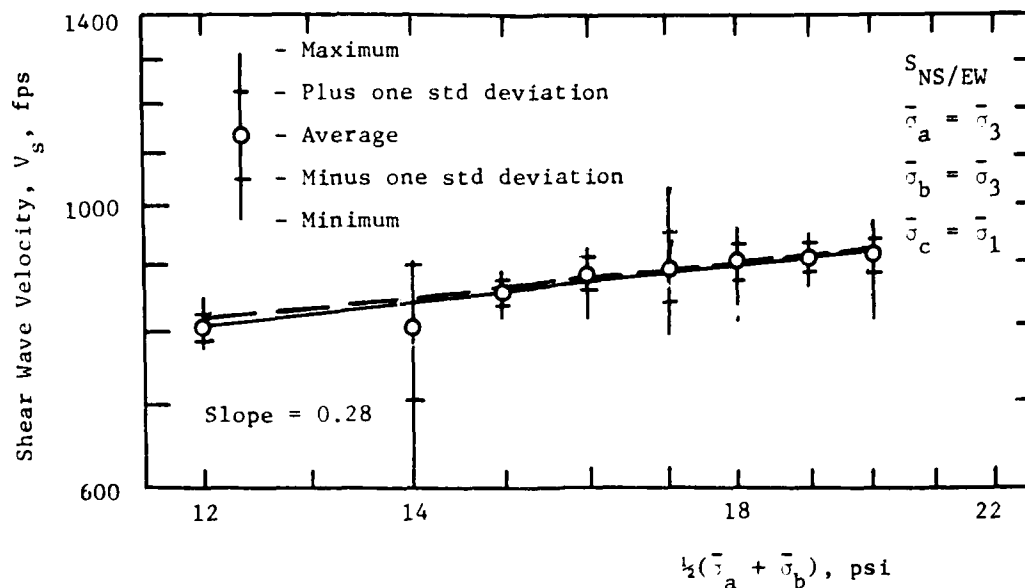
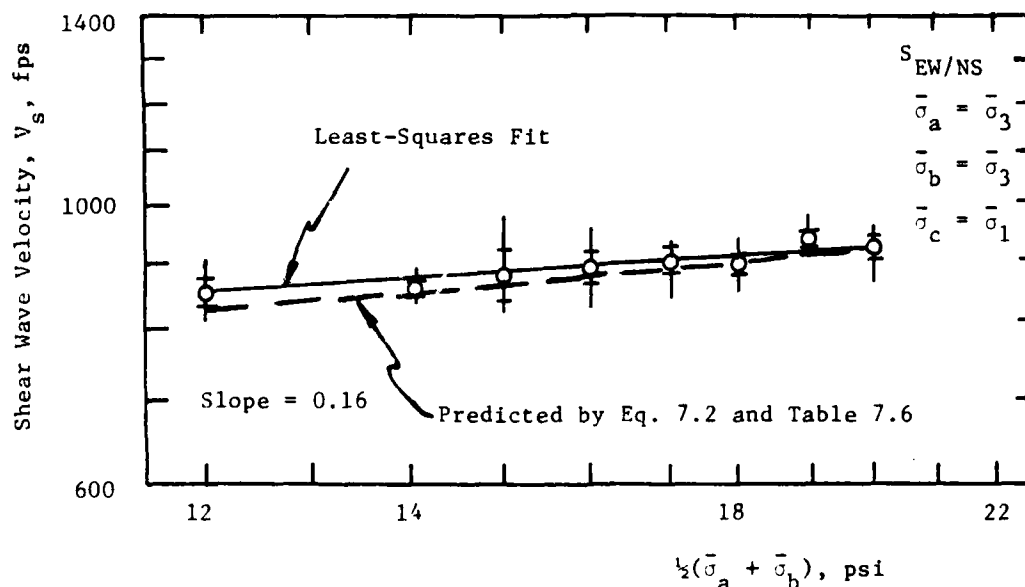
a) For the  $S_{NS/EW}$ -Waveb) For the  $S_{EW/NS}$ -Wave

Fig. 7.22 - Variation of Shear Wave Velocity with Directions of Wave Propagation and Particle Motion for NS-EW Plane of Motion for Biaxial Confinement with a Constant  $\bar{\sigma}_0$

TABLE 7.10

Effect on  $V_s$  of Principal Stresses in Directions  
of Wave<sup>s</sup> Propagation and Particle Motion

Plane of Motion	Shear Wave Type*	Slope of $\log V_s - \log \frac{1}{2}(\bar{\sigma}_a + \bar{\sigma}_b)$ Relationship	Average Slope for each Plane of Motion	Predicted Slope for each Plane of Motion***
(1)	(2)	(3)	(4)	(5)
TB-NS	TB/NS	0.11	0.11	0.07
	NS/TB	0.12		0.07
TB-EW	TB/EW	0.23	0.10	0.09
	EW/TB	-0.04		0.04
NS-EW**	NS/EW	-0.28	-0.22	-0.18
	EW/NS	-0.16		-0.18

\* The first two letters denote the direction of wave propagation and the second two letters denote the direction of particle motion.

\*\* For this biaxial test series,  $\frac{1}{2}(\bar{\sigma}_a + \bar{\sigma}_b)$  decreased from 20 psi to 12 psi.

\*\*\* Based on Table 7.6 and Eq. 7.2.

Based on Table 7.10, there is a definite scatter in these slopes of the  $\log V_s - \log \frac{1}{2}(\bar{\sigma}_a + \bar{\sigma}_b)$  relationship. The measured slopes are all less than the predicted values for Eq. 7.2, although the relative ratios between the planes of motion seem to be similar. Both the TB-NS and NS-EW planes of motion have fair agreement between the measured and predicted values of the slopes. However, for the TB-EW plane there is a poor correlation for the two shear waves. One of the shear wave slopes was 0.23 and the other was -0.04. The reason for this variation is unclear for this biaxial series, and it should be noted that a similar extreme variation occurred during triaxial confinement at constant  $\bar{\sigma}_0$  for the same TB-EW plane (see Section 8.5.1). The possible reasons for the large variation of slopes for this plane of motion are unknown but could include experimental scatter, pressure variations within the sample or in the loading membranes, and/or structural anisotropy.

Therefore, the generalization of a shear wave velocity independent of the level of shearing stress cannot and should not be made. For this study, shear wave velocity varied with the effective principal stresses in the directions of wave propagation and particle motion. As a result, the determination of  $V_s$  depends on the stress components  $\bar{\sigma}_a$  and  $\bar{\sigma}_b$  rather than on the more conventional term  $\bar{\sigma}_0$  previously used in the literature.

#### 7.5.2 Comparison Between Measured and Predicted Shear Wave Velocities

To further check the validity of the expressions for shear wave velocity developed in Section 7.3.5, measured values of  $V_s$  for

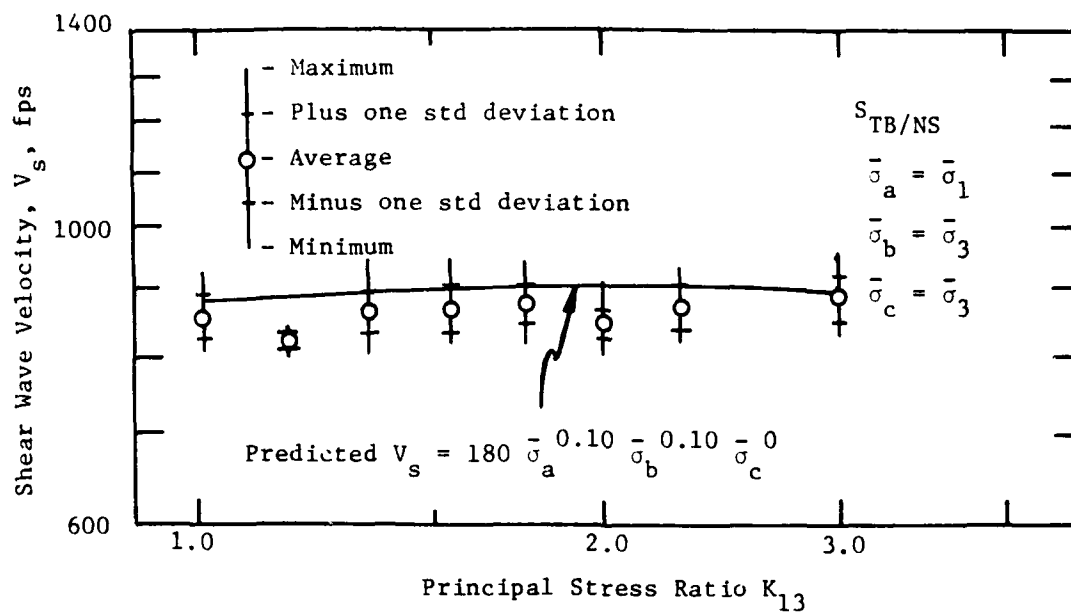
this series of tests with a constant  $\bar{\sigma}_0$  were compared to values predicted from Eq. 7.2 using the values presented in Table 7.6. This comparison was made for each of the six different types of shear waves. Two methods of comparison were performed: 1. plotting the measured shear wave velocity data and predicted  $V_s$  versus the log of  $K_{13}$ , and 2. presenting a ratio of the measured value of  $V_s$  to the predicted  $V_s$  (see Section 7.3.6) versus the log of  $K_{13}$ .

The results of these comparisons are shown in Figs. 7.23 through 7.28. Based on these figures, the ratio of the measured  $V_s$  to the predicted  $V_s$  for  $\pm$  one standard deviation typically ranges from 0.92 to 1.05 with values as high as 1.11. This indicates that the equations developed in Section 7.3.5 to predict  $V_s$  for this test series are generally within 10 percent for each of the shear wave types. Most importantly though, this correlation of measured to predicted values of  $V_s$  means that, in fact, shear wave velocity is not controlled by the level of mean effective principal stress (as previously assumed) but by the effective principal stress in the directions of wave propagation and particle motion. It is the variation of these two stress components that largely affect the variation of  $V_s$ .

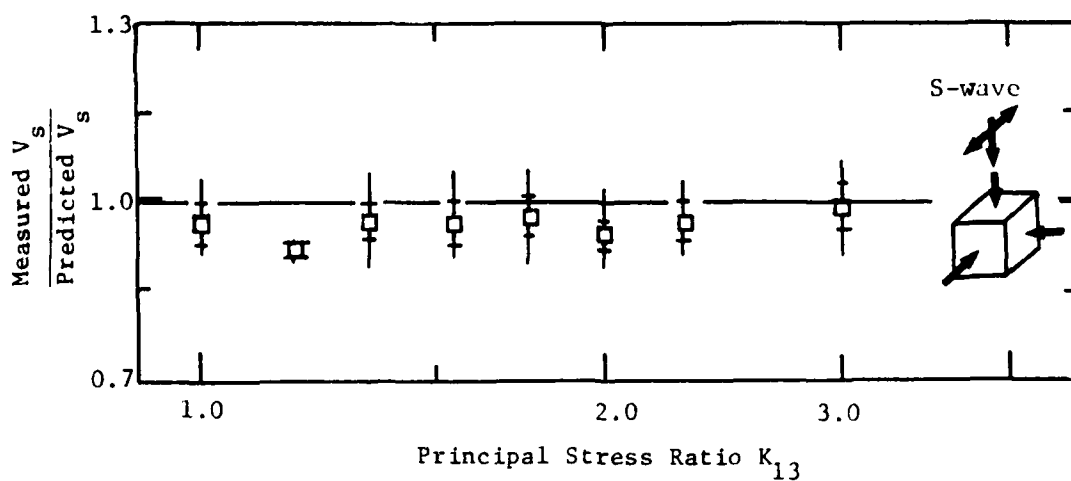
## 7.6 SUMMARY AND CONCLUSIONS

To attain the condition of biaxial confinement, the major principal stress,  $\bar{\sigma}_1$ , was applied along one axis of the cube and the minor principal stress,  $\bar{\sigma}_3$  was applied along the remaining two



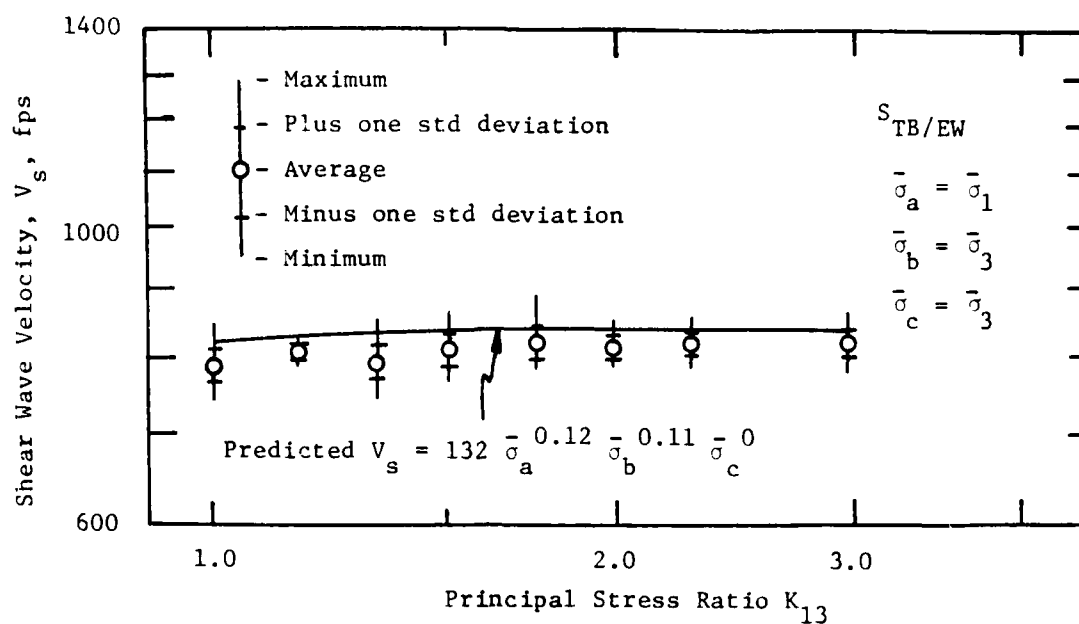


a) Absolute Values of Shear Wave Velocities

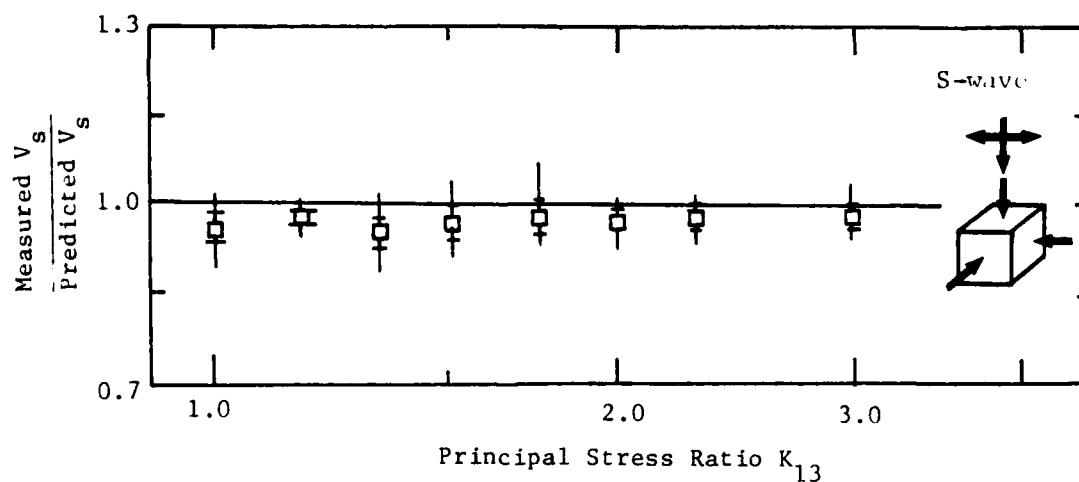


b) Ratio of Shear Wave Velocities

Fig. 7.23 - Comparison of Measured and Predicted Shear Wave Velocities for  $S_{TB/NS}$ -Wave for Biaxial Confinement with a Constant  $\bar{\sigma}_o$

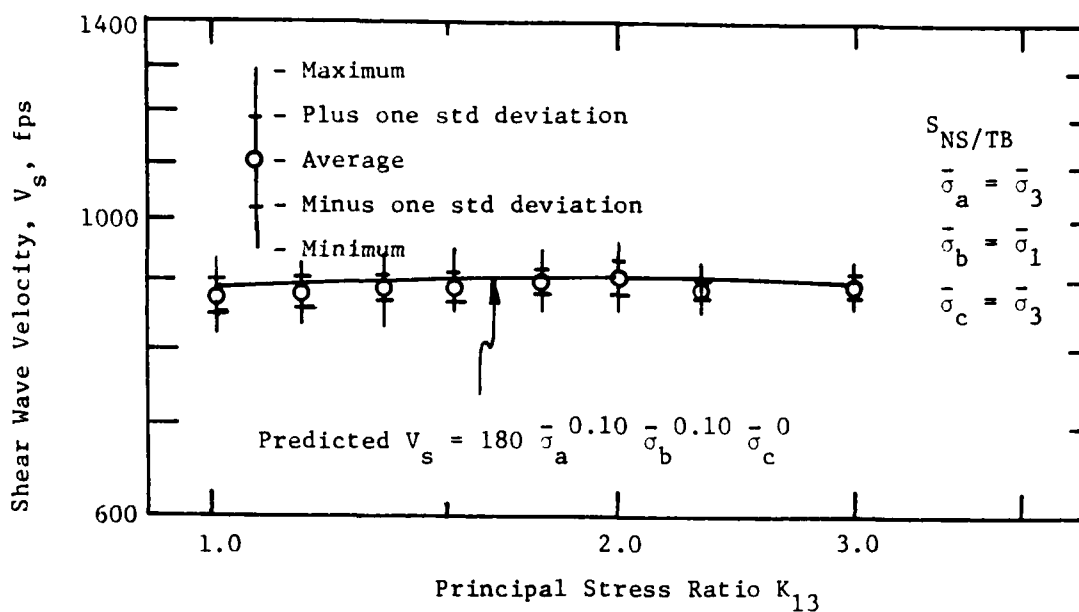


a) Absolute Values of Shear Wave Velocities

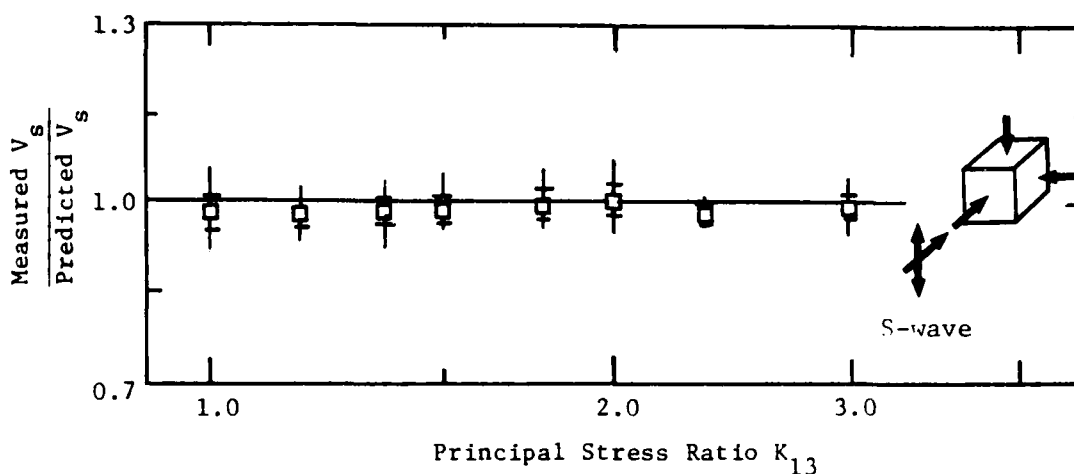


b) Ratio of Shear Wave Velocities

Fig. 7.24 - Comparison of Measured and Predicted Shear Wave Velocities for  $S_{TB/EW}$ -Wave for Biaxial Confinement with a Constant  $\bar{\sigma}_o$

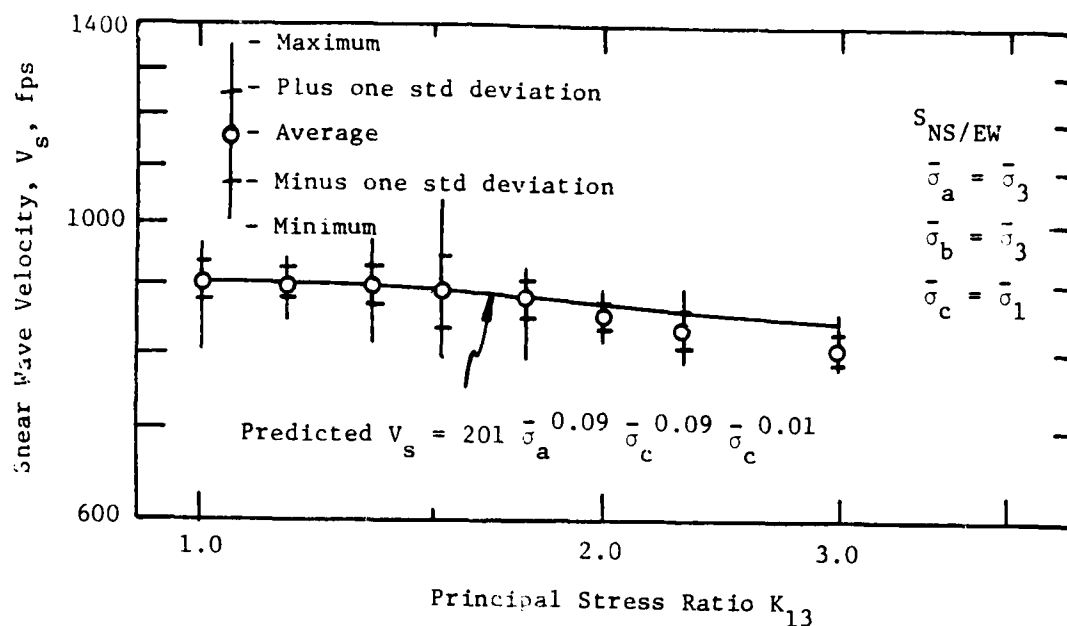


a) Absolute Values of Shear Wave Velocities

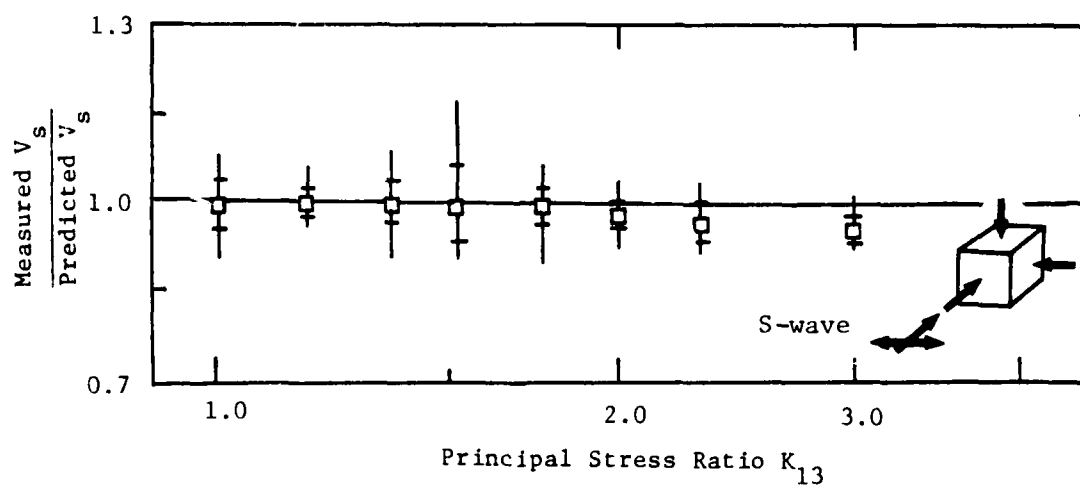


b) Ratio of Shear Wave Velocities

Fig. 7.25 - Comparison of Measured and Predicted Shear Wave Velocities for  $S_{NS/TB}$ -Wave for Biaxial Confinement with a Constant  $\bar{\sigma}_0$

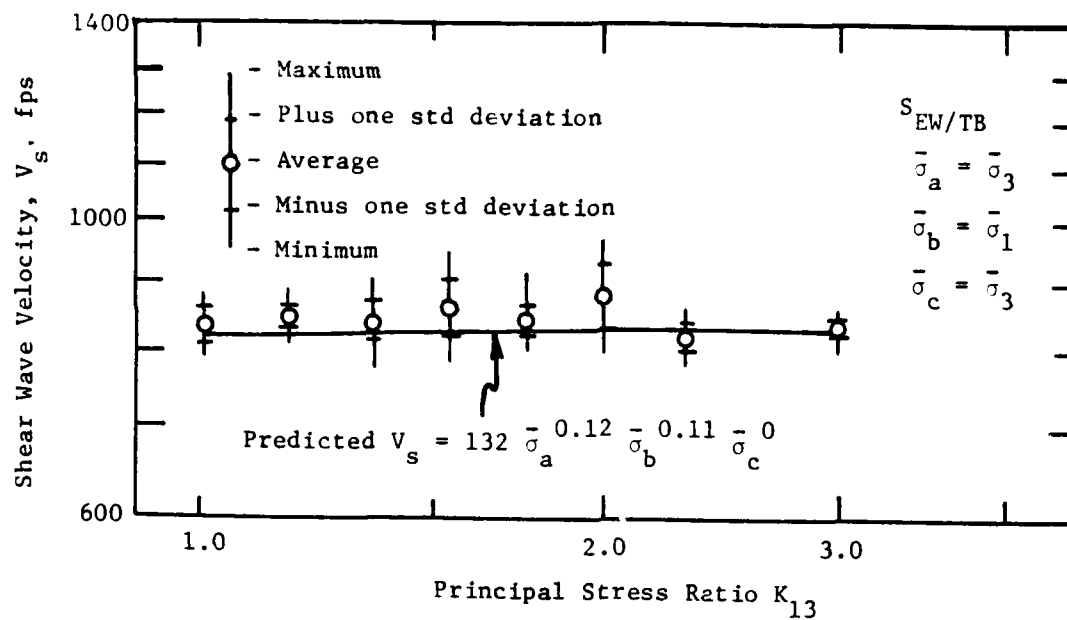


a) Absolute Values of Shear Wave Velocities

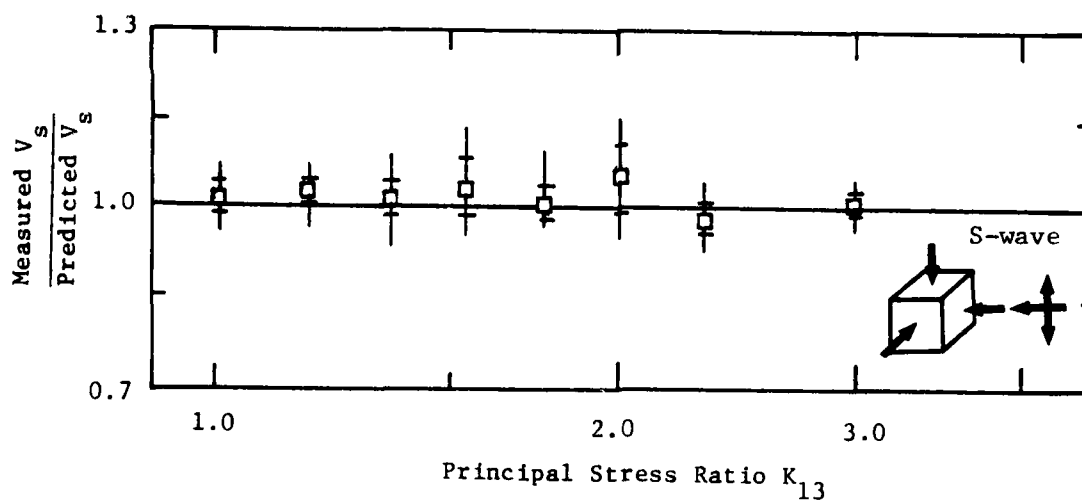


b) Ratio of Shear Wave Velocities

Fig. 7.26 - Comparison of Measured and Predicted Shear Wave Velocities for  $S_{NS/EW}$ -Wave for Biaxial Confinement with a Constant  $\bar{\sigma}_o$

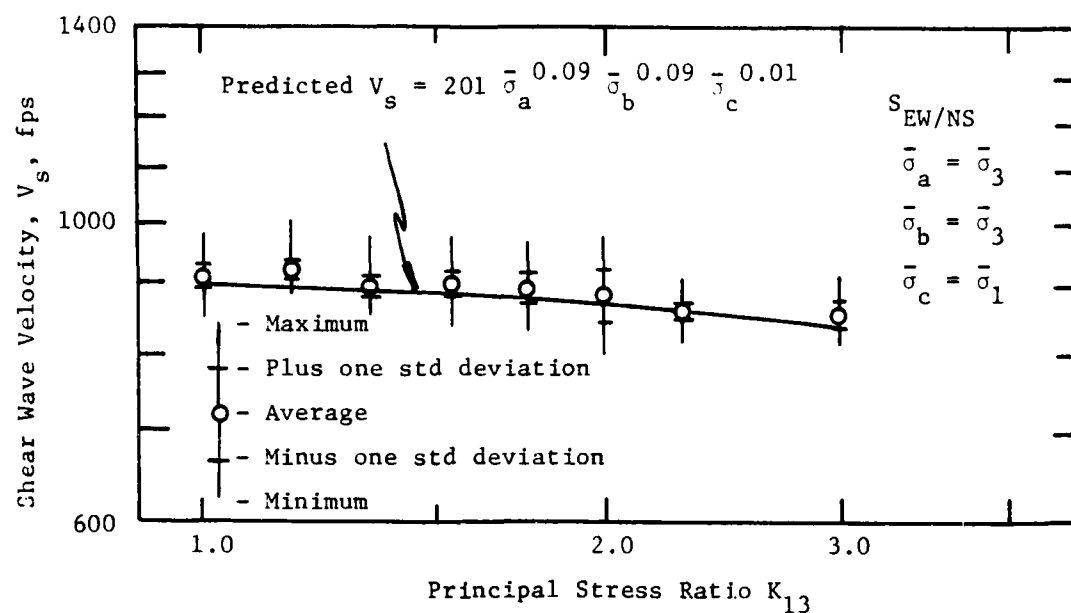


a) Absolute Values of Shear Wave Velocities

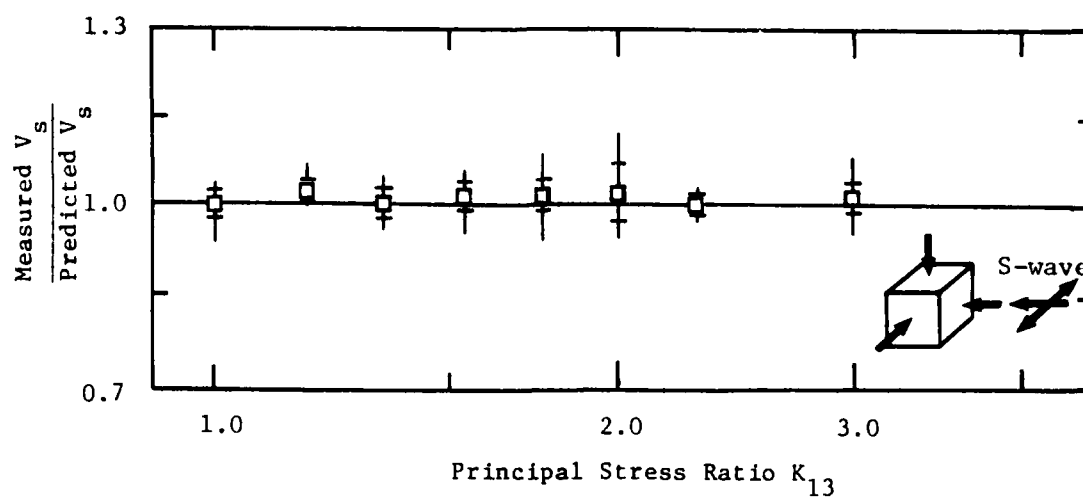


b) Ratio of Shear Wave Velocities

Fig. 7.27 - Comparison of Measured and Predicted Shear Wave Velocities for  $S_{EW/TB}$ -Wave for Biaxial Confinement with a Constant  $\bar{\sigma}_o$



a) Absolute Values of Shear Wave Velocities



b) Ratio of Shear Wave Velocities

Fig. 7.28 - Comparison of Measured and Predicted Shear Wave Velocities for  $S_{EW/NS}$ -Wave for Biaxial Confinement with a Constant  $\bar{\sigma}_o$

axes. For biaxial confinement, the principal stresses were no longer all the same and so principal stresses had to be described relative to the motions associated with each shear wave. As such, the following notation was used to refer to the principal stress components:  $\bar{\sigma}_a$ , the effective principal stress in the direction of wave propagation;  $\bar{\sigma}_b$ , the effective principal stress in the direction of particle motion; and  $\bar{\sigma}_c$ , the out-of-plane direction.

Two patterns of stress variation were used in the biaxial confinement series: 1. tests with a variable mean effective principal stress, and 2. tests with a constant mean effective principal stress. Tests with a variable  $\bar{\sigma}_o$  were designed to examine the variation of  $V_s$  with the individual stress components and to study structural anisotropy in the sample. Tests with a constant mean effective principal stress were performed to evaluate the effect on  $V_s$  of varying levels of shearing stress for a constant  $\bar{\sigma}_o$ .

For tests performed with a variable mean effective principal stress, principal stresses varied from 15 to 40 psi (103.4 to 275.6 kPa) with a resulting range in principal stress ratio,  $K_{13}$ , of 1.0 to 2.67. This pattern of stress variation was examined to evaluate each stress component alone, and so only one stress component was varied at a time. Based upon the test results, it was found that  $\bar{\sigma}_a$  and  $\bar{\sigma}_b$  are the dominant stress components in determining  $V_s$ . Each of these two components was about equally important in the equation, Eq. 7.2, developed to predict  $V_s$ . Values of the slope of the  $\log V_s - \log \bar{\sigma}_a$  relationship ranged from

0.09 to 0.11, with these values depending on the plane of motion. The third stress component,  $\bar{\sigma}_c$ , the out-of-plane principal stress, was found to be unimportant, with the value of the slope of the  $\log V_s - \log \bar{\sigma}_c$  relationship ranging from -0.01 to 0.01.

Stress history had no significant affect on the relationship between  $V_s$  and the stress components. Although the loading and unloading data exhibited slightly different values of the constants as shown in Table 7.6, there was no consistent trend, and the variation was assumed to be due to experimental scatter.

To predict shear modulus, Eq. 7.3 was developed for biaxial confinement with the constants shown in Table 7.8. The sum of the exponents ( $na + nb + nc$ ) was found to be slightly less than the values obtained by resonant column testing.

A comparison was made between measured and predicted shear wave velocities for the biaxial test series with a variable  $\bar{\sigma}_o$ . It was found that the Eq. 7.3 yielded values of  $V_s$  within about 10 percent of the average of the measured values of shear wave velocity.

Structural anisotropy was further examined by rotation of the  $\bar{\sigma}_1$  axis. As with isotropic confinement, shear waves were separated into three planes of motion because of the anisotropic nature of the sample. It was determined that the structural anisotropy relationship between the planes of motion did not affect the basic relationships between  $V_s$  and the principal stress components, although the absolute values of  $V_s$  varied for each plane.



Biaxial tests were also performed with a constant  $\bar{\sigma}_0$  to evaluate the effect on  $V_s$  of varying shear stress. It was found that  $V_s$  depends on the variation of the stress components in the directions of wave propagation,  $\bar{\sigma}_a$ , and particle motion,  $\bar{\sigma}_b$ , and not on  $\bar{\sigma}_0$  as usually assumed. It follows that  $V_s$  depends on the level of shearing stress only to the extent that it relates to  $\bar{\sigma}_a$  and  $\bar{\sigma}_b$ .

Further comparison between measured and predicted values of  $V_s$  was made for the test series with a constant  $\bar{\sigma}_0$ . Results showed that Eq. 7.2 and the values from Table 7.6 predicted  $V_s$  within about 10 percent of the average of the test data.

## CHAPTER EIGHT

### TRIAXIAL CONFINEMENT

#### 8.1 INTRODUCTION

Testing was concluded with the case of triaxial confinement ( $\bar{\sigma}_1 > \bar{\sigma}_2 > \bar{\sigma}_3$ ) which was performed to examine the effect of a truly three-dimensional state of stress on shear wave velocity. The triaxial phase of testing consisted of three different series of tests. The test series were designed to study and re-examine:

1. the variation of  $V_s$  under a constant mean effective principal stress with varying deviatoric stress components, 2. the importance on  $V_s$  of each stress component with respect to direction of wave propagation, direction of particle motion, and the out-of-plane direction, and 3. the effect of structural anisotropy on  $V_s$  for triaxial confinement. Measured shear wave velocities were examined to study and quantify each of these effects, including further evaluation of the validity of equations developed in Chapter Seven to predict  $V_s$  for biaxial confinement. In this chapter, the triaxial states of stress are briefly reviewed, and the variation of  $V_s$  with triaxial confinement and structural anisotropy are summarized.

## 8.2 TRIAXIAL STATES OF STRESS

To obtain the condition of triaxial confinement, the major effective principal stress was applied along one axis of the cube, the minor effective principal stress along another axis, and the intermediate effective principal stress along the remaining axis. Typically, the major principal stress was oriented in the top-bottom (vertical) direction, and the intermediate principal stress was oriented in the north-south direction. However, for the triaxial series which was designed to study structural anisotropy of the sample,  $\bar{\sigma}_1$  and  $\bar{\sigma}_2$  were reversed so that  $\bar{\sigma}_1$  was now rotated to the north-south axis and  $\bar{\sigma}_2$  was rotated to the top-bottom axis of the cube.

### 8.2.1 Notation of Stress Components

For triaxial confinement, as with biaxial confinement, the principal stresses were no longer all the same. Therefore, the effect of the stress components could be reinvestigated for triaxial confinement. The notation used for biaxial confinement, that is  $\bar{\sigma}_a$ ,  $\bar{\sigma}_b$ , and  $\bar{\sigma}_c$ , was also used for triaxial confinement to describe the directions of the principal stresses relative to the directions of motions associated with the shear waves. A discussion of the notation is presented in Section 7.2.1 and is illustrated in Fig. 7.1.

### 8.2.2 Patterns of Stress Variation

The variation in stresses for the three triaxial confinement series followed one of two general patterns used for biaxial confinement. In the first pattern, referred to as triaxial loading with a variable mean effective principal stress, one of the principal stresses ( $\bar{\sigma}_2$ ) was changed, while the remaining principal stresses were held constant. Rows one and two in Table 8.1 (the second row is for the study of structural anisotropy) show the variation of stress components relative to wave motions for tests with a varying mean effective principal stress. For both of these rows, one stress component varied since only one principal stress was changed.

The second pattern of stress variation, referred to as triaxial loading with a constant mean effective principal stress, involved changing all the principal stresses (and, therefore, all the stress components) simultaneously, while maintaining a constant mean effective principal stress. The variation of stress components for this pattern is shown in Row three of Table 8.1. This pattern allowed  $\bar{\gamma}_s$  to be examined for constant  $\bar{\sigma}_o$  but with increasing levels of shearing stress due to stress differences between  $\bar{\sigma}_1$  and  $\bar{\sigma}_2$ ,  $\bar{\sigma}_1$  and  $\bar{\sigma}_3$ , or  $\bar{\sigma}_2$  and  $\bar{\sigma}_3$ .

### 8.2.3 Review of Simplifications and Data Analysis

Because of the inherent pressure gradients in the triaxial cube, a truly triaxial state of stress existed only on the horizontal plane at the mid-height of the cube. The pressure gradients

TABLE 8.1  
Variation of Stress Components for Triaxial Test Series

Triaxial Test Series (1)	Pattern of Stress Variation (2)	Shear Wave Type* (3)	Direction of Varying Stress Component (4)
1. Testing with variable mean effective principal stress	Varying $\bar{\sigma}_2$ oriented along north-south direction with constant $\bar{\sigma}_1$ along top-bottom and constant $\bar{\sigma}_3$ along east-west directions.	TB/NS TB/EW NS/TB NS/EW EW/TB EW/NS	Particle Motion Out-of-Plane Wave Propagation Wave Propagation Out-of-Plane Particle Motion
2. Testing with variable mean effective principal stress ( $\bar{\sigma}_2$ ) to study structural anisotropy.	Varying $\bar{\sigma}_2$ oriented along top-bottom direction with constant $\bar{\sigma}_1$ along north-south and constant $\bar{\sigma}_3$ along east-west directions.	TB/NS TB/EW NS/TB NS/EW EW/TB EW/NS	Wave Propagation Wave Propagation Particle Motion Out-of-Plane Particle Motion Out-of-Plane
3. Testing with constant mean effective principal stress.	Varying $\bar{\sigma}_1$ oriented along top-bottom axis with varying $\bar{\sigma}_2$ along north-south and varying $\bar{\sigma}_3$ along east-west axes.	TB/NS TB/EW NS/TB NS/EW EW/TB EW/NS	All Components Varied All Components Varied All Components Varied All Components Varied All Components Varied All Components Varied

\* The first two letters denote the direction of wave propagation, and the second two letters denote the direction of particle motion (TB = top-bottom, NS = north-south, EW = east-west).

were ignored, however, because of their small mathematical significance on  $V_s$  and the assumed state of stress within the cube, as discussed in Section 6.2.

Data analysis for triaxial confinement was the same as for the preceding isotropic and biaxial test series. Shear wave velocity was based upon both short-interval and long-interval velocity measurements because this approach yielded the results which were felt to be most representative of experimental scatter. As with the previous data analysis, direct velocities were discarded as being unrepresentative of  $V_s$  (see Section 6.3).

A complete set of recorded waveforms, data input and resultant computer output for a representative test is included in Appendix E.

#### 8.2.4 Principal Stress Ratio

The principal stress ratio was first used for biaxial confinement to reference the effect on  $V_s$  of the level of shear stress, measured by the stress difference between  $\bar{\sigma}_1$  and  $\bar{\sigma}_3$ . For triaxial confinement, with the three principal stresses all different, there are two principal stress ratios required to describe the level of shear stress between the principal axes. The first stress ratio,  $K_{13}$ , was also used for biaxial confinement and relates the major principal stress,  $\bar{\sigma}_1$ , to the minor principal stress,  $\bar{\sigma}_3$ , as given by Eq. 7.1.

A second stress ratio,  $K_{23}$ , is needed for triaxial confinement to relate the intermediate principal stress,  $\bar{\sigma}_2$ , to the minor principal stress,  $\bar{\sigma}_3$ , as:

$$K_{23} = \frac{\bar{\sigma}_2}{\bar{\sigma}_3} \quad (8.1)$$

Both of these stress ratios are used for triaxial confinement to describe the change in  $V_s$  with shearing stress.

### 8.3 TESTING WITH A VARIABLE MEAN EFFECTIVE PRINCIPAL STRESS

Two series of tests were conducted with triaxial confinement in which the mean effective principal stress varied. Both series were designed to study the effect on  $V_s$  of the stress components in the directions of wave propagation, particle motion and out-of-plane. The second series presented in this section and in Section 8.4 was also performed to examine the effect of structural anisotropy.

The first triaxial series began at a biaxial state of stress with a vertical stress,  $\bar{\sigma}_1$ , of 40 psi (275.6 kPa) and with the horizontal stresses,  $\bar{\sigma}_2$  along the north-south direction and  $\bar{\sigma}_3$  along the east-west direction, equal to 15 psi (103.4 kPa). The intermediate principal stress  $\bar{\sigma}_2$  along the north-south direction was then increased in 5-psi (34.5 kPa) increments to 40 psi (275.6 kPa), while the other principal stresses remained constant. Wave test measurements were conducted after each incremental pressure change. The test sequence was then reversed to examine

the effect of stress history on the sand sample. These tests are numbered 45 through 50, and 50 through 55 in Table B.1 for the loading and unloading portions, respectively. The load history can be seen in Fig. B.2 during the times of August 11 through August 14, 1981 for the loading portion and from August 14 through August 17, 1981 for the unloading portion. The stress ratio,  $K_{13}$ , for this test series was constant at 2.67, and the other stress ratio,  $K_{23}$ , varied from 1.0 to 2.67.

The second triaxial series, designed to study structural anisotropy, also began at a biaxial state of stress, with  $\bar{\sigma}_1$  of 40 psi (275.6 kPa) rotated to the north-south direction,  $\bar{\sigma}_2$  of 15 psi (103 kPa) rotated to the vertical direction, and  $\bar{\sigma}_3$  of 15 psi (103 kPa) along the east-west direction. The intermediate principal stress was then increased in 5-psi (34.5 kPa) increments to 40 psi (275.6 kPa) while the two remaining stresses were held constant. There was no reversed sequence performed to examine stress history. This series of tests is numbered 61 through 66 in Table B.1, and the load history can be seen in Fig. B.1 during the time of August 18 and August 19, 1981. Results from this test series are discussed in Section 8.4. The stress ratio,  $K_{13}$ , for this series was held constant at 2.67 and the other stress ratio,  $K_{23}$ , varied from 1.0 to 2.67.

### 8.3.1 Effect of Each Stress Component on $V_s$

The equation used for biaxial confinement to examine how each stress component affects  $V_s$  was also used for the case of



triaxial confinement. In doing this, the values of  $C_1$ ,  $ma$ ,  $mb$ , and  $mc$  could be recalculated for triaxial confinement from Eq. 7.2

(after Roesler (1979)) as:

$$V_s = C_1 \bar{\sigma}_a^{ma} \bar{\sigma}_b^{mb} \bar{\sigma}_c^{mc} \quad (8.2)$$

where:  $V_s$  = shear wave velocity in fps,

$C_1$  = constant in  $\text{ft}^{(3-ma+mb+mc)}/\text{sec-lb}^{(ma+mb+mc)}$ ,

$ma$  = slope of  $\log V_s - \log \bar{\sigma}_a$  relationship,

$mb$  = slope of  $\log V_s - \log \bar{\sigma}_b$  relationship, and

$mc$  = slope of  $\log V_s - \log \bar{\sigma}_c$  relationship.

Each of the stress components (expressed in psf) are incorporated into this equation to predict the resultant  $V_s$ . The sum of the exponents of the stress components ( $ma + mb + mc$ ) should be similar for triaxial and biaxial confinement and should equal the slope  $m$  in Eq. 6.1 (slope of the  $\log V_s - \log \bar{\sigma}_o$  relationship for isotropic confinement) for each shear wave type.

As with biaxial confinement, it was decided to evaluate this expression for the three planes of motion (NS-EW, TB-EW, and TB-NS) rather than for the six individual shear waves. This was done because the structural anisotropy study for isotropic confinement showed that the six shear waves could be paired into three wave groups with similar planes of motion (see Fig. 6.12).

### 8.3.2 Effect of Principal Stress in Direction of Wave Propagation

For both of these triaxial confinement series with a variable mean effective principal stress, only one principal stress (and therefore only one stress component) was varied at a time. Those triaxial tests where the effects of  $\bar{\sigma}_a$  on  $V_s$  could be isolated involved varying  $\bar{\sigma}_2$  only.

With  $\bar{\sigma}_2$  oriented along the north-south axis, tests were performed for both loading and unloading pressure variations for the TB-NS and NS-EW planes of motion. These results are shown in Figs. 8.1 and 8.2. Each figure shows a sloping straight line depicting the least-square line fitted to the data. Also shown at the various pressures are a circle depicting the average of all test data for that pressure, a vertical line representing the scatter between the minimum and maximum values measured at that pressure, and two tick marks on the vertical line representing  $\pm$  one standard deviation from the average point. Also included on each figure is a representation of the cube showing the state of stress for the test series. Along with each cube are two crossed arrows signifying the motion associated with the shear wave used during the test, a single-headed arrow oriented along the direction of wave propagation and a double-headed arrow oriented in the direction of particle motion.

For  $\bar{\sigma}_2$  oriented along the vertical axis of the cube (to examine structural anisotropy), tests were only performed for a loading pressure sequence. The loading data are shown in Fig. 8.3

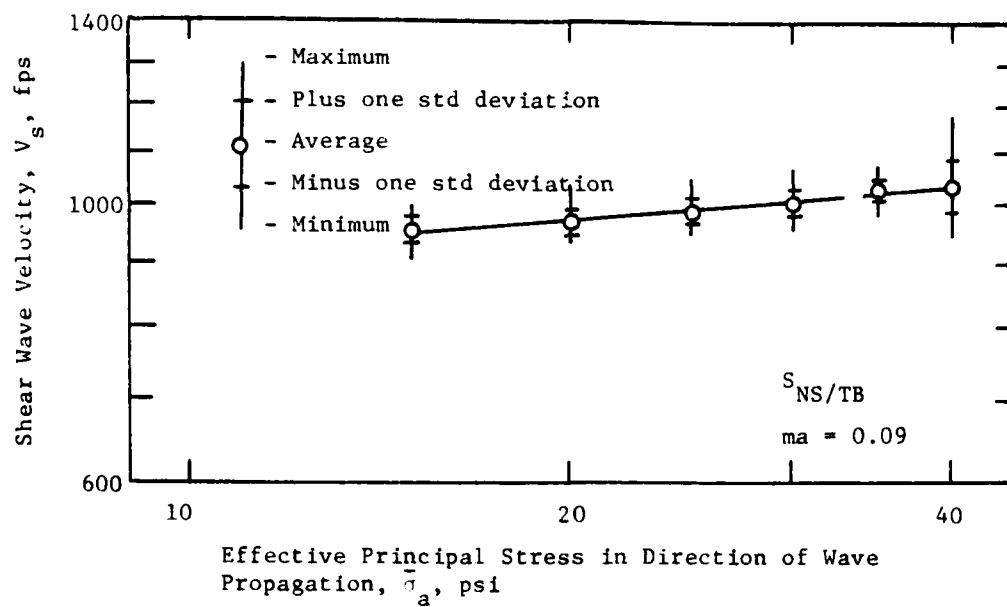
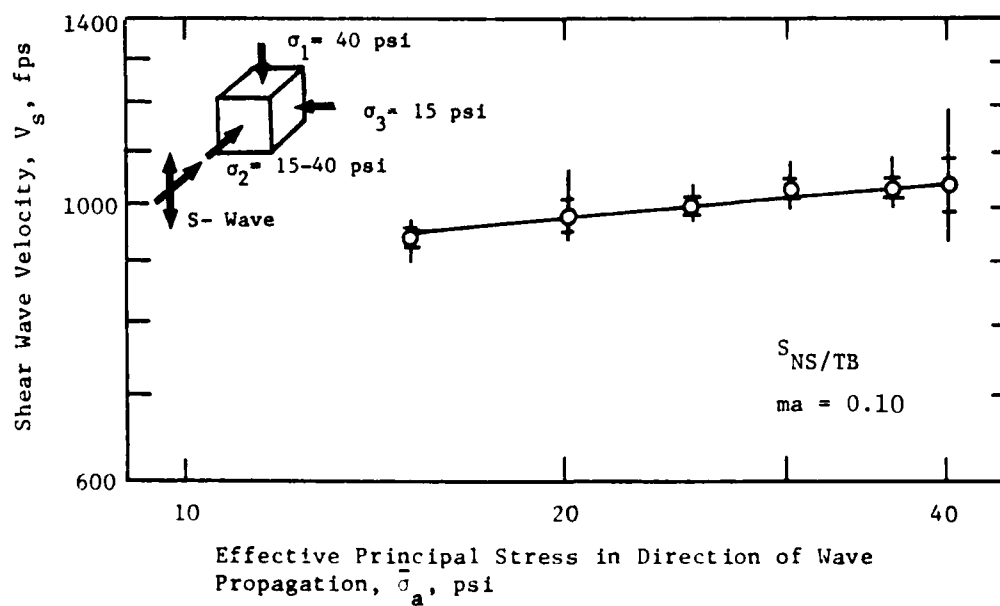
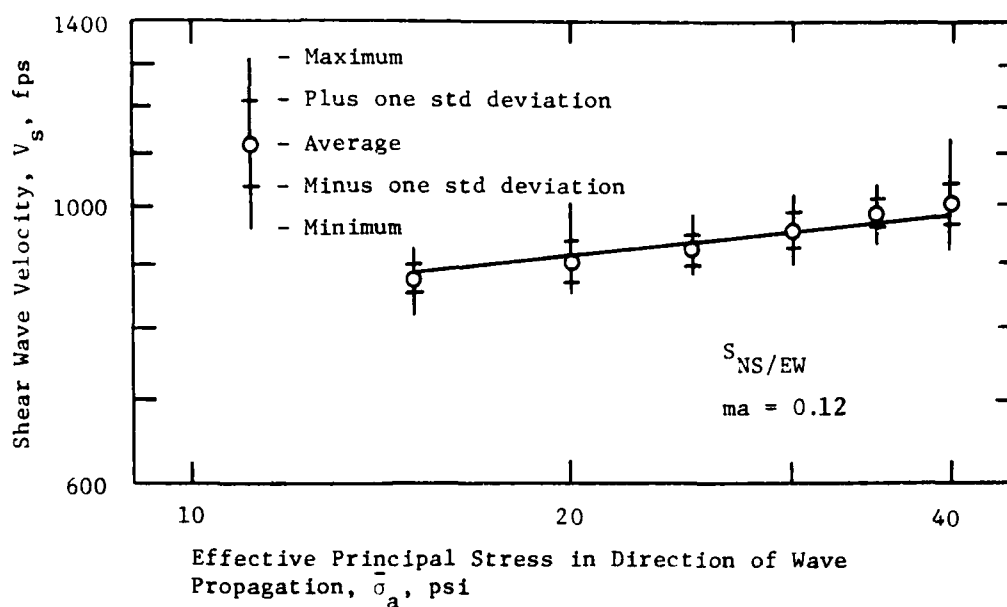
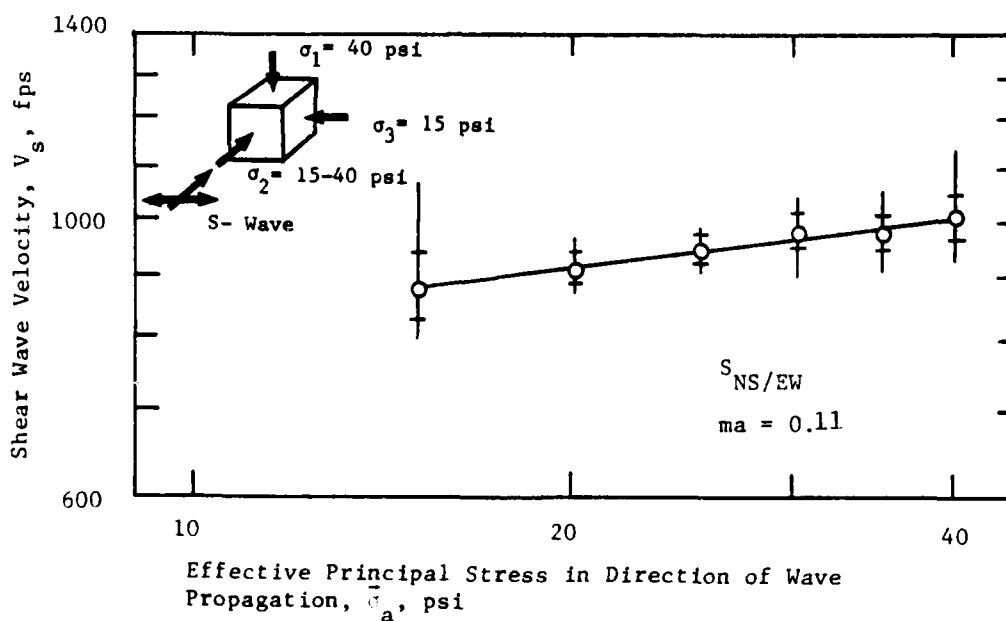
a) Loading Sequence with  $S_{NS/TB}$ -Waveb) Unloading Sequence with  $S_{NS/TB}$ -Wave

Fig. 8.1 - Variation of Shear Wave Velocity with Principal Stress in Direction of Wave Propagation for NS-TB Plane of Motion for Triaxial Confinement



a) Loading Sequence with  $S_{NS/EW}$ -Wave



b) Unloading Sequence with  $S_{NS/EW}$ -Wave

Fig. 8.2 - Variation of Shear Wave Velocity with Principal Stress in Direction of Wave Propagation for NS-EW Plane of Motion for Triaxial Confinement

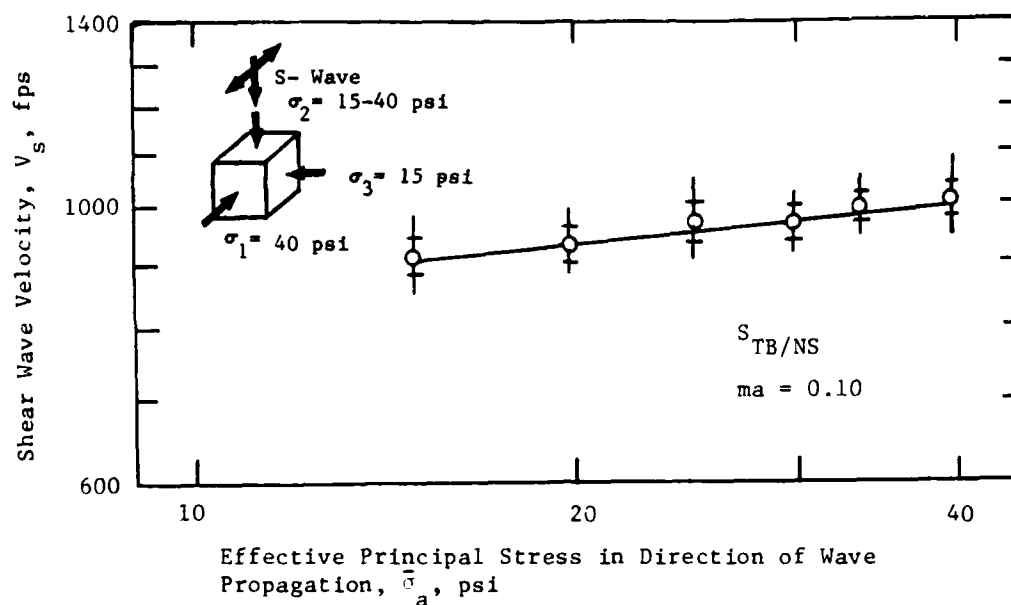
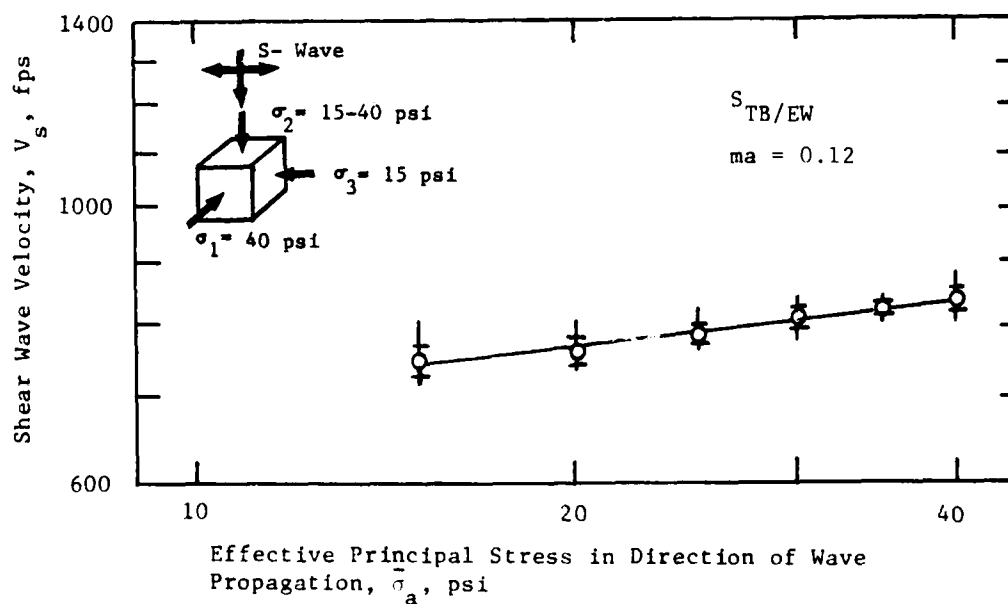
a) Loading Sequence with  $S_{TB/NS}$ -Waveb) Loading Sequence with  $S_{TB/EW}$ -Wave

Fig. 8.3 - Variation of Shear Wave Velocity with Principal Stress in Direction of Wave Propagation for TB-NS and TB-EW Planes of Motion for Triaxial Confinement

for this test in which only  $\bar{\sigma}_2$  varied for the TB-NS and TB-EW planes of motion.

The results of the variation in  $V_s$  with  $\bar{\sigma}_a$  ( $\bar{\sigma}_b = \bar{\sigma}_c =$  constant) are summarized in Table 8.2, based on the least-squares fit to the data in Figs. 8.1, 8.2, and 8.3. From Table 8.2, the slope of the  $\log V_s - \log \bar{\sigma}_a$  relationship varies from 0.10 to 0.12 for all three wave groups. This variation in slope is well within that expected for experimental scatter and, hence, the slopes agree closely. There is no apparent effect on  $V_s$  of stress history, since the value of  $ma$  is similar for the loading and unloading pressure sequences. The effect of structural anisotropy is discussed in Section 8.4.

It is interesting to note that this range of  $ma$  is similar to the range obtained for biaxial confinement, although the values for each plane of motion differ slightly between triaxial and biaxial confinement (0.10 to 0.13 as shown in Table 7.3).

### 8.3.3 Effect of Principal Stress in Direction of Particle Motion

Examination of the effect on  $V_s$  of  $\bar{\sigma}_b$  was performed in a manner similar to that used to study the  $\log V_s - \log \bar{\sigma}_a$  relationship. For  $\bar{\sigma}_2$  oriented along the north-south axis of the cube, the  $\log V_s - \log \bar{\sigma}_b$  relationships for the TB-NS and NS-EW planes of motion are shown in Figs. 8.4 and 8.5, respectively, for loading and unloading pressure sequences. For  $\bar{\sigma}_2$  oriented along the

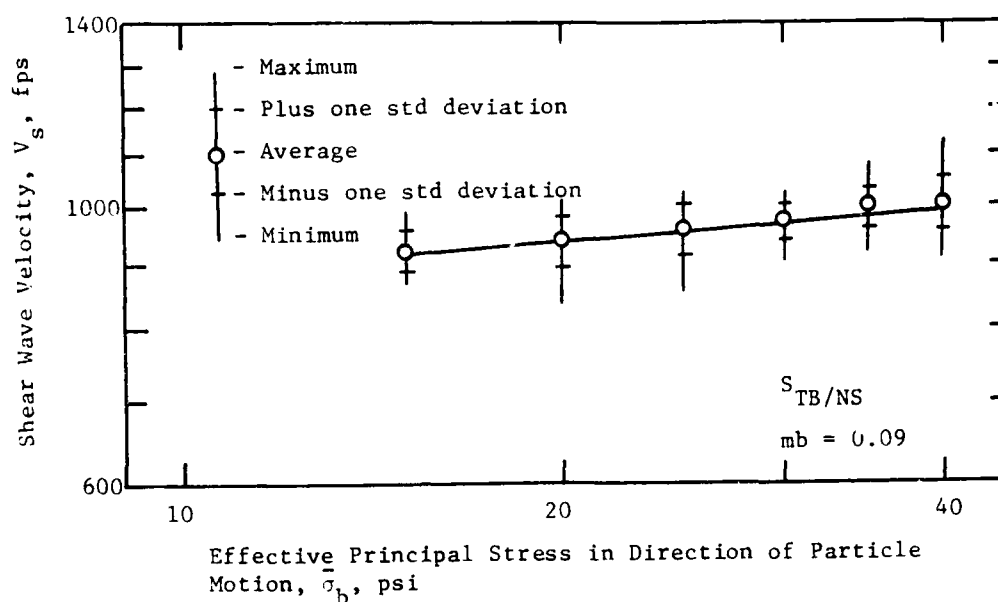
TABLE 8.2

Effect on  $V_s$  of Principal Stress in Direction of Wave  
Propagation for Triaxial Confinement

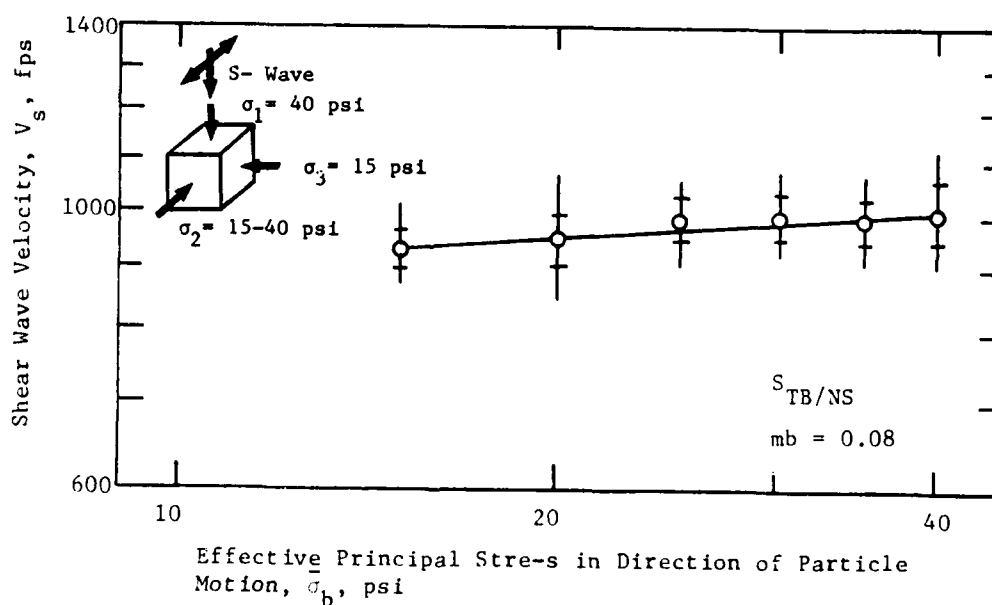
Plane of Motion	Slope of $\log V_s - \log \bar{\sigma}_a$ Relationship*		
	Loading ma	Unloading ma	Average ma
(1)	(2)	(3)	(4)
TB-NS	0.10	0.10	0.10
TB-EW	0.12	**	**
NS-EW	0.12	0.11	0.11

\* Eq. 8.2:  $V_s = C_1 \bar{\sigma}_a^{ma} \bar{\sigma}_b^{mb} \bar{\sigma}_c^{mc}$

\*\* Not determined because only performed loading pressure sequence.



a) Loading Sequence with  $S_{TB/NS}$ -Wave



b) Unloading Sequence with  $S_{TB/NS}$ -Wave

Fig. 8.4 - Variation of Shear Wave Velocity with Principal Stress in Direction of Particle Motion for TB-NS Plane of Motion for Triaxial Confinement



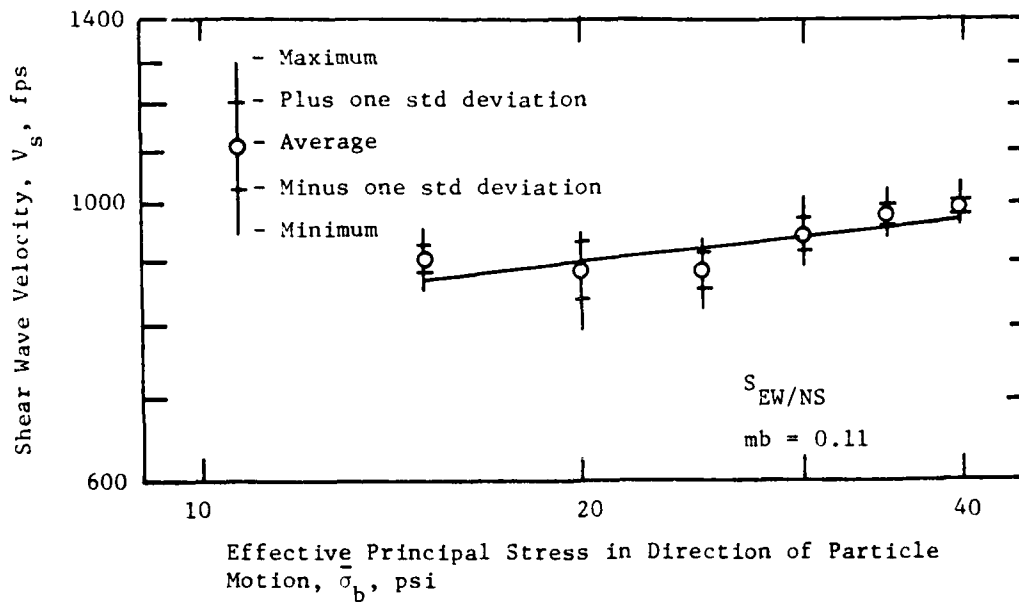
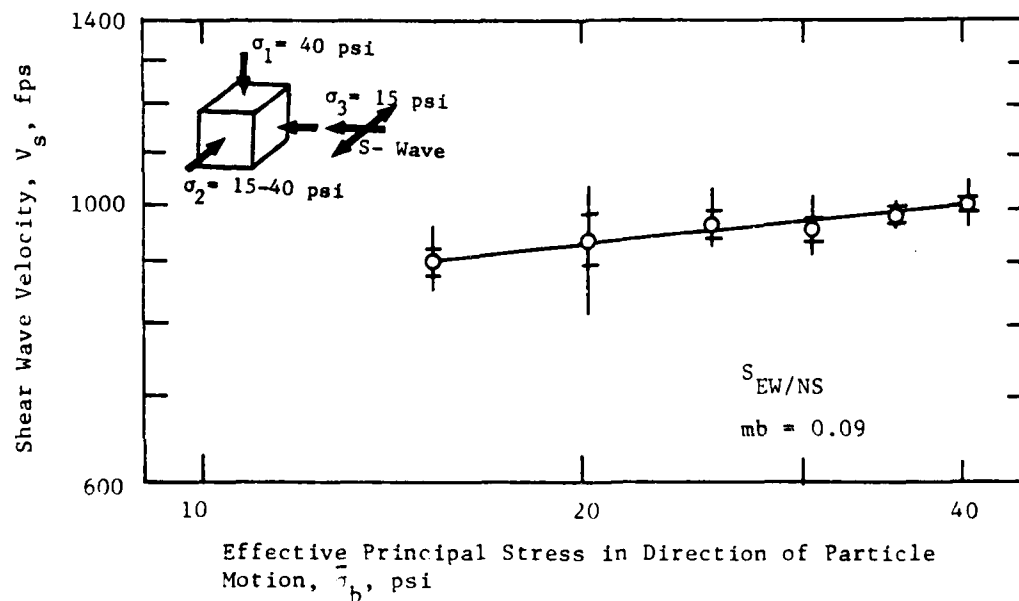
a) Loading Sequence with  $S_{EW/NS}$ -Waveb) Unloading Sequence with  $S_{EW/NS}$ -Wave

Fig. 8.5 - Variation of Shear Wave Velocity with Principal Stress in Direction of Particle Motion for EW-NS Plane of Motion for Triaxial Confinement

vertical axis of the cube, Fig. 8.6 shows the effect on  $V_s$  of  $\bar{\sigma}_b$  for the TB-NS and TB-EW planes of motion for loading pressure sequences only. Included on all of these figures are the average of all interval velocity data for the test pressure, the minimum and maximum values of the data,  $\pm$  one standard deviation from the average at each pressure, and the cube representation showing the state of stress and shear wave motions for the testing sequence.

A summary of the  $\log V_s - \log \bar{\sigma}_b$  relationships shown in Figs. 8.4, 8.5, and 8.6 is presented in Table 8.3. Using a least-squares fit for the data, the value of  $mb$  varies from 0.08 to 0.11 for the three wave groups. Stress history has no apparent effect on  $mb$  in that similar values were measured for both loading and unloading pressure sequences. The effect of structural anisotropy on  $\bar{\sigma}_b$  is discussed in Section 8.4.

As with biaxial confinement, the values of  $mb$  for triaxial confinement are equal to or slightly less than the values of  $ma$  obtained in Section 8.3.2. This would tend to confirm that the shear wave velocity is about equally dependent on the principal stresses in the directions of wave propagation and particle motion for this sand. The range of values of  $mb$  obtained for triaxial confinement are also similar to those obtained for biaxial confinement (0.09 to 0.11 as shown in Table 7.4).

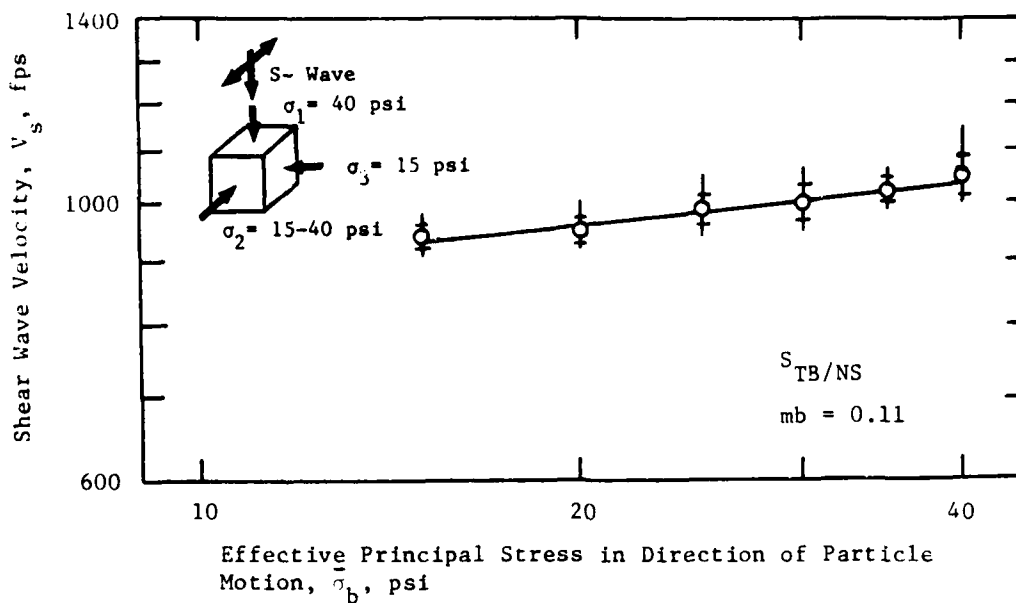
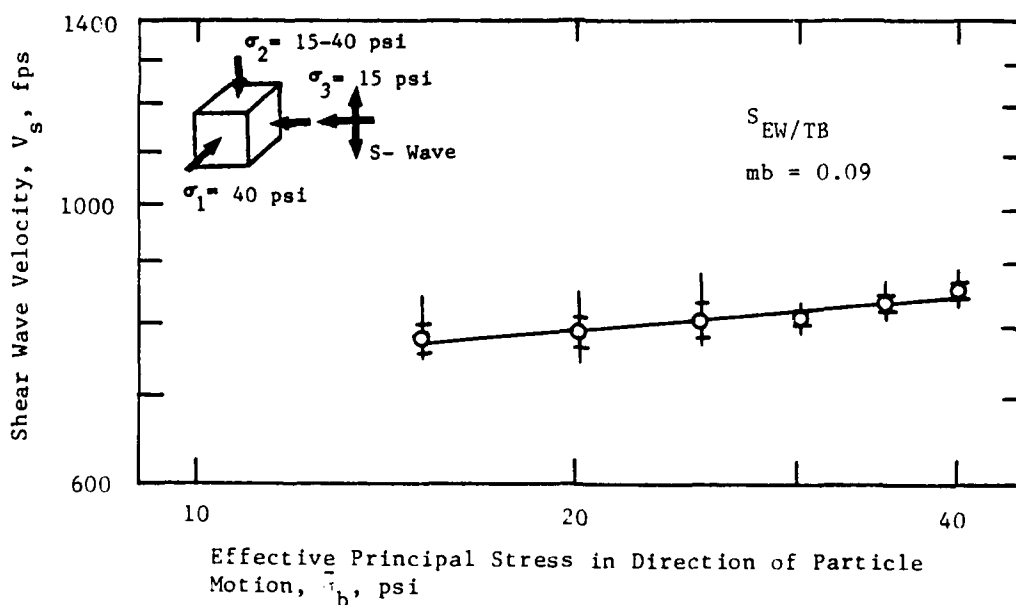
a) Loading Sequence with  $S_{TB/NS}$ -Waveb) Loading Sequence with  $S_{EW/TB}$ -Wave

Fig. 8.6 - Variation of Shear Wave Velocity with Principal Stress in Direction of Particle Motion for TB-NS and TB-EW Planes of Motion for Triaxial Confinement

TABLE 8.3

Effect on  $V_s$  of Principal Stress in the Direction of  
Particle Motion for Triaxial Confinement

Plane of Motion	Slope of $\log V_s - \log \bar{\sigma}_b$ Relationship*		
	Loading mb	Unloading mb	Average mb
(1)	(2)	(3)	(4)
TB-NS	0.10	0.08	0.09
TB-EW	0.09	**	**
NS-EW	0.11	0.09	0.10

\* Eq. 8.2:  $V_s = C_1 \bar{\sigma}_a^{ma} \bar{\sigma}_b^{mb} \bar{\sigma}_c^{mc}$

\*\* Not determined because only performed loading pressure sequence.

#### 8.3.4 Effect of Principal Stress in the Out-of-Plane Direction

The manner of analysis used for  $\bar{\sigma}_a$  and  $\bar{\sigma}_b$  was continued for the examination of the  $\log V_s - \log \bar{\sigma}_c$  relationship. Figure 8.7 shows the  $\log V_s - \log \bar{\sigma}_c$  relationship for the TB-EW plane of motion for the loading and unloading pressure sequences when  $\bar{\sigma}_2$  was oriented along the north-south axis of the cube. For  $\bar{\sigma}_2$  oriented along the vertical axis, Fig. 8.8 shows the values of mc for the NS-EW plane of motion for loading pressure sequences only.

The results of the least-squares fit of the data in Figs. 8.6 and 8.8 are summarized in Table 8.4. As seen in this table, the value of mc for the TB-EW plane of motion was zero (or slightly less than zero), while the value of mc for the NS-EW plane of motion was significantly greater than zero. This larger value of mc is assumed to be primarily due to experimental scatter. It must be noted that only loading pressure sequences were available for the NS-EW plane of motion with no unloading data to compare with the value of mc. The small value of mc for the TB-EW plane of motion (and the relatively small value for the NS-EW plane of motion) seem to agree with the assumptions made for biaxial confinement that the shear wave depends very little on the principal stress in the out-of-plane direction. As with  $\bar{\sigma}_a$  and  $\bar{\sigma}_b$ , there is no apparent effect of stress history on the values of mc, although only one plane of motion was studied in detail.

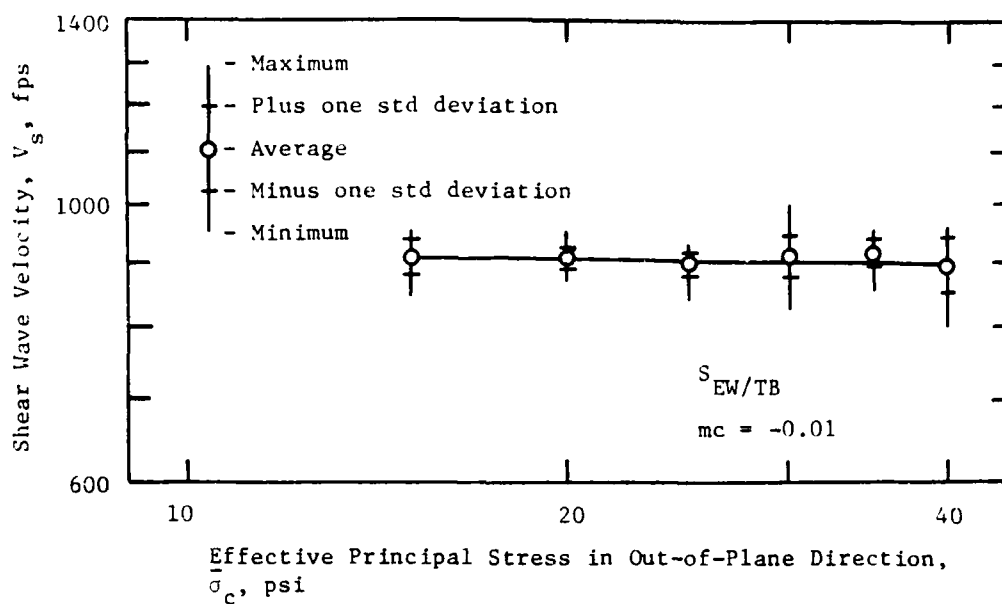
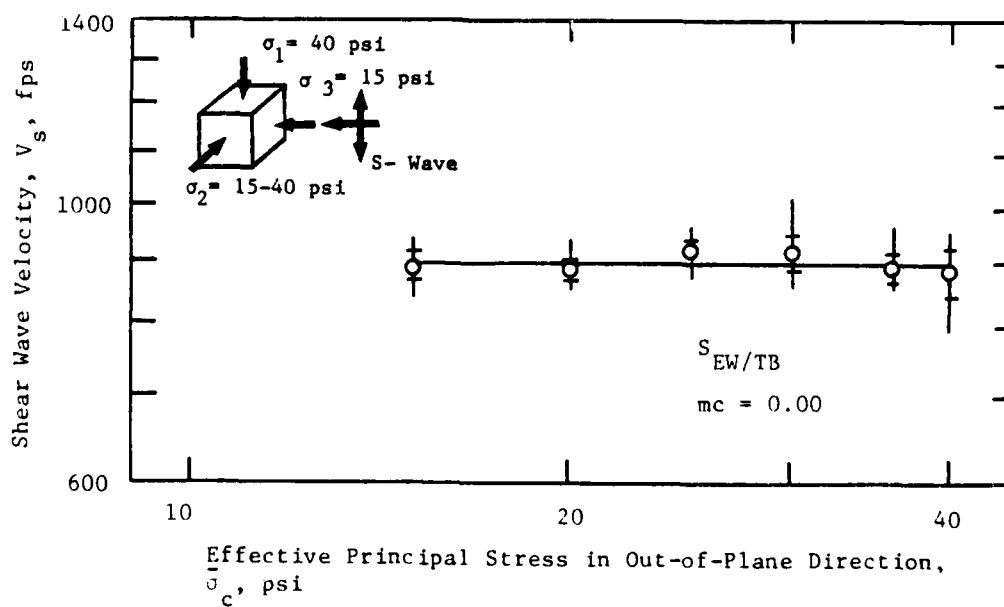
a) Loading Sequence with  $S_{EW/TB}$ -Waveb) Unloading Sequence with  $S_{EW/TB}$ -Wave

Fig. 8.7 - Variation of Shear Wave Velocity with Principal Stress in Out-of-Plane Direction for TB-EW Plane of Motion for Triaxial Confinement

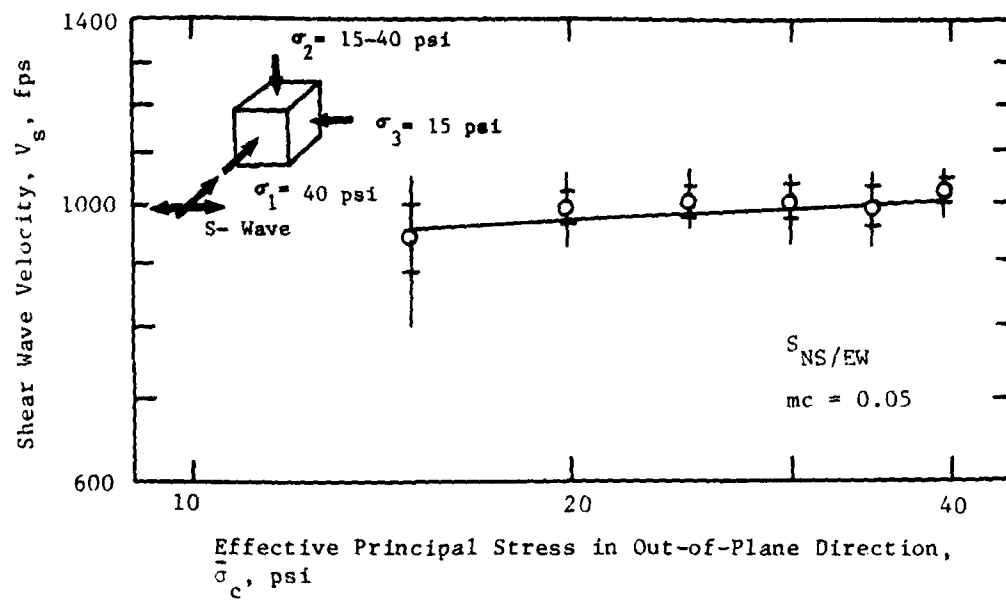
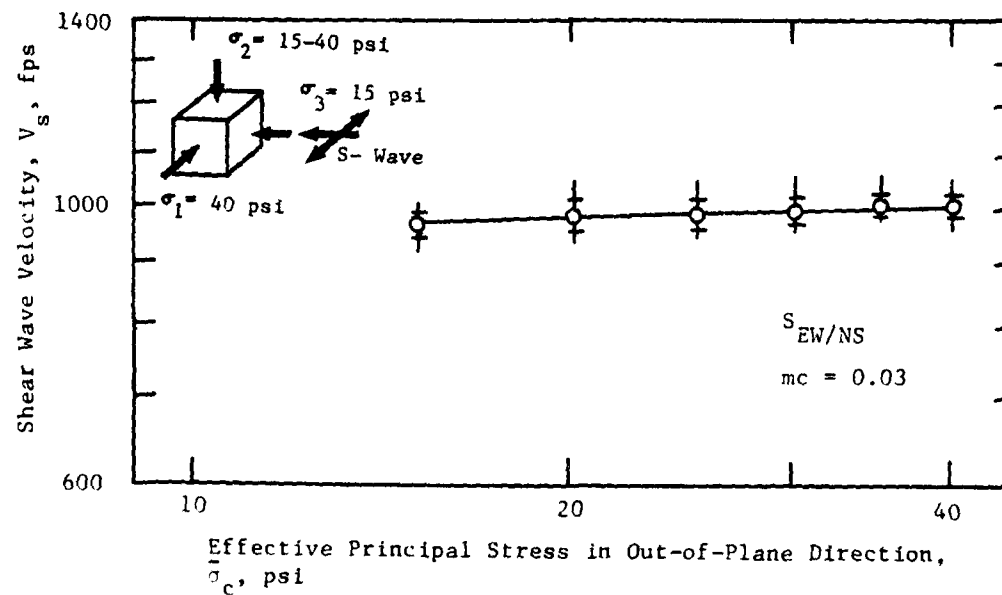
a) Loading Sequence with  $S_{NS/EW}$ -Waveb) Loading Sequence with  $S_{EW/NS}$ -Wave

Fig. 8.8 - Variation of Shear Wave Velocity with Principal Stress in Out-of-Plane Direction for NS-EW Plane of Motion for Triaxial Confinement

TABLE 8.4

Effect on  $V_s$  of Principal Stress in Out-of-Plane  
Direction for Triaxial Confinement

Plane of Motion	Slope of $\log V_s - \log \bar{\sigma}_c$ Relationship*		
	Loading mc	Unloading mc	Average mc
(1)	(2)	(3)	(4)
TB-NS	***	***	***
TB-EW	-0.01	0.00	0.00
NS-EW	0.04	**	**

\* Eq. 8.2:  $V_s = C_1 \bar{\sigma}_a^{ma} \bar{\sigma}_b^{mb} \bar{\sigma}_c^{mc}$

\*\* Not determined because only loading pressure sequences performed.

\*\*\* Not determined because no tests performed for this stress configuration.



### 8.3.5 Summary of Effect of Principal Stresses on $V_s$

Values of  $m_a$ ,  $m_b$ , and  $m_c$  were not determined for all possible testing configurations because of the limited number of tests performed. Average values of the slopes could not be determined when only loading pressure sequences were performed, and there were no tests conducted where  $\bar{\sigma}_c$ , the out-of-plane direction, was varied for the TB-NS plane of motion. Since triaxial confinement has all different principal stresses, there was no intermediate stage of testing, as for biaxial confinement, where two similar principal stresses were varied simultaneously. The remaining triaxial test series had all principal stresses varying and so these tests were not used to compute the missing values of  $m_a$ ,  $m_b$ , and  $m_c$ , since two of the slopes would have to be assumed to calculate the remaining slope. The values previously determined for  $m_a$ ,  $m_b$ , and  $m_c$  are summarized in Table 8.5.

Once the evaluation of the slopes was completed, the constant  $C_1$  for Eq. 8.2 was determined where possible for each plane of motion. This was accomplished by dividing the measured average shear wave velocity for each test pressure by the three principal stress components for that pressure raised to the appropriate power. The values of  $C_1$  for each plane of motion are included in Table 8.5.

The values of  $C_1$  calculated for the TB-NS and NS-EW planes of motion involved assumptions concerning  $m_c$ . The value for  $m_c$  of 0.04 was used to calculate  $C_1$  for the loading pressure

TABLE 8.5

Summary of Effects on  $V_s$  of Orientation of Principal  
Stresses Relative to Planes of Motion  
for Triaxial Confinement

Variable in Eq. 8.3*	Plane of Motion	Loading	Unloading	Average
(1)	(2)	(3)	(4)	(5)
ma	TB-NS	0.10	0.10	0.10
	TB-EW	0.12	**	**
	NS-EW	0.12	0.11	0.11
mb	TB-NS	0.10	0.08	0.09
	TB-EW	0.09	**	**
	NS-EW	0.11	0.09	0.10
mc	TB-NS	**	**	**
	TB-EW	-0.01	0.00	0.00
	NS-EW	0.04	**	**
C <sub>1</sub> ****	TB-NS***	173	207	182
	TB-EW	149	**	**
	NS-EW	129	163	146

\* For the equation  $V_s = C_1 \frac{ma}{\sigma_a} \frac{mb}{\sigma_b} \frac{mc}{\sigma_c}$

\*\* Could not be determined for triaxial confinement.

\*\*\* Calculated with assumed  $mc = 0.00$

\*\*\*\*  $(ft^{3-t} lb^{-t} sec^{-1})$  where  $t = ma + mb + mc$

sequence of the NS-EW plane of motion. The remaining values of  $C_1$  were calculated using the results from biaxial confinement (0.00 for the TB-NS and 0.01 for the NS-EW planes of motion).

Based on this table, the conclusion made for biaxial confinement that the stress components do not contribute equally to the shear wave velocity is also true for triaxial confinement. The stress components in the directions of wave propagation and particle motion again dominate. It appears for this sand that the principal stresses in these directions contribute about equally to  $V_s$ .

Further, the principal stress in the out-of-plane direction affects the shear wave velocity very little and can be neglected. This conclusion is made despite the fact that  $mc$  varied up to 0.06 for triaxial confinement, since it was felt that these higher slopes for  $mc$  were inconsistent with all other results for biaxial and triaxial confinement. The higher slopes were attributed, therefore, to the experimental scatter inherent in the testing technique.

Stress history had no marked effect on the values of the slopes in Table 8.5. Similar values were calculated for the loading and unloading pressure sequences. Stress history, therefore, can be ignored for triaxial confinement, as it could for biaxial confinement.

The  $V_s$  - stress component relationships developed for the triaxial data are similar to those obtained by Roesler (1979)

(as was the biaxial data). In both experiments, the stress component in the out-of-plane direction was not found to affect shear wave velocity and, hence, should be ignored. The stress components in the directions of wave propagation and particle motion were found by this study to almost equally affect the shear wave velocity, with slopes ranging from 0.08 to 0.12. Roesler, in his experiments, found that the direction of wave propagation was more dominant than the component in the direction of particle motion ( $m_a$  equal to 0.15 versus  $m_b$  equal to 0.11). This difference in dominance can be due to the sand sample, experimental scatter, or other inherent differences between the test apparatus used by Roesler and the one used in this study.

#### 8.3.6 Comparison of Stress Component Relationships for Isotropic, Biaxial, and Triaxial Confinement

A comparison was made between the values of the sum of the slopes ( $m_a + m_b + m_c$ ) and  $C_1$  for triaxial and biaxial confinement with the comparable values for isotropic confinement. This comparison, shown in Table 8.6, was made to examine whether or not the slope of the  $\log V_s - \log \bar{\sigma}$  relationship was consistent. The values are compared in Table 8.6 for each of the three planes of motion, and as noted in the table, some of the values are based on loading pressure sequences only or on values of  $m_c$  which are considered good estimates of the  $\log V_s - \log \bar{\sigma}_c$  relationship.

TABLE 8.6

Comparison of Average Effect of Principal Stress  
Orientation on Shear Wave Velocity for  
Isotropic, Biaxial, and Triaxial Confinements

Plane of Motion	Type of Confinement	log $V_s$ - log $\bar{\sigma}$ Relationship*	
		(ma+mb+mc) or m	$C_1$ (ft <sup>3-t</sup> <sub>lb</sub> <sup>-t</sup> sec <sup>-1</sup> ) <sup>#</sup>
(1)	(2)	(3)	(4)
TB-NS	Isotropic	0.18	217
	Biaxial	0.20	180
	Triaxial	0.19	182
TB-EW	Isotropic	0.22	142
	Biaxial	0.23	132
	Triaxial**	0.21	149
NS-EW	Isotropic	0.19	199
	Baixial	0.19	201
	Triaxial***	0.22	173

\* Eq. 7.2 and Eq. 8.2 for biaxial and triaxial confinement:

$$V_s = C_1 \bar{\sigma}_a^{ma} \bar{\sigma}_b^{mb} \bar{\sigma}_c^{mc}$$

Eq. 6.1 for isotropic confinement:  $V_s = C_1 \bar{\sigma}_o^m$

\*\* Based on loading pressure sequence only.

\*\*\* Based on value of mc equal to biaxial value of 0.01.

#  $t = ma + mb + mc$

As can be seen in Table 8.6, there is a good comparison between the values of the slopes and constant for each plane of motion. Values agree within ten percent of the average of the minimum and maximum values for any plane of motion. The ten percent variation is due to experimental scatter, inherent in this study, and is within tolerable limits expected for this type of experiment.

One of the purposes of this study was to determine how each of the principal stress components affected shear wave velocity. A relationship was found for both biaxial and triaxial confinement, and it was decided to compare these relationships in detail. Table 8.7 shows the comparison of  $m_a$ ,  $m_b$ ,  $m_c$ , and  $C_1$  for the three planes of motion for both states of confinement. An average value for each variable is included in column 5 of the table. The values show good correlation between the biaxial and triaxial states of stress. The individual variables for biaxial and triaxial confinement are within the expected experimental scatter of about ten percent. In general, the results of the examination of the effect on  $V_s$  of the principal stress components under triaxial confinement yield similar results to biaxial confinement as discussed in Chapter 7.

#### 8.3.7 Effect of Principal Stresses on Shear Modulus

The shear modulus can be expressed in the simplified form first used for biaxial confinement as (after Hardin, 1978):

TABLE 8.7

Comparison of Influence on  $V_s$  of Orientation of  
Principal Stresses Relative to Planes of  
Shear Wave Motions for Biaxial and Triaxial Confinements

Variable in Eqs. 7.2 and 8.2*	Plane of Motion	Type of Confinement		Average Value
		Biaxial	Triaxial	
(1)	(2)	(3)	(4)	(5)
ma	TB-NS	0.11	0.10	0.11
	TB-EW	0.12	0.12**	0.12
	NS-EW	0.09	0.11	0.10
mb	TB-NS	0.10	0.09	0.09
	TB-EW	0.11	0.09**	0.10
	NS-EW	0.09	0.10	0.09
mc***	TB-NS	0.00	0.00	0.00
	TB-EW	0.00	0.00	0.00
	NS-EW	0.01	0.01	0.01
$C_1$ ****	TB-NS	180	182	180
	TB-EW	132	149**	141
	NS-EW	201	173	187

\* Eq. 8.2:  $V_s = C_1 \bar{\sigma}_a^{ma} \bar{\sigma}_b^{mb} \bar{\sigma}_c^{mc}$

\*\* Based on loading pressure sequence only.

\*\*\* Values of mc for TB-NS and NS-EW planes of motion were assumed the same for biaxial and triaxial confinement.

\*\*\*\*  $(ft^{3-t} lb^{-t} sec^{-1})$  where  $t = ma + mb + mc$

$$G_{\max} = \frac{C}{0.673} P_a^{1-(n_a+n_b+n_c)} \bar{\sigma}_a^{-n_a} \bar{\sigma}_b^{-n_b} \bar{\sigma}_c^{-n_c} \quad (8.3)$$

where:  $G_{\max}$  = shear modulus in desired units,

$C$  = constant (dimensionless),

$n_a$  = slope of  $\log G_{\max} - \log \bar{\sigma}_a$  relationship,

$n_b$  = slope of  $\log G_{\max} - \log \bar{\sigma}_b$  relationship,

$n_c$  = slope of  $\log G_{\max} - \log \bar{\sigma}_c$  relationship, and

$P_a$  = atmospheric pressure in same units as  $G_{\max}$ .

For this equation,  $\bar{\sigma}_a$ ,  $\bar{\sigma}_b$ , and  $\bar{\sigma}_c$  are all expressed in the same units as  $G_{\max}$ . The values of  $n_a$ ,  $n_b$ , and  $n_c$  are equal to two times the values of  $m_a$ ,  $m_b$ , and  $m_c$ , respectively.

Equation 8.3 was evaluated for each plane of motion, using the average values presented in Table 8.7, and the results are shown in Table 8.8. The sum of the slopes for the stress components ( $n_a + n_b + n_c$ ) is consistently less than the slope of 0.48 of the  $\log G - \log \bar{\sigma}_o$  relationship determined from the resonant column tests. However, the sum of the slopes for triaxial confinement compares quite well with the sum of the slopes for uniaxial confinement and the slope  $n$  for the  $\log G - \log \bar{\sigma}_o$  relationship for isotropic confinement in the cube. Differences in testing procedures or in the sand samples tested between the laboratory resonant column tests and the cube may explain the difference in slopes calculated from these two test methods.



TABLE 8.8

Influence on  $G_{\max}$  of Orientation of Principal Stresses  
Relative to Planes of Shear Wave Motions

Plane of Motion (1)	na* (2)	nb* (3)	nc* (4)	C* (5)	na+nb+nc* (6)
TB-NS	0.22	0.18	0.00	678	0.40
TB-EW	0.24	0.20	0.00	603	0.44
NS-EW	0.20	0.18	0.02	748	0.40

\*Eq. 8.3:  $G_{\max} = \frac{C}{0.673} Pa^{1-(na+nb+nc)} \frac{na}{\sigma_a} \frac{nb}{\sigma_b} \frac{nc}{\sigma_c}$

#### 8.4 STRUCTURAL ANISOTROPY

For both isotropic and biaxial confinement, it was determined that the sand had some degree of structural anisotropy (see Sections 6.7 and 7.4). The degree of structural anisotropy was studied once more for the case of triaxial confinement to see if consistent trends were determined for the sand sample. Structural anisotropy of the sand is caused by the realignment of the sand grains as they are placed, which for this study, varied with each axis of the cube.

The structural anisotropy was analyzed for each of the three planes of motion using the values summarized in Table 8.7 for triaxial confinement. Based on these equations, a ratio of shear wave velocities for each plane of motion can be computed as:

$$V_{TB-EW} = (0.86 \bar{\sigma}_a^{0.01} \bar{\sigma}_b^{-0.01} \bar{\sigma}_c^{-0.01}) V_{EW-NS} \quad (8.4)$$

$$V_{NS-TB} = (1.05 \bar{\sigma}_a^{-0.01} \bar{\sigma}_b^{-0.01} \bar{\sigma}_c^{-0.01}) V_{EW-NS} \quad (8.5)$$

These equations involve both a scalar factor and an exponential factor for each stress component.

The relationship of structural anisotropy for the planes of motion for triaxial confinement show much less of a variance than the comparable Eqs. 7.4 and 7.5 for biaxial confinement. The equations do involve positive and negative slopes interrelating the planes of motion.

Although the sum of the slopes of the stress components in equations 8.4 and 8.5 ranges from -0.01 to -0.03, the scalar factor varies by about 20 percent. This indicates that the degree of structural anisotropy dominates the scalar factor, while having much less significance on  $V_s$  within the slopes of the principal stress components. Despite the fact that it is evident that  $V_s$  varies with the planes of motion, it can be seen that the relationship on  $V_s$  of each principal stress component is not altered by the structural anisotropy. Hence, the domination of  $V_s$  by the directions of wave propagation and particle motion and the insignificance on  $V_s$  of the out-of-plane direction is not changed by the structural anisotropy of the sample. Although the degree of structural anisotropy affects the values of  $C_1$ ,  $m_a$ ,  $m_b$ , and  $m_c$  in Eq. 8.2, the critical relationships between  $V_s$  and the principal stress components is not affected.

#### 8.5 TESTING WITH A CONSTANT MEAN EFFECTIVE PRINCIPAL STRESS

One triaxial series was conducted in which the mean effective principal stress remained constant. This test was designed as a supplement to the biaxial confinement data to:

1. study the variation of  $V_s$  under a constant mean effective principal stress with varying shearing stress components, and
2. provide further  $V_s$  measurements to verify the validity of the expressions developed to predict shear wave velocity.

The series began at an isotropic confining pressure of 20 psi (137.8 kPa). The vertical principal stress,  $\bar{\sigma}_1$ , was then increased in 2-psi (13.8 kPa) increments (except for a final 6-psi (41.4 kPa) increment) while simultaneously the horizontal stresses,  $\bar{\sigma}_2$  and/or  $\bar{\sigma}_3$  were varied in 2-psi (13.8 kPa) increments. This variation of the principal stresses kept  $\bar{\sigma}_0$  constant while the level of shearing stresses (measured by the coefficients  $K_{13}$  and  $K_{23}$ ) was varied. The variation of stresses continued until a biaxial state of stress was reached ( $\bar{\sigma}_1 = 36$  psi (248 kPa),  $\bar{\sigma}_3 = 12$  psi (82.7 kPa)), with a value of  $K_{13}$  of 3.0. An unloading pressure sequence was performed using larger increments of pressure change until values of  $K_{13}$  of 2.08 and  $K_{23}$  of 1.92 were reached. This triaxial series consisted of tests 13 through 23 from Table B.1, which can be seen on Fig. B.1 between the dates of July 23 and August 5, 1981. The principal stress ratios varied for this series from 1 to 3.0 for  $K_{13}$  and from 1 to 1.92 for  $K_{23}$ .

#### 8.5.1 Effect of Shearing Stress with Constant $\bar{\sigma}_0$

Examination of the effect on shear wave velocity of shearing stress for a constant mean effective principal stress was first performed by investigating the variation of  $V_s$  with  $K_{13}$  and  $K_{23}$ . These results are presented in Figs. 8.9 through 8.14 for each of the six types of shear waves generated in the three planes of motion. The top half of each figure shows shear wave velocity data for each test pressure plotted against the logarithm

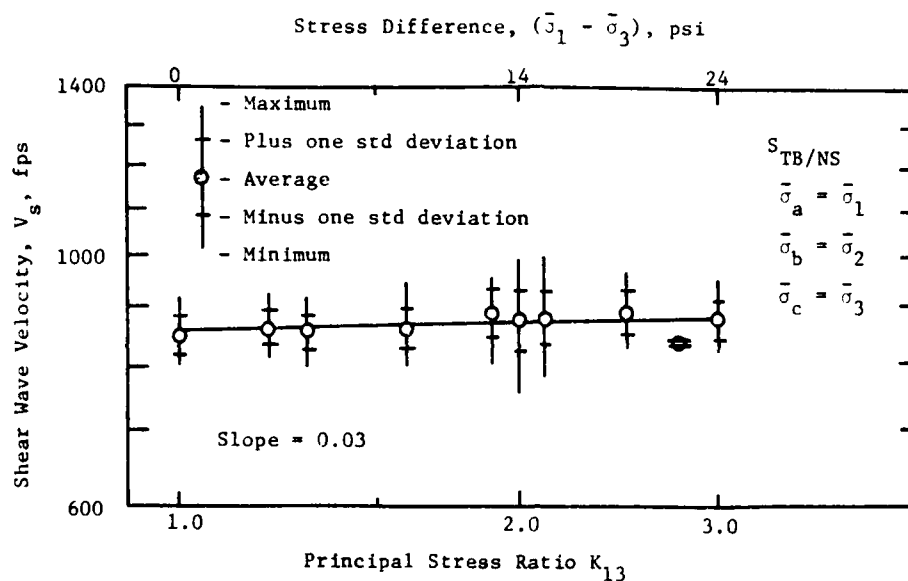
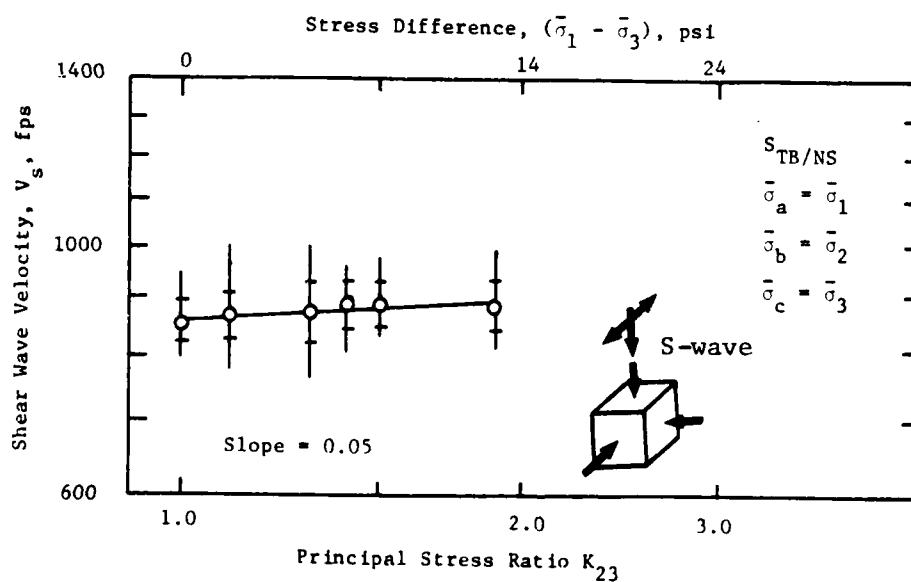
a) Variation in  $V_s$  with  $K_{13}$ b) Variation in  $V_s$  with  $K_{23}$ 

Fig. 8.9 - Variation of Shear Wave Velocity with Principal Stress Ratios  $K_{13}$  and  $K_{23}$  for  $S_{TB/NS}$ -Wave for Triaxial Confinement with a Constant  $\bar{\sigma}_o$

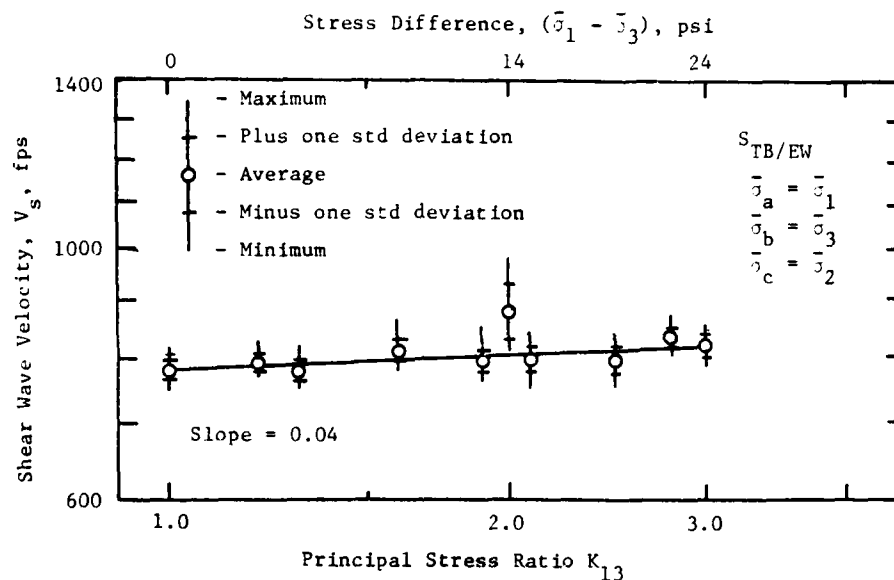
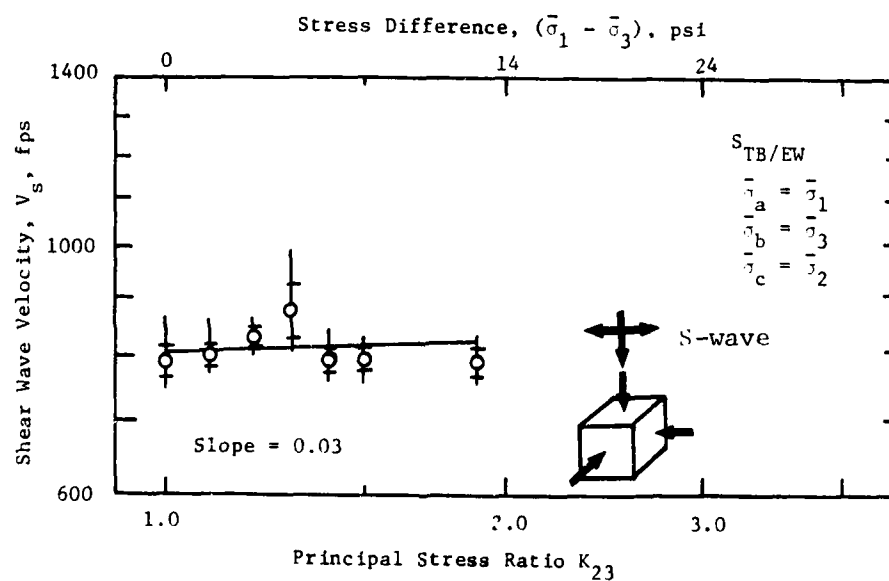
a) Variation in  $V_s$  with  $K_{13}$ b) Variation in  $V_s$  with  $K_{23}$ 

Fig. 8.10 - Variation in Shear Wave Velocity with Principal Stress Ratios  $K_{13}$  and  $K_{23}$  for  $S_{TB/EW}$ -Wave for Triaxial Confinement with a Constant  $\bar{\sigma}_o$

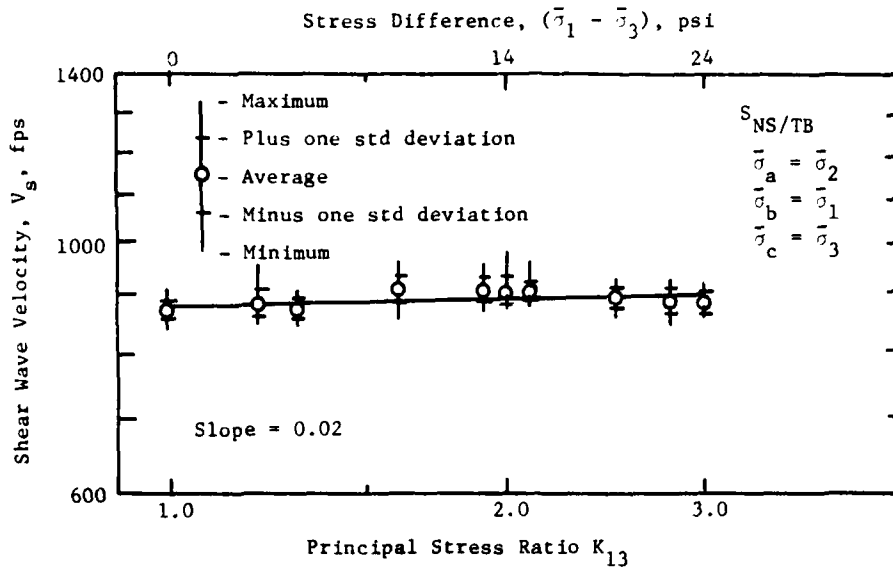
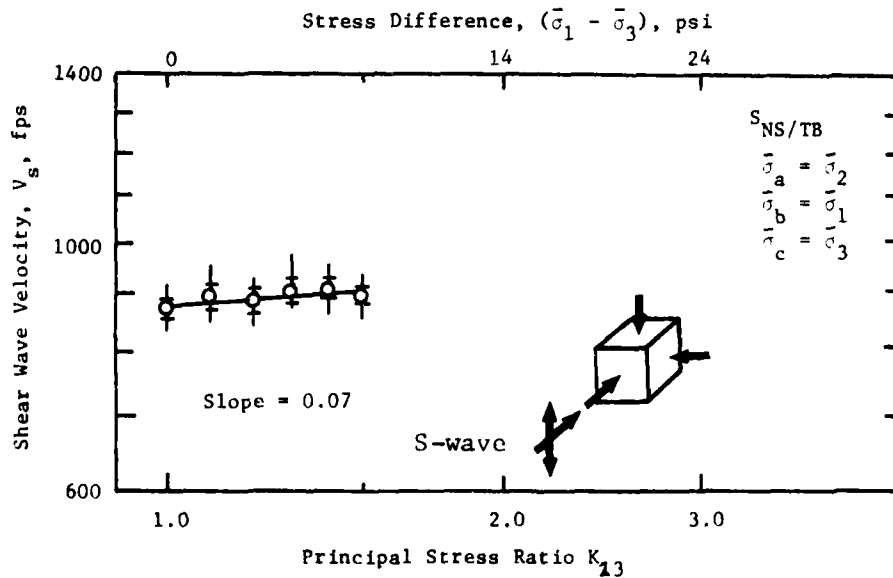
a) Variation in  $V_s$  with  $K_{13}$ b) Variation in  $V_s$  with  $K_{23}$ 

Fig. 8.11 - Variation of Shear Wave Velocity with Principal Stress Ratios  $K_{13}$  and  $K_{23}$  for  $S_{NS/TB}$ -Wave for Triaxial Confinement with a constant  $\bar{\sigma}_0$

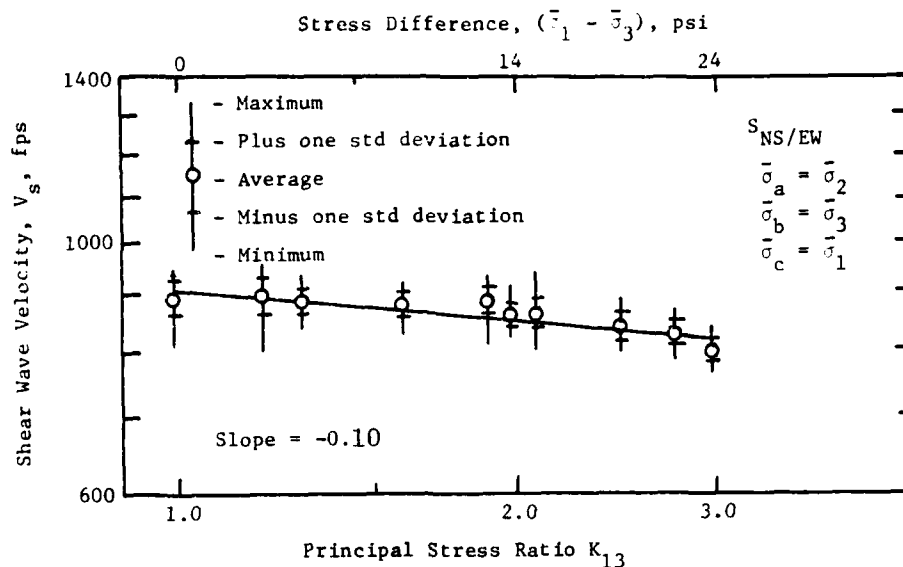
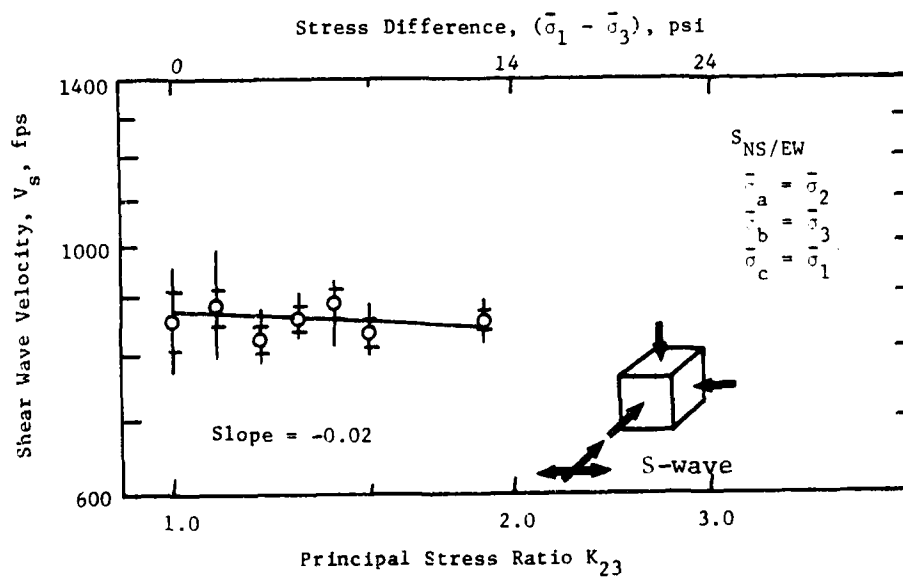
a) Variation in  $V_s$  with  $K_{13}$ b) Variation in  $V_s$  with  $K_{23}$ 

Fig. 8.12 - Variation of Shear Wave Velocity with Principal Stress Ratios  $K_{13}$  and  $K_{23}$  for  $S_{NS/EW}$ -Wave for Triaxial Confinement with a constant  $\bar{\sigma}_0$



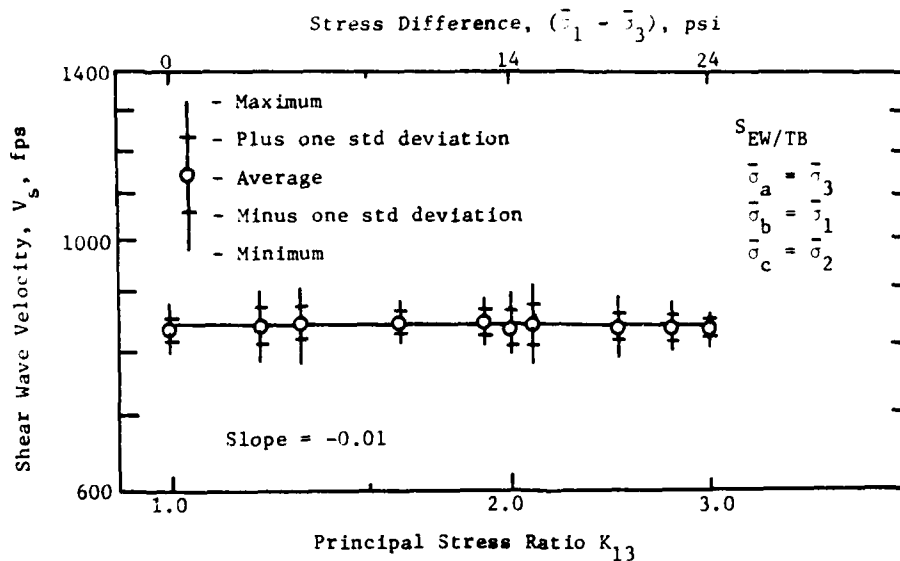
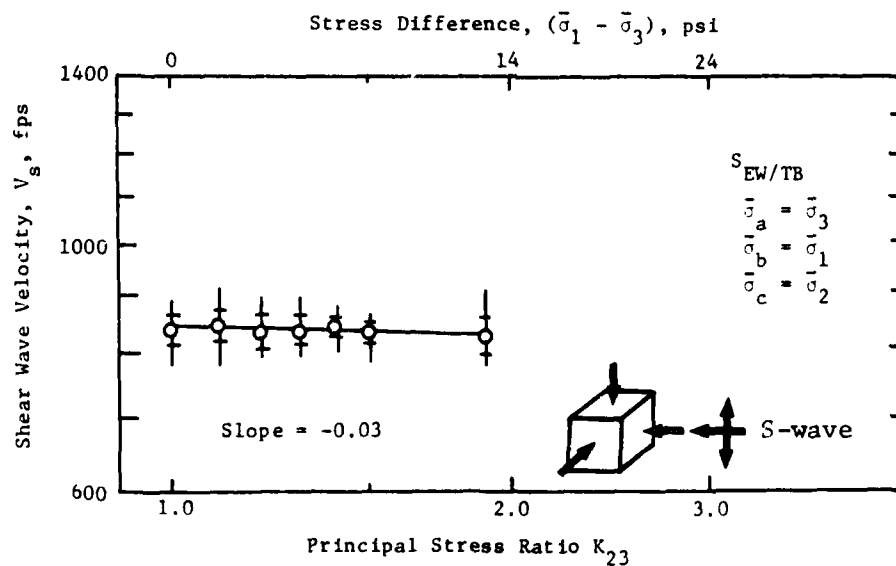
a) Variation of  $V_s$  with  $K_{13}$ b) Variation of  $V_s$  with  $K_{23}$ 

Fig. 8.13 - Variation of Shear Wave Velocity with Principal Stress Ratios  $K_{13}$  and  $K_{23}$  for  $S_{EW/TB}$ -Wave for Triaxial Confinement with a constant  $\bar{\sigma}_o$

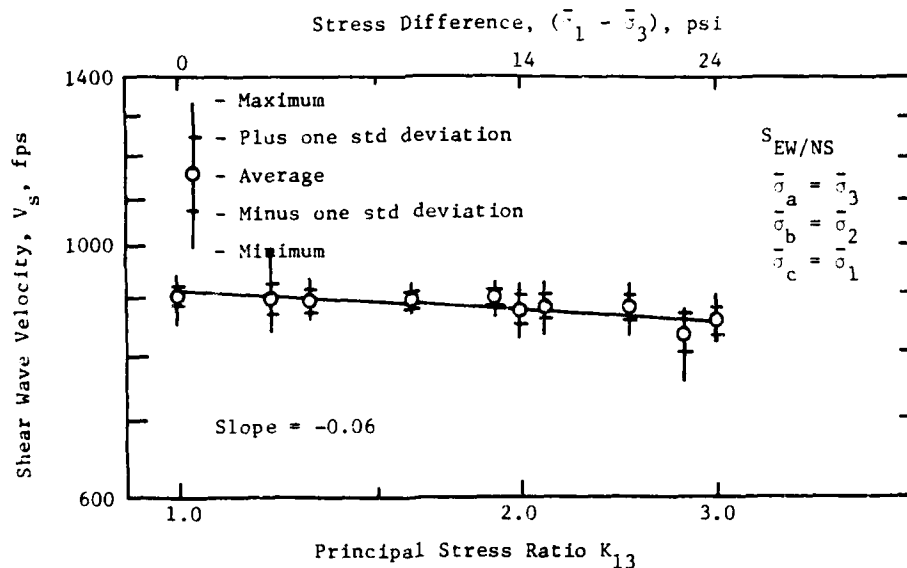
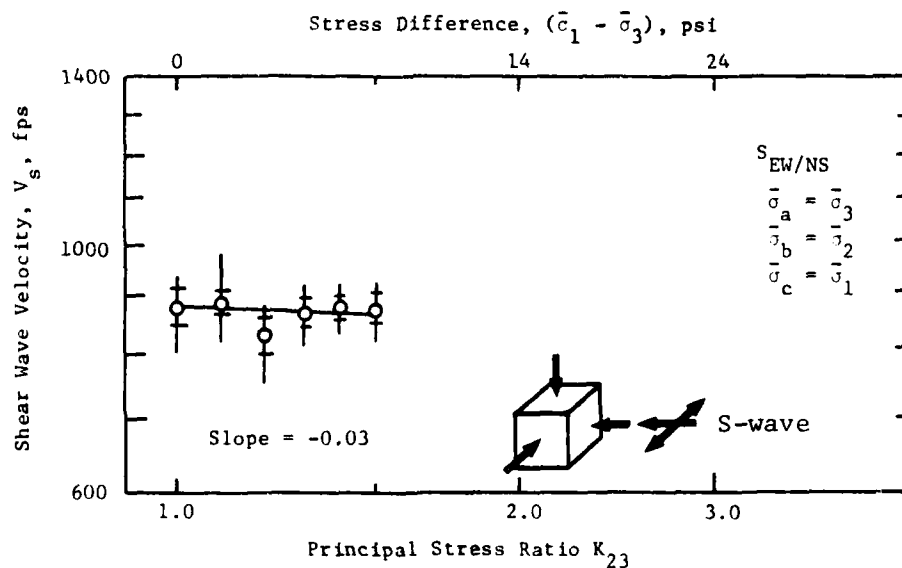
a) Variation in  $V_s$  with  $K_{13}$ b) Variation in  $V_s$  with  $K_{23}$ 

Fig. 8.14 - Variation of Shear Wave Velocity with Principal Stress Ratios  $K_{13}$  and  $K_{23}$  for  $S_{EW/NS}$ -Wave for Triaxial Confinement at a Constant  $\bar{\sigma}_0$

of  $K_{13}$  and the bottom half of each figure shows the same shear wave velocity data plotted against the logarithm of  $K_{23}$ . The principal stress ratio was used as the horizontal axis for these figures in place of  $\bar{\sigma}_0$  as is the usual method. This was done because testing was performed at only one value of  $\bar{\sigma}_0$ . A least-squares fit was performed to determine the slope of the data, and a summarization of the results is given in Table 8.9. It should be noted that the calculated slopes are not the same as  $m_a$ ,  $m_b$ , or  $m_c$  since the horizontal axes are in terms of  $K$ 's and not  $\sigma$ 's.

Based upon Table 8.9,  $V_s$  appears to be only slightly sensitive to the level of shearing stress at a constant  $\bar{\sigma}_0$  for either the TB-NS or TB-EW planes of motion. The slopes of the  $\log V_s - \log K_{13}$  relationships ranged from -0.01 to 0.04, with an average value of 0.02. This range of slope produced a change in  $V_s$  of up to 4.8 percent over the test range. However, if  $V_s$  only depended on  $\bar{\sigma}_0$ , then all of the slopes should have been zero.

The variation of the slopes of the  $\log V_s - \log K_{13}$  relationship for the TB-NS and TB-EW planes under triaxial confinement is similar to the variation of the slopes for the same relationship determined for biaxial confinement (Table 7.9). Therefore, the state of stress in terms of a biaxial or triaxial state of stress was not important for this relationship. Also, as with biaxial confinement, the least consistent trends in  $V_s$  for triaxial confinement occurred for the TB-EW plane of motion. It is unclear if this is due to experimental scatter and coincidence or

TABLE 8.9

Variation of Shear Wave Velocity with Shearing Stress for Tests Performed with a Constant  $\bar{\sigma}_o$  for Triaxial Confinement

Plane of Motion	Shear Wave Type*	Slope**		V ***		Percent Change in V ***	
		K <sub>13</sub>	K <sub>23</sub>	K <sub>13</sub> fps	K <sub>23</sub> fps	K <sub>13</sub> %	K <sub>23</sub> %
(1)	(2)	(3)	(4)	(5)	(6)	(7)	(8)
TB-NS	TB/NS	0.03	0.05	24	27	2.8	3.1
	NS/TB	0.02	0.07	17	25	1.9	2.8
TB-EW	TB/EW	0.04	0.03	38	18	4.8	2.2
	EW/TB	-0.01	-0.03	-9	17	-1.0	2.0
NS-EW	NS/EW	-0.10	-0.02	-90	-13	-9.8	-1.5
	EW/NS	-0.06	-0.03	-59	-11	-6.4	-1.2

\* The first two letters denote the direction of wave propagation, and the second two letters denote the direction of particle motion.

\*\* Slope of the  $\log V_s - \log K_{13}$  or  $\log V_s - \log K_{23}$  relationship.

\*\*\*  $V_s$  at  $K_{13} = 1.0$  minus  $V_s$  at  $K_{13} = 3.0$  or  $V_s$  at  $K_{23} = 1.0$  minus  $V_s$  at  $K_{23} = 1.90$

\*\*\*\*  $\frac{V_{K_{13}=1.0} - V_{K_{13}=3.0}}{V_{K_{13}=1.0}} \times 100\%$  or  $\frac{V_{K_{23}=1.0} - V_{K_{23}=1.9}}{V_{K_{23}=1.0}} \times 100\%$

if there is some reason connected with testing which would cause this variation in  $V_s$ .

The remaining plane of motion, the NS-EW plane, exhibited a more pronounced variation in  $\log V_s - \log K_{13}$  relationship. Slopes ranged from -0.06 to -0.10 with an average value of -0.08 resulting in a change in  $V_s$  of almost ten percent over the testing range employed. Again, this range of slope for the  $K_{13}$  relationship is similar to the range obtained for biaxial confinement.

In examining the variation of  $V_s$  with  $K_{13}$ , the trend of change in the stress components for the triaxial state of stress is similar to that for biaxial confinement. For instance, for triaxial confinement with a constant  $\bar{\sigma}_0$ , when  $\bar{\sigma}_1$  in the vertical direction was increased,  $\bar{\sigma}_2$  and/or  $\bar{\sigma}_3$  along the sides of the cube decreased accordingly. In general, as  $\bar{\sigma}_1$  increased,  $\bar{\sigma}_2$  and  $\bar{\sigma}_3$  tended to decrease. Since it has been determined for this study that  $V_s$  is about equally a function of the effective principal stress in the directions of wave propagation and particle motion and is not affected by the stress in the out-of-plane direction, it is logical to study the variation of  $V_s$  with  $\bar{\sigma}_a$  and  $\bar{\sigma}_b$ , instead of  $K_{13}$ ,  $K_{23}$ , or  $\bar{\sigma}_0$ .

For both the TB-NS and TB-EW planes of motion,  $\bar{\sigma}_a$  and  $\bar{\sigma}_b$  varied in opposite directions. Hence, as the increasing stress components increased  $V_s$ , the other decreasing stress component reduced  $V_s$ . Typically,  $\bar{\sigma}_1$  was increased by two times the amount that  $\bar{\sigma}_3$  was decreased so that  $\bar{\sigma}_0$  remained constant. The net effect

was an increase in the sum of the stress components on the TB-NS and TB-EW planes. This should cause a positive slope in the  $\log V_s - \log K_{13}$  relationship, indicative of an increase in  $V_s$  due to the net increase in stress. This positive slope is shown in Table 8.9 for the TB-NS and TB-EW planes of motion.

However, for the NS-EW plane, both horizontal stresses tended to decrease and so that  $\bar{\sigma}_a$  and  $\bar{\sigma}_b$  tended to decrease, thereby lowering the value of  $V_s$ . The increase in the vertical  $\bar{\sigma}_1$  to keep  $\bar{\sigma}_o$  a constant should have no effect on  $V_s$  since the vertical direction involved  $\bar{\sigma}_c$  for the NS-EW plane. The net effect of the decrease of both  $\bar{\sigma}_a$  and  $\bar{\sigma}_b$  would be a significant negative slope for the  $\log V_s - \log K_{13}$  relationship for the NS-EW plane of motion as shown in Table 8.9.

Since the change in  $V_s$  could be explained by the variation in  $\bar{\sigma}_a$  and  $\bar{\sigma}_b$  (rather than by the variance of  $\bar{\sigma}_o$  or the shearing stress), the next logical step was to analyze  $V_s$  in relation to these two stress components. This comparison between  $V_s$  and  $\bar{\sigma}_a$  and  $\bar{\sigma}_b$  was made based on the assumptions that: 1.  $\bar{\sigma}_a$  and  $\bar{\sigma}_b$  equally effected  $V_s$ , and 2.  $\bar{\sigma}_c$  had no effect on  $V_s$ . As with the case of biaxial confinement,  $\frac{1}{2}(\bar{\sigma}_a + \bar{\sigma}_b)$  was chosen to replace  $K_{13}$  on the horizontal axis, with this new term representing the influence on  $V_s$  of the state of stress.

Figures 8.15, 8.16, and 8.17 show the  $\log V_s - \log \frac{1}{2}(\bar{\sigma}_a + \bar{\sigma}_b)$  relationship for the TB-NS, TB-EW, and NS-EW planes of motion, respectively. Each figure shows the variation of  $V_s$  for the two

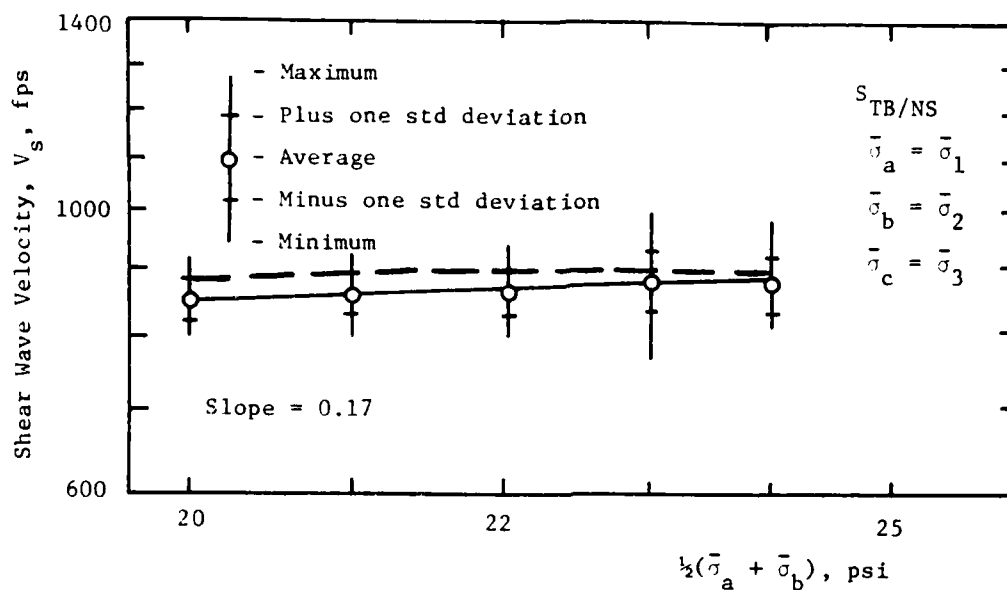
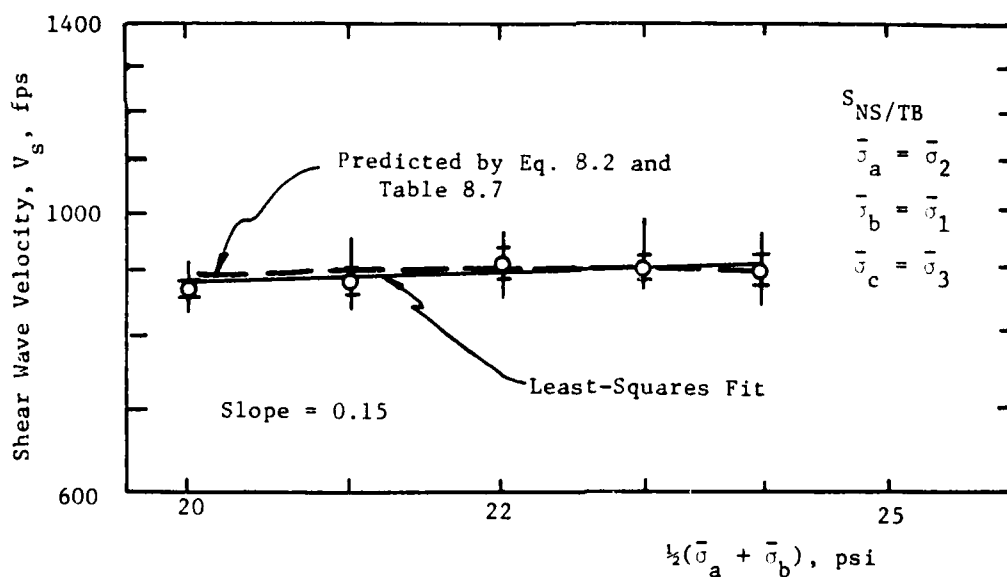
a) For the  $S_{TB/NS}$ -Waveb) For the  $S_{NS/TB}$ -Wave

Fig. 8.15 - Variation of Shear Wave Velocity with Directions of Wave Propagation and Particle Motion for TB-NS Plane of Motion for Triaxial Confinement with a Constant  $\bar{\sigma}_0$

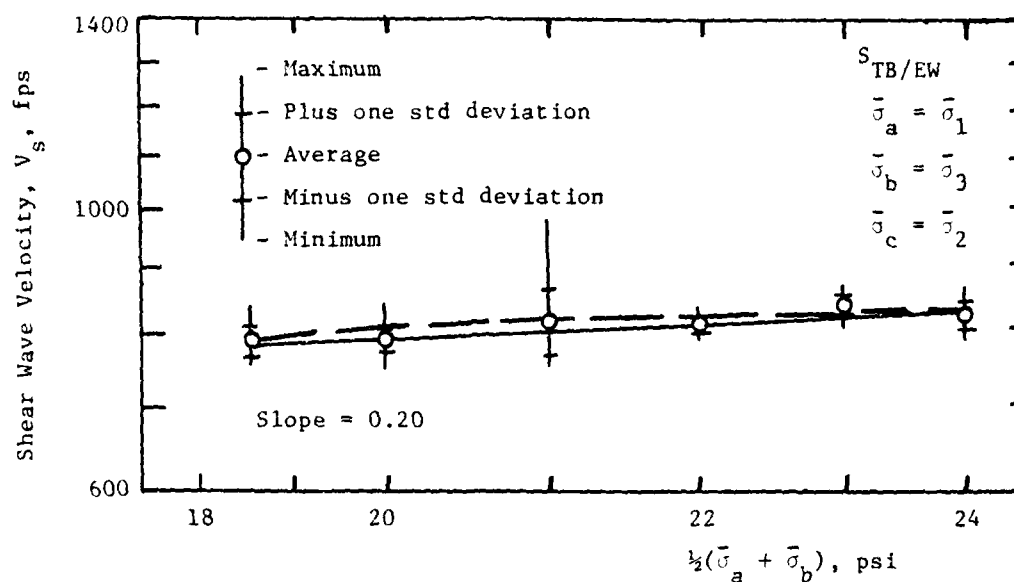
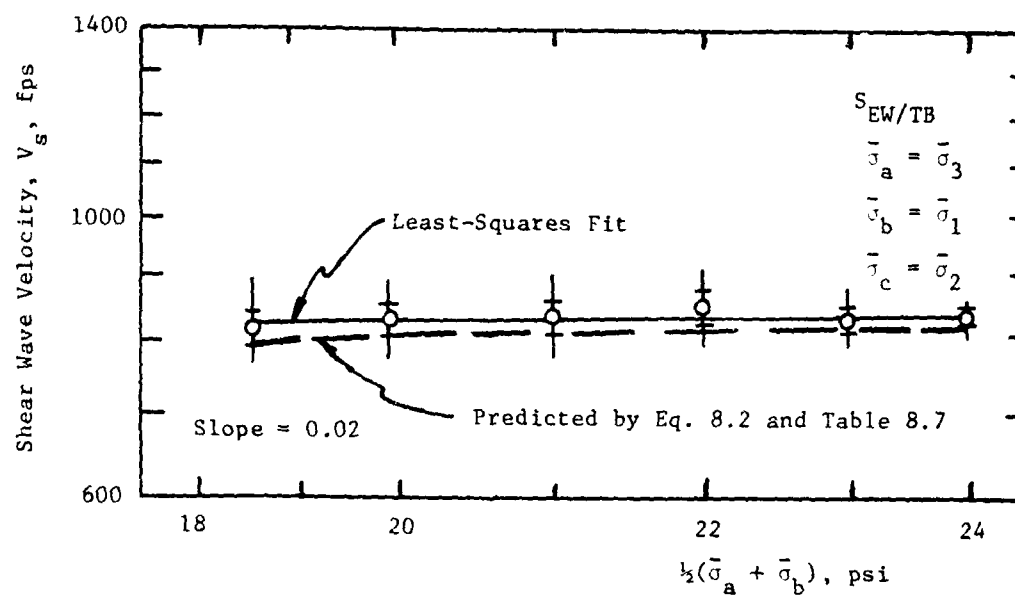
a) For the  $S_{TB/EW}$ -Waveb) For the  $S_{EW/TB}$ -Wave

Fig. 8.16 - Variation of Shear Wave Velocity with Directions of Wave Propagation and Particle Motion for TB-EW Plane of Motion for Triaxial Confinement with a Constant  $\bar{\sigma}_c$



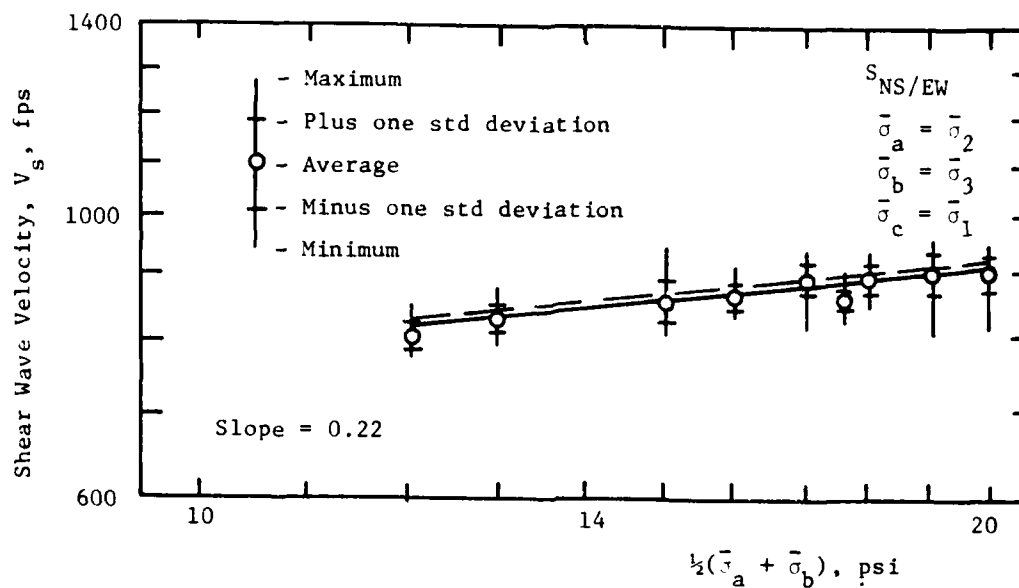
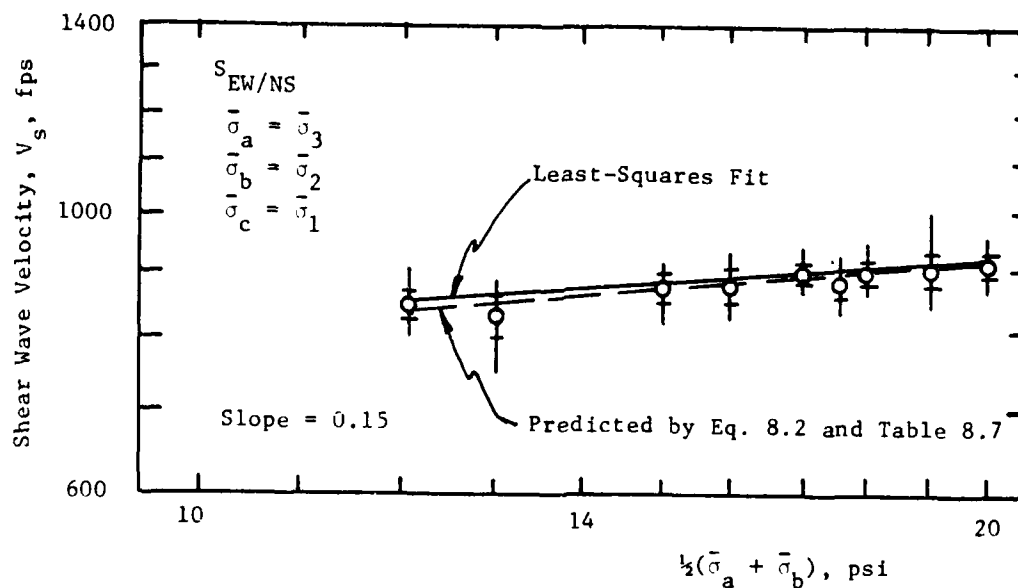
a) For the  $S_{NS/EW}$ -Waveb) For the  $S_{EW/NS}$ -Wave

Fig. 8.17 - Variation of Shear Wave Velocity with Directions of Wave Propagation and Particle Motion for NS-EW Plane of Motion for Triaxial Confinement with a Constant  $\bar{\sigma}_0$

shear wave types defined by each plane. A least-squares fit was performed on the shear wave velocity data at each test pressure and is shown in each figure by the solid line. The results of the least-squares fit are summarized in Table 8.10. In addition, the predicted shear wave velocity (based on Eq. 8.2 and the values in Table 8.7) is included in these figures as a dashed line and the slopes of the  $\log V_s - \log \frac{1}{2}(\bar{\sigma}_a + \bar{\sigma}_b)$  relationships for these lines are also included in Table 8.10.

The results presented in Table 8.10 must be examined with careful attention paid to the change in  $\bar{\sigma}_a$  and  $\bar{\sigma}_b$  for each plane of motion. The general patterns of principal stress variation were:

1. for the TB-NS plane, the vertical major principal stress was increased about two times as much as the intermediate stress along the north-south axis was decreased;
2. for the TB-EW plane, the vertical major principal stress was increased less than two times as much as the minor stress was decreased along the east-west axis;
- and 3. for the NS-EW plane, the minor principal stress along the east-west axis was decreased slightly more than the intermediate principal stress along the north-south axis was decreased. Because of the constant  $\bar{\sigma}_o$ , incremental pressure changes were twice as large for the TB-NS and TB-EW planes of motion as for the EW-NS plane. The net result of these pressure increments should be a 2:1.5:2 ratio for the slopes of the  $\log V_s - \log \frac{1}{2}(\bar{\sigma}_a + \bar{\sigma}_b)$  relationship for the TB-NS:TB-EW:NS-EW planes (given that  $\bar{\sigma}_a$  and  $\bar{\sigma}_b$  control  $V_s$ ). It does not matter whether  $\bar{\sigma}_a$  or  $\bar{\sigma}_b$  are oriented along the

TABLE 8.10

Variation of  $V_s$  with Principal Stresses in Directions of Wave Propagation<sup>s</sup> and Particle Motion for Triaxial Confinement

Plane of Motion	Shear Wave Type*	Slope of $\log V_s - \log \frac{1}{2}(\bar{\sigma}_a + \bar{\sigma}_b)$ Relationship	Average Slope for Each Plane of Motion
(1)	(2)	(3)	(4)
TB-NS	TB/NS	0.17	0.16
	NS/TB	0.15	
TB-EW	TB/EW	0.20	0.11
	EW/TB	0.02	
NS-EW**	NS/EW	(-)0.22	(-)0.18
	EW/NS	(-)0.15	

\* The first two letters denote the direction of wave propagation, and the second two letters denote the direction of particle motion.

\*\* For this test series,  $\frac{1}{2}(\bar{\sigma}_a + \bar{\sigma}_b)$  decreased.

changing principal stress axis since it was assumed that both of these stress components have equal importance on  $V_s$ .

This 2:1.5:2 ratio relating the slopes of the three planes of motion can be seen in column 4 in Table 8.10. It must be noted that the slopes of the shear waves in the TB-EW plane have significantly different slopes, although the average of the slopes is reasonable. This large difference in slopes for the TB-EW plane was also found for biaxial confinement (see Section 7.5.1). There is no obvious reason for the difference in slopes, although possible explanations include experimental scatter, principal stress variations at the loading membrane along the east-west axis or structural anisotropy. Therefore, the conclusion can be made that  $V_s$  is controlled by the effective principal stress in the direction of wave propagation and particle motion and not by the mean effective principal stress. Further,  $V_s$  is not independent of shearing stress to the extent that the shearing stress affects the values of  $\bar{\sigma}_a$  and  $\bar{\sigma}_b$ .

#### 8.5.2 Comparison Between Measured and Predicted Shear Wave Velocities

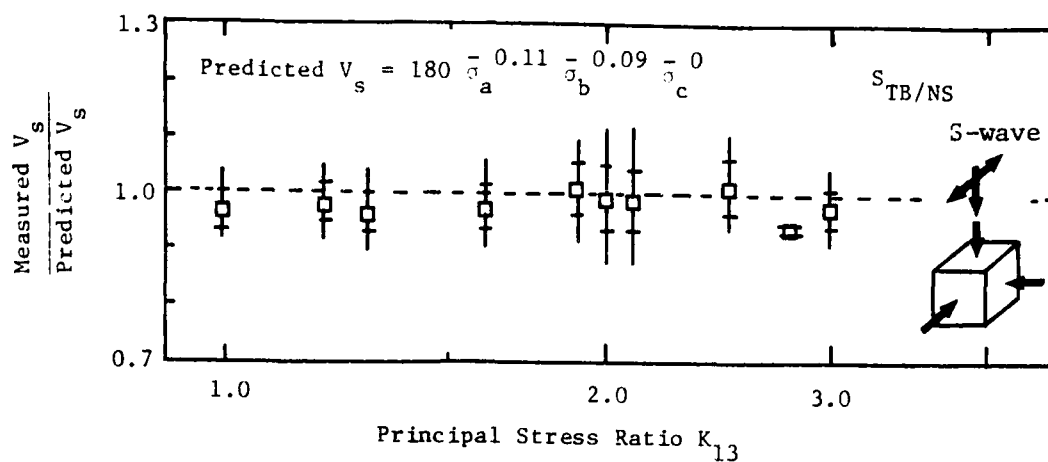
To further check the validity and accuracy of the expressions for shear wave velocity developed in Section 8.3.5, measured values of  $V_s$  for the triaxial series of tests with a constant  $\bar{\sigma}_o$  were compared to values predicted from Eq. 8.3 using the values presented in Table 8.7. This comparison was made for each of the six different types of shear waves. A ratio of the

measured value of  $V_s$  to the predicted  $V_s$  versus the log of  $K_{13}$  was determined for all the tests.

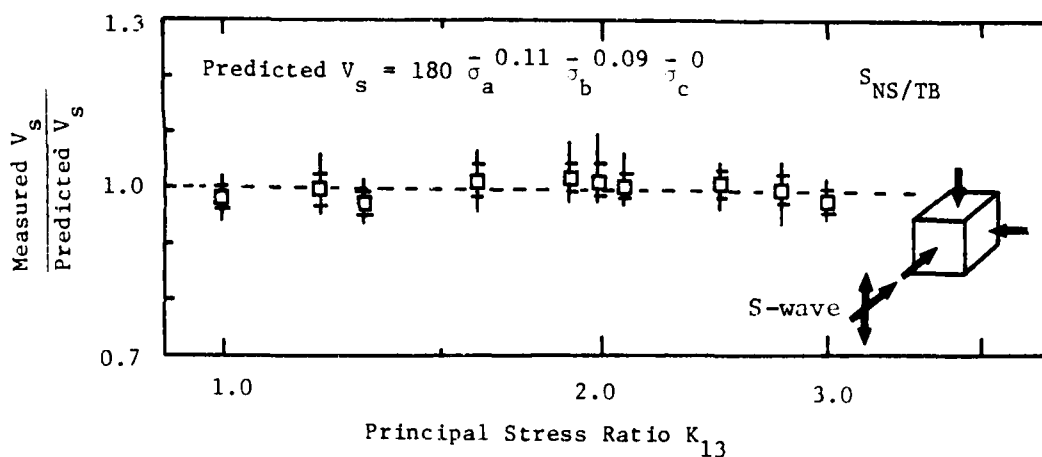
The results of these comparisons are shown in Figs. 8.18, 8.19, and 8.20. Based on these figures, the ratio of measured to predicted  $V_s$  for  $\pm$  one standard deviation typically ranges from 0.92 to 1.08 with one value as high as 1.12. This uniform scatter about one indicates that the equations developed in Section 8.3.5 to predict  $V_s$  for body waves are generally within ten percent for each of the shear wave types. This correlation of measured to predicted values of  $V_s$  means that shear wave velocity is not controlled by the level of hydrostatic stress (as previously assumed; Hardin and Black, 1966; Lawrence, 1965; Schmertmann, 1978) but by the effective principal stress in the directions of wave propagation and particle motion. It is the variation of these two stress components that largely affect the change in  $V_s$ .

## 8.6 SUMMARY AND CONCLUSIONS

The condition of triaxial confinement was obtained by applying the major principal stress,  $\bar{\sigma}_1$ , the intermediate principal stress,  $\bar{\sigma}_2$ , and the minor principal stress,  $\bar{\sigma}_3$ , along the three axes of the cube. Because the principal stresses were all different, the stresses had to be described relative to the motions associated with each shear wave. The stress components were referred to as  $\bar{\sigma}_a$ ,  $\bar{\sigma}_b$ , and  $\bar{\sigma}_c$ , continuing with the same notation used for biaxial confinement. In addition, the notation used for the principal

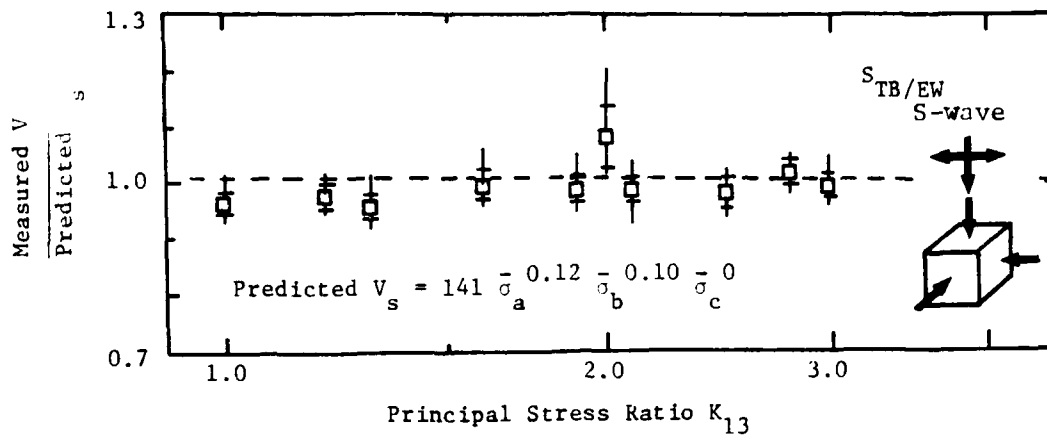


a) Ratio of Shear Wave Velocities for the  $S_{TB/NS}$ -Wave

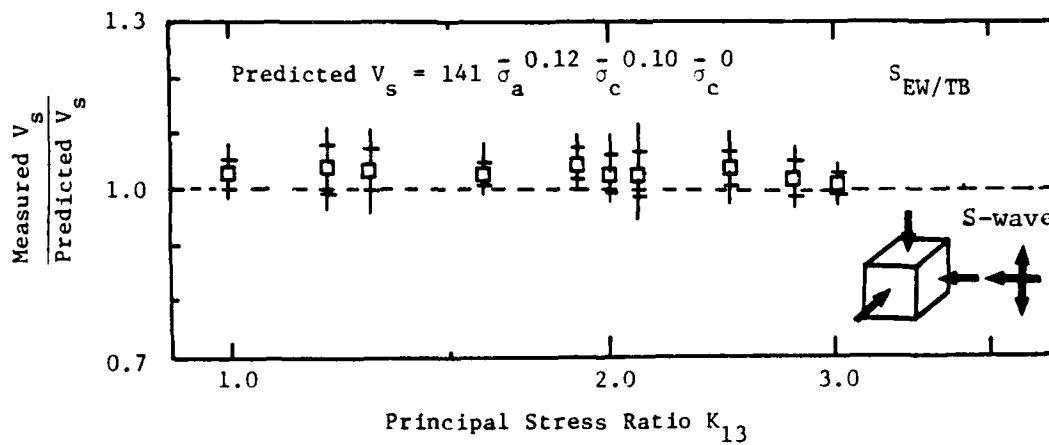


b) Ratio of Shear Wave Velocities for the  $S_{NS/TB}$ -Wave

Fig. 8.18 - Comparison of Measured and Predicted Shear Wave Velocity for TB-NS Plane of Motion for Triaxial Confinement with a Constant  $\bar{\sigma}_0$

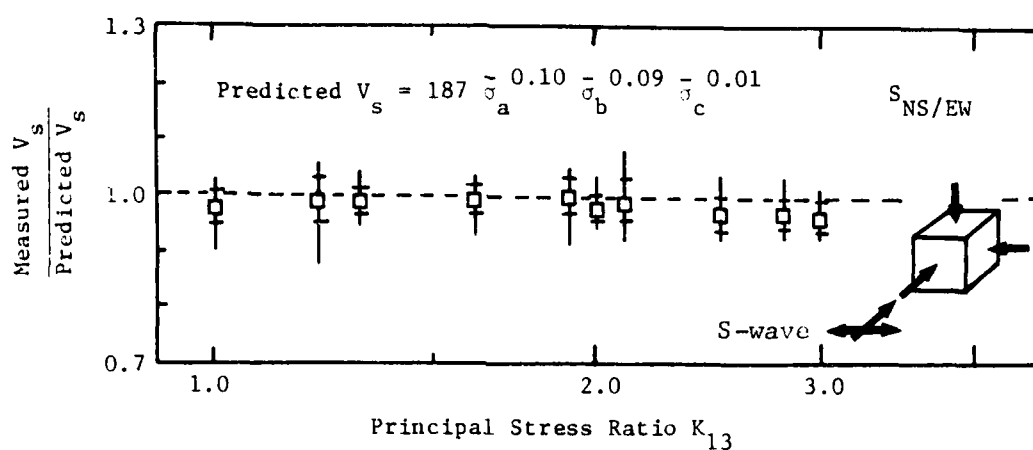


a) Ratio of Shear Wave Velocities for the  $S_{TB/EW}$ -Wave

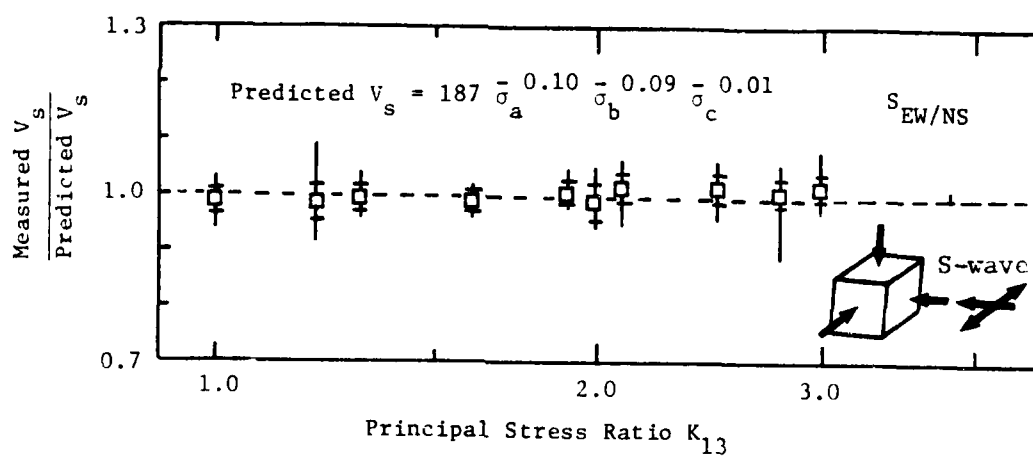


b) Ratio of Shear Wave Velocities for the  $S_{EW/TB}$ -Wave

Fig. 8.19 - Comparison of Measured and Predicted Shear Wave Velocities for TB-EW Plane of Motion for Triaxial Confinement with a Constant  $\bar{\sigma}_0$



a) Ratio of Shear Wave Velocities for the  $S_{NS/EW}$ -Wave



b) Ratio of Shear Wave Velocities for the  $S_{EW/NS}$ -Wave

Fig. 8.20 - Comparison of Measured and Predicted Shear Wave Velocities for NS-EW Plane of Motion for Triaxial Confinement with a Constant  $\bar{\sigma}_o$



stress ratio,  $K$ , was expanded to describe the ratio of  $\bar{\sigma}_1$  to  $\bar{\sigma}_3$  and  $\bar{\sigma}_2$  to  $\bar{\sigma}_3$ , denoted as  $K_{13}$  and  $K_{23}$ , respectively.

Two patterns of variation of stress were used in the triaxial confinement series. Tests were performed with a variable mean effective principal stress to examine the effect on  $V_s$  of the individual stress components and to study structural anisotropy. Tests were also performed with a constant mean effective principal stress to evaluate the effect on  $V_s$  of shearing stress at a constant  $\bar{\sigma}_o$  and to further examine the variation of  $V_s$  with the stress components.

For those tests performed with a variable mean effective principal stress, stresses varied from 15 to 40 psi (103.4 to 275.6 kPa) for a range in  $K_{13}$  of 1.0 to 2.67. Only one of the stress components was varied at a time so that the individual effects on  $V_s$  of the stress components could be studied. From these tests, it was found that  $\bar{\sigma}_a$  and  $\bar{\sigma}_b$  are the dominant stress components. Each of these two components were equally important in the prediction of  $V_s$  by Eq. 8.3. Values of the slope of the  $\log V_s - \log \bar{\sigma}_a$  relationship ranged from 0.10 to 0.12, and values of the slope for the  $\log V_s - \log \bar{\sigma}_b$  relationship ranged from 0.08 to 0.11, with the values of the slopes dependent on the particular plane of motion. The remaining stress component,  $\bar{\sigma}_c$ , was found to have very little effect on  $V_s$ , with the value of the slope of the  $\log V_s - \log \bar{\sigma}_c$  relationship ranging from -0.01 to 0.04. As a result,

triaxial confinement results yielded similar results to biaxial confinement for the effect on  $V_s$  of the stress components.

Stress history had no significant effect on  $V_s$  or the stress component relationships. Loading and unloading data exhibited slightly different values of the factors in Table 8.5, but there was no trend in the variation, and it was assumed to be due to experimental scatter. Stress history could be ignored for this study since it had no effect for either biaxial or triaxial confinement.

In an effort to predict shear modulus, Eq. 8.4 was re-evaluated for triaxial confinement with the constants shown in Table 8.8. The sum of the exponents ( $na + nb + nc$ ) were again found to be slightly less than the value of  $n$  obtained by resonant column testing.

Measured and predicted shear wave velocities were compared for the tests with a variable  $\bar{\sigma}_0$ . It was determined that Eq. 8.2 and the results presented in Tables 8.5 and 8.7 yielded values of  $V_s$  within  $\pm 10$  percent for  $\pm$  one standard deviation from the average of the measured values of shear wave velocity.

Structural anisotropy was examined by the rotation of  $\bar{\sigma}_1$  and  $\bar{\sigma}_2$ . Shear waves exhibited an anisotropic nature, with wave velocity dependent on the particular plane of motion. The structural anisotropy relationship between the planes was similar for triaxial and biaxial confinements. It was concluded that for the shear waves within any particular plane of motion, the effect of structural

AD A120 426

EFFECT OF STATE OF STRESS ON VELOCITY OF LOW-AMPLITUDE  
SHEAR WAVES PROPAG. (U) TEXAS UNIV AT AUSTIN  
GEOTECHNICAL ENGINEERING CENTER D P KNOX ET AL. MAR 82

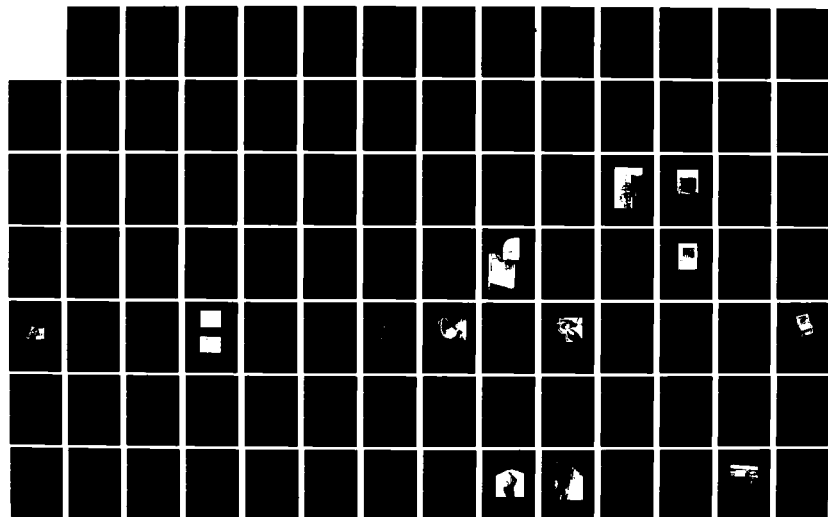
4/6

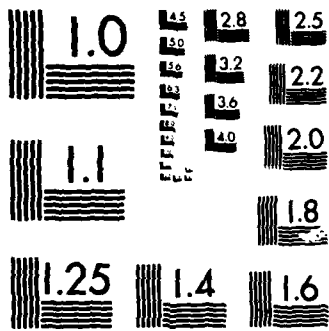
UNCLASSIFIED

GR82-23 AFOSR-TR-82-0908 AFOSR-80-0031

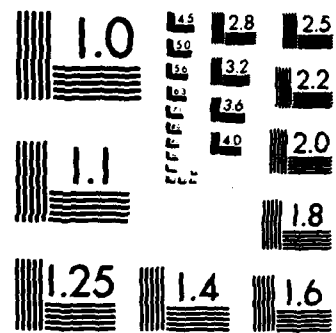
F/G 20/11

NL

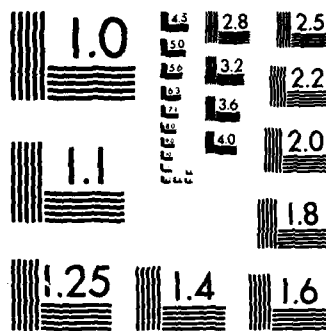




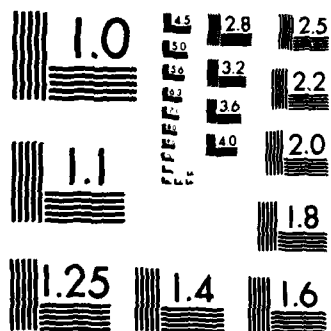
MICROCOPY RESOLUTION TEST CHART  
NATIONAL BUREAU OF STANDARDS-1963-A



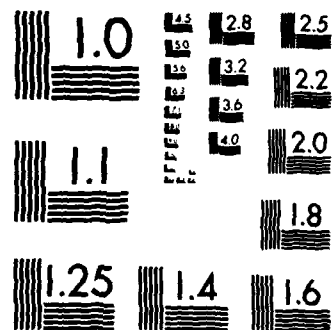
MICROCOPY RESOLUTION TEST CHART  
NATIONAL BUREAU OF STANDARDS-1963-A



MICROCOPY RESOLUTION TEST CHART  
NATIONAL BUREAU OF STANDARDS-1963-A



MICROCOPY RESOLUTION TEST CHART  
NATIONAL BUREAU OF STANDARDS-1963-A



MICROCOPY RESOLUTION TEST CHART  
NATIONAL BUREAU OF STANDARDS-1963-A

anisotropy could be ignored. Only when comparing results from different planes of motion were corrections for structural anisotropy required.

Tests were also performed with a constant  $\bar{\sigma}_o$  to evaluate the effect on  $V_s$  of shearing stress. Normal stresses varied from 12 to 36 psi (82.7 to 248 kPa) for a range in  $K_{13}$  of 1.0 to 3.0. It was found for shearing stress that shear wave velocity was dependent on the variation of the normal stress components in the directions of wave propagation,  $\bar{\sigma}_a$ , and particle motion,  $\bar{\sigma}_b$ . Hence, it is these two components which determine  $V_s$  rather than the more common  $\bar{\sigma}_o$ , which assumes equal dependency of  $V_s$  on  $\bar{\sigma}_a$ ,  $\bar{\sigma}_b$ , and  $\bar{\sigma}_c$  (the out-of-plane direction). It follows that  $V_s$  depends on shearing stress only when  $\bar{\sigma}_a$  or  $\bar{\sigma}_b$  are changed as a result of shearing stresses.

## CHAPTER NINE

## RE-EXAMINATION OF RESULTS FROM PREVIOUS EXPERIMENTS

## 9.1 INTRODUCTION

As the final step, shear wave velocity data was re-examined from previous studies in light of the conclusions drawn for this study. Hence, shear wave measurements from comparable experiments were examined to determine if  $V_s$  was, in fact, equally affected by the principal stresses in the directions of wave propagation ( $\bar{\sigma}_a$ ) and particle motion ( $\bar{\sigma}_b$ ), and was relatively independent of the principal stress in the out-of-plane direction ( $\bar{\sigma}_c$ ). Three experiments were found applicable for this analysis: Lawrence (1965), Hardin and Black (1966), and Roesler (1979). For each of these publications, sufficient shear wave velocity measurements and principal stress data were included to permit the analysis. These experiments were all conducted with dry sand under isotropic and biaxial states of stress.

Examination of the shear wave velocity data was principally directed at the relationship of  $V_s$  to  $\bar{\sigma}_a$  and  $\bar{\sigma}_b$ . The decision was made to compare measured values of  $V_s$  with  $\frac{1}{2}(\bar{\sigma}_a + \bar{\sigma}_b)$  because of the approximately equal dependence of  $V_s$  on these two stress components found for the sand used in this study. It should be noted, however, that this similarity of effect on  $V_s$  could depend on the method of

soil placement and construction as well as the type of soil being tested. The possible effect of soil type on the relative importance of  $\bar{\sigma}_a$  and  $\bar{\sigma}_b$  on  $V_s$  was minimized by reviewing experiments which had only used dry sand.

In this chapter, each of the three experiments used are briefly reviewed, and the results of the analysis of the  $\log V_s - \log \frac{1}{2}(\bar{\sigma}_a + \bar{\sigma}_b)$  relationship are presented.

## 9.2 REVIEW OF PREVIOUS EXPERIMENTS

Each of the experiments used in this analysis were first discussed in Chapter Two. However, brief summaries directed toward those aspects of the experiments which are pertinent to this analysis are presented herein.

Lawrence (1965) performed shear wave velocity measurements in dry sand using a modified triaxial cell with piezoelectric crystals as shear wave generators (see Sections 2.2.2 and 2.4.1). Lawrence performed a test series on the same sand sample which included five repetitive loading paths in which the cell pressure,  $\bar{\sigma}_3$ , was held constant (at a different pressure for each loading path) while the axial stress,  $\bar{\sigma}_1$ , was increased. For this method of stress variation, neither shearing stress or mean effective principal stress remained constant. Because vertically propagating waves were generated,  $\bar{\sigma}_1$  is synonymous with  $\bar{\sigma}_a$ , and  $\bar{\sigma}_3$  is synonymous with  $\bar{\sigma}_b$  and  $\bar{\sigma}_c$ .

Hardin and Black (1966) used resonant column testing to measure shear wave velocity in dry sand (see Sections 2.2.1 and 2.4.2). A loading path was followed which consisted of an initial loading sequence and a subsequent unloading and reloading sequence. During the source of these sequences, the sample was subjected to a variety of isotropic and biaxial states of stress in which the axial stress,  $\bar{\sigma}_1$ , and the cell pressure,  $\bar{\sigma}_3$ , were varied either one at a time (the remaining stress held constant) or in unison. Hence, the shearing stress and  $\bar{\sigma}_0$  could be independently controlled. All testing was performed with one sample of sand.

Data was presented by Hardin and Black in terms of shear modulus,  $G$ , rather than shear wave velocity. The conversion was made from  $G$  to  $V_s$  using Eq. 7.4 along with a calculated value for sand density of 111 pcf ( $1796 \text{ kg/m}^3$ ). This density was determined for a void ratio of 0.52 and an assumed water content of one percent.

Roesler (1979) conducted shear wave velocity measurements with a torsional shear wave exciter embedded in a small cube of sand (see Sections 2.2.4 and 2.4.7). The sand sample could be subjected to a cell pressure ( $\bar{\sigma}_3$ ) and an additional axial load ( $\bar{\sigma}_1$ ) which, by rotation of the sample, could be applied along any principal axis of the cube. This ability to rotate  $\bar{\sigma}_1$  allowed Roesler to conduct three sets of tests, with each set having the axial load varying along one particular principal axis while  $\bar{\sigma}_3$  remained constant. Hence, any one of the stress components could be varied while the other two remained constant. Since no mention was made, it was



assumed that one sand sample was used for the sets of tests in which  $\bar{\sigma}_a$  and  $\bar{\sigma}_b$  varied. Two sand samples were used for the test set in which  $\bar{\sigma}_c$  was varied.

### 9.3 SUMMARY OF EFFECT OF STRESS COMPONENTS ON $V_s$

Analysis was first performed for the relationship of  $V_s$  with the individual stress components by examining the change in  $V_s$  as only one of the stress components was varied. Lawrence (1965) performed tests in which only  $\bar{\sigma}_a$  was varied. Hardin and Black (1966) performed four series of tests in which only  $\bar{\sigma}_a$  was varied and two series of tests in which both  $\bar{\sigma}_b$  and  $\bar{\sigma}_c$  were varied simultaneously (cell pressure changed). Roesler performed tests in which each stress component was individually varied. A least-squares fit was performed to determine the slope of the  $\log V_s - \log \bar{\sigma}$  relationship for each varying stress component, and the results are summarized in Table 9.1.

Based on Table 9.1 for the data from Hardin and Black (1966) and Roesler (1979), the slopes of both the  $\log V_s - \log \bar{\sigma}_a$  and  $\log V_s - \log \bar{\sigma}_b$  relationships range from 0.11 to 0.14. (For the data of Hardin and Black, it was assumed that the slope of the  $\log V_s - \log \bar{\sigma}_c$  portion of the data was negligible as found by Roesler and by this study.) As seen in Table 9.1, although Roesler found the slope of  $\bar{\sigma}_a$  was slightly larger than for  $\bar{\sigma}_b$ , the data for Hardin and Black show the opposite trend. The range in values of slope can be attributed to differences in methods of sample

TABLE 9.1

Influence on Shear Wave Velocity of Orientation of Principal Stresses from Data Presented by Lawrence (1965), Hardin and Black (1966), and Roesler (1979)

Varying Stress Component	Test	Slope of $\log V_s - \log \bar{\sigma}$ Relationship
(1)	(2)	(3)
$\bar{\sigma}_a$	Lawrence (1965) Path 1 Path 2 Path 3 Path 4 Path 5	0.16 0.12 0.10 0.07 0.14
$\bar{\sigma}_a$	Hardin and Black (1966) Tests 5-19 Tests 12-19 Tests 24-34 Tests 39-50	0.11 0.13 0.11 0.11
$\bar{\sigma}_a$	Roesler (1979)	0.14
$\bar{\sigma}_b$ and $\bar{\sigma}_c$	Hardin and Black (1966) Tests 56-60 Tests 64-69	0.13 0.14
$\bar{\sigma}_b$	Roesler (1979)	0.11
$\bar{\sigma}_c$	Roesler (1979)	0.00

construction, different sand types, and experimental scatter. Nonetheless, it appears from these results that both  $\bar{\sigma}_a$  and  $\bar{\sigma}_b$  have a similar effect on  $V_s$ .

The results for the data presented by Lawrence shows no trend in the slope of the  $\log V_s - \log \bar{\sigma}_a$  relationship. Load path five, which had the highest values of pressure for  $\bar{\sigma}_a$ , had a similar slope to load path one, which had the lowest values of pressure for  $\bar{\sigma}_a$ . Therefore, the relationships between  $V_s$  and the stress components seems to be consistent over a wide range in pressures (20 to 180 psi; 137.8 to 1240.2 kPa).

#### 9.4 VARIATION OF $V_s$ WITH DOMINANT STRESS COMPONENTS

Based upon the conclusion that  $V_s$  is equally affected by  $\bar{\sigma}_a$  and  $\bar{\sigma}_b$ , the  $\log V_s - \log \frac{1}{2}(\bar{\sigma}_a + \bar{\sigma}_b)$  relationships for Lawrence (1965), Hardin and Black (1966), and Roesler (1979) are shown in Figs. 9.1, 9.2, and 9.3, respectively. Figure 9.2 separates the data presented by Hardin and Black into the loading sequence shown in the upper figure and the unloading and reloading sequences shown in the lower figure. A least-squares fit was performed for the data included in Figs. 9.1, 9.2 and 9.3 with the  $\log V_s - \log \frac{1}{2}(\bar{\sigma}_a + \bar{\sigma}_b)$  relationship shown as a sloping straight line in each figure.

The slopes of the  $\log V_s - \log \frac{1}{2}(\bar{\sigma}_a + \bar{\sigma}_b)$  relationships are summarized in Table 9.2. These slopes ranged from 0.24 to 0.28. The high values of the coefficient of correlation indicate

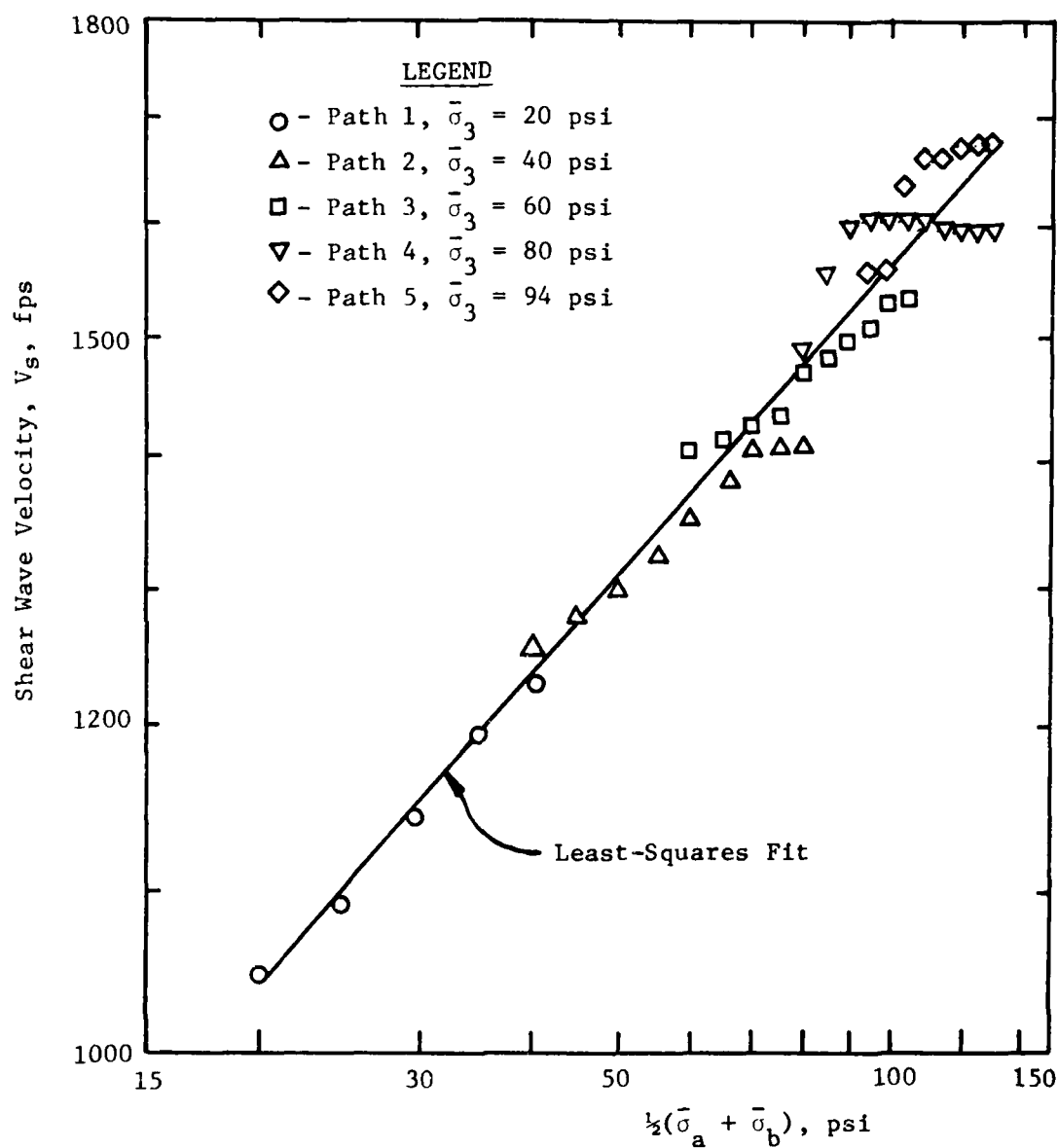
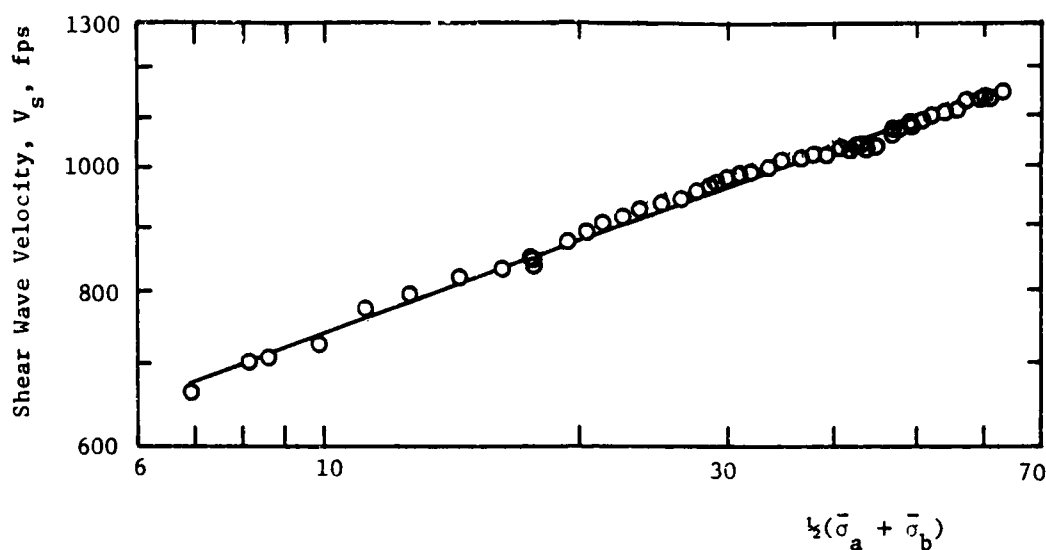
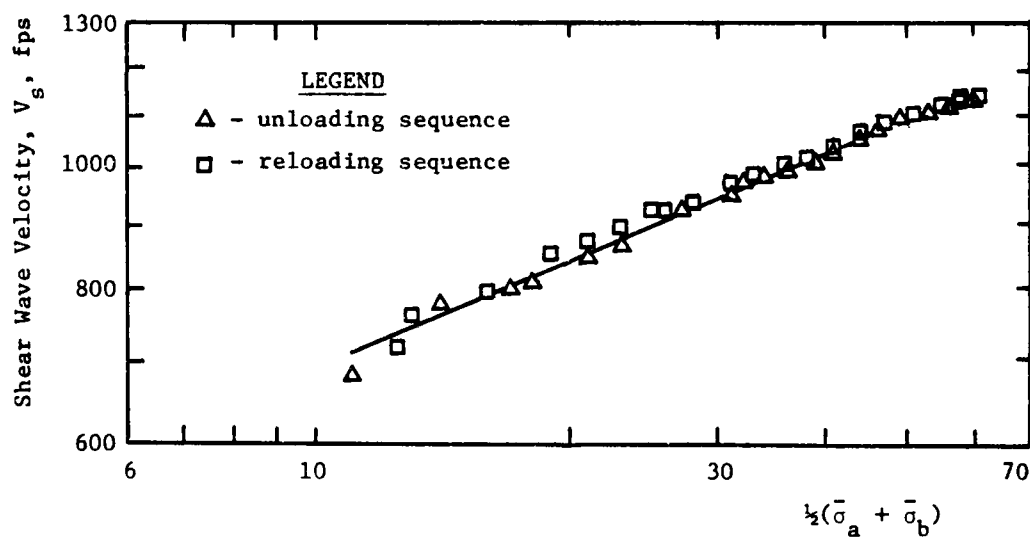


Fig. 9.1 - Variation of Shear Wave Velocity with Directions of Wave Propagation and Particle Motion Based on Data Presented by Lawrence (1965)



a) Loading Pressure Sequence



b) Unloading and Reloading Pressure Sequences

Fig. 9.2 - Variation of Shear Wave Velocity with Directions of Wave Propagation and Particle Motion Based on Data Presented by Hardin and Black (1966)

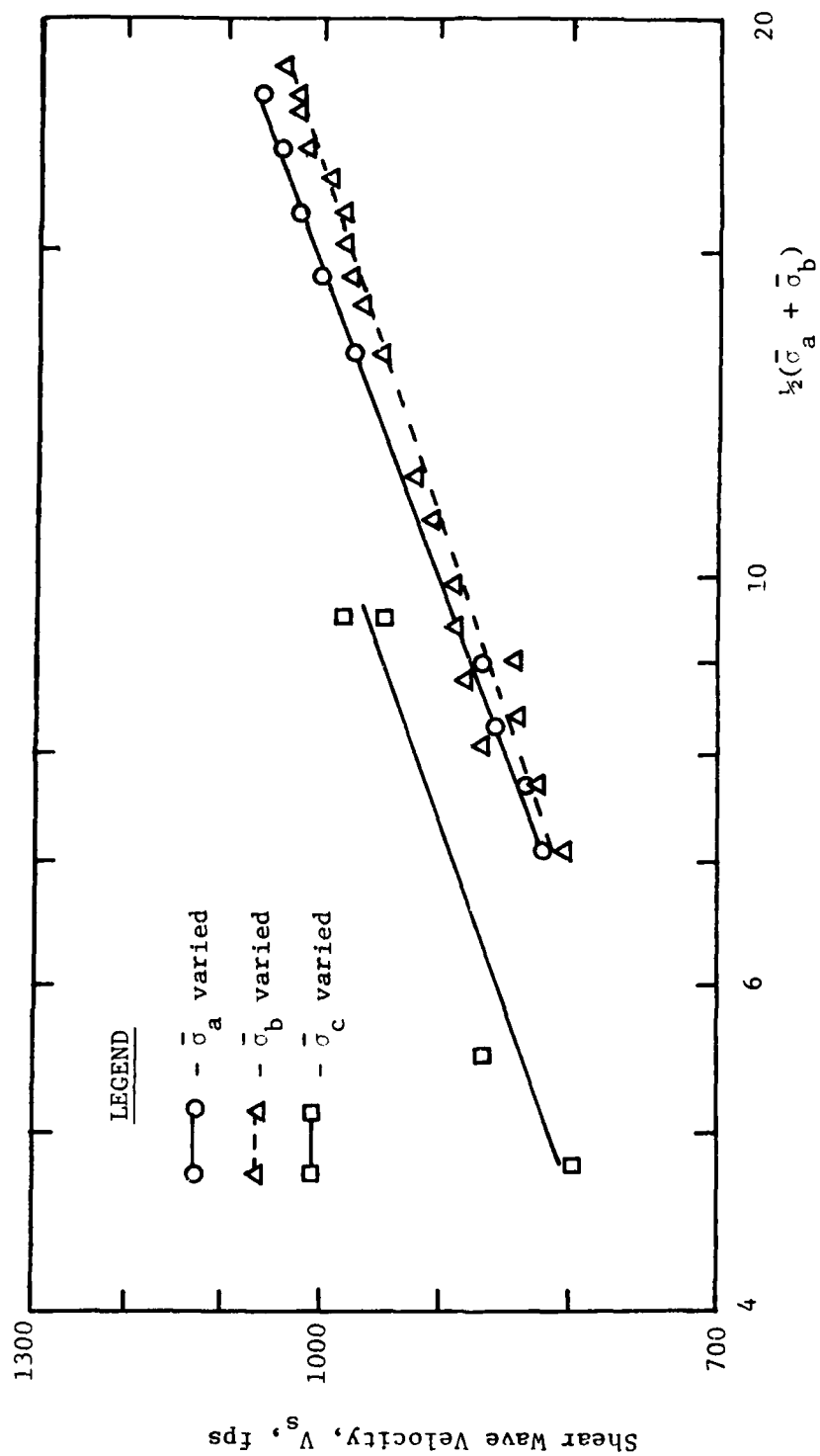


Fig. 9.3 - Variation of Shear Wave Velocity with Directions of Wave Propagation and Particle Motion Based on Data Presented by Roesler (1979)

TABLE 9.2

Variation of Shear Wave Velocity with Directions of Wave Propagation and Particle Motion for Data Presented by Lawrence (1965), Hardin and Black (1966) and Roesler (1979)

Test	Description of Test	Slope of $\log V_s -$ $\log \frac{1}{2}(\bar{\sigma}_a + \bar{\sigma}_b)$ Relationship	Coefficient of Correlation
(1)	(2)	(3)	(4)
Lawrence (1965)			
Path 1	$\bar{\sigma}_a$ increases as $\bar{\sigma}_b, \bar{\sigma}_c$ constant	0.25	0.99
Path 2	$\bar{\sigma}_a$ increases as $\bar{\sigma}_b, \bar{\sigma}_c$ constant	0.18	0.98
Path 3	$\bar{\sigma}_a$ increases as $\bar{\sigma}_b, \bar{\sigma}_c$ constant	0.17	0.99
Path 4	$\bar{\sigma}_a$ increases as $\bar{\sigma}_b, \bar{\sigma}_c$ constant	0.10	0.64
Path 5	$\bar{\sigma}_a$ increases as $\bar{\sigma}_b, \bar{\sigma}_c$ constant	0.24	0.89
Overall		0.26	0.98
Hardin and Black (1966)			
Tests 1-56	increasing $\bar{\sigma}_o$	0.24	0.99
Tests 56-74	decreasing $\bar{\sigma}_o$ (unloading)	0.28	0.99
Tests 74-105	increasing $\bar{\sigma}_o$ (reloading)	0.27	0.99
Roesler (1979)			
	$\bar{\sigma}_a$ increases as $\bar{\sigma}_b, \bar{\sigma}_c$ constant	0.28	0.99
	$\bar{\sigma}_b$ increases as $\bar{\sigma}_a, \bar{\sigma}_c$ constant	0.25	0.99
	$\bar{\sigma}_c$ increases as $\bar{\sigma}_a, \bar{\sigma}_b$ constant	0.25	0.97

that there is a high correlation between  $V_s$  and  $\frac{1}{2}(\bar{\sigma}_a + \bar{\sigma}_b)$ , suggesting that  $\bar{\sigma}_a$  and  $\bar{\sigma}_b$  effect  $V_s$  in a similar manner and that  $\bar{\sigma}_o$  is not the controlling factor for  $V_s$ .

#### 9.5 SUMMARY AND CONCLUSIONS

The results from three experiments (Lawrence, 1965; Hardin and Black, 1966; and Roesler, 1979) were reviewed to examine the shear wave velocity data in light of the conclusion that  $V_s$  is equally dependent on  $\bar{\sigma}_a$  and  $\bar{\sigma}_b$  for sand. Because the dependency of  $V_s$  on  $\bar{\sigma}_a$  and  $\bar{\sigma}_b$  may be effected by the method of sample construction and soil type, only tests performed on dry sand were examined.

Analysis showed that similar slopes were obtained for both the  $\log V_s - \log \bar{\sigma}_a$  and  $\log V_s - \log \bar{\sigma}_b$  relationships, with values ranging from 0.11 to 0.14. The slopes did not seem to be a function of the level of stress. There was a high degree of correlation for the  $\log V_s - \log \frac{1}{2}(\bar{\sigma}_a + \bar{\sigma}_b)$  relationship indicating that there is a relationship between these values. Therefore, the conclusion that  $V_s$  depends equally on only  $\bar{\sigma}_a$  and  $\bar{\sigma}_b$  is reasonable from examination of data presented in these three independent experiments.



## CHAPTER TEN

## SUMMARY, CONCLUSIONS AND RECOMMENDATIONS FOR FUTURE WORK

## 10.1 SUMMARY AND CONCLUSIONS

The general purpose of this research project was to evaluate the effect of the three-dimensional state of stress on the dynamic properties of soil. As this was the initial effort within the project, this segment of the research dealt with:

1. the design and construction of a triaxial testing device, and
2. the investigation of the effect of state of stress on the velocity of shear waves propagating along principal stress directions in dry sand.

10.1.1 Triaxial Testing Device

Much of the effort of this study was directed towards the development of a triaxial testing device, the key component of this research. For the study of wave propagation in soil, a device was desired to apply confining stresses on a soil mass which would model a wide range in stress states to which soil is subjected in the field. The device was constructed of reinforced steel and was designed to hold a cubical soil sample measuring 7 ft (2.1 m) on a side. These dimensions were preferable since it produced a large central portion of soil which was relatively free of boundary effects.

Loading of the soil mass was achieved with rubber membranes placed between the sand and steel walls of the cube. The membranes were placed on three mutually perpendicular sides of the cube, corresponding to the three principal stress directions of the soil sample. Hydraulic loading was used to apply a confining stress on the soil mass which ranged from 10 to 40 psi (78.9 to 275.6 kPa).

A wave source, excitable from outside the cube, was used to generate waves at the boundary of the soil mass. The source hammer could be struck parallel or perpendicular to the side of the cube to generate shear or compression waves, respectively. Source hammers were located along each of the three principal axes of the soil mass. Shear and compression wave motions were monitored by a spacial array of three-dimensional accelerometers placed within the cube. Two digital oscilloscopes were used to record the output from the accelerometers for later analysis.

The waveforms recorded by the oscilloscopes were used for this study to determine direct and interval velocities and frequencies of shear waves generated at the various states of stress. Six types of shear waves were generated at all test pressures, with two types propagated along each of the three principal axes of the cube (top-bottom, north-south, east-west). For each direction of propagation, shear waves were generated in two perpendicular directions of particle motion.

In addition, stress and strain measurements were recorded for various states of stress. The results of the data analysis for

shear waves is presented herein, while the results of the compression waves are presented by Kopperman et al (1982). Although not analyzed for this study, attenuation characteristics were also recorded for the shear waveforms to be used in future analysis.

The test sample itself was composed of a dry, medium to fine, washed mortar sand. The sand was rained into the cube from a minimum height of 2.5 ft (0.76 m) to obtain a soil sample of medium density.

#### 10.1.2 Stress-Strain Measurements

The cube was loaded so that the planned state of stress occurred on the horizontal plane at the mid-height of the cube, with stresses corrected for overburden pressure, hydraulic gradient, and differing piezometric elevations. Because of problems with the strain equipment, no readings were taken for the first half of the test series. As a result, only crude estimates of volume change were possible for the strains occurring within the soil mass. Stress measurements were recorded for the full test series, but these measurements were subject to the significant high scatter typical of these electronic devices.

Based on the stress-strain data available, only small strains (less than 0.3 percent) were created within the sand. A large initial strain was believed to have been caused by seating of the membranes, whereby spaces between the membranes and the steel walls of the cube were filled before pressure was exerted on the

sand. After initial seating, the stress-strain relationship was fairly elastic with no evidence of stress history.

#### 10.1.3 Effect of State of Stress on $V_s$

Shear wave velocities were measured under a number of isotropic, biaxial, and triaxial states of stress. All waves generated for this study were body waves since they were propagated through the soil mass itself. The following conclusions were based on the results of shear waves propagated through dry sand.

The velocity of the shear wave depended about equally on the normal principal stresses in the directions of wave propagation and particle motion and was relatively independent of the normal principal stress in the out-of-plane directions. Prior to this study, it was generally assumed that  $V_s$  was related to the mean effective principal stress,  $\bar{\sigma}_o$ , which is a function of all three principal stresses. In addition, the generalization that  $V_s$  was not affected by the level of shearing stress for a constant  $\bar{\sigma}_o$  was found to be incorrect. Shear wave velocity was found to be controlled by  $\bar{\sigma}_a$  and  $\bar{\sigma}_b$ , and if the average of these stresses,  $\frac{1}{2}(\bar{\sigma}_a + \bar{\sigma}_b)$ , varied, then  $V_s$  changed accordingly even for a constant  $\bar{\sigma}_o$ .

As expected, stress history had little effect on shear wave velocity for the sand used in this study. For the initial isotropic series of tests, values of  $V_s$  differed by a maximum of six percent with an average variation of three percent. For the

subsequent biaxial and triaxial tests, similar shear wave velocities for loading and unloading pressure sequences were measured, with experimental scatter less than 10 percent. This range of scatter was considered reasonable, and, therefore, it was concluded that stress history had little effect on this sand.

Structural anisotropy was found in the sand sample. Structural anisotropy grouped the shear waves into three planes of motion, that is planes which were defined by the directions of wave propagation and particle motion. A maximum difference of 18 percent was determined between all three planes of motion. This difference in  $V_s$  between planes of motion did not, however, affect the relationship between  $V_s$  and  $\bar{\sigma}_a$  and  $\bar{\sigma}_b$ . Shear wave velocity was found to depend equally on  $\bar{\sigma}_a$  and  $\bar{\sigma}_b$  for all the planes of motion, although the exact relationship did vary slightly from plane to plane.

The relationships of  $V_s$  to the stress directions may be expressed in a general form as (after Roesler, 1979):

$$V_s = C_1 \bar{\sigma}_a^{ma} \bar{\sigma}_b^{mb} \bar{\sigma}_c^{mc} \quad (10.1)$$

where:  $V_s$  = shear wave velocity in fps,

$C_1$  = constant,

$\bar{\sigma}_a$  = effective principal stress in the direction of wave propagation, in psf,

$ma$  = slope of  $\log V_s - \log \bar{\sigma}_a$  relationship,

$\bar{\sigma}_b$  = effective principal stress in the direction of  
particle motion, in psf,

mb = slope of  $\log V_s - \log \bar{\sigma}_b$  relationship,

$\bar{\sigma}_c$  = effective principal stress in the out-of-plane  
direction in psf, and

mc = slope of  $\log V_s - \log \bar{\sigma}_c$  relationship (typically mc  
was found to be zero).

Constants for Eq. 10.1 were determined for each plane of  
motion with similar values found for isotropic, biaxial, and  
triaxial states of stress. The range and average values determined  
for these constants for this sand are summarized in Table 10.1.

Shear wave velocity at small strains is related to the  
shear modulus at small strains,  $G_{\max}$ , and can be expressed in  
non-dimensional form as (after Hardin, 1978):

$$G_{\max} = \frac{C}{0.3+0.7e^2} P_a^{1-(na+nb+nc)} \bar{\sigma}_a^{na} \bar{\sigma}_b^{nb} \bar{\sigma}_c^{nc} \quad (10.2)$$

where  $G_{\max}$  = shear modulus in desired units,

C = dimensionless constant,

na = slope of  $\log G_{\max} - \log \bar{\sigma}_a$  relationship,

nb = slope of  $\log G_{\max} - \log \bar{\sigma}_b$  relationship,

nc = slope of  $\log G_{\max} - \log \bar{\sigma}_c$  relationship,

$P_a$  = atmospheric pressure in same units as  $G_{\max}$ , and

e = void ratio.

For Eq. 10.2,  $\bar{\sigma}_a$ ,  $\bar{\sigma}_b$ , and  $\bar{\sigma}_c$  are expressed in the same units as  $G_{\max}$ .

TABLE 10.1

Summary of Values of Constants Determined for Eqs. 10.1\* and 10.2\*\* for Each Plane of Motion for Isotropic, Biaxial, and Triaxial States of Stress

Constant***	Plane of Motion					
	TB-NS			TB-EW		
	Range (2)	Average (3)	Range (4)	Average (5)	Range (6)	Average (7)
$C_1^{***}$	168-207	180	113-149	141	129-204	187
ma	0.10-0.12	0.11	0.11-0.13	0.12	0.09-0.12	0.10
mb	0.08-0.11	0.09	0.09-0.11	0.10	0.09-0.11	0.09
mc	-0.01-0.00	0.00	-0.01-0.00	0.00	-0.01-0.04	0.01
C	668-678	674	569-603	590	711-748	723
na	0.20-0.22	0.21	0.24	0.24	0.18-0.20	0.19
nb	0.18-0.20	0.19	0.20-0.21	0.18	0.18	0.18
nc	0.00	0.00	0.00	0.00	0.02	0.02

\* Eq. 10.1:  $V_s = C_1 \frac{ma}{a} \frac{mb}{b} \frac{mc}{c}$

\*\*\* All constants dimensionless except  $C_1$  where  $C_1$  in  $(ft^3-t_{lb}^{-t}sec^{-1})$ , where  $t = ma + mb + mc$ .

\*\* Eq. 10.2:  $C_{max} = \frac{C}{0.3+0.7e^2} \frac{1-(na+nb+nc)}{a} \frac{na}{a} \frac{nb}{b} \frac{nc}{c}$

The values of the constants were determined for this equation and are also included in Table 10.1.

#### 10.1.4 Importance to Laboratory and Field Testing

The conclusion that the velocity of the shear wave propagating through sand depends on the stress in the directions of wave propagation and particle motion is important in the comparison of laboratory and field tests. Shear wave velocity along principal stress directions for the field may be predicted for any state of stress based on dynamic laboratory tests, provided that the sum of  $\bar{\sigma}_a$  and  $\bar{\sigma}_b$  in the field is equal to the sum of these two stresses in the laboratory.

Kopperman et al (1982) determined that compression wave velocity for body waves was controlled only by the principal stress in the direction of wave propagation. Therefore, dynamic properties for shear and compression waves can be related in laboratory tests only where the sum of  $\frac{1}{2}(\bar{\sigma}_a + \bar{\sigma}_b)$  for shear waves equals  $\bar{\sigma}_a$  for the compression waves.

#### 10.2 RECOMMENDATIONS FOR FUTURE WORK

The recommendations presented in this section deal with improvements in the triaxial testing device and suggestions for future testing within the original scope of this study.

The present source hammer should be redesigned to eliminate the problems of limited access for the hand-held hammer to generate waves, sand leakage around the hammer, and the tendency



of the source to rotate. In this area, the hand-held hammer itself should be modified to reduce the hitting area and to lessen the weight of the hammer. This would greatly increase the control of the generated wave amplitudes. The possibility of using a mechanical source to generate waves should also be explored. Finally, an accelerometer should be placed on the source so that the input wave motion could be examined before it was altered by the soil.

A new raining device for the sand should be constructed to attempt to build a more uniform and homogeneous soil sample. This rainer would hopefully reduce the effect of structural anisotropy which was found for this study. There are two other suggestions in the area of sand raining. First, the greased sheets adjacent to the membranes should be sealed with the WD-40 in them so that the fluid will not leak out or dry up. Second, the greased sheets should be weighted on the bottom so that they will not tend to be blown upwards due to air currents from the sand raining.

An additional membrane should be placed along each face of the cube opposite to the present membranes. The second membrane would ensure a more continuous stress across the soil sample, but it must still allow contact of the source hammer with the soil.

The stress cells and soil strain gages should be calibrated and used to gather stress-strain data from the soil in the cube. Care must be given to: the accuracy of the measurements,

the method of placement, and placement locations in the cube. Because of the inherent scatter with the stress cells, it is suggested that at least three be used along each axis of the cube. This would mean the purchase of additional stress cells, or since they are expensive, the use of the three cells already purchased along any one axis of the cube for each soil sample. Statistically, this would provide more reliable results of the stresses in the soil.

Additional samples of dry sand should be tested under similar states of stresses in the cube. The samples would provide additional data so that the conclusions reached in this study can be reviewed to determine if the method of sample placement is a significant factor. Additional tests would also permit evaluation of the improvements made on the triaxial testing device.

As an aside, should additional samples of dry sand be tested, it is recommended that an area be set aside where sufficient amounts of sand can be stored in a dry environment. The process of drying the sand is a time consuming and tedious task and should have to be done only once.

Subsequent tests should be performed on a variety of soils to determine if the conclusions about the relationship of shear wave velocity and state of stress for dry sand are dependent on the type of soil tested. Other soil types would include saturated or partially saturated sands, sands with cobbles, or rock

inclusions, and cohesive soils. The testing of saturated soils and cohesive soils will present unique problems.

Finally, testing for this study was conducted only along the principal stress axes of the soil. Future tests should be performed with the shear waves propagated at oblique angles to principal stress directions.

APPENDIX A

TRIAxIAL TESTING DEVICE

Taken in Full from Kopperman et al (1982)

## APPENDIX A

## TRIAXIAL TESTING DEVICE

## A.1 INTRODUCTION

Much of the effort in this project was necessarily directed toward the design, fabrication, and readiness for testing of the triaxial cube and associated equipment. This chapter discusses the design of the triaxial cube and associated equipment and reviews the development and evolution of each system within the triaxial testing device.

The triaxial cube is essentially a steel box with interior dimensions of 7 ft (2.1 m) on a side. Equipment associated with the cube is used to: 1. place the sand in a uniform state within the cube, 2. pressurize the sand mass to a desired stress state, 3. excite compression or shear waves in the sand, 4. monitor and digitally record these waveforms, and 5. monitor the stress and strain throughout the sand sample during testing. A schematic drawing of the cube and its associated systems is shown in Fig. A.1. The cube and associated equipment are located at the Phil M. Ferguson Structural Engineering Laboratory at the Balcones Research Center of The University of Texas at Austin.

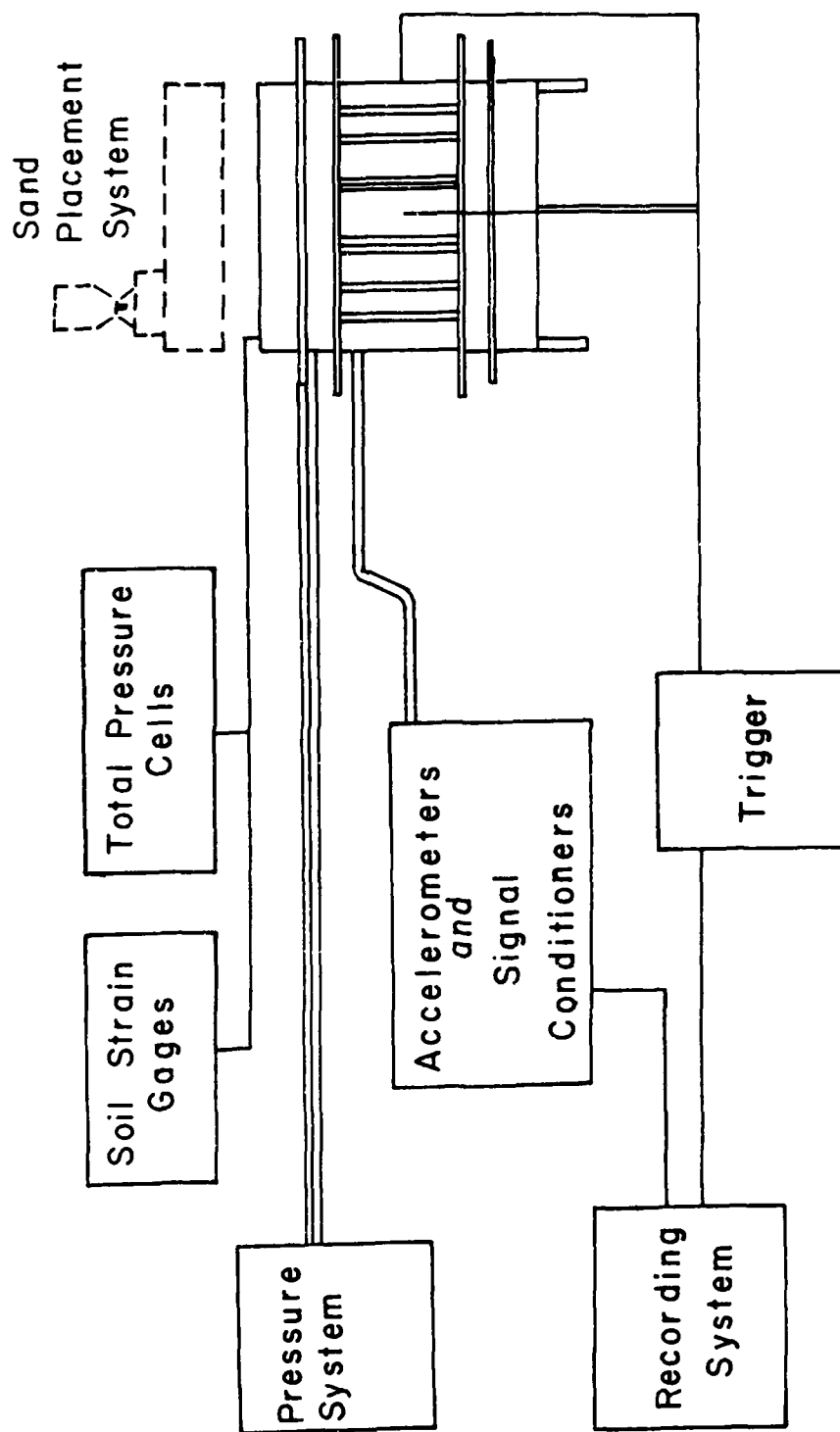


Fig. A.1 - Schematic Diagram of Model Cube and Associated Systems

## A.2 STRUCTURE OF THE CUBE

### A.2.1 Design Considerations

The cube was planned to provide a cubic sample, 7 ft (2.1 m) on a side, through which wave propagation tests could be performed. It was desired to form as large a sample as practical in order to obtain a central portion of sand which would be relatively free of any boundary effects. One boundary effect results from the loading system creating uncertain stresses in the sand along the sides and especially in the corners of the cube. The dimensions selected for the cube provide a central, 4-ft (1.2 m) cubic portion of sand which is considered free from edge effects.

In its simplest form, the cube was initially envisioned as a large box composed of interconnected steel plates approximately 7 ft (2.1 m) square. However, subsequent calculations showed that a plate thickness of 1 $\frac{1}{2}$  in. (30.5 cm) would be required to restrict the bending of the plates to an acceptable value under the desired maximum working pressure of 50 psi (345 kPa). Plates of this size were impractical because of high fabrication costs and excessive weight. A compromise between reduced plate thickness and substantial reinforcement was chosen to reduce the cost of the material and weight of the cube to acceptable values. In the final design, 0.357-in. (0.95 cm) thick, mild steel plates were employed to form all six sides of the cube. These steel plates were reinforced with longitudinal I-beams and lateral angle and plate bracing so that

the cube could withstand a working pressure of 50 psi (345 kPa) over any side. The gross weight of the steel structure is estimated to be about 5 tons (4500 kg).

#### A.2.2 Cube Construction

The cube was designed to be built in three separate sections: 1. the bottom with four base legs, 2. the four sides, and 3. the top. These three sections were then bolted together to form the completed structure. In typical use, the four sides remain bolted to the bottom section and only the top is removed as the cube is filled or emptied of sand. The construction procedure for these sections was: 1. complete the bottom section with base legs, 2. tack weld the four sides together and bolt them to the bottom, 3. complete the top of the cube and examine the fit with the four sides, and 4. with the top removed, finish welding the four sides of the cube together.

The top and bottom sections are similar in design except for the addition of four legs on the bottom section. Each section begins with a 7-ft (2.1 m) square steel plate. Steel reinforcement is then welded to the plate as shown in Figs. A.2 and A.3. Along the edges of the plate, angle sections are welded which have bolt holes fabricated in them to allow the top and bottom sections to be secured to the four sides. The angle sections on the east and west edges are L2x2 each with a row of seven equally spaced 0.625 in. (1.58 cm) diameter bolt holes, and the sections on the north and



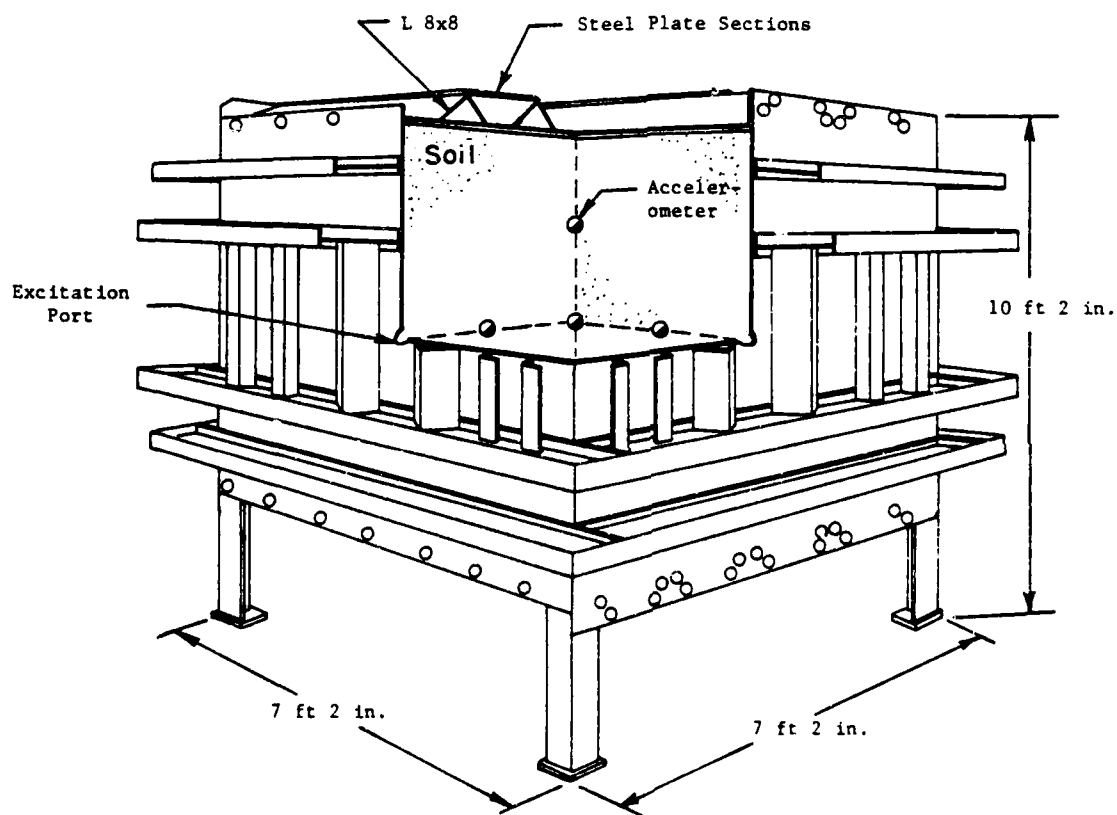


Fig. A.2 - Cut-Away, Isometric View of Triaxial Cube  
Showing Top Reinforcement Details

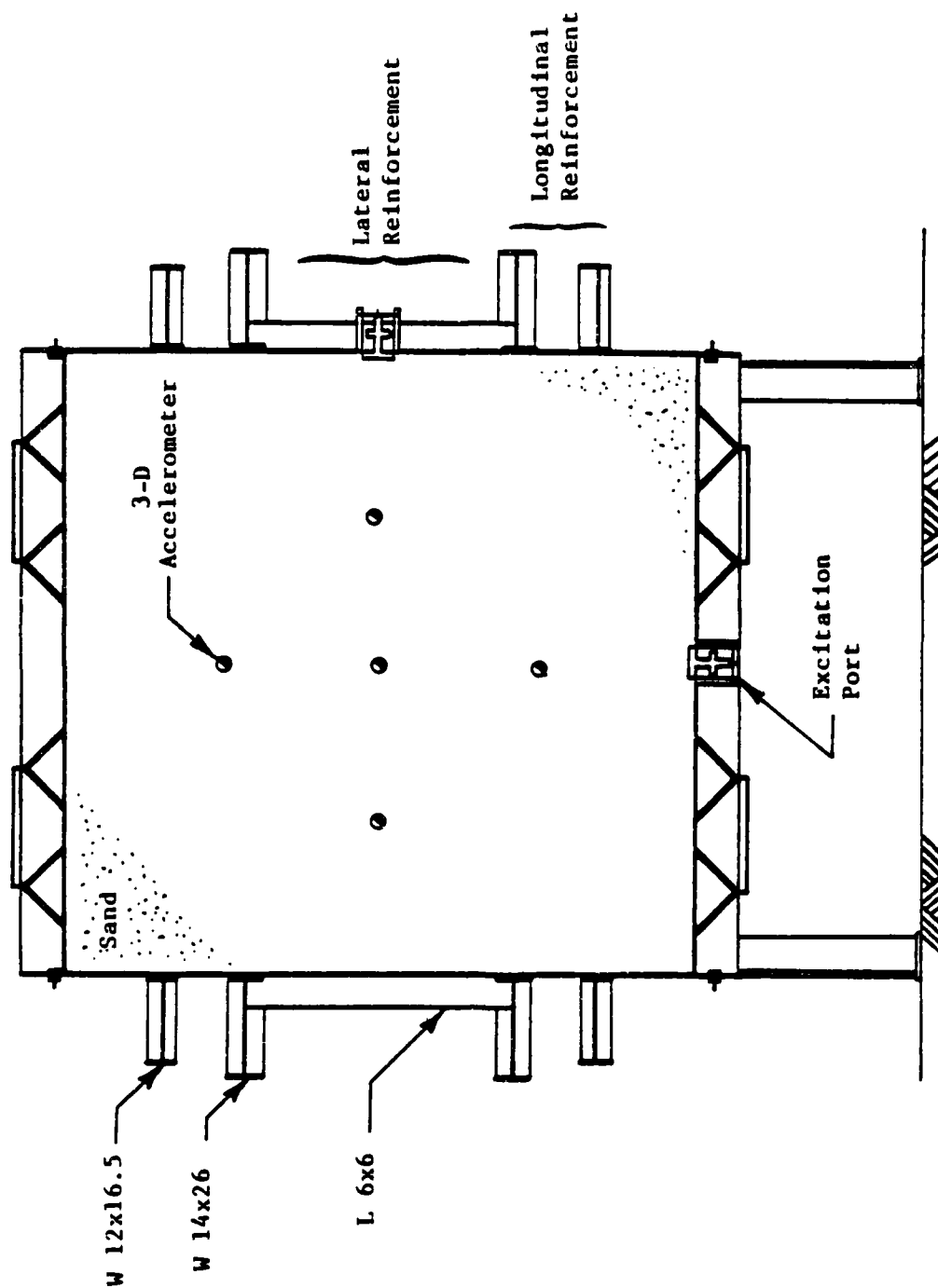


Fig. A.3 - Cross-Sectional View Along Central Vertical Plane in Triaxial Cube

south edges are  $L6 \times 3\frac{1}{2}$  each with a pattern of seventeen 1.0-in. (2.54 cm) diameter bolt holes. Four  $L8 \times 8$  angles are welded across the steel plate in two pairs, each pair centered on half of the steel plate. Additional reinforcement of 0.5-in. (1.27 cm) thick steel plate is welded between the adjacent  $L8 \times 8$  angles for their entire length of 7 ft (2.1 m).

The legs on the bottom section are included in the design to allow access to the bottom of the cube with its excitation port (see Section A.3). The legs are fabricated from  $L5 \times 5$  angles and elevate the bottom of the cube 2.5 ft (.76 m) above the floor surface. Reinforcement of 0.5-in. (1.27 cm) thick steel plate is included above each leg to prevent punching through the bottom face of the cube by the legs when the cube is filled with sand. Small sections of 0.5-in. (1.27 cm) thick steel plate are welded onto the leg angles to withstand any buckling or bending moment in the legs due to the weight of the sand and cube.

For the top and bottom sections, the reinforcement was first tack welded to the steel plates and then completely welded together as a unit. Unfortunately, these sections had to be welded without being secured in place with the cube framework. This permitted some slight bowing of the steel plates due to the welding heat which was corrected in the final stage of welding.

The four sides of the cube are constructed of 0.375-in. (0.95 cm) thick, steel plates with angle and I-beam reinforcement. The steel plates are 7-ft wide (2.1 m) with two plates 7.5-ft (2.3 m)

high and the other two plates 8.2-ft (2.5 m) high. The additional height contains fabricated bolt holes corresponding to those of the angles along the top and bottom sections. Steel angles are vertically welded as lateral reinforcement around the mid-section of the sides as shown in Figs. A.3 and A.4. Each side has four,  $L3\frac{1}{2} \times 3\frac{1}{2}$  and two,  $L6 \times 6$  angles. The angles transfer the load to two, longitudinal, 14-in. (35.6 cm),  $W14 \times 26$  I-beams. The I-beams are horizontally welded to form two continuous rings around the cube with the lateral reinforcement between them. Two more longitudinal rings of 12-in. (30.5 cm),  $W12 \times 16\frac{1}{2}$  I-beams restrict the bending of the upper and lower regions of the steel plates. The longitudinal reinforcement is shown in Figs. A.3 and A.5. The extreme edges of the steel plates are rigid due to the plate-to-plate welding on the sides and the bolt connections along the top and bottom sections.

The procedure used in constructing the sides of the cube consisted of: 1. tack welding the reinforcement to the side plates, 2. bolting each side to the already completed bottom, 3. tack welding the four sides together while bolted to the bottom, and 4. final welding of the reinforcement to the side plates. The procedure was followed in order to reduce the possible deformation of the thin, flat steel plates due to the welding heat. Initial tack welding secured the reinforcement to the side plates with a minimum of heat created in the plates, thereby reducing the curvature produced in the side plates. With the four sides bolted to the bottom, tack welding of the plates together ensured that the

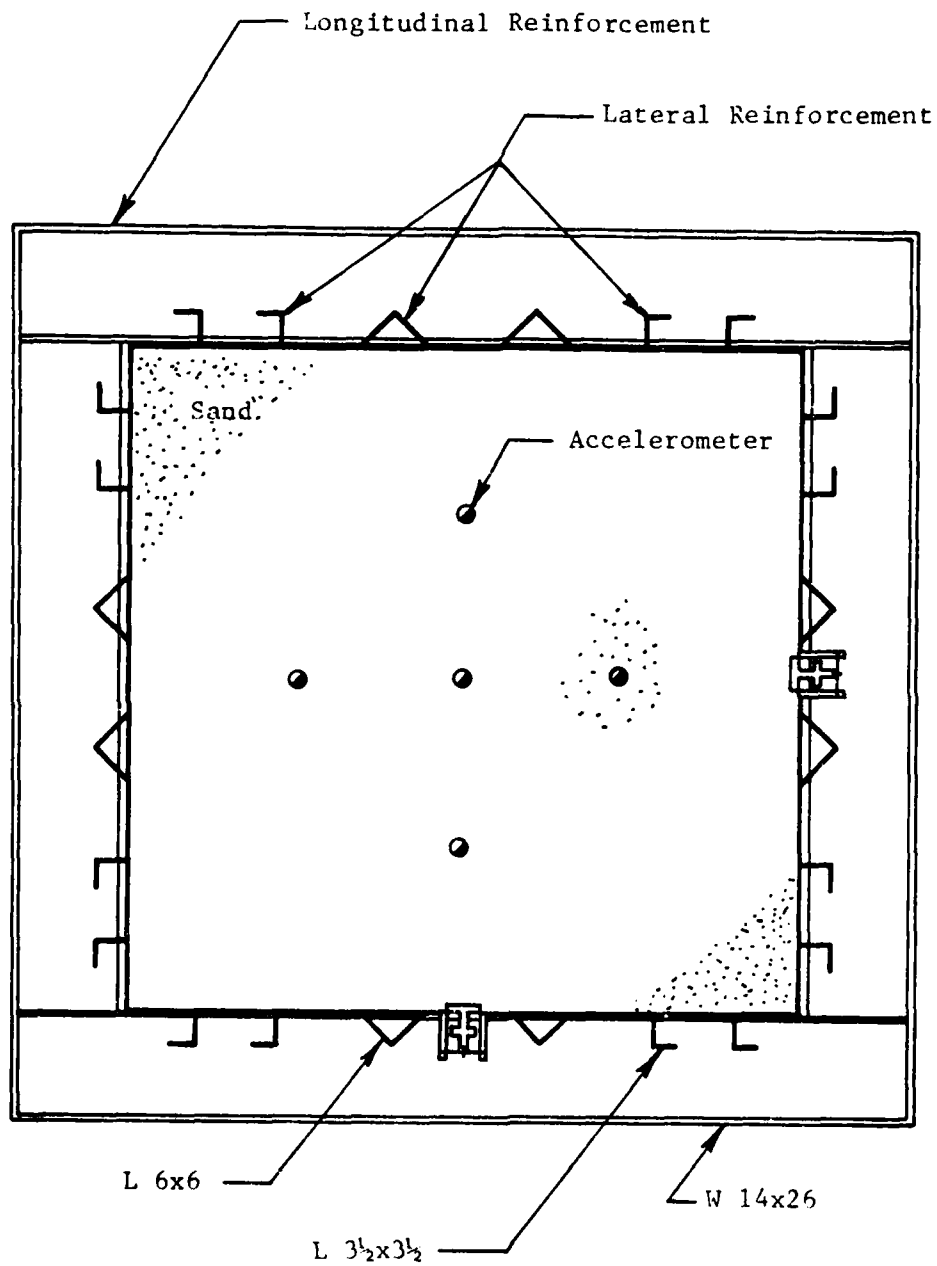
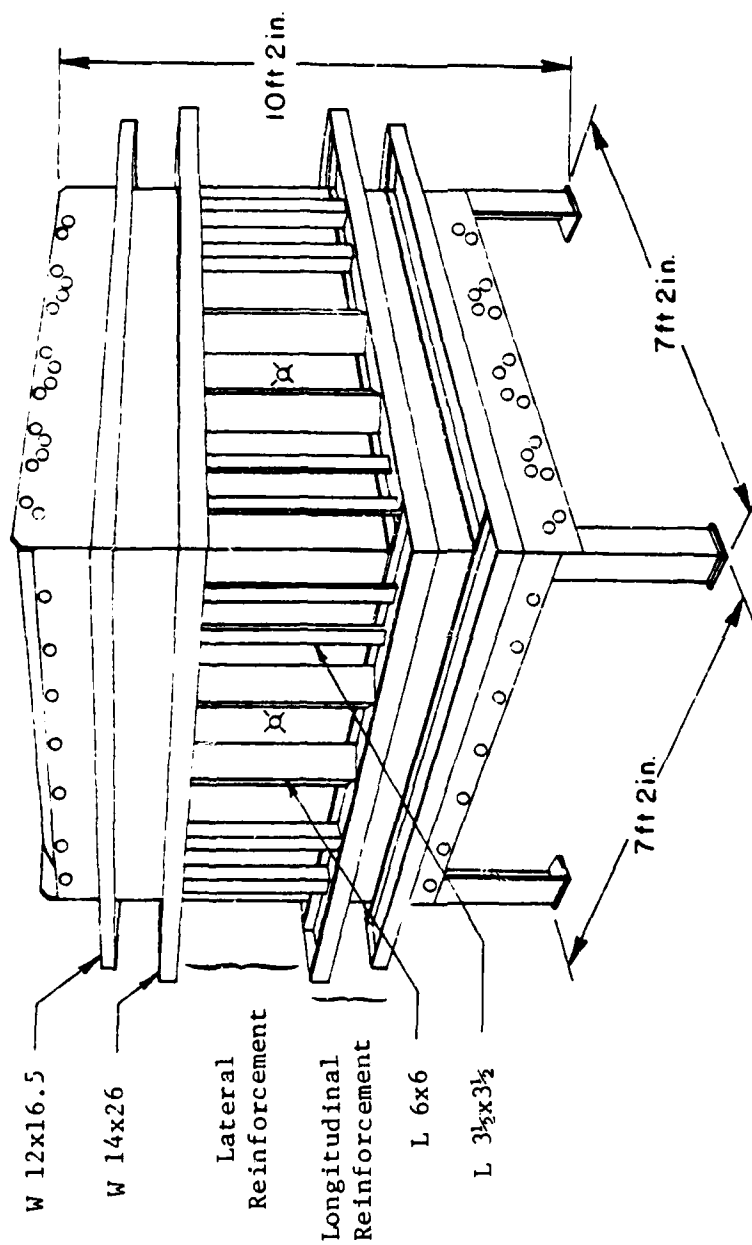


Fig. A.4 - Cross-Sectional View Along Central Horizontal Plane in Triaxial Cube



Note: See Figs. 3.3 and 3.4 for  
Cross-Sectional Detail Views

Fig. A.5 - Isometric View of Triaxial Cube Showing Side Reinforcement Details

final shape would not deform considerably from the design shape. Measurements of the finished cube verified that there was no significant deviation of the cube from the desired shape. The final interior dimensions measured along the edges and across the center of all plates varied by less than  $\pm 0.785$  in. (2.0 cm) from the designed length of 7 ft (84 in. or 213.4 cm), or 0.9 percent.

#### A.2.3 Special Features of the Cube Structure

The final design of the structure incorporates several desirable features. The cube has been designed as a free-standing structure without the need of any external support. This permits the cube structure to be located at any site where the associated equipment has adequate support. In addition, lifting lugs are provided on the top section of the cube to permit movement of the cube, whether full or empty of soil, with the 25-ton (22,700 kg) overhead crane available at the Ferguson Laboratory. Further, excitation ports were fabricated in each face of the cube to provide complete versatility in the location of wave generation. A source hammer can, therefore, be placed in any of the six faces.

To make access to the cube easier and safer during operation, a steel ladder and wood scaffolding were constructed. The steel ladder was built at the same height as the uppermost I-beam, approximately 9 ft (2.7 m) above the floor surface. This allows easy access to the top of the cube and provides a safe elevated working platform. Rollers were included on the ladder to

facilitate movement around the cube as space restrictions dictate. Wood scaffolding was constructed to provide large working platforms at the same height as the uppermost I-beam and to run along two sides of the cube. The scaffolds provide a safe walkway during cube filling operations. After the cube is filled with sand the scaffolds can be easily dismantled and stored near the cube. Figure A.6 shows the assembled scaffolding next to the cube.

The cube was painted two shades of blue on the outside, light blue on the steel plates and dark blue on the reinforcement. All of the inside of the cube was painted light blue. The steel ladder was also painted light blue. Figure A.7 shows the completed cube structure.

### A.3 LOADING SYSTEM

To study wave propagation in soil, it is necessary to apply confining stresses on the soil mass which attempt to model those three-dimensional stresses the soil is subject to in the field. By designing a loading system which simulates field conditions, the resulting wave propagation data can be examined more realistically. Non-rigid membranes were desired for the loading system in order to model stress-controlled conditions. A non-rigid, stress controlled boundary allows non-uniform strains in the sand mass but better simulates desired conditions of uniform stresses within the sand (Arthur and Menzies, 1972). Rigid, strain-controlled boundaries can cause mechanical problems due to sample deformation



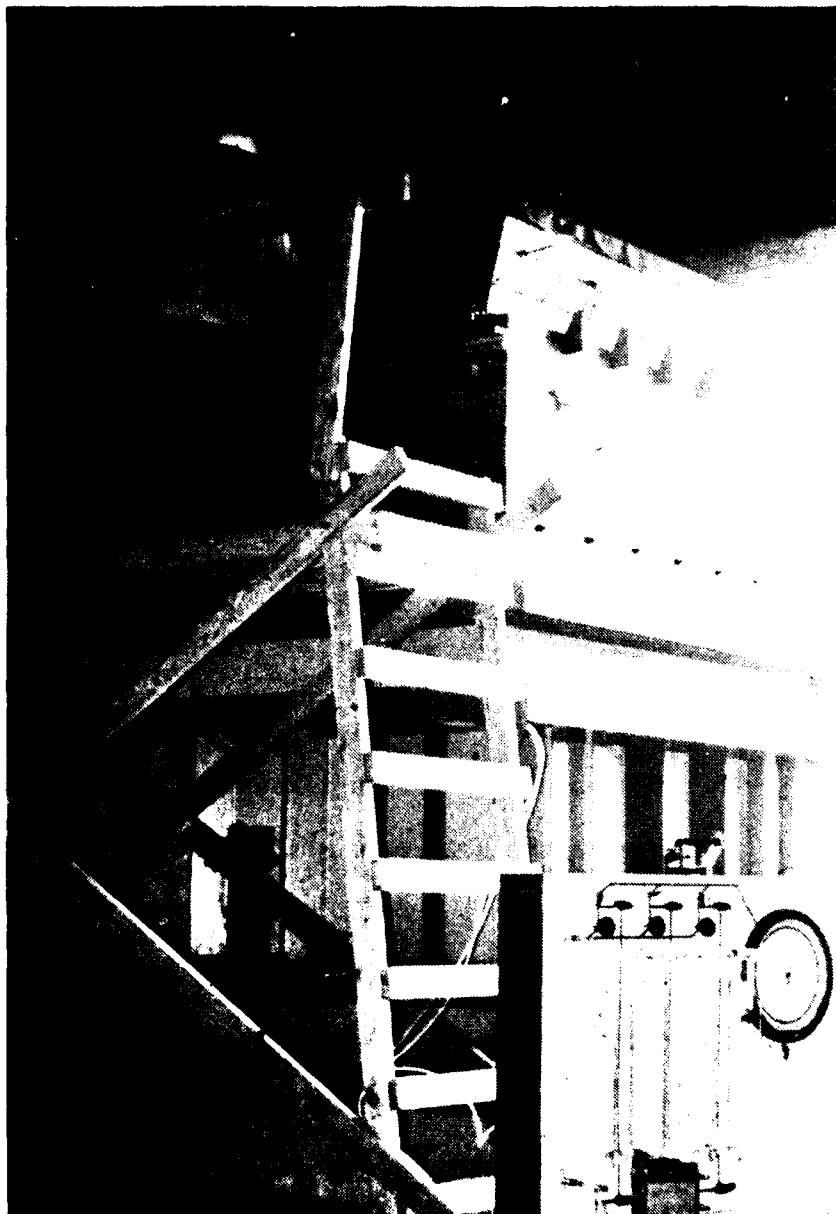


Fig. A.6 - Sand Filling Operation in Progress  
With Wood Scaffolding in Place

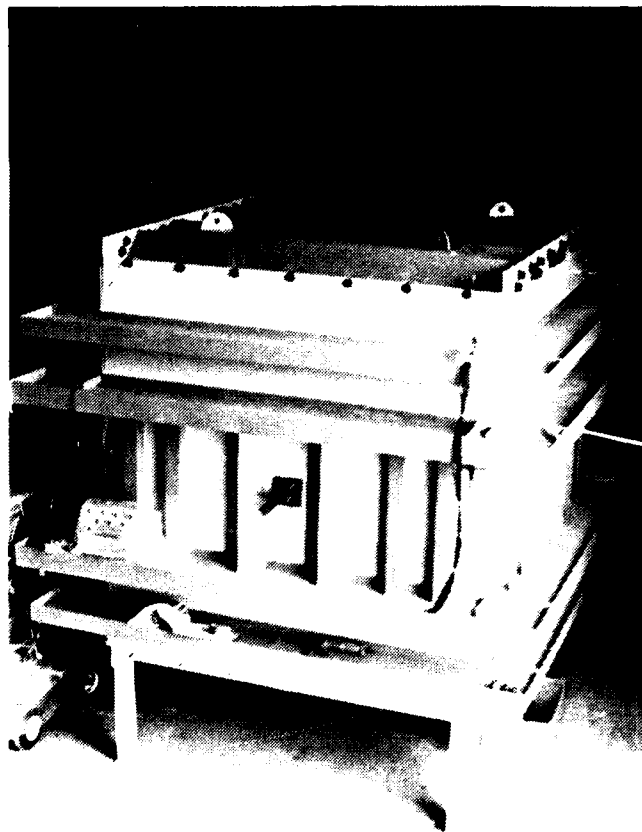


Fig. A.7 - Completed Cube Structure

in the corners of the cube. Further, rigid boundaries, although causing uniform displacements, do not guarantee uniform stresses in the sand mass.

#### A.3.1 Membrane Operation

Confining stresses are applied to the sand mass by three membranes placed on the inside of the cube: one along the top and one on each of two adjacent sides. An exploded view of the membranes within the cube is shown in Fig. A.8. In this configuration, one membrane is used to apply pressure along each of the three principal axes of the cube. The membranes are confined along their perimeter by steel ribs of  $3/4 \times 3/16$  in. (1.9 cm x 0.48 cm) bar section welded along the edges of the inside faces of the cube at 45-degree angles away from the plane of the cube face. These ribs are assumed to confine the membrane edges from expanding toward an adjacent membrane, thereby preventing the tendency of the membranes to stretch and burst along the edges (Sutherland and Mesdary, 1969; Arthur and Menzies, 1972). With this confinement, each membrane is isolated from the others, and so each membrane exerts a pressure only along its respective axis. This arrangement permits independent control of the pressure in each of the three principal directions. Loading conditions on the sand can then be isotropic ( $\sigma_1 = \sigma_2 = \sigma_3$ ), biaxial ( $\sigma_1 > \sigma_2 = \sigma_3$ ), or true triaxial ( $\sigma_1 > \sigma_2 > \sigma_3$ ).

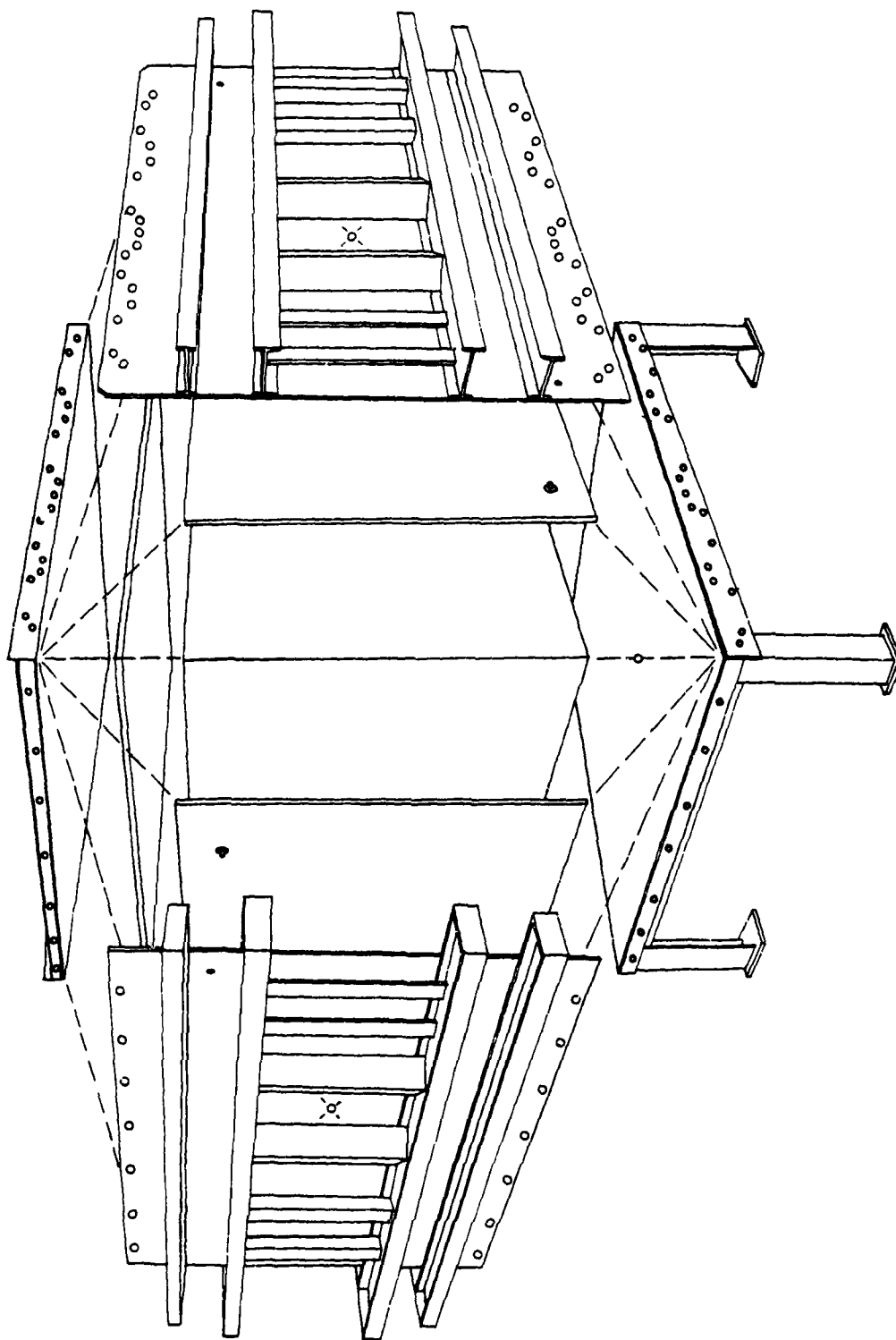


Fig. A.8 - Exploded View of Triaxial Cube

### A.2.2 Membrane Characteristics

Initial discussion of the loading system lead to an ideal membrane design which would: 1. be capable of attaining and indefinitely maintaining the maximum desired pressure of 50 psi over the entire cube face, 2. have rugged and durable construction with puncture and tear resistant materials, 3. present no operational hazards, 4. be simple and quick to pressurize, 5. be manageable, and 6. have a reasonable cost. It was felt that the final membrane design should incorporate an optimum mixture of these characteristics. Triaxial cells of much more limited size possess membranes with similar characteristics (Ko and Sture, 1974; Ko and Scott, 1967; Laier, Schmertmann, and Schaub, 1975).

An important design consideration of the membranes was the decision to use water and not air to pressurize the membranes. Fluid under these pressures is safer than air because of the incompressibility of the fluid. Leakage detection in the membranes would be easier with water filled membranes since water can be visually monitored while air cannot. Water entering the membranes would be indicative of leakage and water elevations in the panel board accumulators (see Section A.3.5) could be easily monitored. Finally, water provides a more desirable vertical pressure distribution on the sand mass, as compared to air. This stems from the fact that, for any elevation in the cube, the water or air and the sand exhibit side forces due to the weight of material above it. This side force is in addition to any pressure in the water or air.

For the water the lateral force would be equal to the weight of water above it ( $K = 1.0$ ), or 62.4 psf per ft (9.8 kPa per m) of elevation head. While for sand, the force is estimated to average about 0.4 of the weight above a given load ( $K = 0.4$ ), or about 40 psf per ft (6.3 kPa per m) of elevation. The density of air is so small that its side forces are negligible. There are organic fluids available which possess densities lighter than water and are therefore more mathematically attractive but their high cost and hazardous properties reduce their value. Therefore, it was decided to use water. Also, it was decided to commence testing at 10 psi to reduce the significance of the non-uniform vertical and horizontal pressure distribution.

#### A.3.3 First-Design Membranes

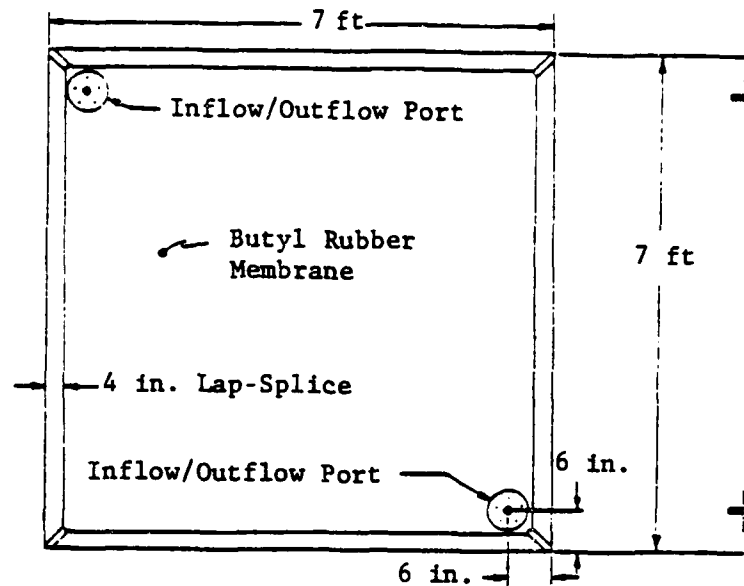
A number of possible membrane solutions were considered, which fell into three general categories: 1. use of a currently manufactured product, either directly as produced or modified as required, 2. use of membranes professionally constructed as per specifications, or 3. construction of membranes ourselves. Those products currently manufactured include dunnage bags, water pressure bags, and utility bags. Each of the solutions contained most of the desired membrane features, with the solutions having a wide range of cost and each solution possessing its own drawbacks.

After examining each of the potential solutions it was decided to construct the membranes ourselves. This choice seemed

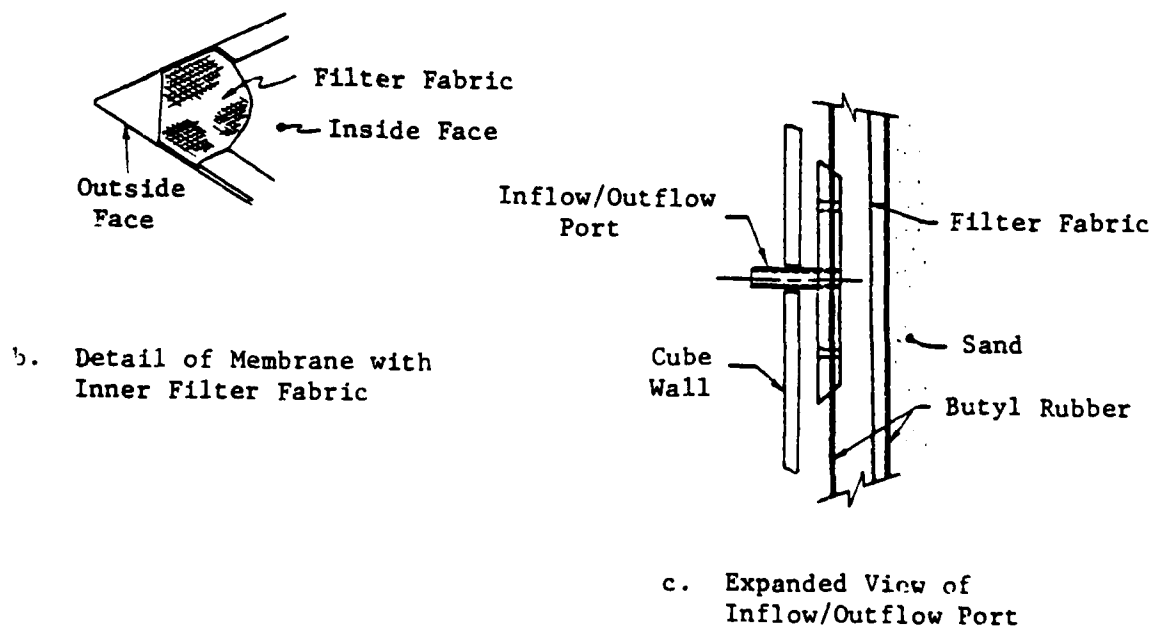
to offer fabricated membranes at the lowest cost and of the precise configuration needed. This version of the loading system consisted of membranes made of 0.063-in. (0.16 cm) thick, Butyl rubber sheets. Each membrane was formed by bonding together the edges of two sheets of Butyl rubber; a smaller sheet cut to the size of the cube face against which it was to be placed, and a larger sheet cut to allow a 4-in. overlap splice along the perimeter edges of the smaller sheet. The edges of these two sheets were bonded together with cement to form a continuous lap seal around the perimeter of the smaller sheet. A sealant was placed inside the membrane along all lap-splice seams to form a water tight seal between the two sheets. In addition, a sheet of filter fabric material was placed between the rubber sheets in each membrane, permitting water to permeate freely throughout the membrane. Water under pressure throughout the membrane would ensure that the pressure would be distributed equally and completely across the cube face in contact with the membrane. Figure A.9 shows the details of construction of these membranes.

The procedure for membrane construction consisted of:

1. cutting and aligning the rubber sheets and filter fabric,
2. cleaning the sheets along the overlap splice with wire brush and heptane, a rubber solvent,
3. applying the sealant with a caulking gun in a continuous bead along the inside fold of the intended overlap splice,
4. placing the bonding cement on the corner sections of the rubber sheets to be sealed and folding over



a. Typical Membrane with Inflow/Outflow Ports



c. Expanded View of Inflow/Outflow Port

Fig. A.9 - Construction of First-Design Membranes



and pressing together the corners, and 5. repeating step 4 along the perimeters of the rubber sheets.

Pressurizing the membranes was to be accomplished through two inflow/outflow ports incorporated in opposite corners of each membrane. These ports provided a channel from the exterior pressure lines through the steel cube walls and into the membranes. These ports consisted of a 4-in. (10.2 cm) long by 0.38-in. (1.0 cm) diameter pipe nipple passing through one of the Butyl sheets. This short pipe was screwed into two, 6-in. (15.2 cm) diameter steel plates between which was fastened the rubber sheet. The plates had a combined thickness of 0.5 in. (1.3 cm). Sealant was placed around the 6-in. (15.2 cm) diameter steel plates of the port and along the screwholes and connections to prevent any water leakage. Once the sand was in place, the membranes would be filled with water through the bottom port while air would be expelled from the top port until the water level in the membrane reached the top port.

The membranes were pretested to determine how well they were sealed. This was performed by pressurizing the membranes while confined in a "test chamber." A load bearing floor which was available at the Ferguson Laboratory was used as the bottom, bearing plate. A wood frame was constructed around the membrane. The wood frame was bolted to the floor and was used to resist lateral expansion of the membranes. The membrane was then placed on the floor with the ports pointing upward. The top of the cube

was set on the wood frame and bolted down to the floor to restrict the expansion room of the membranes as they were filled and pressurized.

Leakage was found in all membranes around the ports and along the seams near the corners. There were two primary reasons for these leaks; the complexity of constructing a large waterproof membrane from Butyl sheets and our own inexperience in working with Butyl rubber and bonding cement. Several solutions were considered: 1. cover the steel plates of the ports and nearby rubber membrane area with extra sealant and patch with an additional sheet of rubber, 2. replace the present ports with ones molded in rubber, 3. mold the membrane corners in a rubber covering, and 4. seal and patch the leaks as found by pressure testing. These solutions were judged too costly, either directly with dollars or indirectly with time, and too uncertain as to their effectiveness in preventing leaks.

The possibility of using air in the leaking membranes instead of water was re-examined. Water had the advantages previously discussed, but air had the advantage that the pressure could be maintained in the membranes, despite leakage, by continually injecting air and continuing to test. The use of air in the leaky membranes was rejected, however, because air leakage would cause vibrations disruptive to the sensitive accelerometer records and could build up a pressure in the sand in the cube so that the effective stress would not be known.

#### A.3.4 Final Membrane Design

It was evident that a new membrane design was needed and so the various solutions were reviewed. Because of the prohibitive cost, having the membranes professionally constructed was eliminated from further consideration. Of those products currently manufactured, dunnage bags and water pressure bags were most applicable. However, both bags would have to be modified in some manner before they could be used in the cube. Essentially both products are similar in design and material. The dunnage bags are intended for air inflation to protect shipped cargo and are only available in certain sizes. The water pressure bags are for water storage and can be manufactured to a variety of dimensions. Each type of bag would need a second fitting installed in the membrane to form the inflow/outflow ports. Both fittings could be placed as per specification. Filter fabric could not be used with either bag because of problems with heat generated during manufacturing and the inability to secure the filter fabric inside the membranes once constructed. In terms of materials, nylon reinforced rubber is used in the construction of both bags and each type of bag could withstand a maximum pressure of 40 psi (276 kPa) under the limited expansion which would occur in the triaxial cube. In terms of cost, water pressure bags are slightly less expensive than dunnage bags.

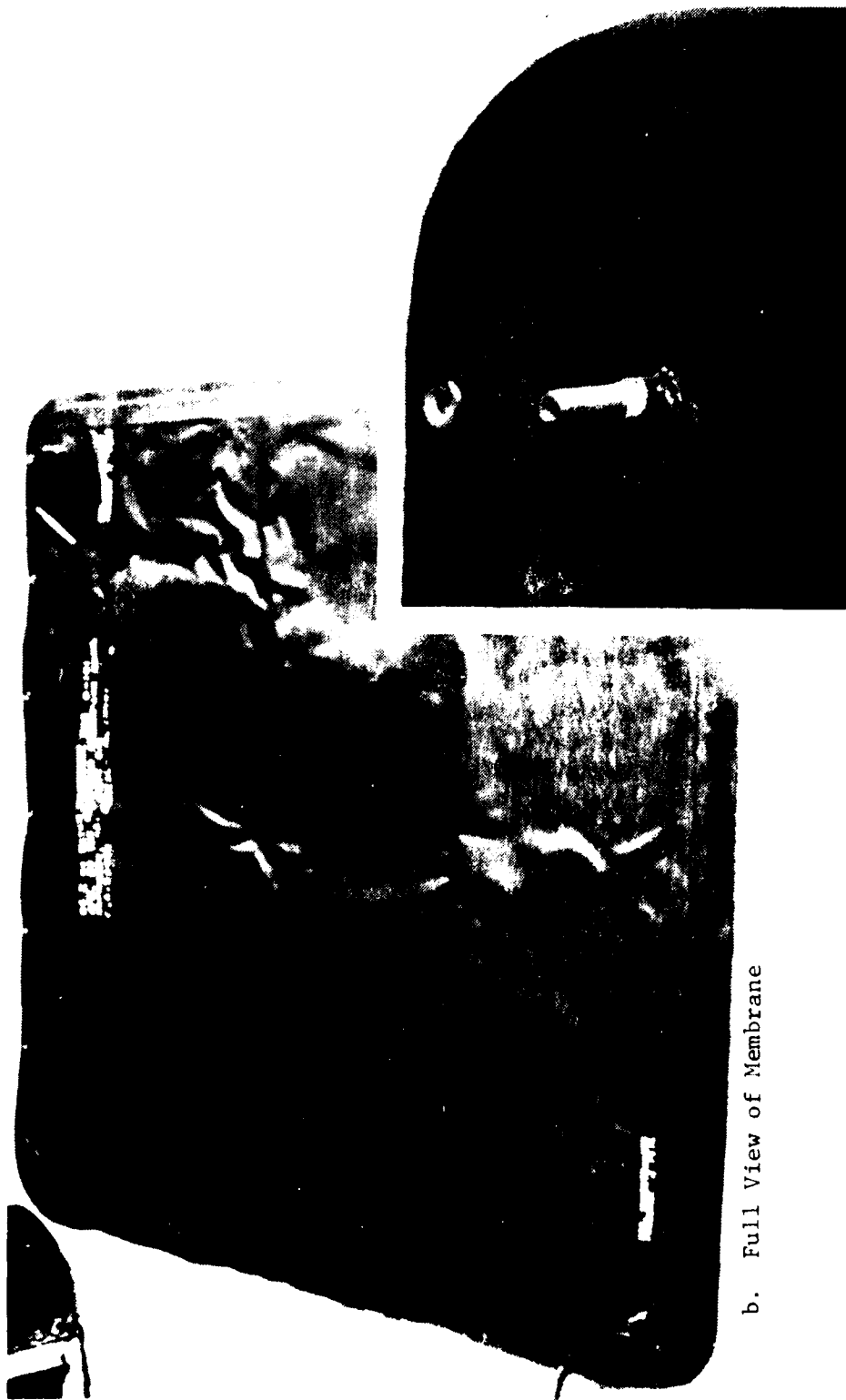
Water pressure bags, manufactured by the Goodyear Aerospace Corporation, were chosen because of the variety of sizes offered and the slightly lower cost. The loading system consists

of membranes made of 1/16-in. (0.16 cm) thick, abrasion-resistant, nylon-reinforced rubber sheeting. Each of the membranes is formed as a one-piece, vulcanized, water retaining unit, manufactured with the same dimensions as the respective cube face. Two fittings are located in opposite corners of the bags as specified. These fittings are 1/4-in. (0.64 cm) diam pipe nipples of 3/4 in. (1.91 cm) length to which pressure lines at the Ferguson Laboratory can be attached. Grommets are installed along what will become the upper edge of the two side membranes to facilitate hanging the bags on the cube during filling. Figure A.10 is a photograph of one of these membranes with a close-up view of one of the fittings.

Both heat and pressure are used to vulcanize these membranes, in a process whereby a bonding compound reacts with the rubber sheets. Paper is placed between the rubber sheets where it is desired to keep the sheets separated. When completed, the membranes are inflated to tear apart the paper which becomes stuck to the rubber sheets during the heat and pressure stages. Personnel at Goodyear felt that the paper on the inside of the membranes would act much like filter paper and allow the water pressure to be evenly distributed over the entire membrane.

#### A.3.5 Hydraulic Loading of Membranes

The membranes are loaded throughout the working pressure range of 10 to 40 psi (69 to 276 kPa). With the membranes full of water, air pressure is used to pressurize the water. This is



b. Full View of Membrane

a. Close-up View of Port

Fig. A.10 - Membrane Used to Apply Load to Sand Sample in Cube

accomplished through a specially constructed panel board shown schematically in Fig. A.11 and by a photograph in Fig. A.12. Air pressure from the Ferguson Laboratory air supply enters a manifold in the panel board at 125 psi and is then independently controlled by three air regulators, one regulator for each membrane.

The air pressure is set using the air regulators in conjunction with a 12-in. Heise type CM pressure gauge (accurate to within  $\pm 0.1$  percent of full scale reading) which is mounted in the panel board. The gauge is also used to monitor the pressure in each membrane during testing. The regulated air pressure for each membrane passes to an air-water accumulator where the air pressure is transformed into water pressure. The water pressure is then directed toward a membrane outlet in the panel board to which a pressure line from the membrane is connected.

The panel board can also be used to fill the membranes as the sand is placed. A water source from the Ferguson Laboratory is connected to the panel board. Water can be pumped directly through the accumulator to the membranes. As a membrane nears full capacity, up to 0.5 gallons (1.9 L) of water can be stored in the accumulator from where it can be forced into the membrane with the aid of air pressure.

#### A.4 EXCITATION PORTS

Since the objective of this research is to study the propagation characteristics of P- and S-waves through a soil mass, a mechanism for generating these waves at the soil boundaries is

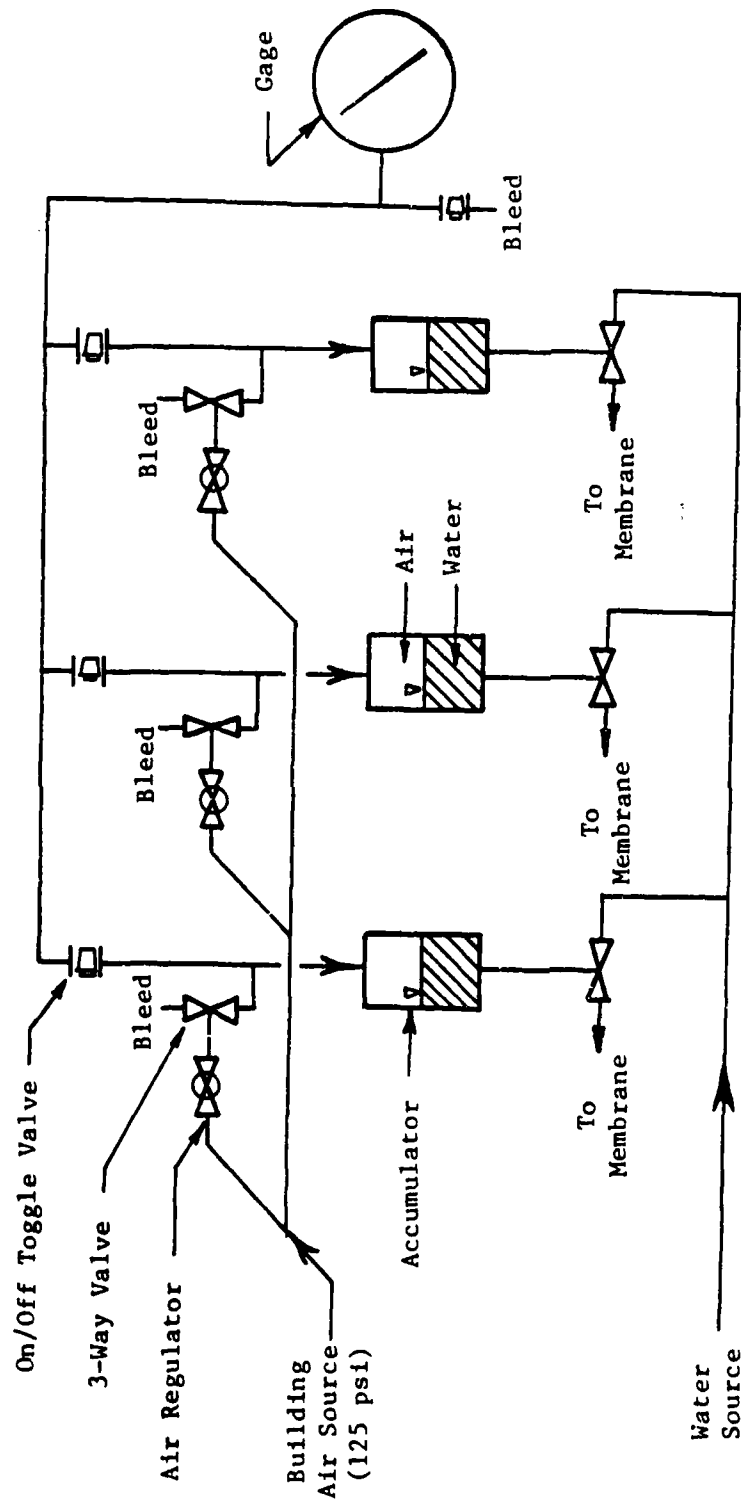


Fig. A.11 - Schematic of Air/Water System Used to Pressurize the Membranes

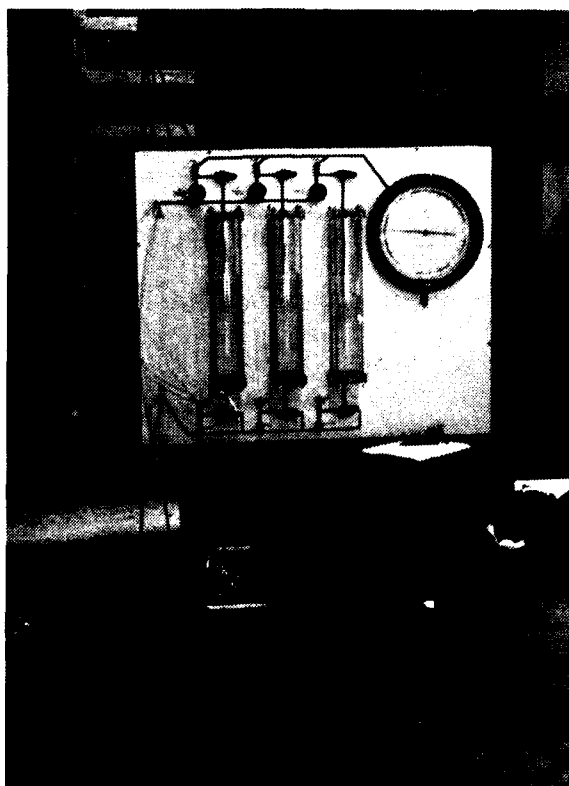


Fig. A.12 - Panel Board Used to Pressurize Membranes  
in Cube



necessary. The ideal situation is a wave source in contact with the boundary of the soil mass inside the cube which is excitable from outside the cube. To achieve this goal, ports (i.e., holes in the cube walls) have been placed in the center of three mutually perpendicular sides of the cube: the bottom and two adjacent sides.

At each port, an excitation system is attached which is composed of: 1. an excitation anvil, 2. a hand-held hammer, 3. an external frame, 4. an external adjustment screw, and 5. an internal frame.

This system (without the hand-held hammer) is shown in Figs. A.13 and A.14.

#### A.4.1 Wave Generation

The excitation port permits generation of P-waves or S-waves at the boundary of the soil mass by striking the anvil with the hand-held hammer. A 3-in. (76.2 mm) square plate at about the midlength of the shaft of the anvil is provided for the striking surface. Shear waves are generated in the soil by striking this plate either horizontally or vertically (parallel to the side of the cube). Compression waves are generated by striking the plate on the anvil in the direction of the axis of anvil (perpendicular to the side of the cube).

#### A.4.2 Soil-Anvil Contact

To generate distinct waves, intimate contact between the soil and base of the anvil is essential. The base of the anvil in contact with the soil is knurled to maximize this contact.

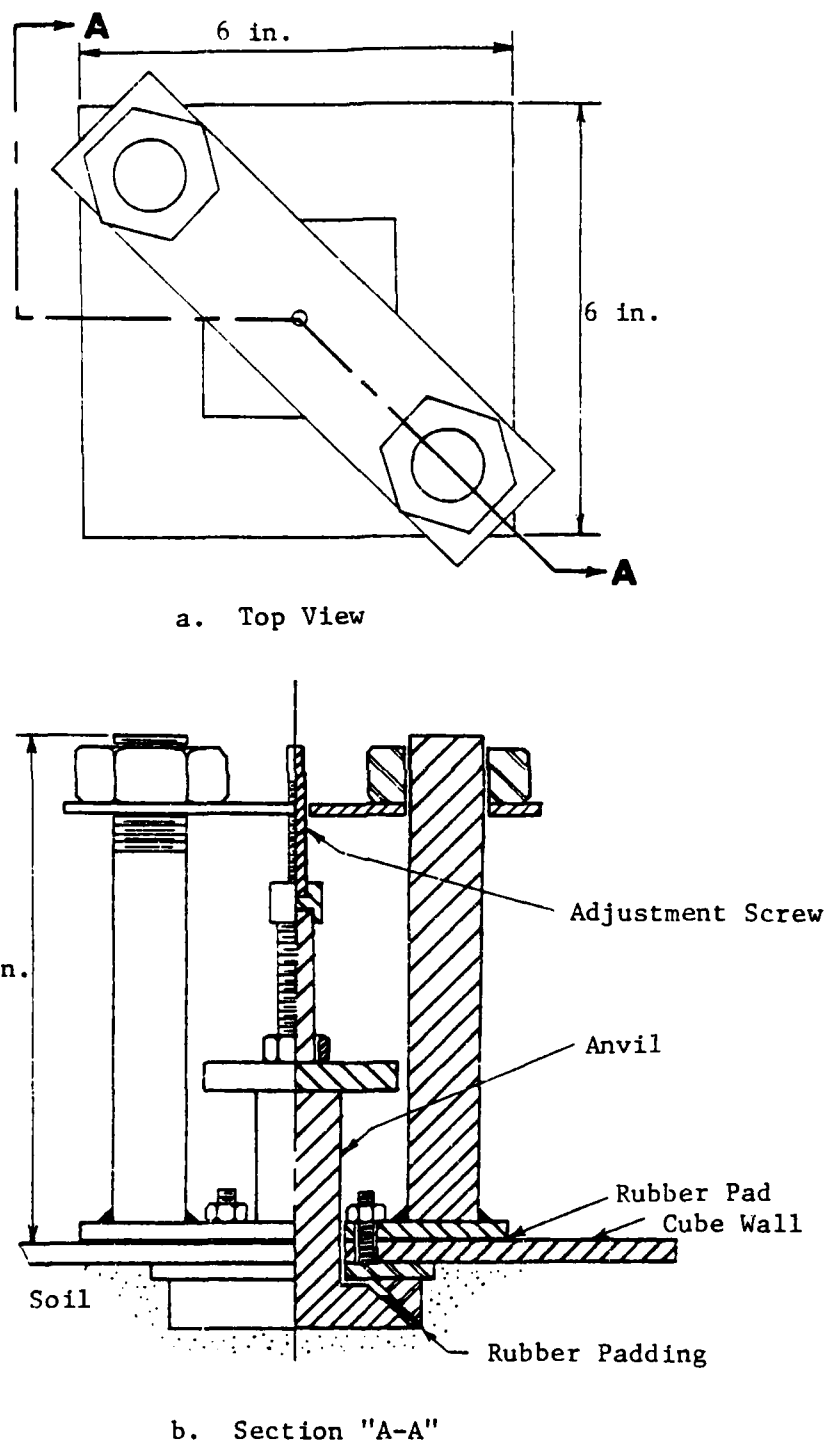


Fig. A.13 - Excitation Hammer in Each Port of Triaxial Cube

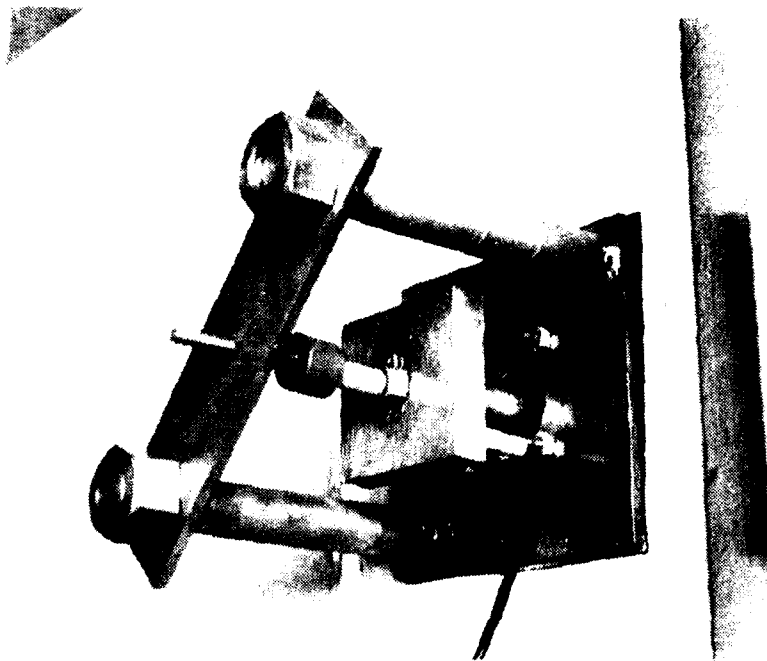


Fig. A.14 - Close-up View of Excitation Port  
Without Impulse Hammer

Additionally, the base of the anvil which is in contact with the soil must maintain the same pressure against the soil as the surrounding face of the cube. This is accomplished by using the adjustment screw shown in Fig. A.13 to push the anvil against the soil. The screw is threaded through a plate and bears against the anvil itself. The plate is part of an external frame which is bolted to the outside of the cube. The bolts holding the external frame on the outside of the triaxial cube are actually part of an internal frame which prevents soil displacement around the base of the anvil inside the cube when the anvil is excited.

#### A.4.3 Additional Design Considerations

Vibrations in the wall of the cube become background noise on the waveform records and must be minimized wherever possible. For this reason, rubber padding has been placed between the external frame and wall of the cube as shown in Fig. A.13.

The excitation port assembly protrudes about 6 in. (15.2 cm) outside of the cube (see Fig. A.14) and about 0.9 in. (2.29 cm) inside of the cube. These sizes were chosen for ease of handling and use. The base of the anvil which contacts the soil is also 3 in. (7.6 cm) square and was selected after investigation of the effect of base size on wave generation characteristics.

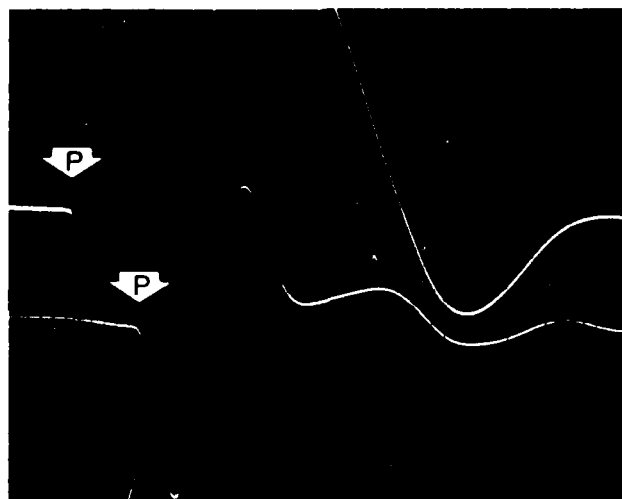
#### A.4.4 Preliminary Testing for Anvil-Base Design

Wave propagation tests were performed in the Dynamic Response Test Facility at the Balcones Research Center of The

University of Texas. This facility is composed of sand that is very similar to that which was used in the initial tests in the cube. Three different sizes of base plates were tested: 2-3/16 in., 3-1/2 in., and 4 in. (5.6 cm, 8.9 cm, and 10.2 cm) in diameter.

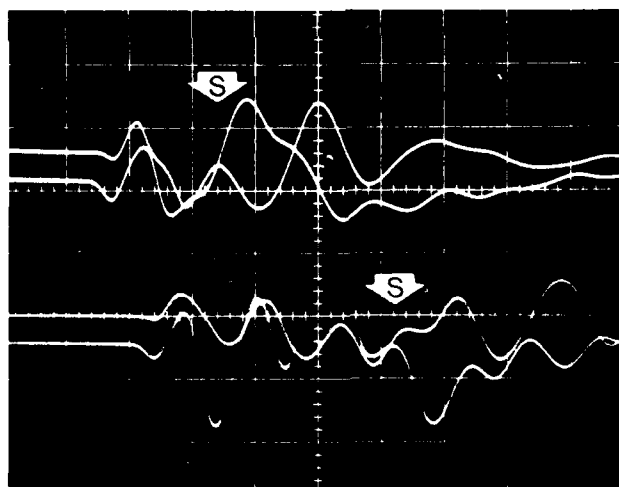
The test set-up mirrored the conditions in the cube. Horizontal and vertical geophones were buried at depths of 12 and 24 in. (30.5 and 61.0 cm) below the ground surface for monitoring the waveforms in a similar fashion to the accelerometers in the cube. The base plates were placed on the ground surface (representing the soil boundary in the cube) directly over the buried geophones. The base plates were then struck vertically and horizontally to generate P-waves and S-waves in the soil. Polaroid pictures of the traces on an analog oscilloscope were used to record the waveforms monitored by the geophones. Typical records are shown in Fig. A.15.

After analysis of over 75 records, it was concluded that the distinctness of the P-wave arrival was the same for all bases, but there was a slight improvement in the distinctness of the S-wave arrival with increasing base size. Since a small port is desirable in the cube to simulate a point source and since the improvement in the S-wave was greater between the 2-3/16-in. (5.6 cm) and 3-1/2-in. (8.9 cm) diameter plates than between the 3-1/2-in. (8.9 cm) and 4-in. (10.2 cm) diameter plates, a 3-in. (7.6 cm) square base plate for the anvil was chosen which has about the same contact area as the 3-1/2-in. (8.9 cm) diameter circular plate.



$$\begin{array}{c} \text{---} 0.001 \text{ sec} \end{array} \quad v_p = \frac{1 \text{ ft}}{0.001 \text{ sec}} = 1000 \text{ fps}$$

- a. Travel Time Record of Compression Wave Using Vertical Geophones



$$\begin{array}{c} \text{---} 0.0028 \text{ sec} \end{array} \quad v_p = \frac{1 \text{ ft}}{0.0028 \text{ sec}} = 360 \text{ fps}$$

- b. Travel Time Record of Shear Wave Using Horizontal Geophones

Fig. A.15 - Typical Travel Time Records for Surface Source and Embedded Receivers

## A.5 MONITORING AND RECORDING SYSTEM

Compression and shear waves propagating through the sand in the cube are monitored and recorded with the electronics shown schematically in Fig. A.16. The core of this measurement system is a spatial array of three-dimensional (3-D) accelerometers buried in the soil. Three, 3-D accelerometers are placed along each of the three principal axes of the sand mass as shown in Figs. A.3 and A.4. A spacing of about 1.5 ft (0.46 m) is used between adjacent 3-D accelerometers. Spacing between the accelerometers closest to the cube wall and the wall is about 2 ft (0.61 m) so that minimum interference is caused by reflections of the waves off of the walls (as discussed in Section 6.8.2). A pair of digital oscilloscopes are used to record the accelerometer signal output.

### A.5.1 Accelerometers

Each 3-D accelerometer package is composed of three accelerometers rigidly attached in a 1.57-in. (44 mm) square wooden block as shown in Figs. A.17 and A.18. One accelerometer is aligned along each of the three principal axes of the cube. Wood (birch) was chosen as the 3-D accelerometer housing material so that the weight of the 3-D package would equal that of the sand displaced by the package and so that the stiffness difference between the block and surrounding sand would be minimized. The average weight of the 3-D packages including accelerometers is 0.31 lb (0.16 kg) resulting in an average density of 100.3 pcf

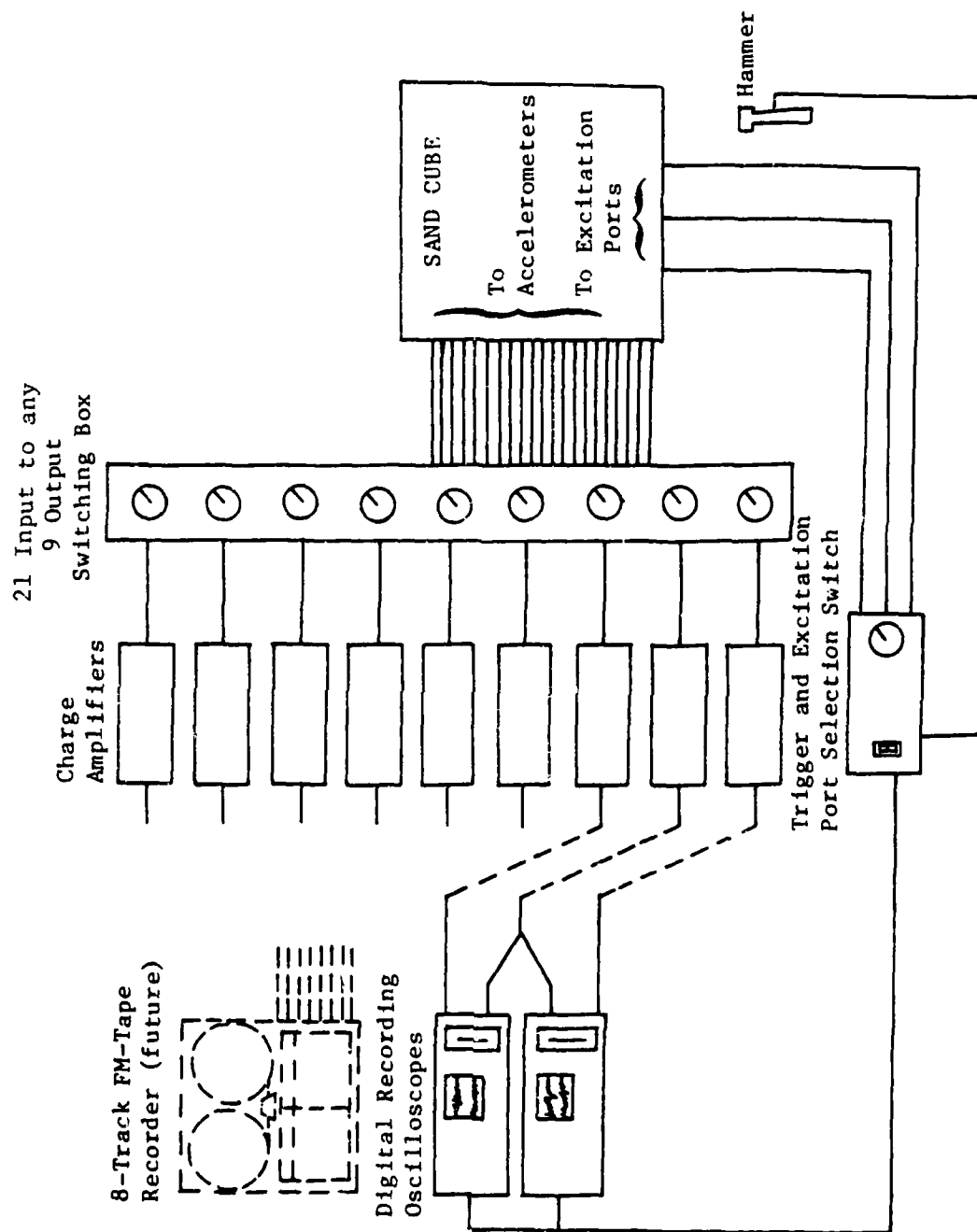


Fig. A.16 - Schematic of Monitoring and Recording Systems



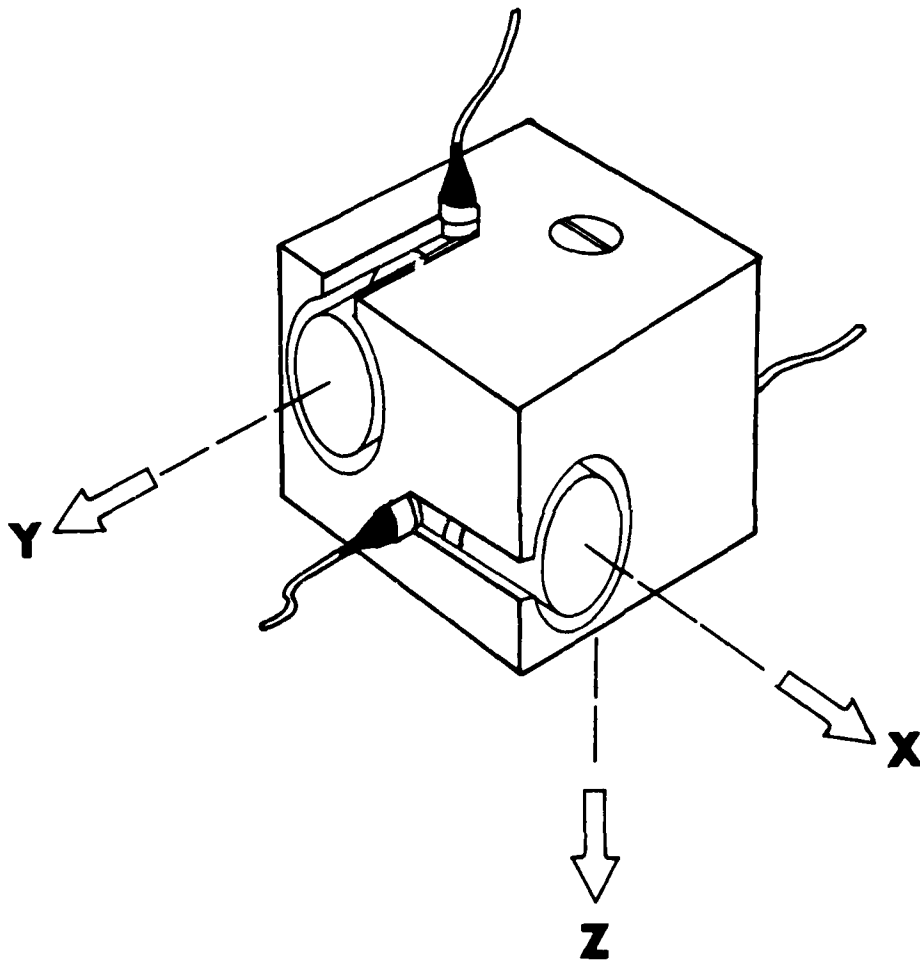


Fig. A.17 - Isometric View of 3-D Accelerometer Package

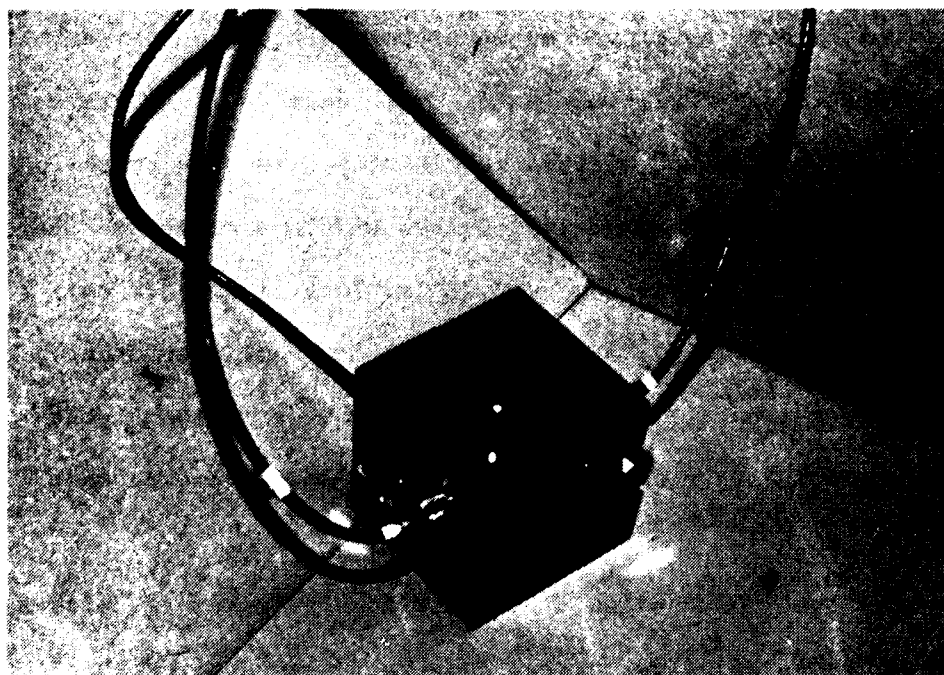


Fig. A.18 - Three-Dimensional Accelerometer  
Block with Accelerometers Installed

(1623 kg/m<sup>3</sup>) compared to an average density of about 96.6 pcf (1563 kg/m<sup>3</sup>) for the sand (see Section B.2.1).

Monitoring of low-amplitude wave propagation through the sand requires highly sensitive accelerometers. Endevco Isoshear accelerometers, model 7701, were used. Each accelerometer has a sensitivity of 0.001 g and a cross sensitivity (sensitivity to movement not along the major axis) of less than one percent. They are small in size (0.625 in. dia. x 0.78 in. long (1.6 x 2.0 cm)) and weight (1.0 oz. (28 g)) so as to create minimum interference as a wave passes and to track closely the particle motion of the wave. Figure A.19 shows the placement of one accelerometer into the wooden block.

The electronic signal from each accelerometer is carried by a coaxial cable of silver plated copperweld conductor with a fused teflon jacket designed for signal reliability. To ensure integrity of the wire in the cube during testing, a soil specimen of the same sand used in the cube was prepared for static triaxial soil testing with a piece of wire embedded in it. After a number of isotropic, drained loading cycles, the sample was sheared under drained conditions. No degradation of the wire or wire covering was evident. Therefore, it was assumed that no additional protection was required for the cables in the triaxial cube.

The electrical cables from the accelerometers pass through two small ports in the east side of the cube. After all the wires are inserted, the ports are sealed against sand loss by a



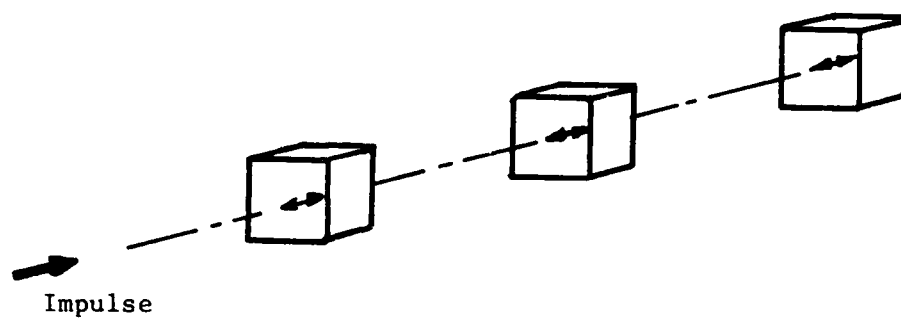
Fig. A.19 - Accelerometer Being Placed into a  
3-D Accelerometer Block

waterproofing rubber sealant applied from the inside of the cube. The 21 wires are connected to a switching box outside the cube so that any nine accelerometers can be connected with charge amplifiers. Any of these nine signals may then be recorded on the digital oscilloscopes, FM digital tape recorder (future), or spectrum analyzer (future).

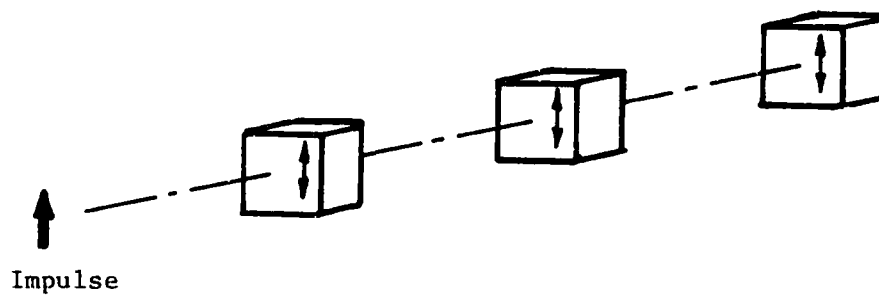
#### A.5.2 Recording Devices

Normally three accelerometers are monitored simultaneously each time an impulse is applied to the source. The three accelerometers of interest lie along the axis of the source being excited and are sensitive along the same direction as the motion of the anvil as illustrated in Fig. A.20. Because each digital oscilloscope is only a two-channel device, two oscilloscopes are required to record the output from the three accelerometers with one accelerometer output being duplicated between the two oscilloscopes for reference. The oscilloscopes are triggered electronically when the hand-held hammer strikes the anvil of the excitation port. At this instant, a voltage drop is sent from the trigger to the oscilloscope by means of a resistance-capacitance circuit initiating the recording cycle. The trigger has a switch to select any of the three excitation ports in use.

With the digital oscilloscope, each waveform is recorded on a floppy diskette for later recall and study. By saving a waveform digitally, the arrival times and amplitudes may be directly



a. P-Wave Accelerometer Orientation



b. Typical S-Wave Accelerometer Orientation

Fig. A.20 - Accelerometer Orientation in 3-D Packages  
Relative to Impulse of Source

read from the oscilloscope upon replaying the digital record. The possibility of future direct oscilloscope-computer hook-up is also possible. In the future, rather than the oscilloscope, an FM digital tape recorder or spectrum analyzer can be used permitting recording for analysis in the laboratory at a later date or direct Fourier analysis.

#### A.6 STRESS MEASUREMENT

Stresses in the sand within the cube were monitored by total stress cells within the sand and by pressure gages measuring the water pressure in the membranes. This was done in an attempt to insure that the pressure in the sand is the same as that applied through the loading system. Three total pressure cells, manufactured by Terra Technology, were used to monitor soil pressure in each of the three principal stress directions. Each cell is a 0.375-in. (0.95 cm) thick by 6-in. (15.2 cm) square unit filled with oil (see Fig. A.21). A change in stress on the square face of the cell changes the pressure that the oil exerts on an electric sensor. The sensor is housed in a 1-in. dia. by 8-in. long (2.5 x 20.3 cm) sensing unit, rigidly attached to the cell by a thin tube approximately 0.38-in. dia. by 6-in. long (.95 x 15.2 cm) which therefore must also be placed in the soil. A pressure change causes a deformation of a small strain gage in the sensor, resulting in a piezoresistive change in the gage full inductance bridge. The signal generated is carried by four-wire cables through

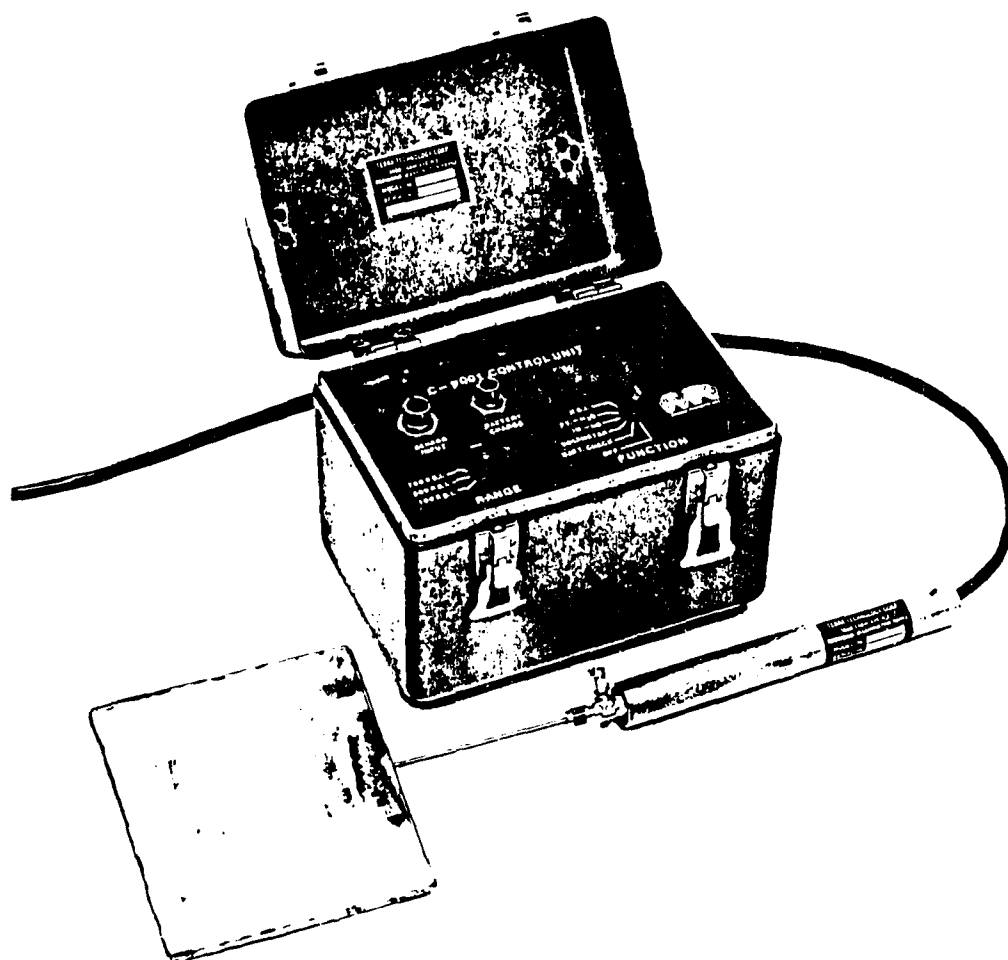


Fig. A.21 - Soil Stress Cell and Control Unit  
(from Terra Technology literature)



sealed holes in the east and south faces of the cube to an external control unit.

The control unit automatically converts the signal from the sensing unit into a digital output for direct pressure reading in units selectable of psi, feet of water, or inches of mercury. Three pressure ranges are available: 0-100 psi, 0-300 psi, 0-750 psi (0-698, 0-2067, 0-5168 kPa). Since the maximum design pressure of the cube is 50 psi (345 kPa), the smallest range, 0-100 psi (0-698 kPa), was used.

The cells were positioned in the cube so that they did not interfere with generation or monitoring of P- and S-waves. Details on the placement and results of the stress cells are discussed in Section B.3.2.

#### A.7 STRAIN MEASUREMENT

To monitor strains in the soil sample during confinement, six pairs of soil strain gages were embedded in the sand when the sample was constructed. Bison soil strain gages, model 4000 series, were used. Each pair of gages consists of two, free-floating, disk-shaped sensors embedded in the sand and separated by a known distance. Two sizes were used in these tests as shown in Fig. A.22: 0.25-in. thick by 2-in. diam (0.64 x 5.1 cm) and 0.38-in. thick by 4-in. diam (0.96 x 10.2 cm). One sensor acts as a driving coil and the other as the receiving coil. The roles are interchangeable and determined by the control unit outside the triaxial cube. The separation of the sensors is related to the electro-magnetic

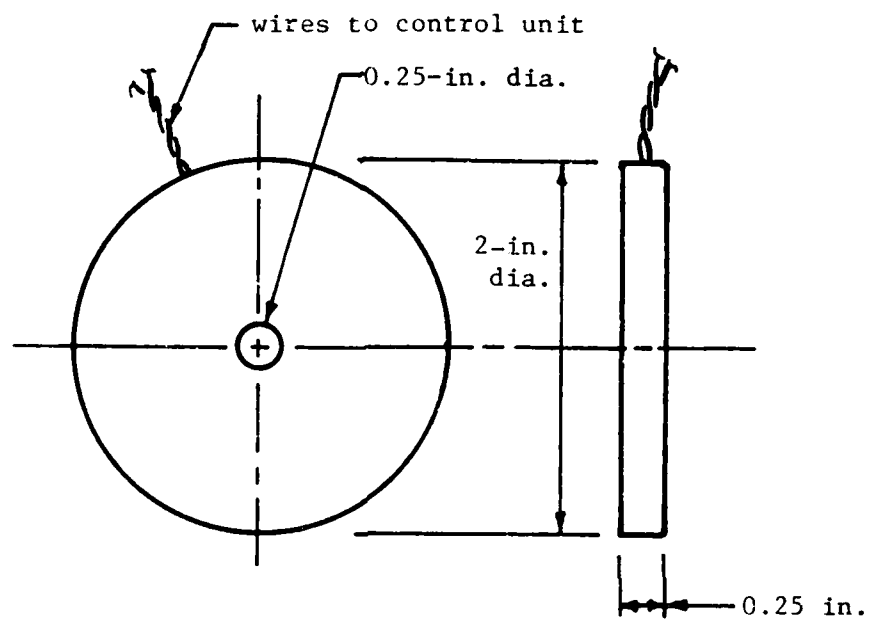


Fig. A.22 - Typical 2-in. Diameter Soil Strain Gage

coupling between the sensors, acting in the same manner as the primary and secondary windings of a transformer (Wetzel and Vey, 1970; Truesdale and Schwab, 1967). The amplitude dial reading resulting from balancing an inductance bridge is calibrated to the absolute spacing of the sensors. Strain may be calculated from the difference between initial and final spacings. The output meter used for balancing may be calibrated to read strain for a single set of coils directly from the offset from null position if the strain is less than four percent. However, in these tests, several sets of coils were used, so strain had to be calculated from the difference between individual readings.

Each pair of gages is used to measure strain only along the axis running from the center of one sensor to the center of the other in the pair with both sensors facing each other. Therefore, six pairs are used in the cube: a 2-in. (5.1 cm) diam pair separated 4 in. (10.2 cm) and a 4-in. (10.2 cm) diam pair separated 8 in. (20.4 cm), each oriented parallel to an axis of the cube. The gages were positioned such that they would not interfere with wave propagation and conversely, any steel components would not interfere with the electro-magnetic field generated by the sensors.

Each sensor size (2-in. and 4-in. (5.1 and 10.2 cm) diameter) has a separate set of calibration curves. Although cable length will affect the calibration within a sensor size, the cables of the sensors used are similar enough so that the same

calibration curves for a given size can be used without any loss of accuracy.

The wires from each sensor were passed through holes that were later sealed in the east face of the cube. The wires were attached to a switching box outside the cube. The sensors may be read one pair at a time on the external control unit which contains all the driving, balancing and output components required to operate the sensors. The control unit has an optional output port which can be attached to a recorder to monitor strain with time. This option is not necessary for the current research.

Details on placement in the sand, problems with the unit, and final results are presented in Section 5.3.3.

## A.8 TEST SAMPLE

### A.8.1 Soil-Cube Boundary

Uniform stress throughout the soil sample can be achieved only if there is no restraint at the soil-cube boundaries; that is, the soil must be free to move parallel to the face (free-free condition) (Rowe and Barden, 1964; Roscoe, 1953; Bishop and Green, 1965). To allow this movement, greased plastic sheets were placed between all six faces of the cube and the sand sample.

The greased sheets were composed of two layers of 4-mil (0.1 mm) polyethylene separated by a thin coat of WD-40 oil. The method of attachment of the sheets to the cube is presented in Section 3.1.

#### A.8.2 Sand Placement

The object of the sand placement system was to fill the cube with sand of a uniform density over the entire height of the cube. The method of raining sand through air (pluviation) was chosen over other methods because of the efficiency and uniformity of placement attainable with this method. Raining sand through air has been shown to yield uniform, medium-dense samples when the height of fall is 2.5 ft (.76 m) or greater (Kilbuszewski, 1948; Beiganousky and Marcusson, 1976). Marcusson and Beiganousky (1977) also found that when they rained sand through several layers of screens with openings of about 0.25 in. (0.64 cm), the variation in density was only  $\pm 0.5$  pcf ( $8 \text{ kg/m}^3$ ) for a given drop height.

The original raining system is shown in Fig. A.23 and is composed of a "V" shaped hopper which can be moved across the top of the cube. The outlet at the bottom of the hopper is 8 in. (20.3 cm) wide by 7 ft (1.73 m) long. The hopper has a gate for flow control and two screens (with mesh openings of 0.25 in. (0.64 cm)) spaced approximately 3 in. (7.6 cm) apart just above the bottom of the hopper. The gate is comprised of a series of twelve, 3-in. by 12-in. (7.6 cm by 30.5 cm) doors that are regulated in tandem by a lever system allowing adjustment of the opening size. The hopper sits on a 30-in. (76.2 cm) high wooden collar which bolts to the top of the cube so that the drop height of the sand into the cube ranges from 9.5 ft (2.9 m) at the start of the filling operation to 2.5 ft (0.8 m) at the conclusion. The volume

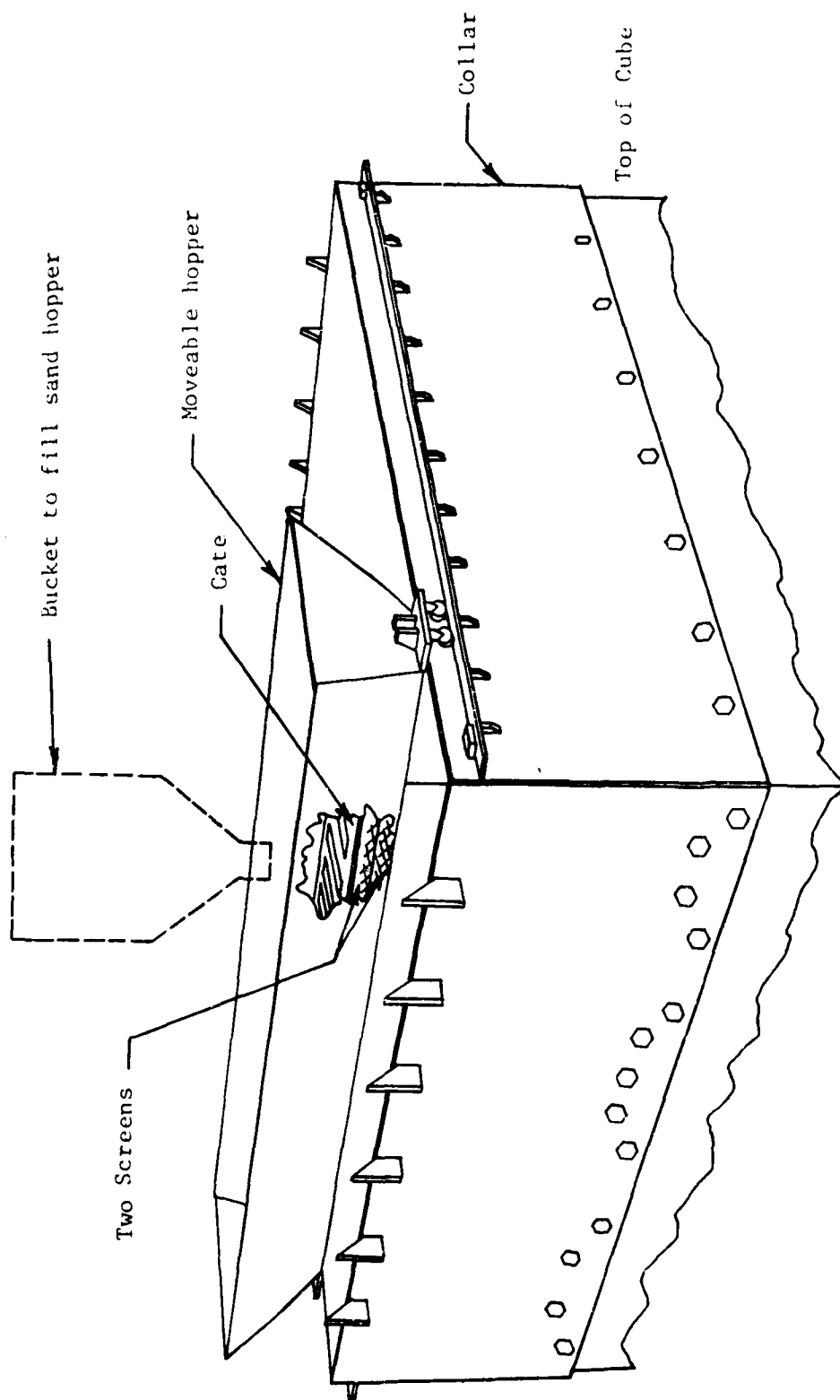


Fig. A.23 - Original Sand Placement System

held by the rainer is approximately 7 cu ft ( $0.2 \text{ m}^3$ ) which results in depositing a layer slightly more than 1-in. (2.5 cm) thick for each filling. For convenience, the bolt holes in the collar match those around the perimeter of the top of the cube so that the collar can easily be attached. The entire system is disassembled and stored when not in use. The method for placing sand using the original raining system and a modified version is discussed in Section 5.3.1.

#### A.8.3 Density Measurement of Sample

A special density device was constructed to measure density of the sand sample during construction to evaluate its uniformity while the cube was being filled. Three identical containers were made of 0.25-in. (.64 cm) thick plexiglass. The containers had an ID of 6 in. (15.2 cm) and a height of 3 in. (7.6 cm), which resulted in a volume of 8.64 cu in. (0.05 cu ft or 142 cu cm). The top edge of the cylinder was machined to an angle of 45 degrees sloping out to minimize additional sand bouncing into the container upon striking the container during the raining process. Details on placement and results are in Section 5.3.1.

#### A.9 SUMMARY

The triaxial testing device was designed and built to hold a soil cube measuring 7 ft (2.1 m) on a side. Membranes were purchased to place between the cube face and the soil to apply pressure from the panel board to the soil. Apparatus for generating, monitoring, and recording P- and S-waves were acquired as

were stress and strain monitoring devices. Methods for raining the sand into the cube and monitoring its density were devised. With the cube and associated equipment complete, the sand was then chosen, and the filling of the cube was begun.



APPENDIX B

TESTING PROGRAM AND PROCEDURES

Taken in Full from Kopperman et al (1982)

## APPENDIX B

### TESTING PROGRAM AND PROCEDURES

#### B.1 INTRODUCTION

The initial testing program for the model cube consisted of measurement of velocity and attenuation of compression and shear waves through a dry sample of sand of medium density. The sample was constructed in May and June, 1981, over a period of six weeks. It was subsequently loaded with the following three pressure sequences: first, a sequence using isotropic confinement; second, a sequence using confinement with a constant mean effective principal stress; and finally, a sequence using confinement with a varying mean effective principal stress. The sequences of loading are listed in Table B.1 and shown graphically with time in Fig. B.1.

##### B.1.1 Isotropic Confinement

Loading with a series of isotropic steps was initially performed to determine the relationship between velocity and mean effective principal stress,  $\bar{\sigma}_0$ , as determined in the cube. These results were also used to: 1. compare with standard laboratory resonant column tests run on the same sand, and 2. evaluate the structural anisotropy of the sample.

TABLE B.1  
Pressure Loading Sequences

Test No.	Date of Test (1981) Month and Day	Effective Vertical Stress	Effective Horizontal Stresses		Mean Effective Principal Stress	Earth Pressure Coefficients	
		$\bar{\sigma}_v$	$\bar{\sigma}_{NS}$	$\bar{\sigma}_{EW}$	$\bar{\sigma}_o$	$K_{13} = \frac{\bar{\sigma}_1}{\bar{\sigma}_3}$	$K_{23} = \frac{\bar{\sigma}_2}{\bar{\sigma}_3}$
(1)	(2)	(psi) (3)	(psi) (4)	(psi) (5)	(psi) (6)	(7)	(8)
1. ISOTROPIC CONFINEMENT							
1	7/8	10	10	10	10	1.00	1.00
2	7/9	20	20	20	20	1.00	1.00
3	7/14	40	40	40	40	1.00	1.00
4	7/14	20	20	20	20	1.00	1.00
5	7/14a	20	20	20	20	1.00	1.00
2. CONSTANT MEAN EFFECTIVE PRINCIPAL STRESS							
5	7/21	22	19	19	20	1.16	1.00
6	7/21	24	18	18	20	1.33	1.00
7	7/21	26	17	17	20	1.53	1.00
8	7/22	28	16	16	20	1.75	1.00
9	7/22	30	15	15	20	2.00	1.00
10	7/22	32	14	14	20	2.29	1.00
11	7/23	28	16	16	20	1.75	1.00
12	7/23	24	18	18	20	1.33	1.00
13	7/23	20	20	20	20	1.00	1.00
14	7/23	22	20	18	20	1.22	1.10
15	7/23	24	18	18	20	1.33	1.00
16	7/24	26	18	16	20	1.63	1.12
17	7/24	26	20	14	20	1.86	1.43
18	7/24	28	18	14	20	2.00	1.28
19	7/24	30	16	14	20	2.14	1.14

TABLE B.1  
Pressure Loading Sequences  
(Continued)

Test No.	Date of Test (1981) Month and Day	Effective Vertical Stress	Effective Horizontal Stresses		Mean Effective Principal Stress	Earth Pressure Coefficients	
		$\bar{\sigma}_v$	$\bar{\sigma}_{NS}$	$\bar{\sigma}_{EW}$	$\bar{\sigma}_o$	$K_{13} = \frac{\bar{\sigma}_1}{\bar{\sigma}_3}$	$K_{23} = \frac{\bar{\sigma}_2}{\bar{\sigma}_3}$
(1)	(2)	(psi) (3)	(psi) (4)	(psi) (5)	(psi) (6)	(7)	(8)
20	8/5	36	12	12	20	3.00	1.00
21	8/5	34	14	12	20	2.83	1.16
22	8/5	30	18	12	20	2.50	1.50
23	8/5	25	23	12	20	2.08	1.92
3. VARYING MEAN EFFECTIVE PRINCIPAL STRESS							
24	8/6	15	15	15	15.0	1.00	1.00
25	8/6	20	15	15	16.7	1.33	1.00
26	8/6	25	15	15	18.3	1.67	1.00
27	8/6	30	15	15	20.0	2.00	1.00
28	8/6	35	15	15	21.7	2.33	1.00
29	8/6	40	15	15	23.3	2.67	1.00
30	8/6	40	20	20	26.7	2.00	1.00
31	8/7	40	25	25	30.0	1.60	1.00
32	8/7	40	30	30	33.3	1.33	1.00
33	8/7	40	35	35	36.7	1.14	1.00
34	8/7	40	40	40	40.0	1.00	1.00
35	8/7	40	35	35	36.7	1.14	1.00
36	8/7	40	30	30	33.3	1.33	1.00
37	8/10	40	25	25	30.0	1.60	1.00
38	8/10	40	20	20	26.7	2.00	1.00
39	8/10	40	15	15	23.3	2.67	1.00
40	8/10	35	15	15	21.7	2.33	1.00

TABLE B.1  
Pressure Loading Sequences  
(Continued)

Test No.	Date of Test (1981) Month and Day	Effective Vertical Stress	Effective Horizontal Stresses		Mean Effective Principal Stress	Earth Pressure Coefficients	
		$\bar{\sigma}_v$	$\bar{\sigma}_{NS}$	$\bar{\sigma}_{EW}$	$\bar{\sigma}_o$	$K_{13} = \frac{\bar{\sigma}_1}{\bar{\sigma}_3}$	$K_{23} = \frac{\bar{\sigma}_2}{\bar{\sigma}_3}$
(1)	(2)	(3) (psi)	(4) (psi)	(5) (psi)	(6) (psi)	(7)	(8)
41	8/10	30	15	15	20.0	2.00	1.00
42	8/10	25	15	15	18.3	1.67	1.00
43	8/11	20	15	15	16.7	1.33	1.00
44	8/11	15	15	15	15.0	1.00	1.00
45	8/11	40	15	15	23.3	2.67	1.00
46	8/11	40	20	15	25.0	2.67	1.33
47	8/11	40	25	15	26.7	2.67	1.67
48	8/11	40	30	15	28.3	2.67	2.00
49	8/14	40	35	15	30.0	2.67	2.33
50	8/14	40	40	15	31.7	2.67	2.69
51	8/14	40	35	15	30.0	2.67	2.33
52	8/17	40	30	15	28.3	2.67	2.00
53	8/17	40	25	15	26.7	2.67	1.67
54	8/17	40	20	15	25.0	2.67	1.33
55	8/17	40	15	15	23.3	2.67	1.00
56	8/17	15	15	15	15.0	1.00	1.00
57	8/17	15	20	15	16.7	1.33	1.00
58	8/17	15	25	15	18.3	1.67	1.00
59	8/17	15	30	15	20.0	2.00	1.00
60	8/18	15	35	15	31.7	2.33	1.00
61	8/18	15	40	15	23.3	2.67	1.00
62	8/18	20	40	15	25.0	2.67	1.33
63	8/18	25	40	15	26.7	2.67	1.67

TABLE B.1  
Pressure Loading Sequences  
(Continued)

Test No.	Date of Test (1981) Month and Day	Effective Vertical Stress $\bar{\sigma}_v$ (psi)	Effective Horizontal Stresses $\bar{\sigma}_{NS}^*$ (psi)	$\bar{\sigma}_{EW}^{**}$ (psi)	Mean Effective Principal Stress $\bar{\sigma}_o$ (psi)	Earth Pressure Coefficients $K_{13} = \frac{\bar{\sigma}_1}{\bar{\sigma}_3}$	$K_{23} = \frac{\bar{\sigma}_2}{\bar{\sigma}_3}$
(1)	(2)	(3)	(4)	(5)	(6)	(7)	(8)
64	8/18	30	40	15	28.3	2.67	2.00
65	8/19	35	40	15	20.0	2.67	2.33
66	8/19	40	40	15	31.7	2.67	2.67
67	8/19	20	20	20	20.0	1.00	1.00
68	8/19	10	10	10	10.0	1.00	1.00

\*  $\bar{\sigma}_{NS}$  = effective principal stress along the north-south (horizontal) axis of the cube

\*\*  $\bar{\sigma}_{EW}$  = effective principal stress along the east-west (horizontal) axis of the cube

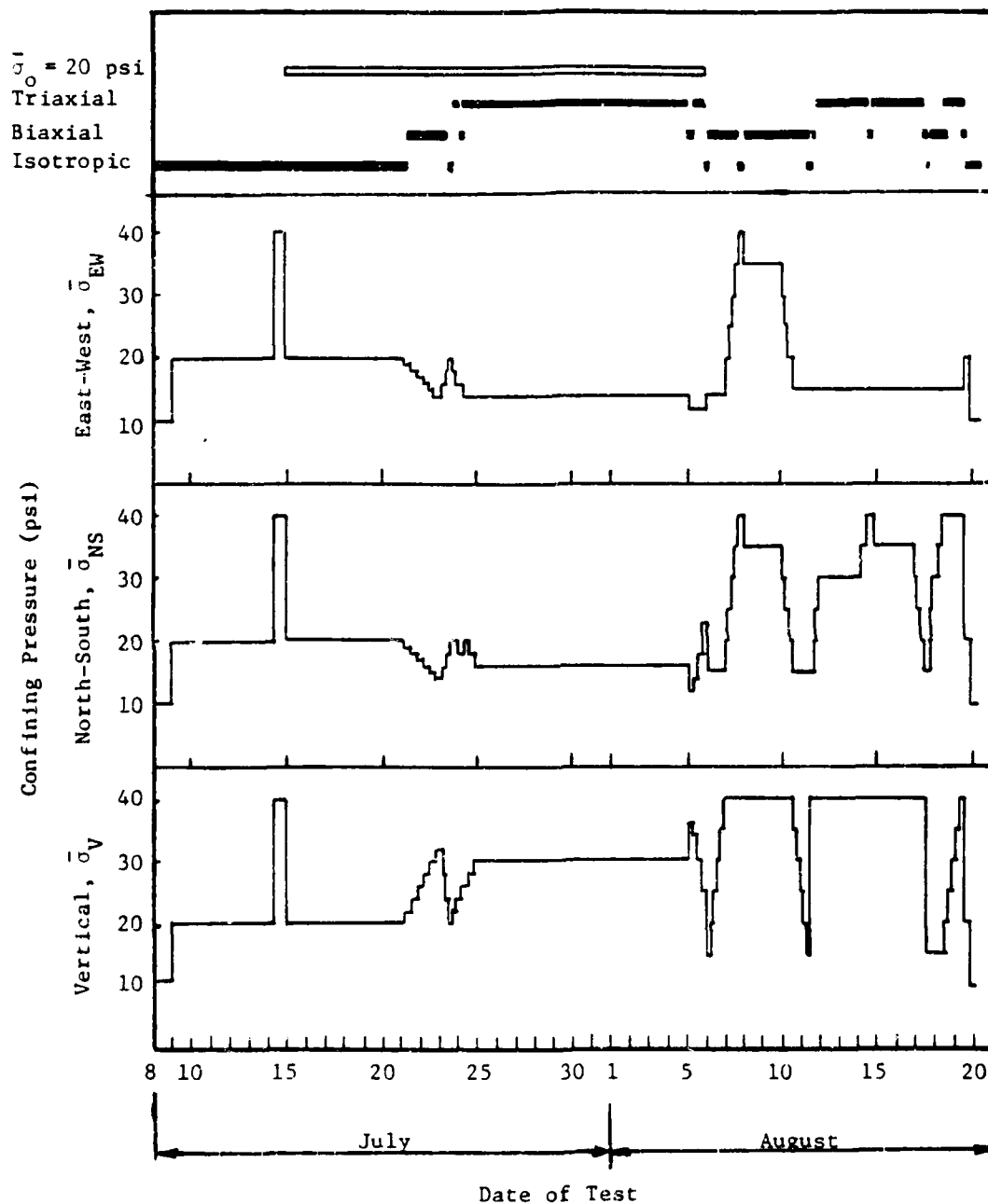


Fig. B.1 - Variation in Confining Pressure Along each Axis of the Cube with Time

### B.1.2 Confinement with Constant Mean Effective Principal Stress

The isotropic series was followed by a series of tests with a constant  $\bar{\sigma}_0$ . These tests included both biaxial and triaxial loadings. In the biaxial series, a lateral pressure coefficient,  $K_{13}$ , was used to describe the tests as:

$$K_{13} = \frac{\bar{\sigma}_1}{\bar{\sigma}_3} \quad (5.1)$$

where:  $\bar{\sigma}_1$  = major effective principal stress, and

$\bar{\sigma}_3$  = minor effective principal stress.

In these tests,  $K_{13}$  was varied while  $\bar{\sigma}_0$  was kept constant at 20 psi (138 kPa). In the triaxial series, a second earth pressure coefficient,  $K_{23}$ , was defined as:

$$K_{23} = \frac{\bar{\sigma}_2}{\bar{\sigma}_3} \quad (5.2)$$

where:  $\bar{\sigma}_2$  = intermediate effective principal stress.

The value of  $K_{23}$  varied in addition to variation of  $K_{13}$ . The value of  $\bar{\sigma}_0$  was kept constant at 20 psi (138 kPa) through the triaxial series. The mean effective principal stress was kept constant to investigate the assumption by Hardin and Black (1966) that the shear wave velocity and attenuation are a function only of  $\bar{\sigma}_0$  and, therefore, should not vary if  $\bar{\sigma}_0$  does not vary.

The biaxial series involved slowly increasing the vertical stress while decreasing the lateral stress. The value of  $K_{13}$  increased from 1.00 (isotropic) to 2.29, but the stress remained safely below the shear failure envelope as shown in Fig. B.2.



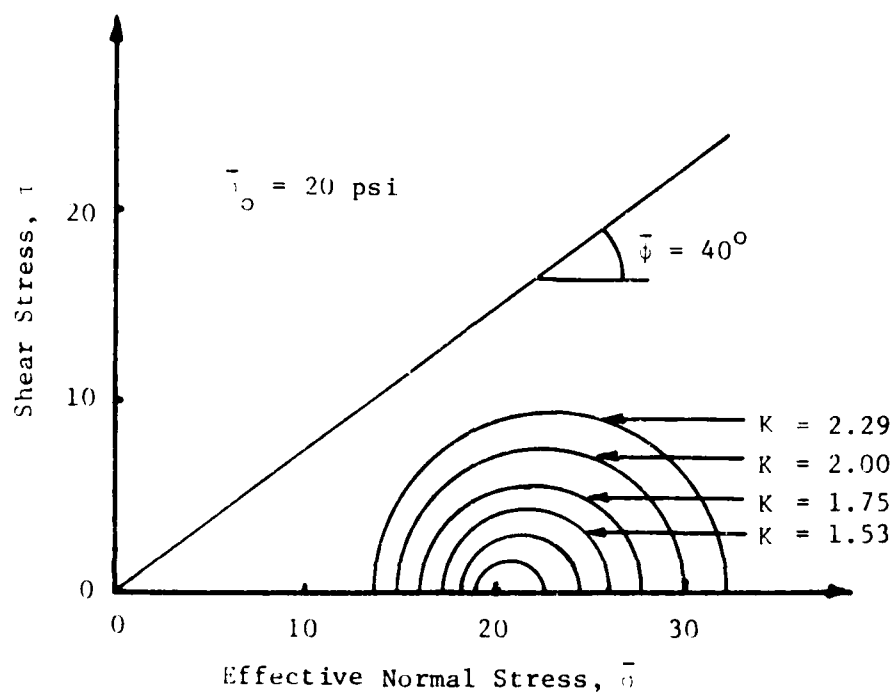


Fig. B.2 - Mohr-Coulomb Envelope for Biaxial Confinement with Constant Mean Effective Principal Stress

The biaxial loading sequence was reversed, and readings were repeated at several previous states of stress to determine if a hysteretic effect existed.

Once the isotropic state of 20 psi (138 kPa) was again achieved upon completion of the biaxial series, the triaxial series of confinement with constant  $\bar{\sigma}_0$  was begun. The vertical stress was increased, and the lateral stress was decreased to maintain a constant  $\bar{\sigma}_0$  and also remain below the failure envelope as shown in Fig. B.3. However, in the triaxial series, the intermediate principal stress was not kept equal to the minor principal stress, thereby permitting  $K_{23}$  to range from 1.00 to 1.90. The limits of  $K_{23}$  are a minimum of 1.00 for isotropic loading and biaxial loading where  $\bar{\sigma}_2$  equals  $\bar{\sigma}_3$ , and a maximum equal to  $K_{13}$  for biaxial loading where  $\bar{\sigma}_2$  equals  $\bar{\sigma}_1$ . The constant  $\bar{\sigma}_0$  sequence was chosen to minimize pressure differences between steps with the usual change being only 2 psi (14 kPa) in any direction.

#### B.1.3 Confinement with Varying Mean Effective Principal Stress

Originally, the first two series were going to complete the initial testing of the sand sample. However, upon examination of the initial results, it was decided to add a third pressure series in which the mean effective principal stress was varied. As a result, additional biaxial and triaxial testing was performed.

To start the series, the sample was lowered to an isotropic pressure of 15 psi (103 kPa). A biaxial sequence was performed by

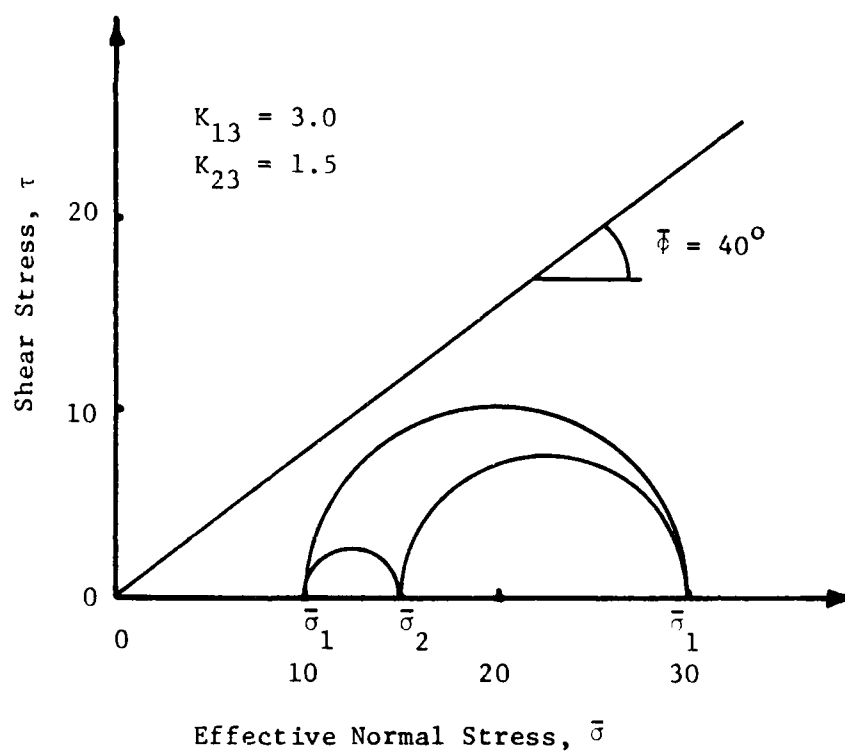


Fig. B.3 - Mohr-Coulomb Envelope for a Typical Test Under Triaxial Confinement

increasing the vertical stress to 40 psi (276 kPa) in 5-psi (34 kPa) increments while maintaining constant horizontal stresses. In this way, the effect on the compression and shear wave velocities of varying only the major principal stress,  $\bar{\sigma}_1$ , could be studied. The horizontal stresses were then increased to 40 psi (276 kPa) in 5-psi (34 kPa) increments while keeping the vertical stress constant at 40 psi (276 kPa). This sequence was performed to study the effect of varying only the minor principal stress,  $\bar{\sigma}_3$ , on  $V_p$  and  $V_s$ .

At this point in testing, the cube was at an isotropic confinement of 40 psi (276 kPa) which was also the maximum pressure achieved at the end of the first isotropic confinement series. The data gathered at this pressure was used together with other such points when an isotropic confinement existed, to study the effect of stress history on the wave velocity. To observe if there was any hysteresis in the data from the biaxial tests, the entire sequence was run again in reverse order: first,  $\bar{\sigma}_3$  was lowered in 5-psi (34 kPa) increments to 15 psi (103 kPa) and then  $\bar{\sigma}_1$  was lowered in 5-psi (34 kPa) increments to 15 psi (103 kPa). The final test in this sequence was again at an isotropic confinement of 15 psi (103 kPa).

To study the effect of the intermediate principal stress,  $\bar{\sigma}_2$ , on compression and shear wave velocities, a triaxial sequence was run. The pressure was set to a maximum biaxial load with the vertical stress equal to 40 psi (276 kPa) and horizontal stresses

equal to 15 psi (103 kPa). One of the horizontal stresses was increased in 5-psi (34 kPa) increments to 40 psi (276 kPa) and then was decreased back to 15 psi (103 kPa) in 5-psi (34 kPa) increments to note any effect of hysteresis.

Structural anisotropy and its possible effect on the biaxial and triaxial series was investigated by running a shortened series of biaxial and triaxial tests. In this series the axes for stresses were rotated with the major principal axis as north-south rather than vertical and the intermediate principal axis as vertical rather than north-south.

## B.2 TESTING PROCEDURES

Once the triaxial cube was constructed and all the associated equipment was thoroughly checked, construction of the sand sample was begun. First, the walls of the cube were cleaned, and the membranes and greased sheets were attached. The sand was then dried in the sun to a moisture content of less than one percent and rained into the cube to form a sample of medium density. At predetermined elevations, raining of the sand was stopped and electronic equipment was placed in the sand. When the soil specimen was completed, the top of the cube was securely fastened. The sample was then loaded, compression and shear waves were generated, and the accelerometer responses were recorded along all three axes at each pressure. The following sections describe, in detail, the work from sample construction through dynamic testing.

### B.2.1 Sample Construction

The first step in constructing the sample was to clean the accumulated dust, oil and dirt from the inside of the cube and to bolt the collar of the raining system (see Section A.8.2) to the top. Next, the greased sheets and membranes were installed inside the cube on the sides and bottom. The two rubber membranes which were used to apply lateral loading were hung on the north and west faces of the cube as shown in Fig. B.4. Rope was passed through the grommets in the top of the membranes and then through the extra bolt holes in the top of the cube which were not used to attach the collar. The ropes were tied off to convenient anchors along the outside of the cube and collar.

On the inside of the cube, two sheets of plastic were placed on the bottom and on each of the four sides, including placement over the membranes previously hung on two sides. The sheets on the sides were held in place by pieces of duct tape. (The tape, in addition to the ropes holding the membranes, was removed before attaching the top of the cube.) Small openings were cut in the plastic sheets as required for the three sources and five holes through which electrical wires passed. The outer sheet of each pair of sheets (which eventually touched the sand) was lifted by one person while another placed a thin layer of WD-40 oil on the inner sheet with a paint roller as shown in Fig. B.5. The outer sheet was allowed to drop back in place and then was pressed smooth with a clean, dry roller. This resulted in a system of a



Fig. B.4 - Rubber Membranes Being Attached to the  
North and West Faces of the Cube



Fig. B.5 - Layer of Oil Being Applied to Plastic Sheet on West Face of Cube



thin layer of oil sandwiched between two plastic sheets having a clean contact with the sand on one side and cube or membrane on the other side. The purpose of the oil was to minimize friction between the layers of plastic and, therefore, between the sand and the walls of the cube so that little shearing stress could develop at the sand-cube boundary. Uniform stresses across each side of the sample could not have been achieved if shearing stresses developed between the sand and cube walls (Section A.8.1).

The string-spring assembly (Section B.2.2) used to determine elevation and levelness of the sand was placed at the 24-in. (61 cm) level, the first level at which raining of the sand was halted for placement of electronics.

The sand for these tests was supposed to be dry which for this work was taken to be a moisture content of less than one percent. However, the sand had to be stored outdoors, exposed to the weather, and was damp. The early summer in Austin is usually sunny and dry with temperatures reaching above 90 degrees F. Unfortunately, May and June of 1981 were unusually damp. Intermittent strong rains, averaging three nights per week, precluded storage of dry sand for more than one day. Several methods of covering the sand were tried in an attempt to keep rain water out of the sand, but all were unsuccessful. Therefore, before placement in the cube, the sand was spread in approximately one cubic yard ( $0.9 \text{ m}^3$ ) lots to a thickness of one to two inches (2.5 to 5.0 cm) and dried in the sun. An acceptable water content could be achieved in one-half

to three hours, depending upon the initial water content (directly related to how recently the last rain was) and the daily humidity. Figure B.6 shows the sand being dried. When dry, this sand was placed in the cube while another layer was spread to dry.

After the sand dried in the sun, it was shoveled into a  $3/4$ -cu yd ( $0.6 \text{ m}^3$ ) concrete bucket which had been moved by forklift to the outdoor drying area. A screen with 0.25-in. (0.64 cm) openings was placed over the top of the bucket before it was filled so that foreign matter that may have found its way into the outdoor storage pile would be removed. (Little foreign matter was found in the sand.) Once the bucket was filled, it was moved by forklift into the building where it was attached to the overhead crane. The crane was used to lift the bucket over the cube so that sand could be rained into the cube.

The initial method for raining sand into the cube was as follows. About one third of the sand in the bucket was emptied into the hopper to fill it. The hopper gate was then opened to give the desired flow rate while the hopper was moved at a constant rate along the rails of the collar attached to the top of the cube. When the hopper was empty, the gate was closed and the process was repeated. Unfortunately, the force of the sand on the gates always forced them to open fully. Because of this problem, after one or two uses, the raining system was modified as described below.

After one bucket load of sand, it was decided to modify the raining system since the force of the sand caused the hopper

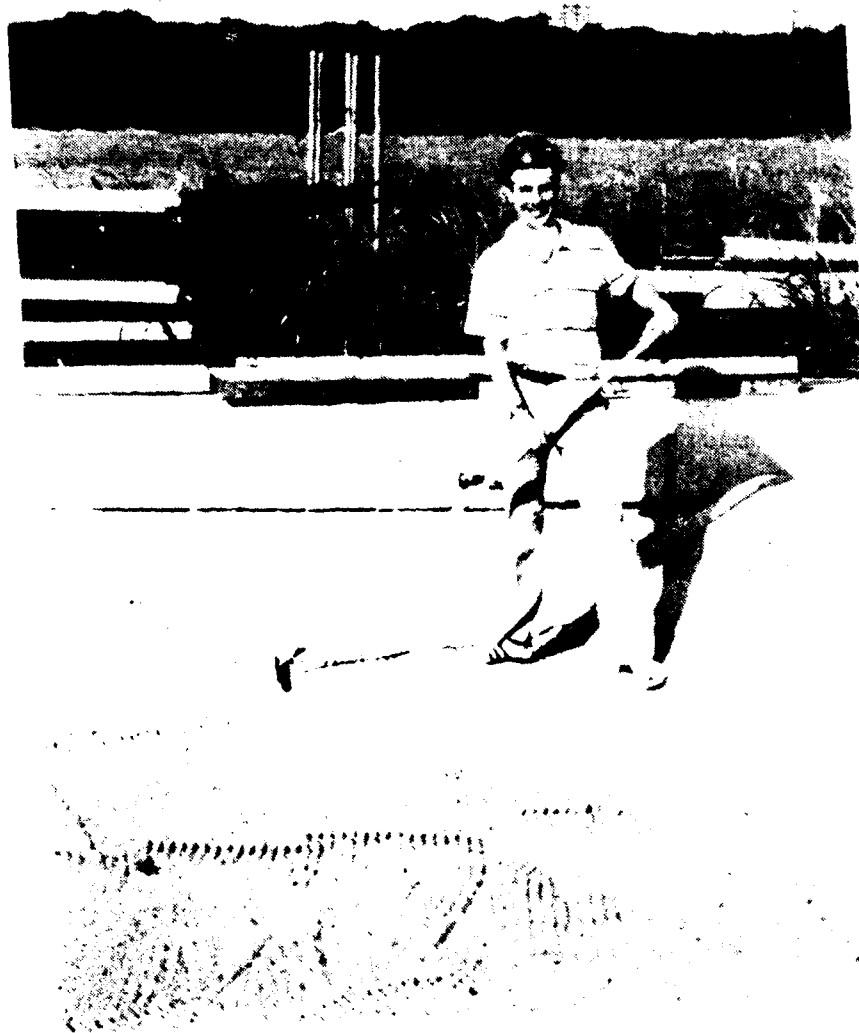


Fig. B.6 - Sand Being Air Dried in Outdoor Storage Bin

to stay in its fully open position. Experimentation revealed that the sand could be placed directly from the concrete bucket at the same rate as through the open rainer, but without the set-up time required to fill the hopper. Therefore, the approach was simply to swing the bucket manually in the north-south direction while the crane moved the bucket in the east-west direction. A 0.25-in. (0.64 cm) wide (north-south) by 10 in. (25.4 cm) long (east-west) rectangular curtain of sand dropped out of the bucket at an initial angle of about 45 degrees causing it to disperse and rain quite evenly over the top surface of the sand in the cube. Since considerable time could be saved using the bucket directly while maintaining a seemingly uniform sample, the cube was filled directly with the bucket.

The sand density was measured at four elevations in the cube. At each measurement elevation, raining of sand into cube was halted, and the special density device described in Section A.7.3. was placed on the current surface of the sand. Several different horizontal locations were chosen as shown in Fig. B.7 so that the density of samples from all sections of the cube could be compared. Raining of the sand continued with the device in place until the sand surface was just above the top of the device, and it was full. The full container was then removed, and the sand in the container carefully transferred to a self-sealing (Ziplock) bag. The bags were transported back to the main campus where they were weighed on

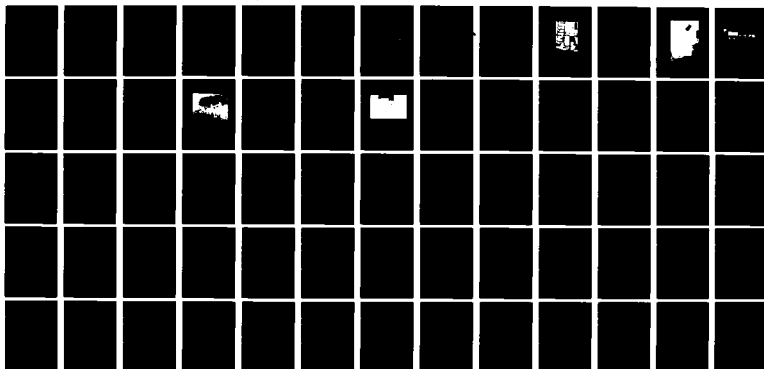
AD-A120 426

EFFECT OF STATE OF STRESS ON VELOCITY OF LOW-AMPLITUDE  
SHEAR WAVES PROPAG. (U) TEXAS UNIV AT AUSTIN  
GEOTECHNICAL ENGINEERING CENTER D P KNOX ET AL. MAR 82  
GR82-23 AFOSR-TR-82-0908 AFOSR-80-0031 F/G 20/11 NL

5/6

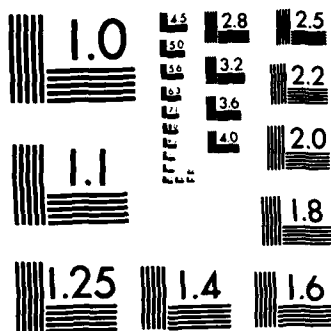
UNCLASSIFIED

NL

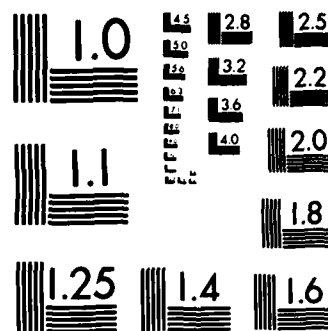


END  
JAN  
1982

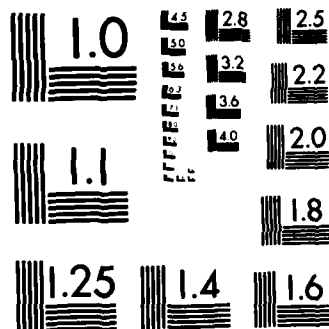
CNT



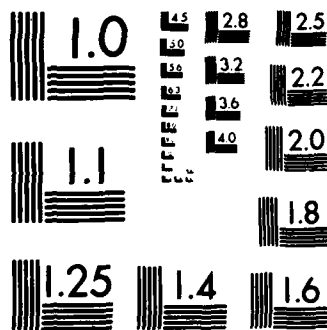
MICROCOPY RESOLUTION TEST CHART  
NATIONAL BUREAU OF STANDARDS-1963-A



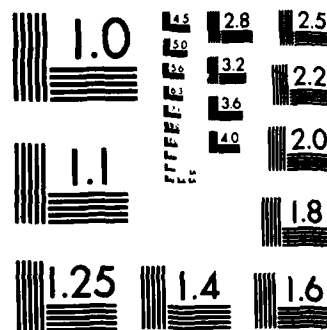
MICROCOPY RESOLUTION TEST CHART  
NATIONAL BUREAU OF STANDARDS-1963-A



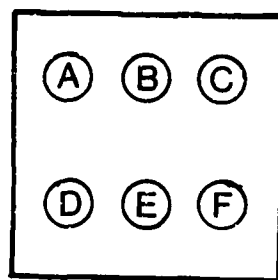
MICROCOPY RESOLUTION TEST CHART  
NATIONAL BUREAU OF STANDARDS-1963-A



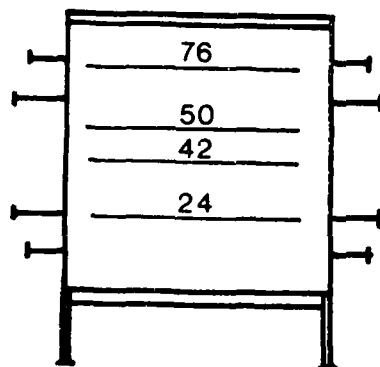
MICROCOPY RESOLUTION TEST CHART  
NATIONAL BUREAU OF STANDARDS-1963-A



MICROCOPY RESOLUTION TEST CHART  
NATIONAL BUREAU OF STANDARDS-1963-A



a. Top View of Cube



b. Elevations Where Raining of Sand was Halted for Density Measurements

Fig. B.7 - Location of Density Measurements Taken During Filling of Cube

a Metler balance. The density was computed by dividing this weight by the known volume of the density device.

The resulting densities and their locations within the cube together with the resulting void ratios are tabulated in Table B.2. The average density is 96.6 pcf ( $1547 \text{ kg/m}^3$ ), and the standard deviation is only about two percent of this value, or 1.9 pcf ( $30 \text{ kg/m}^3$ ). Therefore, the sample can be considered quite uniform as deposited by the modified sand raining system.

#### B.2.2 Placement of Electronics

It is crucial that the exact distances between accelerometers in the cube be known for computation of wave travel times. It is also important that the stress and strain cells be oriented in the correct direction to eliminate cross interference. To satisfy both requirements, a surveying system was developed. The system consisted of small eyebolts attached at predetermined elevations along the fins of the cube which surround each membrane to prevent lateral expansion under load. Two string-spring assemblies were hooked into sets of eyebolts in opposite corners to form an "x" across the middle of the cube. The springs maintained tension in the string to minimize sagging at the center so that the "x" was at a known elevation.

This "x" provided many useful functions. The center of it was the center of the horizontal plane in the cube which was directly over the source in the bottom. This center was used in



TABLE B.2  
Densities and Void Ratios of Sand at  
Various Elevations in the Cube

Height Above the Bottom in.	Location*	Density pcf	Void Ratio** e
(1)	(2)	(3)	(4)
24	D	94.7	0.77
42	C	97.7	0.71
42	D	97.9	0.70
42	F	100.0	0.67
50	B	95.4	0.75
50	F	97.8	0.71
50	D	97.5	0.71
70	E	95.5	0.75
70	A	95.7	0.75
70	C	93.7	0.78
Average		96.6	0.73
Std. Deviation		1.9	0.03

\* See Fig. 5.7.

$$** \quad e = \frac{\gamma_w G_s}{\gamma_d} - 1 \quad \text{where } G_s = 2.68$$

horizontally locating the accelerometers. Also, the strings formed a nearly level plane which was used to monitor filling of the cube and to level the placement of accelerometers, stress devices, and strain devices. Finally, since the "x" was at a known elevation, the vertical distance from the level plane to any item could be measured by use of a plumb-bob. In this manner, the location of the accelerometers was determined. Each time an accelerometer package was placed in the center of the cube, a plumb-bob was hung from wooden rod inserted through the open, center bolt hole in the top of the north and south walls to verify the horizontal distances.

Raining of the sand in the cube was halted five times to allow placement of electronic devices at the following elevations above the bottom: 24 in., 42 in., 50 in., 56 in., and 60 in. (60.9, 106.7, 127.0, 142.2, and 152.4 cm). At the 24-in. (60.9 cm) level, two pairs of horizontal strain sensors were placed along with the first 3-D accelerometer package as seen in Fig. B.8. The second level, 42 in. (106.7 cm), represented the mid-height of the sample. All three stress cells were placed at this level along with five, 3-D accelerometer packages and the lower strain sensor of the vertical 4-in. (10.3 cm) diameter pair as shown in Fig. B.9. The second strain sensor of the 4-in. (10.3 cm) diameter pair was the only item placed at the 50-in. (127.0 cm) level. The lower 2-in. (5.1 cm) diameter vertical strain sensor was placed along with the two, 2-in. (5.1 cm) diameter horizontal

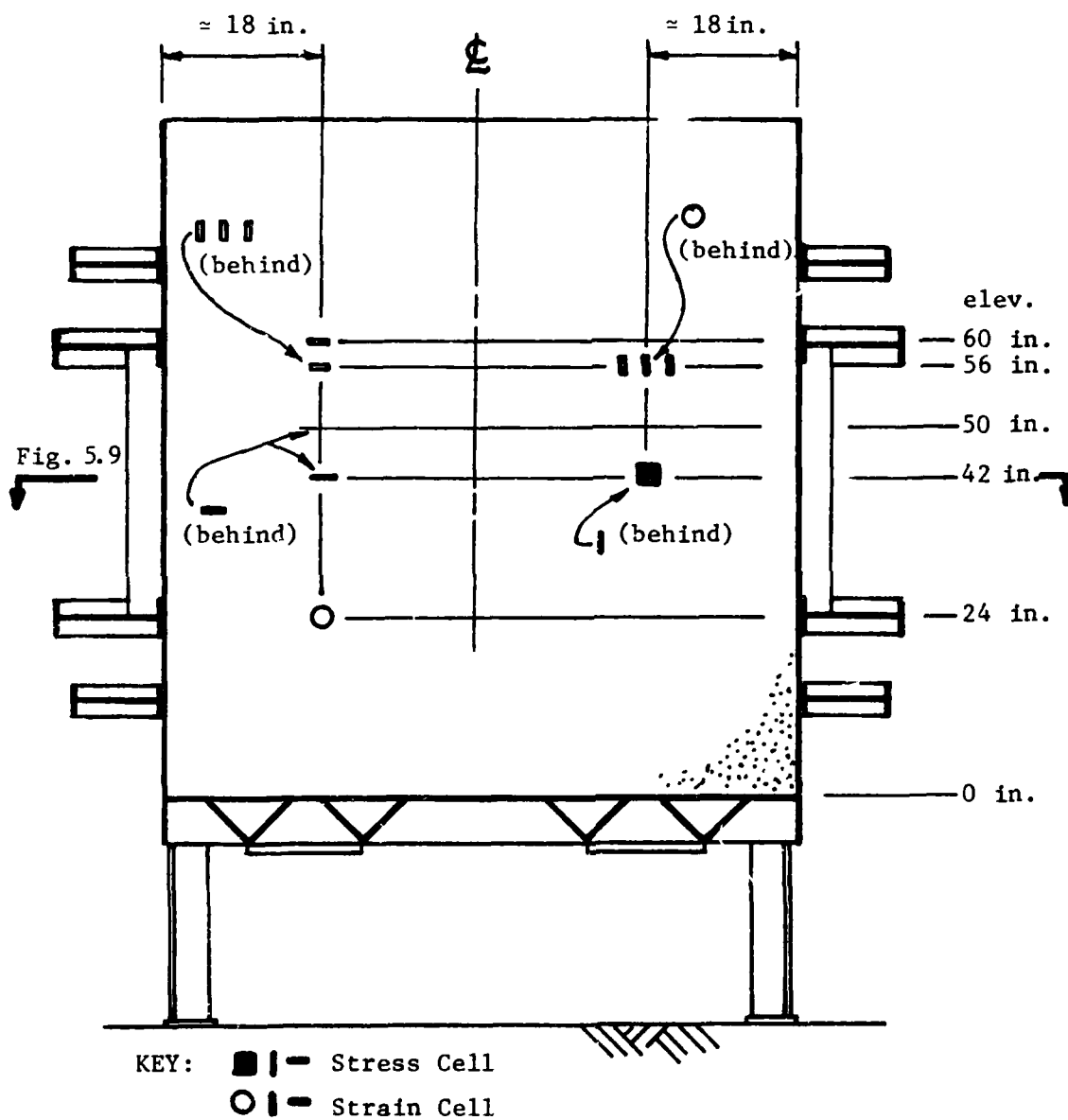


Fig. B.8 - Location of Stress and Strain Measuring Devices in Cube When Looking West Through The Cube

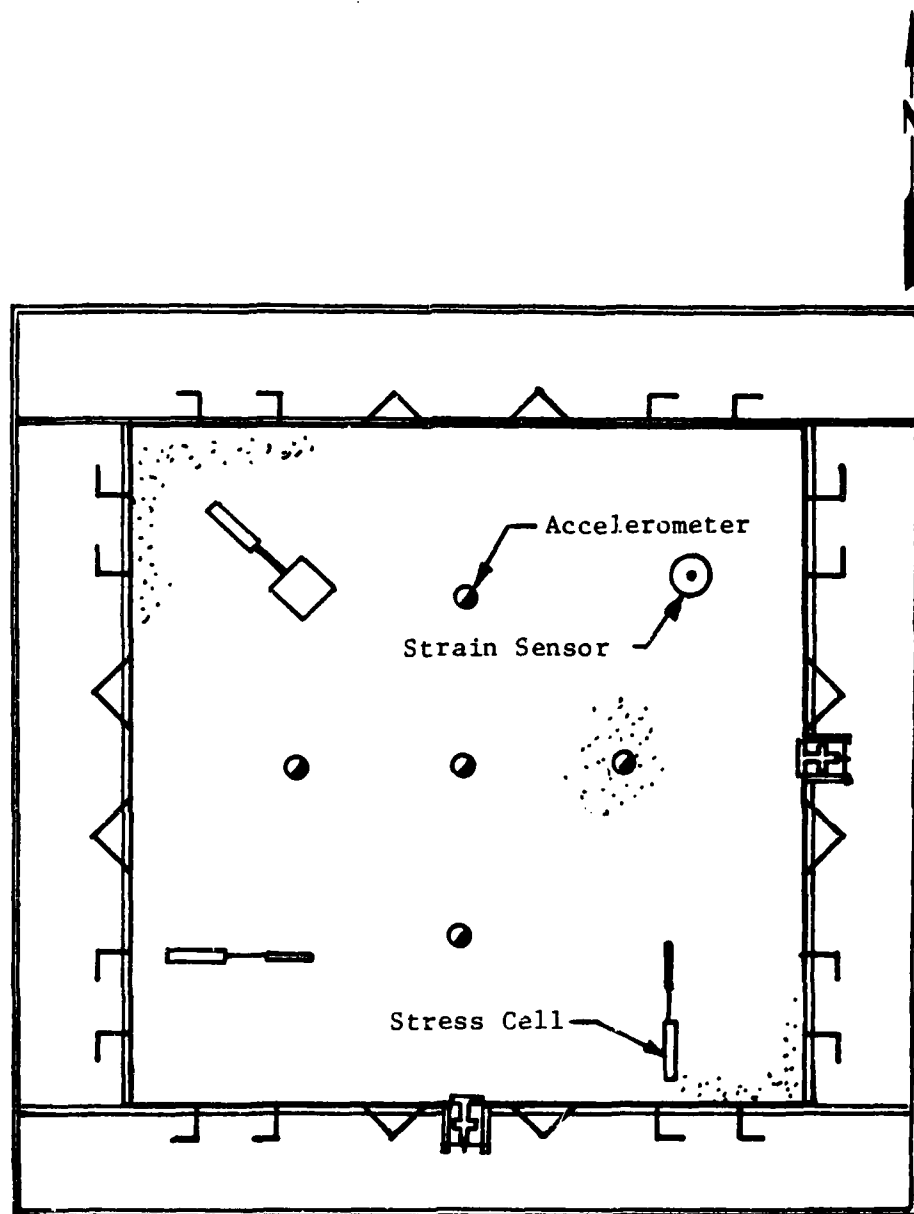


Fig. B.9 - Horizontal Location of Stress and Strain Measuring Devices at Mid-Height of Cube

strain sensor and the final 3-D accelerometer package. The final accelerometer-to-source distances are listed in Table B.3.

To place the electronic devices in the sample, the raining of sand was stopped, and a person in a personnel cage was lowered by crane into the cube. As shown in Fig. B.10, the cage has an open side to permit hand placement of devices and measurement of distances. There are rubber bumpers on the sides to prevent damage to the interior of the cube, and the cage was never permitted to touch the sand surface so that no disturbance of the sand occurred. After completing placement of devices at a given level, the string-spring assembly was moved to a higher level, the wires were passed through holes in the wall of the cube, and raining was resumed.

The stress cells were positioned at mid-height of the cube so that they did not interfere with generation or monitoring of P- and S-waves. The cell used to monitor pressure in the vertical direction was simply placed directly on the level sand surface as shown in Figs. B.11a and B.12. The two cells used to monitor horizontal stresses in the sand were oriented parallel to the vertical walls of the cube and were slightly embedded on their side as shown in Figs. B.11b and B.13. The wires from the cells were passed through three holes in the south and east walls as can be seen in Fig. B.14. Raining of the sand was continued until sand covered the cells. This placement method is essentially the same as that described by Hadala (1967).

TABLE B.3  
Source-Accelerometer Distances Determined  
After Placement

Source*	Receiver	Axis of Sensitivity	Distance (ft)
(1)	(2)	(3)	(4)
1	1	Vertical	1.99
2	1		1.94
3	1		1.97
1	2		3.34
2	2		3.50
3	2		3.44
1	3		4.91
2	3		5.00
3	3		4.94
1	1	North-South	1.99
2	1		1.94
3	1		1.94
1	2		3.40
2	2		3.44
3	2		3.44
1	3		4.96
2	3		4.94
3	3		4.94
1	1	East-West	1.93
2	1		2.00
3	1		2.00
1	2		3.35
2	2		3.50
3	2		3.50
1	3		4.79
2	3		5.00
3	3		5.00

\* 1 = Vertical, 2 = South, 3 = East.

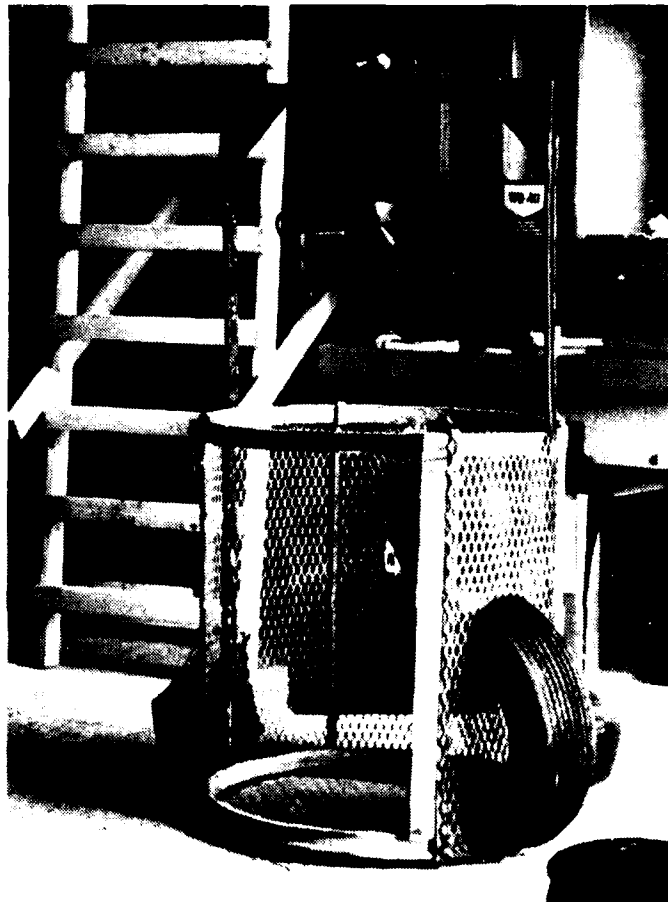
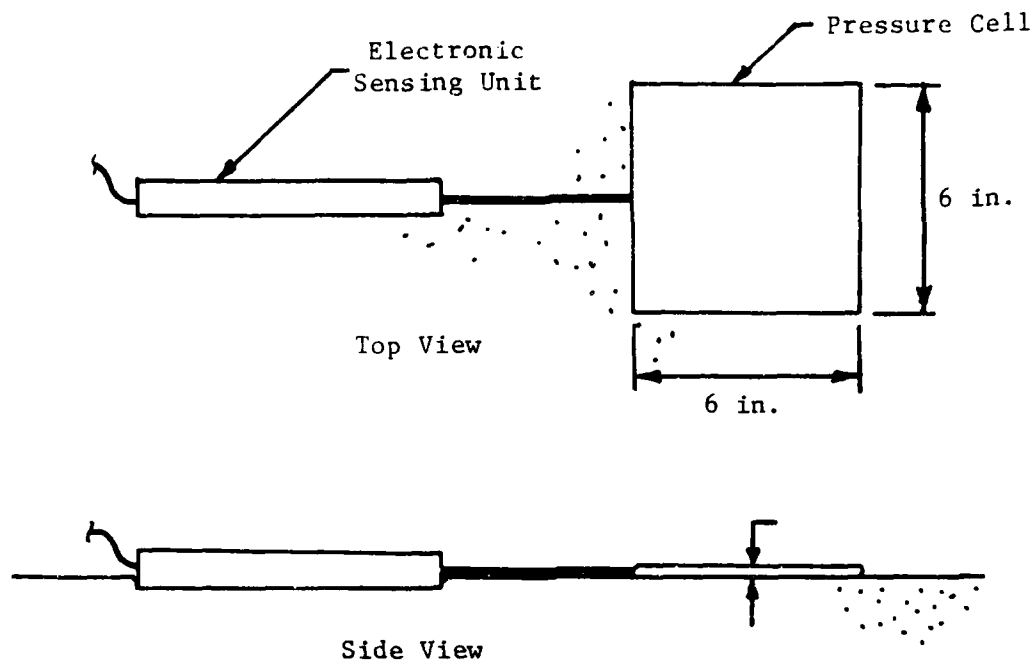
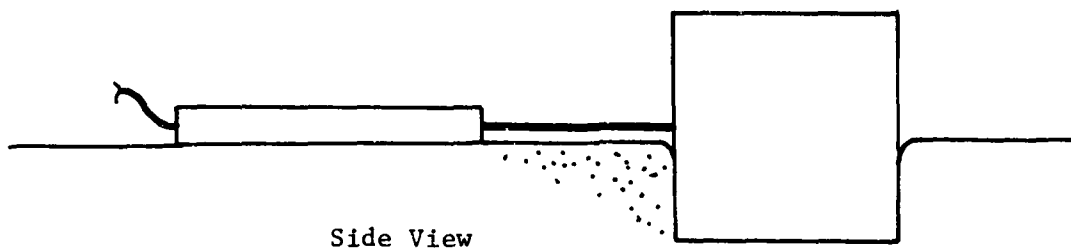


Fig. B.10 - Personnel Cage Used in Placement of Electronics into Sand During Filling Operation



a) Horizontal Orientation of Cell Monitoring Vertical Stress



b) Vertical Orientation of Cells Monitoring Horizontal Stress

Fig. B.11 - Placement of Total Stress Cells When the Cube Was Half Filled





Fig. B.12 - Total Stress Cell for Vertical Stress  
Measurement Placed on Sand Surface  
During Building of Sample

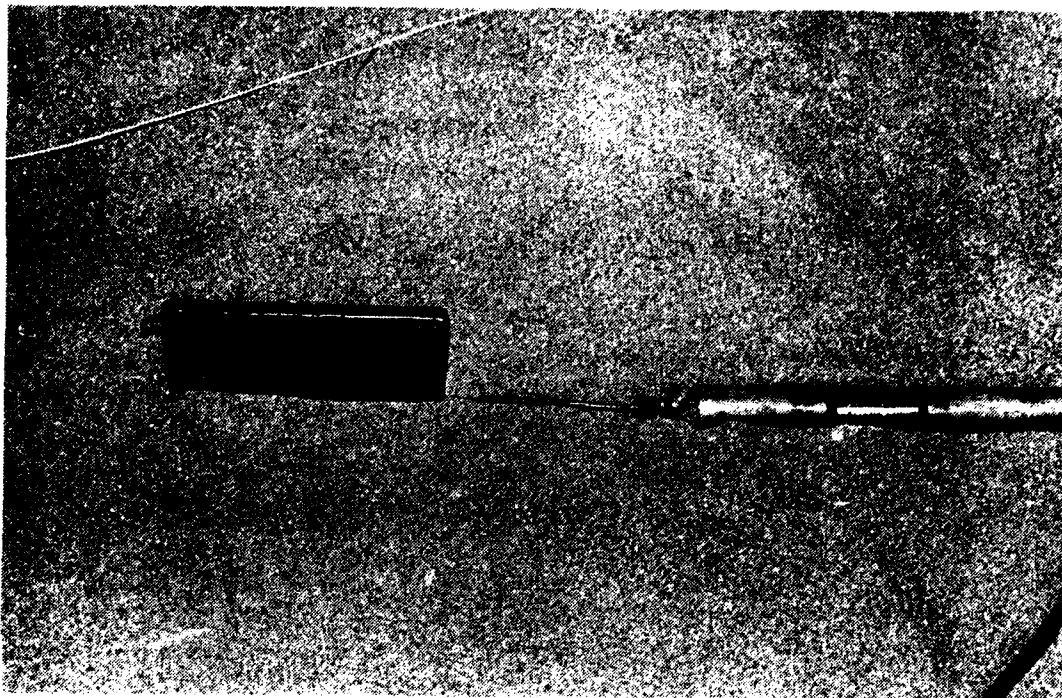


Fig. B.13 - Total Stress Cell for Horizontal Stress  
Measurement Placed on Sand Surface  
During Building of Sample

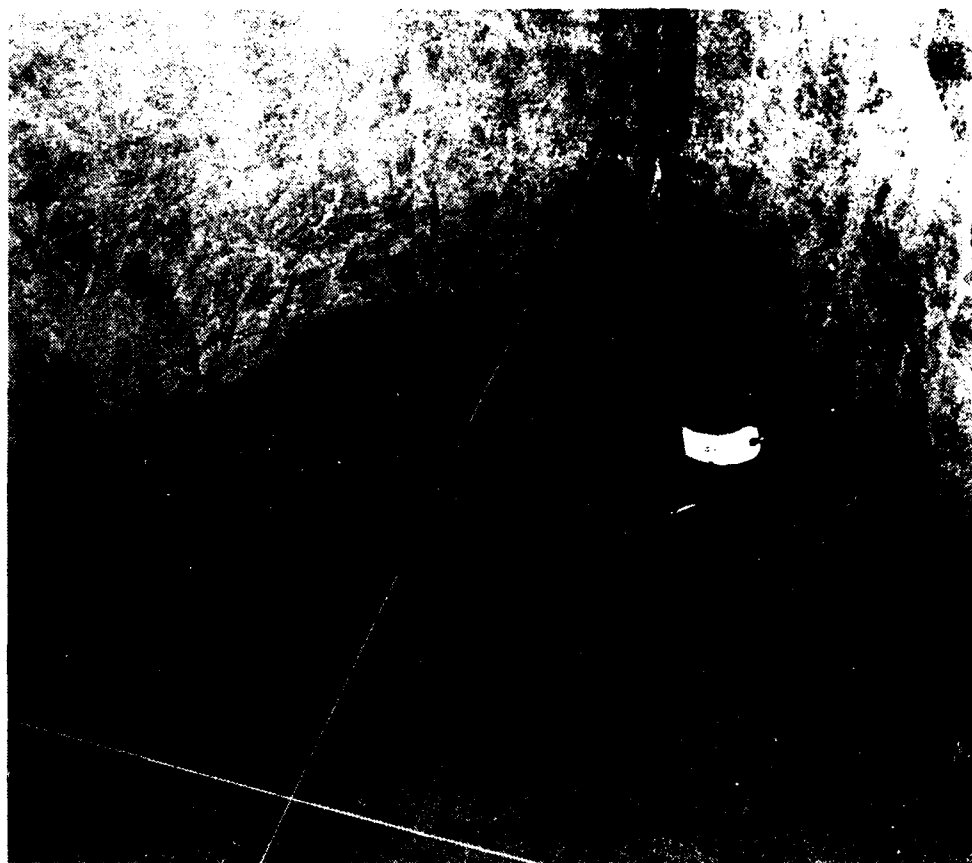


Fig. B.14 - Wires from Stress Cells Fed Through  
East Wall of the Cube

Hadala experimented with three methods of placing stress cells in dry sand which was rained into a container. Although the stress cells used by Hadala were of a slightly different construction, i.e. different manufacturer and smaller size, the results of his tests can be applied to the stress cells used in the cube. Hadala found the best method for placement in dry sand to be setting of the gage directly on the sand surface and continuation of the filling around it. This method resulted in smaller scatter in measured pressures and a lower, mean over-registration ratio,  $R$ , where  $R$  is defined as:

$$R = \frac{1}{n} \sum_{i=1}^n \frac{\sigma_i}{\bar{\sigma}} \quad (3.3)$$

where  $n$  = number of gages,

$\sigma_i$  = stress reading of gage  $n$ , and

$\bar{\sigma}$  = actual stress on gage  $n$ .

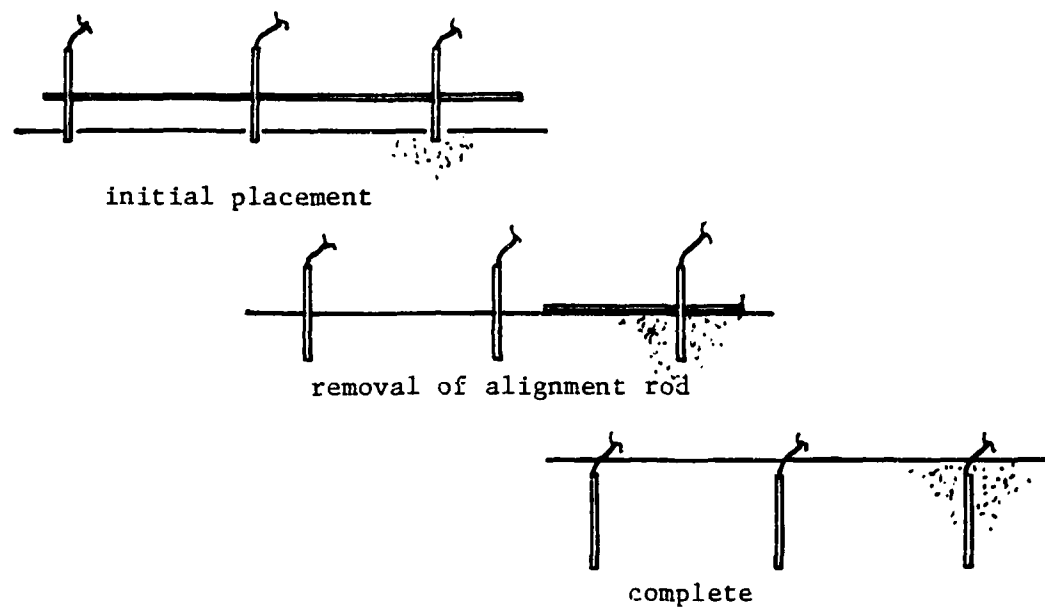
The typical value of  $R$  in his experiments was about 22 percent for the placement method described above. Larger values, up to 40 percent, were found for tamping the stress cell into the sand and the raised-mound method. The raised-mound method involves excavating sand, placing the stress cell and replacing and tamping the excavated sand over the cell.

Each pair of strain sensors had to be oriented with respect to each other so that certain surfaces of the disks faced each other. Unfortunately, this orientation could only be determined by connecting the cells to the control unit. The control unit was

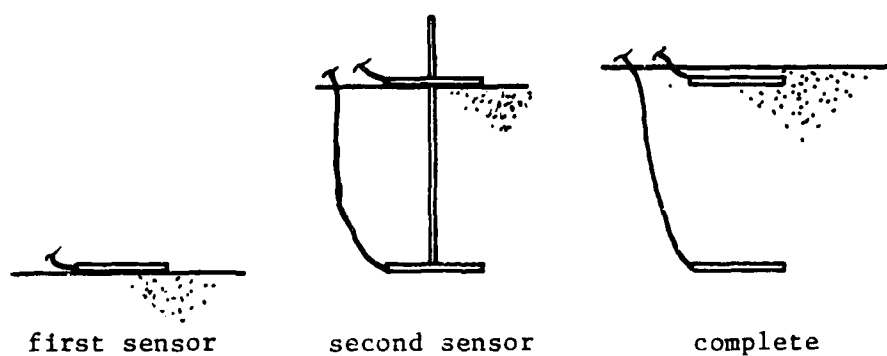
not available until the middle of testing because of a problem with the needle of the meter on the unit which stuck whenever it was deflected full-scale to the left. The manufacturer, Bison, Inc., took approximately six months to correct this minor problem. Rather than delay the tests, it was decided to place three sensors, rather than two, at each horizontal location in the cube. This method doubled the chances of having one operational pair at each location. When the control unit finally arrived back in working order (it was first returned, unfixed, in four months), it was found that four pairs of the six sets were operational.

Each sensor has a small hole in the center to aid in placement in the sand. For horizontal strain measurement, three sensors were placed on an alignment rod at a spacing of twice the sensor diameter as shown in Fig. B.15a. The assembly was then set on the sand with the rod parallel to the level surface and pointing along the axis to be measured. Sand raining was then continued until the bottom of the rod was just at the sand surface. The rod was removed at this point because the sand could support the sensors for the remainder of the filling operation as shown in Fig. B.16.

For vertical strain measurement, a sensor was placed on its face on the level sand surface as shown in Fig. B.15b after the raining was stopped. An alignment rod was placed in the hole of the sensor perpendicular to the sand surface. Raining of the sand was continued until the sand level reached the mark on the rod indicating a distance of two diameters. The second sensor was



a) Horizontal Placement



b) Vertical Placement

Fig. B.15 - Placement of Strain Sensors When the Cube was Partially Filled

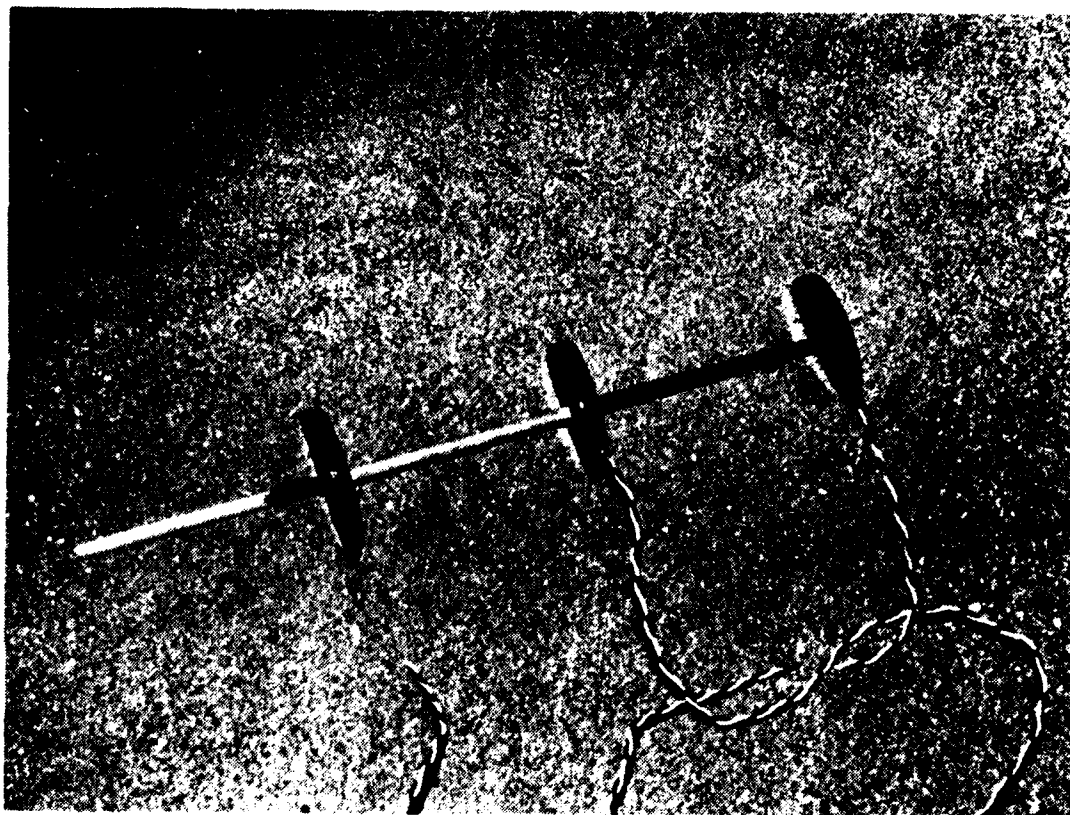


Fig. B.16 - Horizontal Strain Sensors Placed in the Sand During the Building of the Sample

inserted onto the alignment rod so that it was over the first sensor at a predetermined separation. The rod was then carefully removed, and sand was poured into the resulting hole. Raining was then continued. This method was similar to that described by Wetzel and Vey (1970).

The wires from all the sensors were fed through either of two holes in the east face of the cube. The holes were sealed with rubber, watertight sealant before the sand covered them.

In both horizontal and vertical strain gage placement, lateral and rotational misalignment must be avoided. Truesdale and Schwab (1967) found that errors in strain measurements will occur if the sensors are displaced laterally more than ten percent of the spacing between sensors or if the sensors are rotated greater than ten degrees off of the axis between the pair. The use of the alignment rod minimizes these problems.

While sand was being placed in the cube, the side membranes were being filled with water. The object was to keep the water elevation approximately one in. (2.5 cm) above the sand elevation to ensure that the membrane did not pinch together, closing off a portion of the membrane. If this pinching occurred, pressure might not be uniform over the face of the sand cube which would cause an unknown stress distribution within the sample.

The height of water in the membranes was kept at a maximum of 3 in. (7.5 cm) above the sand surface to prevent any localized passive failure of the top edge of the sand. Water was added



through the air-water panel board to the lower ports of the membranes while the upper ports were open to allow air to escape. When the water elevation reached the top port, a quick-connect was attached to the port and a simple piezometer tube was attached to monitor the final few inches of filling.

Filling of the cube was stopped one in. (2.5 cm) below the top to allow room for the top membrane. The rope supporting the side membranes was removed as was the duct tape supporting the greased sheets. The wooden collar was removed, and the sand surface leveled as shown in Fig. B.17. A precut sheet of plastic was laid over the top surface and WD-40 oil applied in a thin coat. A second plastic sheet was then placed on top of the oiled sheet after which the top (final) membrane was placed. The steel top was attached and securely bolted. The top membrane was filled with water to fill the void between the top of the sand and the top of the cube. Pressure within the membrane was monitored to ensure that the sand was not subjected to any loading.

The cube and surrounding area was thoroughly cleaned and testing was commenced.

#### B.2.3 Loading the Soil

Each membrane was connected to a separate pressure outlet in the panel board (Fig. 3.12) so that the stress along each axis could be individually controlled and monitored. The sample was loaded and tested along each step of the series listed in Table B.1.

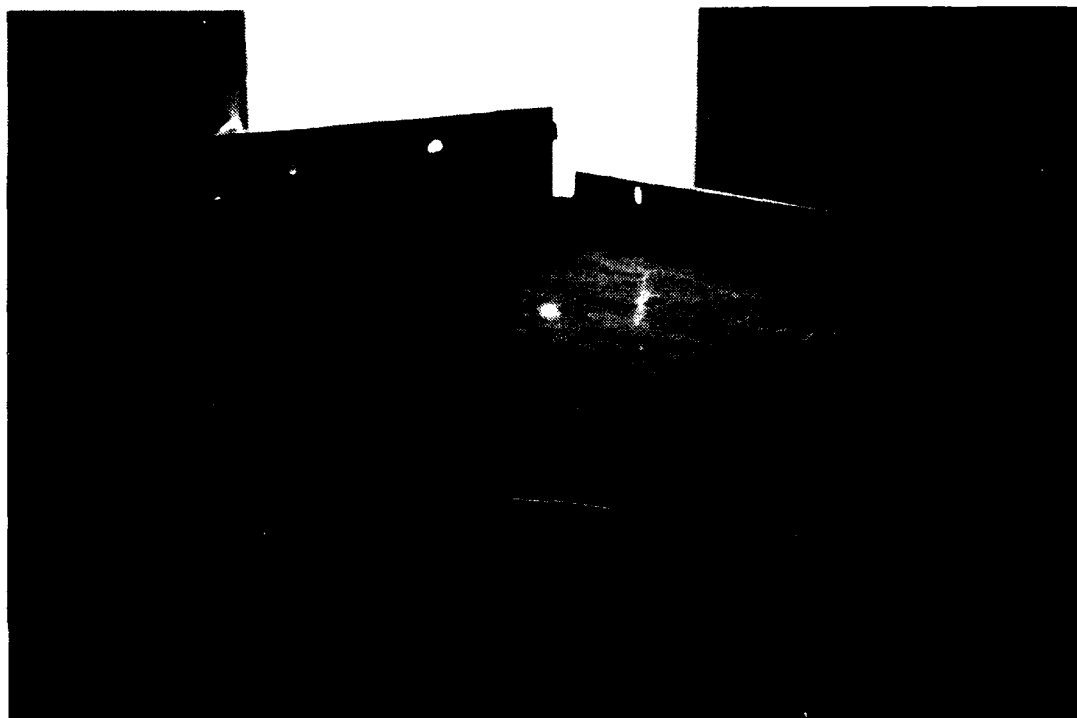


Fig. B.17 - Sand Surface upon Completion of  
Building of the Sample

To ensure that the stress path initially followed isotropic loading and later maintained a constant mean effective principal stress, the pressure was varied by less than 0.5-psi (3 kPa) increments in a linear progression between pressure steps. This was accomplished by pressurizing all three axes at once and monitoring the rate of change in pressure and adjusting the settings as required.

The stresses and strains at each sub-step were measured on the stress cells and strain sensors to monitor the stress level in the cube and verify the magnitude of the strains as discussed in Section B.3.4. The change in volume of the membranes (amount of water flowing into or out of the membranes) was also monitored.

The cube was loaded so that the planned state of stress occurred at the center of the cube. Therefore, the effects of overburden pressure, hydraulic gradient, and differing piezometric elevations between the membranes and the pressure panel board had to be taken into account when reading the gage at the panel board. The necessary corrections can be expressed in terms of the following equations:

$$\text{Vertical Correction: } P_G = P_C - 2.4 + -0.036h \quad (B.4)$$

$$\text{Horizontal Correction: } P_G = P_C - 1.5 + 0.036h \quad (B.5)$$

where:  $P_G$  = reading on pressure gage at panel board, in psi,  
 $P_C$  = pressure at center of cube, in psi, and  
 $h$  = difference in elevation between top of cube and  
 air/water interface at panel board, in inches.

The difference in elevation between the top of the cube and the air-water interface at the panel board,  $h$ , is not constant. As the soil compacts or dilates, the column of water falls or rises, respectively. However, the change in elevation of one in. (2.5 cm) results in less than a 0.04 psi (0.25 kPa) change in pressure, or a change of the entire 18-in. (45.7 cm) high accumulator on the panel board results in only a 0.6 psi (4.4 kPa) change in pressure. Therefore, the pressure can be considered constant using a constant value for  $h$  and maintaining the water level at an approximately constant level.

#### B.2.4 Problems in Use of Stress and Strain Measuring Devices

Problems arose in attempting to use the stress and strain devices which significantly reduced their usefulness. The problem with the strain sensors was not in the device itself, but rather with the manufacturer. As mentioned in Section B.2.2, the control unit for the sensors originally arrived from Bison, Inc. in disrepair. The unit was returned for repair with the understanding that the delay would be short. The unit was returned four months later when the cube was about to be filled, and no repairs had been made. It was again sent to the manufacturer, and two months later the unit was returned in time to record data for the second half of the testing only.

The available data from the strain gages are plotted against pressure in Fig. B.18 for the three axes. A strain of 0.1 percent was arbitrarily chosen for the strain up to the loading

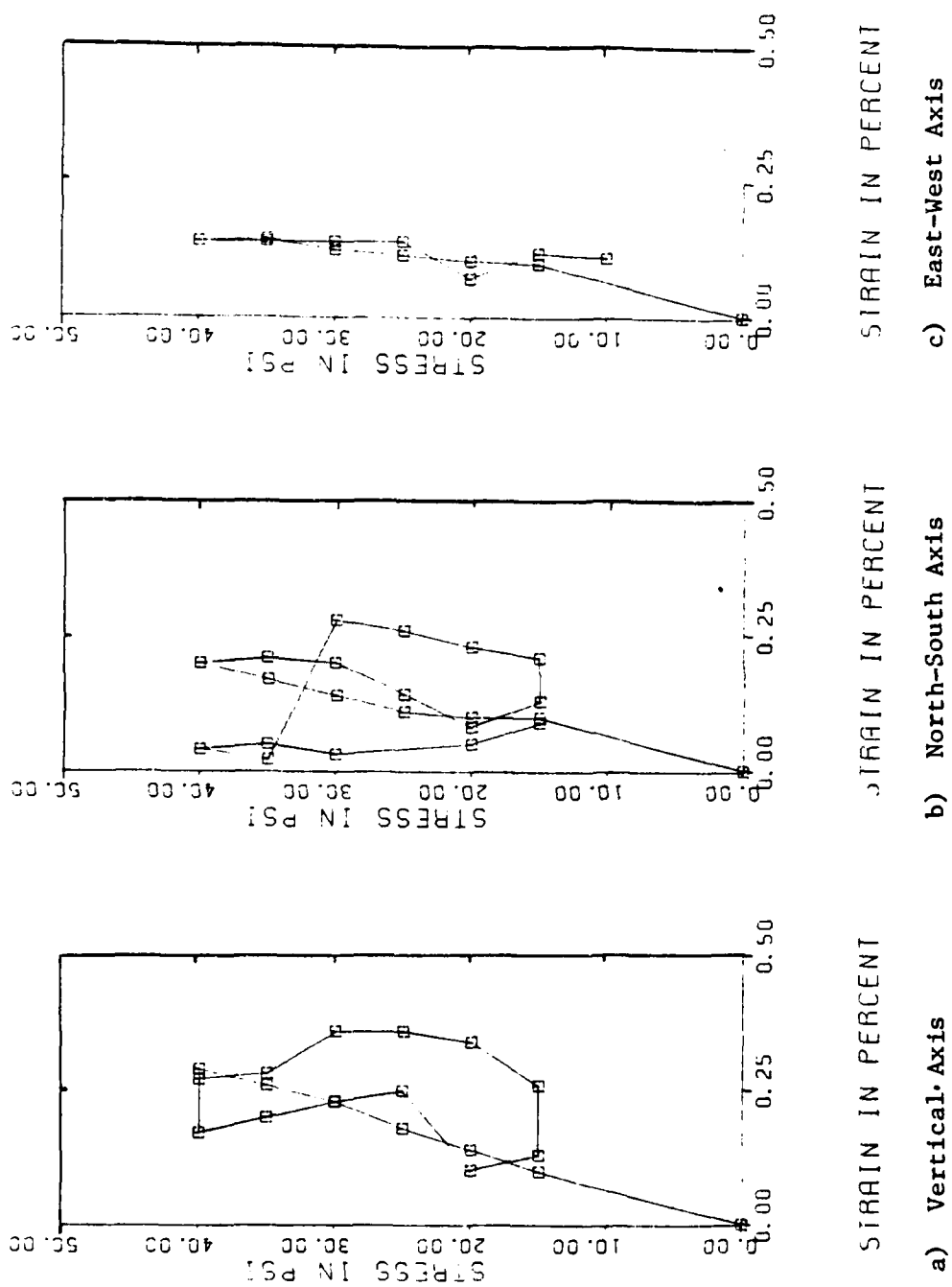
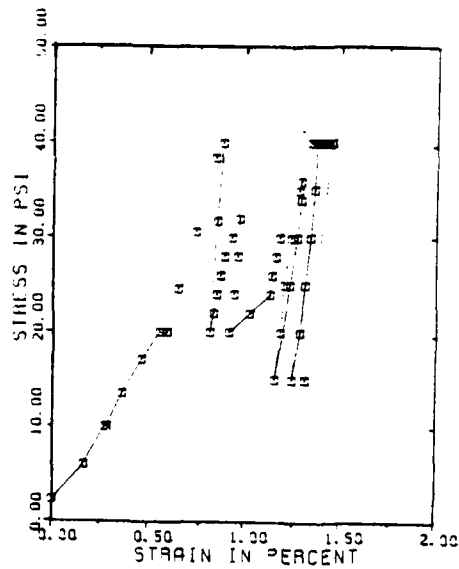


Fig. B.18 - Stress-Strain Curves for Each Axis of the Cube Based on Strain Gages

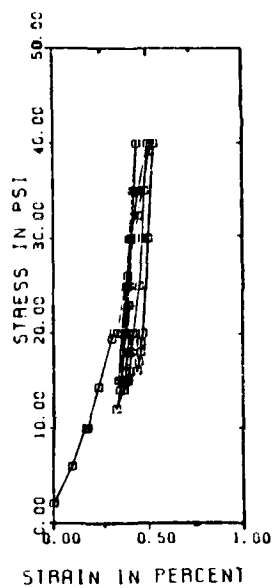
of 15 psi (103 kPa) when the strain gages began to operate. From this limited data, the stress-strain properties cannot be predicted because of the scatter and lack of data points. The loading, however, may be considered small-strain loading because the maximum strain is about 0.3 percent over the range in pressures measured.

A rough estimate of strain with respect to change in stress was made by monitoring the number of times the accumulator had to be filled or drained because of water flowing into or out of the membranes during loading. This volumetric strain along each axis is shown in Fig. B.19. The large initial strain is believed to have been caused by seating of the membranes in the cube. Any voids between the membranes and face of the cube and in the corners of the cube had to be filled before the membrane could exert pressure on the sand. After the initial seating, the stress-strain relationship is fairly linear with no evidence of stress history. The actual strains are probably less than the volumetric strain because of the unmeasurable compliance in the loading system. The values of the elastic modulus,  $E$ , derived from the slopes of the curves are 18,000 psi (124,000 kPa), vertical, and 16,000 psi (110,000 kPa), north-south and east-west.

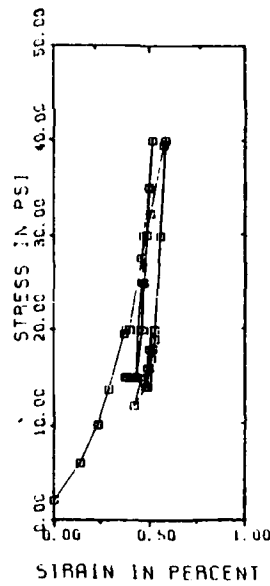
The stress cells were supposed to be calibrated so that a digital pressure readout was possible. Hadala (1967) discussed the inherent errors associated with stress cells in cohesionless soil. The major problem occurs from sand arching around the cell. Proper placement of the cell can minimize this problem (Section B.2.2),



a) Vertical Axis



b) North-South Axis



c) East-West Axis

Fig. B.19 - Stress-Strain Curves for Each Axis of the Cube Based on Water Flowing Into and Out of Membranes

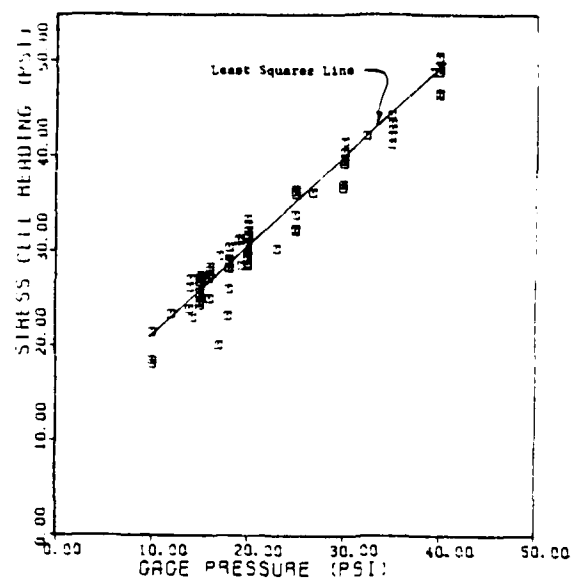
but even the best placement method results in an average range of 22 percent over- or under-reading. A minor error inherent to the type of stress cell used in these tests was that the soil pressure caused a comparable oil pressure which deflects a strain gage in the unit. Problems may arise from the slight compressibility of the soil and possible small non-linearity of the strain gage.

Figure B.20 shows the stress applied by the loading system versus the stress read by the stress cell along each axis. Within some scatter, the variation is linear, but not a direct correspondence. Therefore, if the cells are to be used in the future, calibration curves can and must be made for each cell in the laboratory before placement in the soil.

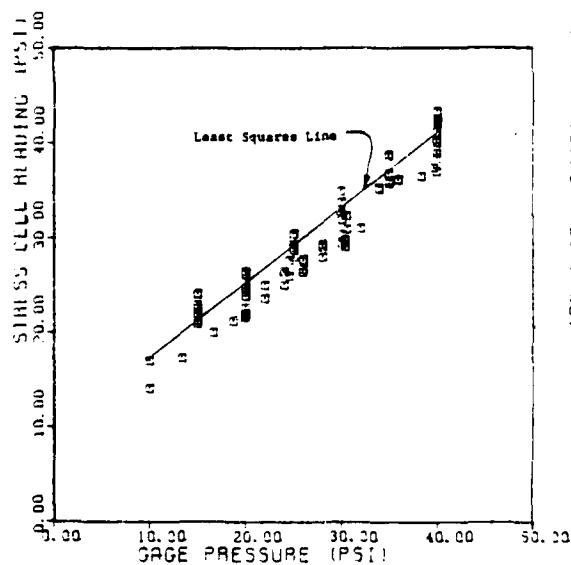
#### B.2.5 Dynamic Testing

Nine sets of waveforms were recorded at each state of stress since a compression wave and two, mutually perpendicular shear waves were generated along each axis. Each set of three waveforms results from the output simultaneously recorded from the three accelerometers positioned along the direction of wave propagation and oriented in the direction of particle motion. For example, a compression wave generated at the east source would be recorded on the horizontal accelerometers sensitive in the east-west direction in the three, 3-D accelerometer packages lying along the east-west axis of the cube. (Operation of the accelerometers is discussed in Section B.5.1.)

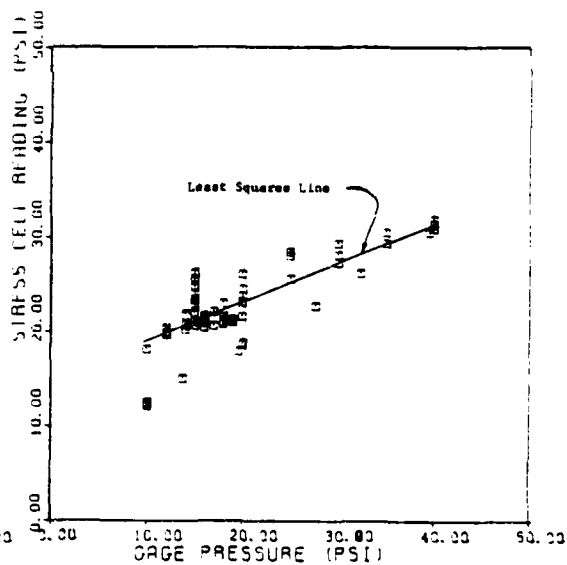




a) North-South Axis



b) Vertical Axis



c) East-West Axis

Fig. B.20 - Stress Cell Reading versus Pressure  
Determined by Panel Board Gage for Each  
Axis of the Cube

Each set of waveforms was generated by striking the anvil of a source on the cube with a hammer. The mechanical action generated a wave through the sand. The direction of the impulse of the hammer determined the direction of the particle motion, and therefore the type of wave. As the hammer struck the source, the two digital oscilloscopes were electrically triggered, starting the recording of the waveforms. Full details of the operation of the trigger and source can be found in Section A.3.

The waves were recorded on the magnetic storage diskettes of a pair of two-channel oscilloscopes with the output from the middle accelerometer recorded on both oscilloscopes as a reference. Appendices C to E show typical sets of S-wave traces along with their data reduction. Data reduction is discussed in Chapter 6.

### B.3 SUMMARY AND CONCLUSIONS

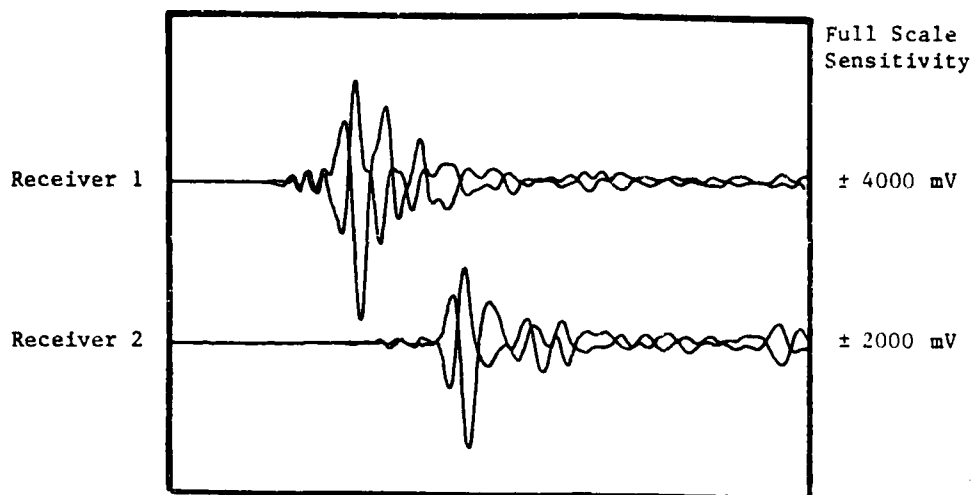
A testing program was selected which permitted testing with: 1. isotropic confinement, 2. confinement with a constant mean effective principal stress, and 3. confinement with a varying mean effective principal stress. The sand was tested in a dry state and therefore could be placed in the cube by a raining technique discussed in the chapter. Raining was halted at predetermined elevations to allow for placement of accelerometers, stress cells, and strain sensors, and to permit determination of density. The density tests showed the sample to be quite uniform with an average density of 96.6 pcf ( $1547 \text{ kg/m}^3$ ). Because of

problems discussed in the chapter, the stress and strain cells were not used to their full potential. Rather, they could only give an estimation of what was occurring in the cube when subjected to load.

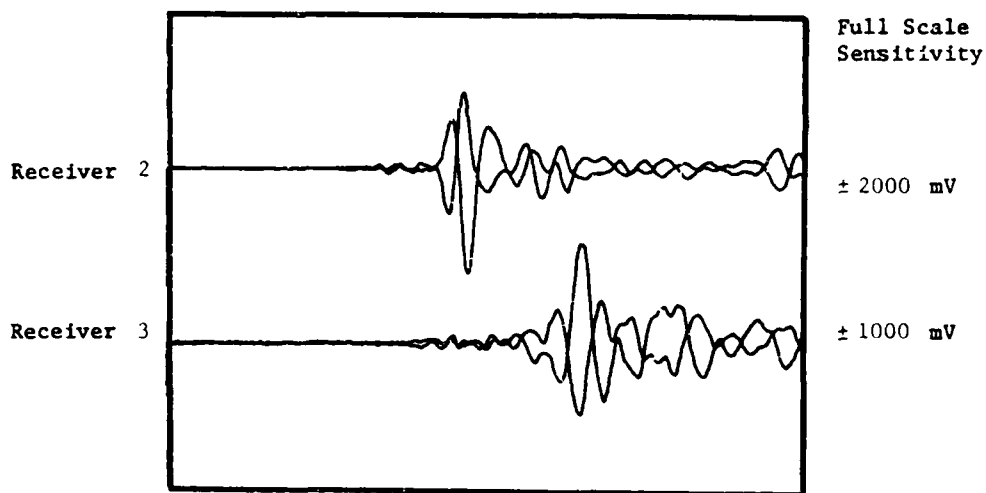
Dynamic testing began on July 8, 1981, and was completed on August 19, 1981. The method of analyzing the data is discussed in Chapter 6, and the results of the testing are discussed in Chapters 6 through 8.

## APPENDIX C

SET OF RECORDED WAVEFORMS, DATA INPUT,  
AND COMPUTER OUTPUT FOR A REPRESENTATIVE  
ISOTROPIC TEST (Wave Reversals are Included)



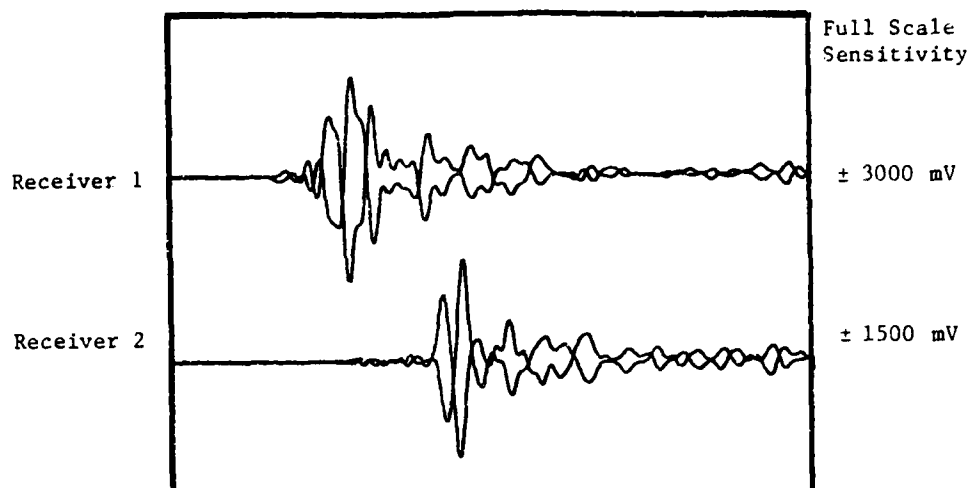
Disk / Track Number: 4-7/5  
Record Length: 10.1 msec.



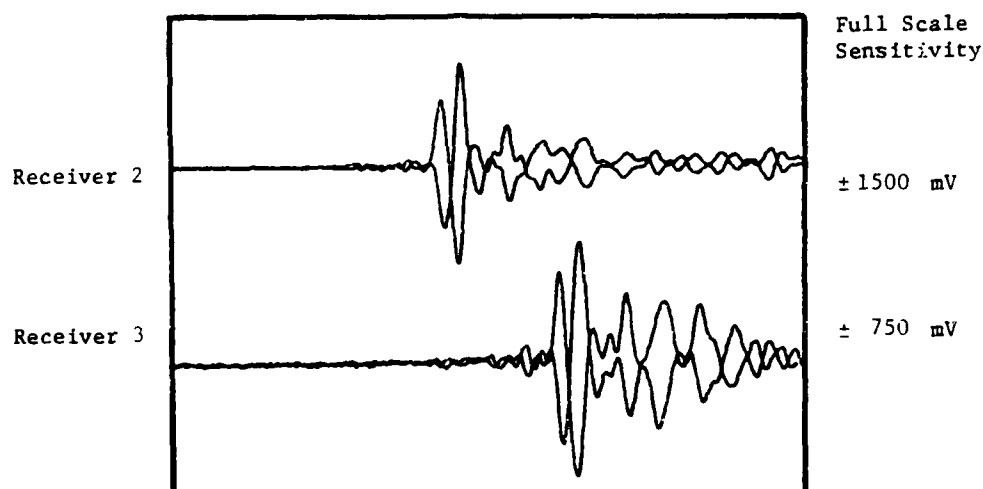
Disk / Track Number: 4-8/5  
Record Length: 10.1 msec.

TEST NUMBER: 13  
DIRECTION OF WAVE PROPAGATION: Top-Bottom      PRESSURE ALONG AXIS: 20 psi  
DIRECTION OF PARTICLE MOTION: North-South      PRESSURE ALONG AXIS: 20 psi

Fig. C.1 - Accelerometer Records of  $S_{TB/NS}$ -Wave for  
Sample Isotropic Data



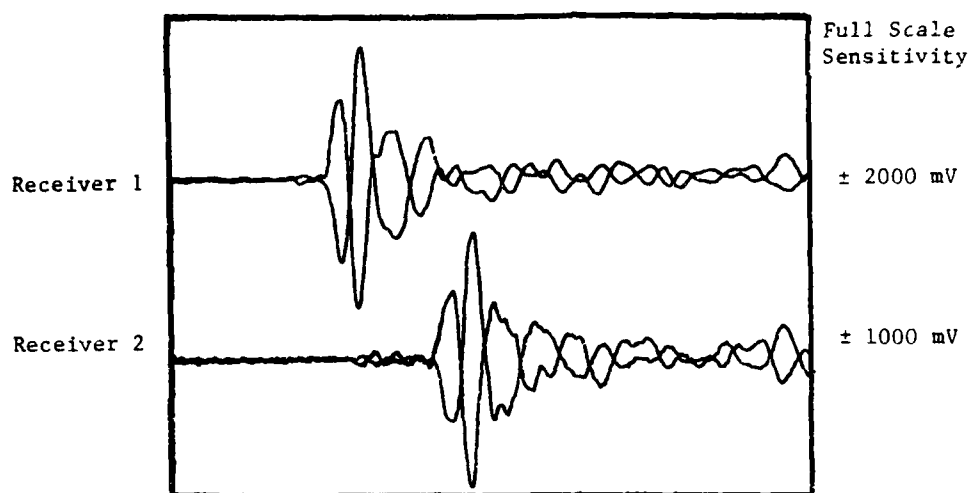
Disk / Track Number: 4-7/4  
Record Length: 10.1 msec.



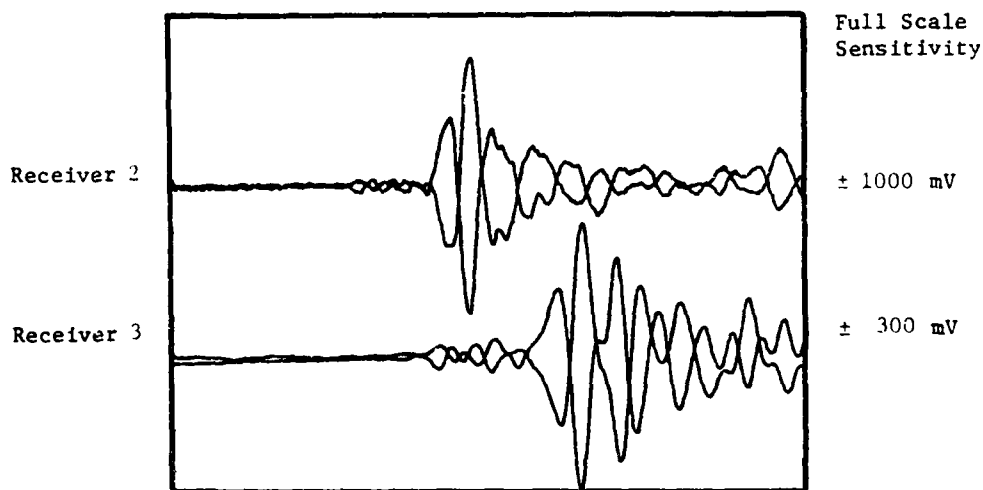
Disk / Track Number: 4-8/4  
Record Length: 10.1 msec.

TEST NUMBER: 13  
DIRECTION OF WAVE PROPAGATION: Top-Bottom PRESSURE ALONG AXIS: 20 psi  
DIRECTION OF PARTICLE MOTION: East-West PRESSURE ALONG AXIS: 20 psi

Fig. C.2 - Accelerometer Records of  $S_{TB/EW}$ -Wave for  
Sample Isotropic Data



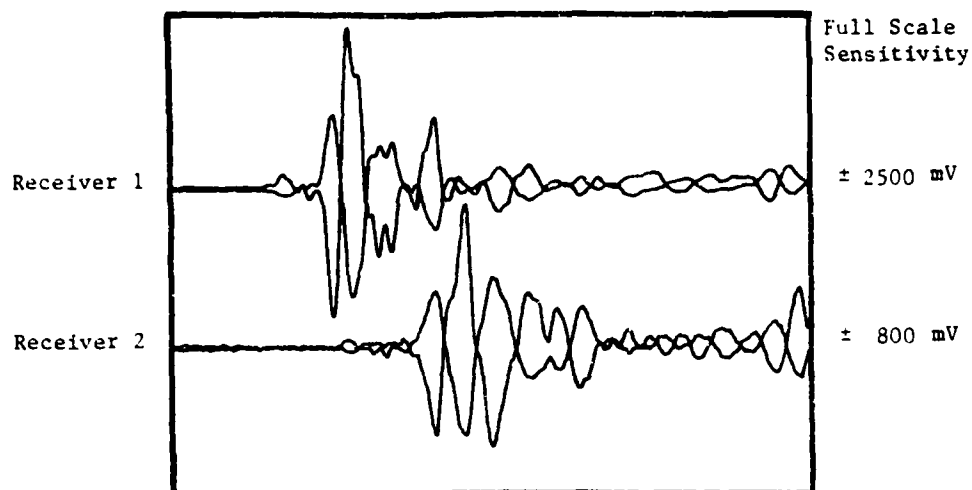
Disk / Track Number: 4-7/3  
Record Length: 10.1 msec.



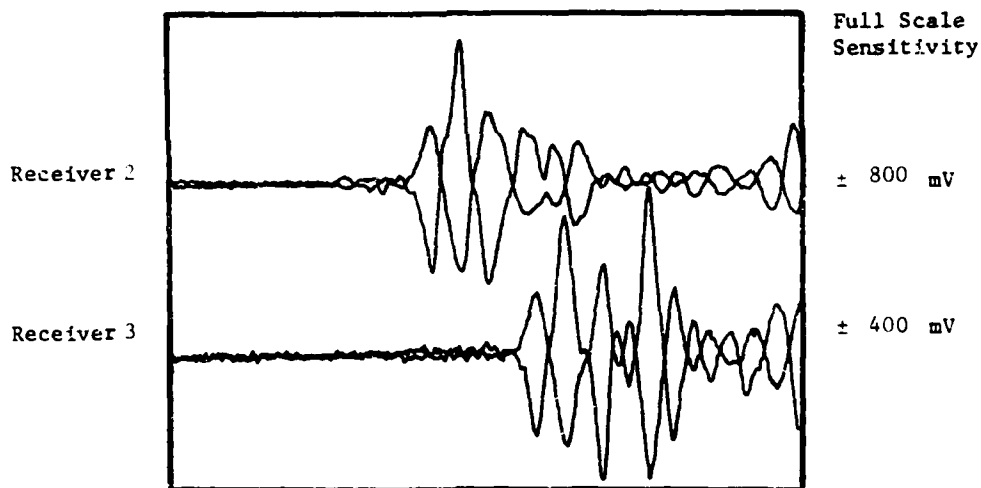
Disk / Track Number: 4-8/3  
Record Length: 10.1 msec.

TEST NUMBER: 13  
DIRECTION OF WAVE PROPAGATION: North-South PRESSURE ALONG AXIS: 20 psi  
DIRECTION OF PARTICLE MOTION: Top-Bottom PRESSURE ALONG AXIS: 20 psi

Fig. C.3 - Accelerometer Records of  $S_{NS/TB}$ -Wave for  
Sample Isotropic Data



Disk / Track Number: 4-7/1  
Record Length: 10.1 msec.

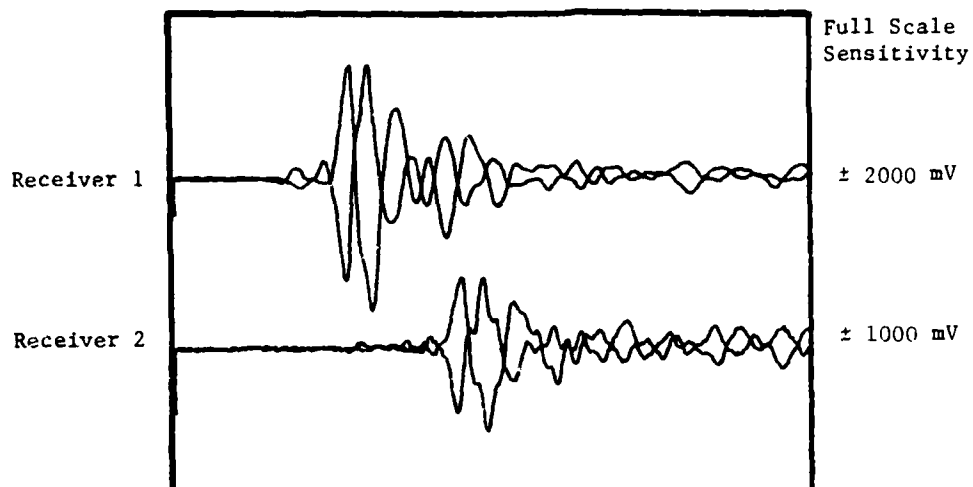


Disk / Track Number: 4-8/1  
Record Length: 10.1 msec.

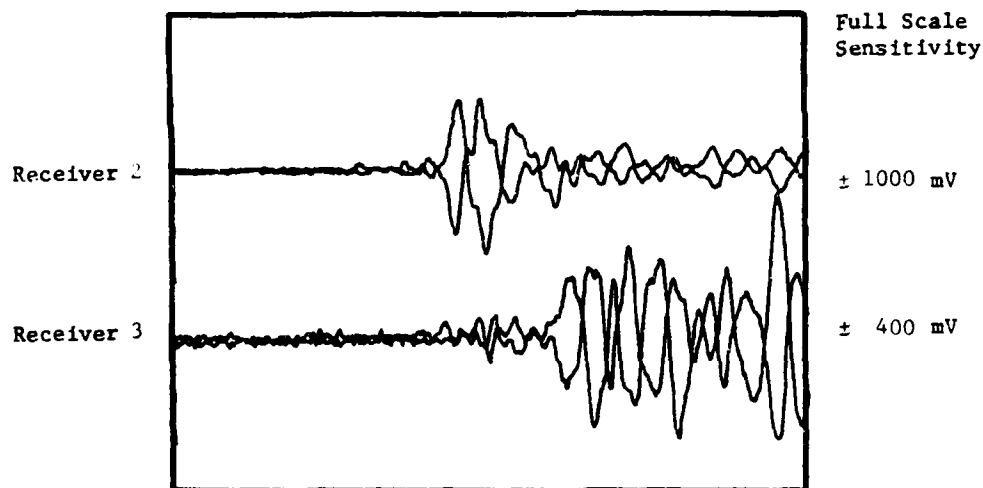
TEST NUMBER: 13  
DIRECTION OF WAVE PROPAGATION: North-South    PRESSURE ALONG AXIS: 20 psi  
DIRECTION OF PARTICLE MOTION: East-West       PRESSURE ALONG AXIS: 20 psi

Fig. C.4 - Accelerometer Records of  $S_{NS/EW}$ -Wave for  
Sample Isotropic Data





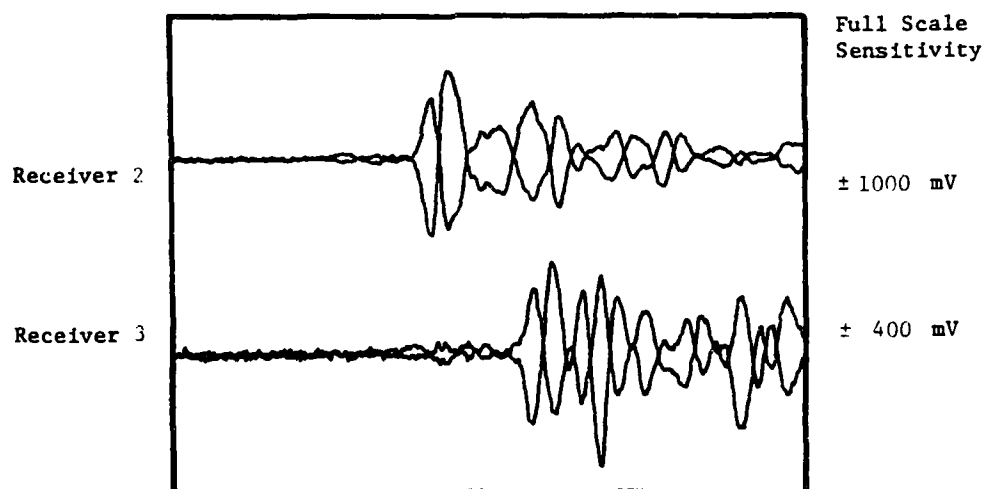
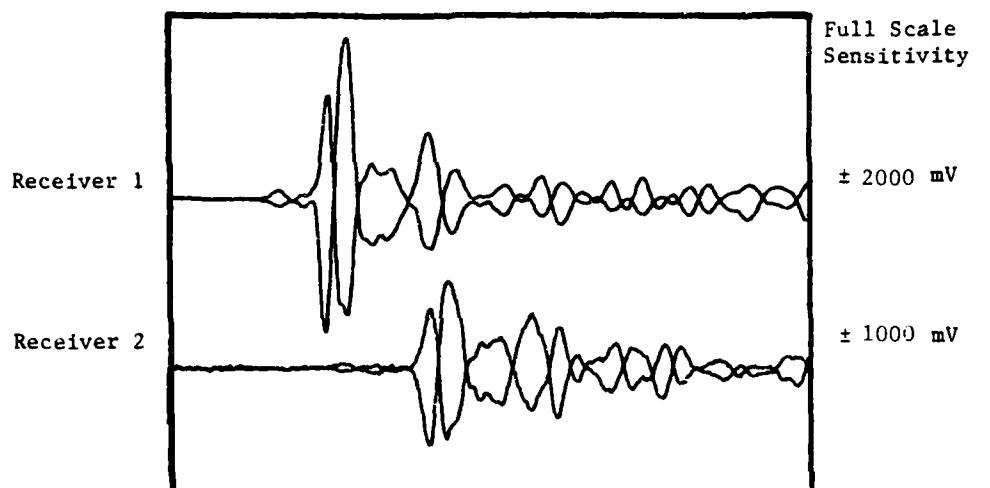
Disk / Track Number: 4-5/8  
Record Length: 10.1 msec.



Disk / Track Number: 4-6/8  
Record Length: 10.1 msec.

TEST NUMBER: 13  
DIRECTION OF WAVE PROPAGATION: East-West      PRESSURE ALONG AXIS: 20 psi  
DIRECTION OF PARTICLE MOTION: Top-Bottom      PRESSURE ALONG AXIS: 20 psi

Fig. C.5 - Accelerometer Records of  $S_{EW/TB}$ -Wave for  
Sample Isotropic Data



TEST NUMBER: 13  
 DIRECTION OF WAVE PROPAGATION: East-West PRESSURE ALONG AXIS: 20 psi  
 DIRECTION OF PARTICLE MOTION: North-South PRESSURE ALONG AXIS: 20 psi

Fig. C.6 - Accelerometer Records of  $S_{EW/NS}$ -Wave for Sample Isotropic Data

TEST NO.: 13  
 DATE: 7/23/81  
 P-DATA BY: -  
 S-DATA BY: DPK

DIRECTION OF AXIS  
 1-1 Top-Bottom  
 2-2 North-South  
 3-3 East-West

PRESSURE AT CENTER  
 OF CUBE  
 20  
 20  
 20  
 (psi)

PRESSURE AT GAGE  
 AT PANEL BOARD  
 19.8  
 20.9  
 20.9  
 (psi)

## REDUCED DATA FOR S-WAVE\*

DISK	TRACE	DIRECTION OF WAVE PROPAGATION	DIRECTION OF PARTICLE MOTION	S-WAVE TYPE **	TRACE 1					TRACE 2					TRACE 3				
					t <sub>11</sub>	t <sub>21</sub>	t <sub>31</sub>	A <sub>11</sub>	A <sub>21</sub>	t <sub>12</sub>	t <sub>22</sub>	t <sub>32</sub>	A <sub>12</sub>	A <sub>22</sub>	t <sub>13</sub>	t <sub>23</sub>	t <sub>33</sub>	A <sub>13</sub>	A <sub>23</sub>
4-7	5	1-1	2-2	NR	2.57	2.81	3.07	.509	1.86	4.30	4.53	4.78	.205	.720	6.07	6.25	6.57	.034	.097
4-8	5	1-1	2-2	R	2.60	2.77	2.99	.272	1.43	4.35	4.50	4.73	.186	.568	6.04	6.20	6.54	.048	.201
4-7	4	1-1	3-3	NR	2.38	2.54	2.86	.528	1.08	4.18	4.35	4.62	.200	.536	6.07	6.21	6.49	.114	.268
4-8	4	1-1	3-3	R	2.42	2.68	2.90	.438	.980	4.21	4.41	4.66	.206	.528	6.12	6.27	6.54	.112	.267
4-7	3	2-2	1-1	NR	2.44	2.72	3.04	.222	.701	4.22	4.44	4.82	.094	.309	5.90	6.22	6.55	.033	.133
4-8	3	2-2	1-1	R	2.44	2.71	2.98	.157	.677	4.24	4.48	4.78	.083	.324	5.94	6.18	6.53	.026	.132

\* Time are in msec, Amplitudes are in volts.

\*\* NR denotes non-reversed shear wave, R denotes reversed shear wave.

Fig. C.7 - Data Input of All Shear Wave Types for Sample Isotropic Data

TEST NO.: 13 Cont.

DATE: 7/23/81

P-DATA BY: -

S-DATA BY: DPK

DIRECTION OF AXIS

1-1 TB

2-2 NS

3-3 EW

PRESSURE AT CENTER OF CUBE

20

20

20

(psi)

PRESSURE AT GAGE AT PANEL BOARD

19.8

20.9

20.9

(psi)

## REDUCED DATA FOR S-WAVE \*

REDUCED DATA FOR S-WAVE\*

DISK	TRACK	DIRECTION OF WAVE PROPAGATION	DIRECTION OF PARTICLE MOTION	S-WAVE TYPE**	TRACE 1				TRACE 2				TRACE 3						
					t <sub>11</sub>	t <sub>21</sub>	t <sub>31</sub>	A <sub>11</sub>	A <sub>21</sub>	t <sub>12</sub>	t <sub>22</sub>	t <sub>32</sub>	A <sub>12</sub>	A <sub>22</sub>	t <sub>13</sub>	t <sub>23</sub>	t <sub>33</sub>	A <sub>13</sub>	A <sub>23</sub>
4-7	1	2-2	3-3	NR	2.35	2.60	2.86	.606	1.38	3.96	4.23	4.70	.134	.380	5.66	5.86	6.33	.055	.176
4-8	1	2-2	3-3	R	2.35	2.61	2.91	.335	.881	3.94	4.22	4.68	.078	.237	5.60	5.89	6.35	.046	.122
4-5	8	3-3	1-1	NR	2.53	2.74	3.10	.315	.703	4.36	4.50	4.92	.089	.225	6.08	6.28	6.67	.032	.077
4-6	8	3-3	1-1	R	2.53	2.81	3.16	.368	.800	4.35	4.58	5.00	.100	.255	6.09	6.35	6.70	.030	.101
4-5	7	3-3	2-2	NR	2.29	2.50	2.81	.482	1.14	3.92	4.18	4.46	.145	.321	5.59	5.76	6.09	.046	.125
4-6	7	3-3	2-2	R	2.29	2.53	2.85	.337	.848	3.90	4.19	4.45	.111	.255	5.64	5.80	6.13	.032	.098

\* Times are in msec, Amplitudes are in volts.

\*\* NR denotes non-reversed shear wave, R denotes reversed shear wave.

Fig. C.7 (Continued) - Data Input of All Shear Wave Types for Sample Isotropic Data

DATA REDUCTION FOR SIGMA(1)= 2.0 SIGMA(2)= 2.0 SIGMA(3)= 20.0

EFFECT (DAMPING) DIRECT (INTERVAL)	FIRST ARRIVAL (TRACE 1) (HALF AMPL)			FIRST THROUGH (TRACE 2) (FULL AMPL)			FIRST PEAK (TRACE 3)			AVG
	1	2	3	1	2	3	1	2	3	
	1-2	2-3	1-3	1-2	2-3	1-3	1-2	2-3	1-3	
SOURCE NO. 1 HWT DIRECTION 2 (S-WAVE)										
INPUT	.02570	.02410	.02370	.0402	1.0590					
INPUT	.04370	.04530	.04780	.2045	.7200					
INPUT	.04670	.04650	.04570	.518	.2626					
DIRECT VEL	774	791	817							794
INTERVAL VEL	818	841	849	821	847	863	825	872	849	853
FREQUENCY	1042	962	1000	1027	1020	1042	1389	741	1000	1030
COEF OF ATTN	.267	.438	.462	.293	.400	.351				.40
LOG DECP..	.221	.527	.381	.242	.334	.208				
DAMPING	.135	.100	.161	.230	.153	.106				
Q	14.	1.	12.	16.	13.	10.				
SOURCE NO. 1 HWT DIRECTION 2 (S-WAVE)										
INPUT	.02200	.02270	.02290	.2720	1.0330					
INPUT	.04430	.04510	.04730	.1855	.5675					
INPUT	.04600	.04620	.04500	.0480	.2016					
DIRECT VEL	765	782	821							786
INTERVAL VEL	816	823	863	815	810	866	810	862	837	856
FREQUENCY	1471	1136	1282	1067	1087	1316	1562	735	1020	1251
COEF OF ATTN	.118	.625	.277	.277	.425	.355				.37
LOG DECP..	.100	.427	.180	.190	.290	.243				
DAMPING	.100	.108	.131	.130	.146	.139				
Q	1.	11.	20.	20.	14.	16.				
SOURCE NO. 1 HWT DIRECTION 3 (S-WAVE)										
INPUT	.02380	.02250	.02260	.6280	1.2810					
INPUT	.04510	.04435	.04620	.2400	.5355					
INPUT	.04670	.04621	.04640	.1136	.2682					
DIRECT VEL	811	841	789							807
INTERVAL VEL	789	762	775	785	774	770	807	774	788	781
FREQUENCY	1562	781	1042	1471	926	1136	1786	803	1190	1190
COEF OF ATTN	.295	.144	.219	.176	.232	.170				.19
LOG DECP..	.192	.290	.143	.260	.151	.110				
DAMPING	.131	.115	.123	.111	.124	.118				
Q	24.	37.	25.	49.	24.	32.				
SOURCE NO. 1 HWT DIRECTION 3 (S-WAVE)										
INPUT	.02420	.02680	.02290	.4380	.6800					
INPUT	.04820	.04410	.04660	.2055	.5275					
INPUT	.04610	.04620	.04650	.1116	.2670					
DIRECT VEL	798	796	783							792
INTERVAL VEL	793	754	773	821	774	777	807	786	786	786
FREQUENCY	962	1136	1042	1250	1000	1111	1667	926	1190	1143
COEF OF ATTN	.145	.176	.160	.148	.225	.137				.14
LOG DECP..	.199	.121	.110	.233	.150	.100				
DAMPING	.116	.119	.118	.105	.125	.115				
Q	35.	29.	32.	90.	24.	37.				

Fig. C.8 - Computer Output of All Shear Wave Types for Sample Isotropic Data

```

SOURCE NO. 2 HWT DIRECTION 1 (S-WAVE)
INPUT .002011 .002721 .003001 .002201 .7111
INPUT .004022 .004044 .004401 .00401 .7191
INPUT .005011 .005221 .005501 .00521 .7321
DIRECT VEL .795 .829 .847 .824
INTERVAL VEL .874 .893 .884 .877 .863 .874 .874 .867 .877 .877
FREQUENCY .871 .781 .831 .1131 .851 .831 .741 .751 .749 .827
COEF OF ATTN .171 .241 .311 .117 .125 .234 .27
LOG DECP .183 .202 .315 .151 .145 .202
DAMPING .29 .171 .151 .225 .151 .141
Q .21 .11 .13 .23 .13 .11

SOURCE NO. 2 HWT DIRECTION 1 (S-WAVE)
INPUT .002011 .002711 .002901 .1571 .770
INPUT .004011 .004011 .004711 .1825 .7215
INPUT .005011 .005111 .005311 .1251 .1311
DIRECT VEL .795 .825 .842 .821
INTERVAL VEL .867 .882 .874 .881 .882 .882 .887 .857 .862 .821
FREQUENCY .921 .924 .921 .1042 .831 .921 .1042 .714 .847 .900
COEF OF ATTN .31 .542 .283 .05 .361 .225 .25
LOG DECP .113 .521 .272 .101 .341 .211
DAMPING .115 .113 .143 .115 .151 .134
Q .09 .11 .15 .31 .13 .11

SOURCE NO. 2 HWT DIRECTION 3 (S-WAVE)
INPUT .002351 .002611 .002811 .1341 .13431
INPUT .003011 .004211 .004711 .1341 .1341
INPUT .005111 .005111 .006311 .1551 .1764
DIRECT VEL .851 .884 .883 .873
INTERVAL VEL .932 .882 .901 .921 .921 .921 .815 .921 .865 .873
FREQUENCY .1012 .982 .981 .971 .532 .674 .1251 .532 .746 .845
COEF OF ATTN .033 .351 .192 .141 .271 .311 .13
LOG DECP .673 .373 .523 .511 .291 .405
DAMPING .111 .150 .183 .182 .146 .164
Q .11 .12 .11 .11 .11 .11

SOURCE NO. 2 HWT DIRECTION 3 (S-WAVE)
INPUT .002351 .002611 .002911 .1351 .8811
INPUT .003011 .00422 .004611 .741 .2365
INPUT .005111 .005111 .006351 .1461 .1211
DIRECT VEL .851 .881 .883 .873
INTERVAL VEL .941 .921 .923 .932 .891 .911 .817 .901 .872 .874
FREQUENCY .742 .813 .893 .893 .543 .671 .812 .543 .617 .741
COEF OF ATTN .501 .111 .151 .511 .121 .351 .13
LOG DECP .711 .121 .111 .511 .242 .111
DAMPING .112 .121 .101 .101 .131 .167
Q .11 .12 .11 .11 .11 .11

SOURCE NO. 3 HWT DIRECTION 1 (S-WAVE)
INPUT .002531 .002711 .003111 .1111 .7131
INPUT .003111 .004011 .004911 .1811 .2251
INPUT .006011 .006211 .006711 .321 .771
DIRECT VEL .771 .781 .813 .813
INTERVAL VEL .871 .872 .817 .815 .713 .811 .811 .857 .832 .793
FREQUENCY .1101 .601 .877 .1711 .595 .803 .1251 .841 .847 .875
COEF OF ATTN .181 .021 .151 .301 .171 .135 .11
LOG DECP .115 .111 .101 .131 .111 .373 .11
DAMPING .111 .151 .162 .151 .145 .151
Q .11 .12 .12 .13 .11 .12

```

Fig. C.8 (Continued) - Computer Output of All Shear Wave Types for Sample Isotropic Data

SOURCE NO. 3 WIT. DIRECTION 1 (S-WAVE)  
 INPUT .00253 .00281 .00314 .00347 .00380  
 INPUT .00435 .00468 .00501 .00534 .00567  
 INPUT .00600 .00633 .00666 .00699 .00732  
 DIRECT VEL. 779. 791. 811. 831. 847. 869. 892. 914. 939. 962. 984. 1006  
 INTERVAL VEL. 3.4. 4.2. 5.0. 5.8. 6.6. 7.4. 8.2. 9.0. 9.8. 10.6. 11.4  
 FREQUENCY 893. 714. 704. 1047. 545. 709. 962. 714. 421. 816. 46  
 COEF OF ATTEN. .513 .554 .572 .61 .672 .344 .342 .342 .342 .342 .342  
 LOG DECP. .524 .564 .516 .51 .51 .51 .51 .51 .51 .51 .51  
 DAMPING .53 .52 .57 .55 .61 .63 .63 .63 .63 .63 .63  
 Q 12. 9. 9. 11. 12. 11. 11. 11. 11. 11. 11.

SOURCE NO. 3 WIT. DIRECTION 2 (S-WAVE)  
 INPUT .00229 .00253 .00281 .00309 .00337  
 INPUT .00365 .00393 .00421 .00449 .00477  
 INPUT .00505 .00533 .00561 .00589 .00617  
 DIRECT VEL. 847. 878. 899. 920. 949. 920. 919. 924. 915. 915. 846  
 INTERVAL VEL. 924. 468. 919. 873. 949. 920. 919. 924. 915. 915. 915  
 FREQUENCY 1194. 846. 912. 912. 893. 924. 1471. 758. 1024. 992. 46  
 COEF OF ATTEN. .419 .53 .474 .463 .389 .426 .426 .426 .426 .426 .426  
 LOG DECP. .385 .487 .436 .425 .357 .301 .301 .301 .301 .301 .301  
 DAMPING .61 .77 .69 .68 .57 .562 .562 .562 .562 .562 .562  
 Q 12. 13. 11. 11. 12. 12. 12. 12. 12. 12. 12.

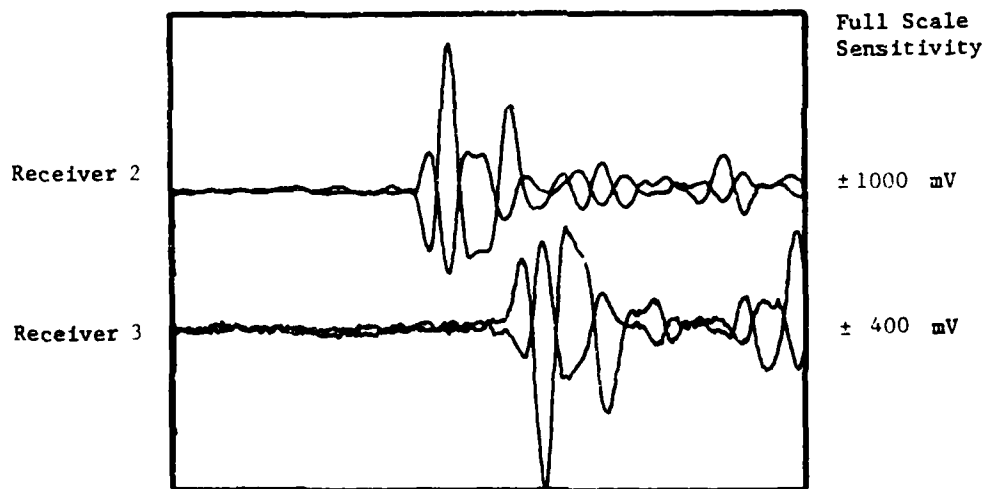
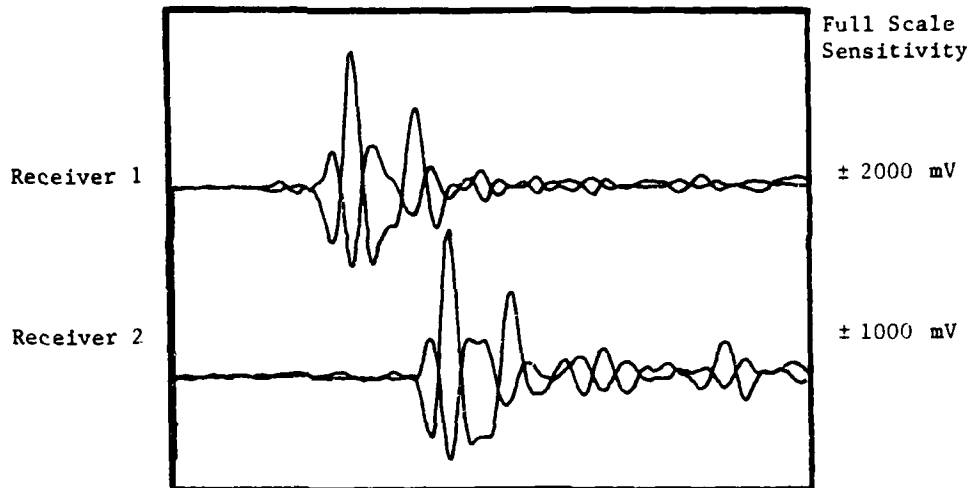
SOURCE NO. 3 WIT. DIRECTION 2 (S-WAVE)  
 INPUT .00229 .00253 .00281 .00309 .00337  
 INPUT .00365 .00393 .00421 .00449 .00477  
 INPUT .00505 .00533 .00561 .00589 .00617  
 DIRECT VEL. 847. 882. 876. 914. 932. 917. 938. 893. 915. 915. 846  
 INTERVAL VEL. 932. 862. 804. 914. 932. 917. 938. 893. 915. 915. 915  
 FREQUENCY 1442. 781. 893. 862. 962. 909. 1563. 758. 1024. 977. 46  
 COEF OF ATTEN. .362 .593 .477 .419 .394 .404 .404 .404 .404 .404 .404  
 LOG DECP. .337 .553 .444 .391 .349 .342 .342 .342 .342 .342 .342  
 DAMPING .54 .788 .471 .462 .459 .459 .459 .459 .459 .459 .459  
 Q 13. 9. 11. 12. 12. 12. 12. 12. 12. 12. 12.

Fig. C.8 (Continued) - Computer Output of All Shear Wave  
 Types for Sample Isotropic Data

## APPENDIX D

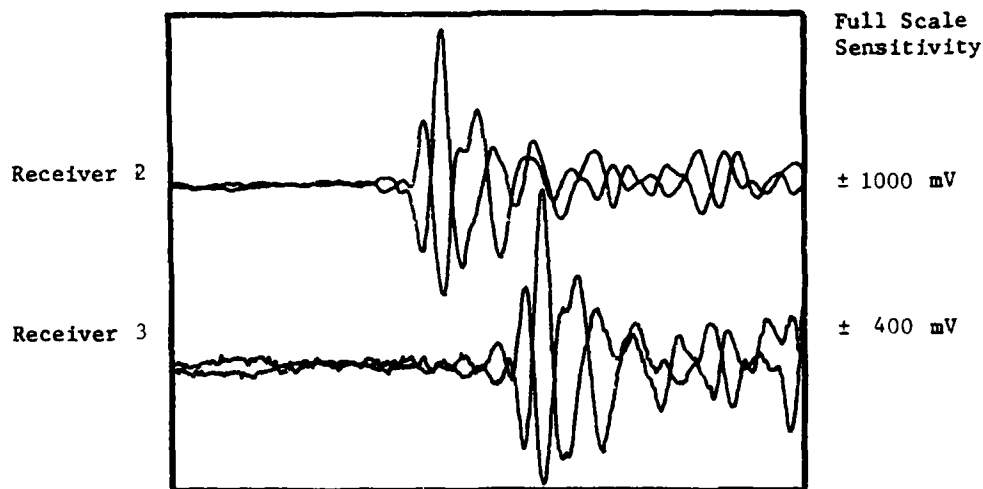
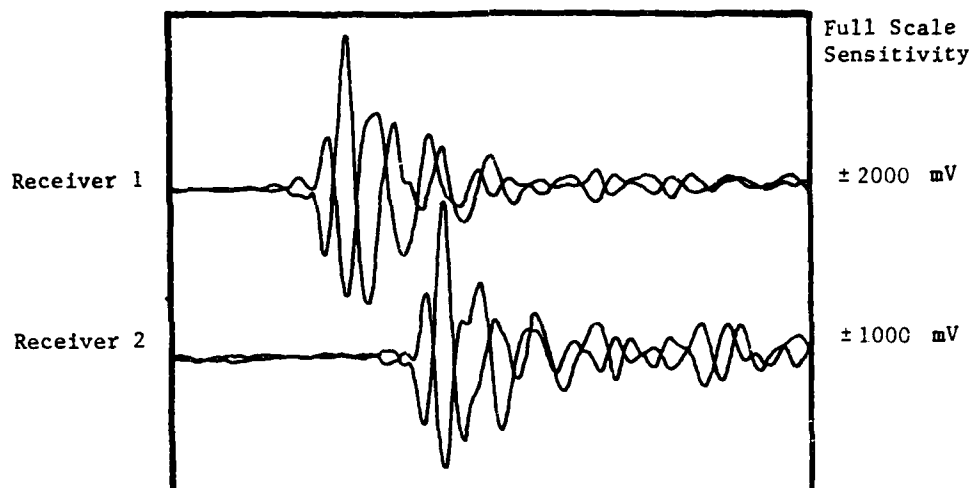
SET OF RECORDED WAVEFORMS, DATA INPUT,  
AND COMPUTER OUTPUT FOR A REPRESENTATIVE  
BIAXIAL TEST (Wave Reversals are Included)





TEST NUMBER: 33  
 DIRECTION OF WAVE PROPAGATION: Top-Bottom  
 DIRECTION OF PARTICLE MOTION: North-South  
 PRESSURE ALONG AXIS: 40 psi  
 PRESSURE ALONG AXIS: 35 psi

Fig. D.1 - Accelerometer Records of  $S_{TB/NS}$ -Wave for  
 Sample Biaxial Data



TEST NUMBER: 33

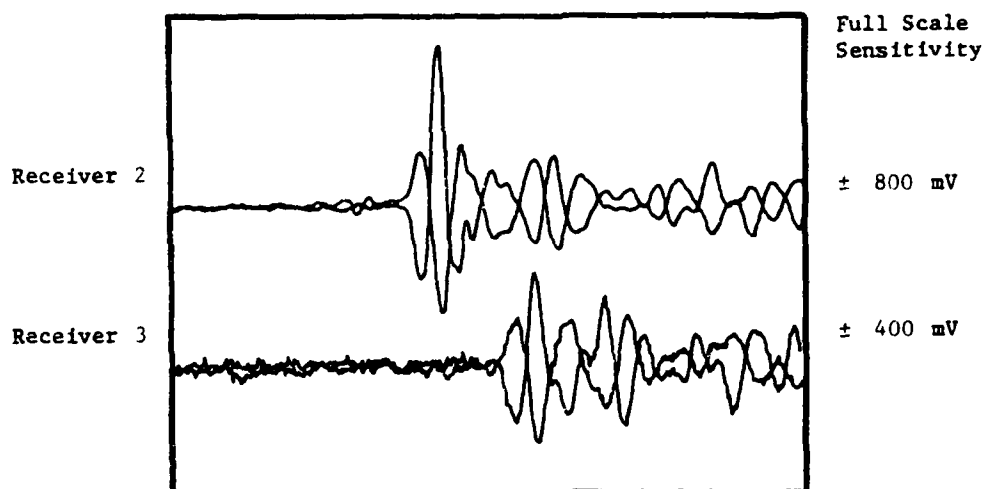
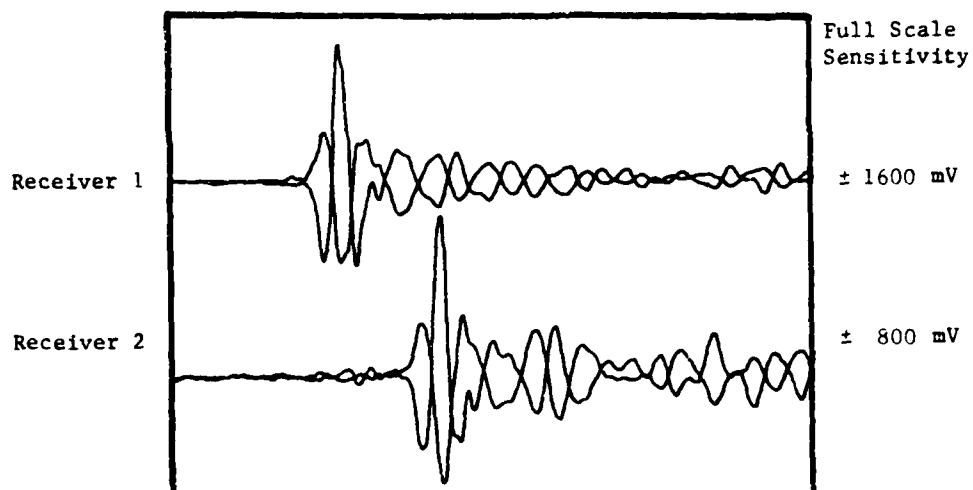
DIRECTION OF WAVE PROPAGATION: Top-Bottom

DIRECTION OF PARTICLE MOTION: East-West

PRESSURE ALONG AXIS: 40 psi

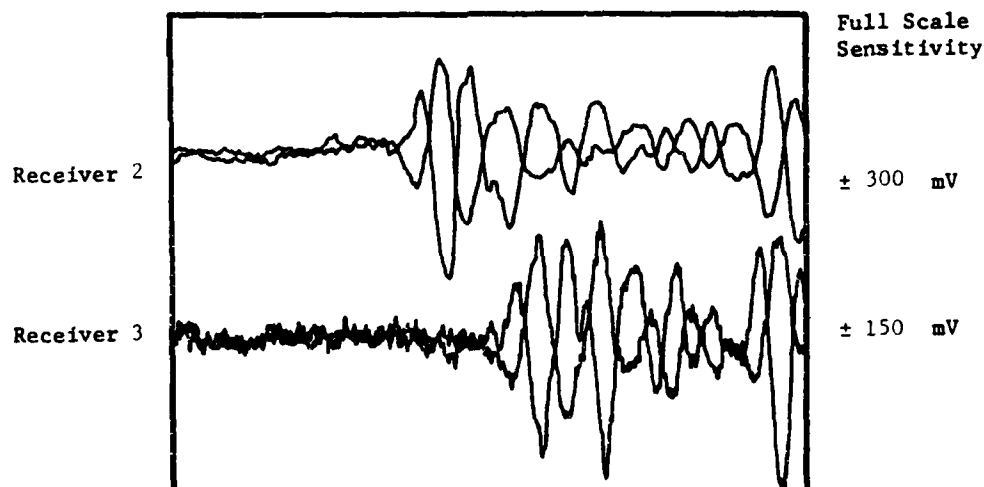
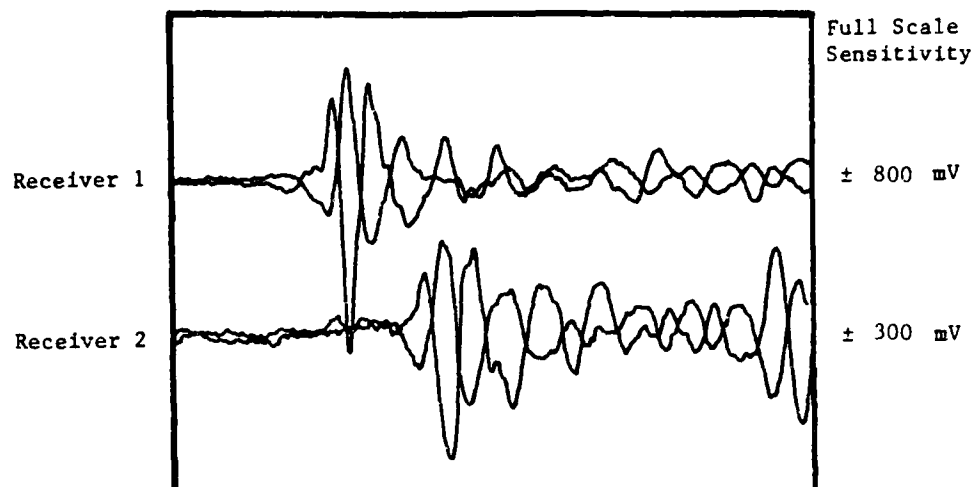
PRESSURE ALONG AXIS: 35 psi

Fig. D.2 - Accelerometer Records of S<sub>TB/EW</sub>-Wave  
for Sample Biaxial Data



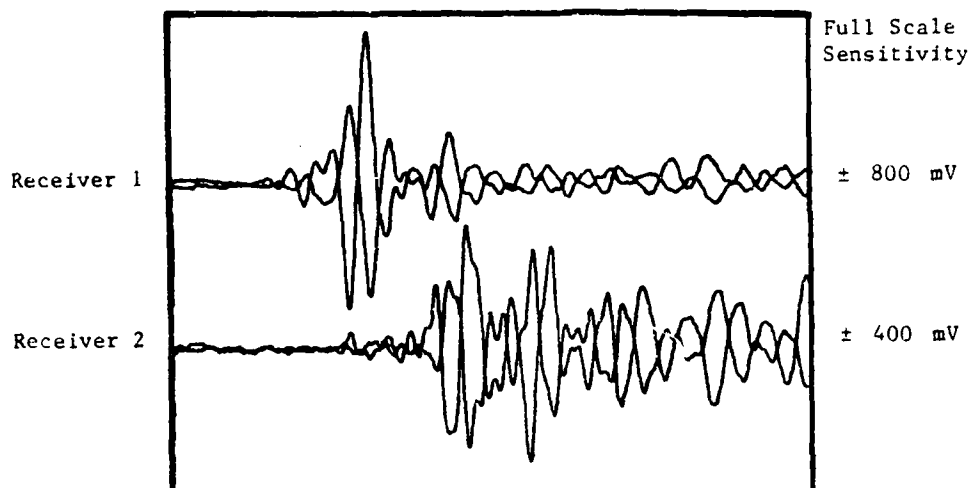
TEST NUMBER: 33  
 DIRECTION OF WAVE PROPAGATION: North-South PRESSURE ALONG AXIS: 35 psi  
 DIRECTION OF PARTICLE MOTION: Top-Bottom PRESSURE ALONG AXIS: 40 psi

Fig. D.3 - Accelerometer Records of  $S_{NS/TB}$ -Wave for Sample Biaxial Data

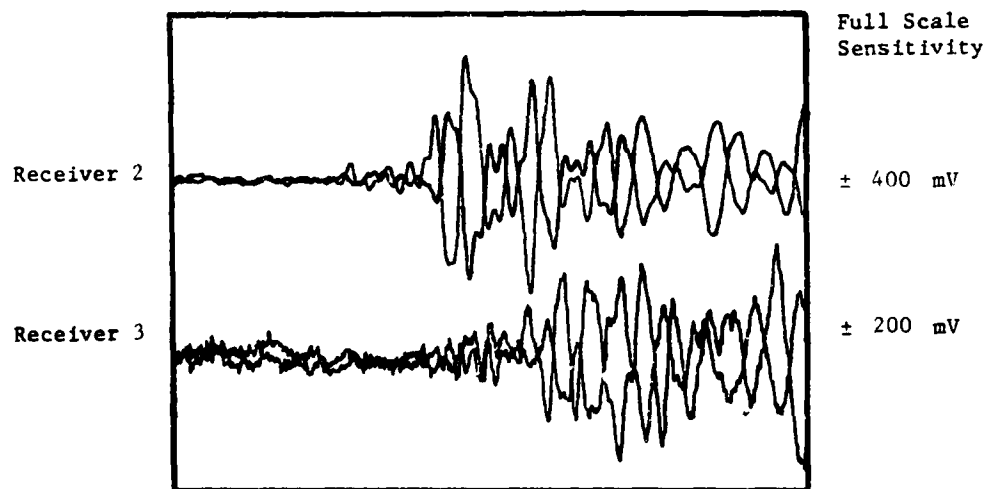


TEST NUMBER: 33  
 DIRECTION OF WAVE PROPAGATION: North-South  
 DIRECTION OF PARTICLE MOTION: East-West  
 PRESSURE ALONG AXIS: 35 psi  
 PRESSURE ALONG AXIS: 35 psi

Fig. D.4 - Accelerometer Records of  $S_{NS/EW}$ -Wave for Sample Biaxial Data



Disk / Track Number: 9-1/8  
Record Length: 10.1 msec.

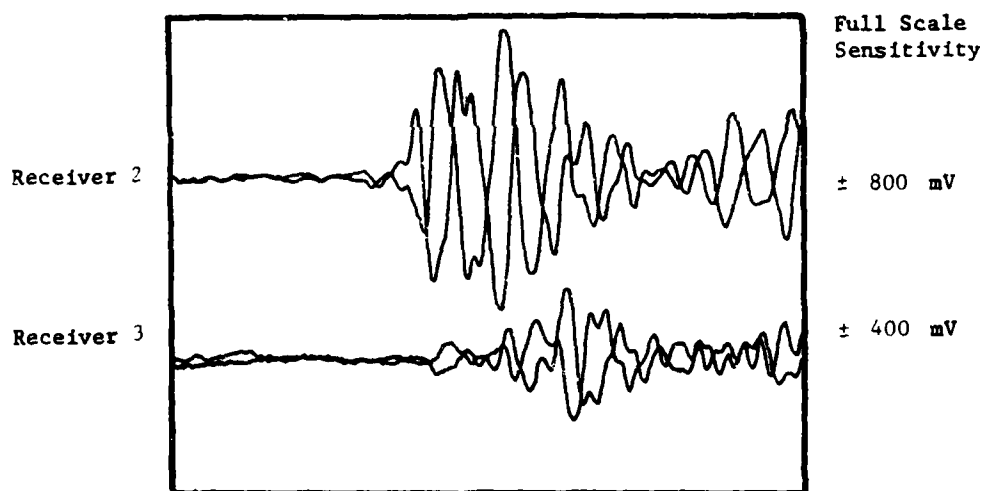
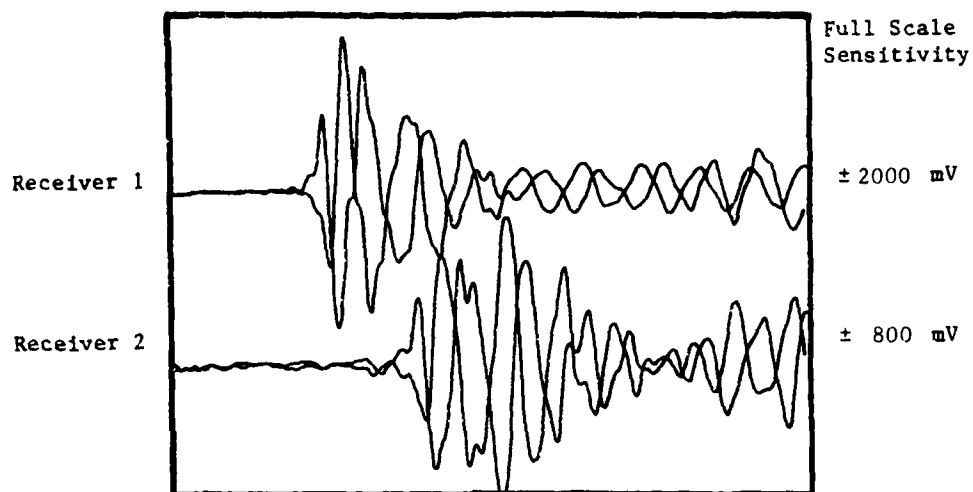


Disk / Track Number: 9-2/8  
Record Length: 10.1 msec.

TEST NUMBER: 33  
DIRECTION OF WAVE PROPAGATION: East-West  
DIRECTION OF PARTICLE MOTION: Top-Bottom

PRESSURE ALONG AXIS: 35 psi  
PRESSURE ALONG AXIS: 40 psi

Fig. D.5 - Accelerometer Records of  $S_{EW/TB}$ -Wave for  
Sample Biaxial Data



TEST NUMBER: 33

DIRECTION OF WAVE PROPAGATION: East-West

DIRECTION OF PARTICLE MOTION: North-South

PRESSURE ALONG AXIS: 35 psi

PRESSURE ALONG AXIS: 35 psi

Fig. D.6 - Accelerometer Records of  $S_{EW/NS}$ -Wave for  
Sample Biaxial Data

TEST NO.: 33  
 DATE: 8/7/81  
 P-DATA BY: -  
 S-DATA BY: DPK

DIRECTION OF AXIS  
 1-1 Top-Bottom  
 2-2 North-South  
 3-3 East-West

PRESSURE AT CENTER  
 OF CUBE  
 40  
 35  
 35

PRESSURE AT GAGE  
 AT PANEL BOARD  
 39.8  
 35.9  
 35.9

(psi)

## REDUCED DATA FOR S-WAVE \*

REDUCED DATA FOR S-WAVE																			
DISK	TRACK	DIRECTION OF WAVE PROPAGATION	DIRECTION OF PARTICLE MOTION	S-WAVE TYPE**	TRACE 1					TRACE 2					TRACE 3				
					t <sub>11</sub>	t <sub>21</sub>	t <sub>31</sub>	A <sub>11</sub>	A <sub>21</sub>	t <sub>12</sub>	t <sub>22</sub>	t <sub>32</sub>	A <sub>12</sub>	A <sub>22</sub>	t <sub>13</sub>	t <sub>23</sub>	t <sub>33</sub>	A <sub>13</sub>	A <sub>23</sub>
9-3	5	1-1	2-2	NR	2.37	2.55	2.87	.115	.537	3.85	4.07	4.36	.077	.230	5.26	5.53	.025	.109	
9-4	5	1-1	2-2	R	2.28	2.54	2.86	.240	.888	3.81	4.08	4.38	.117	.390	5.29	5.52	.054	.213	
9-3	4	1-1	3-3	NR	2.29	2.52	2.81	.242	.725	3.86	4.07	4.35	.122	.322	5.45	5.65	.079	.182	
9-4	4	1-1	3-3	R	2.29	2.47	2.82	.283	1.00	3.81	4.02	4.35	.111	.409	5.42	5.61	.079	.240	
9-3	3	2-2	1-1	NR	2.18	2.46	2.70	.242	.677	3.76	4.00	4.31	.089	.290	5.25	5.48	.034	.092	
9-4	3	2-2	1-1	R	2.19	2.47	2.73	.137	.400	3.78	4.01	4.33	.056	.203	5.28	5.49	.022	.076	

\* Times are in msec, Amplitudes are in volts.

\*\* NR denotes non-reversed shear wave, R denotes reversed shear wave.

Fig. D.7 - Data Input of All Shear Wave Types for Sample Biaxial Data

TEST NO.: 33 Cont.

DATE: 8/7/81

P-DATA BY: -

S-DATA BY: DPK

DIRECTION OF AXIS

1-1 TB

2-2 NS

3-3 EW

PRESSURE AT CENTER OF CUBE

40

35

35

PRESSURE AT GAGE AT PANEL BOARD

39.8

35.9

35.9

(psi)

# REDUCED DATA FOR S-WAVE\*

DISK	TRACK	DIRECTION OF WAVE PROPAGATION	DIRECTION OF PARTICLE MOTION	S-WAVE TYPE**	TRACE 1				TRACE 2				TRACE 3						
					t <sub>11</sub>	t <sub>21</sub>	t <sub>31</sub>	A <sub>11</sub>	A <sub>21</sub>	t <sub>12</sub>	t <sub>22</sub>	t <sub>32</sub>	A <sub>12</sub>	A <sub>22</sub>	t <sub>13</sub>	t <sub>23</sub>	t <sub>33</sub>	A <sub>13</sub>	A <sub>23</sub>
9-3	1	2-2	3-3	NR	2.34	2.49	2.79	.027	.241	3.66	3.90	4.31	.023	.085	5.21	5.41	5.84	.012	.051
9-4	1	2-2	3-3	R	2.39	2.56	2.82	.114	.412	3.87	4.01	4.38	.096	.123	5.25	5.50	5.89	.021	.058
9-1	8	3-3	1-1	NR	2.22	2.45	2.86	.065	.222	3.94	4.16	4.41	.023	.083	5.58	5.68	5.96	.009	.023
9-1	8	3-3	1-1	R	2.18	2.44	2.83	.109	.363	3.94	4.14	4.39	.067	.139	5.53	5.66	5.95	.024	.053
9-1	7	3-3	2-2	NR	2.38	2.54	2.77	.192	.791	3.89	4.04	4.30	.043	.229	5.29	5.44	5.79	.045	.084
9-1	7	3-3	2-2	R	2.26	2.43	2.67	.212	.741	3.74	3.94	4.18	.078	.241	5.18	5.36	5.69	.049	.087

\* Time are in msec, Amplitudes are in volts.

\*\* NR denotes non-reversed shear wave, R denotes reversed shear wave.

Fig. D.7 (Continued) - Data Input of All Shear Wave Types for Sample Biaxial Data



DATA REDUCTION FOR SIGMA(1)= 41.1 SIGMA(2)= 35.0 SIGMA(3)= 35.1

	FIRST ARRIVAL (TRACE 1) (HALF AMPL)			FIRST TROUGH (TRACE 2) (FULL AMPL)			FIRST PEAK (TRACE 3)			AVG
(FREQ.) (DAMPING) DIRECT (INTERVAL)	1 1-2	2 2-3	3 1-3	1 1-2	2 2-3	3 1-3	1 1-2	2 2-3	3 1-3	
SOURCE NO. 1 HIT DIRECTION 2 (S-WAVE)										
INPUT	.02371	.02551	.02870	.1150	.5370					
INPUT	.13451	.147	.1361	.1770	.231					
INPUT	.15261	.15531	.16840	.251	.1021					
DIRECT VEL.	.843	.893	.943							.889
INTERVAL VEL.	.953	.116	.1028	.928	.1687	.997	.946	.1154	.1008	.1000
FREQUENCY	.1349	.781	.1101	.1136	.862	.980	.926	.86	.862	.971
COEF OF ATTE	.45	.472	.206	.221	.237	.229				.21
LOG DECH.	.2	.197	.214	.231	.246	.238				
DAMPING	.1	.179	.134	.137	.39	.338				
Q		.1	.14	.17	.16	.17				
SOURCE NO. 1 HIT DIRECTION 2 (S-WAVE)										
INPUT	.02281	.02540	.02860	.2400	.4881					
INPUT	.13411	.14040	.14381	.1171	.3910					
INPUT	.15291	.15521	.16861	.2541	.2130					
DIRECT VEL.	.873	.892	.939							.911
INTERVAL VEL.	.922	.1054	.967	.916	.1083	.997	.928	.1154	.900	.902
FREQUENCY	.962	.781	.862	.926	.833	.877	.1087	.715	.877	.882
COEF OF ATTE	.131	.251	.195	.204	.146	.173				.16
LOG DECH.	.146	.245	.212	.229	.160	.195				
DAMPING	.23	.405	.335	.336	.26	.31				
Q	.25	.14	.14	.17	.22	.19				
SOURCE NO. 1 HIT DIRECTION 3 (S-WAVE)										
INPUT	.12201	.12521	.12810	.2420	.7251					
INPUT	.13461	.1417	.14350	.1220	.3221					
INPUT	.15451	.15651	.16021	.201	.1821					
DIRECT VEL.	.843	.868	.879							.883
INTERVAL VEL.	.904	.908	.915	.916	.911	.914	.922	.917	.920	.913
FREQUENCY	.1087	.862	.962	.1191	.897	.1020	.1254	.926	.1084	.1028
COEF OF ATTE	.94	.453	.274	.183	.148	.165				.12
LOG DECH.	.83	.147	.145	.163	.131	.147				
DAMPING	.113	.114	.113	.120	.121	.123				
Q	.41	.60	.51	.23	.27	.25				
SOURCE NO. 1 HIT DIRECTION 3 (S-WAVE)										
INPUT	.02291	.02471	.02820	.2831	.10110					
INPUT	.13411	.14021	.14350	.1111	.4091					
INPUT	.15421	.15611	.16010	.1701	.2410					
DIRECT VEL.	.843	.870	.884							.889
INTERVAL VEL.	.934	.894	.914	.916	.906	.911	.924	.911	.920	.915
FREQUENCY	.1349	.711	.903	.1194	.758	.926	.1316	.711	.981	.1000
COEF OF ATTE	.271	.212	.125	.241	.122	.181				.155
LOG DECH.	.248	.100	.117	.221	.112	.186				
DAMPING	.39	.10	.19	.35	.118	.126				
Q	.16	.1	.31	.18	.31	.22				

Fig. D.8 - Computer Output of All Shear Waves for  
Sample Biaxial Data

SOURCE NO. 2 HIT DIRECTION 1 (S-WAVE)  
 INPUT .02141 .02460 .02771 .0321 .0777  
 INPUT .03761 .04080 .04391 .0483 .0928  
 INPUT .05251 .05570 .05881 .0632 .0928  
 DIRECT VEL. .821 .831 .952  
 INTERVAL VEL. .247. 10.7. 997. 1013. 1014. 1013. 947. 1020. 994. 1001. 924.  
 FREQUENCY .893. 1012. 962. 1002. 8.6. 909. 1027. 833. 903. 946.  
 COEF OF ATTEN. .263 .444 .332 .105 .528 .343 .33.  
 LOG DECK.. .279 .227 .351 .175 .558 .363  
 DAMPING .04 .04 .05 .028 .080 .058  
 Q 15. 11. 12. 21. 9. 12.

SOURCE NO. 2 HIT DIRECTION 1 (S-WAVE)  
 INPUT .02191 .02447 .02732 .0370 .0400  
 INPUT .03731 .0401 .04332 .0501 .2131  
 INPUT .05201 .05491 .0581 .0221 .0761  
 DIRECT VEL. .846. 926. 967.  
 INTERVAL VEL. .941. 10.0. 99. 1013. 1014. 1013. 975. 1000. 947. 907.  
 FREQUENCY .893. 962. 924. 1007. 741. 909. 1100. 735. 909. 932.  
 COEF OF ATTEN. .195 .445 .244 .057 .417 .233 .26.  
 LOG DECK.. .209 .112 .303 .05 .446 .249  
 DAMPING .35 .045 .040 .01 .071 .040  
 Q 18. 11. 11. 55. 11. 10.

SOURCE NO. 2 HIT DIRECTION 3 (S-WAVE)  
 INPUT .02311 .02490 .02791 .0271 .0412  
 INPUT .03301 .03900 .04311 .0231 .0552  
 INPUT .05211 .05411 .05801 .0120 .0510  
 DIRECT VEL. .855. 956. 962.  
 INTERVAL VEL. 1136. 964. 1045. 1044. 993. 1027. 947. 984. 944. 1021.  
 FREQUENCY 1067. 833. 1111. 1002. 614. 749. 1250. 901. 794. 962.  
 COEF OF ATTEN. .266 .196 .033 .322 .103 .212 .04.  
 LOG DECK.. .0.000 .208 .0.000 .341 .100 .225  
 DAMPING .0.000 .033 .0.000 .054 .017 .06  
 Q 0. 18. 0. 13. 32. 17.

SOURCE NO. 2 HIT DIRECTION 3 (S-WAVE)  
 INPUT .02391 .02501 .02420 .0144 .0412  
 INPUT .03471 .04010 .04320 .0400 .0231  
 INPUT .05251 .05501 .05801 .0211 .0560  
 DIRECT VEL. .837. 901. 962.  
 INTERVAL VEL. 1014. 1007. 1040. 1034. 1007. 1020. 962. 993. 977. 1016.  
 FREQUENCY 1071. 962. 1153. 1786. 676. 940. 1000. 641. 741. 1051.  
 COEF OF ATTEN. .259 .775 .259 .033 .263 .348 .33.  
 LOG DECK.. 1.000 .757 .259 .418 .255 .336  
 DAMPING 1.000 .118 .0. 0.000 .040 .053  
 Q 0. 8. 10. 11. 10. 13.

SOURCE NO. 3 HIT DIRECTION 1 (S-WAVE)  
 INPUT .02221 .02245 .02260 .0454 .0222  
 INPUT .03041 .0416 .0413 .0231 .0331  
 INPUT .05541 .0568 .05961 .0000 .0231  
 DIRECT VEL. .847. 871. 845.  
 INTERVAL VEL. .855. 915. 804. 860. 987. 920. 944. 964. 958. 882.  
 FREQUENCY 1007. 611. 781. 1136. 1000. 1064. 2500. 893. 1316. 1150.  
 COEF OF ATTEN. .328 .300 .350 .091 .614 .054 .01.  
 LOG DECK.. .262 .307 .284 .232 .490 .362  
 DAMPING .042 .049 .045 .037 .074 .054  
 Q 15. 14. 14. 17. 10. 12.

Fig. D.8 (Continued) - Computer Output of All Shear Wave  
Types for Sample Biaxial Data

## SOURCE NO. 3 HIT DIRECTION 1 (S-WAVE)

INPUT	.02133	.02443	.02833	.1201	.3633					
INPUT	.03993	.04413	.04893	.673	.139					
INPUT	.05533	.05953	.06553	.1217	.533					
DIRECT VEL.	9.4	973	433							802
INTERVAL VEL.	835	913	437	855	987	922	942	952	952	922
FREQUENCY	262	641	769	1250	1031	1111	1923	802	1102	1079
COEFF OF ATTEN	.044	.043	.223	.274	.442	.338				.26
LOG DECR.	.001	.379	.171	.234	.343	.289				
DAMPING	.001	.61	.27	.37	.55	.46				
Q		12	22	17	13	14				

## SOURCE NO. 3 HIT DIRECTION 2 (S-WAVE)

INPUT	.02333	.02543	.02773	.1920	.7913					
INPUT	.03893	.04443	.04333	.1430	.2290					
INPUT	.05223	.05443	.05793	.1450	.0840					
DIRECT VEL.	815	834	934							878
INTERVAL VEL.	993	1071	1031	1000	1071	1434	980	1117	903	1021
FREQUENCY	1602	1047	1282	1607	962	1220	1667	714	1000	1240
COEFF OF ATTEN	.010	.272	.172	.445	.427	.436				.30
LOG DECR.	.507	.001	.102	.366	.342	.359				
DAMPING	.41	.001	.23	.158	.156	.157				
Q	10	1	25	12	12	12				

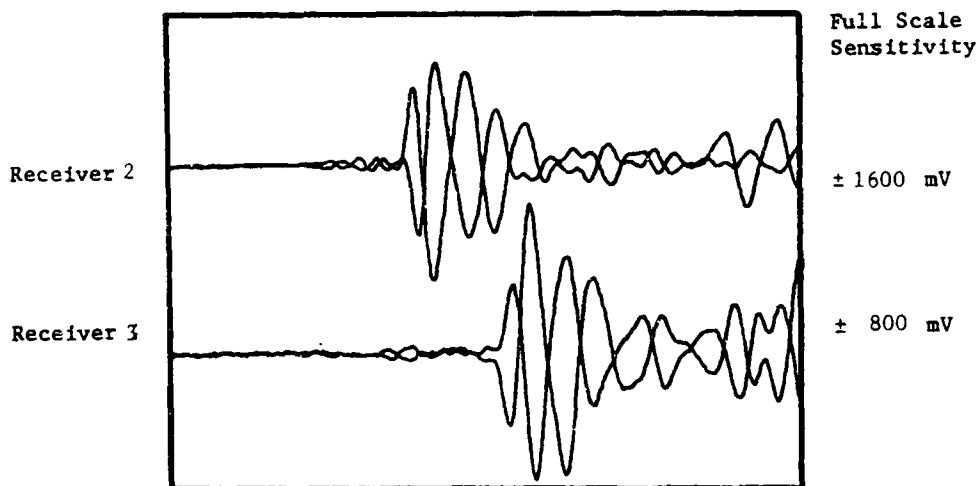
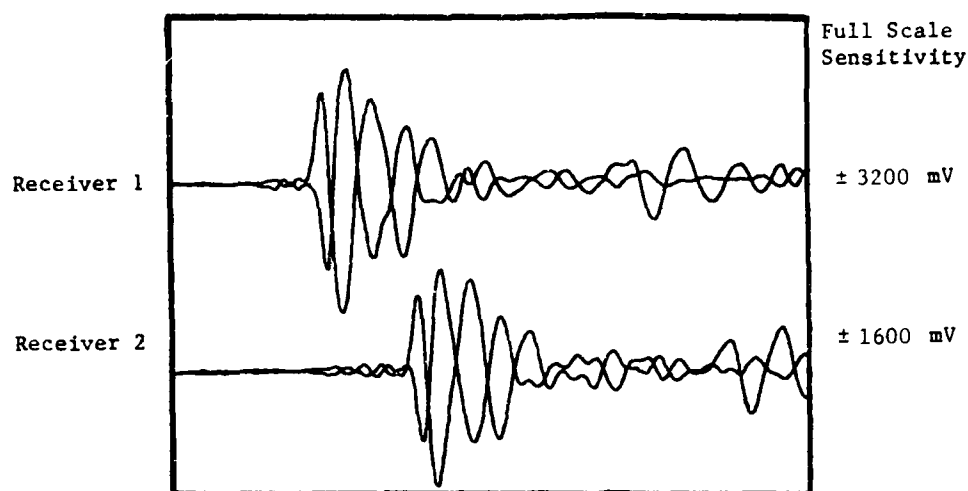
## SOURCE NO. 3 HIT DIRECTION 2 (S-WAVE)

INPUT	.02263	.02433	.02673	.2120	.7413					
INPUT	.03743	.03943	.04123	.1781	.2413					
INPUT	.05143	.05363	.05693	.1401	.0871					
DIRECT VEL.	858	923	954							911
INTERVAL VEL.	1014	1042	1027	993	1056	1024	993	993	903	1015
FREQUENCY	1471	1042	1220	1250	1042	1136	1349	758	980	1103
COEFF OF ATTEN	.285	.060	.177	.367	.438	.402				.29
LOG DECR.	.253	.041	.157	.326	.380	.357				
DAMPING	.44	.11	.25	.452	.462	.457				
Q	10	15	23	13	12	12				

Fig. D.8 (Continued) - Computer Output of All Shear Wave Types for Sample Biaxial Data

## APPENDIX E

SET OF RECORDED WAVEFORMS, DATA INPUT,  
AND COMPUTER OUTPUT FOR A REPRESENTATIVE  
TRIAXIAL TEST (Wave Reversals are Included)

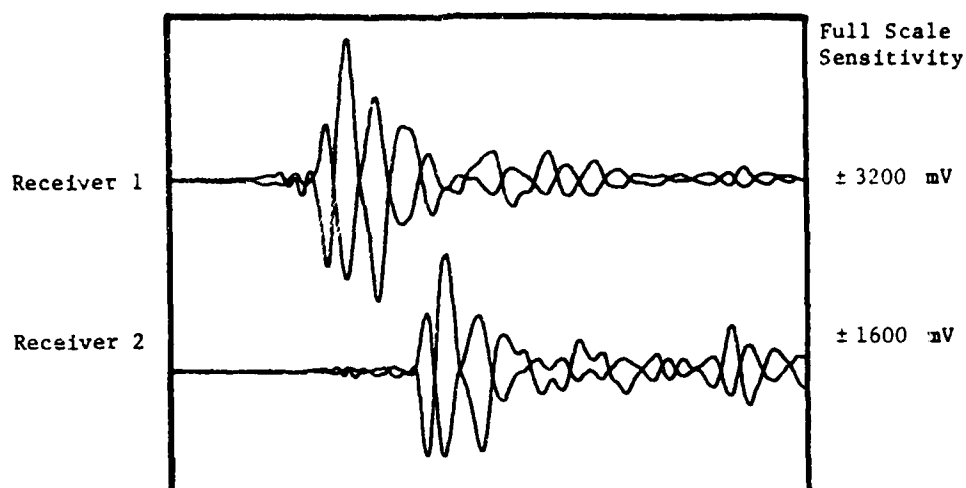


TEST NUMBER: 52

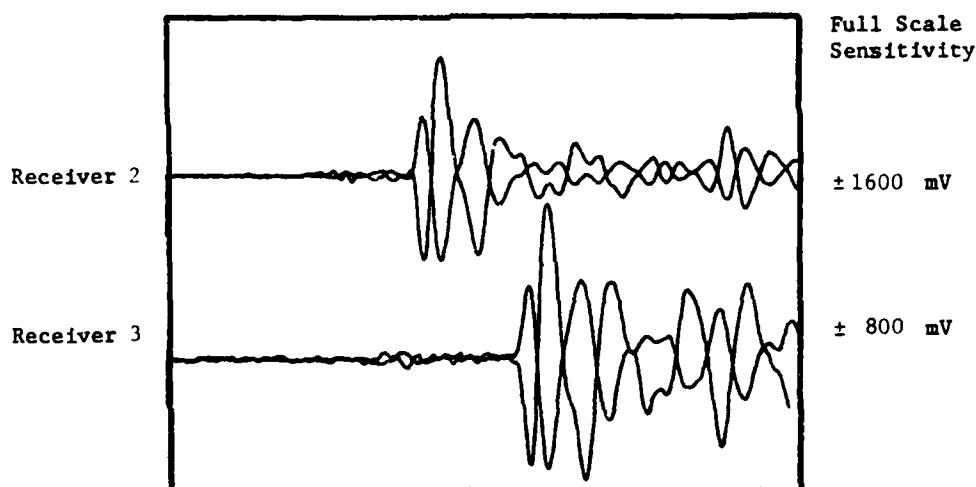
DIRECTION OF WAVE PROPAGATION: Top-Bottom  
DIRECTION OF PARTICLE MOTION: North-South

PRESSURE ALONG AXIS: 40 psi  
PRESSURE ALONG AXIS: 30 psi

Fig. E.1 - Accelerometer Records of  $S_{TB/NS}$ -Wave for  
Sample Triaxial Data



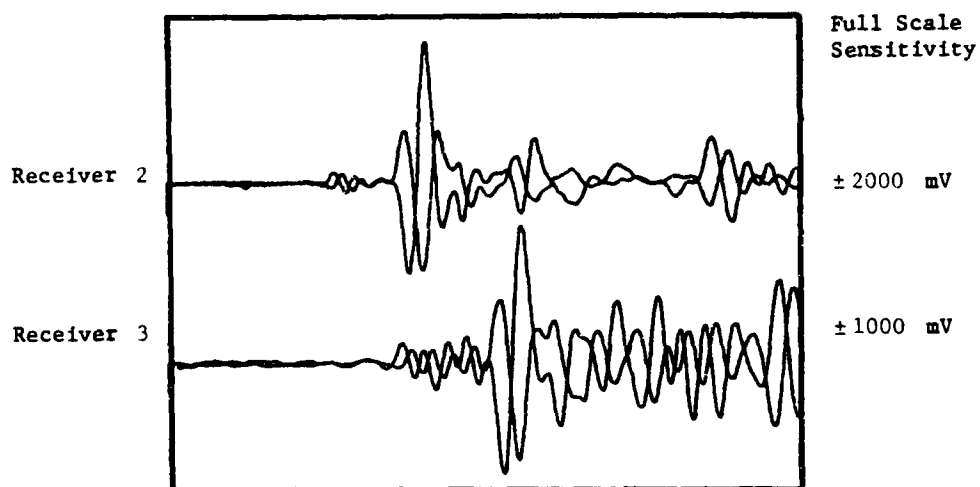
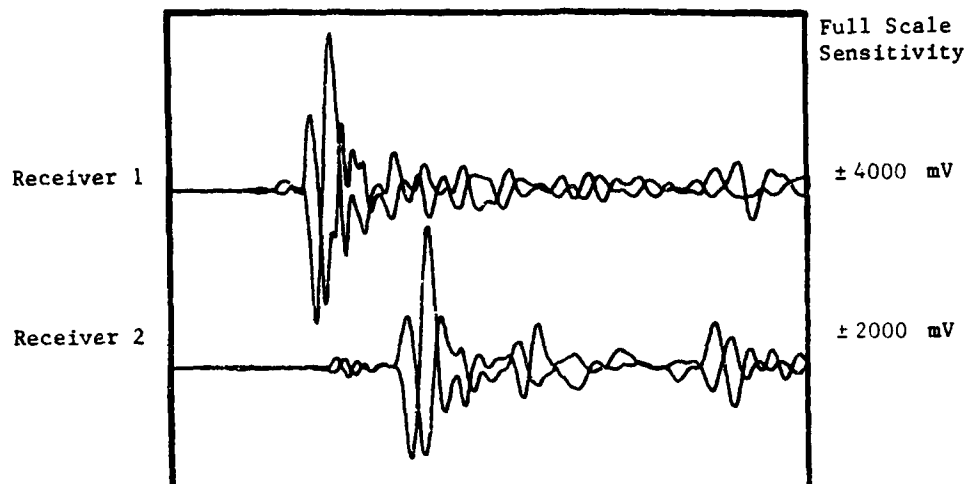
Disk / Track Number: 13-5/3  
Record Length: 10.1 msec.



Disk / Track Number: 13-6/3  
Record Length: 10.1 msec.

TEST NUMBER: 52  
DIRECTION OF WAVE PROPAGATION: Top-Bottom  
DIRECTION OF PARTICLE MOTION: East-West  
PRESSURE ALONG AXIS: 40 psi  
PRESSURE ALONG AXIS: 15 psi

Fig. E.2 - Accelerometer Records of  $S_{TB/EW}$ -Wave for  
Sample Triaxial Data

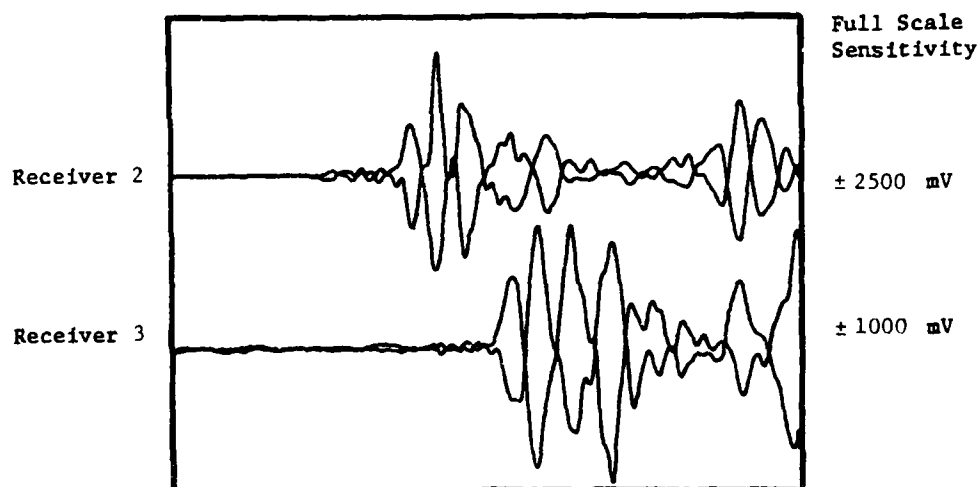
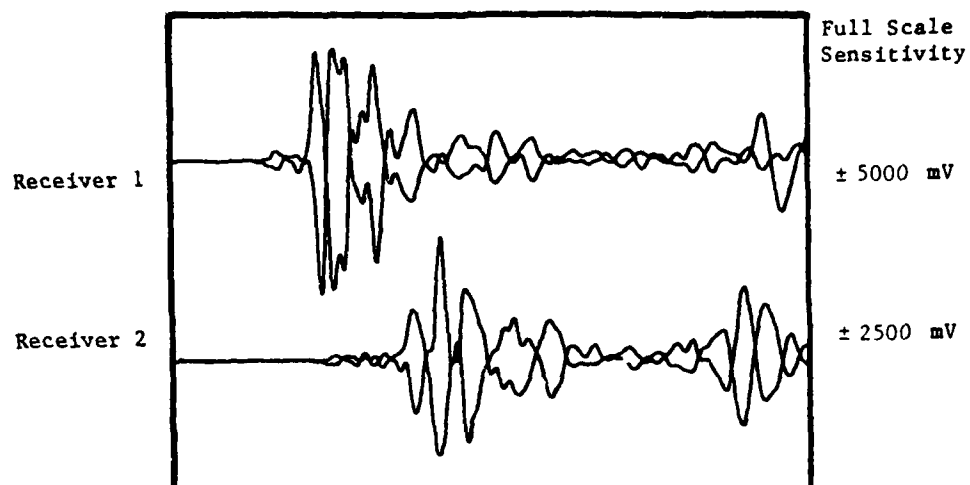


TEST NUMBER: 52

DIRECTION OF WAVE PROPAGATION: North-South  
DIRECTION OF PARTICLE MOTION: Top-Bottom

PRESSURE ALONG AXIS: 30 psi  
PRESSURE ALONG AXIS: 40 psi

Fig. E.3 - Accelerometer Records of  $S_{NS/TB}$ -Wave for  
Sample Triaxial Data



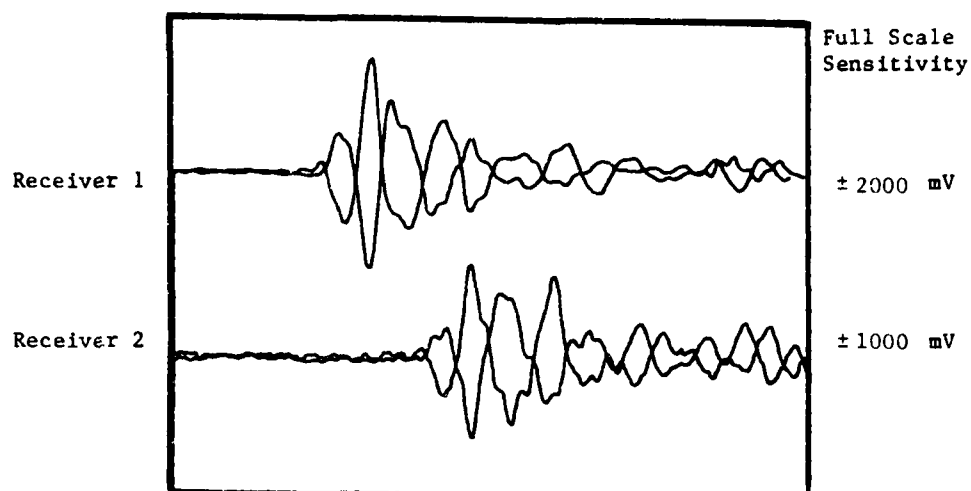
TEST NUMBER: 52

DIRECTION OF WAVE PROPAGATION: North-South  
DIRECTION OF PARTICLE MOTION: East-West

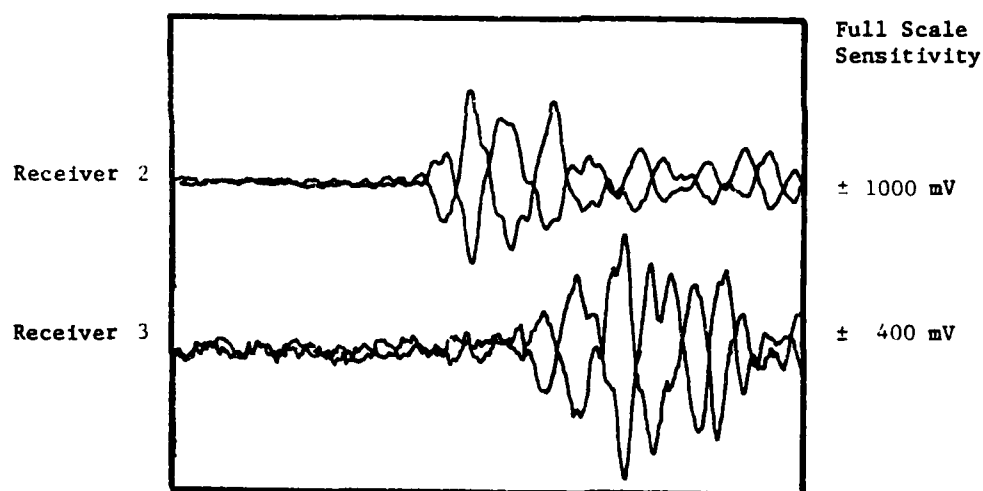
PRESSURE ALONG AXIS: 30 psi  
PRESSURE ALONG AXIS: 15 psi

Fig. E.4 - Accelerometer Records of  $S_{NS/EW}$ -Wave for  
Sample Triaxial Data





Disk / Track Number: 13-5/7  
Record Length: 10.1 msec.



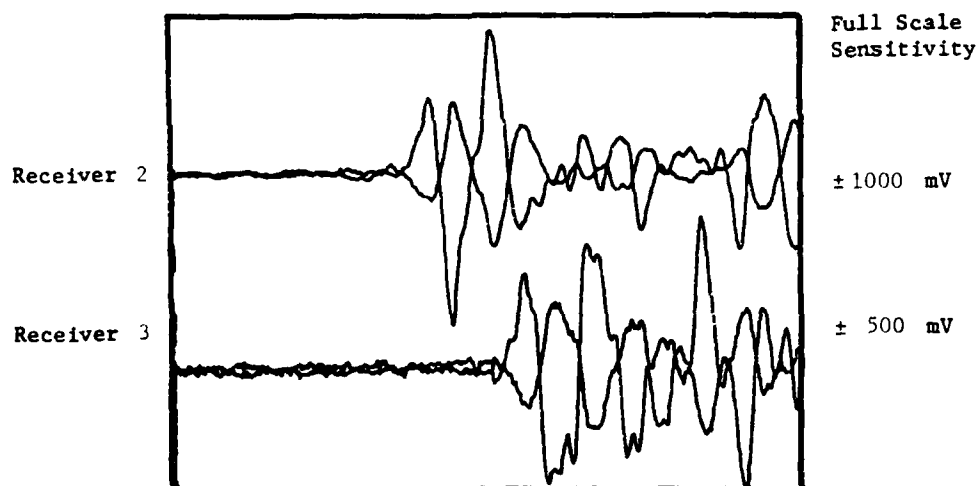
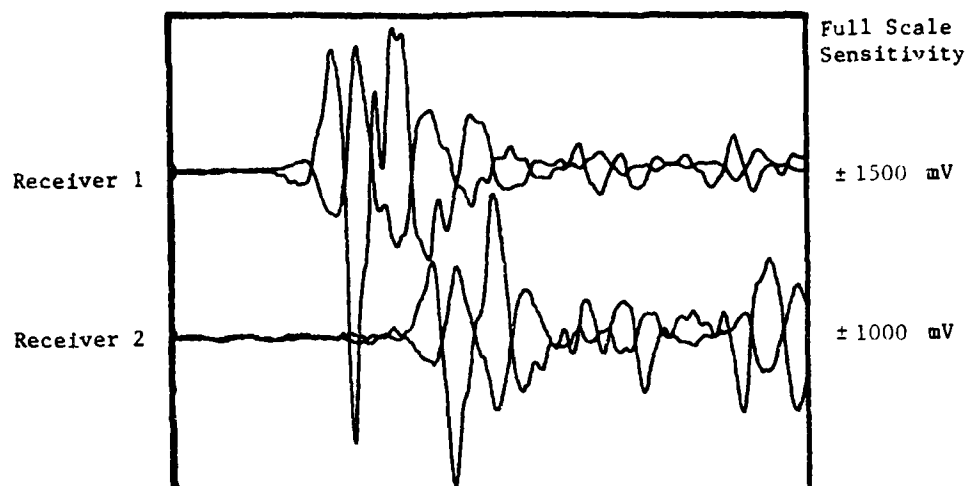
Disk / Track Number: 13-6/7  
Record Length: 10.1 msec.

TEST NUMBER: 52

DIRECTION OF WAVE PROPAGATION: East-West  
DIRECTION OF PARTICLE MOTION: Top-Bottom

PRESSURE ALONG AXIS: 15 psi  
PRESSURE ALONG AXIS: 40 psi

Fig. E.5 - Accelerometer Records of  $S_{EW/TB}$ -Wave for  
Sample Triaxial Data



TEST NUMBER: 52

DIRECTION OF WAVE PROPAGATION: East-West

DIRECTION OF PARTICLE MOTION: North-South

PRESSURE ALONG AXIS: 15 psi

PRESSURE ALONG AXIS: 30 psi

Fig. E.6 - Accelerometer Records of  $S_{EW/NS}$ -Wave for Sample Triaxial Data

TEST NO.: 52  
 DATE: 8/17/81  
 P-DATA BY: -  
 S-DATA BY: DPK

DIRECTION OF AXIS  
 1-1 Top-Bottom  
 2-2 North-South  
 3-3 East-West

PRESSURE AT CENTER OF CUBE  
 40  
 30  
 15  
 (psi)

PRESSURE AT CAGE AT PANEL BOARD  
 39.8  
 30.9  
 15.9  
 (psi)

## REDUCED DATA FOR S-WAVE \*

REDUCED DATA FOR S-WAVE

DISK	TRACK	DIRECTION OF WAVE PROPAGATION	DIRECTION OF PARTICLE MOTION	S-WAVE TYPE **	TRACE 1				TRACE 2				TRACE 3						
					t <sub>11</sub>	t <sub>21</sub>	t <sub>31</sub>	A <sub>11</sub>	A <sub>21</sub>	t <sub>12</sub>	t <sub>22</sub>	t <sub>32</sub>	A <sub>12</sub>	A <sub>22</sub>	t <sub>13</sub>	t <sub>23</sub>	t <sub>33</sub>	A <sub>13</sub>	A <sub>23</sub>
13-5	2	1-1	2-2	NR	2.20	2.44	2.75	.558	1.43	3.71	3.94	4.24	.261	.631	5.21	5.42	5.78	.101	.346
13-6	2	1-1	2-2	R	2.28	2.51	2.82	.648	1.305	3.81	4.01	4.30	.244	.566	5.27	5.49	5.84	.101	.313
13-5	3	1-1	3-3	NR	2.28	2.53	2.84	.367	1.02	3.89	4.11	4.40	.207	.473	5.58	5.78	6.08	.095	.257
13-6	3	1-1	3-3	R	2.27	2.54	2.87	.633	1.49	3.92	4.12	4.41	.301	.667	5.60	5.80	6.09	.144	.360
13-5	4	2-2	1-1	NR	2.16	2.36	2.62	.893	1.893	3.63	3.87	4.16	.305	.764	5.13	5.37	5.66	.150	.330
13-6	4	2-2	1-1	R	2.15	2.29	2.59	.527	1.25	3.63	3.81	4.10	.156	.460	5.06	5.32	5.61	.095	.211

\* Times in msec, Amplitudes in volts.

\*\* NR denotes non-reversed shear wave, R denotes reversed shear wave.

Fig. E.7 - Data Input of All Shear Wave Types for Sample Triaxial Data

TEST NO.: 52 Cont.

DATE: 8/17/81

P-DATA BY: -

S-DATA BY: DPK

DIRECTION OF AXIS

1-1 TB

2-2 NS

3-3 EW

PRESSURE AT CENTER OF CUBE

40

30

15

(psi)

PRESSURE AT GAGE AT PANEL BOARD

29.8

30.9

15.9

(psi)

# REDUCED DATA FOR S-WAVE\*

REDUCED DATA FOR S-WAVE.

DISK	TRACK	DIRECTION OF WAVE PROPAGATION	DIRECTION OF PARTICLE MOTION	S-WAVE TYPE**	TRACE 1					TRACE 2					TRACE 3				
					t <sub>11</sub>	t <sub>21</sub>	t <sub>31</sub>	A <sub>11</sub>	A <sub>21</sub>	t <sub>12</sub>	t <sub>22</sub>	t <sub>32</sub>	A <sub>12</sub>	A <sub>22</sub>	t <sub>13</sub>	t <sub>23</sub>	t <sub>33</sub>	A <sub>13</sub>	A <sub>23</sub>
13-5	6	2-2	3-3	NR	2.20	2.41	2.69	1.49	2.76	3.74	3.89	4.20	.278	.991	5.21	5.50	5.88	.123	.418
13-6	6	2-2	3-3	R	2.13	2.33	2.69	1.22	2.66	3.69	3.85	4.24	.213	.819	5.16	5.47	5.84	.156	.450
13-5	7	3-3	1-1	NR	2.41	2.76	3.16	.147	.382	4.10	4.34	4.77	.046	.154	5.58	5.94	6.44	.031	.058
13-6	7	3-3	1-1	R	2.46	2.73	3.15	.080	.314	4.08	4.36	4.78	.033	.131	5.58	5.92	6.47	.025	.052
13-5	8	3-3	2-2	NR	2.17	2.54	2.94	.163	.547	3.74	4.09	4.51	.046	.186	5.39	5.67	6.11	.027	.085
13-6	8	3-3	2-2	R	2.15	2.54	2.87	.429	1.29	3.77	4.12	4.47	.134	.449	5.38	5.62	6.13	.087	.166

\* Times are in msec, Amplitudes are in volts

\*\* NR denotes non-reversed shear wave, R denotes reversed shear wave.

Fig. E.7 (Continued) - Data Input of All Shear Wave Types for Sample Triaxial Data

ATC DIRECTION FOR SIG ACCE= 11. SIGMAC(2)= 31.0 SIGMA(13)= 16.1

	FIRST ARRIVAL (TRACE 1)			FIRST TOPPED (TRACE 2)			FIRST PEAK (TRACE 3)			AVG
(FREQ.) (AMPLITUDE) DIRECT (INTERVAL)	(HALF AMPLE)			(FULL AMPLE)						
	1	2	3	1	2	3	1	2	3	
	1-2	2-3	1-3	1-2	2-3	1-3	1-2	2-3	1-3	
SOURCE NO. 1 HIT DIRECTION 2 (S-WAVE)										
INPUT	1224	219	275	558	1030					
INPUT	1371	390	124	261	631					
INPUT	521	512	578	1010	346					
DIRECT VEL.	95	91	95							924
INTERVAL VEL.	934	1043	987	948	1054	997	946	1013	940	984
FREQUENCY	1002	816	919	1007	833	943	1100	844	877	921
COEF OF ATTN	.159	.367	.269	.200	.143	.170				.21
LOG DECH.	.167	.389	.266	.212	.152	.181				
DAMPING	.127	.62	.145	.134	.024	.029				
Q	22	12	14	18	24	21				
SOURCE NO. 1 HIT DIRECTION 2 (S-WAVE)										
INPUT	1224	251	282	480	1310					
INPUT	1381	1010	1330	240	506					
INPUT	1527	1549	1550	1010	313					
DIRECT VEL.	873	892	941							902
INTERVAL VEL.	922	1068	993	980	1054	997	953	1013	943	961
FREQUENCY	1007	816	926	1250	862	1020	1136	714	877	964
COEF OF ATTN	.313	.323	.313	.215	.138	.175				.24
LOG DECH.	.322	.332	.327	.221	.142	.179				
DAMPING	.51	.53	.52	.035	.023	.029				
Q	13	13	13	14	25	21				
SOURCE NO. 1 HIT DIRECTION 3 (S-WAVE)										
INPUT	1228	253	280	471	1020					
INPUT	1349	1411	1411	270	673					
INPUT	1550	1578	1550	950	257					
DIRECT VEL.	816	861	852							855
INTERVAL VEL.	882	852	867	899	862	884	910	847	883	877
FREQUENCY	1000	816	893	1136	862	944	1250	853	1000	973
COEF OF ATTN	.15	.293	.155	.153	.175	.164				.15
LOG DECH.	.13	.260	.139	.134	.158	.148				
DAMPING	.12	.112	.22	.122	.125	.124				
Q	237	15	26	26	23	25				
SOURCE NO. 1 HIT DIRECTION 3 (S-WAVE)										
INPUT	1227	254	287	433	1000					
INPUT	1392	1412	1411	301	667					
INPUT	1550	1580	1500	1000	360					
DIRECT VEL.	850	855	855							853
INTERVAL VEL.	861	857	859	899	857	877	922	857	888	875
FREQUENCY	926	758	833	1251	862	1020	1251	862	1020	976
COEF OF ATTN	.135	.264	.200	.178	.180	.179				.18
LOG DECH.	.121	.237	.179	.150	.161	.160				
DAMPING	.19	.134	.122	.125	.126	.126				
Q	29	17	21	23	23	23				

Fig. E.8 - Computer Output of All Shear Wave Types  
for Sample Triaxial Data

SOURCE NO. 2 HIT DIRECTION 1 (S-WAVE)  
 INPUT .00210 .0236 .0242 .0231 .0290  
 INPUT .00365 .0387 .0416 .0351 .0490  
 INPUT .00510 .0537 .0566 .0511 .0630  
 DIRECT VEL. 890. 964. 975. 940.  
 INTERVAL VEL. 1.51. 1.51. 1.31. 1.33. 1.11. 1.07. 1.03. 1.11. 1.10.  
 FREQUENCY 1250. 942. 1067. 1042. 862. 943. 1042. 862. 943.  
 COEF OF ATTEN. .310. .235. .274. .242. .322. .261.  
 LOG DECH.. .310. .240. .279. .240. .328. .260.  
 DAMPING .51. .39. .44. .33. .50. .42.  
 Q 13. 16. 15. 19. 13. 15.

SOURCE NO. 2 HIT DIRECTION 1 (S-WAVE)  
 INPUT .00210 .0229 .0250 .0270 .0250  
 INPUT .00363 .0381 .0411 .0360 .0400  
 INPUT .00510 .0532 .0561 .0501 .0511  
 DIRECT VEL. 902. 960. 984. 952.  
 INTERVAL VEL. 1.54. 1.49. 1.52. 1.46. 993. 1010. 1033. 943. 1013. 1.25.  
 FREQUENCY 1790. 833. 1130. 1349. 862. 1060. 962. 862. 949. 1040.  
 COEF OF ATTEN. .42. .303. .251. .263. .242. .272.  
 LOG DECH.. .378. .47. .236. .247. .265. .256.  
 DAMPING .61. .44. .37. .39. .40. .41.  
 Q 12. 39. 17. 16. 15. 16.

SOURCE NO. 2 HIT DIRECTION 3 (S-WAVE)  
 INPUT .00220 .0241 .0260 .0260 2.7000  
 INPUT .00374 .0389 .0420 .0381 .0910  
 INPUT .00520 .0550 .0580 .0530 .0480  
 DIRECT VEL. 900. 976. 960. 935.  
 INTERVAL VEL. 974. 1020. 907. 1014. 932. 971. 993. 843. 940. 970.  
 FREQUENCY 1190. 808. 1020. 1067. 860. 1047. 862. 858. 746. 902.  
 COEF OF ATTEN. .740. .310. .520. .310. .338. .324.  
 LOG DECH.. .730. .200. .510. .343. .330. .317.  
 DAMPING .115. .108. .182. .148. .52. .45.  
 Q 8. 14. 11. 14. 13. 13.

SOURCE NO. 2 HIT DIRECTION 3 (S-WAVE)  
 INPUT .00210 .0233 .0260 .0220 2.6000  
 INPUT .00360 .0385 .0420 .0381 .0190  
 INPUT .00510 .0547 .0580 .0561 .0510  
 DIRECT VEL. 900. 960. 960. 962.  
 INTERVAL VEL. 962. 1021. 900. 947. 924. 955. 964. 937. 952. 966.  
 FREQUENCY 1250. 670. 893. 1562. 641. 949. 860. 876. 735. 947.  
 COEF OF ATTEN. .790. .310. .380. .412. .161. .287.  
 LOG DECH.. .402. .310. .405. .439. .172. .335.  
 DAMPING .133. .110. .164. .170. .27. .49.  
 Q 8. 11. 11. 11. 22. 14.

SOURCE NO. 3 HIT DIRECTION 1 (S-WAVE)  
 INPUT .00240 .0270 .0310 .0470 .3820  
 INPUT .00410 .0434 .0477 .0460 .1540  
 INPUT .00550 .0590 .0640 .0310 .0540  
 DIRECT VEL. 817. 830. 885. 847.  
 INTERVAL VEL. 870. 1111. 937. 930. 934. 934. 913. 898. 905. 847.  
 FREQUENCY 714. 625. 667. 1042. 581. 740. 694. 544. 541. 683.  
 COEF OF ATTEN. .411. .22. .215. .239. .410. .325.  
 LOG DECH.. .557. .230. .291. .324. .555. .441.  
 DAMPING .48. .105. .140. .151. .188. .170.  
 Q 9. 10. 14. 13. 9. 11.

Fig. E.8 (Continued) - Computer Output of All Shear Wave Types for Sample Triaxial Data

## SOURCE NO. 3 HIT DIRECTION 1 (S-WAVE)

INPUT .002461 .00273 .03151 .04114 .3148  
 INPUT .00344 .00436 .03781 .0381 .1319  
 INPUT .00544 .00592 .04471 .25 .0524

DIRECT VEL.	881.	883.	885.							883
INTERVAL VEL.	907.	910.	952.	902.	902.	931.	912.	888.	885.	926
FREQUENCY	926.	595.	725.	893.	595.	714.	735.	455.	562.	889
COEF OF ATTN	.223	.156	.122	.215	.375	.296				.16
LOG DECR.	.300	.111	.111	.291	.510	.396				
DAMPING	.48	.111	.114	.146	.81	.163				
Q	14.	9.	32.	14.	14.	11.				

## SOURCE NO. 3 HIT DIRECTION 2 (S-WAVE)

INPUT .002171 .002541 .002941 .0631 .5474  
 INPUT .003741 .004191 .004511 .061 .1861  
 INPUT .005391 .005871 .006111 .0271 .2850

DIRECT VEL.	894.	920.	917.							91.
INTERVAL VEL.	955.	910.	932.	948.	949.	958.	955.	957.	906.	908
FREQUENCY	876.	825.	849.	714.	595.	649.	893.	508.	694.	870
COEF OF ATTN	.162	.114	.263	.337	.281	.319				.20
LOG DECR.	.644	.161	.401	.473	.321	.434				
DAMPING	.113	.25	.164	.175	.163	.164				
Q	9.	23.	11.	14.	12.	11.				

## SOURCE NO. 3 HIT DIRECTION 2 (S-WAVE)

INPUT .002151 .002541 .002471 .0200 .1298  
 INPUT .003771 .004121 .004171 .0341 .0491  
 INPUT .005331 .005821 .006131 .070 .1604

DIRECT VEL.	902.	912.	914.							911
INTERVAL VEL.	926.	932.	920.	949.	1400	974.	938.	904.	920.	901
FREQUENCY	891.	758.	894.	714.	714.	714.	1002.	420.	667.	715
COEF OF ATTN	.394	.147	.220	.322	.422	.372				.20
LOG DECR.	.512	.161	.291	.424	.556	.490				
DAMPING	.182	.111	.146	.167	.188	.178				
Q	10.	54.	14.	11.	9.	14.				

Fig. E.8 (Continued) - Computer Output of All Shear Wave  
Types for Sample Triaxial Data

## REFERENCES

1. Arthur, J. R. F. and Menzies, B. K. (1972), "Inherent Anisotropy in a Sand," Geotechnique, Vol. 22, No. 1, pp. 115-128.
2. Atkinson, R. H. and Ko, H. Y (1973), "A Fluid Cushion, Multiaxial Cell for Testing of Cubical Rock Specimens," International Journal of Rock Mechanics and Mineral Science, Vol. 10, pp. 351-361.
3. Beiganousky, W. A., and Marcusson, W. F., III (1976), "Uniform Placement of Sand," Journal of the Geotechnical Engineering Division, ASCE, Vol. 102, No. GT3, March, pp. 229-233.
4. Berends, B. E. (1977), "Development of a Multiaxial Testing Cell for Cohesive Soils," M.S. Thesis, University of Colorado, Boulder, 1977.
5. Bishop, A. W. and Green, G. E. (1965), "The Influence of End Restraint on the Compression Strength of a Cohesionless Soil," Geotechnique, Vol. 15, No. 3, pp. 423-266.
6. Drnevich, V. P. and Richart, F. E. Jr. (1970), "Dynamic Prestraining of Dry Sand," Journal of Soil Mechanics and Foundations Division, ASCE, Vol. 96, No. SM2, March, pp. 453-469.
7. Hadala, P. F. (1967), "The Effect of Placement Method on Response of Soil Stress Gages," Proceedings, International Symposium on Wave Propagation and Dynamic Properties of Earth Materials, Albuquerque, N.M.
8. Hardin, B. O. (1978), "The Nature of Stress-Strain Behavior of Soils," Proceedings of the Earthquake Engineering and Soil Dynamics Conference, ASCE, Pasadena, CA, June 19-21, 1978, Vol. I, pp. 3-90.
9. Hardin, B.O. and Black, W. L. (1966), "Sand Stiffness Under Various Triaxial Stresses," Journal of the Soil Mechanics and Foundations Division, ASCE, Vol. 92, No. SM2, March, pp. 27-43.
10. Hardin, B. O. and Drnevich, V. P. (1972a), "Shear Modulus and Damping in Soils: Measurement and Parameter Effects," Journal of the Soil Mechanics and Foundations Division, ASCE, Vol. 98, SM6, June, pp. 603-624.



11. Hardin, B. O. and Drnevich, V. P. (1972b), "Shear Modulus and Damping in Soils: Design Equations and Curves," Journal of the Soil Mechanics and Foundations Division, ASCE, Vol. 98, No. SM7, July, pp. 667-692.
12. Hardin, B. O. and Richart, F. E., Jr. (1963), "Elastic Wave Velocities in Granular Soils," Journal of the Soil Mechanics and Foundations Division, ASCE, Vol. 89, No. SM1, February, pp. 33-65.
13. Hoar, R. J. and Stokoe, K. H., II (1978), "Generation and Measurement of Shear Waves in Situ," Dynamic Geotechnical Testing, ASTM STP 654, pp. 3-29.
14. Kilbuszewski, J. J. (1948), "General Investigation of the Fundamental Factors Controlling Loose Packing of Sands," Proceedings of the Second International Conference on Soil Mechanics, Rotterdam, Vol. 7, pp. 47-49.
15. Ko, H. Y. and Scott, R. F. (1967), "A New Soil Testing Apparatus," Geotechnique, Vol. 17, No. 1, pp. 40-57.
16. Ko, H. Y. and Sture, S. (1974), "Three-Dimensional Mechanical Characterization of Anisotropic Composites," Journal of Composite Materials, Vol. 8, April, pp. 173-190.
17. Kopperman, S. E., et al (1982), "Effect of State of Stress on Velocity of Low-Amplitude Compression Waves Propagating Along Principal Stress Directions in Sand," Research Report GR22-22, Department of Civil Engineering, University of Texas at Austin.
18. Laier, J. E., Schmertmann, J. H., and Schaub, J. H. (1975), "Effect of Finite Pressuremeter Length in Dry Sand," Proceedings of Specialty Conference on In-Situ Measurement of Soil Properties, ASCE, Vol. 1, pp. 241-259.
19. Lawrence, F. V. (1963), The Response of Soils to Dynamic Loadings, Report 14: Propagation Velocity of Ultrasonic Waves Through Sand, Massachusetts Institute of Technology, Department of Civil Engineering, Research Report R63-8, March, 54 pp.
20. Lawrence, F. V. (1965), Ultrasonic Shear Wave Velocities in Sand and Clay, Massachusetts Institute of Technology, Department of Civil Engineering, Research Report R65-05, January, 24 pp.

21. Marcusson, W. F., III and Beiganousky, W. A. (1977), "Laboratory Standard Penetration Tests on Fine Sands," Journal of the Geotechnical Engineering Division, ASCE, Vol. 103, No. GT6, June, pp. 565-588.
22. Pearce, J. A. (1971), "A New True Triaxial Apparatus," Stress-Strain Behavior of Soils, Proceedings of the Roscoe Memorial Symposium, Cambridge University, pp. 330-339.
23. Richart, F. E., Jr., Hall, J. R., Jr., and Woods, R. D. (1970), Vibrations of Soils and Foundations, Prentice Hall, 414 pp.
24. Roesler, S. K. (1979), "Anisotropic Shear Modulus Due to Stress Anisotropy," Journal of the Geotechnical Engineering Division, ASCE, Vol. 105, No. GT5, July, pp. 871-880.
25. Roxcoe, K. H. (1953), "An Apparatus for the Application of Simple Shear to Soil Samples," Proceedings, Third International Conference on Soil Mechanics and Foundations, Zurich, Vol. 1.
26. Rowe, P. W. and Barden, L. (1964), "Importance of Free Ends in Triaxial Testing," Journal of Soil Mechanics and Foundation Division, ASCE, Vol. 90, No. SMI, January, pp. 1-27.
27. Schmertmann, J. H. (1978), Effect of Shear Stress on Dynamic Bulk Modulus of Sand, U.S. Army Engineering Waterways Experiment Station, Technical Report S-78-16, October, 92 pp.
28. Schwarz, S. C. and Musser, J. M. (1972), "Various Techniques for Making In Situ Shear Wave Velocity Measurements -- A Description and Evaluation," Proceedings of the International Conference on Microzonation for Safer Construction, Research and Application, Vol. 2, Seattle, Washington, pp. 593-608.
29. Shannon, W. C., Yamane, G., and Dietrich, R. J. (1959), "Dynamic Triaxial Tests on Sand," Proceedings, First Panamerican Conference on Soil Mechanics and Foundation Engineering, Mexico City, Vol. 1, pp. 473-486.
30. Silver, M. L. and Park, T. K. (1975), "Testing Procedure Effects on Dynamic Soil Behavior," Journal of the Geotechnical Engineering Division, ASCE, Vol. 101, No. GT10, pp. 1061-1083.
31. Sutherland, H. B. and Mesdary, M.S. (1969), "The Influence of the Intermediate Principal Stress on the Strength of Sand," Proceedings of the Seventh International Conference on Soil Mechanics, Mexico City, Vol. 1, pp. 391-399.

32. Truesdale, W. B. and Schwab, R. B. (1967), "Soil Strain Gage Instrumentation," Proceedings, International Symposium on Wave Propagation and Dynamic Properties of Earth Materials, Albuquerque, N.M.
33. Wetzel, R. A. and Vey, E. (1970), "Axisymmetric Stress Wave Propagation in Sand," Journal of the Soil Mechanics and Foundations Division, ASCE, Vol. 96, No. SM5, September, pp. 1763-1786.
34. Wilson, S. D. and Miller, R. P. (1962), "Discussion of "Foundation Vibrations," Transactions, ASCE, Vol. 127, Part I, pp. 913-917.
35. Woods, R. D. (1978), "Measurement of Dynamic Soil Properties," Proceedings of the Earthquake Engineering and Soil Dynamics Conference, ASCE, Pasadena, CA, Jun 19-21, 1978, Vol. I, pp. 91-178.

AD-A120 426

EFFECT OF STATE OF STRESS ON VELOCITY OF LOW-AMPLITUDE  
SHEAR WAVES PROPAG. (U) TEXAS UNIV AT AUSTIN  
GEOTECHNICAL ENGINEERING CENTER D P KNOX ET AL. MAR 82  
GR82-23 AFOSR-TR-82-0908 AFOSR-80-0031

F/G 20/11

NL

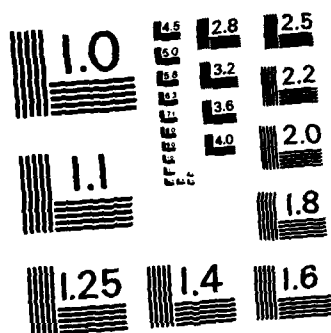
UNCLASSIFIED



END

DATA  
FILMED

DTIC



MICROCOPY RESOLUTION TEST CHART  
NATIONAL BUREAU OF STANDARDS-1963-A

**SUPPLEMENTAR**

**INFORMATION**

REPORT DOCUMENTATION PAGE		READ INSTRUCTIONS BEFORE COMPLETING FORM												
REPORT NUMBER <b>AFOSR-TR- 82 - 0908</b>	2. GOVT ACCESSION NO. <b>ADA120426</b>	1. RECIPIENT'S CATALOG NUMBER												
TITLE (and Subtitle) <b>EFFECT OF STATE OF STRESS ON VELOCITY OF LOW-AMPLITUDE SHEAR WAVES PROPAGATING ALONG PRINCIPAL STRESS DIRECTIONS IN DRY SAND</b>		5. TYPE OF REPORT & PERIOD COVERED <del>ANNUAL</del> <b>Final</b> <b>1 Oct 79 - 31 Dec 81</b>												
AUTHOR(s) <b>DAVID P. KNOX, KENNETH H. STOKOE, II, AND STEWART E. KOPPERMAN</b>		6. PERFORMING ORG. REPORT NUMBER												
PERFORMING ORGANIZATION NAME AND ADDRESS <b>UNIVERSITY OF TEXAS AT AUSTIN DEPARTMENT OF CIVIL ENGINEERING AUSTIN, TX 78712</b>		8. CONTRACT OR GRANT NUMBER(s) <b>AFOSR-80-0031</b>												
11. CONTROLLING OFFICE NAME AND ADDRESS <b>AIR FORCE OFFICE OF SCIENTIFIC RESEARCH/NA BOLLING AFB, DC 20332</b>		10. PROGRAM ELEMENT, PROJECT, TASK AREA & WORK UNIT NUMBERS <b>61102F 2307/C1</b>												
14. MONITORING AGENCY NAME & ADDRESS (if different from Controlling Office)		12. REPORT DATE <b>March 1982</b>												
		13. NUMBER OF PAGES <b>421</b>												
		15. SECURITY CLASS. (of this report) <b>Unclassified</b>												
		15a. DECLASSIFICATION/DOWNGRADING SCHEDULE												
16. DISTRIBUTION STATEMENT (of this Report)  <b>Approved for Public Release; Distribution Unlimited.</b>														
17. DISTRIBUTION STATEMENT (of the abstract entered in Block 20, if different from Report)														
18. SUPPLEMENTARY NOTES														
19. KEY WORDS (Continue on reverse side if necessary and identify by block number)  <table border="0"> <tr> <td>SHEAR WAVES</td> <td>TRIAxIAL TESTING</td> <td>STRUCTURAL ANISOTROPY</td> </tr> <tr> <td>SEISMIC VELOCITY</td> <td>BIAXIAL TESTING</td> <td></td> </tr> <tr> <td>SHEAR MODULUS</td> <td>LOW AMPLITUDE BODY WAVES</td> <td></td> </tr> <tr> <td>DAMPING</td> <td>STRESS HISTORY</td> <td></td> </tr> </table>			SHEAR WAVES	TRIAxIAL TESTING	STRUCTURAL ANISOTROPY	SEISMIC VELOCITY	BIAXIAL TESTING		SHEAR MODULUS	LOW AMPLITUDE BODY WAVES		DAMPING	STRESS HISTORY	
SHEAR WAVES	TRIAxIAL TESTING	STRUCTURAL ANISOTROPY												
SEISMIC VELOCITY	BIAXIAL TESTING													
SHEAR MODULUS	LOW AMPLITUDE BODY WAVES													
DAMPING	STRESS HISTORY													
20. ABSTRACT (Continue on reverse side if necessary and identify by block number)  <p>The effect of state of stress on shear wave velocity was examined for shear waves propagated as body waves through a sand mass. Testing was performed in a triaxial testing device, which was designed to hold a cubic soil sample measuring 7 ft (2.1 m) on a side and which was used to apply an isotropic, biaxial or triaxial state of stress to the sample. The triaxial device is essentially a steel box, constructed of reinforced steel, which uses rubber membranes to apply a confining pressure along each of the principal axes</p>														

UNCLASSIFIED

20. Cont.

of the cube. Dry sand was placed in the cube for this initial testing program.

Shear waves were propagated along the principal axes of the cube over the pressure range from 10 to 40 psi (68.9 to 276 kPa). Shear wave particle motion was monitored by three-dimensional accelerometers embedded in the sand. Stress cells and strain sensors were also embedded in the sand mass to examine stress-strain properties of the sand for the applied loading. All wave testing was performed at low-amplitude strains and at wave frequencies less than 2400 Hz. Therefore, it was assumed that the shear modulus was rate independent in this study.

Based on the results of this study, shear wave velocity was found to depend about equally on the principal stresses in the direction of wave propagation and particle motion and was determined to be relatively independent of the principal stress in the out-of-plane direction (the direction in which no shear wave particle motion occurs). As a result, the typical procedure of relating shear wave velocity to the mean effective principal stress is not correct, since the mean effective stress involves all three of the principal stresses. Stress history was found to have not significant effect on shear wave velocity for this sand. Structural anisotropy was found to cause up to an 18 percent variation in shear wave velocity, with velocities apparently grouped according to planes of motion, the plane determined by the direction of wave propagation and particle motion.